EFFECTS OF HYDROGEN IN AN ALUMINIUM-MAGNESIUM-SILICON ALLOY DURING THE PRODUCTION OF EXTRUSION INGOTS

A thesis submitted for the degree of

Doctor of Philosophy

by

Masood Al Rais

April, 1995.

Brunel, The University of West London,

Uxbridge, Middlesex, UB8 3PH.

Brunel, The University of West London
Department of Materials Technology,
Uxbridge,
Middlesex, UB8 3PH.

M. Al Rais.

Title: Effects of Hydrogen in an Aluminium-Magnesium-Silicon Alloy During the Production of Extrusion Ingots.

Ph. D.
1995.

ABSTRACT

Hydrogen causes defects, for which aluminium alloy products are rejected. The behaviour of hydrogen in aluminium-magnesium-silicon alloy extrusion ingots, has been studied throughout the course of manufacture from freshly reduced aluminium.

It is shown that hydrogen in the liquid metal is produced by temperature-dependent reaction between the metal and water vapour in the atmosphere. As the metal is received from the reduction cells, its temperature is ~850 °C and its hydrogen content, >0.4 cm^3/100 g, is too high for casting sound ingots. The metal is transferred first to a so-called melting furnace, where it is alloyed and stirred, thence to a holding furnace, where the composition is adjusted, the metal is degassed by gas sparging and allowed to settle before casting. The metal cools throughout these operations and as the temperature falls, the calculated value for the hydrogen content in equilibrium with the atmosphere falls in response to the reduced hydrogen solubility. The actual hydrogen content of the metal exhibited marked hysteresis in following the equilibrium value. Significant reduction of the hydrogen content occurred only when the metal was agitated. The hydrogen content never fell below the equilibrium value even during the nominal degassing operation, leading to the conclusion that gas sparging in a furnace does not positively remove hydrogen but only assists the equilibration.

The hot-top DC casting process yielded a 8 m x 0.18 m diameter ingot with a virtually uniform hydrogen content. When this ingot was homogenised by heating it to 590 °C in a 7h cycle, a significant proportion of the hydrogen content was lost from the surface zone. By matching the loss to a theoretical model assuming diffusion control, it was shown that the loss of hydrogen is attenuated by trapping in micropores.

The effects of simulated industrial atmospheres on the loss or absorption of hydrogen by the solid alloy were investigated in an extended series of laboratory heat-treatments. The interaction of the metal with these atmospheres was found to be determined by the nature of the oxide films formed and therefore the films were investigated by XPS and SIMS surface analysis techniques. In clean atmospheres the absorption or loss of hydrogen was determined by the balance between inward migration of protons and outward diffusion of hydrogen atoms through the oxide. Pollution of the air by chlorine or especially sulphur stimulated hydrogen absorption to a degree which seriously damaged the metal by pore growth. These effects are explained by modified compositions and structures in the surface oxide.

ACKNOWLEDGEMENTS

I wish to express my thanks to the following:

Dr. D. E. J. Talbot, Brunel University for support and advice.

The United Arab Emirates for provision of a studentship.

Dubai Aluminium Company for leave of absence and financial assistance.

Mr M. J. Roberts of Dubai Aluminium Company for his encouragement.

Professor Brian Ralph and Dr M. J. Folkes of the Department of Materials Technology, Brunel University ,for provision of facilities.

Mr R. Bulpett of the Experimental Techniques Centre at Brunel University for advice and provision of electron optical facilities.

My wife, Afsaneh for her patient support and encouragement.

Contents

1. INTRODUCTION

1.1 Philosophy Of Approach

This thesis describes a project designed to develop a scientific approach to a serious industrial problem.

In Industry, recurrent difficulties associated with a chronic problem incur unacceptable costs and disruption. They must be rectified expeditiously as they arise, if necessary by empirical means, and incentives to address the fundamental principles underlying the problem diminish with temporary remission of immediate difficulties.

Conversely, a University has resources and opportunity for impartial study but the small scale of the work and artificial conditions applied to control experiments often leads to oversimplified models which are unrelated or even irrelevant to the industrial problems they are intended to address. A few examples illustrate the point. Small-scale experiments cannot simulate the behaviour of liquid metal handled in bulk. The atmospheres in industrial melting or heat-treatment furnaces are not amenable to the same degree of evaluation and control as atmospheres simulated in laboratories. Isothermal heat-treatment of solid metal in batch furnaces is usually impossible because of the thermal capacity of the load and the finite time needed for heat conduction through large pieces. Above all, idealised procedures are often excluded by costs.

In the present work, the project was devised to combine the advantage of the author's continuing association with the plant of a large aluminium producer with extended access to the scientific attitudes and resources of a University. Various aspects of the project were conducted in the plant and in the laboratory as appropriate. This approach has its particular frustrations. Industrial experiments require Management sanction because they disrupt the regular operation of the plant and can seldom be repeated. Bulk materials selected for study must be accepted as they are and cannot be conditioned to aid interpretation of the results obtained from them. However, the merit of the approach is that any conclusions drawn are both fundamentally sound and directly relevant to the real problems of interest.

1.2 Purpose And Objectives

The occlusion and effects of hydrogen in aluminium and its alloys have been extensively investigated both empirically and in the laboratory. Nevertheless, the interactions which can occur are so complex and variable that aluminium producers and manufacturers can still experience intractable problems attributable to hydrogen occluded in the metal.

An example of such a problem is the unpredictable sporadic incidence of fine blisters, 1-3 mm in diameter on the surface of aluminium-magnesium-silicon alloy extrusion billets, within the AA6063 specification, occurring after "homogenisation". The incidence of blistering does not correlate with any obvious variations in metal origin or production procedures, both of which are nominally consistent. As used in the Aluminium Industry, the word homogenisation does not necessarily have its usual meaning of eliminating variations in composition but is an established term describing any production process in which cast material is heat-treated for several hours at high temperatures, to develop desirable characteristics for subsequent fabrication.

This particular problem was selected for study because it has many features typical of the industrial difficulties which remain through insufficient information on the underlying fundamental principles and their application. A comprehensive approach was adopted in which carefully designed and executed experiments in a major aluminium plant were integrated with corresponding laboratory experiments at Brunel University. In this way, a systematic assessment was built up to explain the interaction of hydrogen with the liquid and solid metal as it progressed through the production sequences by which the extrusion billet is produced.

The objectives were:

- to identify conditions which influence the hydrogen of the liquid metal, with special reference to metal transfer operations and to degassing procedures.
- to identify and quantify factors which control the absorption or loss of hydrogen by interaction of the solid metal with the atmosphere to which it is exposed during heat-treatment.

- to identify factors which promote un-soundness, i. e: porosity and blisters, generated by hydrogen in the metal.
- to optimise existing practices or to suggest alternative procedures to minimise unsoundness in commercially-produced AA6063 extrusion ingots.

1.3 Scope And Organisation

1.3.1 The Industrial Context

The production of aluminium alloy ingots is dominated by the need to ensure that high quality is maintained, because defects of any kind in the ingots are inherited by semi-finished products fabricated from them. Such products are supplied for critical applications in a cost-conscious market in which there is intense competition between manufacturers.

The thesis begins by describing the industrial context to which the work is related. Section 2 is a comprehensive review of the theory and practice of metal treatment processes by which liquid metal is prepared and solidified as ingots. This is followed in Section 3 by a more detailed description of direct chill (DC) casting, which controls the structure of the ingots and which has been intensively developed, culminating in advanced techniques such as the Airslip® process by which the material used in the present work was cast.

1.3.2 Theoretical and Practical Aspects of the Effects of Hydrogen

The extensive theory which underlies the effects of hydrogen in aluminium alloys is critically reviewed in Section 4. This covers the nature of hydrogen occlusion, the thermodynamics of metal-hydrogen systems , and theories and measurements of solubility and diffusivity. Practical matters considered include methods of measurement and effects of hydrogen in manufactured products.

1.3.3 Quantitative Approach

The essence of the approach adopted was to obtain quantitative information for interpretation and the accurate determination of the hydrogen of the metal is the basis of the investigation. From a review of the available techniques given in Section 5 a decision was made to base the investigation on the hot vacuum extraction (Ransley) method, supported by in-plant measurements made with the Telegas. The principles of these techniques and the construction, calibration and commissioning of suitable equipment is described in Section 6.

The first stage of the experimental work was designed to examine the behaviour of hydrogen in the liquid metal throughout the industrial processes in which the metal was received from the reduction furnaces, alloyed, degassed and cast into ingots.

The second stage was to characterise the distribution of hydrogen within a selected actual industrially-cast ingot before and after homogenisation.

The third stage was to examine the absorption or loss of hydrogen from samples of metal in laboratory experiments simulating homogenisation. In these experiments, the temperature and furnace atmosphere were systematically varied to represent conditions which could conceivably prevail in a production environment. The experimental atmospheres used included clean air and air contaminated with sulphur or with chlorides, representing industrial and marine pollution. In the course of these experiments, it became clear that the factor controlling the absorption or loss of hydrogen was the nature of the oxides formed on the metal in these various environments. Composition profiles of these oxides were therefore studied by surface analysis techniques including XPS and SIMS.

Finally, the new information was assessed and used to evaluate existing industrial processes and to suggest possible modifications.

2. THE PRODUCTION OF EXTRUSION INGOT

Aluminium is produced by electrolytic reduction of Alumina (Al_2O_3). The principal commercial process in present day operation was developed in 1886 by Charles M. Hall (USA) and Paul T. Heroult (France), thus is generally known as the Hall-Heroult process.

The process consists of dissolving the alumina into molten cryolite (Na_3AlF_6) and electrolysing the solution in electrolytic cell or "pot", as it is termed in industry. The cell process is very complex but the overall reaction may be summarised by:

$$4Al_2O_3 = 2\,Al^{3+} + 6AlO_2^- \qquad \text{(primary ionisation)}$$

$$6AlO_2^- + 3C\,(\text{anode carbon}) = 3Al_2O_3 + 3CO + 6e \qquad \text{(anode reaction)}$$

$$2\,Al^{3+} + 6e = 2\,Al \qquad \text{(cathode reaction)}$$

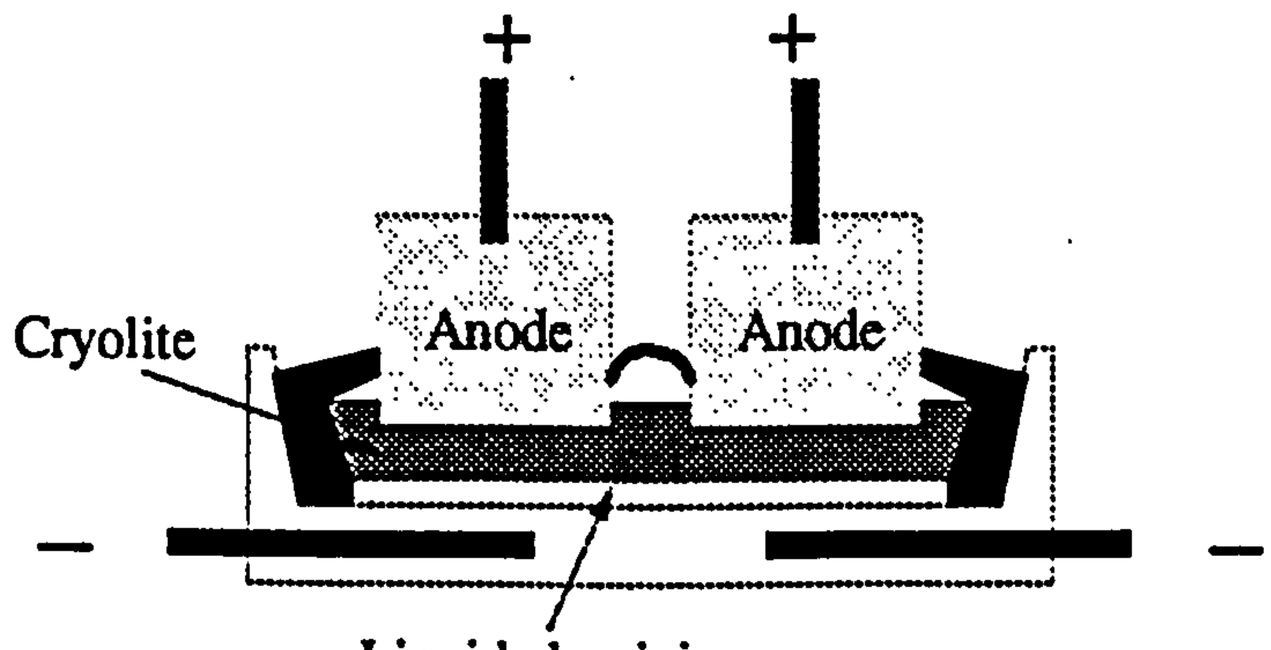

Figure 2.1 End view of a pre-backed pot.

Figure 2.1 shows an end view sketch of a pre-baked type pot.

The aluminium produced is normally in the commercial purity[1] range of 99.50 - 99.79% pure. High purity[1] grade of 99.80 - 99.949% pure aluminium can also be produced by Hall-Heroult process if great care is taken and high quality raw materials are used in the process.

2.1 Metal Quality And Liquid Metal Treatment

The extracted metal is delivered to the cast house or cast shop to be cast in a suitable intermediate product i.e. ingot.

The electrolysed metal is often not suitable for immediate casting and must undergo some refining and treatment to achieve the required chemical composition and metal quality.

Metal quality is a composite of three interrelated components, which are the level of alkali and alkali earth trace elements, hydrogen, and inclusions in the metal. The components are impurities of both elemental and compound state. The main sources of these impurities in aluminium are:

- The electrolysis process, e.g. Na and Ca,
- the alloying elements, e.g. MgO, SiO_2 ,
- turbulence in the transfer and treatment of liquid metal, e.g. Al_2O_3 ,
- chemical reaction of fluxing agent, e.g. $AlCl_3$, $MgCl_2$,
- the reaction of liquid aluminium with water vapour which is the source of hydrogen.

A survey of impurities in the metal from the electrolysis cell and impurities attributed to alloying elements are listed in table 2.1[2,3,4] and 2.2[3] respectively. In an un-treated aluminium melt, the inclusion concentration could be 0.005 - 0.02[5] volume fraction (5000 - 20000 ppm). The observed inclusion particle size[5] range from MgO dispersoids of a few μm in size to Al_2O_3 films and clusters that extend several millimetres. The concentration of alkaline and alkali earth metals in un-treated liquid aluminium can be as high as 80 ppm.

Hydrogen is a major detrimental impurity which is the main subject of the work at hand, and will be dealt with in detail on its own.

Table 2.1
A survey of impurities in aluminium
from electrolysis cells.

Impurity	Concentration (wt ppm)	Typical size (μm)
H	0.2 - 0.5	
C	5 - 13*	
Na	40 - 80	
Mg	10 - 20	
Si	300 - 700	
Ca	3 - 10	
Ti	30 - 50	
V	100 - 200	
Mn	10 - 30	
Fe	500 - 2000	
Ni	10 - 80	
Cu	5 - 30	
Zn	20 - 200	
Ga	80 - 180	
Carbides	1 - 5	0.1 - 20
Borides	0.1 - 1	0.1 - 10
Nitrides	0.3 - 2	
Oxides	0.3 - 3	10 - 300
Salts	~ 0.1	10 - 20

*C content is nearer to 50 ppm and is precipitated as TiC or ZnC.

Therefore an aluminium melt is refined prior to casting. The degree of refinement necessary is dictated by requirements in the subsequent fabrication process, and ultimately by the final product, for example although many products require the particle size of an inclusion population to be less than 50 μm^5 , much smaller particles size of several μm could have a deleterious effect in the production of 5 μm (thickness) aluminium foil.

The treatment of aluminium melt typically involves:

- Settling, floatation, and filtration for removal of inclusions,
- fluxing out dissolved alkali impurities,
- degassing for hydrogen removal.

Table 2.2
Impurities in alloying elements.

Alloying elements	Mg 99.8%	Si 98.4%	Ti 99.8%	Mn 99.9%	Fe 96%	Cu 99.9%	Zn 99.9%
Impurity	(ppm)	(ppm)	(ppm)	(ppm)	(ppm)	(ppm)	(ppm)
H_2	0.2 - 3			150			
C		1000-1500	30		3 - 1.5%		
S					100 - 350		
Ca		2000					
Ti		1200					
Fe	100 - 300	4500					500-2000
Oxides	10 - 40	1000	370			400	
Carbides	1.5 - 7	300					
Sulphate				140			
Sulphide				176			

2.1.1 Settling

Settling entails simple gravity sedimentation of inclusions heavier than the melt, which is achieved by leaving the melt undisturbed for 0.5 to 2.0 hours in the holding furnace, thus is an in-furnace melt treatment.

The mechanism of settling is commonly expressed[5.6.7.] by Stokes law:

$$V_s = \frac{2R_p^2}{9\eta_{Al}}(\rho_p - \rho_{Al})\,g \qquad (2.1)$$

Where;

V_s = settling velocity,
R_p = particle radius,
η_{Al} = viscosity of aluminium,
ρ_p, ρ_{Al} = particle and aluminium densities and,
g = gravitational acceleration (9,80665 m sec^{-2})

Based on Stokes law Martin et al[8] predicted that all MgO inclusions (density = 3.58 g cm^{-3}) with diameters greater than 30 μm can be separated out, over a distance of 1 m, in half an hour, but the results of their experimental investigations did not fit the static model, however modifying the model to include the inclusions capture mechanism was said to have improved its correspondence to the observed trends. Nevertheless the investigations confirmed the benefit of settling treatment by reporting significant reduction (over 60%) in the inclusions concentration. Common industrial practice is to include settling along with other melt treatment.

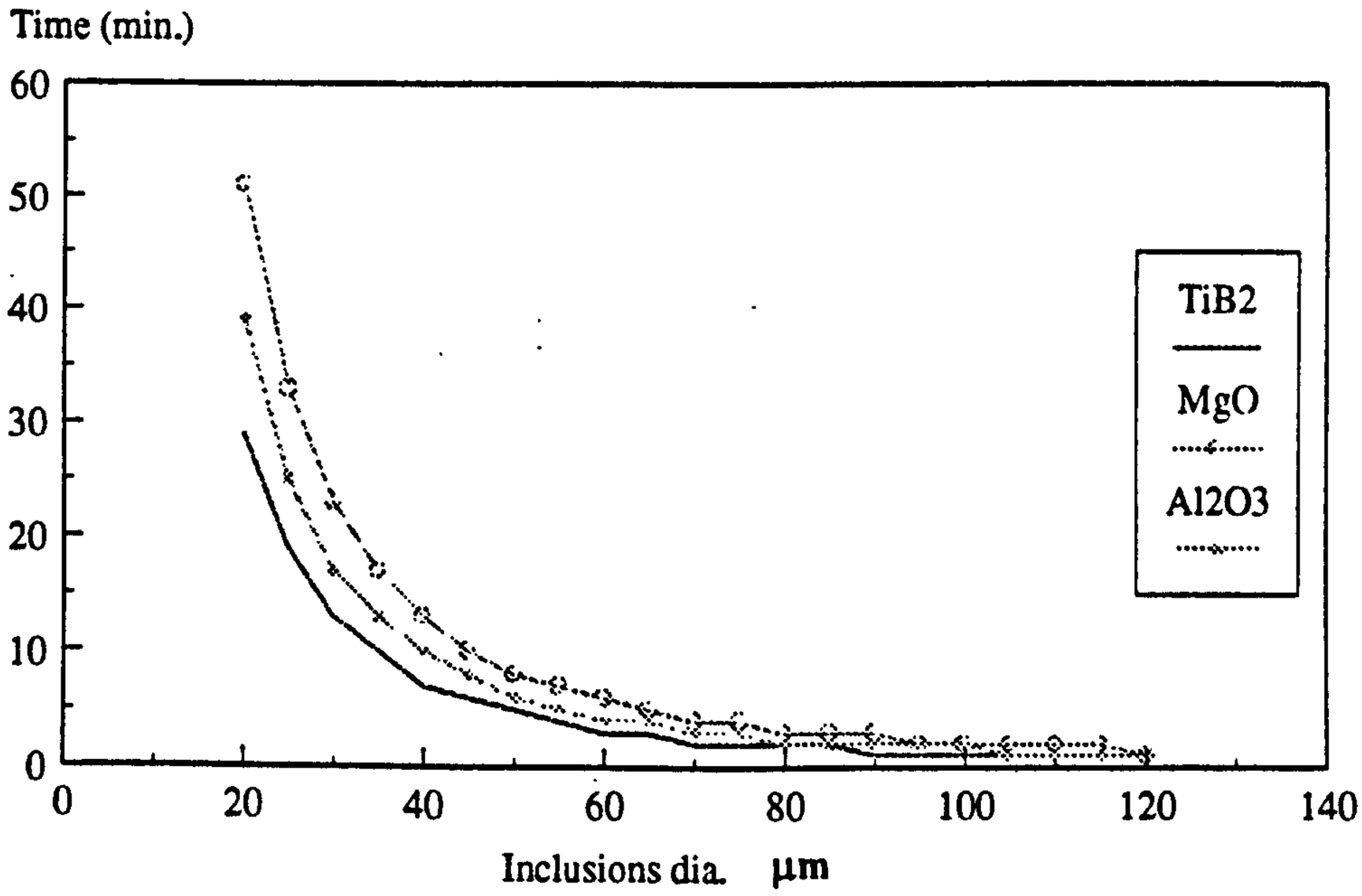

Figure 2.2 Settling of inclusions.

2.1.2 Melt Treatment by Gas Sparging

The floatation of inclusions, fluxing of the alkali impurities and the removal of hydrogen or "degassing" are carried out by sparging the melt with an inert gas (argon or nitrogen) or with a mixture of an active gas (mainly chlorine) and an inert gas.

The gas sparging may be performed in the holding or casting furnace in which case it is known as in-furnace melt treatment, or in a dedicated reactor unit in in-line melt treatment.

2.1.2.1 In-furnace Melt Treatment

In furnace melt treatment consists of either injecting the sparging gas through a lance into the melt, or by submerging a reactive compound such as hexachloroethane (C_2Cl_6), which generate the sparging gasses of Cl_2 and $AlCl_3$.

Although still widely practised, this process suffers a numbers of drawbacks:

- The holding furnace commonly a large (typically 30-50 tonne) reverberatory type is designed for thermal efficiency is not suited for gas purging thus leading to poor gas utilisation,
- the process produces large gas bubbles[9] (45 mm dia.), which contribute to refining inefficiency,
- the large gas bubbles rise up rapidly through the melt causing extremely turbulent melt surface, thus contributing to inclusion content[10].
- the sparging gas reacts with water moisture in the atmosphere resulting in environmental pollution with HCl , $2AlCl_3 + 3H_2O = Al_2O_3 + 6HCl$ (g)

However Nilmani et al[9] suggest that adding diffusers to the lance, or by using helical plug lance the efficiency of the process is improved, and Grandfield[6] reports significant reduction in inclusion content can be achieved if chlorine is added to the purge gas.

2.1.2.2 In-line Melt Treatment

To improve melt treatment efficiency and productivity in-line melt treatment was adopted.

An in-line melt treatment process is defined as a continuous refining of the melt during casting. Liquid aluminium is continuously fed into the treatment vessel from the holding furnace. The treated metal which leaves the vessel is then often filtered before it is cast.

The early versions (still used) of in-line systems consisted of a vessel containing fine tabular alumina balls, tabular alumina flakes and a graphite, quartz or porcelain enamelled steel tube[11] to inject purging gas at the bottom of the vessel. This set up provided for melt treatment by filtration and gas sparging. Alcoa's 181 (Figure 2.3), 469

and British Aluminium's FILD are some examples of this type of system.

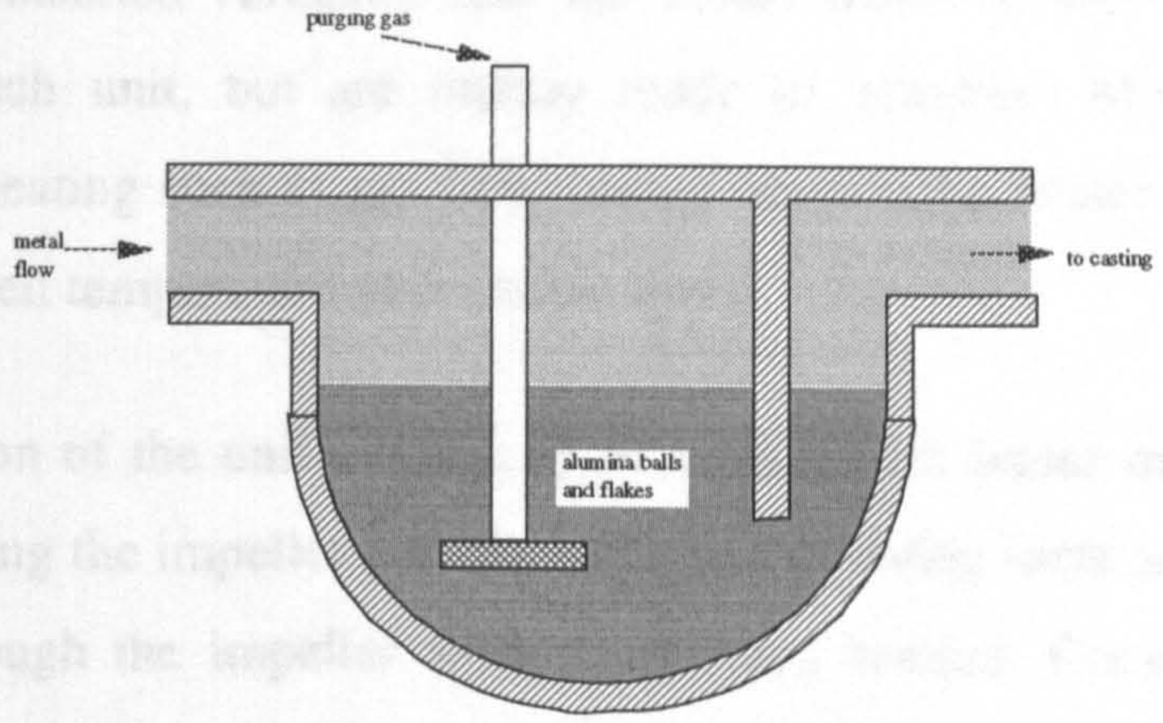

Figure 2.3 Alcoa 181.

The efforts to understand bubble dynamics and the behaviour of gas bubbles in molten metals, particularly in steel, resulted in the concept of gas injection into the melt through rotating impeller. The first embodiment of this technology for the aluminium industry[6.] was the introduction of Spinning Nozzle Inert Flotation (SNIF™) unit by Union Carbide in the early seventies.

Currently the in-line melt treatment by rotating-impeller gas injection is the dominant technology in the aluminium industry. There are numerous units of this type commercially available, such as; Alcoa's 622 (Figure 2.4), Pechiney's Alpur, Norsk Hydro's Hycast, and others.

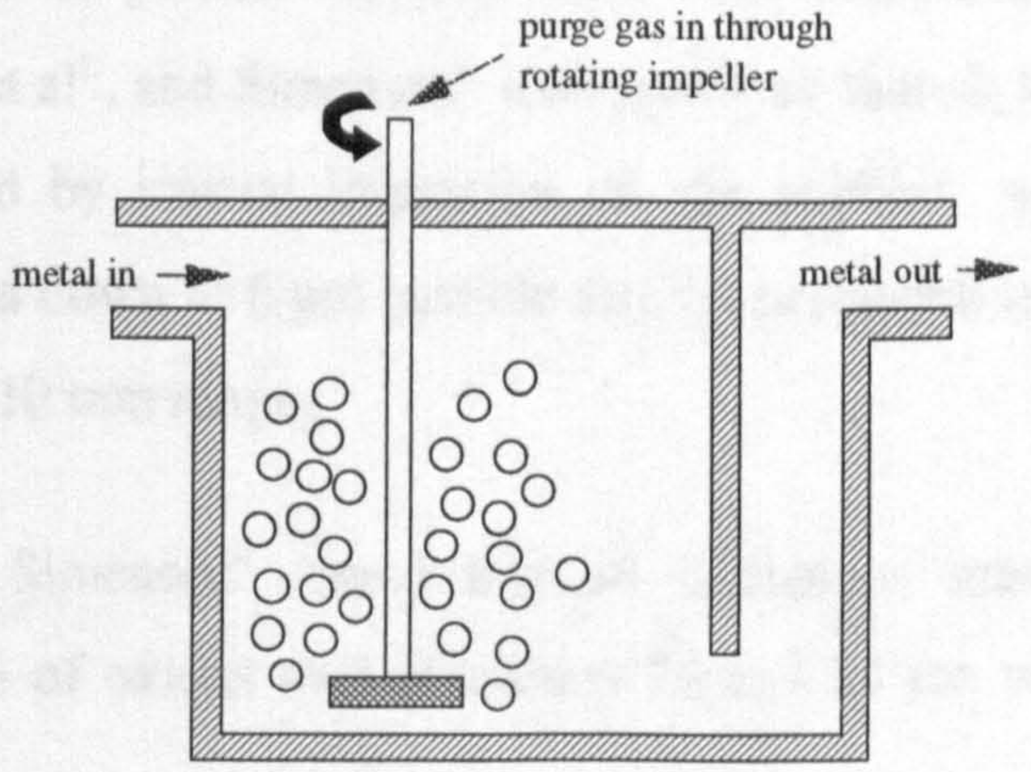

Figure 2.4 Alcoa 622.

The system consists of a refractory lined vessel, and one or more impeller assemblies which can be inserted vertically into the vessel from the top. The impellers design varies with each unit, but are mainly made of graphite. Most systems include a provision for heating such as gas fired burner, immersion heater or induction heater to maintain the melt temperature at desirable level.

The operation of the unit consists of feeding it with liquid metal from the holding furnace, lowering the impeller into the melt, and injecting inert or mixture of inert with active gas through the impeller while it is being rotated. Consequently the metal is sparged with well dispersed fine gas bubbles. The gas bubbles refine the liquid metal by:

- Floatation of inclusions,
- fluxing out of active elements,
- degassing.

These refining mechanisms are discussed next.

2.1.2.3 Flotation

One of the major benefits of gas purging is the removal of inclusions by floatation. The theory of operation is that if a gas bubble contacts a particle non-wetted by the melt the two join and the particle is carried to the surface with the bubble.

The mechanisms of particle flotation have been comprehensively investigated by Szekely[12], Eckert et al[5], and Simensen[4] who predicted that all large particles (> 80 μm) should be removed by inertial impaction on gas bubbles and an efficient particle removal is expected down to 6 μm particle size by peripheral interception if the size of bubbles is in the 1-10 mm range.

Experimentally Simensen[4] found that all inclusions greater than 100 μm and approximately 90% of oxides with diameters 75 and 25 μm were removed by in-line treatment.

Simensen[4] also reported that oxide films 100 μm long had been observed to have escaped being removed and had passed through the in-line treatment, which he

explained could occur if the oxide is oriented with its major axis parallel to the velocity vector of the bubbles, in which case the bubble can "see" a much smaller inclusion (thickness 1-2 μm).

All theoretical and experimental investigations have shown that the effectiveness of melt treatments by gas purging are inversely related to the gas bubbles size. A simplified expression for 100% inclusion removal for various gas bubble diameters is derived by Eckert et al[5], which is:

$$d_p = 0.222\ d_b^2 \tag{2.2}$$

Where: d_p and d_b are particle and bubble dia. in μm and mm. This expression is plotted in figure 2.5.

The addition of chlorine to the purge gas is believed to be beneficial by increasing the probability of capturing oxide inclusions by the salt formed on the gas bubbles as inclusions are well wetted by the salt and not by the melt[4], and also by reducing melt loss by promoting dry dross[12].

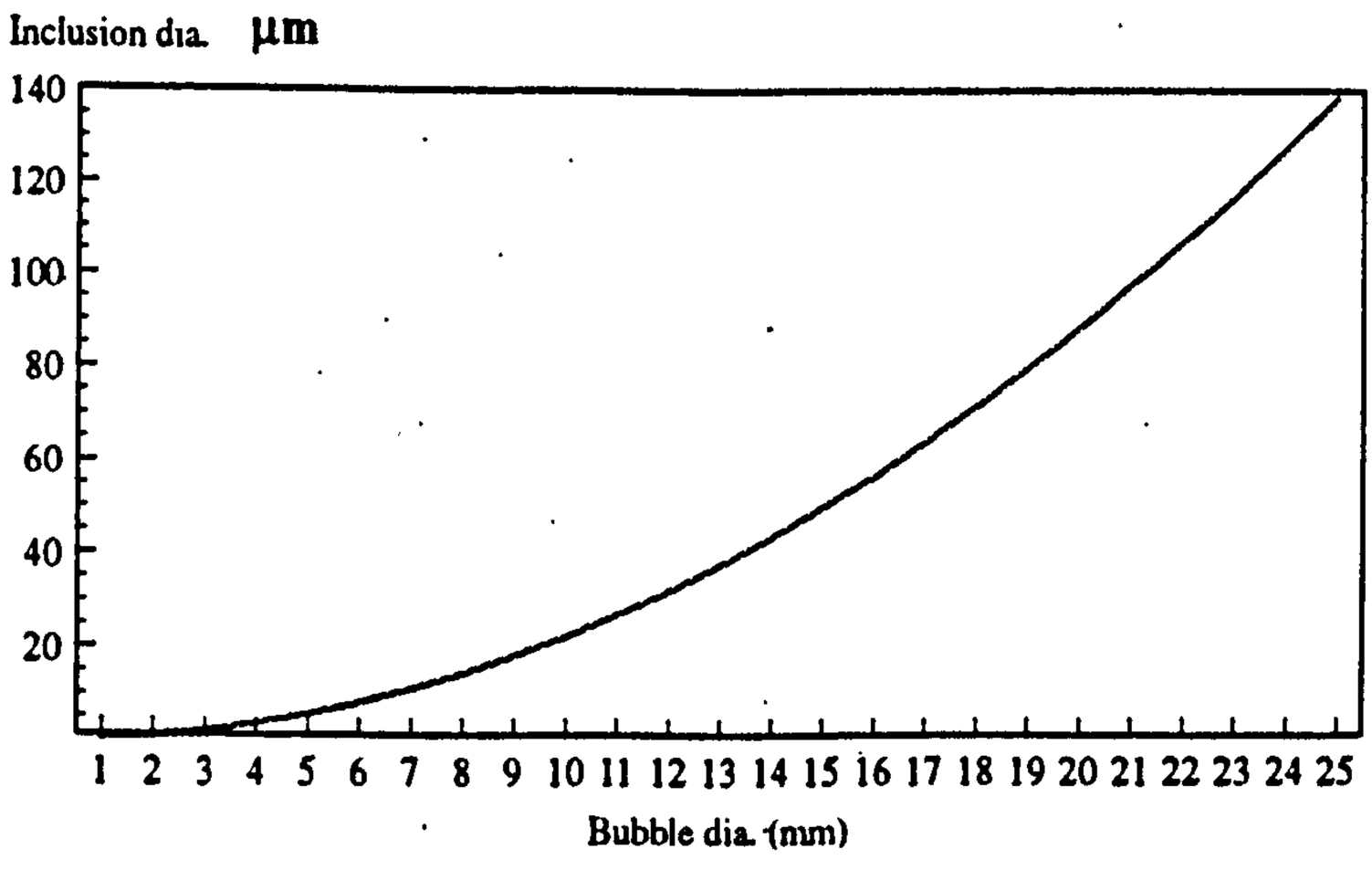

Figure 2.5 Bubble size for 100% inclusion removal

2.1.2.4 Fluxing

The removal of alkali and alkali earth metals by their reactions with $AlCl_3$ in the gas bubbles is often termed as fluxing.

Significant reduction in sodium content of the melt, as a consequence of settling and sparging with inert gas, due to its high vapour pressure has been reported[13]. But if extremely low level of sodium, calcium and lithium is required, which is the case for some rolling ingots, then gas sparging with a mixture of chlorine-inert gas is required[14].The fluxing out of alkali and alkali earth impurities by chlorine is due to the higher chemical affinity of chlorine for these elements versus aluminium. And the more stable chloride an element forms the easier it is to remove, i.e. calcium will be removed to its thermodynamically lowest concentration[7], followed by sodium and lithium. If the amount of chlorine used is in excess of that required for alkali and alkali earth removal, magnesium level will start to be reduced.

The theoretical chlorine requirement (l min^{-1}) in the purge gas, for the removal of Na, Li, and Ca, can be estimated by the following expression[7]:

$$Q_{Cl_2} = F(2.24F_m)\left\{ \frac{(wt.\%Na)_i-(wt.\%Na)_e}{2M_{Na}} + \frac{(wt.\%Li)_i-(wt.\%Li)_e}{2M_{Li}} + \frac{(wt.\%Ca)_i-(wt.\%Ca)_e}{M_{Ca}} \right\} \qquad (2.3)$$

Where:

F_m = metal flow rate (kg min^{-1}),
M = molecular weigth,
i = inlet condition,
e = equilibrium condition,
Q_{Cl_2} = flow rate of chlorine (l min^{-1}), and,
F = correction factor ~ 2-3, as actual Cl_2 utilization is not 100%.

2.1.2.5 Degassing

The term degassing in aluminium industry is often used to describe the whole melt treatment system, as in in-line degassing or in-furnace degassing which are in-line and in-furnace melt treatment systems.

A more accurate definition of the term is, the removal of hydrogen from liquid aluminium or its alloys by gas sparging, which may be said to be a primary objective of the melt treatment systems mentioned above.

Hydrogen dissolved in molten aluminium has a relatively high vapour pressure[7], and this fact is the basis for its removal by gas sparging. Atomic hydrogen passes from the liquid metal phase to the gas phase (sparging gas bubbles) where it forms di-atomic hydrogen gas. The hydrogen concentration difference between these two phases being the driving force for mass transport. This phenomenon can be represented by the following reaction:

$$2\,[H]_{Al} = (H_2)_g$$

For hydrogen to be removed by the ascending gas bubble, it is transferred by a series of steps outlined below and in Figure 2.6.

1. Transport of atomic hydrogen in the melt to the vicinity of a gas bubble by a combination of convection and diffusion,
2. Diffusive transport through the liquid boundary layer, to the bubble surface,
3. The chemical adsorption on to the outside and subsequent desorption from the inside of the bubble surface, and the formation of di-atomic hydrogen.
4. Diffusion as a gaseous species into the gas bubble.

The mechanism and efficiency of hydrogen removal by gas purging have been extensively investigated by Engh et al[13, 14, 15], and others. The following equation by Engh, expresses the efficiency of gas purging (Z), as a function of "dimensionless" melt/gas contact area (ϕ_A) .

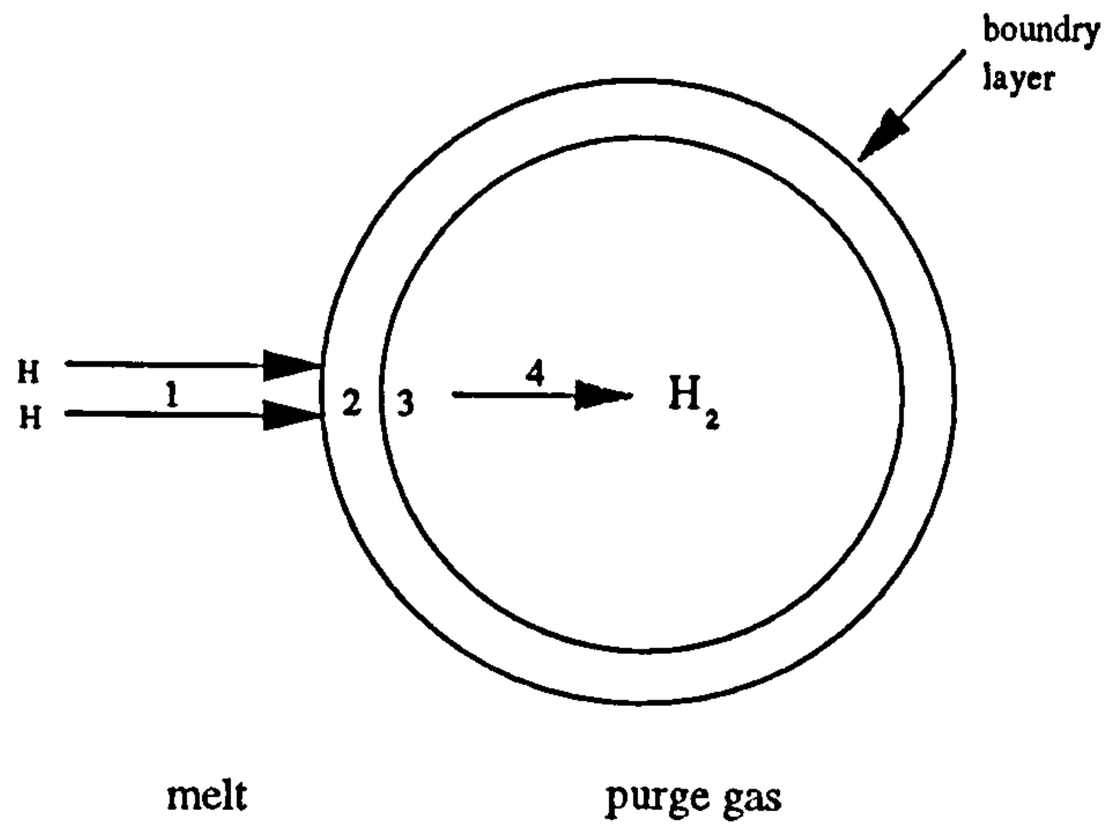

Figure 2.6 Hydrogen removal by purge gas

$$Z = 1 - \exp(-\phi_A) \tag{2.4}$$

and,

$$\phi_A = \frac{k_t \, \rho_m \, A \, P_{inert}}{100 \cdot m_x \, \dot{G} \, f_x \, K} \tag{2.5}$$

where:

k_t = total mass transfer coefficient (m s^{-1}),
ρ_m = density of the metal (kg m^{-3}),
A = interfaccial contact area (m^2),
P_{inert} = partial pressure of inert gas (atm),
m_x = molar mass of component x (kg $kmol^{-1}$),
$\dot{G}$ = flow of gas (kmol s^{-1}),
f_x = activity coefficient for component x in melt and,
K = equilibrium constant.

From Equation 2.5, it is apparent that ϕ_A increases with the ratio between contact area and gas flow rate $\frac{kA}{\dot{G}}$, it also increases when equilibrium constant K is small. When K is small, the bubble in equilibrium will have a low partial pressure of x (hydrogen) and the "x-capacity" of the bubble is low. Similarly ϕ_A increases with P_{inert} which is approximately equal to the total pressure. When the total pressure is high, the gas volume available to be "filled" with hydrogen is low.

To approach equilibrium, $Z = 1$ (100% efficiency), ϕ_A must be greater[14.] than 3. Engh[15.] has estimated that gas purging efficiency (Z) for in-furnace treatment by lance and for in-line treatment by spinning impeller to be ~0.1 and ~0.7 respectively.

The addition of chlorine has traditionally been believed to increase hydrogen removal. But recently this beneficial effect has been questioned, with Engh et al[15.] stating that chlorine will not react with hydrogen, therefore based on thermodynamic reasoning there seems to be no advantage in its use. Grandfieled et al[16.] adding that the chloride formed on the gas bubble may present a diffusion barrier preventing the hydrogen removal from the melt, and this view is supported experimentally by Stevens et al[17.].

Nevertheless, Engh[14.] suggests that if the degassing process is mass transfer controlled; that is, if bubbles are large, the chlorine may improve hydrogen removal, because the mass transfer coefficient increases by about two times in the presence of halogen, but the mass transfer coefficient is not important if very small purge gas bubbles are present, as the efficiency is already nearly 100 percent

2.1.3 Filtration

Filtration of liquid aluminium and its alloys is another mean of removing inclusions, which is widely employed either as an integral part of the in-line melt treatment unit as in Alcoa 469 or as a separate unit located immediately before the casting unit, supplementing the melt treatment by gas sparging.

Filtration consist of passing the melt through a porous medium designed to arrest and retain particulate matters..

The porous media available for filtration of liquid aluminium can be classified in the following types:

2.1.3.1 Woven glass fibre filter

Is the simplest type of filter, made of woven glass fibre, shaped in the form of bag of various sizes which are commonly known as filter or trough "sock", which can be fitted in the trough or over the mould at the liquid metal feeding point.

The filtration efficiency of this type of filters are limited to large particulates. (> 500 μm) but they are often used to supplement other filter types, with the aim of removing particles such as pieces of trough lining or foreign objects which may enter the liquid metal between the main filtration unit and the casting unit.

2.1.3.2 Packed bed filter

It is usually constructed of a refractory lined steel "box" packed with loose ceramic particulate such as tabular alumina flakes and/or alumina balls, which form the filter "bed". The filter bed varies in size, but 50-70 cm may be a common thickness range.

Liquid metal enters on to the top of the filter bed and is collected from the bottom. Thus the unit must be engineered between the casting furnace and the casting station. If an in-line gas sparging unit is used, then the filter is located immediately after it.

If designed with proper filter factor i.e. filter bed surface area appropriate for the metal flow rate, packed bed filter or deep bed filter as they are commonly known are considered to be the most efficient[18. 19.] type of filter. Netter et al[20.] predict efficient removal of inclusions down to 6 μm in size by deep bed filtration.

Packed bed filters such as British Aluminium FILD, Swiss Aluminium DUFFI, Alcoa 469 and 528, were the predominant filtration technology until the ceramic foam filters where introduced on to the market in the seventies.

2.1.3.3 Ceramic foam filter (CFF)

They are available in plate shape, typically 17"x17" or 20"x20" and 2" thick, made by replication of reticulated polyurethane foam, and are currently produced in a range

of compositions[21]. including phosphate bonded alumina, sintered alumina, zirconia/alumina and others.

The filters are characterised by their pore size in term of number of pores per linear inch (ppi). The phosphate bonded alumina filters in the pore size range of 20-60 ppi are commonly used in aluminium casting[21]. Each filter is normally used once and for one cast.

To accommodate the filter and provide for rapid filter changing, a filter holder (filter "bowl") is fitted in the trough immediately before the casting station.

For CFF of 30 ppi, an efficiency of 80-100% is expected[6] for oxide and boride particles larger than 50 μm.

2.1.3.4 Rigid media filters (RMF)

Rigid media filters are made of alumina or silicon carbide refractory grains which are bonded together. This type of filter is characterised by its grain size or grit number, with a 6 grit designation being most appropriate[22] for use with aluminium extrusion billet casting.

Rigid media filter in form of tube was developed by Tokyo Koyo Rozai and has been in use in Japan since the seventies, but due to cost consideration it has not been widely used elsewhere. RMF (TKR HC) is claimed[22] to have a filtration efficiency of >80% for particles >8 μm as determined by PoDFA type assessment..

2.1.4 Mode of filtration

The mode and mechanism of filtration have been extensively investigated[5,20,23,24], therefore only a brief description of modes will follow:

2.1.4.1 Filtration by straining

If the inclusions are larger than the filter pores, they will be retained on the filter's inlet surface by straining, this is the primary filtration mode for glass fibre type filter.

2.1.4.2 Cake mode filtration

When the particles size are large compared to the filter pore size and their concentrations are high (>500 ppm)[6], they form a layer on the inlet surface of the filter effectively reducing the pores sizes, leading to the build up of more layers of smaller particles. The accumulation of these inclusion layers on the inlet surface is termed cake formation.

2.1.4.3 Depth or deep bed filtration

Normally the melt has already been treated prior to filtration, thus should only contain low concentration (< 100 ppm)[6] of small inclusions, which can not be removed by straining and cake mode. Therefore the particles will follow the melt through the filter until they contact the filter where they are retained.

Eckert et al[5] state that " it is believed that impingement is the main transport mechanism in aluminium melt filtration, and pressure Van der Waal forces are responsible for particle attachment" to the filter media.

Table 2.3
Inclusion removal efficiency for various types of filter

Filter type	Thickness (cm)	Melt veloc. (cm/s)	Inclusion 6-12 µm	Inclusion 13-20 µm	Inclusion 20-30 µm	Inclusion >30 µm
Packed bed	20(fine)or 50(coarse)	0.1	90-100%	100%	100%	100%
Packed bed	20(fine)or 50(coarse)	0.4	60-85%	85-98%	98-100%	100%
RMF	2	0.03	55-80%	85-95%	95-98%	>98%
RMF	2	0.06	30-70%	70-90%	90-95%	>95%
CFF 40 ppi	5	0.25	25-50%	50-70%	70-85%	>85%
CFF 40 ppi	5	1	22-35%	35-55%	55-70%	>70%

Inclusion removal efficiency for various types of filters based on the removal of TiB_2 (density of 4.5 $g.cm^{-3}$) are listed[20] in Table 2.3.

2.3 Aluminium- Magnesium- Silicon Alloys

In 1906 Alfred Wilm[26.] (Germany) discovered the phenomenon of precipitation hardening at room temperature (natural ageing) following quenching. The aluminium alloy contained about 4% Cu, 0.5% Mg, 0.5% Mn, and the usual Fe and Si impurities that were around 0.5% each.

Wilm's discovery led to a search for other alloys that could age-harden. In 1921 a copper-free alloy containing 1% Si and 0.5% Mg (AA 6051) was successfully heat treated in the United States[26.]. Following this success a major class of age-hardenable aluminium alloy, AA 6XXX was developed. Some of the major alloys within this class are listed[26.27.28.] in table 2.6 .

The ratio of magnesium to silicon added is normally 1.73:1 (wt%) or with slight excess silicon which leads to the formation of Mg_2Si intermetallic compound.

The equilibrium-phase diagram (Figure 2.7) is pseudo binary Al-Mg_2Si with the pseudo binary eutectic horizontal at 868 K. The composition of the eutectic liquid is 8.15 wt% magnesium and 4.74 wt% silicon in equilibrium with aluminium solid solution containing 1.13 wt% magnesium and 0.67 wt% silicon (~ 1.85 wt% Mg_2 Si)[29.].

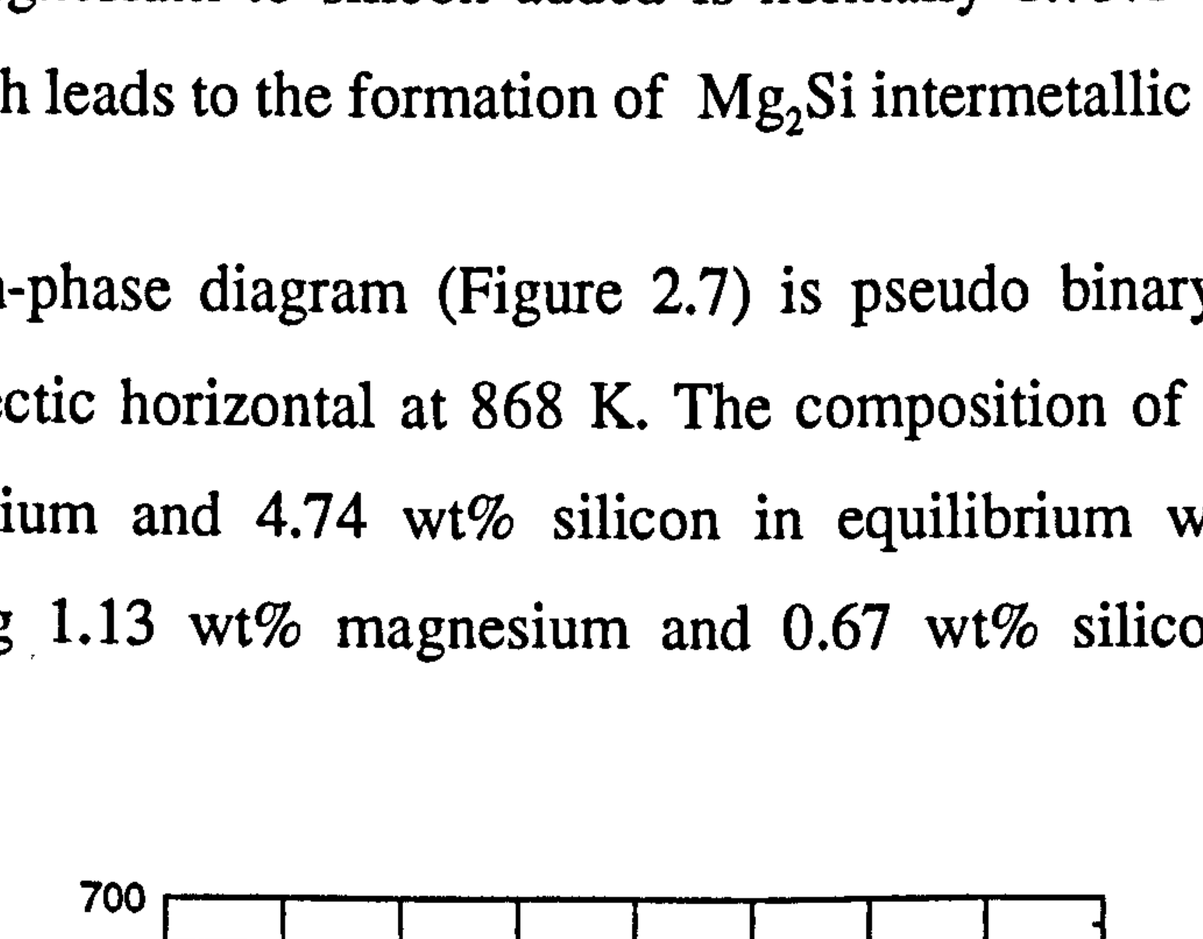

Figure 2.7 Al - Mg_2 Si phase diagram.

2.2 Aluminium Alloys

Most of the aluminium used is alloyed, with the principal alloying elements being copper, manganese, silicon, magnesium and zinc. Other elements are also added in smaller amount for grain refinement and to develop special properties; e.g. titanium, strontium etc.

Since there are wide variety of aluminium alloys, special designation were developed by the Aluminium Association[25.] (AA) as listed in Tables 2.4 for wrought and 2.5 for cast alloys.

Table 2.4
Designation system for wrought aluminium alloys

Alloy series	Description or major alloying element
1XXX	99.00% minimum aluminium
2XXX	Copper
3XXX	Manganese
4XXX	Silicon
6XXX	Magnesium and Silicon
7XXX	Zinc
8XXX	Other elements
9XXX	Unused series

Table 2.5
Designation system for cast aluminium alloys.

Alloy series	Description or major alloying element.
1XX.X	99.00% minimum aluminium
2XX.X	Copper
3XX.X	Silicon plus Copper and/or Magnesium
4XX.X	Silicon
5XX.X	Magnesium
6XX.X	Unused series
7XX.X	Zinc
8XX.X	Tin
9XX.X	Other elements

Table 2.6 Chemical composition of some aluminium alloys, AA6XXX series

Alloy	6151	6351	6061	6063	6066	6070	6009	6013
Year introd.	1928		1935	1944	1954	1962	1976	
Si	0.6-1.2	0.70-1.30	0.4-0.8	0.2-0.6	0.9-1.8	1.0-1.7	0.6-1.6	0.6-1.0
Fe	1.00	0.50	0.70	0.35	0.50	0.50	0.50	0.50
Cu	0.35	0.10	0.15-0.4	0.10	0.7-1.2	0.15-0.40	0.15-0.6	0.6-1.1
Mn	0.20	0.40-0.8	0.15	0.10	0.6-1.1	0.40-1.0	0.2-0.8	0.20-0.8
Mg	0.45-0.8	0.40-0.8	0.8-1.2	0.45-0.9	0.8-1.4	0.50-1.2	0.4-0.8	0.8-1.2
Cr	0.15-0.35	--	0.04-0.35	0.10	0.40	0.10	0.10	0.10
Zn	0.25	0.20	0.25	0.10	0.25	0.25	0.25	0.25
Ti	0.15	0.20	0.15	0.10	0.20	0.15	0.10	0.10
Others (each)	0.05	0.05	0.05	0.05	0.05	0.05	0.05	0.05
Others (total)	0.15	0.15	0.15	0.15	0.15	0.15	0.15	0.15
Al	Balance	Balance	Balance	Balance	Balance	Balance	Balance	Balance
Composition given in wt% either as maximum or range.								

2.3.1 AA 6063 Aluminium alloys

The alloy nominally contains 0.67% Mg and 0.4% Si, but more versions of this alloy are probably made than there are versions of any other alloy[26].

The favourable characteristics of this alloy family includes, moderately high strength (see Table 2.7), relatively low quench sensitivity[1], good corrosion resistance and good extrudability (see Table 2.8) in case of AA6063 extrusion ingot.

Table 2.7 AA6063 Mechanical properties at various heat treatment[27].

Temper	Ultimate Tnsile Strength MPa	Yield Tensile[a] Strength MPa	Elongation % in 50 mm	Hardness BHN[b]	Shear Strength MPa	Fatigue limit[c] MPa
0	90	50	...	25	70	55
T1	150	90	20	42	95	70
T4	170	90	22	...	110	...
T5	185	145	12	60	115	70
T6	240	215	12	73	150	70
T83	255	240	9	82	150	...
T831	205	185	10	70	125	...
T832	290	270	12	95	185	...

(a) At 0.2% offset, (b) 500 kg load 10 mm ball, (c) Based on 500 million cycle using R. R. More-Type rotating machine.

Table 2.8 Relative extrudability of aluminium alloys[27].

Alloy	1350	1100	3003	6063	6061	2011	5086	2014	5083	2024	7075	7178
Extrudability*	160	135	120	100	60	35	25	20	20	15	9	8

* Extrudability, % of rate for AA6063. The key factors which are often used in determining extrudability are "break in pressure", extrusion speed, and surface condition of the extrusion.

2.4 Solidification

Following all the necessary liquid metal treatment and alloying, the metal is cast into suitable ingot. Although an intermediate product, the quality and the metallurgical properties of the ingot has profound effect on the efficiency of the operations that follows[30,31] the ingot casting e. g. extrusion and rolling.

To appreciate the factors that govern the as-cast structure it is necessary to first consider some fundamental aspects of solidification science.

2.4.1 Nucleation

For solidification to occur it requires an out flow of heat which changes the free energies, and therefore the relative thermodynamic stability of the phases present. Then if the atoms cluster into "embryo" in the liquid or on a foreign substrate and at some

temperature below the thermodynamic equilibrium melting temperature they reach a critical size, they can become a stable nucleus and grow to form a solid grain.

2.4.1.1 Homogeneous nucleation.

When a solid forms with its own melt without the aid of foreign materials, it is said to nucleate homogeneously.

The free energy change for the homogeneous nucleation of a spherical embryo is given by[32.33.]:

$$\Delta G_r = 4 \pi r^2 \sigma + 4/3 \pi r^3 \Delta G_V \qquad (2.6)$$

where:

ΔG_r is the free energy (J mol^{-1}) to form the embryo of radius r,
σ is the solid-liquid interfacial energy (J m^{-2}),
ΔG_V is the free energy per unit volume (J m^{-3}), and

$$\Delta G_V = \frac{\Delta H_f \Delta T}{T_f V_m} \qquad (2.7)$$

where;

ΔH_f is laten heat of fusion per mole (J mol^{-1}),
ΔT is undercooling (K),
T_f is the melting point of pure substance (K), and
V_m is molar volume of the embryo (m^3 mol^{-1}).

The variation of the different free energy terms and the overall change in free energy Equation 2.6 is illustrated in figure 2.8. Any embryo which form above[34.] T_f will rapidly disperse. On the other hand below T_f, provided the embryo reaches a critical size with radius r^*, at which

$$(\partial (\Delta G) / \partial r) = 0$$

it is equally probable that it will disperse or that it will grow as a stable nucleus. To

form this critical nucleus a random fluctuation producing a localised energy change ΔG^* is required. differentiating Equation 2.6 and allowing for the sign of ΔG_V,

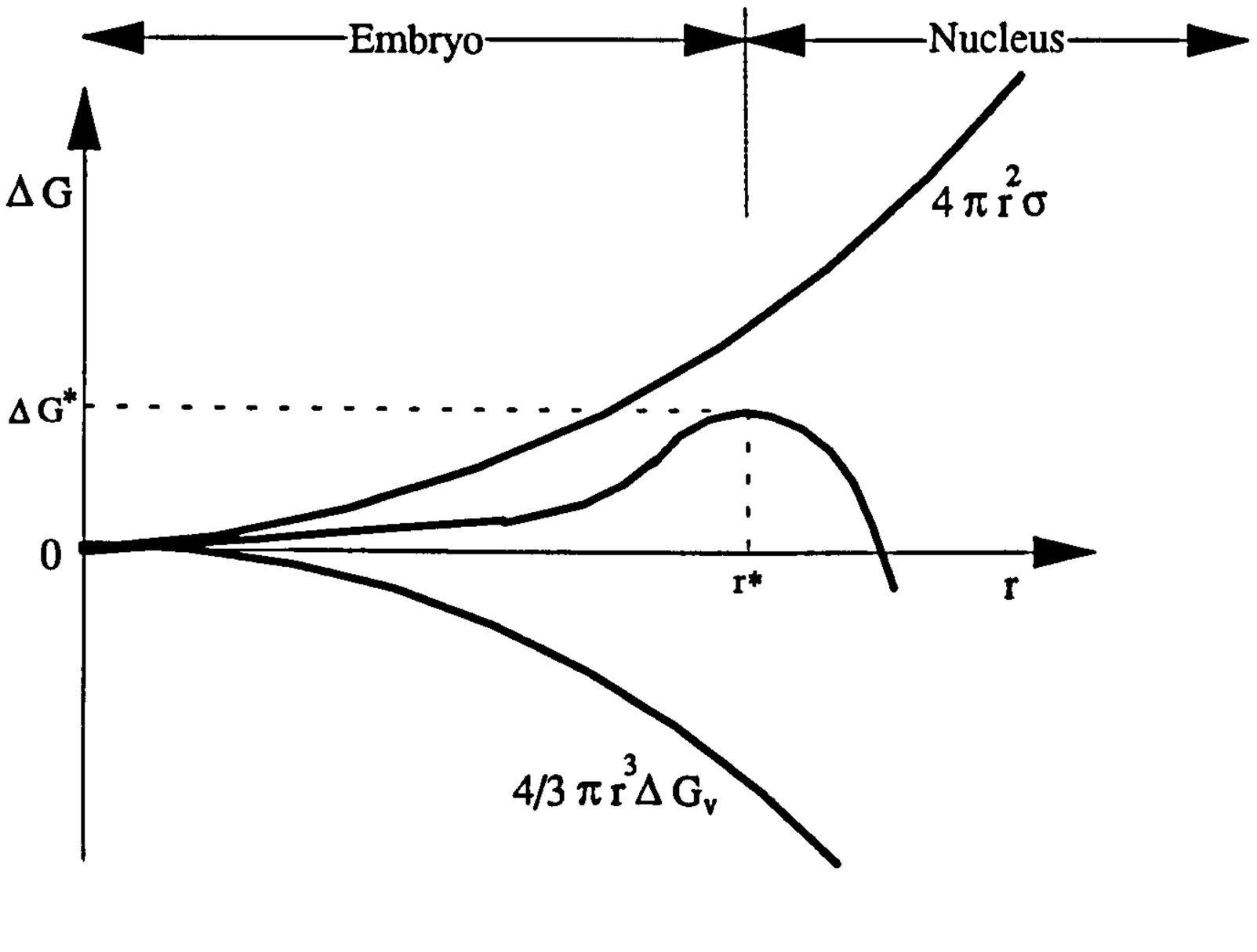

Figure 2.8 The free energy change resulting from homogeneous nucleation of sphere of radius *r*.

$$r^* = -\frac{2\sigma}{\Delta G_V} = -\frac{2\sigma T_f V_m}{\Delta H_f \Delta T} \tag{2.8}$$

The localised energy change or the activation energy for nucleation[35]. ΔG^* can be determined by introducing r^* into Equation 2.6:

$$\Delta G^* = \frac{16\pi\sigma^3}{3\Delta G_V^2} = \frac{16\pi\sigma^3 T_f^2 V_m^2}{3\Delta H_f^2 (\Delta T)^2} \tag{2.9}$$

Since ΔG_V increases approximately linearly as temperature falls (see Equation 2.7), the critical radius r^* decreases rapidly as does the activation energy of nucleation (ΔG^*) as illustrated in figure 2.9.

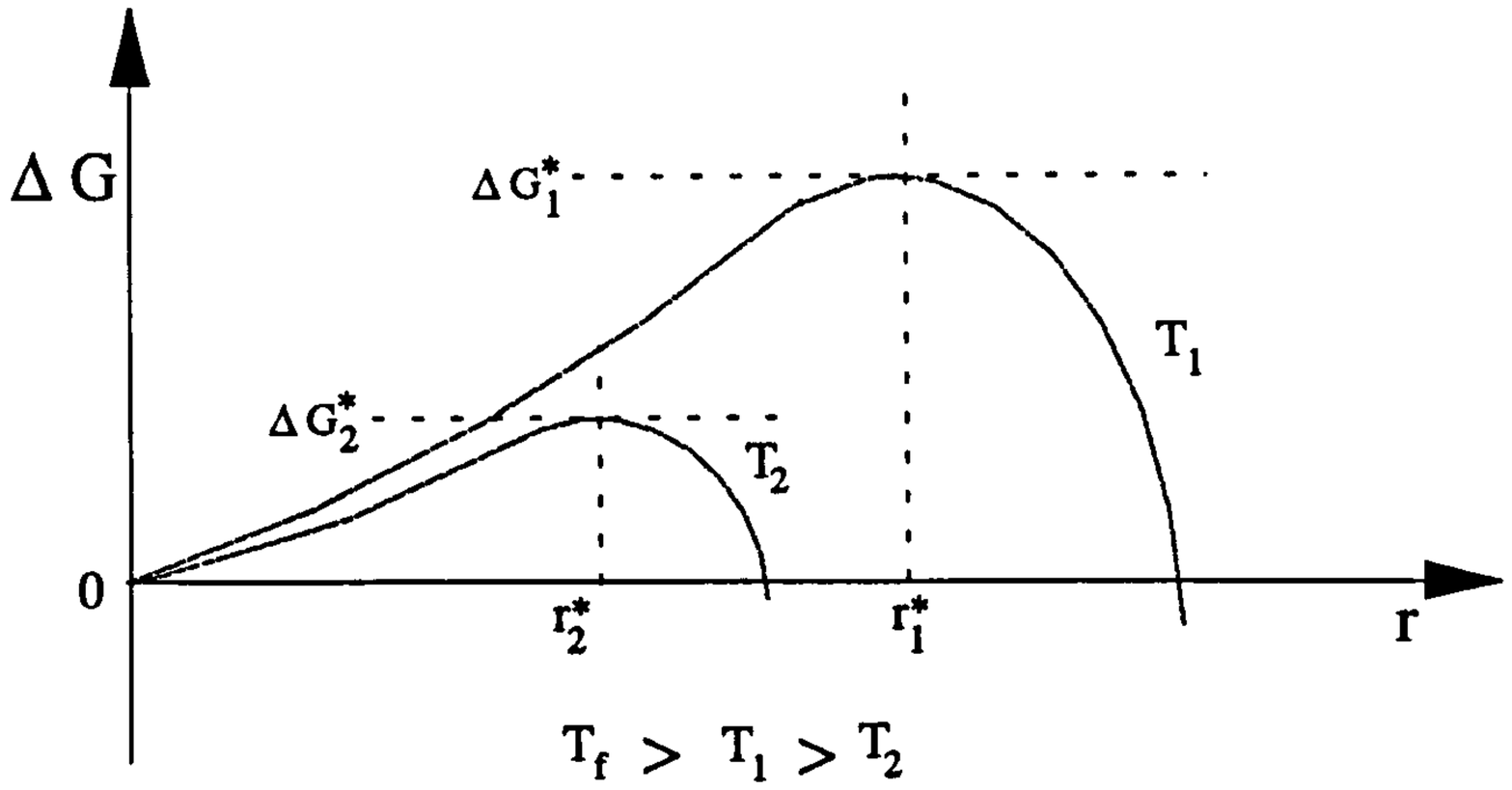

Figure 2.9 The effect of decreasing temperature on the critical radius for nucleation and on the activation energy for nucleation.

2.4.1.2 Heterogeneous nucleation

When the melt contains solid particles, or is in contact with a crystalline container or oxide layer, nucleation may be facilitated if the number of atoms, or activation energy required for nucleation, are reduced. This is known as heterogeneous nucleation.

Turnbull[36.] showed, that when the solid-liquid interface of the substance is partly replaced by an area of low-energy solid-solid interface between the crystal and a foreign particle, nucleation can be enhanced, and the magnitude of the effect was expressed as:

$$f(\theta) = \frac{(2 + Cos\,\theta)(1 - Cos\,\theta)^2}{4} \qquad (2.10)$$

Where θ is the wetting angle, in the presence of the melt, between a growing spherical cap of solid (nucleus) and solid substrate (particle or mould), illustrated in Figure 2.10.

Numerical values of $f(\theta)$, based on equation 2.10, are listed[35.] in Table 2.9, and show that, under conditions of good solid-solid wetting (small θ) between the crystal nucleus and the foreign substrate in the melt, a large decrease in ΔG^* (activation

energy for nucleation) can be expected.

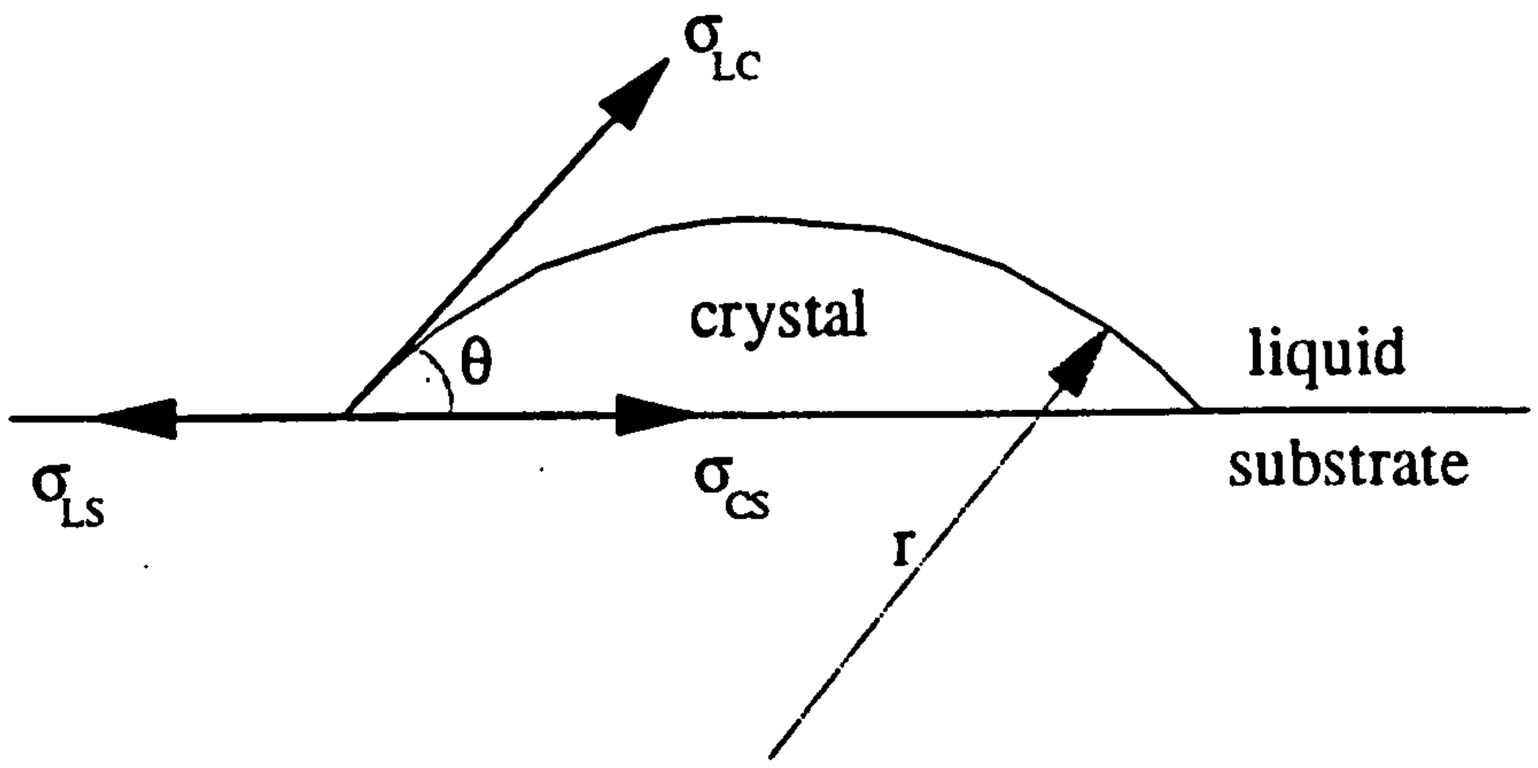

Figure 2.10 Heterogeneous nucleation of spherical cap of solid formed on a planar substrate.

Table 2.9 Calculated values for $f(\theta)$, based on equation 2.10.

θ °	Type of nucleation	$f(\theta)$
0 complete wetting	no nucleation barrier (immediate growth can occur).	0
10	heterogeneous	0.00017
20	heterogeneous	0.0027
30	heterogeneous	0.013
40	heterogeneous	0.038
50	heterogeneous	0.084
70	heterogeneous	0.25
90	heterogeneous	0.5
110	heterogeneous	0.75
130	heterogeneous	0.92
150	heterogeneous	0.99
170	heterogeneous	0.9998
180	homogeneous	1

For spherical cap nucleus representation[32] ΔG^* is expressed as:

$$\Delta G^* = \frac{16 \pi \sigma_{LC}^3}{3 \Delta G_V^2} f(\theta) \qquad (2.11)$$

The critical nucleus radius (r^*) is unaffected by nucleation site.

2.4.1.3 Rate of nucleation

An expression for the rate of nucleation (I), essentially equivalent to that derived by Turnbull and Fisher[32], based on earlier work[37] of nucleation of droplets from the vapour, can be stated as:

$$I = I_O \exp\left(\frac{\Delta G^* + \Delta G_d}{kT}\right) \qquad (2.12)$$

where:

I_O is a pre-exponential factor,
ΔG_d is the activation energy for diffusion through the solid-liquid interface,
k is Boltzmann's constant, and
T is temperature (K).

In Equation 2.12, ΔG^* varies as $-1 / T(\Delta T)^2$, while ΔG_d as $-1 / T$. An increase in ΔT, giving more numerous and smaller nuclei of critical size (see Equation. 2.8 - 2.11), is accompanied by a decrease in T. i.e. lower diffusion . These opposing tendencies lead to a maximum in nucleation rate at a critical temperature, which is approximately[38] at $\sim 0.2\, T_f$ undercooling for most metals for homogeneous nucleation but at only $\sim 0.02\, T_f$ undercooling for heterogeneous nucleation as shown[34] in Figure 2.11.

At low undercooling, equation 2.12 can be[35] approximated to :

$$I = 10^{39} \exp\left(-\frac{\Delta G^*}{kT}\right) \qquad (2.13)$$

Kurz and Fisher[35] illustrated (figure 2.12) that due to the exponential relationship, variation in the value of the term, ($\Delta G^* / kT$), have a remarkable effect upon the rate of nucleation, I . If, for an observable rate of $I = 1\ cm^{-3}\ s^{-1}$, the exponential term is changed by a factor two, from 50 to 100 for example, the resultant change in the nucleation rate is of the order of 10^{22} . When $\Delta G^* / kT$ is equal to 50, 10^8 nuclei per

litre of melt per microsecond are formed. If the latter term is equal to 100, only one nucleus will be formed per litre of melt over a period of 3.2 years.

Thus changing the temperature or changing the value of ΔG^* can enormously increase or decrease the nucleation rate.

Minimisation of the activation energy for nucleation (ΔG^*) by the use of foreign crystalline particles which are readily wet by the growing nucleus is the basis for the inoculation and grain refining in the metallurgical industry.

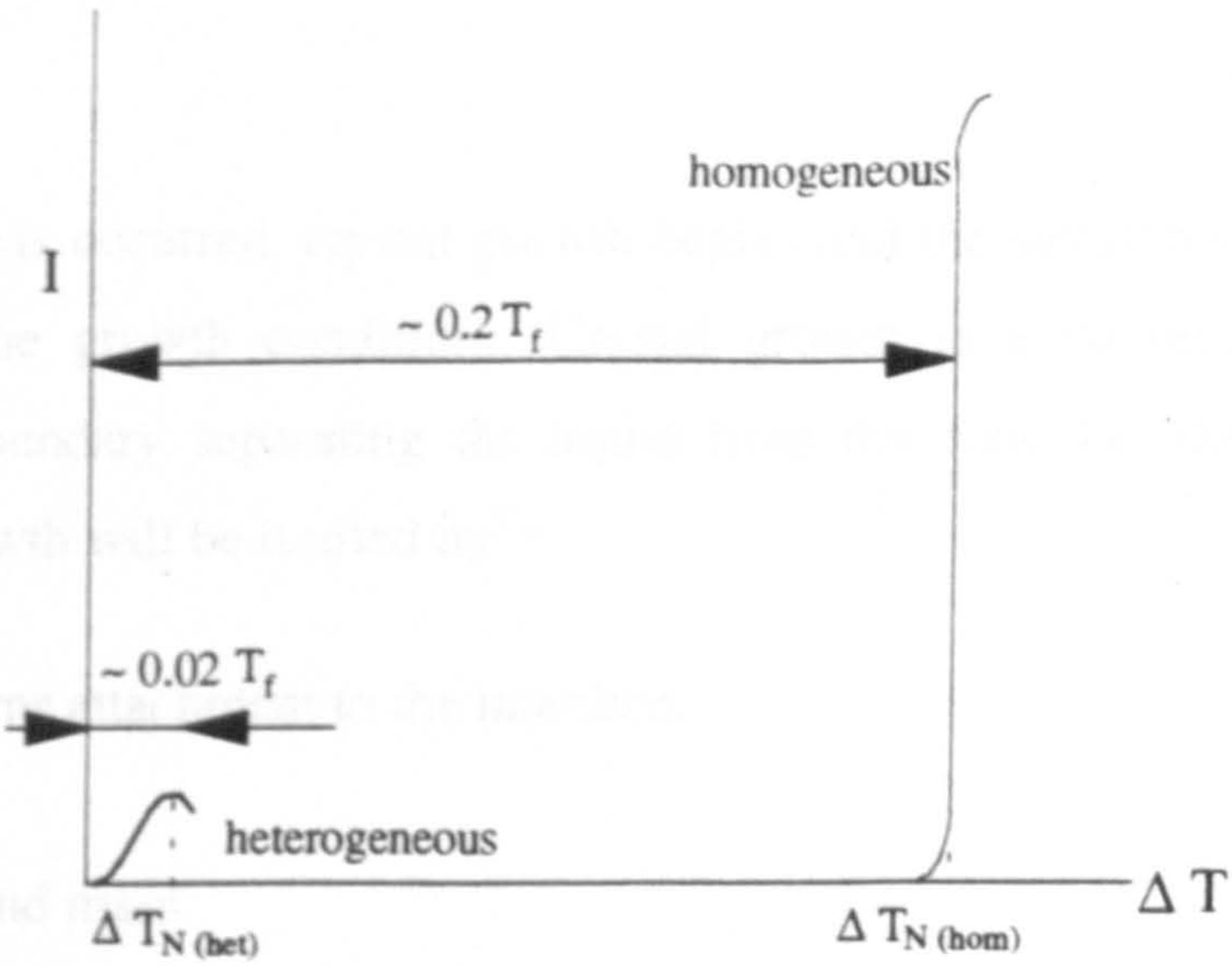

Figure 2.11 The critical undercooling for homogeneous and heterogeneous nucleation

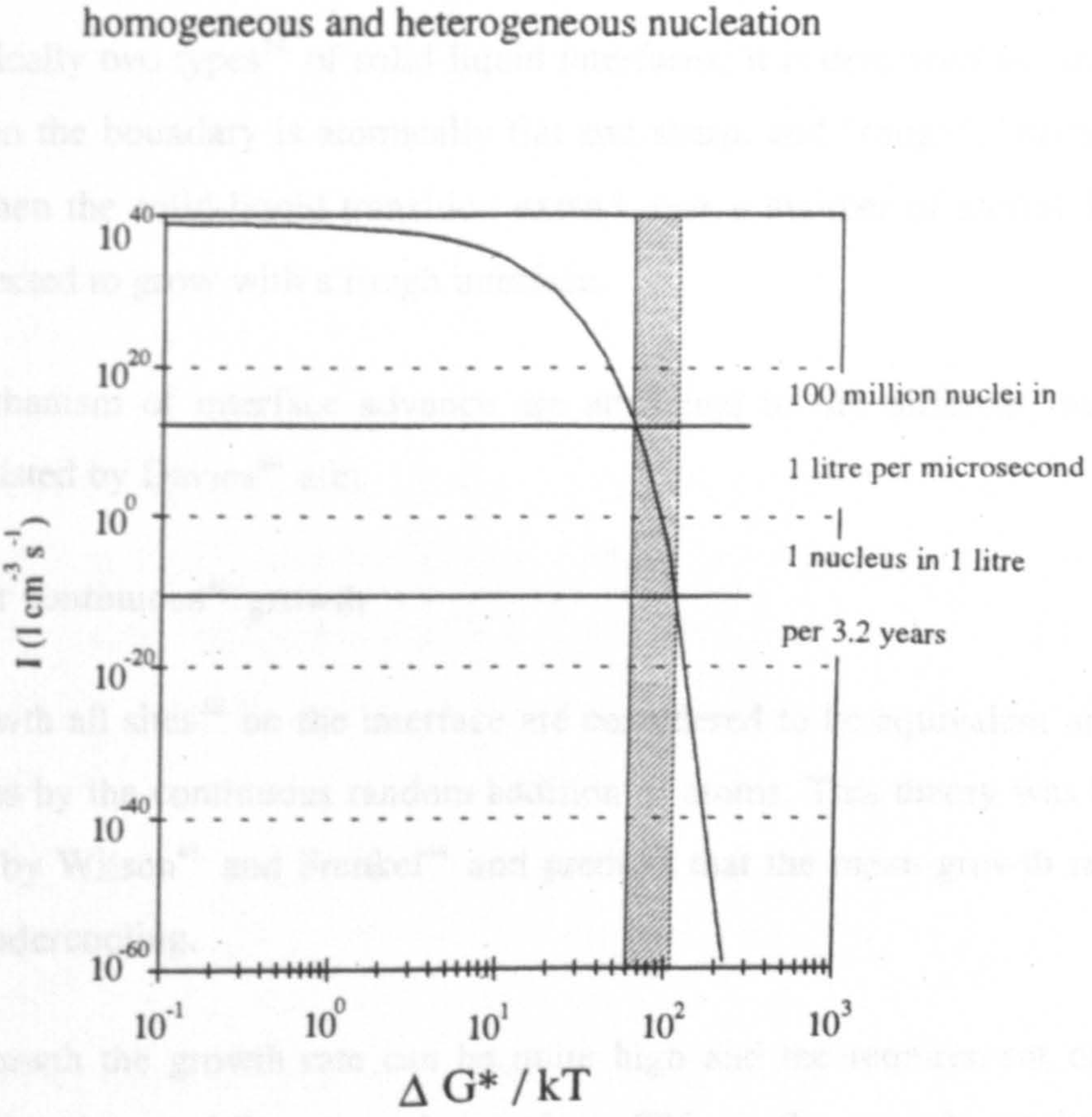

Figure 2.12 Nucleation rate as a function of activation energy ΔG^* .

2.4.2 Crystal growth

Once nucleation has occurred, crystal growth begins and the structures that develop can be related to the growth conditions. Crystal growth is a consequence of the movement of the boundary separating the liquid from the solid i.e. the solid-liquid interface. Such a growth will be limited by[35]:

- the kinetics of atoms attachment to the interface,
- capillarity,
- diffusion of heat and mass.

The relative importance of each of these factors depends upon the substance in question and upon the solidification conditions.

There are basically two types[39] of solid-liquid interfaces; it is described as "smooth" or "faceted" when the boundary is atomically flat and sharp, and "rough", "diffuse" or "non-faceted" when the solid-liquid transition extend over a number of atomic layers. Metals[40] are expected to grow with a rough interface.

Different mechanism of interface advance are attributed to the different interface forms, the three listed by Davies[34] are:

2.4.2.1 Normal or continuous[41] growth

In normal growth all sites[42] on the interface are considered to be equivalent and the interface advances by the continuous random addition of atoms. This theory was based on earlier works by Wilson[43] and Frenkel[44] and predicts that the mean growth rate, is proportional to undercooling.

For normal growth the growth rate can be quite high and the requirement of site equivalence implies the need for a rough interface. This is the growth mechanism considered applicable to most metals.

2.4.2.2 Growth by surface mechanism or lateral[41.] growth,

This theory[33.45.] assumes that the crystal interface is smooth and that growth proceeds by the homogeneous nucleation of new layers in the form of disc nuclei which grow laterally until a complete layer is formed. This is shown schematically in Figure 2.13. The theory predicts growth rates which are negligibly slow at low undercooling.

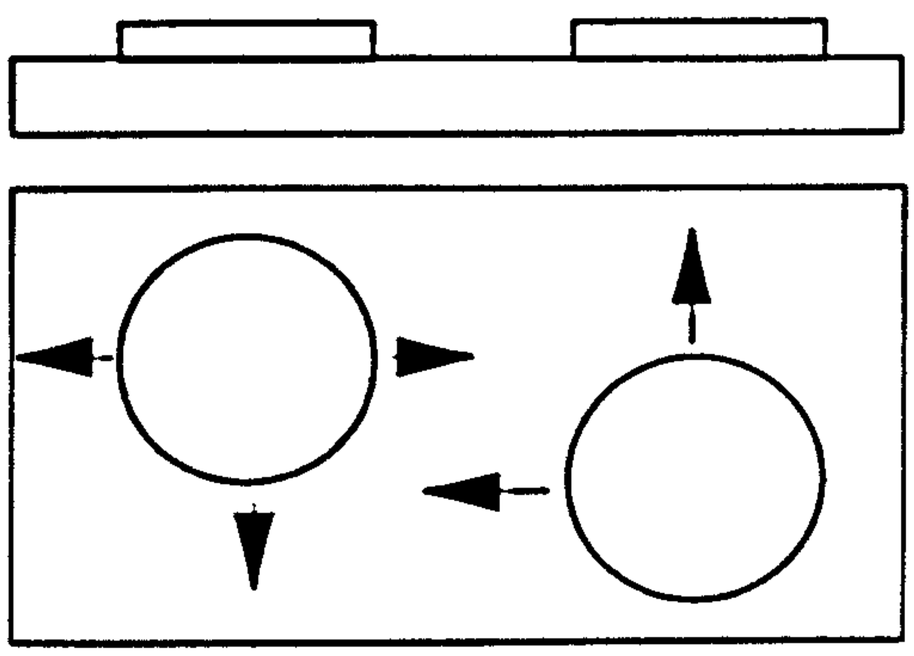

Figure 2.13 Crystal growth by surface mechanism.

2.4.2.3 Growth on imperfections,

Here the assumption is that some form of continuous growth steps exists at which atoms can be added. The simplest form of step is that formed when a screw dislocation emerges at a crystallographically smooth interface. The theory of growth on screw dislocation has been treated by Frank[46.] and Hillig and Turnbull[47.]. In this case the predicted growth rates are also very low and this is due to restriction on the number of available growth sites.

2.5 Solidification of Pure Metals

Presuming the casting takes place in a container (mould), the solidification begins with the initiation of crystallisation at the mould wall immediately after the liquid is poured, thus forming a thin layer of solid metal there; for pure metals and in absence of inoculant, the solidification proceeds[48.49.50.51.] by gradual thickening of this layer of solid metal i.e. by "skin formation". It had been[52.] "tacitly assumed that the solidification front (solid-liquid interface) advancing from a plane mould wall is itself substantially

plane". Works by Chalmers, Weinberg and their associates[53,54,55,56], demonstrated that certain conditions e.g. thermal gradient, constitutional supercooling, can cause instability in the planar interface leading to cellular and dendritic morphology.

The morphology of the advancing solid-liquid interface of pure metal is determined by the thermal gradient, which refers to the gradient in the liquid (G_L) away from the interface. In keeping with Tiller et al[55] convention, if the temperature increases, the temperature gradient is considered to be positive and vice versa.

As illustrated[34] in Figure 2.14, the growth of pure metals in a region of positive temperature gradient is controlled by the flow of heat away from the interface through the solid. Provided the interface is at a temperature below the equilibrium temperature, just necessary to provide sufficient undercooling (ΔT) the interface should grow in a stable planar form. Any localised instability formed on the interface would project into a region at a temperature higher than the melting temperature (T_m) and would remelt to restore the isothermal interface (Figure 2.14 b).

However, if a state of metastability is created on the growing interface in a region of negative temperature gradient (see Figure 2.15), the growing planar interface will break down as shown in Figure 2.15 (b).

In reality solidification morphology and the transition of solid-liquid interface from planar to cellular and to dendritic is extremely complex and has been the subject of numerous investigations, the latest of which are a series of papers by Trivedi and Kurz and co-workers[57,58,59,60].

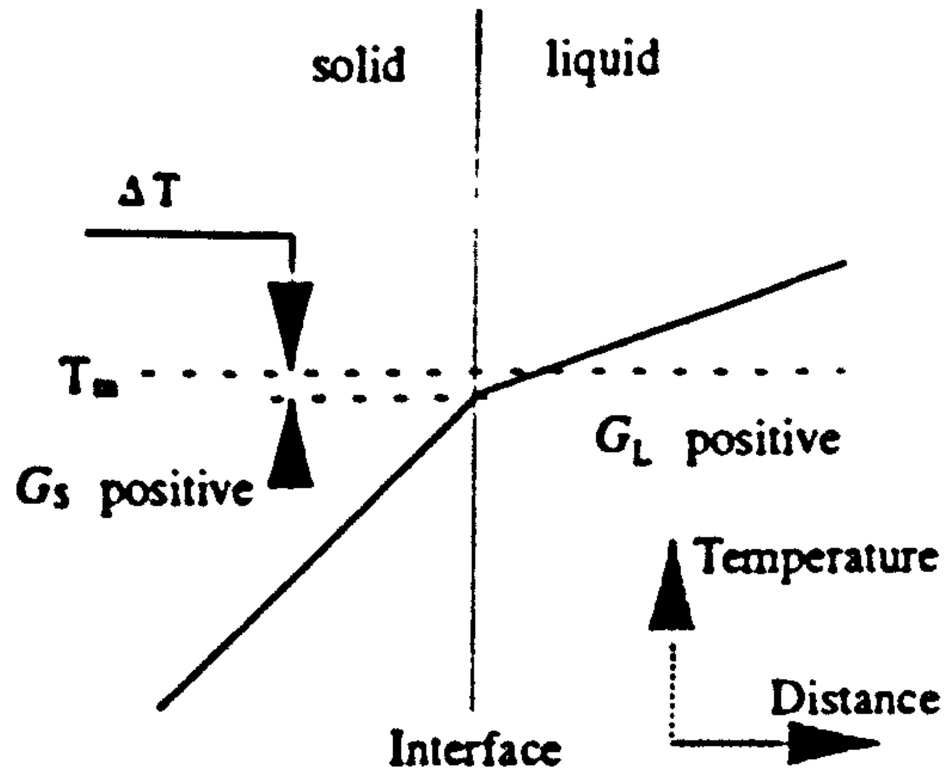

(a)

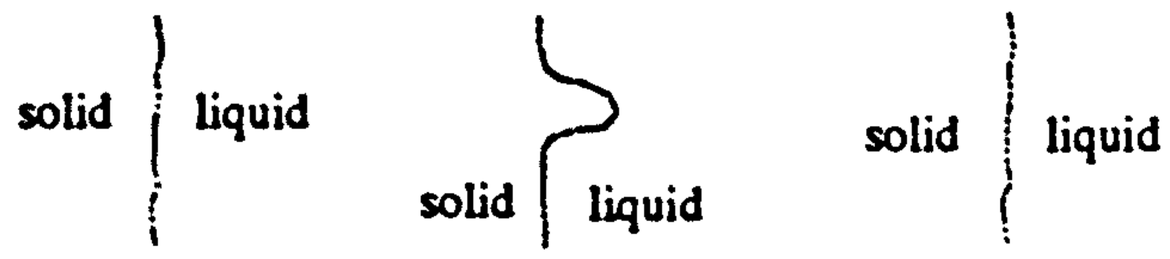

(b)

Figure 2.14 Interface growing into liquid with positive temperature gradient

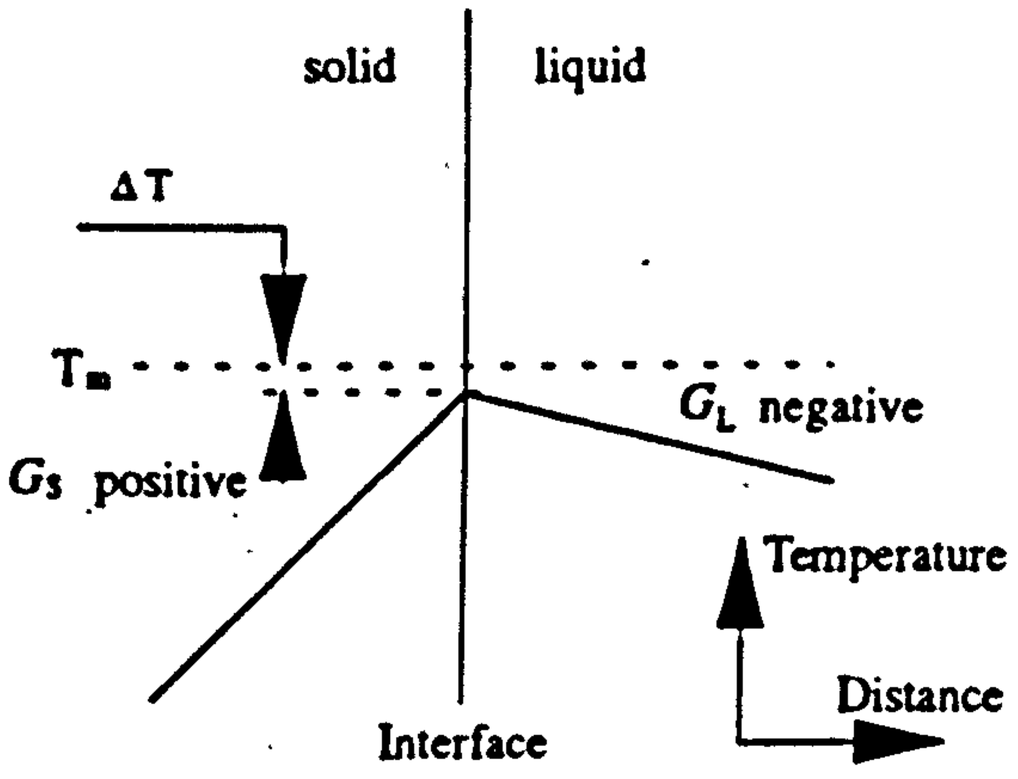

(a)

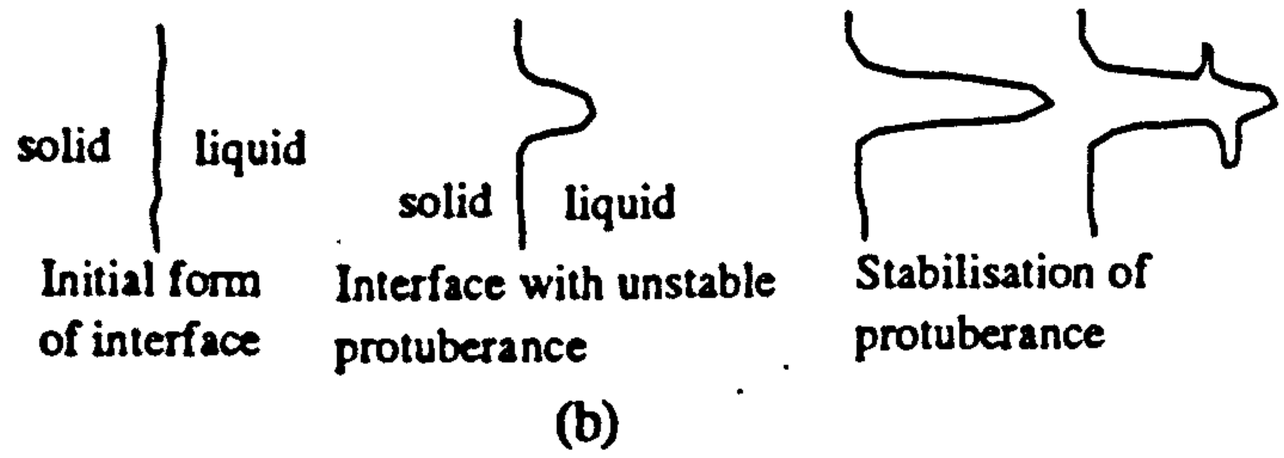

(b)

Figure 2.15 Interface growing into liquid with negative temperature gradient

2.6 Alloy Solidification

The solidification of pure metal is rarely encountered in practice. Even commercially pure metals contain sufficient impurities to change the characteristics of solidification from pure metal to alloy behaviour.

When a liquid solution of uniform composition, is solidified, the distribution of solute in the solid is different from that in the liquid, although the total amount is unchanged.

2.6.1 Solute redistribution

Consider the freezing of binary eutectic alloy of composition C_o shown in figure 2.16 (a). The first solid to freeze, at the liquidus temperature T_L , has the composition kC_o , where the partition coefficient (k) equals C_s / C_L (where C_L is approximately equal to C_o at liquidus temperature). If it is assumed that there is no diffusion in the solid and complete diffusion in the liquid, then during subsequent solidification the liquid becomes richer in solute and the solid that forms is of higher solute content at later stages of solidification. This sequence of events is shown schematically in figure 2.16 (b-d). A quantitative expression may be obtained by equating the solute rejected when a small amount of solid forms with the resulting solute increase in the liquid. This balance is

$$(C_L - C^*_s)\, df_s = (1 - f_s)\, dC_L \qquad (2.14)$$

Substituting the equilibrium partition ratio (k) and integrating $C^*_s = k\, C_o$ at $f_s = 0$ yields the composition of the solid at the liquid-solid interface C_s^* as a function of fraction solid.

$$C^*_s = k\, C_o\, (1 - f_s)^{(k-1)} \qquad (2.15)$$

or, in terms of liquid composition and fraction liquid,

$$C_L = C_o f_1^{(k-1)} \tag{2.16}$$

Equations 2.15 and 2.16 were first derived by Gulliver[61] and later by Scheil[62], and are termed the non-equilibrium lever rule, or the Scheil equation.

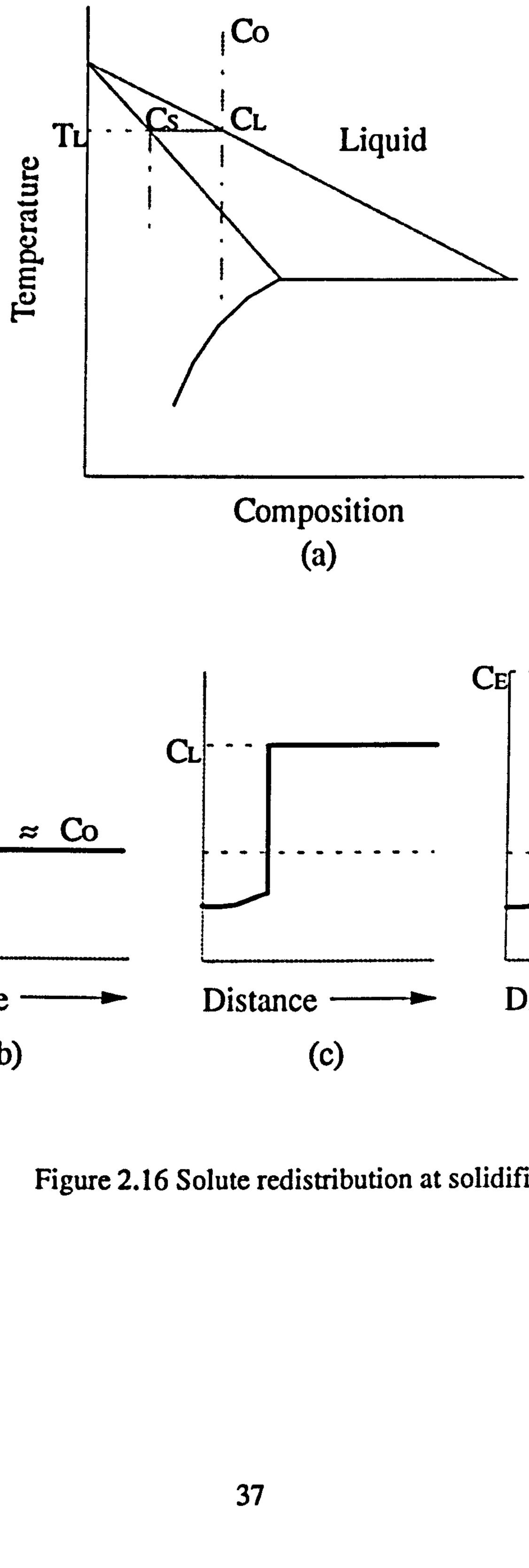

Figure 2.16 Solute redistribution at solidification.

2.6.2 Constitutional supercooling

The consequence of limited diffusion in the liquid is the development of a solute-rich boundary layer ahead of the growing interface. Chalmers and co-workers[55] quantified the concept and applied it to crystal growth from the melt. Figure 2.17 shows how the driving force for instability of the planar front develops.

As illustrated in Figure 2.17(b), the concentration of solute at the interface (I) reaches a maximum C_0/k then decreases according to the equation:

$$C_L = C_0\left[1+\frac{1-k}{k}\exp\left(-\frac{R}{D}X\right)\right] \tag{2.17}$$

where R = rate of solidification, D = diffusion rate of solute in the liquid and X = distance ahead of the interface.

If the liquidus line is assumed to be linear the liquidus temperature of any composition is related to the freezing temperature of pure metal by the expression:

$$T_L = T_0 - mC_L \tag{2.18}$$

so that;

$$T_L = T_0 - mC_0\left[1+\frac{1-k}{k}\exp\left(-\frac{R}{D}X\right)\right] \tag{2.19}$$

where T_0 = freezing temperature of pure metal, m = slope of the liquidus. The rise in equilibrium liquidus temperature with distance from the interface is shown schematically in Figure 2.17(c).

From equation 2.18:

$$T_I = T_0 - m\frac{C_o}{k} \tag{2.20}$$

where T_I is the interface temperature.

Thus the temperature in the liquid at a point X is:

$$T = T_I + GX \tag{2.21}$$

or

$$T = T_0 - m\frac{C_0}{k} + GX \tag{2.22}$$

where G is the temperature gradient in the liquid. When the real temperature is superimposed upon the equilibrium freezing temperature the situation is as in 2.17(d).

Note that this zone of supercooling is eliminated if the slope of the actual temperature equals or exceeds the slope of the liquidus temperature curve. The constitutional supercooling criteria given by Chalmers and co-workers is:

$$\frac{G}{R} \geq m\frac{C_0}{D}\left(\frac{1-k}{k}\right) \tag{2.23}$$

Figure 2.17(d) shows two conditions, one in which the actual temperature T' ahead of the interface is above the equilibrium liquidus temperature and the other, T'', where it is below the liquidus. In the former case the planar interface is stable because any instability that would give rise to a protuberance will find itself in a super-heated environment and melt-back. On the other hand, for T'', the melt is below the liquidus temperature and is therefore supercooled. Constitutional supercooling results in instability of the interface since any protuberance forming on the planar front would be in supercooled liquid and would not remelt.

The factors that tend to maximise this zone, ahead of the advancing interface, are important in the control of the as-cast grain structure. For heterogeneous nuclei to grow in the melt, ahead of the interface, it is essential that there is a supercooled region.

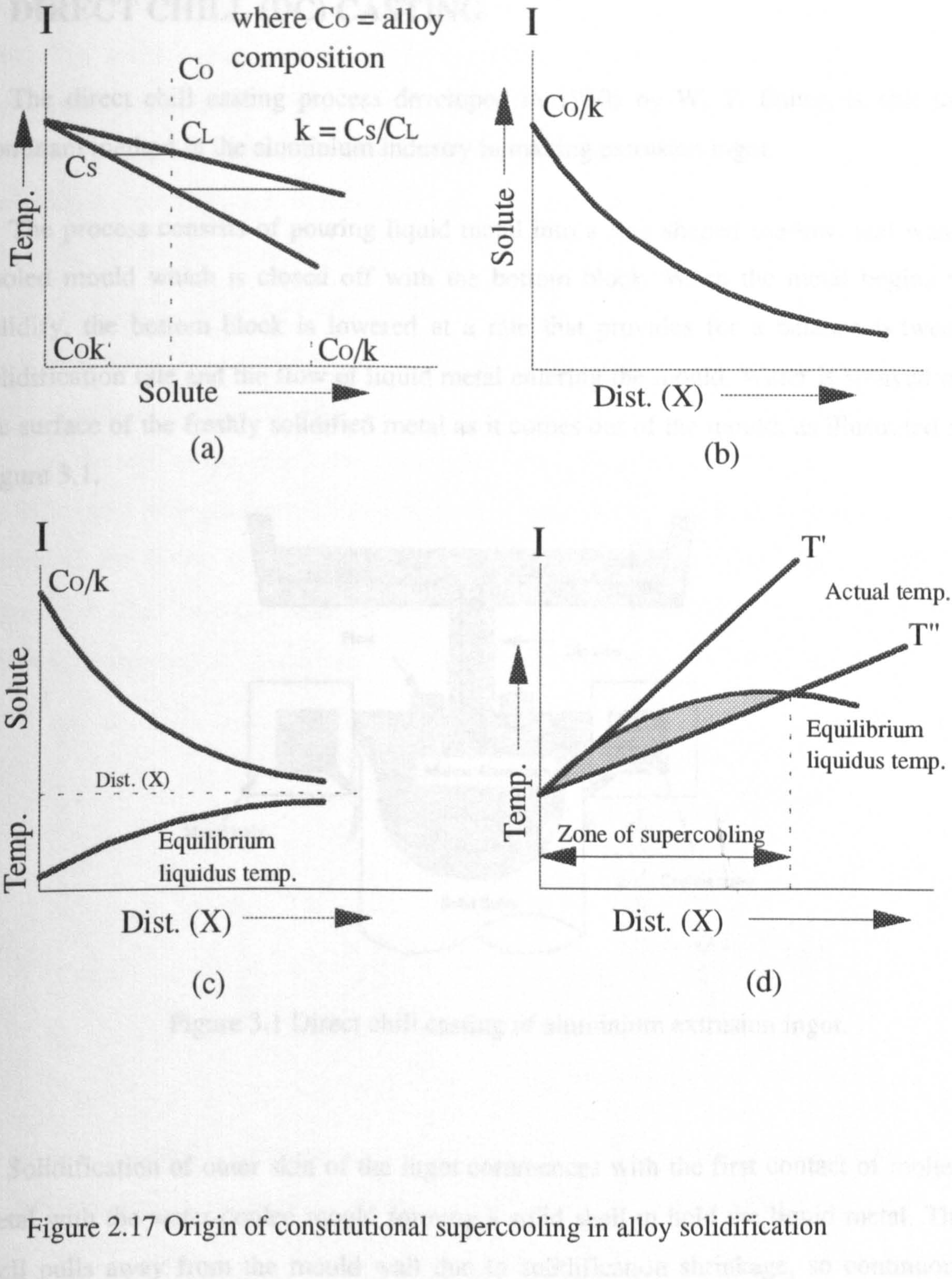

Figure 2.17 Origin of constitutional supercooling in alloy solidification

3. DIRECT CHILL (DC) CASTING

The direct chill casting process developed in 1930s by W. T. Ennor, is still the dominant method in the aluminium industry in making extrusion ingot.

The process consists of pouring liquid metal into a ring shaped shallow, and water cooled mould which is closed off with the bottom block. When the metal begins to solidify, the bottom block is lowered at a rate that provides for a balance between solidification rate and the flow of liquid metal entering the mould. Water is sprayed on the surface of the freshly solidified metal as it comes out of the mould, as illustrated in Figure 3.1.

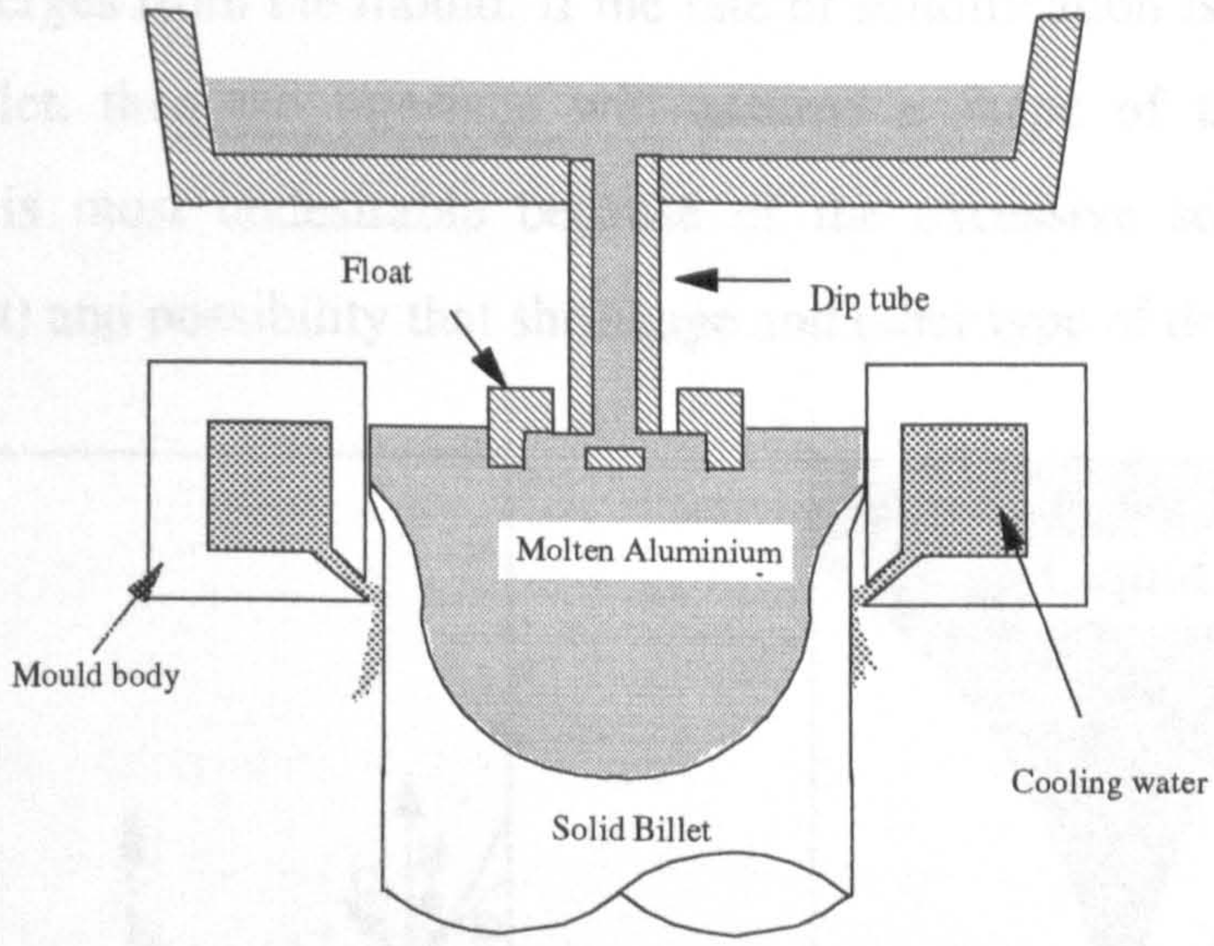

Figure 3.1 Direct chill casting of aluminium extrusion ingot.

Solidification of outer skin of the ingot commences with the first contact of molten metal with the water-cooled mould forming a solid shell to hold the liquid metal. The shell pulls away from the mould wall due to solidification shrinkage, so continuous removal of the ingot from the mould is made possible.

Direct chill casting method is a semi-continuous process, in which the rate at which the process can be conducted is determined[63] largely by the problem of the removal of the latent heat and the flow of the metal during solidification. An important characteristic of this process, is that a steady state is maintained. This corresponds to a constant shape of the liquid-solid interface (solidification front), and a solidification

rate that depends only on the position relative to the surface (metal head) and not on time. The solidification rate is clearly not uniform, because as shown in Figure 3.2 solidification at A and B (and at all points on the solidification front) must take place at rate such that the longitudinal components of the rates, AA' and BB', are equal to the withdrawal ("casting") rate of the billet (v_C) . The rate of solidification, however, is the rate along the local normal to the interface (BC), which is equal to BB' Sin ϕ , where ϕ is the local inclination of the interface to the direction of motion. It follows that, in order to achieve an interface shape of the kind shown in[63.] Figure 3.2, it is necessary to provide cooling conditions such that the rate of extraction of latent heat is greater at A (i.e., on the axis of the billet) and least at D. This necessitate the secondary cooling of the billet as it emerges from the mould. If the rate of solidification is a minimum at the centre of the billet, then the interface will assume a shape of the type shown in Figure 3.3. This is most undesirable because of the excessive solute accumulation (terminal transient) and possibility that shrinkage and other type of defects can occur.

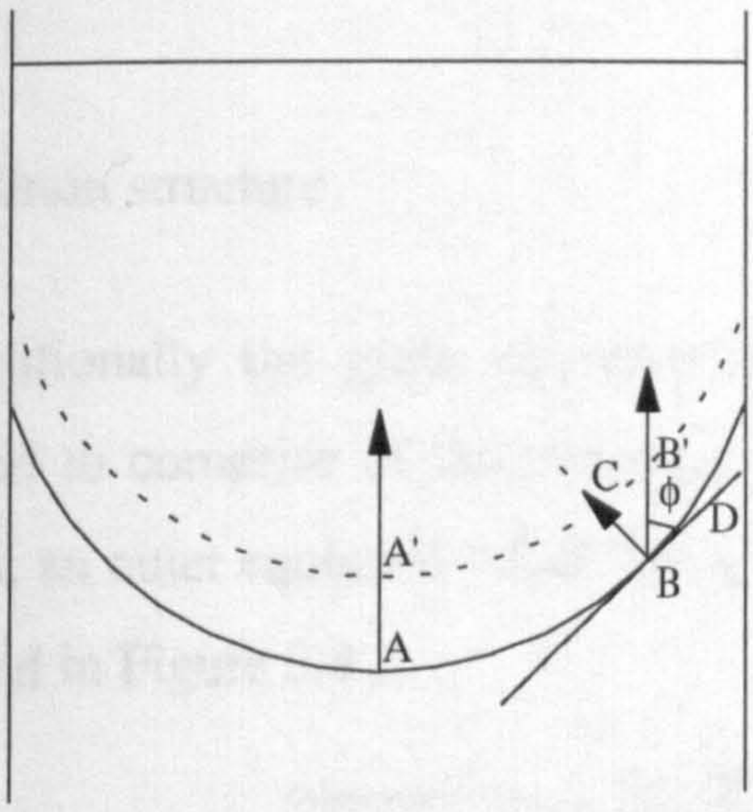

Figure 3.2 Interfacial shape and rate of solidification in continuous casting.

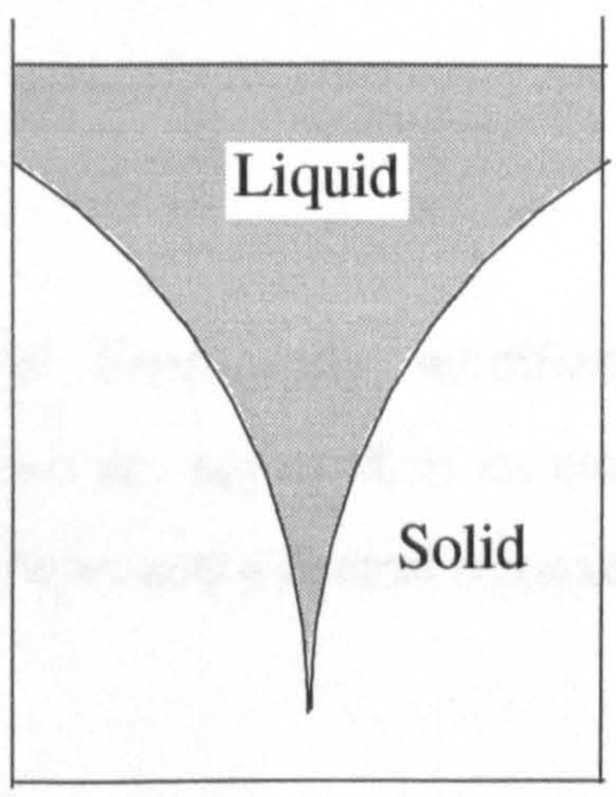

Figure 3.3 Alternative interface shape in continuous casting.

The quantitative aspect of continuous casting of cylindrical billet are discussed by Boichenko[64.], who expressed the depth of the liquid core, h_c , by the equation:

$$h_c = \frac{I \gamma R^2 v_c}{4K(T_f - T_s)} \qquad (3.1)$$

where ;

I is latent heat plus heat extracted, for unit mass, during fall of temp. from T_f to $(T_f + T_s) / 2$,
γ is density,
R is radius of billet,
v_c rate of withrawal of billet (casting rate),
K is thermal conductivity of the solid metal,
T_f melting point and,
T_s is surface temperature (assumed uniform).

3.1 Structural Characteristics of D C Cast Ingot.

As illustrated schematically in figure 3.1, the combination of water-cooled mould and direct impingement of water on the hot ingot surface as it emerges from the mould result in moderately high cooling rate, (0.5 - 2 Ks^{-1})[65.] and rapid solidification[66.].

3.1.1 Grain structure.

Traditionally the grain structure of rapidly and directionally solidified ingot is depicted to comprise of three distinct regions, which are apparent in an etched ingot section; an outer equiaxed "chill" zone, a columnar zone, and a central equiaxed zone as sketched in Figure 3.4 .

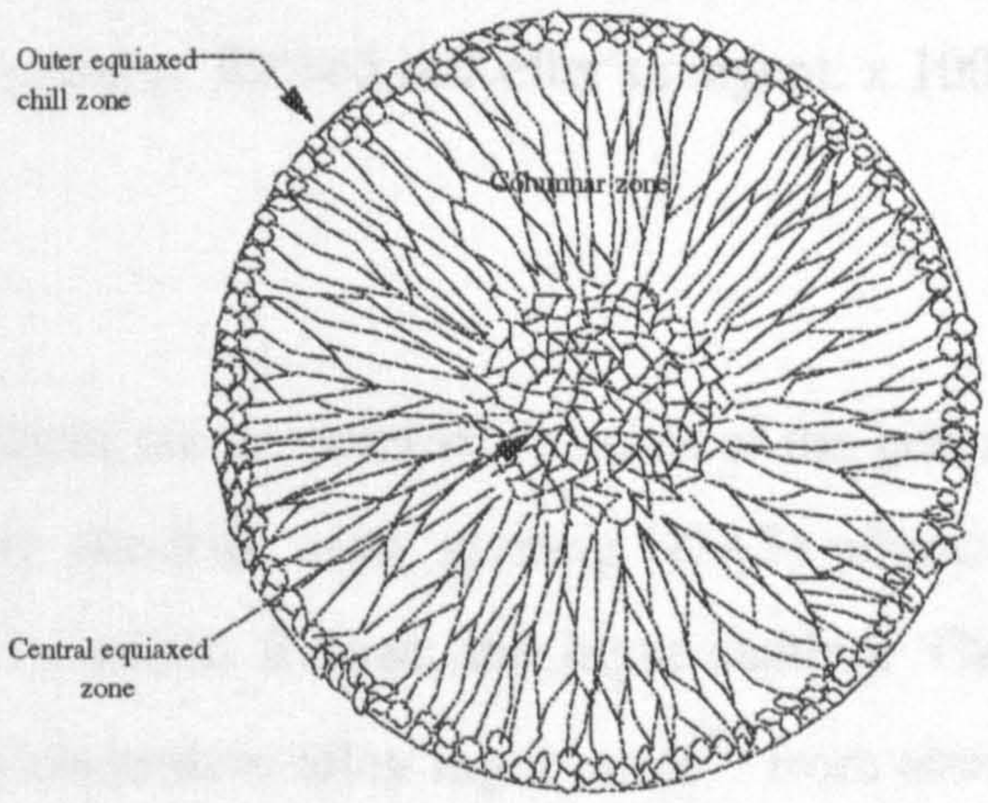

Figure 3.4 Variation of shape and orientation of grains across an ingot section.

Nevertheless, modern DC casting process, result in ingot with complete fine equiaxed dendritic grain structure, which is attributed to either or combination of constitutional supercooling[67], "crystal multiplication" [68,69,70], and convection[71,72].The grain size ranges[73] from about 50 to 500 μm in a grain-refined DC cast ingot.

Master alloys containing finely distributed TiB_2 prticles are used to obtain a uniform and fine equiaxed grain structure. The master alloy must have higher Ti/B ratio than stoichiometric as the grain-refinement is thought to be by TiAl complex overlaid on TiB_2 particles.

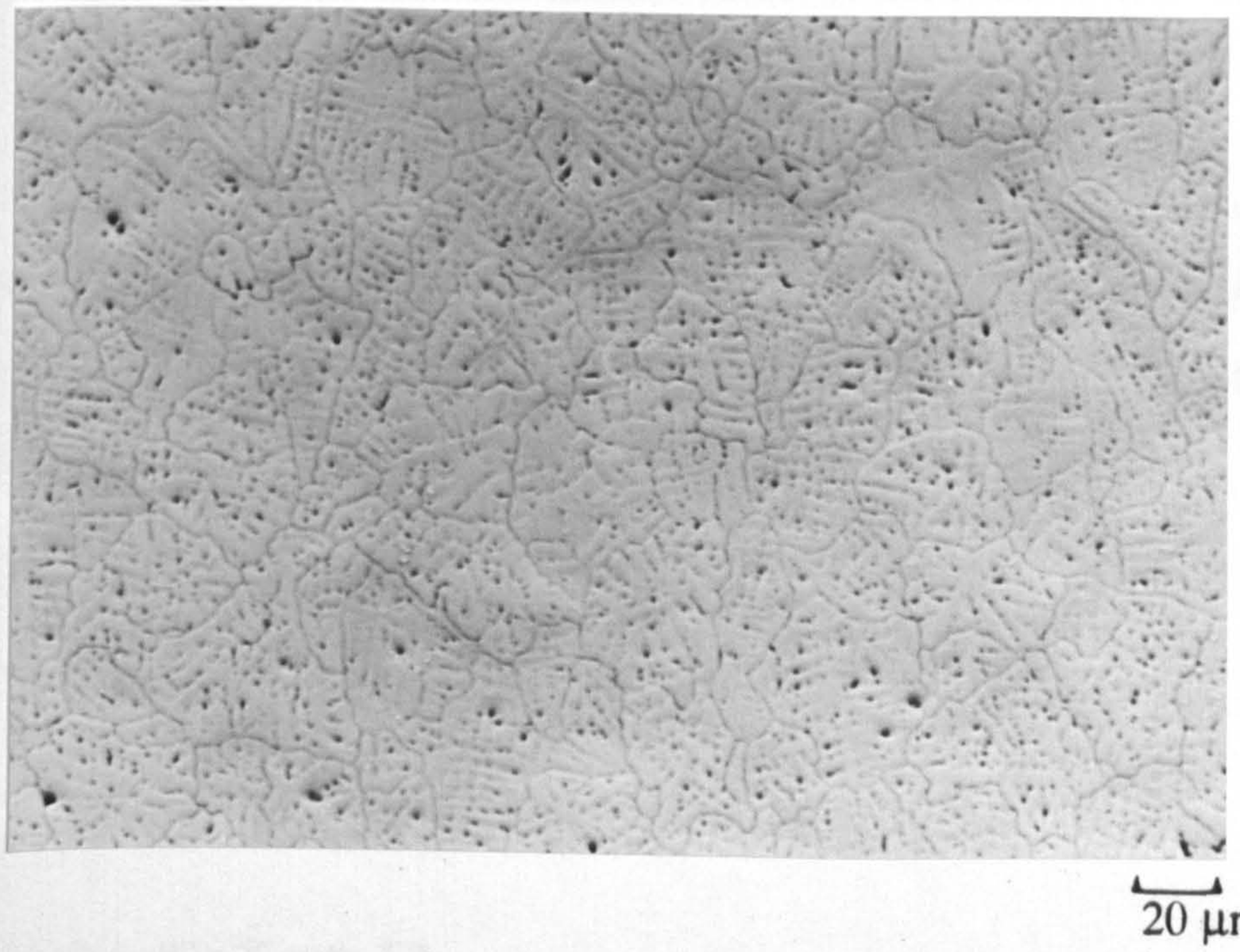

Figure 3.5 Dendritic structure of equiaxed grains in DC cast AA6063 extrusion ingot. Etched in Keller's reagent. x 100.

Cells or dendrites are the internal features of the grains, see Figure 3.5. The cell size or the secondary dendrite arms spacing (DAS) affects the heat treatment operation (homogenisation), which follows the ingot casting. The cell size or DAS, for grain refined DC cast aluminium alloy ingot range[73] from about 10 to 100 μm. An empirical equation has been developed[74], where the secondary dendrite arm spacing, d (in μm) is

correlated to the average local cooling rate during solidification, ε_{Avg} (°C s^{-1}), or local solidification time[75.] (time available for coarsening), t_f , by:

$$d = a\,\varepsilon_{Avg}^{-n} \tag{3.2}$$

or

$$d = b\,t_f^{n} \tag{3.3}$$

where

$$\varepsilon_{Avg} = \frac{(T_L - T_S)}{t_f} \tag{3.4}$$

and (T_L - T_s) is the solidification temperature range, a and b are constants, and n is an exponent which experimentally is found[76.] to be between 1/4 and 2/5, and theoretically is expected to be 1/3. An approximate plot of dendrite arm spacing against the cooling rate is given[76.] in Figure 3.6 .

A review of extensive experimental data was found[77.] to correspond closely to a straight line, which can be expressed as:

$$d = 7.5\,t_f^{0.39}$$

which is plotted in Figure 3.7 .

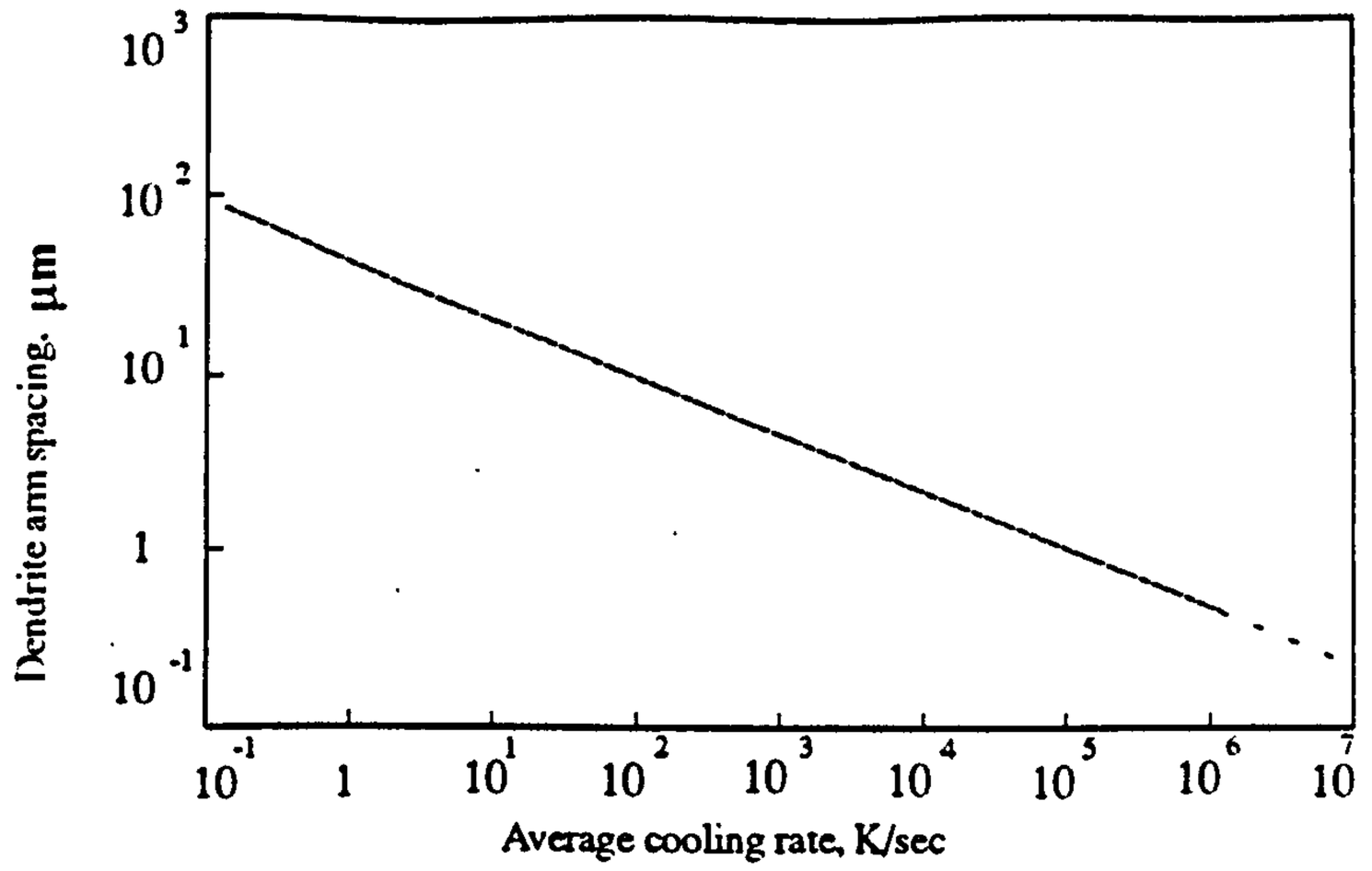

Figure 3.6 An approximate plot of dendrite arm spacing aginst cooling rate of an aluminium alloy.

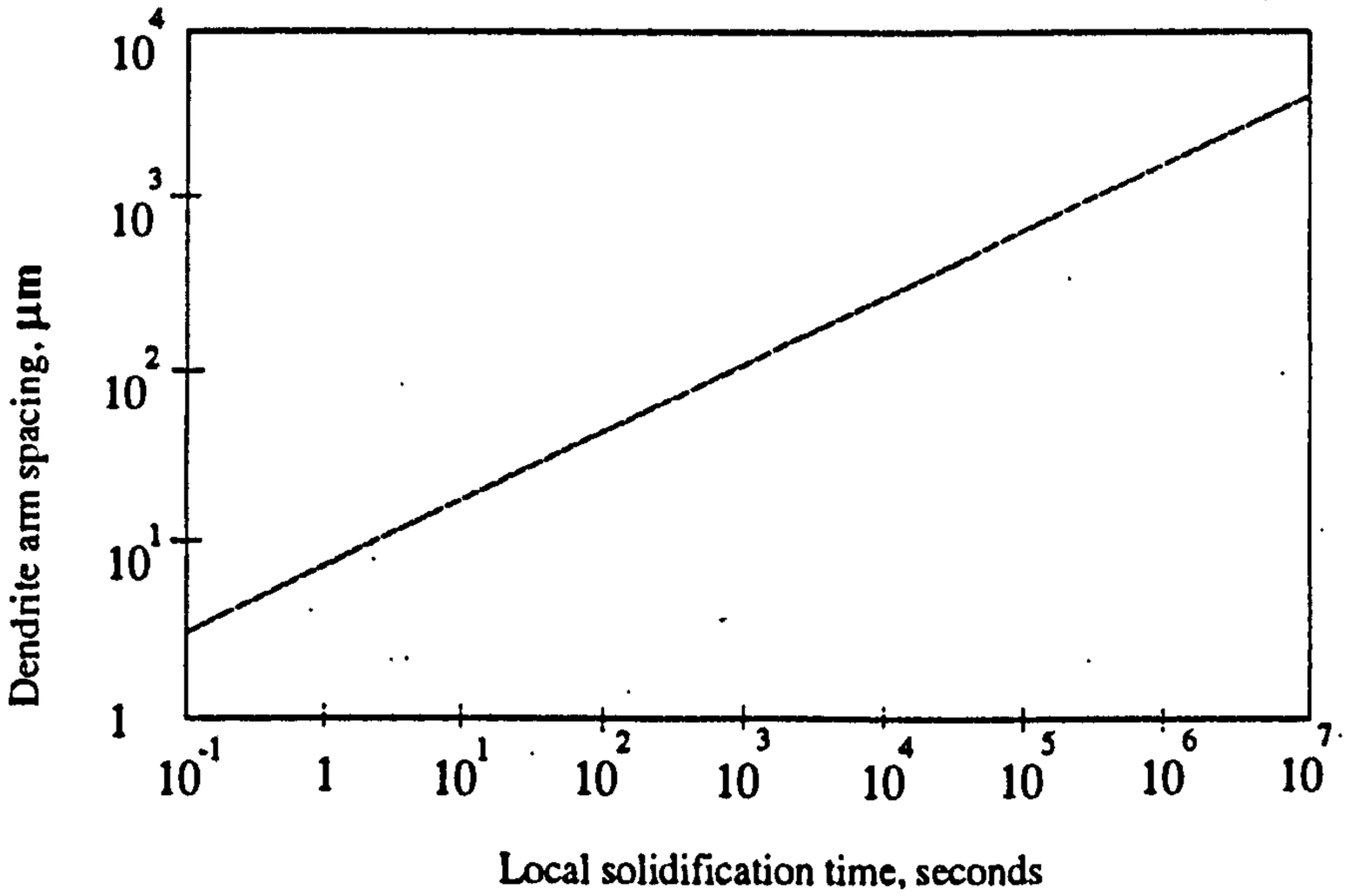

Figure 3.7 Relationship between dendrite arm spacing and local solidification time, in Al - 4.5 % Cu alloy.

3.2 Segregation

The redistribution of solute during solidification results in chemical and structural heterogeneities or segregation. The fundamental theory was briefly discussed in previous sections, therefore what follows is a short review of the segregation phenomena as they pertain to the industrial production of aluminium ingot.

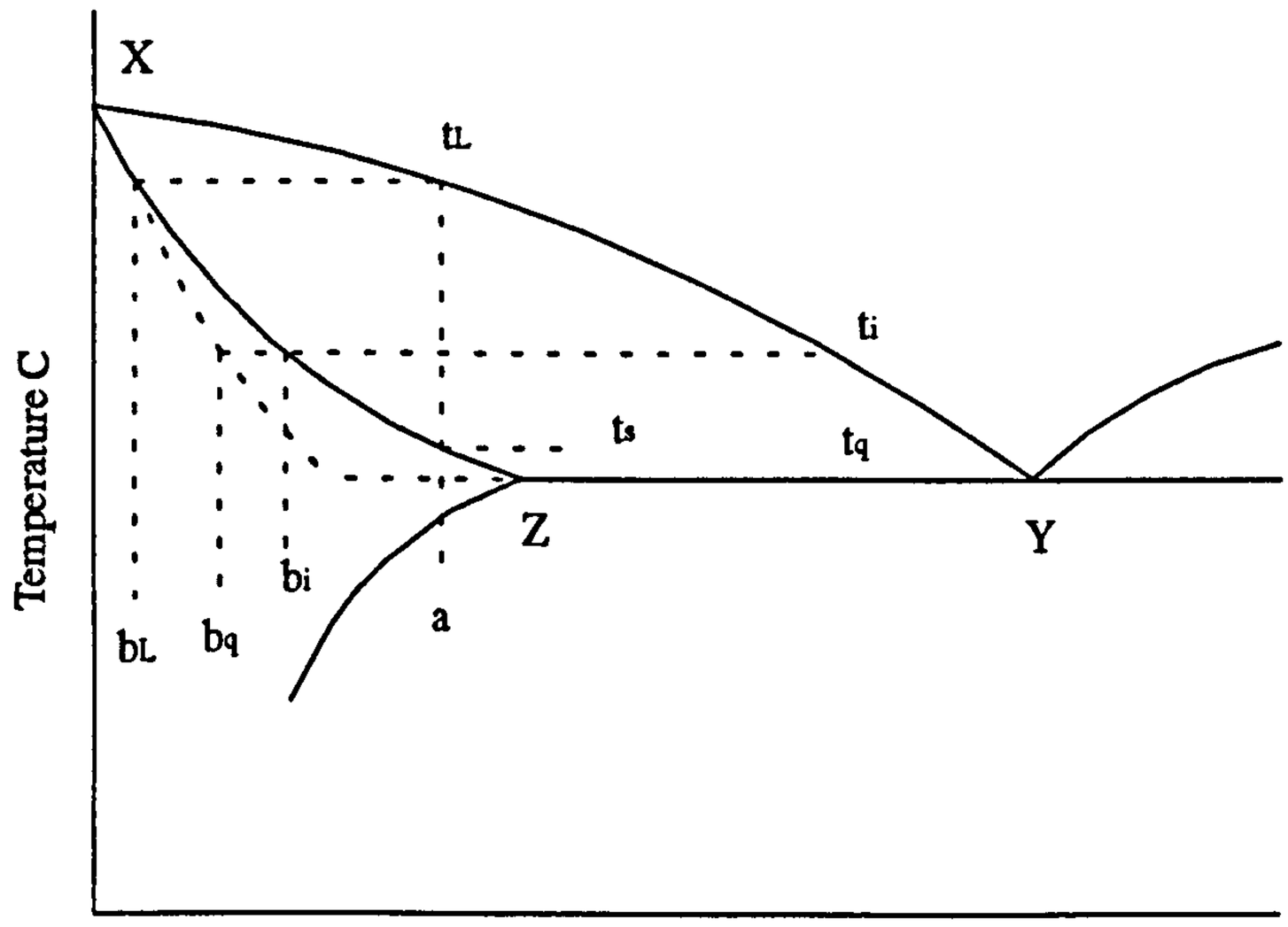

Figure 3.8 Partial phase diagram of a typical binary eutectic alloy.

With either equilibrium or non-equilibrium conditions of cooling, the composition of the primary nuclei which form during the initial stages of solidification is the same, being that of point b_L , as illustrated[78.] in Figure 3.8. The composition of the material which solidifies to form the secondary and tertiary arms of the dendrites can be read from the same diagram, for the metal has a composition corresponding to progressively lower points on the solidus line XZ. At each successively lower temperature the metal which separates contains more and more of the solute than is present in either the original nuclei or the solid deposited at any preceding stage. Solidification under non-equilibrium conditions does not provide sufficient time for the process of diffusion to remove the gradient of concentration with in the crystal, and thereby to induce a uniform composition throughout the solid.. As a consequence, the average composition

of a growing crystal at an intermediate temperature, t_i , during solidification is b_q instead of b_i , as it would be if cooling were taking place under equilibrium conditions.

Depending whether the concentration gradient is the result of[79] short-range or long-range mass transport, it is classified as micro- or macrosegregation accordingly.

3.2.1 Microsegregation

Segregation on the scale of dendrite arms spacing or across a grain would be classed as microsegregation and is usually expressed by Scheil equation (Equation 2.15).

3.2.1.1 Coring

Concentration gradient between dendrite arms is known as coring, and it determines[80] the extent of homogenisation which is required after casting.

3.2.1.2 Grain boundary segregation

Another type of microsegregation which is also effected by homogenisation, is grain boundary segregation, which is primarily the result of the accumulation of mainly insoluble elements and intermetallic compounds (mainly Fe, and Fe-bearing compounds), at the grain boundary.

3.2.2 Macrosegregation

Macrosegregation as stated before, refers to long range variation in composition, such as those found between the outside and the centre of an ingot.

3.2.2.1 Normal segregation

This type of segregation is defined[63] in terms of motion of solute parallel to the direction of solidification, and can be represented by a single curve, relating the concentration of a solute to the distance from the start of solidification as shown in Figure 3.9.

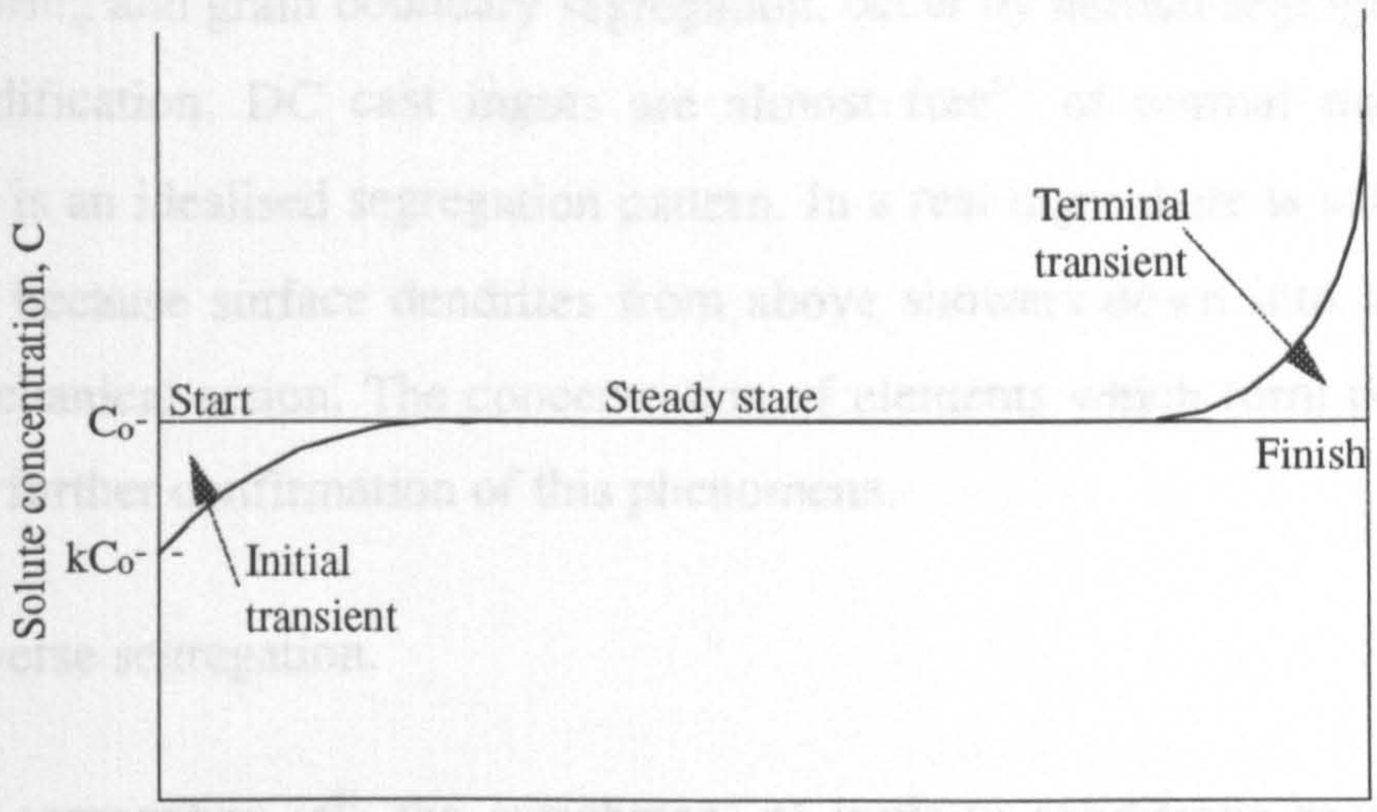

Figure 3.9 Normal segregation.

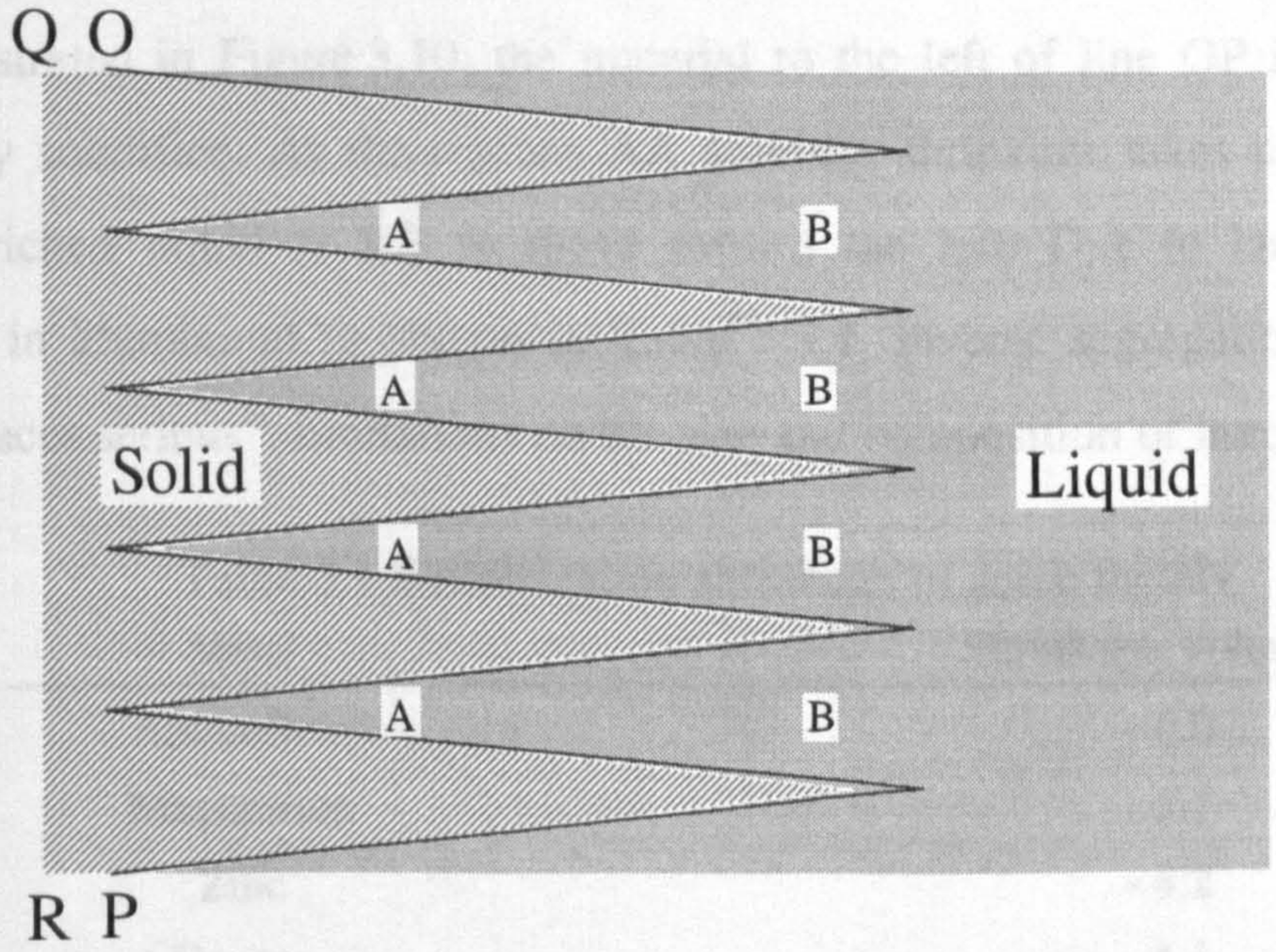

Figure 3.10 Inverse segregation.

Both coring and grain boundary segregation, occur by normal segregation, but due to rapid solidification, DC cast ingots are almost free[66.] of normal macrosegregation. Figure 3.9 is an idealised segregation pattern. In a real ingot there is solute depletion at the centre because surface dendrites from above showers down into the centre under purely mechanical action. The concentration of elements which form peritectics, at the centre is a further confirmation of this phenomena.

3.2.2.2 Inverse segregation.

Inverse segregation is[81.] the enrichment of initially solidifying regions with lower melting point compositions due to the flow-back along the interdendritic channels of normally segregated residual liquid. The cause and mechanism of inverse segregation has been extensively investigated and discussed[80.82.83.84.85.86.87.88.], a consensus of opinion supported by experiments (originally proposed by Scheil[89.]), identify the shrinkage that in most alloys accompanies solidification as the cause of the "flow-back" of the solute enriched liquid in a direction opposite to that of the solidification front.

As illustrated in Figure 3.10, the material to the left of line OP is assumed to be completely solidified. As the regions AA solidify, shrinkage takes place, causing the solute enriched liquid at BB to move toward the left. Due to large solidification shrinkage in aluminium as shown in Table[63.] 3.1, inverse segregation in DC casting process places serious[86.] limitations on the size and composition of ingot made.

Table 3.1 Solidification shrinkage of some metals.

Metal	Shrinkage, volume %
Aluminium	- 6.0
Magnesium	- 5.1
Zinc	- 4.2
Copper	- 4.1
Sodium	- 2.5
Iron	- 2.2
Lithium	- 1.65
Gallium	+ 3.2
Bismuth	+ 3.3

The inverse segregation with serious practical implication as discussed by Kirkaldy and Youdelis[81], and Yu and Granger[86], occurs when eutectic or other low melting point liquid, which are high in solute, are sucked out through the boundary QR (Figure 3.10) by a difference of pressure arising from the contraction of solidifying metal away from the mould i.e. by exudation mechanism. The liquid which has exuded, solidified on the surface of the metal, in the form of small drops, known as "sweat" or "bleb" or in extreme case "bleed" or "liquation".

A typical inverse segregation in the "chill" zone of a DC cast extrusion ingot is shown in Figure 3.11.

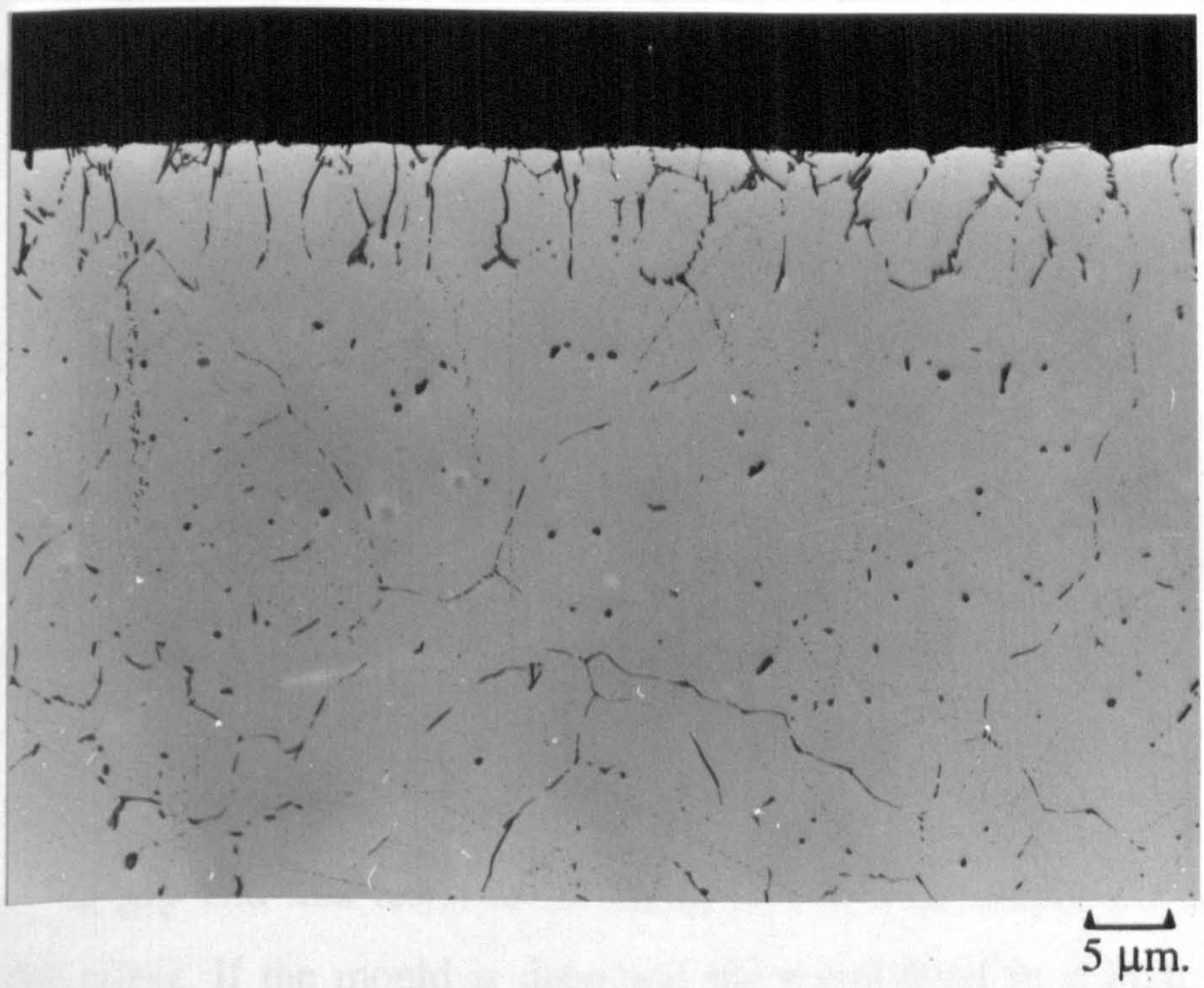

Figure 3.11 Typical inverse segregation zone in DC cast AA6063 extrusion ingot. x 400

3.3 D C Ingot Casting Process Development.

The effort to improve the quality of DC cast ingot as well as improve the economy of the process, has been fruitful particularly in the development of level transfer or hot top casting and the implementation of shallow mould or low head DC casting.

3.3.1 Level transfer or Hot top casting,

Conventionally liquid metal would be delivered to a distribution basin, and then lowered to the individual moulds through refractory tubes ("dip tube") and a floating flow regulator ("float"), as shown schematically in Figure 3.12. The bilevel delivery of the molten metal to the moulds was thought to cause excessive turbulence, disturbing the oxide skin on the molten metal surface, leading to further oxide, "dirty metal" and hydrogen pick up.

The solution to the problems was the level transfer or hot top casting, whereby the moulds are fitted in the metal distribution basin (casting table), eliminating the bilevel delivery as shown in Figure 3.13.

3.3.2 Shallow mould or Low head casting,

In the DC casting process, the liquid metal is subjected to primary cooling by conduction of heat through the wall of the water-cooled mould and to secondary cooling through direct application of water to the solid shell as it emerges from the mould. At some point after the primary cooling, the solidifying metal shrinks away from the mould leaving an air-gap. Extraction of heat through the mould wall is greatly reduced by the air-gap and this leads to reheating of the shell before the secondary cooling can take effect. If the mould is deep and the metal level in it high, then the air-gap will extend over a greater length of the mould, which could leave to the formation of subsurface band of coarse cell[90.] grains, severe inverse segregation and even liquation. Therefore a shallow mould or low head casting has been adopted. Figures 3.14 and 3.15, illustrate the heat extraction for conventional and low head casting.

Modern DC casting technology incorporates both hot top and low head casting .

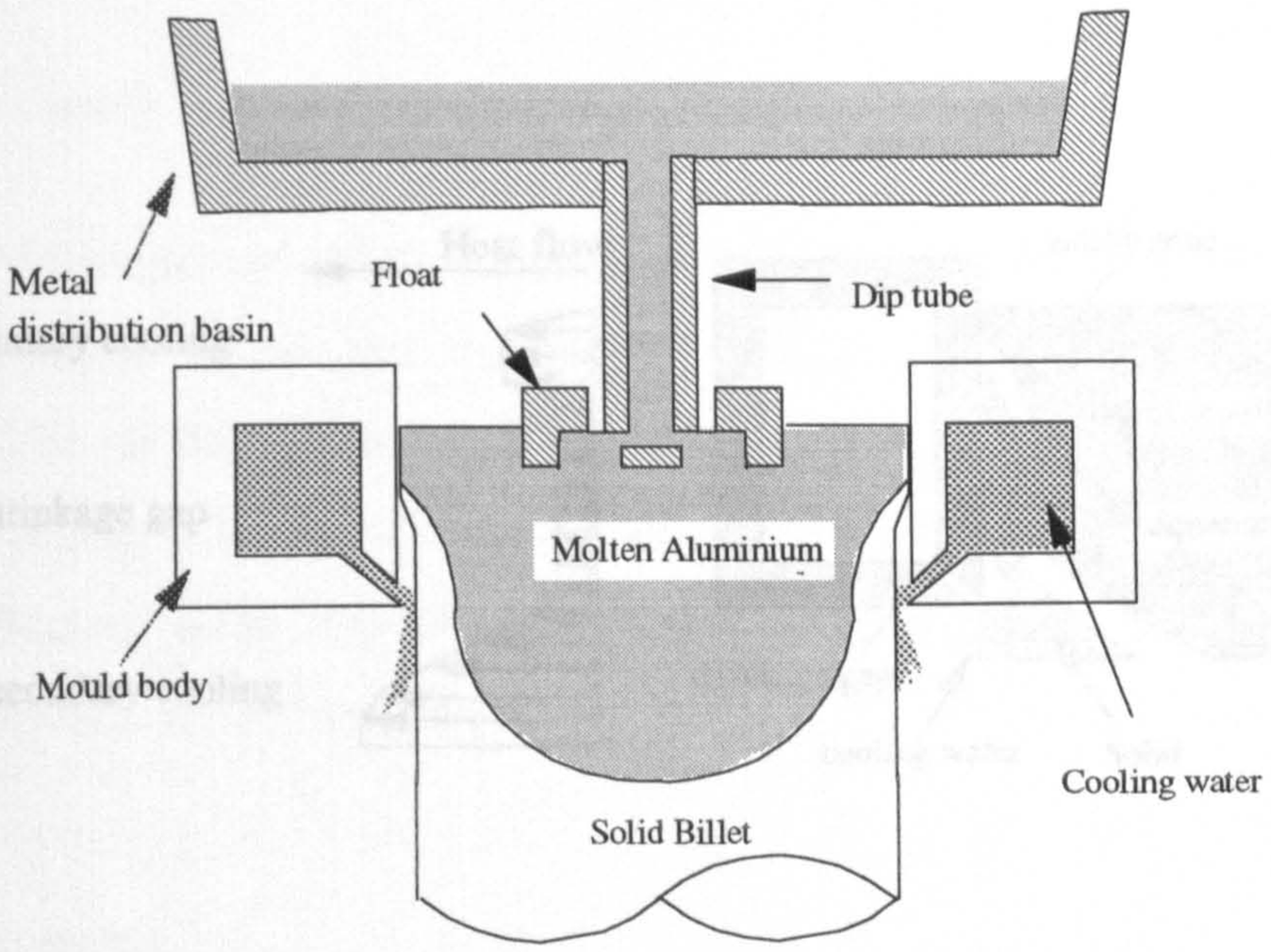

Figure 3.12 Conventional D C casting

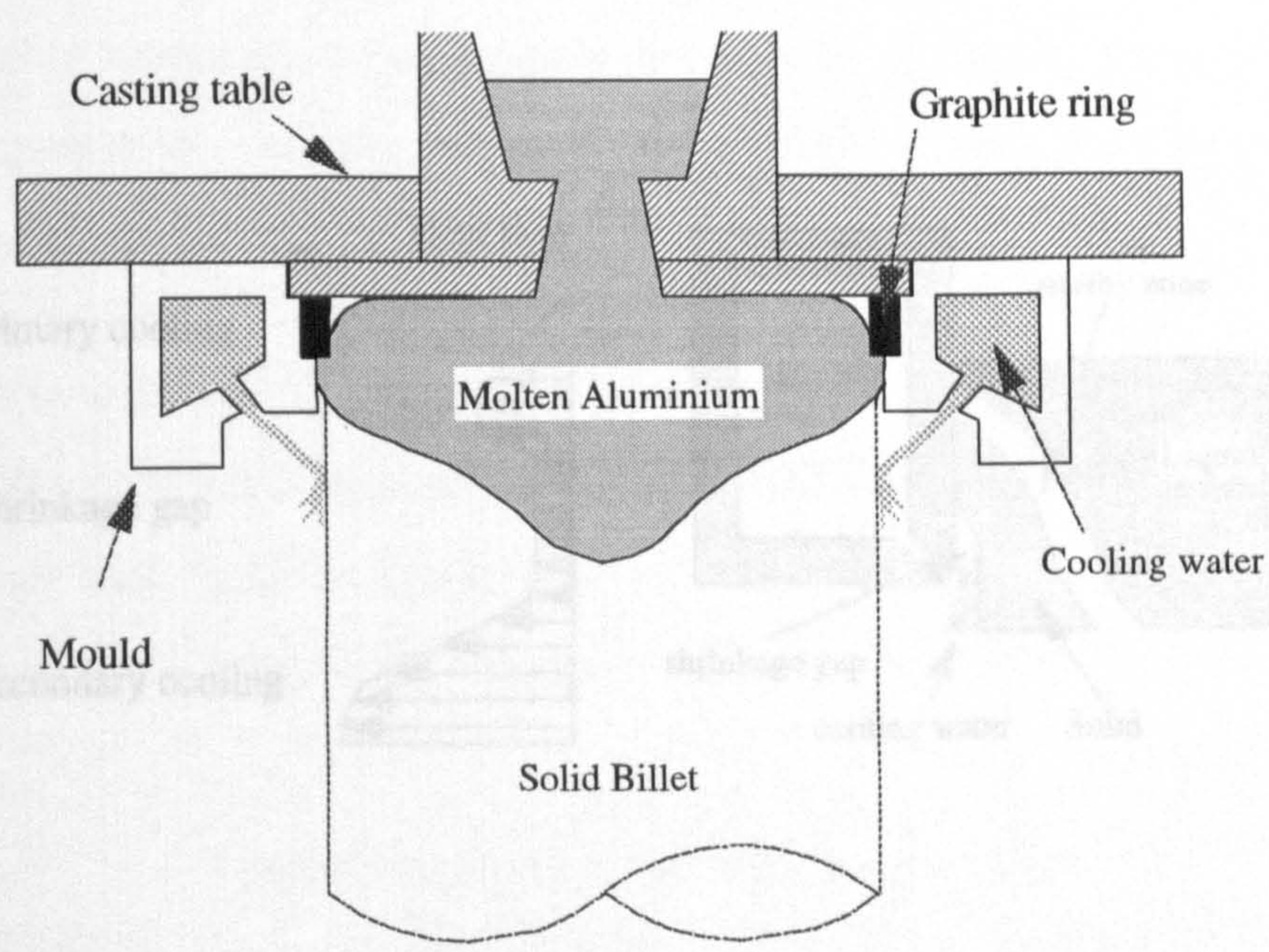

Figure 3.13 Hot top D C casting

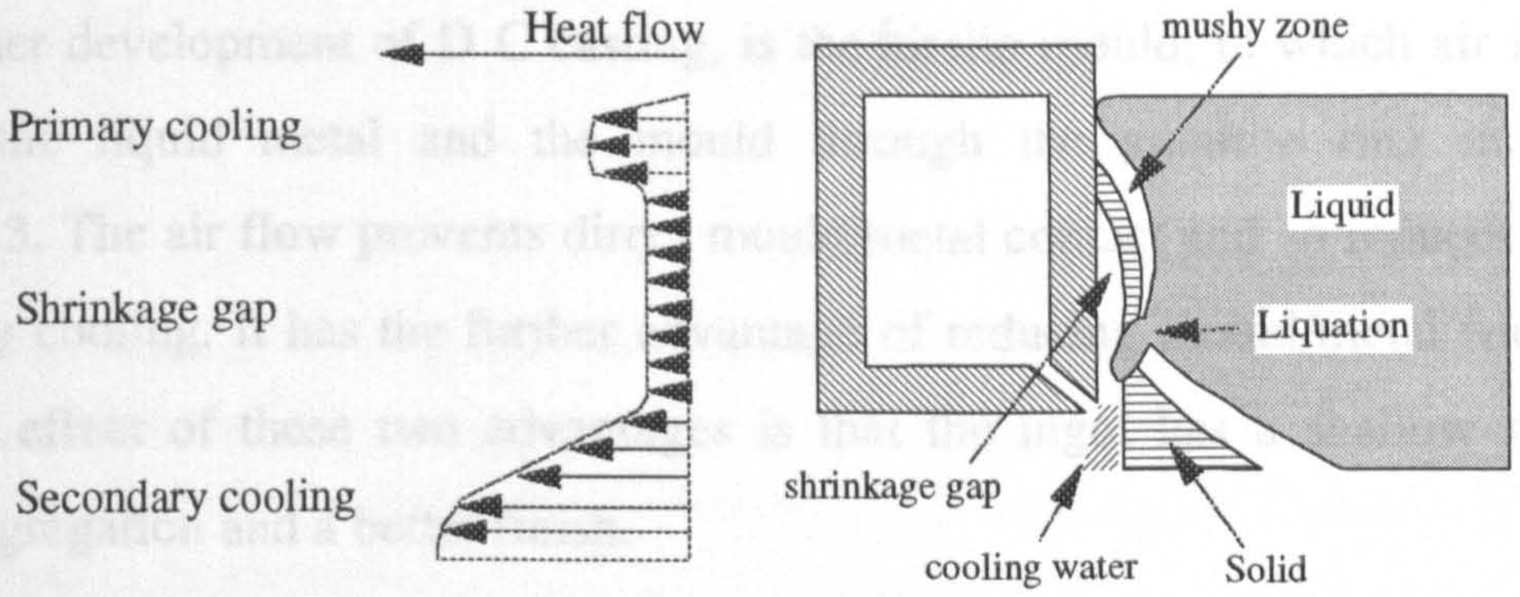

Figure 3.14 Liquation in shrinkage gap zone in conventional casting.

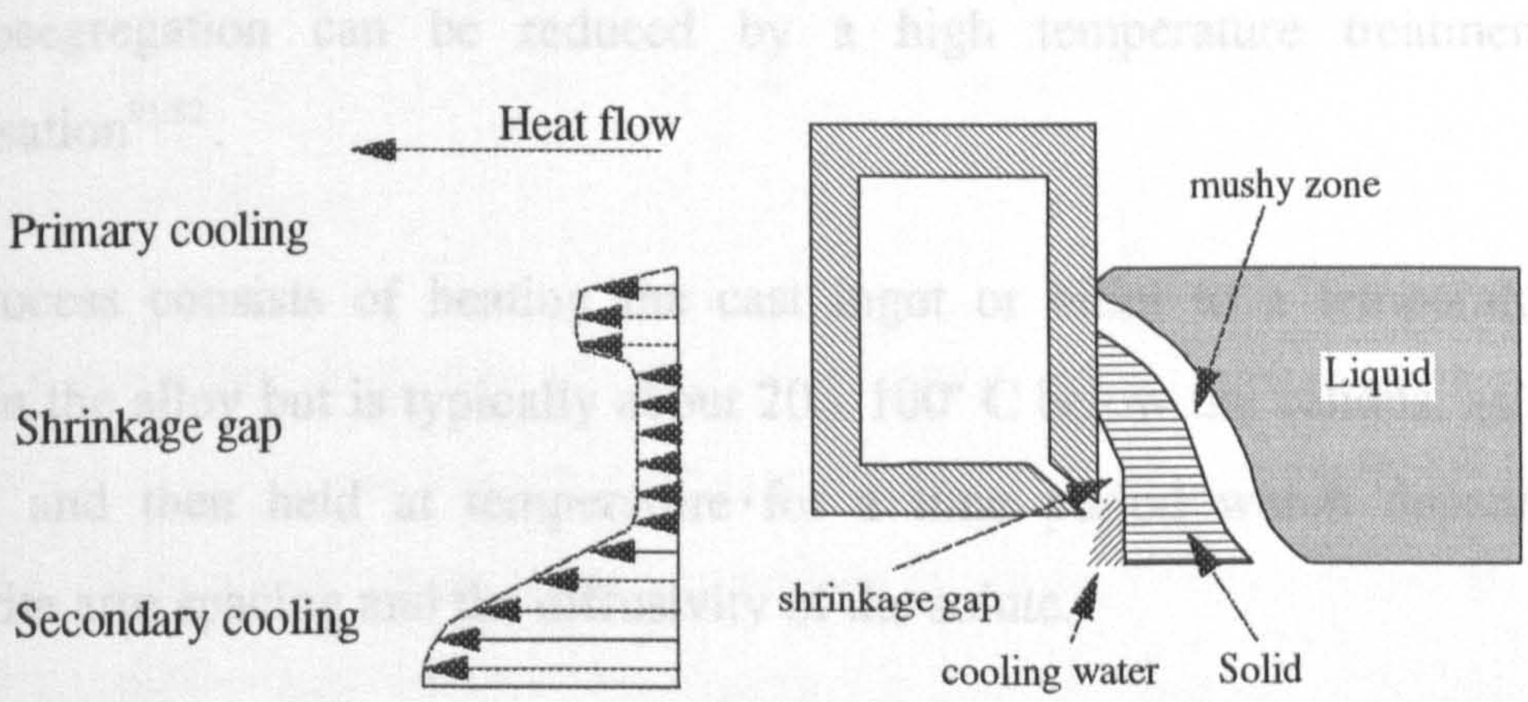

Figure 3.15 Low head casting.

3.3.3 Airslip casting

A further development of D C casting, is the Airslip mould, in which air is injected between the liquid metal and the mould through the graphite ring indicated in Figure 3.13. The air flow prevents direct mould/metal contact and so reduces the effect of primary cooling. It has the further advantage of reducing mould/metal friction. The combined effect of these two advantages is that the ingot has a shallow sump, less surface segregation and a better finish.

3.4 Homogenisation

Industrial casting processes including DC casting of aluminium extrusion ingot (billet), involves rapid and non-equilibrium solidification, resulting in heterogeneities, namely micro- and macrosegregation which were discussed.

Unacceptably severe macrosegregation can only be physically removed by scalping, but microsegregation can be reduced by a high temperature treatment termed homogenisation[91.92].

The process consists of heating the cast ingot or billet to a temperature which depends on the alloy but is typically about 20 - 100° C below the solidus, as listed[93] in Table 3.2, and then held at temperature for a time period which depends on the interdendrite arm spacing and the diffusivity of the solute.

Table 3.2
Typical homogenisation temperature range.

Alloy series	Solidus (° C)	Homogenization temp. (° C)
1000	640 - 650	560 - 600
2000	500 - 650	480 - 530
3000	630 - 645	530 - 620
5000	570 - 630	380 - 550
6000	580 - 620	560 - 600
7000	> 500	400 - 440

A useful expression for approximate prediction of times and temperature required to homogenise a given cast structure is given by Flemings[41]:

$$\delta_i = e^{-\pi (D_s t / l_o^2)} \tag{3.5}$$

where;

δ_i is the index of residual microsegregation, = 1 before any homogenization and = 0 after complete homogenization,
D_S is the diffusion coefficient in the solid at the temp. of homogenisation of element (assumed to be constant)
t is the homogenization time and,
l_o is one-half the dendrite arm spacing.

Therefore the effectiveness of homogenisation is strongly dependent on the diffusion distance, that is the dendrite arm spacing and the diffusivity of the alloying elements and the impurities.

Simultaneous with constitutional equalisation, however, a number of additional diffusion related processes may occur[94], some of which are:

3.4.1 Surface oxidation

Extensive surface oxidation of the casting results during thermal exposure unless a very low O_2 and H_2O partial pressure is maintained[95] in the furnace atmosphere. The problem is particularly severe with magnesium containing alloys where blackening due to MgO formation can occur. The blackening can be reduced or eliminated by the introduction of fluorides and the control of moisture in the furnace atmosphere[96,97].

3.4.2 Hydrogen loss or pickup

Normally, homogenisation results in the drop of dissolved hydrogen content of the casting. The hydrogen release is related to the temperature and the heating rate. Too low a temperature results in ineffective release, too high temperature and rapid heating result in sudden gas release and large subsurface and interdendritic voids left by the escaping hydrogen[94]. If surface oxidation occurs during thermal exposure, the escape of

hydrogen across the casting surface is impeded by the oxide layer[91.] and large sub-surface cavities or surface blistering often result in the homogenised material.

Heat treatment in certain atmospheres, e.g. high humidity[98.99.] or sulphur[100.] contaminated atmosphere an increase in the hydrogen content of metal i.e. hydrogen pick-up has been observed. Magnesium containing alloys are particularly prone to surface oxidation and hydrogen pick-up.

3.4.3 Localised melting

Heavily cored areas of the casting, such as cell boundary (microsegregation), ingot surface (inverse-segregation) and centreline segregation (normal-macrosegregation), can undergo localised melting during the homogenisation.

4. THEORY OF HYDROGEN IN ALUMINIUM

Hydrogen is the only gas which is appreciably soluble in both solid and liquid aluminium and its alloys.

Sieverts' classic observations that the solubility of hydrogen in dilute solution is a parabolic function of the pressure in the diatomic gas phase established empirically that hydrogen dissociates on dissolution in metals, yielding a monatomic solute:

$$(H_2)_g = 2[H]_{Al} \qquad (4.1)$$

A combination of x-ray investigation and direct density measurements[101], established that the solid solution was of the interstitial type when the system was in a state of thermodynamic equilibrium.

Other experiments supporting the interstitial character of the gas-metal solutions are the measurements of diffusivities of gases in metals. Fast[101] cites the examples of diffusion coefficients of nitrogen and carbon in iron (interstitial solution) at 700°C, which are approximately 10^4 times larger than that of sulphur and 10^5 times larger than that for phosphorous (substitutional solutions) under the same conditions.

4.1 The Interstices In The Rigid Sphere Models.

The face centred cubic (fcc) structure of aluminium provides two potential interstices for the hydrogen atom in aluminium hydrogen system namely the octahedral and the tetrahedral interstices.

Calculating the radii of the largest spheres that can be accommodated in the octahedral (r_6), and the tetrahedral (r_4) interstices without distorting the structure, from: $r_6 = 0.414\,R$ and $r_4 = 0.225\,R$, where R is the atomic radii of the metal, and assuming the Bohr radius, 0.053 nm to represent the "size" of the hydrogen atom. The octahedral interstice appears to be the more feasible site for the hydrogen in the fcc metals. The sizes of the interstices for various metals are tabulated in Table 4.1.

Table 4.1
Atomic radii and the sizes of interstices in some metals (nm).

Metal	atomic radii (R)**	octahedral (r_6) *	tetrahedral (r_4) *
Al (fcc)	0.143	0.059	0.032
Ag	0.144	0.060	0.032
Cu	0.128	0.053	0.029
Fe	0.126	0.052	0.028
Ni	0.125	0.052	0.028
Co	0.126	0.052	0.028
Ti (hcp)	0.171	0.071	0.038
Zr	0.160	0.066	0.036
Ti (bcc)	0.173	0.020	0.050
Zr	0.161	0.018	0.047
Fe	0.128	0.015	0.037

* For bcc metals; $r_6 = 0.115\ R$ $r_4 = 0.291\ R$, and for hcp metals, the same as for fcc.
** Gold-schmidt atomic radii, Smithells Metal Reference Book, 7th edition, Butterworth-Heinemann Ltd., Oxford, 1992.

4.2 Electronic And Chemical Factors.

The rigid sphere model discussed in the previous section illustrated the influence of the size factor on the solubility of hydrogen in a metal.

Nevertheless it assumes the solvent metal to be composed of rigid spherical atoms which are in contact with each other. Further more it implies that the solute atoms occupy completely void interstices without any interaction with the solvent atoms. Therefore this model does not accommodate the electronic theory of metals.

This theory[102], describes a metal as a three dimensional lattice of positive ions, floating freely as it were, in a dense electron "gas" filling the space between the ions. The mutual electrostatic repulsion of the ions causes them to stay as much apart as possible and their distances adjust themselves such that the pressure of the electron gas, the electrostatic attraction between the ions and the electrons and the mutual repulsion of the ions compensate each other. This results in the ions arranging themselves in a regular lattice.

In some metals the ions are relatively[102.] far part, e.g. in sodium 70% of the metal volume is taken up by the electrons gas. In copper, however, the ions are very closely together.

The space between the metal atoms can therefore, in many cases, be larger than would be expected from the rigid spheres model. On the other hand, this space is not empty as in the model, because they are filled with electrons. Consequently, the introduction of an atom into an interstice implies a strong electronic interaction with the metal.

4.2.1 The embedded atom theory.

The embedded atom theory is a relatively new semi-empirical theory, proposed by a number of physicists[103.104.105.], to explain various hydrogen phenomena in metals and is based on the "quasi-atom"[106.] or "effective medium" [107.] theory.

This model is[108.] an extension of the simple free-electron model; only the valence electrons of the metal are considered to contribute to the electron charge density, and the ion-cores (the nuclei plus inner-shell electrons) are represented by a smeared-out positive charge of density equal to that of the free electron. The electron charge distribution within the bulk of the metal is uniform.

4.3 Thermodynamics Of Solution

With the assumption that the solute is accommodated as non-interacting atoms, all occupying equivalent interstitial sites, no impurities are present in the system which can form stable hydrides, the dissolution process can be represented by (Equation. 4.1):

$$(H_2)_g = 2[H]_{Al}$$

Assuming ideal behaviour for the gas and that for the dilute interstitial solution, Henry's law is applicable, the equilibrium can be stated by:

$$K = \frac{a^2_{[H]}}{a_{(H_2)}} = \frac{(m/m^{\ominus})^2}{p/p^{\ominus}} \tag{4.2}$$

which yields the Sievert's isotherm:

$$\frac{m}{m^{\ominus}_p} = \left[\frac{p}{p^{\ominus}}\right]^{0.5} \tag{4.3}$$

where:

$a_{(H_2)}$ is the activity of the gas referred to the pure gas at a standard pressure, $p^{\ominus}$, usually chosen as 101325 Pa (1 atm.),
$a_{[H]}$ is the activity of the solute in equilibrium with $a_{(H_2)}$,
m is the solute molality in equilibrium with a pressure, p,
$m^{\ominus}_p$ is the solute molality in equilibrium with the pressure, $p^{\ominus}$,and,
$m^{\ominus}$ is a value of molality within the range of Henrian activity selected as the standard state for the solute.

The variation of equilibrium constant with temperature is described by an equation known as the van't Hoff isochore. The isochore is derived[109.] by combining the van't Hoff isotherm;

$$\Delta G^{\ominus} = -RT \ln K \tag{4.4}$$

and the Gibbs-Helmholtz equation:

$$\frac{d(\Delta G^{\ominus})}{dT} = \frac{\Delta G^{\ominus} - \Delta H^{\ominus}}{T} \tag{4.5}$$

Differentiating the van't Hoff isotherm with respect to temperature yields,

$$\frac{d(\Delta G^{\ominus})}{dT} = -R \ln K_p - RT \frac{d(\ln K_p)}{dT}$$

multiplying both sides by T gives;

$$T \frac{d(\Delta G^{\ominus})}{dT} = -RT \ln K_p - RT^2 \frac{d(\ln K_p)}{dT}$$

and substitution of $T \frac{d(\Delta G^{\ominus})}{dT} = \Delta G^{\ominus} - \Delta H^{\ominus}$ and

$-R\,T\,\ln\,K_p\,=\,\Delta\,G^{\ominus}$ in the above equation produces;

$$\Delta\,G^{\ominus}\,-\,\Delta\,H^{\ominus}\,=\,\Delta\,G^{\ominus}\,-\,R\,T^2\,\frac{d(\,\ln\,K_p\,)}{d\,T}$$

and hence rearranging, gives the van't Hoff isochore:

$$\frac{d(\,\ln\,K_p\,)}{d\,T}\,=\,\frac{\Delta\,H^{\ominus}}{R\,T^2} \qquad (4.6)$$

Based on equation 4.2 and the isochore, the van't Hoff isobar is arrived at:

$$\frac{d}{d\,T}(\,\ln\,K_p\,)\,=\,2\,\frac{d}{d\,T}\left(\ln\left(\frac{m}{m^{\ominus}}\right)\right)_p\,=\,\frac{\Delta\,H^{\ominus}}{R\,\,T^2} \qquad (4.7)$$

Since for a restricted temperature range, the standard enthalpy of solution ($\Delta\,H^{\theta}$) can be considered constant, integration of Equation 4.7 yields:

$$\ln\left(\frac{m}{m^{\ominus}}\right)_p\,=\,-\,\frac{\Delta\,H^{\ominus}}{2\,R\,T}\,+\,\text{constant} \qquad (4.8)$$

The Equation 4.8 can be modified to incorporate pressure as a variable yielding:

$$\ln\left(\frac{m}{m^{\ominus}}\right)\,-\,1/2\,\ln\left(\frac{p}{p^{\ominus}}\right)\,=\,-\,\frac{\Delta\,H^{\ominus}}{2\,R\,T}\,+\,\text{constant} \qquad (4.9)$$

4.4 Interstitial Hydrogen Solution in FCC Metals

4.4.1 Entropy of solution

The solution of hydrogen in pure metals reflects the random distribution of hydrogen atoms among the available lattice interstices. The entropy of mixing is determined by the statistical distribution of the solute atoms among identical interstitial sites and is expected to be the same for metals of the same crystallographic form.

The constant in Equation 4.9 includes a term, X, relating the different standard states to which the activities of the diatomic gas and the atomic solute are referred and the

particular units adopted for the hydrogen content but is otherwise determined by entropy change in the solution, i.e.:

$$\text{Constant} = X + \Delta S_d + \Delta S_p + \Delta S_m \qquad (4.10)$$

where:

ΔS_d is the entropy of dissociation of diatomic hydrogen

ΔS_p is due to change in partition function for the atoms on dissolution

ΔS_m is the entropy of mixing for solute atoms in the metal.

The value of X is determined by the convention adopted and the contributions from ΔS_d and ΔS_p are due to inherent characteristics of the gas, so that any difference found in the value of the constant for metal/hydrogen system must be due only to differences in the entropy of mixing for the solute, ΔS_m.

In Figure 4.1, hydrogen solubilities in equilibrium with the gas at a pressure of 1 atm (101325 Pa) for some pure FCC metals are fitted to Equation 4.9, using critically assessed values[110.] expressed as ratios of numbers of solute atoms, N_H, to the numbers of interstitial sites, N_I. The extrapolations converge to the same intercept at $1/T = 0$, confirming that the entropies of mixing for hydrogen in the various metals are equal.

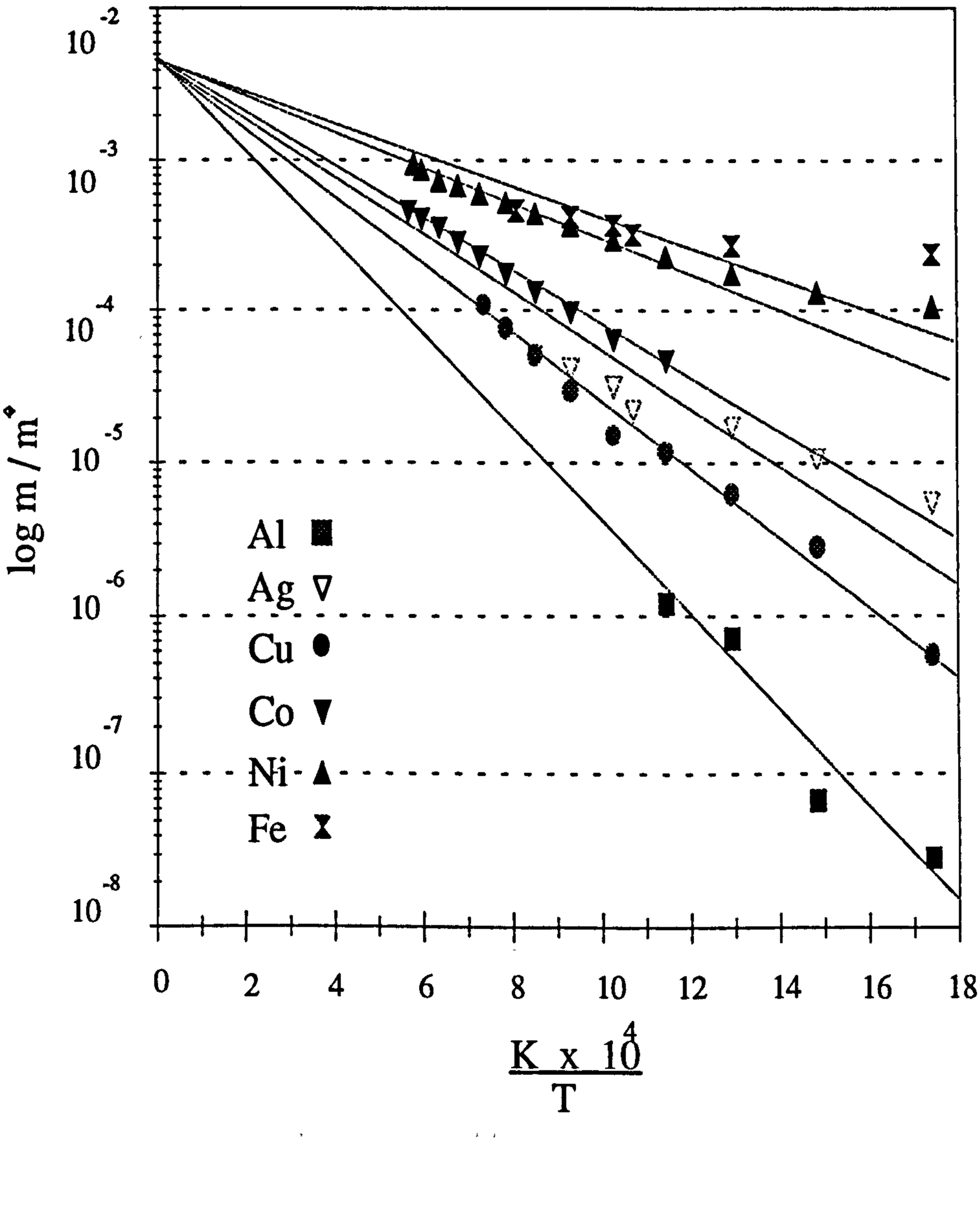

Figure 4.1 Solution of hydrogen in FCC metals

4.5 Units and Symbols for Hydrogen Content,

In the SI system the quantitative relation between a solute, B and its solvent, A, is represented by either the molality, $m_B = n_B / n_A M_A$ or the concentration, $C_B = n_B / V$ where, n_B , n_A , M_A and V are respectively the number of moles of B, the number of moles of A, the mass of A and the volume of the phase.

However, hydrogen content is commonly expressed in a pseudo-unit, the "$cm^3/100g$" which is:

- neither a recognised unit in SI system,
- nor, it is rational to express a quantity of atomic solute in terms of the volume occupied by its gaseous diatomic equivalent, especially when the temperature and pressure at which the volume of the diatomic gas is to be measured are not given explicitly.

The matter can be resolved[111.] by a simple expedient. In the SI system the molality of a solute, m, can be referred to any standard value. Since hydrogen is virtually ideal at temperatures of interest, the unit "cm^3/ 100g" can be assimilated into SI system by setting the standard value, m^{θ} , equal to 8.93×10^{-4} mol kg^{-1} , which is the molality of a solution of atomic hydrogen formed when 1 cm^3 of diatomic hydrogen measured at 273 K and 101325 Pa (1 atm), dissolves in 100 g of metal.

This both satisfies international conventions on units and symbols[112.113.] and yields values for m / m^{θ} numerically equal to and interchangeable with values given elsewhere as "cm^3 / 100g". Throughout the thesis "cm^3 / 100g" and m / m^{θ} are synonymous terms for arbitrary hydrogen content. To accord with established practice, another synonym, "s / s^{θ}", is used where the value of m / m^{θ} is a "solubility", i.e. the hydrogen content in equilibrium with the gas phase at standard pressure p^{θ} , usually 101325 Pa (1 atm).

4.6 Solubility of Hydrogen in Aluminium,

Considering the solubility of hydrogen in aluminium in idealised solution, outlined in sections 4.1 to 4.3, the intrinsic solubility would be implied.

Talbot defines[111.]: "The intrinsic solubility of hydrogen in aluminium or a phase in one of its alloys is the quantity of hydrogen contained in a prescribed mass of a single crystal with an undisturbed lattice, containing the equilibrium vacancy population when in equilibrium with a gas phase of normal diatomic hydrogen at prescribed temperature and pressure."

Obviously such a structural perfection and compositional homogeneity is unrepresentative of industrially produced metal and difficult to achieve even under laboratory conditions.

Even when gross defects are not present the failure[114] of Equation 4.3 and 4.8 to represent observed behaviour and anomalous diffusion effect discussed later indicates, that hydrogen is partitioned between the interstitial solution and other occluded forms, referred to as hydrogen trap sites[115].

$$1/2\ H_2 = [H]_{(\text{interstitial solution})} = H_{(\text{trap sites})} \qquad (4.11)$$

The identified trap sites can be divided into three main types[115],

4.6.1 Atomic traps,

In principle the association of solute atoms with lattice defects is expected[116]. Foster et al[117] produced direct autoradiographic evidence for an association of hydrogen with dislocations and other defects in aluminium loaded with radioactive isotope ^3H (tritium).

Other evidences are the work of Wriedt and Darken[118], which showed that prior cold working enhanced the solubility of nitrogen in steel which they attributed to dislocations generated by plastic deformation. Mokaram[119] also attributed the anomalous diffusion of hydrogen in copper to the association of the solute with quenched in lattice vacancies.

4.6.2 Molecular traps

There are two kinds of molecular trap, the first kind is the gross internal flaws which are generated in the course of manufacture. The most familiar are:

1. Interdendritic porosity in ingots cast from liquid melt with excessive hydrogen content[115],

2. Extraneous inclusions, notably fragments of oxide entrapped in the liquid metal during melting and casting[120],
3. Defects generated mechanically during fabrication, including cracks, and incomplete welding at roll-bonded core/cladding interface.

The other kind of trap is due to spontaneous precipitation of hydrogen with in the solid metal producing widely distributed very small spherical pores identified by Talbot and Granger[121].

4.6.3 Chemical traps

The trapping of hydrogen due to the formation of stable hydrides is termed chemical trapping.

Neither pure nor the common alloys of aluminium form stable hydrides under conditions of metallurgical interest, therefore chemical trapping is not a consideration for aluminium and its alloys except for:

1. Hydride formation by sodium impurity in very pure aluminium[122].
2. The potential for hydride formation in aluminium-lithium alloys.

4.7 Determination Of Solubility

As stated in section 4.6, when experimentally determined, the term solubility denotes the total hydrogen contained in interstitial solution and other occluded forms.

There are three basic methods which have been used to determine the solubility of hydrogen in metals.

1. Sieverts' method[123]. This method, as used by Ransley and Neufeld[124] and Opie and Grant[125], consist of determining the volume of a system above the molten metal, known as the "dead space"[124], at a given temperature and pressure, using an insoluble gas. The system is then evacuated and the soluble gas is introduced at the same temperature and until the same pressure is reached. Obviously a larger volume of soluble gas will be required, the difference in volume being the solubility.

2. Eichenauer's method[126.127]. Eichenauer equilibrated the liquid metal with a hydrogen atmosphere and then rapidly evacuated the system above the sample. The quantity of dissolved hydrogen was then determined by collection in a low pressure system as it subsequently diffused out of the metal.
3. Quenching method. To determine the solubility of hydrogen in liquid copper alloys, Jones and Pehlke[128] and Thomas[129], equilibrated the metal with hydrogen and then rapidly quenched solid samples. The hydrogen content of these samples was then determined using a low pressure collection system.

Similar method was adopted by Ransley and Neufeld[124], and Anyalebechi[130] in determining the solubility of hydrogen in solid aluminium and some of its alloys.

4.7.1 Solubility of hydrogen in liquid pure aluminium

The solubility of hydrogen in liquid aluminium using one or another of the three techniques discussed have been extensively determined.

The reported solubility at 973K and 101325 Pa, from works extending back to 1932 are listed in Table 4.2.

Table 4.2 Hydrogen solubility in liquid pure aluminium at 973K and 101325 Pa.

Author	Year	Solubility $cm^3/100g$
Rotgen and Braun[131]	1932	0.08
Bircumshaw[132]	1935	0.23
Baukloh and Oesterlen[133]	1938	0.95
Baukloh and Redjali[134]	1942	0.45
Ransley and Neufeld[124]	1948	0.92
Opie and Grant[125]	1950	0.90
Ransley and Talbot[135]	1955	0.89
Eichenauer et al[136]	1961	0.63
Anyalebechi[130]	1985	0.93

More recently the solubility of hydrogen in aluminium had been systematically measured , in works carried out at Brunel university under the supervision of Dr Talbot. Their results are presented and discussed next.

Figure 4.2 is a Van't Hoff plot of the results in Table 4.3 with equivalent results by Ransley and Neufeld[124.] and Opie and Grant[125.].

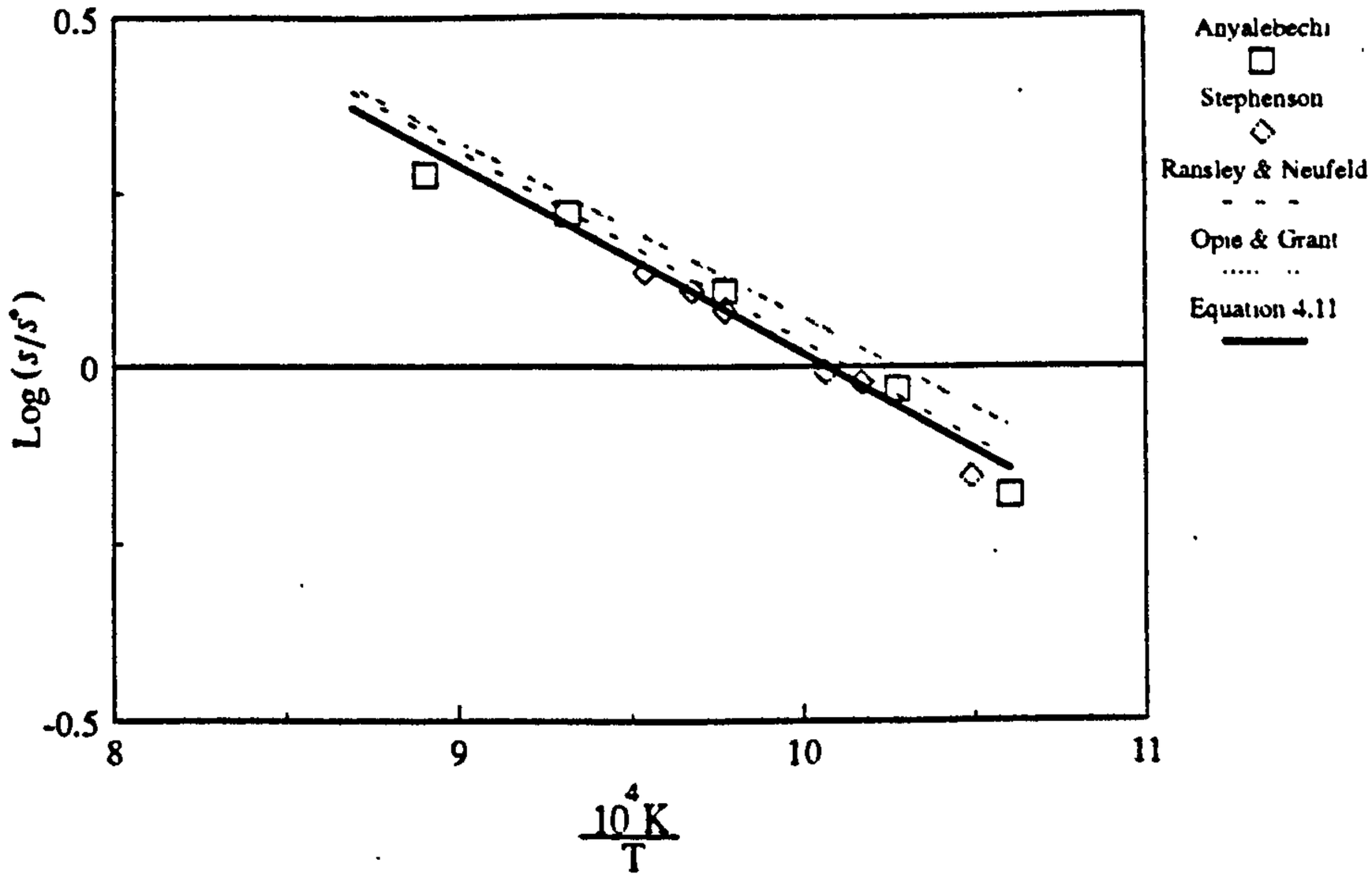

Figure 4.2 Van't Hoff isobar at 101325 Pa (1 atm) for solution of hydrogen in liquid pure aluminium.

Table 4.3 Temperature dependence of hydrogen solubility in liquid pure aluminium for 101325 Pa (1atm)[130.137.].

Temperatue / K	Solubility / (cm^3 / 100g) = (m/m^θ), reported by:	
	Stephenson	Anyalebechi*
943		0.66
953	0.70	
973		0.93
983	0.95	
993	0.98*	
1023	1.20	1.28
1033	1.28**	
1048	1.36*	
1073		1.66
1123		1.89

*mean of duplicate values.

Table 4.4 Pressure dependence of hydrogen solubility in liquid pure aluminium[111.] at 973K

Pressure/ kPa	$(p/p^{\theta})^{1/2}$	Solubilty*/(cm^3/100g) (m/m^{θ})	$(m/m^{\theta}) / (p/p^{\theta})^{1/2}$
67	258	0.78	3.0×10^{-3}
80	283	0.82	2.9×10^{-3}
93	305	0.89	2.9×10^{-3}
101 (1atm)	318	0.93	2.9×10^{-3}
107	327	0.97	3.0×10^{-3}
113	337	0.99	2.9×10^{-3}

* mean of duplicate values.

The linear plot given in Figure 4.2 and the constancy of the ratio $(m/m^{\theta})/(p/p^{\theta})^{1/2}$ given in table 4.4, show that these results fit the Equations 4.3 (Sieverts' isotherm) and 4.8 (Van't Hoff isobar). This is a necessary criterion[111.] for the acceptability of the results.

After a comprehensive and critical review of all the available results, Talbot[111.] concluded that the best values for the solubility of hydrogen in liquid pure aluminium are those derived from the works of Ransley and Neufeld[124.], Opie and Grant[125.] and Anyalebechi[130.].

Based on these results Talbot[111.], recommended the following equation for the solubility, at 101325 Pa (1atm);

$$\log\left(\frac{s}{s^{\Theta}}\right) = -\frac{2700}{T/K} + 2.72 \qquad (4.12)$$

Introducing pressure as a variable:

$$\log\left(\frac{s}{s^{\Theta}}\right) - 1/2\log\left(\frac{p}{p^{\Theta}}\right) = -\frac{2700}{T/K} + 2.72 \qquad (4.13)$$

where: s is solubility (cm^3/100g), $p^{\theta} = 101325$ Pa and $s^{\theta} = 1$ cm^3/100g.

4.7.2 Solubility of hydrogen in solid pure aluminium

Due to the extremely small solubility and difficulty in experimental detection, the solubility of hydrogen in solid pure aluminium has only been systematically measured on two occasions, by Ransley and Neufeld[124] and by Eichenauer and Pebler[127]. Both sets of investigators fitted their results to the Van't Hoff isobar, Equation 4.8, and Sieverts' isotherm, Equation 4.3, yielding:

Ransley and Neufeld:

$$738 < T/K < 893 \qquad \log\left(\frac{s}{s^{\ominus}}\right) - 1/2\log\left(\frac{p}{p^{\ominus}}\right) = -\frac{2080}{T/K} + 0.788 \qquad (4.14)$$

Eichenauer and Pebler:

$$743 < T/K < 863 \qquad \log\left(\frac{s}{s^{\ominus}}\right) - 1/2\log\left(\frac{p}{p^{\ominus}}\right) = -\frac{4254}{T/K} + 3.35 \qquad (4.15)$$

The results are plotted in Figure 4.3 and tabulated as in Table 4.5. They agree reasonably well at temperature approaching the melting point of the metal but diverge at temperatures < 800 *K*.

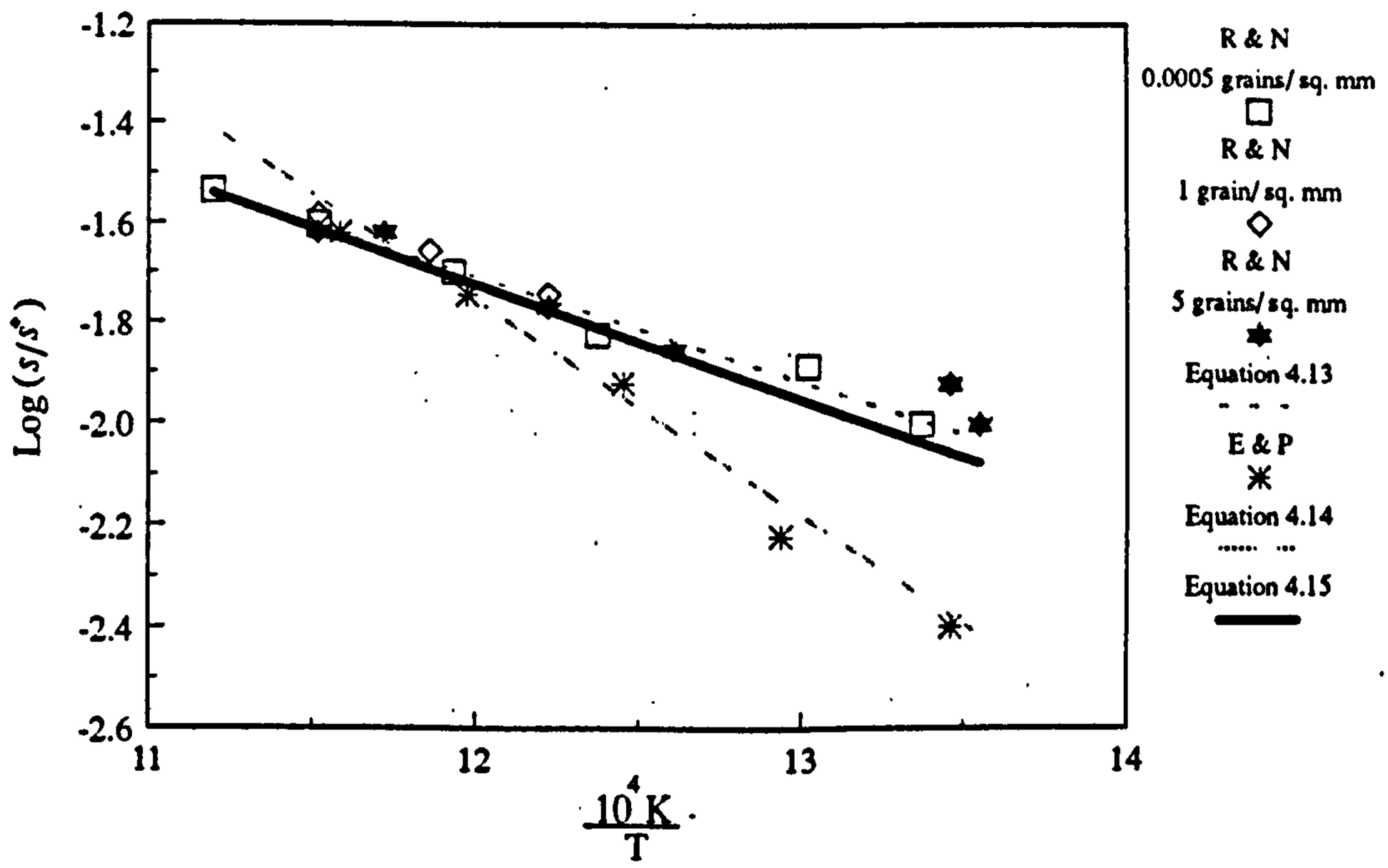

Figure 4.3 Van't Hoff isobar at 101325 Pa (1 atm) for solution of hydrogen in solid pure aluminium.

Table 4.5 Temperature dependence of hydrogen solubility in solid aluminium for 101325 Pa, [Ransley and Neufeld[124.], and Eichenauer and Pebler[127.]]

Temperature *T/K*	Solubility/ (cm^3/100g)	Metal purity%	Sample form	Grain size (grains mm^2)	Investigator
893	0.029	99.99	cylinder	'0.0005	R & N
878	0.029	99.2	cylinder	50	R & N
868	0.026	99.99	cylinder	1	R & N
868	0.024	99.99	cylinder	5	R & N
868	0.025	99.99	cylinder	'0.0005	R & N
863	0.024	99.5		unspecified	E & P
853	0.024	99.99	cylinder	5	R & N
843	0.022	99.99	cylinder	1	R & N
838	0.020	99.99	cylinder	'0.0005	R & N
835	0.018	99.5		unspecified	E & P
818	0.018	99.99	cylinder	1	R & N
818	0.017	99.99	cylinder	5	R & N
818	0.015	99.2	cylinder	0.3	R & N
808	0.015	99.99	cylinder	'0.0005	R & N
803	0.011	99.5	cylinder	unspecified	E & P
803	0.012	99.5		unspecified	E & P
793	0.014	99.99	cylinder	5	R & N
773	0.006	99.5	cylinder	unspecified	E & P
773	0.008	99.5		unspecified	E & P
768	0.013	99.99	cylinder	'0.0005	R & N
748	0.010	99.99	cylinder	'0.0005	R & N
743	0.004	99.5	cylinder	unspecified	E & P
743	0.012	99.99	cylinder	5	R & N
738	0.010	99.99	cylinder	5	R & N

In the absence of further reliable experimental results, Talbot[111.] combined the results of both sets of investigators[124.127.] for the temperature range 800 - 900 *K*, in which they agree, yielding the following equation:

$$800 < T/K < 900 \qquad \log\left(\frac{s}{s^{\ominus}}\right) - 1/2\log\left(\frac{p}{p^{\ominus}}\right) = -\frac{2270}{T/K} + 1.0 \qquad (4.16)$$

Extrapolating equation 4.16, the solubility of hydrogen in the solid pure metal at the melting point, 660 °C (933*K*), is 0.037 cm^3 / 100g.

The value for the liquid metal at the melting point, similarly derived from equation 4.12, is 0.67 cm^3 / 100g. The quotient yields 18 for the partition coefficient of hydrogen between the liquid and solid phase during solidification.

4.7.3 Solubility of hydrogen in aluminium alloys

Apart from the works carried out at the Brunel university under the supervision of Dr Talbot[130.138.139.] on aluminium-lithium alloys, the only other available systematic results for hydrogen solubility in aluminium alloys are those determined by Opie and Grant[125.] for liquid binary aluminium-copper and aluminium-silicon alloys.

Values for the temperature range 700 - 1000°C (973 - 1273 *K*) are given by the equations:

Al- 2wt% Cu	$\log\left(\frac{s}{s^{\Theta}}\right) - 1/2\log\left(\frac{p}{p^{\Theta}}\right) = -\frac{2950}{T/K} + 2.90$	(4.17)
Al- 4wt% Cu	$\log\left(\frac{s}{s^{\Theta}}\right) - 1/2\log\left(\frac{p}{p^{\Theta}}\right) = -\frac{3050}{T/K} + 2.94$	(4.18)
Al- 8wt% Cu	$\log\left(\frac{s}{s^{\Theta}}\right) - 1/2\log\left(\frac{p}{p^{\Theta}}\right) = -\frac{3150}{T/K} + 2.94$	(4.19)
Al- 16wt% Cu	$\log\left(\frac{s}{s^{\Theta}}\right) - 1/2\log\left(\frac{p}{p^{\Theta}}\right) = -\frac{3150}{T/K} + 2.83$	(4.20)
Al- 32wt% Cu	$\log\left(\frac{s}{s^{\Theta}}\right) - 1/2\log\left(\frac{p}{p^{\Theta}}\right) = -\frac{2950}{T/K} + 2.57$	(4.21)
Al- 2wt% Si	$\log\left(\frac{s}{s^{\Theta}}\right) - 1/2\log\left(\frac{p}{p^{\Theta}}\right) = -\frac{2800}{T/K} + 2.79$	(4.22)
Al- 4wt% Si	$\log\left(\frac{s}{s^{\Theta}}\right) - 1/2\log\left(\frac{p}{p^{\Theta}}\right) = -\frac{2950}{T/K} + 2.91$	(4.23)
Al- 8wt% Si	$\log\left(\frac{s}{s^{\Theta}}\right) - 1/2\log\left(\frac{p}{p^{\Theta}}\right) = -\frac{3050}{T/K} + 2.95$	(4.24)
Al- 16wt% Si	$\log\left(\frac{s}{s^{\Theta}}\right) - 1/2\log\left(\frac{p}{p^{\Theta}}\right) = -\frac{3150}{T/K} + 3.00$	(4.25)
Al- 1wt% Li	$\log\left(\frac{s}{s^{\Theta}}\right) - 1/2\log\left(\frac{p}{p^{\Theta}}\right) = -\frac{2113}{T/K} + 2.568$	(4.26)
Al- 2wt% Li	$\log\left(\frac{s}{s^{\Theta}}\right) - 1/2\log\left(\frac{p}{p^{\Theta}}\right) = -\frac{2797}{T/K} + 3.329$	(4.27)
Al- 3wt% Li	$\log\left(\frac{s}{s^{\Theta}}\right) - 1/2\log\left(\frac{p}{p^{\Theta}}\right) = -\frac{2889}{T/K} + 3.508$	(4.28)
Al- 2wt% Li- 2.5wt% Cu	$\log\left(\frac{s}{s^{\Theta}}\right) - 1/2\log\left(\frac{p}{p^{\Theta}}\right) = -\frac{2243}{T/K} + 3.019$	(4.29)

When fitting the result to Van't Hoff isobar for solid aluminium-lithium alloys, the alloys exhibited[111.130.] a two part Van't Hoff isobar with a discontinuity at a composition-dependent critical temperature. Thus two equations are given for every alloy[111.].

Al- 1wt% Li :

$$473 < T/K < 680 \qquad \log\left(\frac{s}{s^{\ominus}}\right) - 1/2\log\left(\frac{p}{p^{\ominus}}\right) = -\frac{358}{T/K} + 0.576 \qquad (4.30)$$

$$680 < T/K < 873 \qquad \log\left(\frac{s}{s^{\ominus}}\right) - 1/2\log\left(\frac{p}{p^{\ominus}}\right) = -\frac{604}{T/K} + 0.620 \qquad (4.31)$$

Al- 2wt% Li :

$$473 < T/K < 740 \qquad \log\left(\frac{s}{s^{\ominus}}\right) - 1/2\log\left(\frac{p}{p^{\ominus}}\right) = -\frac{273}{T/K} + 0.597 \qquad (4.32)$$

$$740 < T/K < 873 \qquad \log\left(\frac{s}{s^{\ominus}}\right) - 1/2\log\left(\frac{p}{p^{\ominus}}\right) = -\frac{676}{T/K} + 0.767 \qquad (4.33)$$

Al- 3wt% Li :

$$523 < T/K < 770 \qquad \log\left(\frac{s}{s^{\ominus}}\right) - 1/2\log\left(\frac{p}{p^{\ominus}}\right) = -\frac{615}{T/K} + 1.272 \qquad (4.34)$$

$$770 < T/K < 873 \qquad \log\left(\frac{s}{s^{\ominus}}\right) - 1/2\log\left(\frac{p}{p^{\ominus}}\right) = -\frac{830}{T/K} + 1.166 \qquad (4.35)$$

Al- 2wt% Li- 2.5wt% Cu (AA2090):

$$473 < T/K < 773 \qquad \log\left(\frac{s}{s^{\ominus}}\right) - 1/2\log\left(\frac{p}{p^{\ominus}}\right) = -\frac{376}{T/K} + 0.889 \qquad (4.36)$$

$$773 < T/K < 893 \qquad \log\left(\frac{s}{s^{\ominus}}\right) - 1/2\log\left(\frac{p}{p^{\ominus}}\right) = -\frac{714}{T/K} + 0.971 \qquad (4.37)$$

Al- 2wt% Li- 2wt% Cu- 1.5wt% Mg (AA2091):

$$473 < T/K < 773 \qquad \log\left(\frac{s}{s^{\ominus}}\right) - 1/2\log\left(\frac{p}{p^{\ominus}}\right) = -\frac{366}{T/K} + 0.880 \qquad (4.38)$$

Copper and silicon decrease[125.] the hydrogen solubility in aluminium, the effect of copper being considerably greater than that of silicon. Lithium on the other hand increases the solubility and copper and magnesium addition to Al-Li alloys enhances the effect of lithium[139.].

4.8 Interstitial Diffusion Of Gases In Metals

Diffusion is the process by which atoms move through the crystal lattice by jumping from one available site to another.

In the simplest cases the net result of the diffusion is that existing differences in concentration are reduced and finally disappear altogether.

Realising the analogy of diffusion mechanism to the transfer of heat by conduction, Fick[140.] adopted the Fourier's[141.] equation for heat conduction to express diffusion in isotropic substances;

$$q = k A \frac{T_1 - T_2}{l} t \qquad \text{(Fourier's equation)} \qquad (4.39)$$

where at the constant temperatures T_1 and T_2 ($T_1 > T_2$) and under steady-state conditions, the amount of heat q , flowing through a transverse cross-section with the area of A in the time t..

In analogy with the fourier's equation, Fick proposed an equation for unidirectional diffusion, now known as Fick's first law. In this equation the flow of heat is replaced by a flow of matter and the temperature T_1 and T_2 by the concentrations C_1 and C_2 of the diffusing substance ($C_1 > C_2$); this results in the equation

$$m = D A \frac{C_1 - C_2}{l} t = - D A \frac{C_2 - C_1}{l} t \qquad (4.40)$$

or, in the differential form:

$$dm = - D A \frac{\partial C}{\partial x} d t \qquad (4.41)$$

In the two equations above, m or dm represents the quantity of substance diffusing in time t or dt through A cm^2 of transverse cross-section. The quantity D is called the diffusion coefficient or diffusivity, and is usually given in terms of square centimetres per seconds ($cm^2\ s^{-1}$).

Fick's first law is commonly written as:

$$J = - D \frac{\partial C}{\partial x} \qquad (4.42)$$

where $J = dm / A\ dt$ is known as the flux.

4.8.1 Steady state diffusion

Fick's first law is only applicable to diffusion problems where the concentration in the flow region does not change with time, i. e. in cases of steady-state diffusion. This is typified by the diaphragm type experiment[142.] used in measuring the rate of diffusion of a gas through a metal, shown schematically in Figure 4.4.

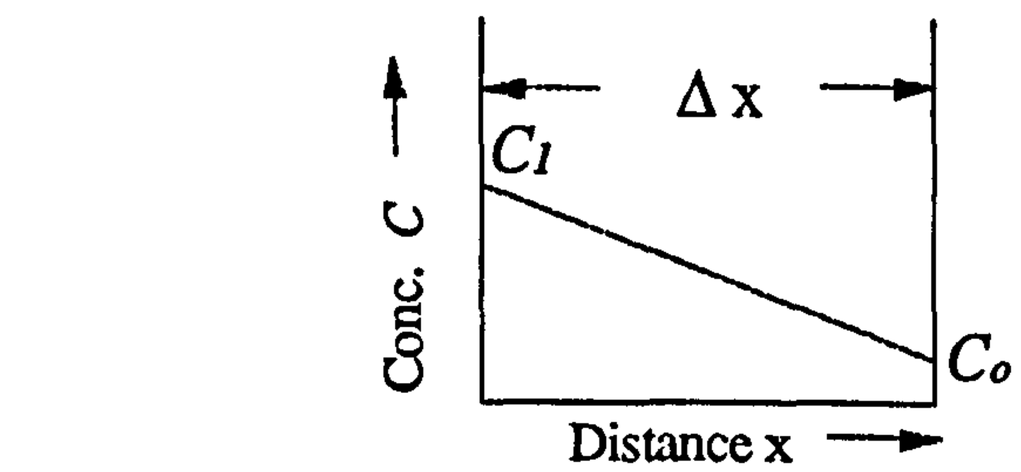

Figure 4.4 Schematic representation of steady-state diffusion.

The gas is maintained at a pressure p_1 on one side of the diaphragm and at a lower pressure p_0 , on the other side. A steady state is achieved when the rate at which the gas enters the metal on the high-pressure side and the rate at which it leaves the low-pressure side become equal, i. e., the flux (J) is constant. If diffusivity (D) is also constant then (see Equation. 4.41) the concentration gradient $\frac{\partial C}{\partial x}$,is also constant and the concentration of gas varies linearly with distance in the flow direction (Figure 4.4).

4.8.2 Non-steady state diffusion,

In this case the concentration gradient varies from point to point and from moment to moment.

Derived from the first law, Fick's "second law", relates the rate of change of the concentration $\left(\frac{\partial C}{\partial t}\right)$ at x and the change in the concentration gradient.

$$\frac{\partial C}{\partial t} = D\frac{\partial^2 C}{\partial x^2} \tag{4.43}$$

Functions fitted to Equation 4.43, satisfying relevant initial and boundary conditions are available for recurrent situations[111.143]. Two examples useful for the geometry of common industrial products are:

1. diffusion into or out of an infinite plate of thickness, $2a$, with an initial uniform solute concentration, C_o, and constant surface concentration, C_s. The instantaneous concentration, C, at point x, referred to as mid-plane of the plates as origin, is given by:

$$\frac{C-C_o}{C_s-C_o} = 1-\frac{4}{\pi}\sum_{n=1}^{\infty}\frac{(-1)^n}{2n+1}+\exp\left[-\frac{D(2n+1)^2\pi^2 t}{4a^2}\right]\cos\left[\frac{(2n+1)\pi x}{2a}\right] \tag{4.44}$$

The fraction of solute, Q_t / Q_∞, entering or leaving the plate after the elapse of time, t, is given by:

$$\frac{Q_t}{Q_\infty} = 1-\frac{8}{\pi^2}\sum_{n=1}^{\infty}\frac{1}{(2n+1)^2}\exp\left[-\frac{D(2n+1)^2\pi^2 t}{4a^2}\right] \tag{4.45}$$

2. diffusion into or out of an infinite cylinder of radius, a, referred to the radial co-ordinate, r, with the same initial and boundary conditions as the plate. The analogous equations are:

$$\frac{C-C_o}{C_s-C_o} = 1-2a\sum_{n=1}^{\infty}\frac{J_o(\beta_n r/a)}{\beta_n^2 J_1(\beta_n)}\exp\left[-\frac{D t \beta_n^2}{a^2}\right] \tag{4.46}$$

and

$$\frac{Q_t}{Q_\infty} = 1-\sum_{n=1}^{\infty}\frac{4}{\beta^2}\exp\left[-\frac{D t \beta_n^2}{a^2}\right] \tag{4.47}$$

where; $J_o(\beta_n)$ and $J_1(\beta_n)$ are the Bessel functions of zero and first orders respectively; β_n is the n^{th} root of the equation, $J_o(\beta_n) = 0$.

4.8.3 The influence of temperature

Many experiments have shown that the dependence of diffusivity on temperature, over a limited temperature range, can be represented by an Arrhenius type expression of the form:

D_o is called the frequency factor and ΔH^* the activation enthalpy.

4.8.4 Intrinsic diffusivity of hydrogen in pure aluminium

Intrinsic diffusivity can be measured only with laboratory artefacts specially prepared to satisfy the assumptions that:

1. The hydrogen is present in solution and not in traps and is uniformly distributed.
2. The desorption rate of the gas from the sample is not controlled by the surface process.
3. The diffusivity is not a function of the concentration.
4. That all the gas measured is hydrogen.

Some of the published results on "diffusivity" determinations are listed in table 4.6.

Table 4.6
Diffusion of hydrogen in aluminium.

Material	Temp. range K	D_o ($m^2 s^{-1}$) x 10^{-5}	ΔH^* kJ mol^{-1}	Investigator(s)
99.999% Al	633-873	1.1	41	Eicheanauer et al[136].
99.999% Al	743-863	2.1	45.6	Eicheanauer and Pebler[127].
99.999% Al	723-863	1.9	40	Papp and Kovacs Csetenyi[144].
99.99% Al	843-903	0.2	50	Matsuo and Hirata[145].
99.9999% Al	573-673	2.6	58.6	Hashimoto and Kino[146].
99% Al	773-873	1.2	61	Andrew et al[147].
99.8% Al	723-863	0.25	90	Papp and Kovacs Csetenyi[148].

The discrepancy in the published results is because some of them refer to samples of industrially prepared materials which are almost certainly subject to hydrogen trapping.

After strict review of the experimental procedure, Talbot[111]. concluded that the results reported by Eichenauer and Pebler[127]. can be confidently accepted where the intrinsic diffusivity, D ($m^2 s^{-1}$), as a function of temperature is expressed as:

$$D = 2.1 \times 10^{-5} \exp\left(\frac{-5505}{T}\right) \qquad (4.51)$$

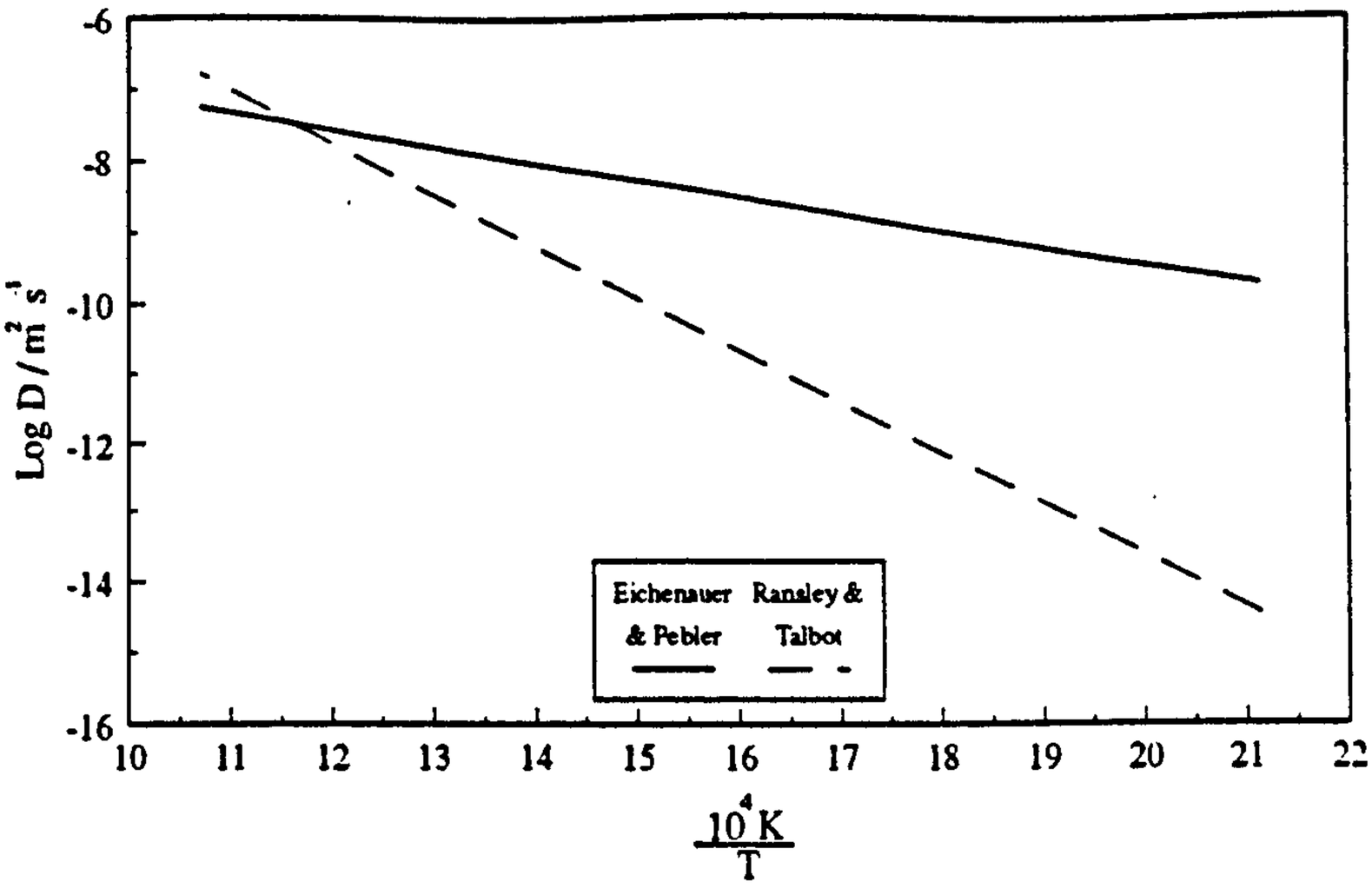

Figure 4.6 Comparison of diffusion coefficients and mobility constants for hydrogen in pure aluminium plotted in Arrhenius' format

4.8.5 Mobility of hydrogen in manufactured aluminium products.

Although the intrinsic diffusivity has important theoretical significance, it offers little guidance in assessing the redistribution of hydrogen in manufactured aluminium products because of the trapping phenomena described earlier in Section 4.5.

In fact, extensive experience with hydrogen content determination by the hot vacuum extraction method shows that the apparent diffusivity, or mobility[111], of hydrogen in small samples of commercially produced metal is much lower than the theoretical values as shown in Figure 4.6. This is in accordance with diffusion in a field of traps, using the approach developed by Crank[143].

In the simplest case, the concentration, S, of trapped substance is directly proportional to the concentration, C, of the substance in true solution, i.e.

$$S = RC \tag{4.52}$$

$$D = D_o \exp\left(\frac{-\Delta G^*}{RT}\right) \tag{4.48}$$

ΔG^*, represent the activation energy which the diffusing atom must overcome.

Within the rigid sphere (hard ball) model of atomic arrangement, the activation energy is required to move apart a number of metal atoms between two interstices to allow the interstitial atom to squeeze through the narrow space, and in the context of the embedded atom theory, the activation energy is required to facilitate diffusion through region of high electron density. Either approach indicate the activation energy to be a sinusoidal function of position of a diffusing interstitial atom. Thus the maximum energy existing at a point midway between any two adjacent equilibrium sites.

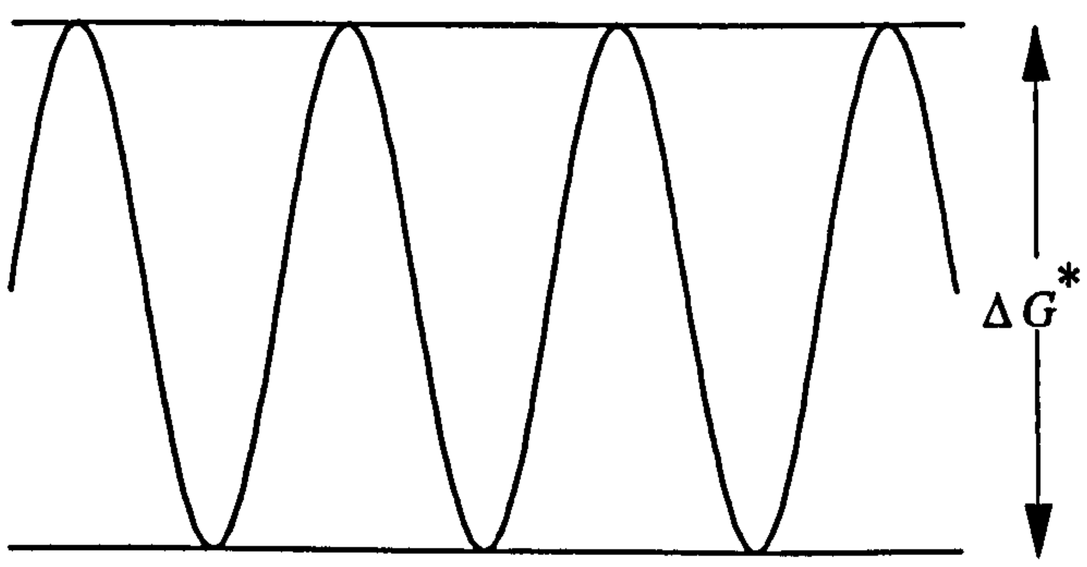

Figure 4.5 Potential energy of a crystal as a function of the position of a diffusing interstitial atom. The minima correspond to the equilibrium positions, the maxima to the energy barriers to be overcome by the diffusing atom.

Equation 4.48 can be written as:

$$D = D_o \exp\left(\frac{-\Delta H^* + T\Delta S^*}{RT}\right) \tag{4.49}$$

Over a limited temperature range ΔS^* is not temperature dependent, thus $\Delta S^* / R$ can be assumed to be constant, therefore,

$$D = D_o \exp\left(\frac{-\Delta H^*}{RT}\right) \tag{4.50}$$

When diffusion occurs in a field of traps, the standard diffusion equation given in Section 4.8.

$$\frac{\partial C}{\partial t} = D\frac{\partial^2 C}{\partial x^2} \tag{4.43a}$$

must be modified to allow for this and becomes:

$$\frac{\partial C}{\partial t} = D\frac{\partial^2 C}{\partial x^2} - \frac{\partial S}{\partial t} \tag{4.53}$$

On substituting for S from (4.51) we obtain,

$$\frac{\partial C}{\partial t} = \frac{D}{R+1}\frac{\partial^2 C}{\partial x^2} \tag{4.54}$$

Equation 4.54 is of identical form to equation 4.43 if a mobility constant, $M = D/R+1$ is substituted for the diffusion coefficient, D:

$$\frac{\partial C}{\partial t} = M\frac{\partial^2 C}{\partial x^2} \tag{4.55}$$

Hence the mobility coefficient in metal where hydrogen is trapped is less than the theoretical diffusion coefficient.

The above treatment is not strictly correct because Equation 4.52 does not apply to hydrogen trapped as diatomic gas in secondary porosity for which it is replaced by the non-linear equation:

$$S = R\,C^2 \tag{4.56}$$

due to the dissociation of hydrogen from the traps by the equation:

$$H_{2\,(gas)} = 2H_{(solution)} \tag{4.57}$$

As Crank points out[143], substitution of Equation 4.57 into Equation 4.53 yields an expression that can only be resolved mathematically by numerical methods.

From empirical measurements, based on several hundreds of determinations, Ransley and Talbot[135.] found that the mobility was remarkably consistent and for pure aluminium was given by the expression:

$$M = 12 \exp\left(\frac{16900}{T}\right) \qquad (m^2\ s^{-1}) \qquad (4.58)$$

This approach has provided extensive evidence that the mobility of hydrogen in commercial products are much less than Equation 4.51 suggests and the difference is greater at lower temperature.

4.9 Hydrogen Content Determination

The precise determination of the hydrogen content in aluminium, either as a characteritic for the quality of an industrial product, or as a fundamental parameter in a research program, is imperative.

The ongoing world-wide effort has lead to the development of numerous quantitative and semi-quantitative techniques with varying degree of sophistication. There are more than 20 reported techniques[149.] that are used in the aluminium industry, a few of the common techniques are reviewed.

4.9.1 Straube-Pfeiffer test

This test is based on the formation of bubbles when molten aluminium or its alloy is solidified under reduced pressure.

An iron crucible containing 100-200 g of molten metal is placed in a vacuum chamber. Pressure is reduced rapidly to a selected value and held during solidification. A qualitative estimate of the hydrogen content of the metal is obtained from the observation of the bubble evolution during the solidification, the apparent density of the sample, and examining cut surface for porosity.

The main drawback of the test is its sensitivity[149.] (or greater than) 0.30 cm^3 /100g, which is far too high for aluminium alloy products for critical applications.

4.9.2 The Initial Bubble test

This test was first proposed by Dardel[150.151.] and is based on Sievert' law,

$$[H] = k\sqrt{P_{H_2}} \tag{4.59}$$

where:

$[H]$ is the concentrtion of the dissolved hydrogen in the melt,
P_{H_2} is the partial pressure of hydrogen in the atmospher,
k is a temperature dependent constant.

The test consist of gradual application of vacuum over small sample of molten metal, which is contained in an electrically heated crucible until the first bubble is observed at the molten surface. The pressure and temperature at which the first bubble appear are recorded. A monograph relating pressure, temperature and hydrogen solubility of the alloy being tested is used to obtain the hydrogen content.

The results obtained by initial bubble test are erratic and not easily reproducible[152.153.].

4.9.3 Telegas Instrument

The Telegas instrument developed by Ransley et al[154.155.] operates on the principle of monitoring the hydrogen activity developed in a small quantity of inert gas or nitrogen continuously recirculated through the molten metal under the test until the gaseous hydrogen diffused in the nitrogen bubbles is in equilibrium with the solute hydrogen in the metal.

The Telegas instrument has proven to be suitable method for absolute determination of hydrogen content of molten aluminium in industrial conditions.

AlScan developed by Alcan and Sumitomo Light Metal (SLM) Hydrogen Determinator are also based on the same principle.

The technique will be further discussed in Section 6.2.

4.9.4 Nitrogen Carrier Fusion Techniques

The technique involves the melting of a solid cylindrical specimen of several grams in a nitrogen gas flow at atmospheric pressure. The hydrogen that evolves from the sample is transported by the nitrogen gas to a thermal conductivity detector (katharometer hot wire) for measurement.

There are two commercially available instruments based on this principle, namely LECO RH, manufactured by Instrument S. A. and Ithac, manufactured by Adamel -Lhomargy (a division of Instrument S. A.).

Although results obtained by Degreve[156.157.] are reported in good agreement with those of hot vacuum extraction method (to be discussed), several other investigators have reported significant disparity between hydrogen content values obtained with Ithac instrument for Al-Mg[158.159.] and Al-Zn[159.] alloys. At very low hydrogen content level (<0.10 $cm^3/100g$) results obtained with LECO instrument are reported[160.] to be erratic and not very reproducible.

The fundamental drawbacks which are attributed for the inaccurate measurements are[149.] :

1. The "surface hydrogen" evolved by the reaction between water absorbed in thin hydrated oxide film on the sample, formed in the atmosphere at room temperature and the metal itself,

$$Al_2O_3 . 3H_2O = Al_2O_3 + 3H_2O \quad (4.60)$$

$$2Al + 3H_2O = Al_2O_3 + 3H_2 \quad (4.61)$$

Although Degreve and Jardin recommended[157.] that surface hydrogen could be eliminated by thermal treatment at 673K prior to melting, Simensen and Lauritzen[159.] found that preheating to 773K is necessary in the case of Al-Mg

4.10.1Interdendritic porosity

When liquid aluminium or any of its alloys is cast by the techniques used in normal production routes, it retains virtually all of the dissolved hydrogen it may contain[124.135.162.163.].

The solubility of hydrogen in pure liquid aluminium at solidification temperature (933 K) is approximately eighteen times greater than in solid state at that temperature, as illustrated in Table 4.7, which also list equilibrium solubility limit for some other metals.

Table 4.7 Hydrogen solubility at solidification temperature for some common metals.

Pure metal	Hydrogen solubility (cm^3/100g)		Ratio of L_s / S_s
	In liquid (L_s)	In solid (S_s)	
Al	0.67	0.037	18
Cu	5.30	2.10	2.5
Mg	25.00	15.00	1.7
Ni	40.00	14.00	2.9

In accordance with general principle of solute redistribution the marked change in solubility at the solidification causes some of the hydrogen to be expelled from the solid crystals into the adjacent liquid. If the concentration of hydrogen in liquid rises to a level sufficient to exceed the sum of the local pressure with in the liquid and the excess pressure attributed to surface tension, then gas bubbles are nucleated. Since this condition is usually reached near the end of solidification, the gas bubbles are constrained to occupy the restricted space between the growing dendrites, so they become irregular, gas-filled cavities with the characteristic shape illustrated in Figure 4.7.

The quantity of porosity in solid aluminium is often expressed as volume percentage, determined by:

$$\text{Percentage porosity} = \frac{\text{(Theoretical Density) - (Actual Density)}}{\text{(Theoretical Density)}} \times 100 \qquad (4.62)$$

alloys. Holding samples at these high temperature could lead to evolution of some of the bulk hydrogen.

2. Reaction between volatile alloying elements, such as Mg, Li and Zn, evaporated from the sample and the water vapour absorbed on the surface of the glass and/or silica (quartz) extraction tube walls on which they condense.
3. Reaction between the sample and water vapour evolved from the walls of the apparatus.
4. Presence of porosity and/or oxide inclusions in the samples. These pores tend to retain moisture which subsequently reacts with the sample during heating.

4.9.5 Hot Vacuum Extraction (Ransley) Method

The Ransley technique, generally referred to as the hot vacuum extraction method, was developed and first described by Eborall and Ransley[98]. and later modified to its present form by Ransley and Talbot[161]. The method comprises the collection and measurement of hydrogen desorbed into an evacuated system from a specially prepared heated solid sample. The technique is a subfusion and direct method which provides absolute hydrogen content values for aluminium alloys but is essentially a laboratory method. It has earned a reputation for reliability and constitute a reference method valuable for any alloy. Hot vacuum extraction is the standard method against which other techniques are calibrated and compared..

This was the technique used in the work at hand, thus will be described in detail in Section 6.1.

4.10 Defects Caused By Hydrogen In Aluminium And Aluminium Alloys

The main defect which has long been recognised and is well documented, is the precipitation of hydrogen gas phase during solidification, leading to porosity in the solid metal.

Characterised by the mechanism and morphology of their formation, two types of porosity have been identified, namely the interdendritic and secondary porosity.

The method to determine the theoretical density to an accuracy of +/- 0.03% is reported to be by[135.] measuring the density of the sample after a hot-pressing operation in a steel die at a pressure of approximately 150 Mpa (10 tons/in^2), and a temperature of about 450°C for 10-15 minutes. The technique is said to be suitable for most aluminium alloys.

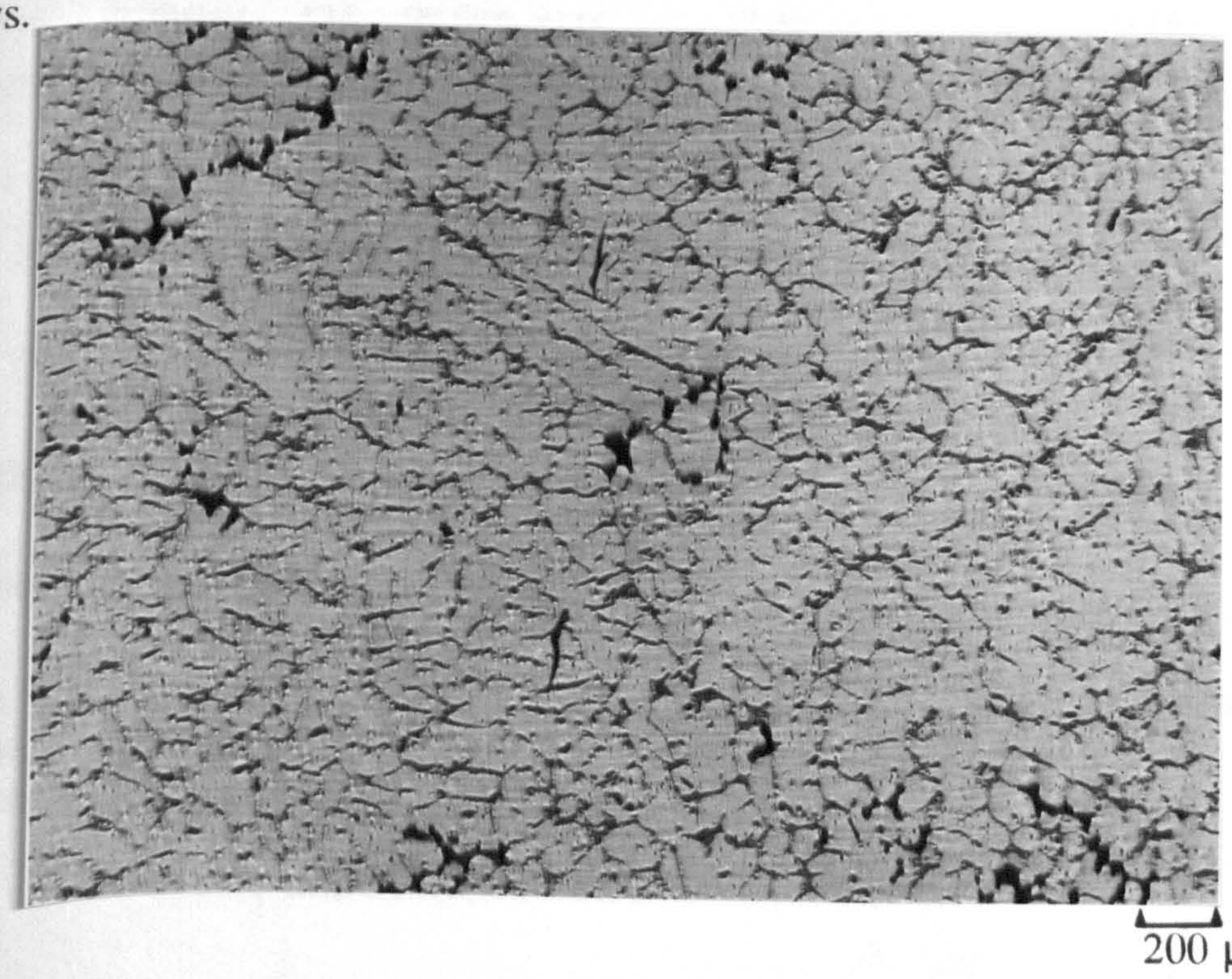

Figure 4.7 Interdendritic porosity direct cast ingot of 99.2% aluminium[115] x12.5.

Plotting the percentage porosity against hydrogen content a linear correlation was observed[124.164.]. Extrapolating the best straight line to zero porosity yields a theoretical threshold gas content for the particular alloy, below which no interdendritic porosity is expected.

Thomas and Gruzleski[165.] plloted percentage porosity against hydrogen content from all the previously reported results and their own work on Al-8 wt% Si. Using a linear regression technique and the best straight line fit, they re-determined the threshold hydrogen content for pore formation for a variety of aluminium alloys, over a wide range of casting conditions. Their results are presented in Table 4.8 and Figure 4.8.

Table 4.8 Threshold hydrogen content for pore formation and experimental details of various investigations.

Investigator(s)	Ref.	Alloy	Casting condtion	Threshold hydrogen content ($cm^3/100g$)[1]	Line[2]
Ransley & Neufeld	124	Commercial purity	Sand cast	0.117	a
Ransley & Talbot	135	99.99% pure	Sand cast	0.168	b
Ransley & Talbot	135	Duralmumin, Al-4.5%Cu	D C	0.167	c
Metcalfe	164	A-4.6%Cu	Sand cast	0.169	d
Jordan etal	162	Al-Cu-Mg	DC (11"dia x 44" ingot)	0.119	e
Jordan etal	162	Al-Cu-Mg	DC (5"dia x 12.5" ingot)	0.141	f
Thomas & Gruzleski	165	Al-8%Si	Water cooled mould (chilled region)	0.150	g
Thomas & Gruzleski	165	Al-8%Si	Water cooled mould (non-chilled region)	0.053	h

1. As determined by Thomas and Gruzleski which in some cases may differ from the value reported by the original investigator.
2. Corresponding to the lines plotted in Figure 4.8.

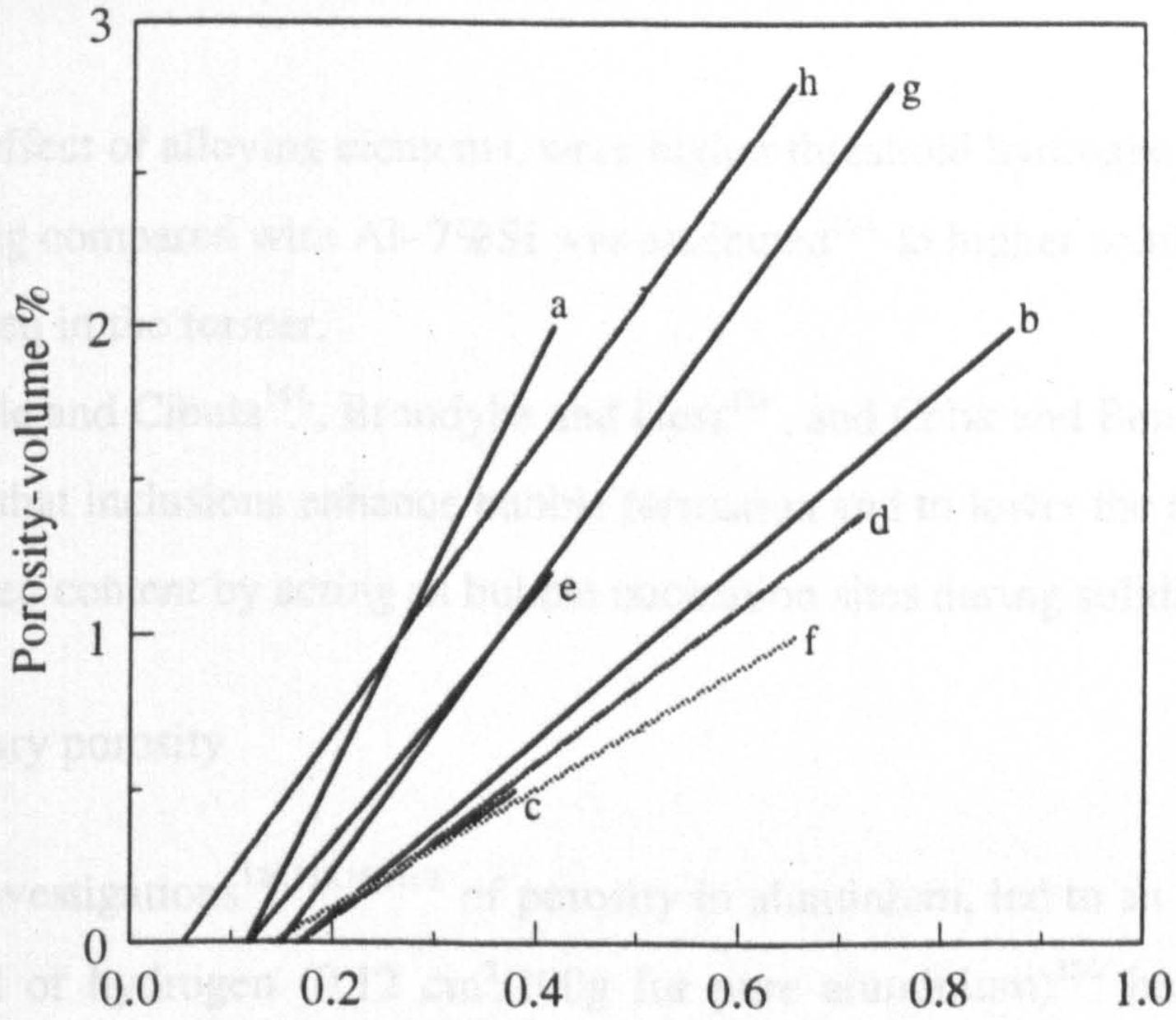

Figure 4.8 Plot of volume percentage porosity vs hydrogen content for aluminium alloys cast under variety of conditions.

The efforts to identify the conditions thus predicting the formation of porosity, have revealed numerous contributory factors which can be broadly classified to:

1. The influence of hydrogen content i.e. the threshold hydrogen content which was discussed.
2. The effect of solidification conditions[166], some of which are tabulated in the following Table 4.9.

Table 4.9 Effects of solidification conditions on hydrogen porosity in aluminium.

Condition	Average pore size	Pore fraction volume	Threshold hydrogen content
Increasing cooling rate	Decrease	Decrease	Increase
Grain refinement[1]	Decrease	Decrease	Increase
Eutectic modification[2]	Increase	Increase	Decrease
Smaller freezing range	Decrease	Decrease	Increase

1. Grain refinement with Al- 5%Ti- 0.2%B master alloy.
2. Eutectic modification with Al- %5Sr.

3. The effect of alloying elements, were higher threshold hydrogen content in Al- 4.7%Mg compared with Al- 7%Si was attributed[104] to higher solubility of hydrogen in the former.
4. Ruddle and Cibula[167], Brondyke and Hess[168], and Celik and Bennet[169] have shown that inclusions enhance bubble formation and to lower the threshold hydrogen content by acting as bubble nucleation sites during solidification.

4.10.2 Secondary porosity

The early investigations[124,135,162,163] of porosity in aluminium, led to an assumption of threshold level of hydrogen (0.12 $cm^3/100g$ for pure aluminium)[124] below which no porosity would form. The hydrogen in excess of the solubility limit was assumed to be in super saturated solution.

Adopting the same reasoning as that advanced by Seitz[170] and Barnes and Mazey[171] and supported by the experimental observation of Doherty and Chalmers[172], Talbot and Granger[121] showed that in the absence of interdendritic porosity, the hydrogen retained

in cast aluminium is partitioned between solid solution and numerous small ~ 1-2 μm diameter pores, which they termed secondary porosity, shown in Figure 4.9.

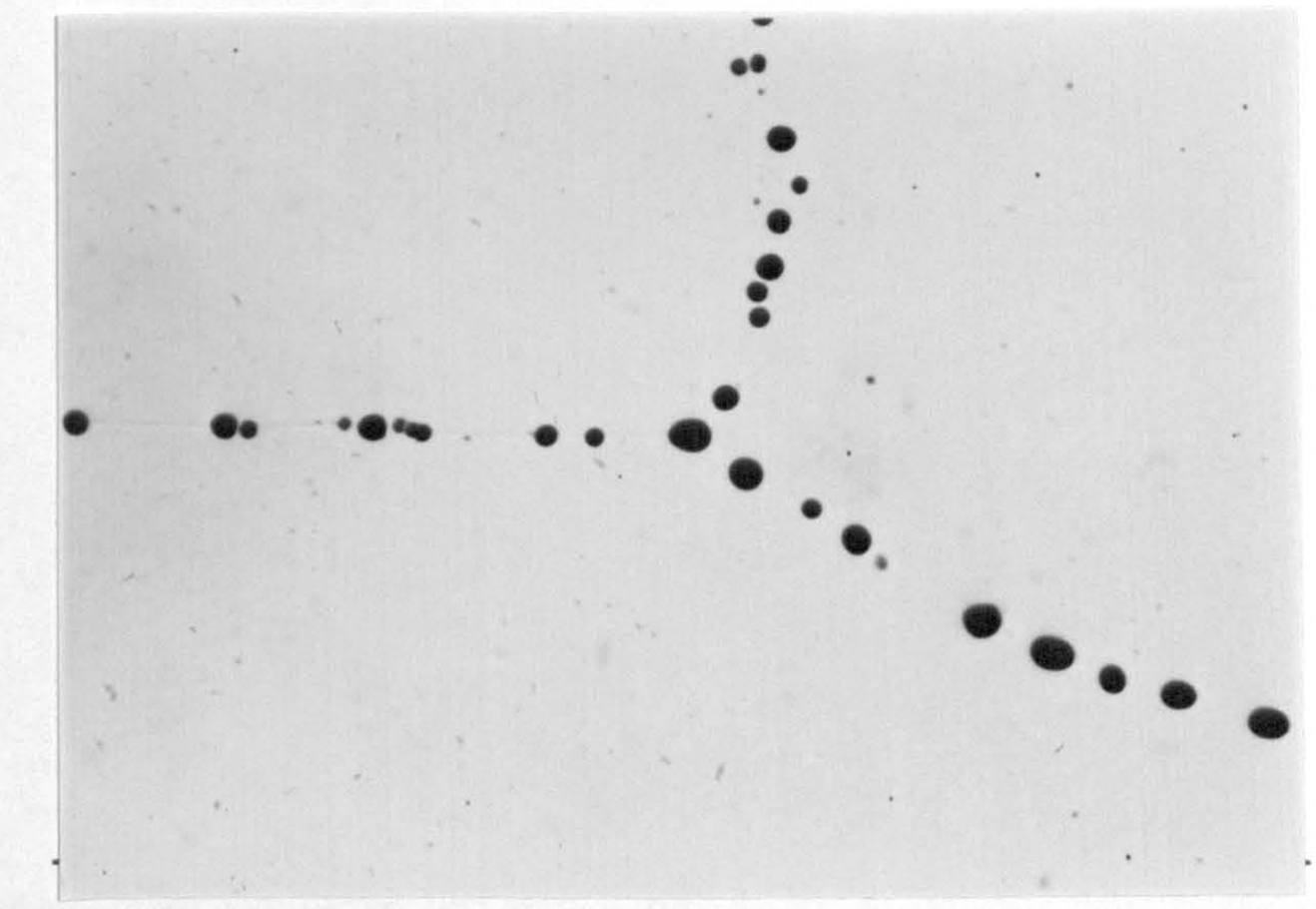

(a)

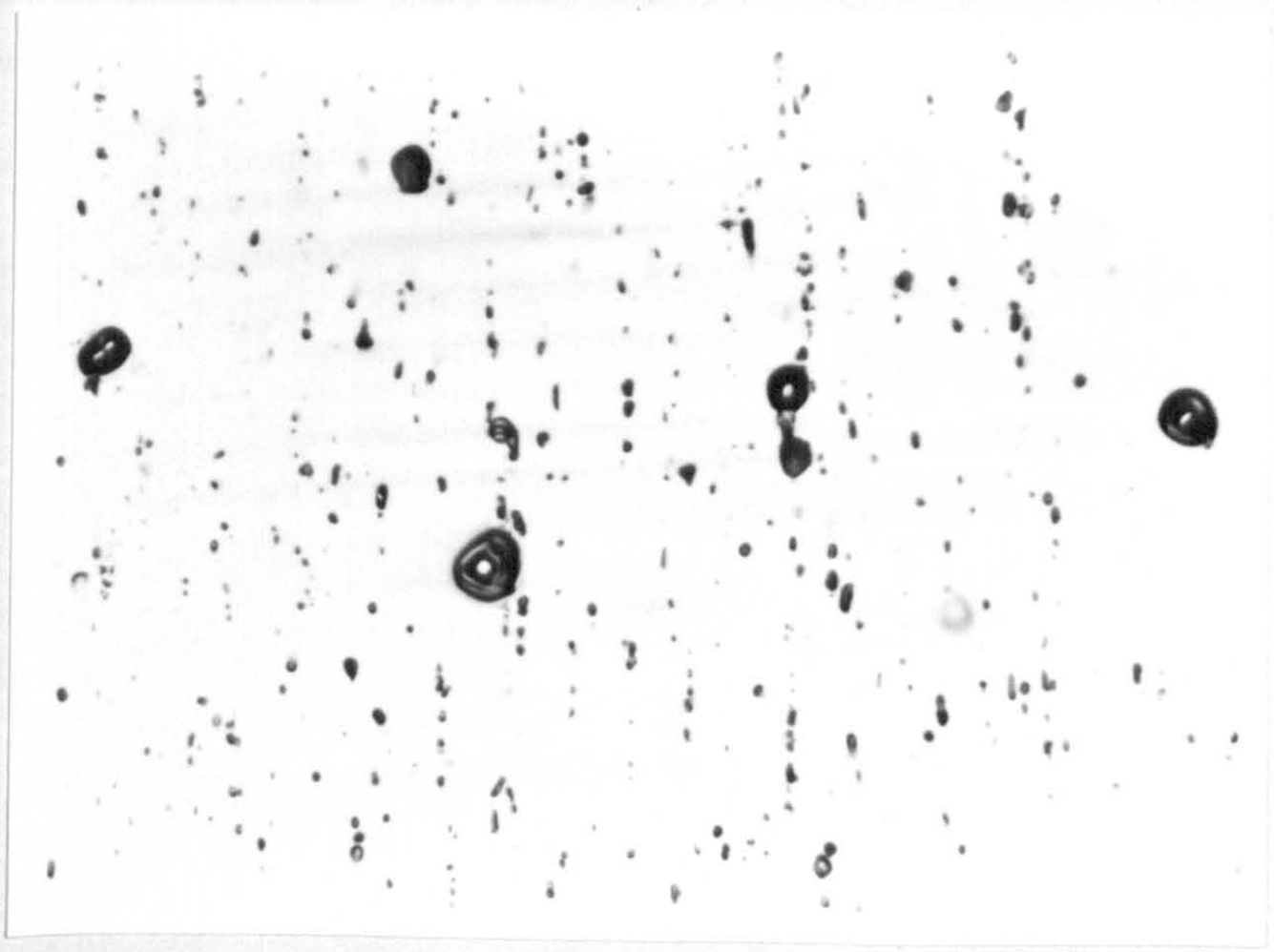

(b)

Figure 4.9 Secondary porosity in (a) direct cast and homogenised 99.99% aluminium x90, (b) hot rolled and annealed 99.2% aluminium plate x350.[121] Electropolished in Perchloric-Ethyl alcohol mixture.

4.10.3Blistering

Surface blistering illustrated in Figure 4.10 is a common form of defect which is encountered on wrought aluminium and aluminium alloy products.

Figure 4.10 Blisters on the surface of aluminium extrusion ingot heat treated in an environment containing SO_2, x 10.

The basic cause is the inflation of internal defects by hydrogen when the overlying metal is soft during heat treatment.

The incidence of blister is determined by the nature and distribution of internal defects and hydrogen content in the metal by one or more of the following mechanism.

4.10.3.1Re-expansion of the existing defects,

If the metal contains interdendritic porosity, the pores tend to concentrate near the surface. At high temperature the gas pressure can exceed the restraining force of the thin overlaying metal leading to surface blistering.

The concentration and size of intermetalic and non-metallic inclusions ("dirt") in the metal have a detrimental effect on the threshold hydrogen content for interdendritic porosity and blistering[173.174].

Blister can be induced in otherwise sound metal if faults are introduced in the course of mechanical working. Naturally, the metal must spend some time at high temperature to allow hydrogen to accumulate in the defects[115] by diffusion because hydrogen is virtually immobile in aluminium at room temperature[98.127.135].

Blister can also be induced by incipient fusion which occurs when solidus temperature of an alloy is exceeded[175].

4.10.3.2Reaction[175] or Diffusion[176] blisters

These type of blisters are caused by reaction of the furnace atmosphere with the surface of solid aluminium leading to marked hydrogen absorption. Consequently spherical cavities grow near the surface and coalesce to form blisters.

Although water vapour in the furnace atmosphere can lead to some absorption of hydrogen, the surface reaction is remarkably catalysed by traces of sulphur[100].

Contamination of the metal surface with chloride ion is also reported[177] to act in a catalytic capacity for the surface reaction. Figure 4.11 is a microsection through a reaction blister.

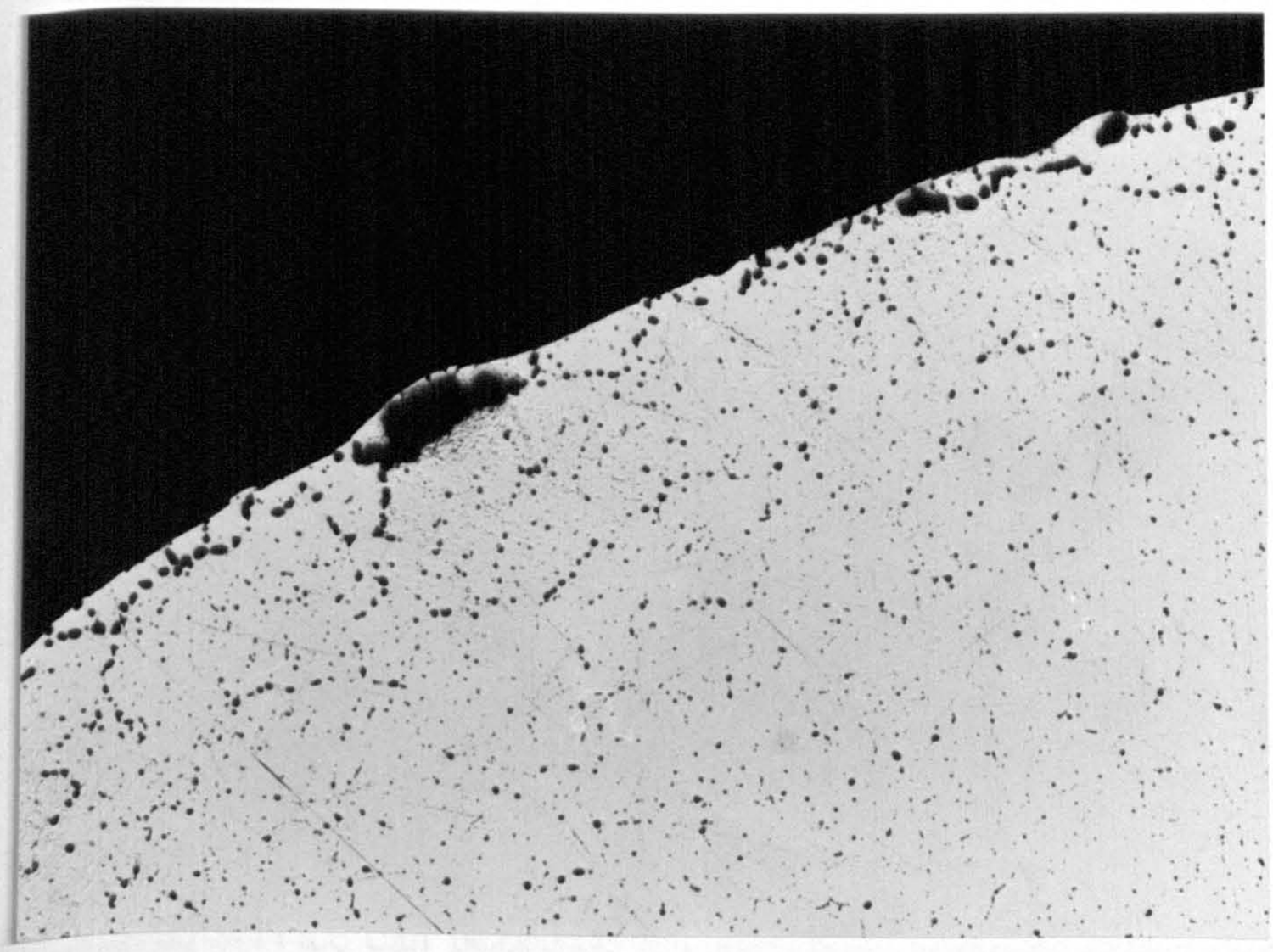

Figure 4.11 Microsection through a reaction blister on a sample of aluminium alloy, AA6063, heat treated in an atmosphere containing SO_2, x 100.

4.10.3.3"High-Temperature Oxidation"

Blistering on the surface of aluminium alloys component after prolonged high temperature heat treatment is sometimes labelled "high-temperature oxidation"[29.178.179.]. Nevertheless based on detailed discussion of the phenomenon published in a series of papers by Polmear[180.181.182.], Mills[183.] and Jenkins[184.], it can not be differentiated from the reaction or diffusion blistering discussed in the previous section.

4.10.4Other defects

4.10.4.1Effects of hydrogen on physical properties,

Interdendritic porosity in cast ingots does not weld up completely in the course of working operations during fabrication, but is flattened into planar discontinuities.[185.186.187.] In thick plate and forging, the loss of load-bearing section and internal notch effects due to the flattened porosity reduce the mechanical properties in the short-transverse direction. Turner and Bryant[189.] measured the short-transverse

strength, ductility, and impact properties of 5 and 7.5 cm thick plate rolled from 28 cm thick semicontinuosly cast ingots of a high-strength Al-Cu-Mg alloy. Their work revealed good correlation between all of these properties and the hydrogen porosity in the ingots.

4.10.4.2Hydrogen embrittlement and Stress Corrosion Cracking (SCC)

There is no reported instance of embrittlement from hydrogen introduced into aluminium alloys during manufacturing.

However, Scamens and his co-workers[188.189.190.] have shown that cathodic hydrogen introduced during service can penetrate the grain boundaries of Al-Mg and Al-Zn-Mg alloys when aged. They put this concept forward as a plausible explanation for stress corrosion cracking.

5. EXPERIMENTAL APPROACH

5.1 Objectives

The project was designed around the production of Al-Mg-Si alloy extrusion billet at a plant in which smelting and ingot casting are integrated. The intention was to apply a range of specialist techniques.

1. to quantify the hydrogen content of the metal throughout the whole process, including treatment of the freshly-reduced liquid metal, the casting process and subsequent homogenisation of the cast ingot.
2. to characterise those aspects of the structure of the metal and its surface oxide film which influence the interaction with hydrogen.

There is apparently no report of such a comprehensive study in the open literature, probably due to difficulty in reconciling expertise in industrial operation with an ability to select and apply appropriate research techniques.

There are two aspects to the experimental work:

1. The selection and use of techniques.
2. The design and implementation experimental procedure.

5.2 Selection of Experimental Techniques

Based on the objectives stated in the previous section, it was necessary to select experimental techniques for hydrogen content determination, structural characterisation and surface analysis.

5.2.1 Hydrogen content determination techniques

The two most reliable techniques for hydrogen content determination in aluminium are the hot vacuum extraction method and the Telegas instrument. Fortunately financial support was granted to construct a dedicated hot vacuum extraction apparatus, and the Telegas instrument was also available in the industrial plant and its application had been well established.

Although much easier and faster, the use of the Telegas instrument is limited to hydrogen determination in the liquid metal and under specific conditions and thus could not be used in the majority of the production stages e.g. for measuring the hydrogen content of the metal in the crucible or in the furnaces.

Therefore the hot vacuum extraction method was selected, as the main technique but the Telegas instrument was also used wherever possible for comparison and confirmation of the results.

5.2.2 Surface analysis

The characterias for selection of the surface analysis techniques were:

1. Sensitivity, the required sensitivity of the technique needs to be better than <0.5 wt% to enable the detection of Mg in the alloy investigated which nominally contained 0.5 wt% Mg.
2. Depth resolution < 10 nm, to provide for detection of natural aluminium oxide which is reported to be in the order of 10 nm.[191.]
3. Depth profile capability, to enable the characterisation of thicker oxides.
4. Practical factors, i.e. availability, cost and analytical time required.

A number of techniques are now available for surface analysis of which x-ray photoelectron spectroscopy (XPS or ESCA), and secondary ion mass spectrometry (SIMS) were utilised and are briefly described in Section 6.3.

Although these techniques derive their usefulness from their true surface sensitivity, which is[192.] 2 nm for XPS , and 1 nm for SIMS, they can be used to determine the composition of much deeper layers. This is normally achieved by sequential (or simultaneous) removal of surface layers by ion beam sputtering and surface analysis. In this way, the composition of a material may be dissected layer by layer to build up what is termed a "composition-depth profile".

Sputter-depth profiling is said to be suitable to a depth of[193.] ~ 2 μm.

5.2.3 Structural characterisation

Macroscopic observation of deep-etched fine machined surface to reveal grain morphology.

Microscopic examination of polished surface to reveal microstructures.

6. DESCRIPTION OF THE EXPERIMENTAL TECHNIQUES

6.1 Hydrogen Content Determination by Hot Vacuum Extraction.

6.1.1 Operating principles[111].

Hydrogen is extracted from a solid sample heated in a evacuated vessel to a temperature below the solidus temperature of the metal. The gas is continuously pumped to a calibrated low pressure system for collection and measurement.

The speed of the determination depends on the diffusion-controlled desorption of the gas from the sample.

6.1.2 Equipment

The equipment, illustrated schematically in figure 6.1, is constructed of hard glass. The joint, B, receives the extraction tube, A, in which a metal sample is heated by an external furnace. It affords access, via a 20 mm bore tap, C, and a liquid-nitrogen cooled trap, D, to a two-stage mercury diffusion collection pump, E, which delivers the gas extracted from the sample into a system with a calibrated volume. The size of vessel, F, is chosen to adjust the total volume of the system to about 1000 cm^3 so that the gas collected from standardised 8-10 g samples is contained at pressure in the optimum range, 0-0.1 Pa, of McLeod gauges, J. The palladium tube, G, is 50 mm long by 1.3 mm diameter with 0.15 mm wall thickness. It is closed at one end and at the open end it is gold-soldered into a platinum thimble sealed to lead-glass. A small electrical heater is provided to heat the tube to 700 °C. A small liquid nitrogen cooled trap, H, to eliminate condensable gasses, e.g. water vapour and carbon dioxide, without significantly affecting the temperature of the permanent gasses present. The system includes a pirani gauge (not shown), but precise pressure measurements are taken on the McLeod gauges, J.

The system can be evacuated by a three stage mercury diffusion pump, not shown in figure 6.1, backed by a rotary pump and can be isolated from it by the tap, K. A by-pass

tap, L, permits evacuation of the extraction tube when a sample is loaded, without admitting air to the system.

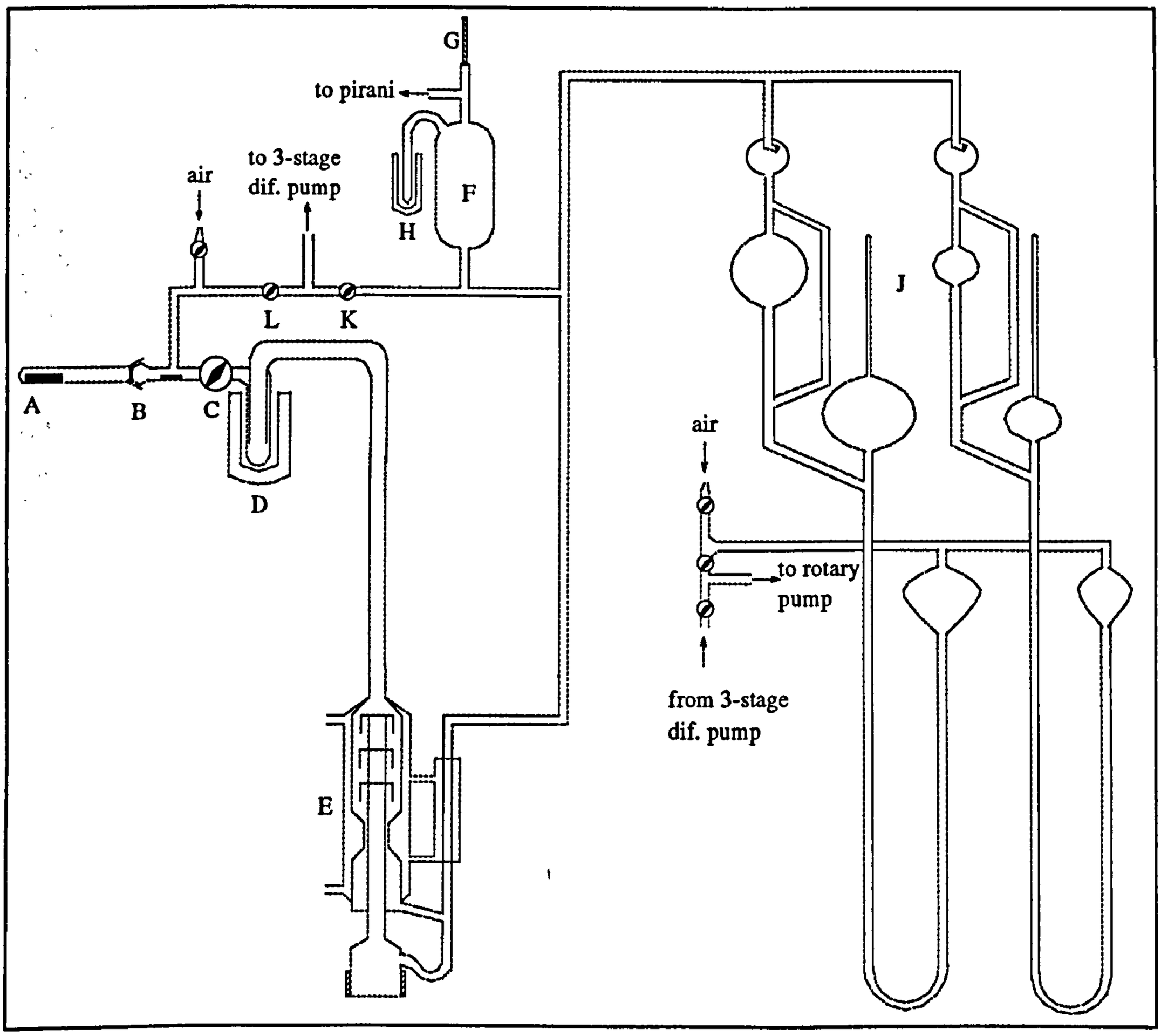

Figure 6.1 Schematic illustration of Hot Vacuum Extraction equipment.

The general construction is shown in figure 6.2. The glass work is erected on a framework permitting access for glass-blowing and servicing, The diffusion pumps are electrically heated. The furnace for pre-heating the extraction tube is suspended from an arm pivoted on the framework, facilitating its alignment with and movement over the end of the extraction tube.

The induction (RF) furnace for heating the sample during extraction is fitted on a separate frame which can easily me moved over the end of the extraction tube at the start of the test.

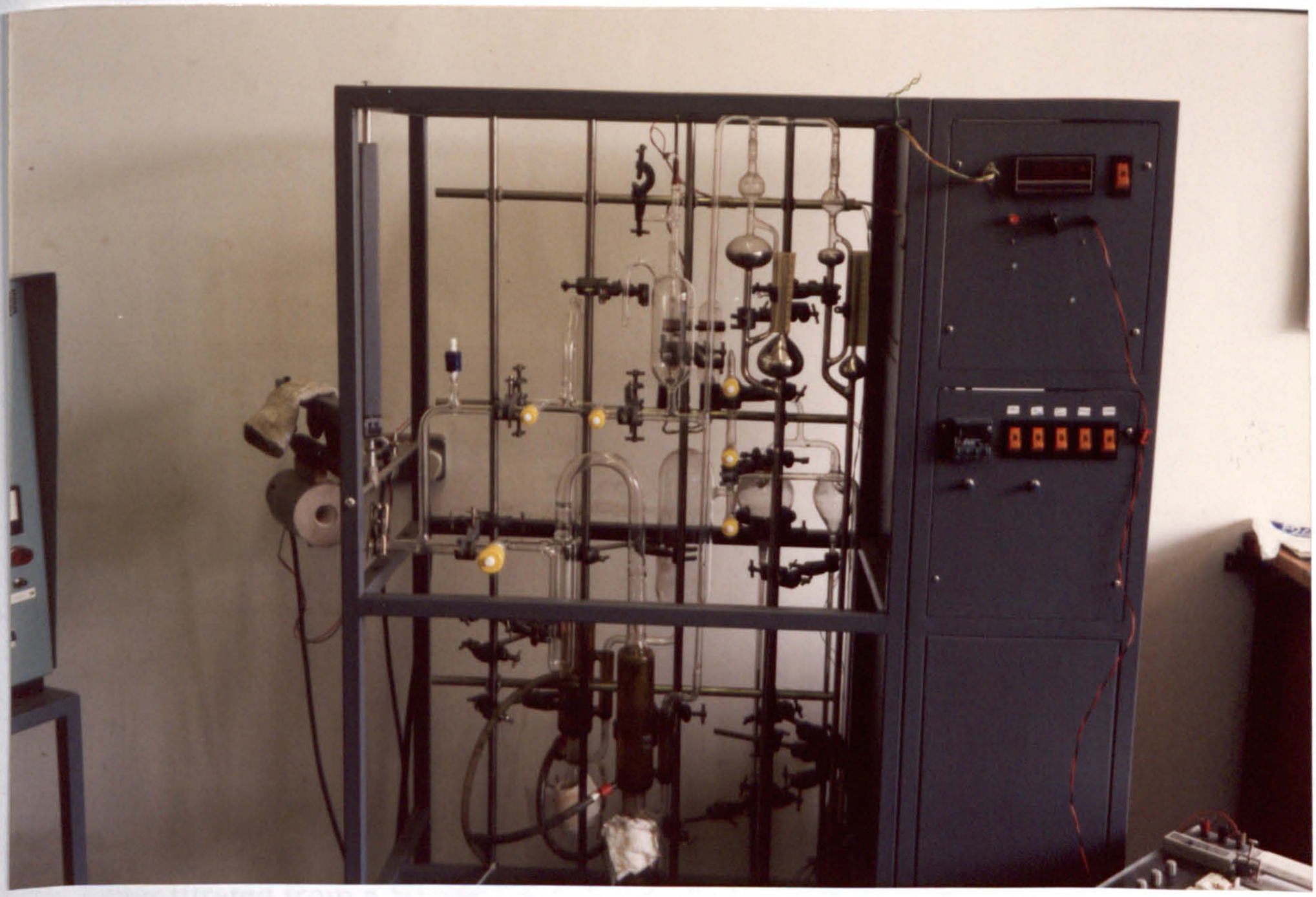

Figure 6.2 General view of Hot Vacuum Extraction equipment.

6.1.3 Commissioning and calibration

New equipment was constructed for the project. The McLeod gauges were calibrated before installation. The new glass, new mercury charge in the pumps and gauges and new oil in the rotary vacuum pump required prolonged pumping to outgas them. At this stage, pinholes in the glass and defects in seals and taps could be identified and rectified. The volume of the gas collection was calibrated when the equipment was leak-free and completely outgassed

6.1.3.1 Calibration of Mcleod Gauges No. 1 (fine scale gauge)

Radius of Capillary Tube

Capillary tube is "Vernida" precision bore tubing of 0.5 mm uniform radius and guaranteed tolerance +/- 1%. The length of a column of mercury in the tube was measured using a travelling microscope. To avoid meniscus error, the end of the column was taken as 1/3 of the distance from the chord to the apex of the meniscus. The mercury was carefully transferred to a small dish and weighed.

		(1)	(2)	(3)
Length of mercury thread (1)/mm	=	69.16	90.77	90.48
Weight of dish (w)/g	=	2.6040	2.6040	2.6040
Weight of dish + mercury (w)/g	=	3.2612	3.4785	3.4560
Weight of mercury (w)/g	=	0.6572	0.8745	0.8520
Room temperature	=	20°C	20°C	20°C
Radius of tube = (w/13.51)/mm	=	0.473	0.476	0.470

Average value of radius r/mm = 0.473

Volume of Bulb

Water titrated from a 50 cm^3 Class B burette into bulb,

Volume of water	(1)	50 + 47.8 = 97.8 +/- 0.01 cm^3
	(2)	50 + 47.7 = 97.7 +/- 0.01 cm^3
	(3)	50 + 47.7 = 97.7 +/- 0.01 cm^3
	(4)	50 + 47.7 = 97.7 +/- 0.01 cm^3

Average value of volume, $V = 97.7\ cm^3 = 9.77 \times 10^4\ mm^3$

McLeod constant, C

A constant, C, relates the column of mercury corresponding to the McLeod reading, R, to the column of mercury which would be supported by the pressure, *p*, in the system:

$$C = \pi r^2/V = (0.473)^2/ 9.77 \times 10^4 = 7.195 \times 10^{-6}\ mm^{-1}$$

6.1.3.2 Calibration of Mcleod Gauges No. 2 (coarse scale gauge)

Radius of Capillary Tube

The capillary tube is of uniform radius but not guaranteed to be precisely the nominal value of 1.0 mm. The length of a column of mercury in the tube was measured using a travelling microscope. To avoid meniscus error, the end of the column was

taken as 1/3 of the distance from the chord to the apex of the meniscus. The mercury was carefully transferred to a small dish and weighed.

		(1)	(2)	(3)
Length of mercury thread (1)/mm	=	96.50	100.60	97.65
Weight of dish (w)/g	=	2.652	2.653	2.653
Weight of dish + mercury (w)/g	=	7.293	7.471	7.336
Weight of mercury (w)/g	=	4.641	4.818	4.683
Room temperature	=	20°C	20°C	20°C
Radius of tube = (w/13.561)/mm	=	1.060	1.06	1.060

Average value of radius r/mm = 1.06

Volume of Bulb

- Water titrated from a 50 cm^3 Class B burette into bulb,

Volume of water	(1)	19.5 +/- 0.01 cm^3
	(2)	19.4 +/- 0.01 cm^3
	(3)	19.5 +/- 0.01 cm^3
	(4)	19.5 +/- 0.01 cm^3

Average value of volume, $V = 19.5\ cm^3 = 1.9 \times 10^4\ mm^3$

McLeod constant, C

A constant, C, relates the column of mercury corresponding to the McLeod reading, R, to the column of mercury which would be supported by the pressure, *p*, in the system:

$$C = \pi r^2/V = (1.06)^2/ 1.9 \times 10^4 = 1.81 \times 10^{-6}\ mm^{-1}$$

6.1.3.3 Gas collection system

McLeod Gauge No. 1 - Factor $7.195 \times 10^{-6}\ mm^{-1}$ Standard Volume 1022 cm^3

Procedure: Hydrogen expanded from standard volume bulb to system volume.

$$\text{Volume of system} = \frac{(M_1)^2-(M_2)^2}{(M_2)^2} \times (\text{standard volume})$$

Where M_1 and M_2 are McLeod gauge readings before and after expansion (Table 6.1).

Table 6.1 McLeod gauge readings

	Before expansion	Mean	After expansion	Mean	Volume cm^3
1	98.9, 98.9, 98.9, 98.9, 98.9, 98.9	98.9	72.9, 72.9, 73.0, 73.3, 73.1, 73.1	73.1	849
2	97.2, 97.0, 97.1, 97.1, 96.9, 97.0	97.1	70.9, 70.9, 71.9, 71.8, 71.2, 71.1	71.3	873
3	87.9, 87.8, 87.5, 87.6, 87.9, 88.0	87.8	64.1, 64.2, 64.1, 64.2, 64.2, 64.2	64.2	889
4	88.4, 88.4, 88.3, 88.4, 88.4, 88.5	88.4	65.0, 65.0, 65.0, 65.0, 65.0	65	868
5	80.2, 80.2, 80.1, 80.2, 80.2, 80.2	80.2	58.6, 58.7, 58.6, 58.5, 58.6, 58.6	58.6	892
6	82.3, 82.1, 82.1, 82.3, 82.3, 82.3	82.2	60.0, 60.0, 60.1, 60.1, 60.0, 60.0	60	896
7	73.8, 73.8, 73.8, 73.9, 73.9, 73.9	73.9	54.4, 54.4, 54.4, 54.4, 54.4, 54.4	54.4	864
8	75.5, 75.5, 75.5, 75.5, 75.5, 75.5	75.5	55.5, 55.5, 55.5, 55.6, 55.6, 55.6	55.6	862
9	91.7, 91.7, 91.7, 91.5, 91.6, 91.6	91.6	66.4, 66.5, 66.6, 66.5, 66.6, 66.7	66.6	911
10	92.9, 92.9, 92.9, 92.8, 92.9, 92.9	92.9	67.8, 67.8, 67.8, 68.0, 68.0, 67.9	67.9	891
11	99.2, 99.2, 99.1, 99.1, 99.1, 99.1	99.1	73.1, 73.2, 73.2, 72.2, 72.3, 72.2	73.2	851
12	98.0, 97.9, 98.0	98	72.6, 72.6, 72.6	72.6	840
13	64.1, 64.1, 64.1	64.1	47.4, 47.3, 47.3	47.3	855
14	96.4, 96.3, 96.3	96.3	71.7, 71.7, 71.7	71.7	822
15	71.7, 71.7, 71.7	71.7	53.0, 53.0,53.0	53	848
16	95.4, 95.4, 95.4	95.4	70.9, 70.9, 70.9	70.9	828
17	70.9, 70.9, 70.9	70.9	52.3, 52.3, 52.3	52.3	856

Average of 17 determination = 864 cm^3 (scatter + 5.4% - 4.9%)

6.1.3.4 System Factor, F

Volume of gas in system = $F \times R^2$

where: $F = V_{system} \times 273/298 \times C/760 \times R^2$

$$= \frac{867 \times 7.195 \times 10^{-6} \times 273}{760 \times 298} R^2$$

$$= 7.519 \times 10^{-6} \text{ cm}^3$$

6.1.3.5 RF heater programme calibrations

Coil: 7 turn 50 mm diameter horizontal coil of 6 mm copper pipe,

Pure Aluminium

Material: AA 1100 (99.2% pure Al) machined from Ransley bar.

Sample: 9.8 mm diameter x 42 mm long cylinder

1. Heating at Full RF Power- First Run, Table 6.2.

Cold junction at ambient temperature, i.e. 18°C (0.70 mV)

Table 6.2 RF heater programme calibration, Pure Aluminium, first run.

Time/s	mV reading for 23.6°C CJ	mV equivalent for 0°C CJ	Temperature °C
0	0.00	0.70	18
5	1.20	1.90	47
10	2.45	3.15	77
15	3.40	4.10	100
20	4.40	5.10	124
25	5.55	6.25	153
35	8.23	8.98	220
40	9.80	10.50	258
45	11.20	11.90	292
50	12.47	13.17	323
55	13.93	14.63	358
60	15.30	16.00	391
65	16.90	17.60	428
70	18.67	19.37	470
75	20.25	20.95	507
90	24.30	25.00	602

2. Heating at Full RF Power- Second Run, Table 6.3.

Cold junction at ambient temperature, i.e. 18°C (0.70 mV)

Table 6.3 RF heater programme calibration. Pure Aluminium, second run.

Time/s	mV reading for 23.6°C CJ	mV equivalent for 0°C CJ	Temperature °C
0	0.00	0.70	18
20	4.83	5.53	130
40	10.00	10.70	263
45	11.60	12.30	302
55	14.55	15.25	373
80	22.33	23.03	556
85	23.95	24.65	594
90	25.40	26.10	628

3. Holding power for constant temperatures

% RF Power	mV reading for 22.6°C CJ	mV equivalent for 0°C CJ	Temperature °C
10	22.10	22.80	550

AA 6063

Material: AA 6063 extruded section.

Sample: 10.0 mm diameter x 40.0 mm long cylinder.

1. Heating at Full RF power, Table 6.4.

Fine wire chromel/alumel thermocouple inserted into end of sample and peened in tightly to make good thermal contact.

Cold junction at ambient temperature, i.e. 25°C (1.06 mV)

Times to reach prescribed temperatures noted.

Table 6.4 RF heater programme calibration, AA 6063 alloy.

Time/s	mV reading for 25°C CJ	mV equivalent for 0°C CJ	Temperature °C
0	0.0	1.0	25
5	1.0	2.0	49
10	2.1	3.1	76
15	3.4	4.4	107
20	4.5	5.5	134

25	5.6	6.6	162
30	7.0	8.0	197
35	8.2	9.2	224
40	9.6	10.6	261
45	11.0	12.0	295
50	12.4	13.4	329
60	15.4	16.4	400
65	17.1	18.1	440
70	18.8	19.8	480
75	20.2	21.2	513
80	22.0	23.0	555

2. Holding power for constant temperatures

% RF Power	mV reading for 25°C CJ	mV equivalent for 0°C CJ	Temperature °C
6	21.70	22.78	540

6.1.4 Sample preparation

To achieve accurate and reproducible results a stringent sample preparation must be adhered to;

1. Cylindrical samples, 40 mm x 10 mm diameter are most convenient.
2. The sample must be machined dry, finishing with a light but fast cut with a slow feed. It is vitally important to remove all the original surface.
3. To avoid contamination, machined sample must not be touched.

6.1.5 Operating procedures

On assembling the apparatus for a determination, the sample is placed in the extraction tube at , N, as shown in figure 6.3.

The tube is evacuated and pre-baked at 800 °C up to the point, M, with the electric radiation furnace for at least one hour. When the tube has been conditioned, the sample is moved to the extraction position, A, using the manipulator, P, actuated by an external magnet and the manipulator is drawn back behind the joint, B.

Liquid nitrogen is applied to traps D and H to eliminate traces of water vapour, which otherwise reacts at the hot sample surface, producing spurious hydrogen. Making sure that taps K and L are closed the extraction tube is connected to the gas collection system by opening the tap C, if the gas collected in 15 minutes is negligible, the test may proceed.

The induction furnace is set to a predetermined set up, to provide a rapid heat up to the prescribed temperature, and is moved into position. After starting the furnace, the pressure in the collection system is monitored continuously by the McLeod and Pirani gauges until it is virtually constant, indicating the end-point. At this point the palladium tube is heated to 700 °C for 10 minutes, allowing the hydrogen to diffuse out. The residual gas is usually < 5% of the total quantity collected. It is a mixture[111] of carbon monoxide, methane and nitrogen, derived partly from the surface of the sample and partly from the system. Its pressure is recorded to apply as a correction.

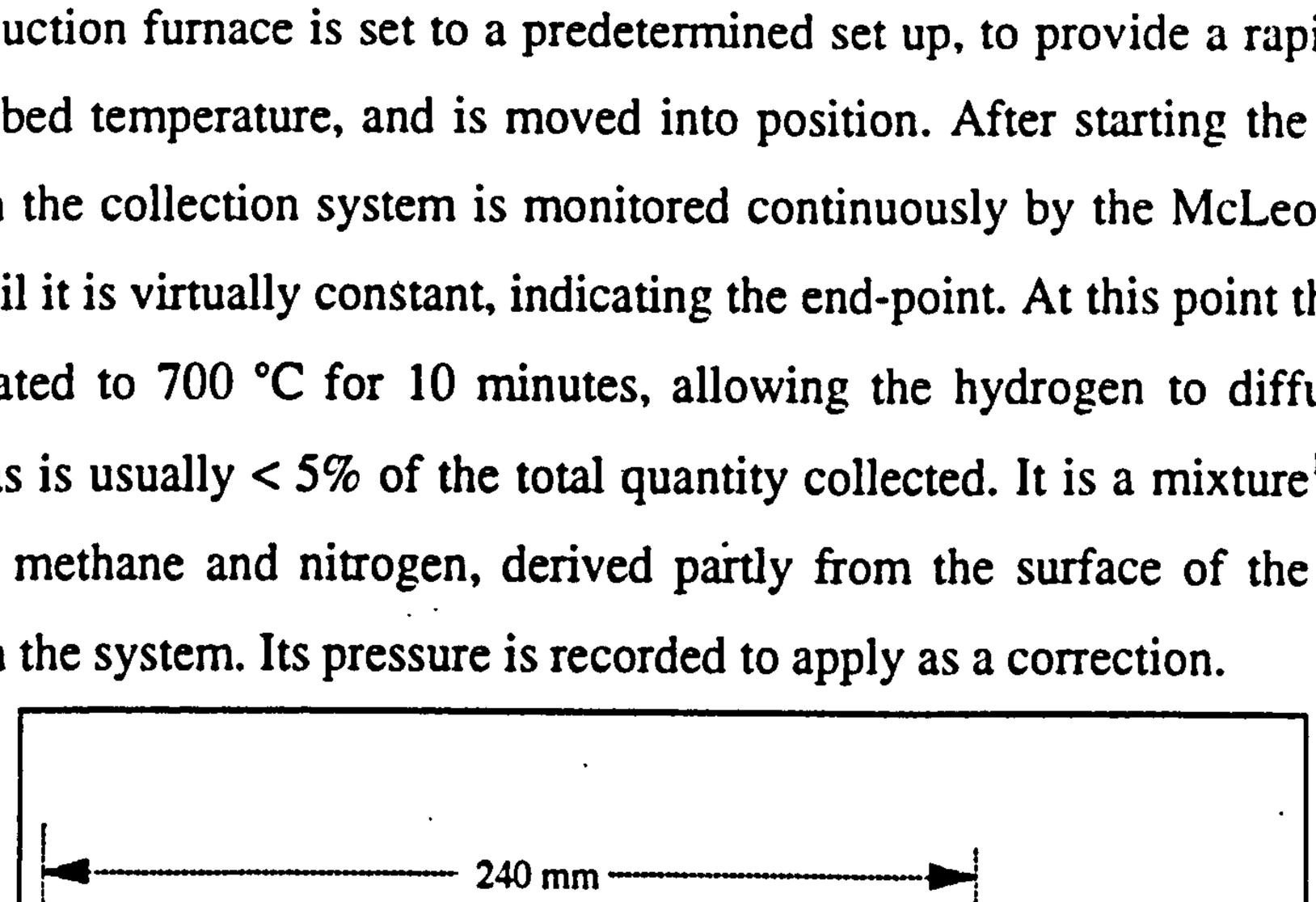

Figure 6.3 Extraction tube assembly

The gas collected is subjected to a further correction for hydrogen evolved at the sample surface, which is evaluated from blank determinations on representative degassed samples after re-preparation to restore the original surface condition. Its value

depends on the sample composition, the preparation, and the state of the equipment and is in the range 1.0-3.5 x 10^{-4} cm^3 of hydrogen per cm^2 of geometric surface area.

6.1.6 Sources of error and validity of results

A standard chart recorder can be connected to the apparatus providing a curve for the evolving gas, enabling the immediate detection of any abnormal gas evolution during the testing.

The reproducibility of the method was illustrated by Talbot[111] by the following results:

1. 14 replicated determinations on the same piece of extruded 99.8% pure aluminium rod yielded results all within the range 0.24-0.28 cm^3/100g with a standard deviation of +/- 0.014 cm^3/100g for a single result.
2. Duplicated determinations on each of 43 samples of various commercial grade of pure metal and alloys containing up to 1.0% magnesium yielded results with a standard deviation of +/- 0.015 cm^3/100g for a single result.
3. Duplicated determinations on each of 16 samples of alloys containing over 5% magnesium, with hydrogen content in the range of 0.14-0.97 cm^3/100g, yielded results with a standard deviation of 0.023 cm^3/100g for a single result.

6.2 Hydrogen Content Determination by Telegas

6.2.1 Operating principle

The principle is to determine the activity of diatomic hydrogen in equilibrium with the liquid solution. Since hydrogen is virtually ideal, this is equivalent to measuring the hydrogen pressure established in an inert gas (usually nitrogen) which is bubbled through the liquid metal. The hydrogen content is then given by Seiverts' isotherm, Equation 4.3, usually written as:

$$G = s^{\Theta} (p/p^{\Theta})^{0.5}$$

where:

G is hydrogen content.
p is the measured pressure.
s^{Θ} is the solubilty for the pressure p^{Θ} = 101325 Pa.

Telegas is designed to measure p. The concentration of hydrogen in solution can then be calculated from the available values for solubility[124.125.194.].

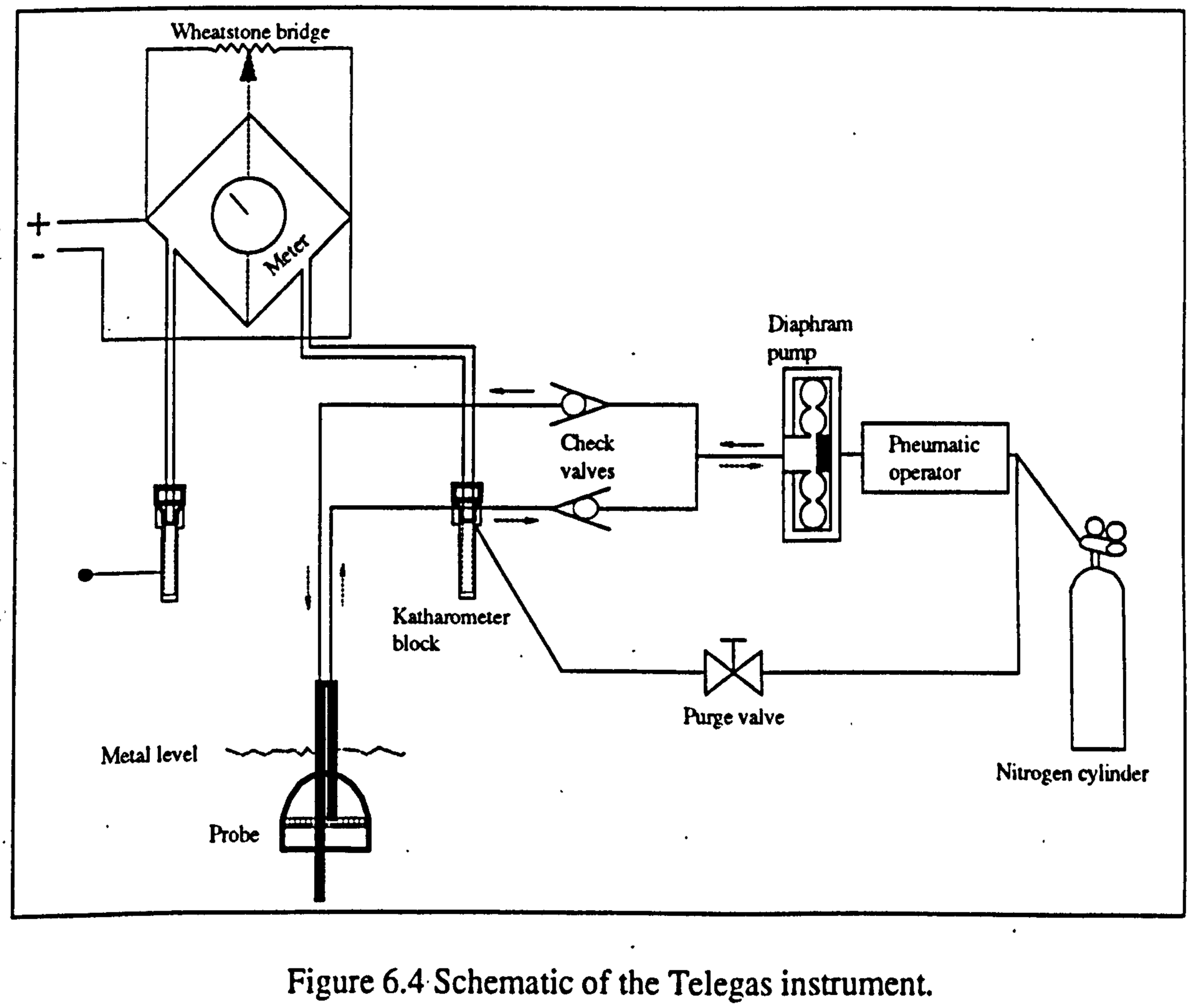

Figure 6.4 Schematic of the Telegas instrument.

6.2.2 Instrument

Figure 6.4 is a schematic[195.196.] of the Telegas instrument. It comprises three basic components[195]: (1) a capillary system around which the nitrogen carrier gas is circulated through the melt via a twin-bore alumina probe (2) a Katharometer (or thermal conductivity cell) for measuring the amount of hydrogen entrained in the nitrogen gas

and (3) a Wheatstone bridge circuit for determining the decrease in resistance of the Katharometer as the amount of the hydrogen in the carrier gas increases.

6.2.3 Operating principle

After pre-heating the probe is inserted into the metal so that the cup is well immersed, i.e. about 4 cm below the surface. During entry into the metal, the carrier gas purge valve is opened, blowing a stream of nitrogen out through the probe to clear away the oxide films. The valve is closed and the pump is operated until the millivoltmeter is steady. The hydrogen content is found from a calibration chart which related meter reading, hydrogen solubility as affected by temperature, and hydrogen content in cm^3 per 100 g of metal.

6.2.4 Validity of results

In the original assessment of the Telegas instrument, results determined with the Telegas for laboratory melts were compared with corresponding results for chill-cast samples[154]. This comparison is reproduced in Figure 6.5, which shows a reasonably good correspondence between the Telegas and Vacuum Extraction results with no detectable systematic error. Similar comparisons have been made on several occasions, for example by Hess[197]. Some authors find a small systematic error, usually with the Telegas instrument reading low[198], which they attribute to slight leaking away of hydrogen along the outside surface of the probe.

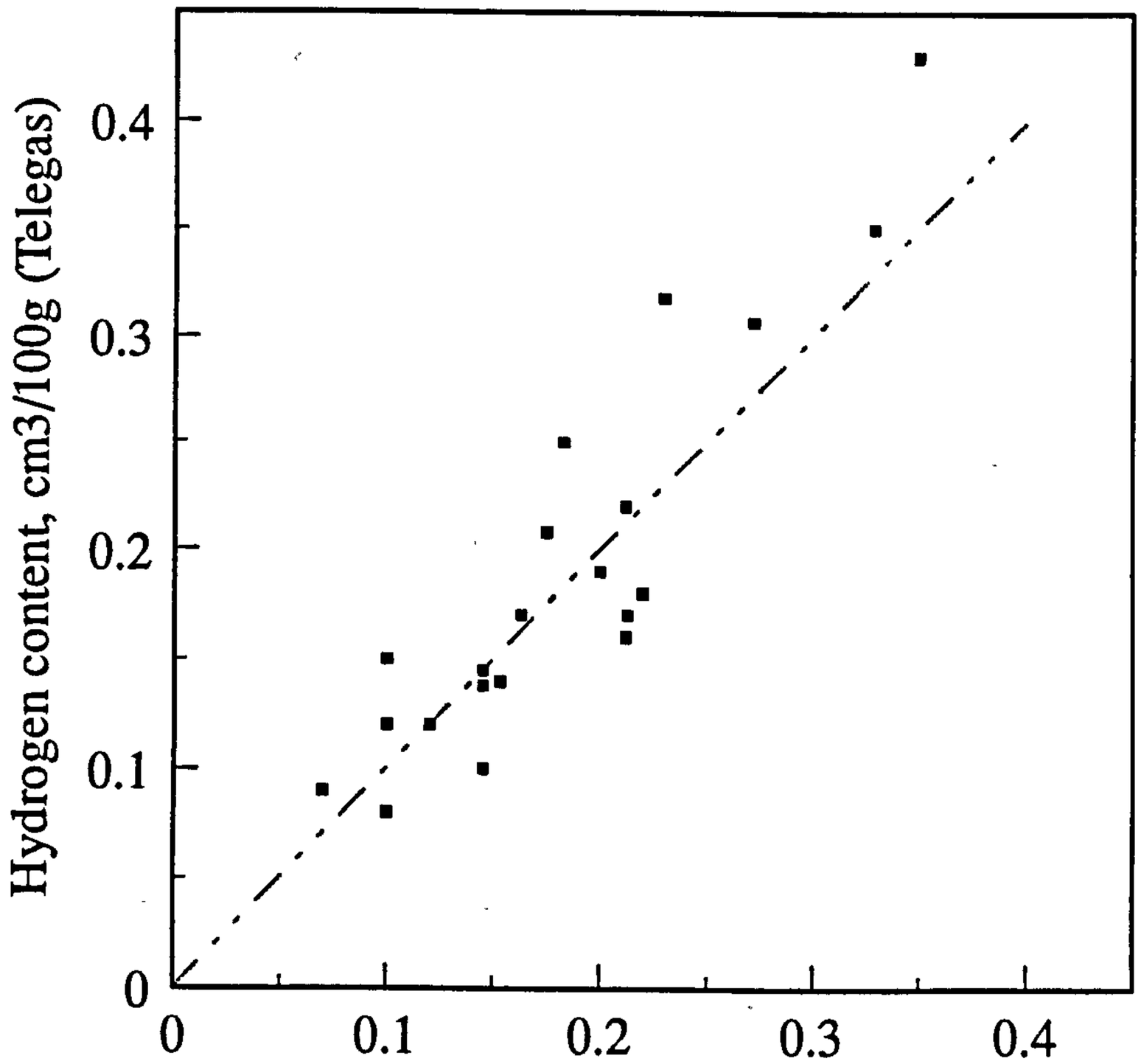

Figure 6.5 Comparison of hydrogen determination results of Telegas instrument with Vacuum Extraction determination of the same metal.

6.3 Surface Analysis Techniques.

6.3.1 X-ray Photoelectron Spectroscopy (XPS),

In XPS, the sample surface is illuminated with a source of soft x-rays, photoionisation of a core level takes place, as illustrated schematically in Figure 6.6. The resultant photoelectrons have a kinetic energy E which is related to the x-ray energy ($h\nu$) by the Einstein relation

$$E = h\nu - E_B - \phi \qquad (6.1)$$

where E_B is the binding energy of the electron in the material and is characteristic of the individual atom and ϕ is the work function of the energy analyser.

In addition, the electron binding energies within any one element are not fixed and small variations[193] of up to 10 eV may occur. These "chemical shifts" are caused by changes in the valence electronic structure of the atoms concerned and so may be used to provide information on chemical bonding.

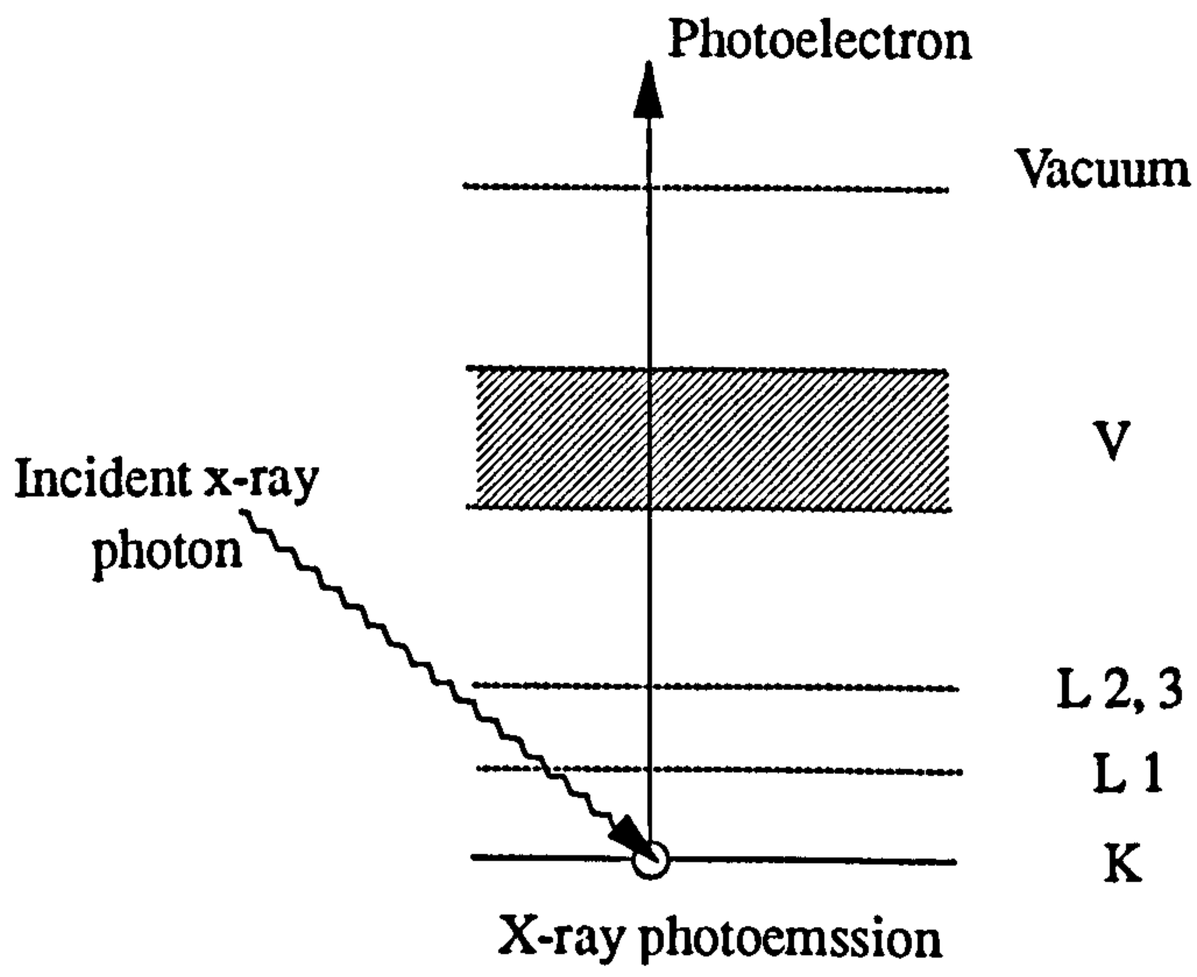

Figure 6.6 A schematic energy level diagram illustrating the photoexcitation of a K shell electron by a low energy X-ray photon ($h\nu$).

Although the incident radiation in XPS may penetrate as deep as[199.] 1 μm into the sample, it is only those electrons which come from the first few atomic layers escape with all their original energy intact. The electrons which originate further within the sample, lose energy in inelastic collisions and may no longer be identified as such. It is estimated that the mean free paths or electron escape depth (λ) range from 1 nm in metals to about 10 nm in organic coatings[200.201.].

6.3.2 Secondary Ion Mass Spectrometry (SIMS),

The basis of SIMS analysis is the sputtering process. A beam of primary ions impinges onto the solid surface of the sample and the atoms in the surface of the sample are sputtered off into the surrounding vacuum. When a primary ion strikes the surface of the sample it can be back-scattered or, more probably, will penetrate into the surface of the sample, losing its initial energy through a series of elastic and inelastic collisions with the atoms of the sample. This collisions cascade process is depicted[202.] in figure 6.7.

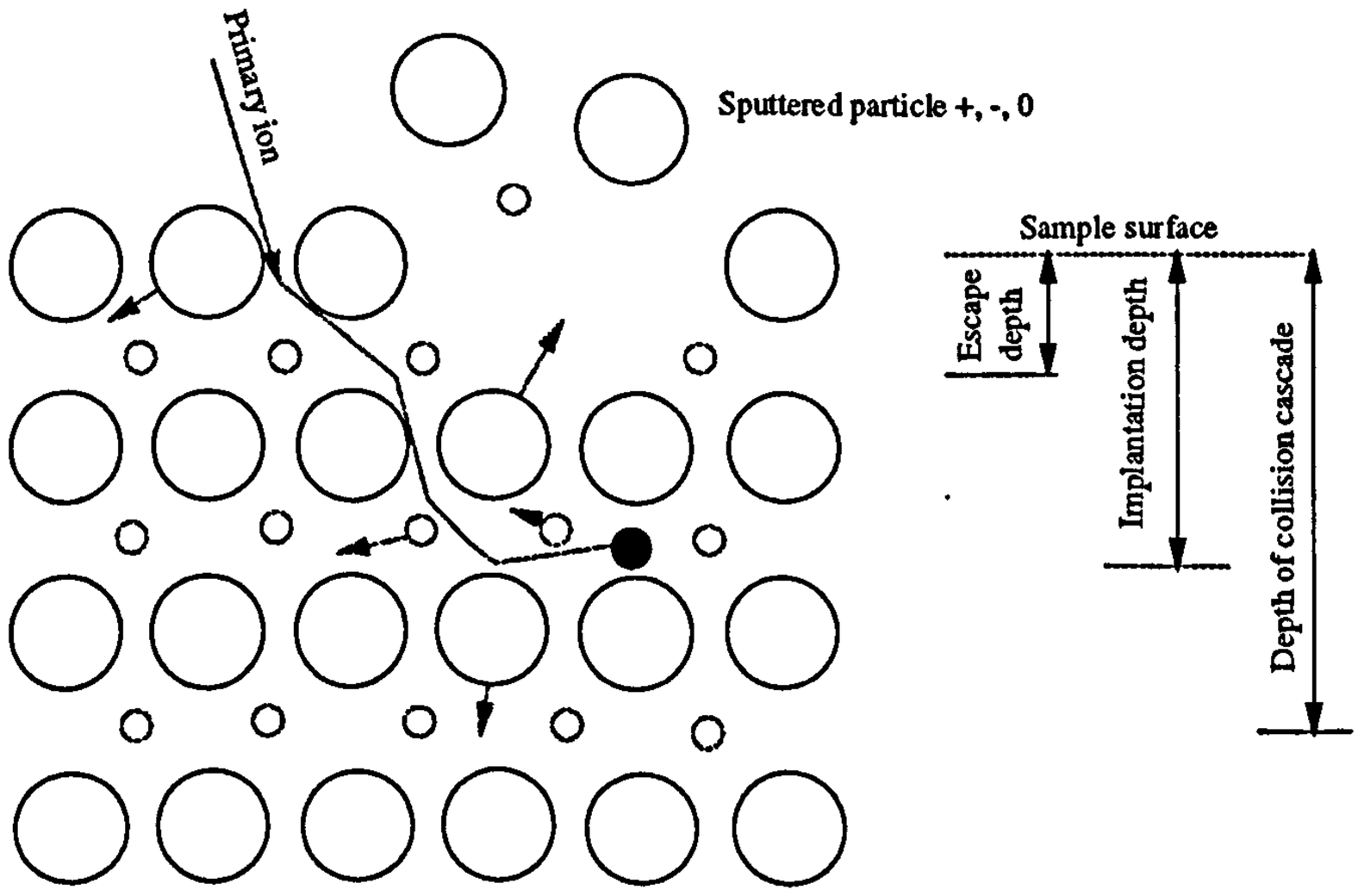

Figure 6.7 Schematic diagram of the sputtering process.

Sputtering takes place when atoms near the surface of the sample receive sufficient energy from the cascade to escape from the surface of the sample. These sputtered

particles can be ejected as atoms or molecules in a neutral, excited or ionised state, but it is only the ionised species that can be used for SIMS analysis.

The characteristics that have generated the considerable interest in SIMS are[203]; high detection sensitivity for the majority of elements, depth concentration profiling of trace constituents with depth resolutions ≤ 5 nm, lateral characterisation of the surface on a micrometer scale, isotopic analysis, and analysis of low atomic number elements (H, Li).

Surface analysis by SIMS falls into two categories; low current density sputtering and high current density sputtering. The categories are determined by the characteristics of the primary ion beam. A low current density sputtering analysis results in a very small fraction of the surface being disturbed, a result that approaches a basic requirement of a true surface analysis method. High current density sputtering with its high surface removal rate, on the other hand, is required for obtaining elemental depth profiles.

6.4 X-Ray Diffraction (X R D)

In principle, XRD can yield chemical information based on the detection of crystal structures which may be present.

Some preliminary experiments were conducted in which both bulk and powder samples were submitted to XRD examination in an attempt to identify species in oxide films on aluminium alloy samples. Unfortunately the results proved to be unclear because the diffraction signals from the aluminium metal were too intense as to overwhelm any signals which originated from the oxide.

6.5 Optical Microscopy and Metallography.

The care needed in preparing scratch free metallographic samples of aluminium alloy is well known . Several suitable procedures using proprietary materials have been developed. The particular procedure used in the present work is as follows:

1. After the usual sectioning and mounting, the sample is rough ground on grinding wheel with P120 (180 G), P400 (320 G), P800 (400 G), and P1200 (800 G) abrasive papers respectively in the usual manner.
   The samples are then fine ground with a grit 600 soft (Microcut by Buehler) abrasive paper.
2. Then the samples are rough polished on an automatic polishing wheel at approximately 100 rpm, with a load of 1.5 kg over Texmet® (by Buehler) polishing cloth and 6 μm diamond polishing compound (paste), lubricated by a water based lubrication (type W by Kemt®).
   A polishing period of 8 - 12 minutes is found to be suitable.
3. The wheel is removed and the automatic polisher is washed, then the final polishing wheel is installed. this wheel is covered by Mastertex® (by Buehler) polishing cloth, and as polishing medium, OP-S® suspension (by Struers), which is SiO_2 particulate suspended in water is used. For best result the OP-S is diluted (50-60%) with distilled water and the polisher is loaded with 1.5 kg weight and the wheel is operated at approximately 100 rpm. A polishing time of 8-12 minuets should be sufficient.
   The samples must be thoroughly washed with water and soap, rinsed with alcohol and dried, particularly prior to and between polishing stages.

7. EXPERIMENTAL PROCEDURES

Before describing the experimental procedure, the layout of the production facility must be described and the production process briefly explained.

7.1 Plant Description

7.1.1 Casting facility layout.

Except for possible minor variations, the set up depicted schematically in Figure 7.1 is a typical layout of D C casting facility for aluminium ingot. It consists of;

- the crucibles, which are ladles with the capacity of ~ 6 tonne, used to deliver the liquid metal from the electrolysis cells (pot rooms) to the casting unit.
- a fixed hearth, reverberatory gas fired furnace with a capacity for 45 tonne, of molten metal. This furnace is known as the melting furnace or simply, the melter,
- two reverberatory, gas fired, tilting furnaces, designated the casting furnaces. The tilting toward the casting table is facilitated hydraulically and provides for the controlled flow of metal for casting. These furnaces are alternatively known as the holding furnace or simply the holders,
- a casting table, which is basically a liquid metal distribution system and it houses the D C casting moulds,
- the launder system comprises refractory lined steel channels, which connect the melting furnace to the casting furnace, and the casting furnace to the casting table,
- the filter bowls, which consist of refractory lined steel boxes, fitted in the launder between the casting furnace and the casting table to accommodate the ceramic foam filter (CFF), and,
- the moulds which are of the air-slip hot-top pattern illustrated in Figure 3.13 and described in Section 3.3.3.

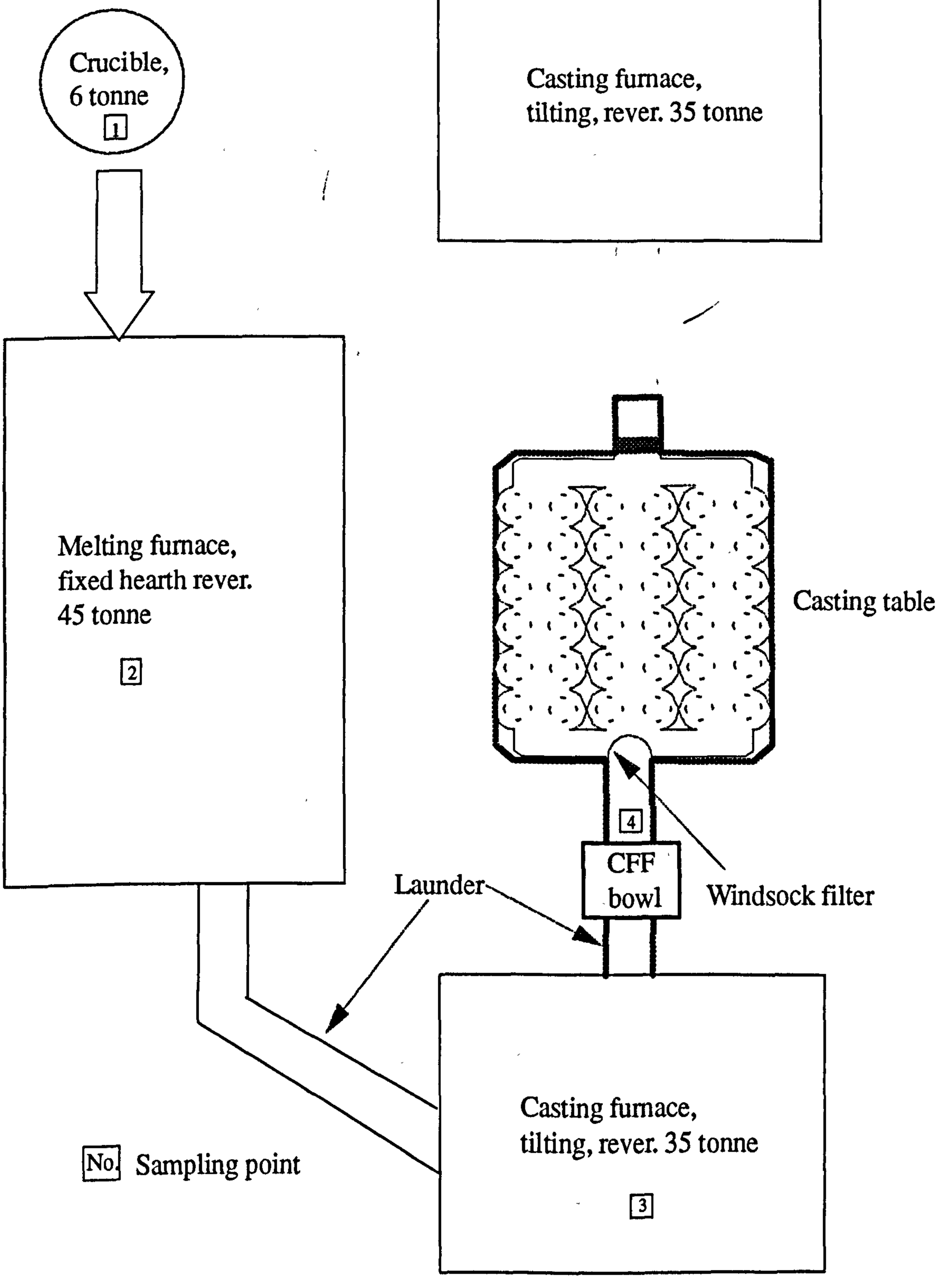

Figure 7.1 D C casting facility layout, top view.

7.1.2 The production process

The process begins with:

1. Filling the melting furnace with commercially pure liquid aluminium, which is delivered in ~ 6 tonne crucibles, and some solid charge, which is the in-house scrap. The liquid metal from the pot rooms, is normally at 800-900 °C, this high temperature facilitates the rapid melting of the solid charge.
   When the furnace is full and all the solid charges have melted, some alloying elements such as silicon and iron are added and the melt is then stirred and skimmed. The metal can now be transferred to the casting furnace.

2. After transferring to the casting furnace, the remaining alloy addition and further stirring is carried out.
   If the chemical composition is satisfactory, the melt is then degassed by solid tablets of hexachlorethane (C_2Cl_6).
   The degassing is accomplished by putting a predetermined amount of the tablets in a steel basket and then submerging into the metal bath, causing a violent reaction that leads to the generation and accumulation of various oxides and inclusions on the melt surface that must be skimmed off.

3. Following the degassing and skimming, the melt is left un-disturbed, i.e. settling for one hour, after which the casting can proceed.

4. To start the casting, the casting furnace is tilted to allow the metal to flow through the launder, and the ceramic foam filter bowl, onto the casting table, where casting commences.

5. Since the casting furnace has a capacity of ~ 40 tonne, whilst one complete casting run produces only ~ 20 tonne of ingot, thus two casting runs or as they are called two "drops" are produced from each furnace preparation (cast).
   The "drops" from the same cast are designated as A and B, corresponding to the first and second drop respectively.

7.2 Effect of Processes on the Hydrogen Content of the Liquid Metal

7.2.1 Sampling procedure

To collect suitable samples, first four sets of Ransley's pin[161] sampling moulds were obtained. The mould provides a suitable cylindrical sample 11 mm in diameter and 100 mm long, which can be easily detached from its liquid metal feeder wedge.

After careful study of the production process and considering the practical limitations, two sampling sequences were adopted covering the whole process.

7.2.1.1 Sampling sequence 1

This sequence of sampling was intended to investigate hydrogen content variation which may be attributed to the liquid metal state and to processes which precede casting. The following sequence was set out;

1. Sampling the liquid metal in the crucible just before charging into the melting furnace, to establish the inherent hydrogen content in the commercially pure metal as received from the pot rooms.

2. To take samples from the melting furnace just before transferring the metal to the casting furnace. The hydrogen content of these samples would identify the effects of the following factors:

	likely effect on hydrogen content
hydrogen in the freshly reduced metal	increase
hydrogen in the solid charge	decrease
hydrogen in the alloying element	increase
moisture on the surface of the solid charge and tools	increase
reducing temperature	decrease
stirring (turbulence)	decrease/increase

There is no point in sampling before this stage, as the metal is extremely heterogeneous both thermally and chemically. The melt is made more homogeneous by stirring prior to transfer.

3. Due to rapid flow of the metal and its shallowness during the transfer, sampling from the transfer launder was extremely prone to contain excessive oxides, rendering the sample un-suitable for hot vacuum extraction technique. Therefore it was decided to sample the metal from the casting furnace immediately after the transfer. The hydrogen content of these samples would identify the effects of the following factors:

	<u>likely effect on hydrogen content</u>
contact of the liquid metal with the launder	increase
turbulence during the transfer	increase/decrease
reducing temperature	decrease

4. The melt was sampled immediately after the final alloying and stirring. The hydrogen content of these samples would identify the effects of the following factors:

	<u>likely effect on hydrogen content</u>
hydrogen in the alloying element	increase
significant turbulence	increase/decrease
reducing temperature	decrease

5. Sampling the metal immediately after degassing and skimming. The hydrogen content of these samples were of particular interest as it follows the process which has as its main objective, the reduction of hydrogen in the melt, by both positive degassing i.e. the mass transport of the hydrogen out of the melt as discussed previously, and by indirect effect i.e. the consequence of equilibration of the melt with its atmosphere due to the turbulence caused by degassing and by floating out the oxides and other inclusions from the melt.
Therefore these samples could provide a good indication of the efficiency of in furnace degassing by hexachlorethane (C_2Cl_6).

6. To determine if the settling (holding) time influences the hydrogen content, the melt was sampled every ten minutes, starting with 10 minutes after the degassing and skimming. A total of five sets of samples was to be collected as the total settling time was 60 minutes.

7. After the start of casting it was not possible to continue sampling the metal from the furnace due to it being tilted, and it was decided to take samples from the launder immediately after the ceramic foam filter, as marked (4) in figure 7.1. The reasons for choosing this point are;

   i. the metal flow and depth was suitable for hydrogen measurement with Telegas as well, and the hydrogen content determined with this technique could be compared with the hot vacuum extraction method,
   ii. the metal had already been filtered, thus any potential effect of filtration was also taken into account,
   iii. and this was thought to be a suitable reference point from which other sampling sequences were to start.

In order to see if the hydrogen content of the melt varies during the casting. The metal was sampled from sampling point 4 (see Figure 7.1), at;

   i. the start of drop A,
   ii. ten minutes into drop A, this is to allow the metal flow to stabilise,
   iii. the end of drop A,
   iv. at the start of drop B,
   v. ten minutes into drop B, and finally,
   vi. the end of drop B.

Simultaneous with sampling the following information were also recorded;

- The metal temperature at sampling point,
- the hydrogen content was measured using the Telegas method whenever possible,
- the relative humidity and the ambient temperature were also noted at least three times during the whole sampling sequence.

The samples were collected in duplicate and the whole sampling sequence was repeated for three casts, yielding a total of 96 samples.

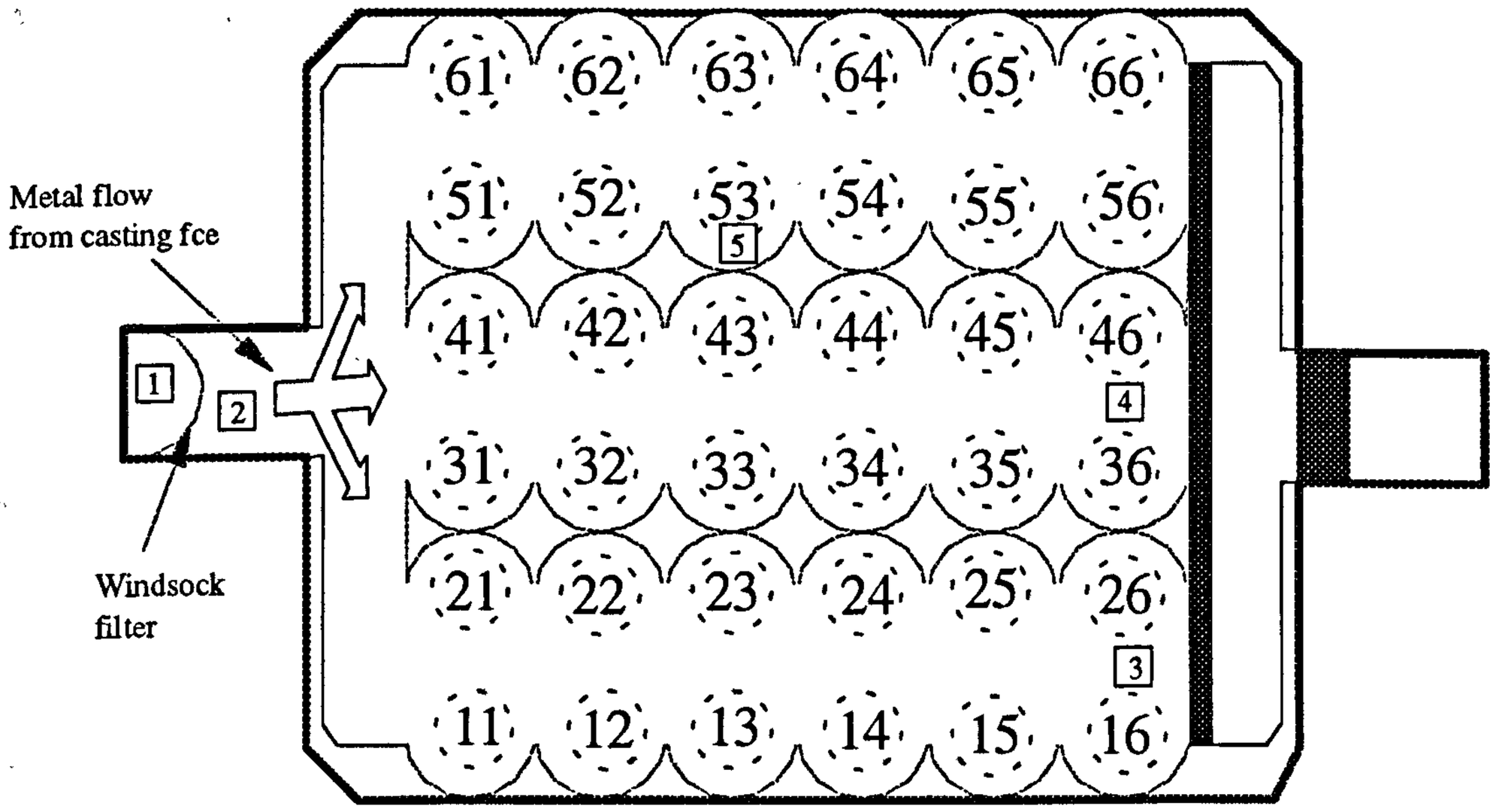

Figure 7.2 Casting table, top view.

7.2.1.2 Sampling sequence 2

Due to variation of the position of moulds relative to the molten metal entry to the casting table, the temperature of the metal delivered to each mould varies. A difference of 20°C or more, is expected. The position of any given mould also determines how long the metal is in contact with the refractory lining and exposed to the prevailing atmosphere. Therefore the position of a mould on the casting table could potentially influence the hydrogen content.

Another factor, unique to Airslip process which was suspected of an effect on the hydrogen content was the phenomenon known as "bubbling moulds", due to maladjustment of the pressure of the injected air.

To investigate these factors, five appropriate sampling points, identified in Figure 7.2 were designated on the casting table.

1. Sampling point no. 1 was on the launder immediately after the ceramic foam filter. This provided a reference sample, representing the state of the metal as delivered to the casting table. Telegas readings were taken at the same point.

2. Sampling points 2, 3, and 4 were selected to yield values for the hydrogen content in the metal entering moulds at the nearest, furthest and intermediate distances from the entry of the metal to the casting table, respectively.
3. To assess any effect due to a bubbling mould, mould 53 was deliberately set to exaggerate the effect, and sampling point 5 was designated accordingly.

Every set of samples included one sample from each of the designated sampling points collected at virtually the same time. Four sets of samples were collected for each of the two drops, A & B, yielding one set every 15 minutes. The metal temperature was recorded for every sampling point as every set of samples was taken.

7.3 Structural Characterisation and Hydrogen Distribution in an Industrially Cast and Homogenised Ingot.

7.3.1 Cast materials

To select an ingot characteristic of those normally produced at the plant, the casting process in which it was produced was carefully monitored to ensure that there were no abnormalities which would detract from the value of the information to be acquired. The ingot was one of a batch of 36 ingots, 178 mm in diameter, produced simultaneously from the casting table in drop A of the cast. The intention was to survey the hydrogen content both laterally and along the length of the ingot. In the time taken to cast the ingot, it was possible that the hydrogen content of the metal delivered to the mould could change, so Ransley pin samples of the liquid metal just above the mould were taken at predetermined intervals corresponding to the locations along the cast length where the solidified ingot was to be sectioned. At the same time intervals, Telegas readings were taken at Sampling point 1, marked in Figure 7.2.

7.3.2 Homogenisation

The selected billet was cut across the length into 15 cm thick slices. A slice was added to the normal full loads in batches homogenised in every one of three different industrial gas-fired furnaces. The furnace zones were set at 580 °C, producing a thermal cycle in which the metal was raised from ambient temperature to 580 °C over a period of 7 hours, spending 3.5 hours at temperatures above 560 °C . This cycle is used because from experience it is known that it is sufficient to take the Mg_2Si phase into solution, thereby improving the extrudability of the material. On completion of the heating cycle, the load is cooled to the touch in 3 hours in a forced air circulation cooler. The atmosphere in the furnaces were the products of combustion from the fuel. The furnaces are unavoidably impregnated with a trace of sodium borofluoride which is routinely used as a normal industrial practice to suppress hydrogen absorption[204]. The sodium borofluoride decomposes at high temperature producing $BF_3(g)$ which covers the surface of the billets creating a barrier against water vapour

7.3.3 Hydrogen content determinations

7.3.3.1 Sampling

Samples for hydrogen content determinations were cut from the cast edge, middle of the radius and centre of the slices as illustrated in Figure 7.3.

7.3.3.2 Distribution of hydrogen in the as-cast ingot

The hydrogen contents of the samples from the cast edge, middle radius and centre of slices taken at 6 locations representing the length of the as-cast ingot were determined by hot vacuum extraction.

7.3.3.3 Distribution of hydrogen in the homogenised ingot

The hydrogen contents of the samples from the cast edge, middle radius and centre of the three industrially homogenised slices were determined by hot vacuum extraction.

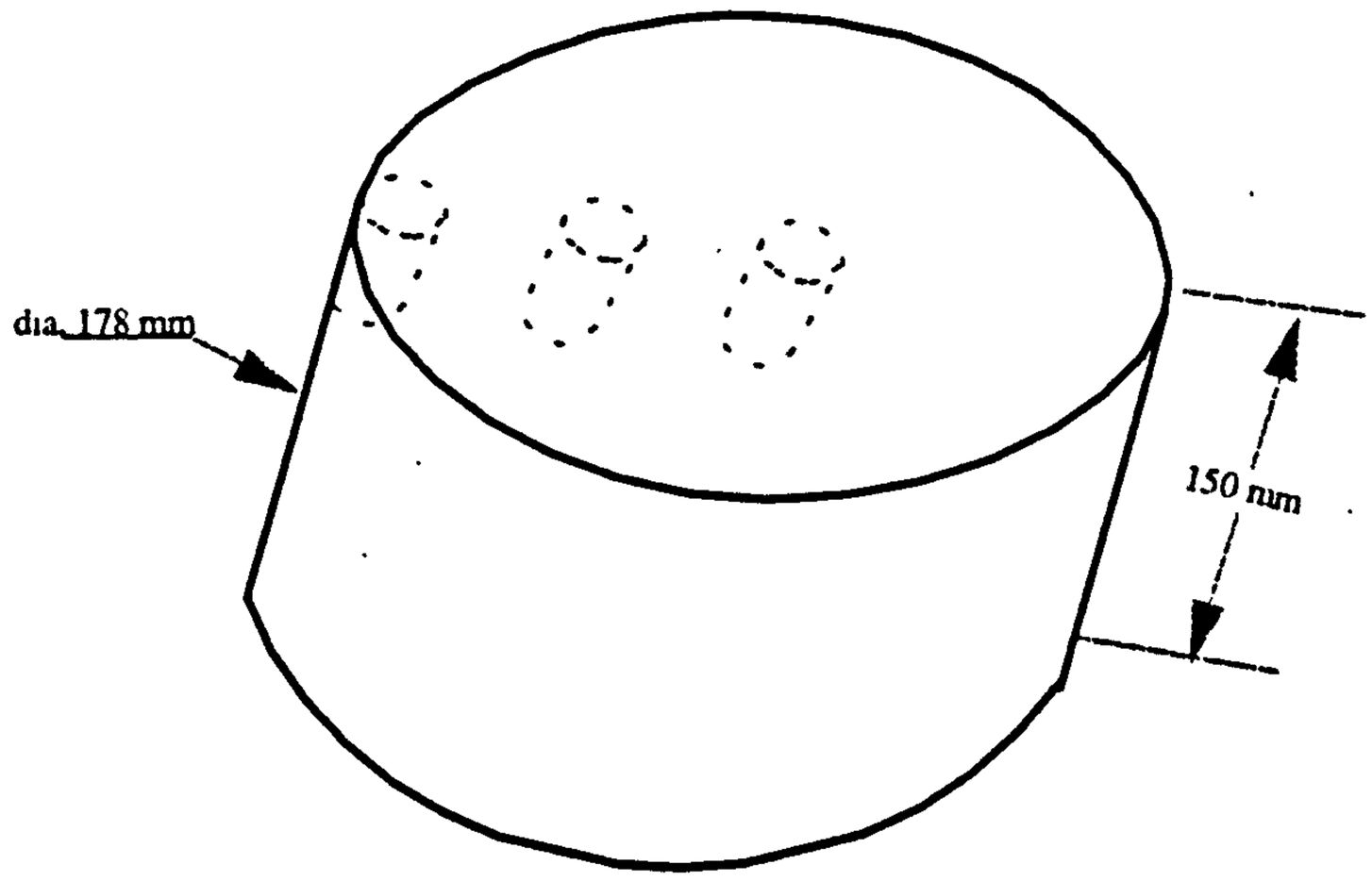

Figure 7.3 Samples cut from ingot slice.

7.3.4 Structural characterisation

The structure of cast metal, broadly includes[63] the size, shape and orientation of the crystals; the distribution of phases, and internal and external topography of the metal such as, porosity and surface shape and finish. These characterisation was carried out by;

- optical microscopy and metallography,
- secondary ion mass spectroscopy of the surface (SIMS).

7.3.4.1 Optical microscopy

The ingot was examined in and across the casting, i.e. longitudinally and in cross-section respectively, as shown in Figure 7.4.

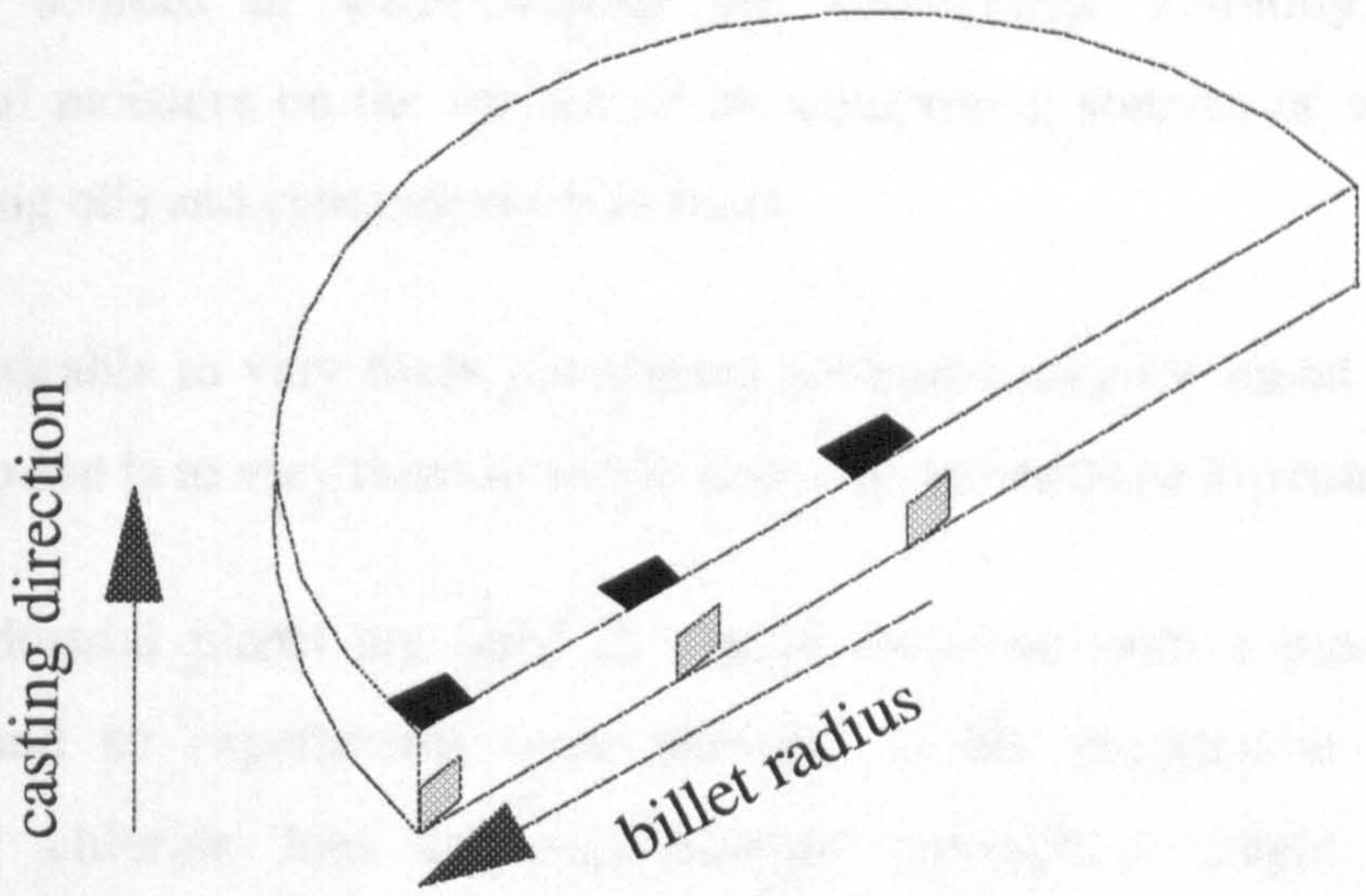

Figure 7.4 Ingot (billet) samples for microscopy.

7.3.4.2 Surface analysis

Samples of the ingot surface from both as-cast and homogenised slices were submitted to analysis by SIMS.

7.4 Effect of Heat-Treatment Environment on the Hydrogen Content and Oxidation of Solid Metal

7.4.1 Purpose

A serious deterioration in the metal quality in term of hydrogen content is often experienced, in high temperature operations which follows the casting. These operations include homogenisation and high temperature deformation processes such as extrusion, forging and rolling.

The factors often suspected of contributing to these deleterious effects are water vapour and sulphur contamination in the industrial environment.

The major sources of water vapour are atmospheric humidity, products of combustion and moisture on the surface of the equipment; sources of sulphur include industrial cutting oils and contamination in fuels.

It is impracticable to vary these parameters systematically for metal in production, and the only option is to vary them in small-scale experimental heat-treatments.

Some industrial plants are sited in coastal locations with a prevailing marine environment and so experiments were included in the programme to assess any influence that chlorine ions in heat-treatment atmosphere might have on the susceptibility of the metal to hydrogen absorption, a condition which has not been investigated before.

Experimental heat treatment was carried out to assess the effects of:

- heat-treatment atmosphere,
- temperature and,
- time of treatment.

7.4.2 Apparatus

Samples were inserted into a fused silica tube, 20 mm diameter x 700 mm long heated along most of its length by a close-fitting electric resistance furnace. A thermocouple was wired to the outside of the tube as a sensor for controlling the furnace temperature. A gas train capable of supplying and measuring an air flow of any required atmosphere was connected to the silica tube. The air flow rate was 50 cm^3/min in every experiment. The general arrangement of the equipment is shown in the photograph given in Figure 7.5.

7.4.3 Sample preparation

The material for these experiments was taken from some of the ingot slices characterised by the observations described in Section 7.3.

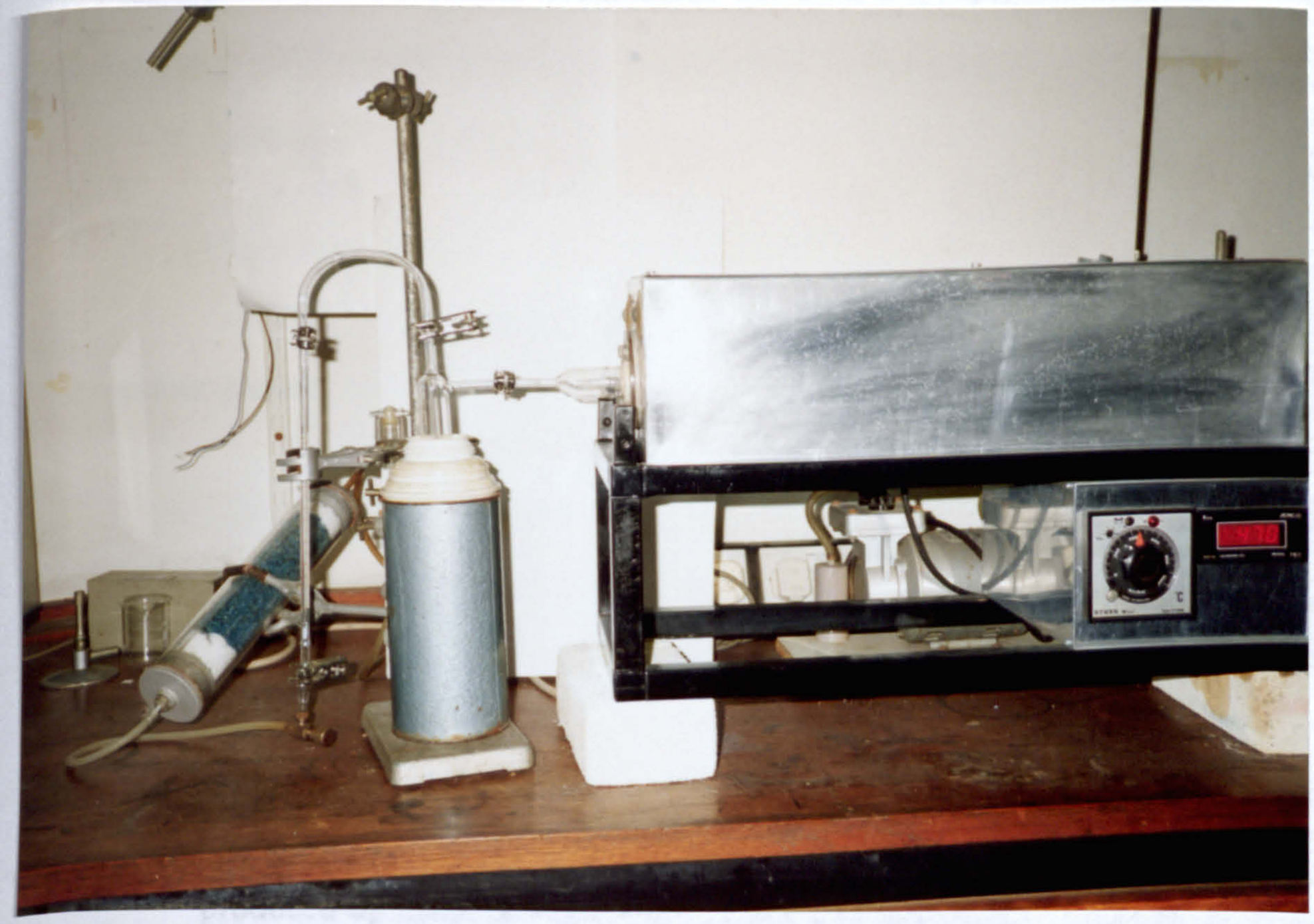

Figure 7.5 Apparatus for experimental heat-treatment, set up for dry air.

A set of four samples was prepared for every heat-treatment, consisting of one machined cylinder, 10.5 mm diameter x 70 mm long and three discs, 10.5 mm diameter and 5 mm thick, every one of which was fine ground (600 grit) on one face.

The samples were placed in an aluminium boat which was pushed into a constant temperature zone in the middle of the silica tube within which the temperature was constant to within 1°C. A chromel/alumel thermocouple was wired tightly to the aluminium boat to record the temperature of the samples.

7.4.4 Experimental conditions

The following experimental parameters were used because they are relevant to industrial practices:

7.4.4.1 Atmospheres

i. Clean dry air

produced by passing ambient air through silica gel and then through a liquid nitrogen trap before entering the furnace shown in Figure 7.5.

ii. Moist air

i.e. water saturated air, produced by bubbling ambient air through water at 20 °C via a fritted glass plug. This yields an atmosphere with a water vapour pressure of 0.023 atm. [205].

iii. Dry air contaminated with sulphur dioxide

produced by injecting 1% of 99.7% pure sulphur dioxide into a dry air stream produced as in (i) at the point just before the furnace.

iv. Moist air contaminated with sulphur dioxide

produced by injecting 1% of 99.7% pure sulphur dioxide into a moist air stream produced as in (ii) at the point just before the furnace.

v. Air contaminated with chlorine

produced as in (ii) but replacing the water with a 25% by volume aqueous solution of hydrochloric acid. Litmus paper placed at the exit of the furnace tube confirmed the presence of HCl vapour in the atmosphere.

vi. Moist air contaminated with sulphur dioxide and chlorine

produced as in (iv) but replacing the water with a 25% by volume aqueous solution of hydrochloric acid.

The air flows were all maintained at 50 cm^3/minute

7.4.4.2 Temperatures

470, 500, 530, 560, and 590°C.

7.4.4.3 Times of heat-treatments

1, 2, 4, 6, and 8 hours.

7.4.5 Examination of heat-treated samples oxide films

Following every heat-treatment, the cylindrical sample was cut to yield one 40 mm long piece and three 5 - 10 mm thick sections which were used to prepare samples for optical microscopy. The three discs with fine ground faces were submitted to surface examination by XPS, and SIMS.

The seven samples from every heat-treatment were examined as follows:

7.4.5.1 Hydrogen content determinations

The hydrogen content of the 40 mm long piece of the cylinder was determined by hot vacuum extraction.

7.4.5.2 Optical microscopy

The three 5 - 10 mm thick sections cut from the cylindrical sample were used to prepare metallographic samples which were examined by optical microscopy.

7.4.5.3 Surface analysis

The three fine ground three fine ground discs of 10.5-10.7 mm diameter and 5-10 mm thick were submitted for analysis by X-ray photoelectron spectroscopy (XPS), and secondary ion mass spectrometry (SIMS).

8. RESULTS.

8.1 Hydrogen Content of Liquid Metal During Production.

8.1.1 Effect of liquid metal treatment

Tables 8.1 to 8.3 give the results for hydrogen content determinations on the samples of liquid metal as described in Section 7.2 as follows:

Table 8.1 Samples taken from Cast 1.

Table 8.2 Samples taken from Cast 2.

Table 8.3 Samples taken from Cast 3.

Tables 8.4 to 8.6 give the chemical analysis of corresponding samples to characterise the composition.

8.1.2 Distribution of hydrogen content in the casting system

Tables 8.7 and 8.8 give the results of hydrogen content determinations on the samples taken from the liquid metal distribution system, as described in Section 7.2 as follows:

Table 8.7 Samples taken from the first drop (A).

Table 8.8 Samples taken from the second drop (B).

Table 8.1

Hydrogen content during the production of aluminium ingot alloy AA6063, cast 1.

Sampling location and sequence		Sampling point (Fig 7.1)	Hydrogen content ($cm^3/100g$)			Metal temperature (°C)	Time (minutes)	%Relative humidity	Ambient temperature (°C)
			Duplicate	Average	Telegas				
Crucible before charging into melter.		1	0.38*	0.38		849	0	60	29
Melting furnace befor transfer.		2	0.36, 0.34	0.35		768	50		
Casting furnace	after transfer.	3	0.35, 0.35	0.35		720	91		
	after stirring.	3	0.26, 0.24	0.25		705	116		
	after degasing	3	0.16, 0.19	0.18		703	190		
	10 min. after degasing	3	0.16, 0.18	0.17		703	200		
	20 min. after degasing	3	0.18, 0.17	0.18		701	210		
	30 min. after degasing	3	0.18,0.16	0.17		700	220		
	40 min. after degasing	3	0.15, 0.16	0.16		700	230		
	50 min. after degasing	3	0.17, 0.17	0.17		699	240	54	30
Launder	start of A drop	4	0.15, 0.16	0.16		676	260		
	10 min. into A drop	4	0.18, 0.16	0.17	0.20	687	270		
	end of A drop	4	0.15, 0.18	0.17	0.18	685	325		
	start of B drop	4	0.16, 0.18	0.17		683	377		
	10 min. into B drop	4	0.14, 0.17	0.16	0.18	688	387	74	33
	end of B drop	4	0.13, 0.17	0.15	0.18	676	439		

* Duplicate sample was damaged in preparation.

Table 8.2
Hydrogen content during the production of aluminium ingot alloy AA6063, cast 2.

Sampling location and sequence		Sampling point (Fig 7.1)	Hydrogen content (cm^3/100g)			Metal temperature (°C)	Time (minutes)	%Relative humidity	Ambient temperature (°C)
			Duplicate	Average	Telegas				
Crucible before charging into melter.		1	0.41, .40	0.40		845	0	54	30
Melting furnace befor transfer.		2	* , 0.32	0.32		736	67		
Casting furnace	after transfer.	3	0.32, 0.32	0.32		709	115		
	after stirring.	3	0.25, 0.26	0.26		701	129		
	after degasing	3	0.16, 0.18	0.17		695	187		
	10 min. after degasing	3	0.18, 0.16	0.17		699	197		
	20 min. after degasing	3	0.14, 0.17	0.16		703	207		
	30 min. after degasing	3	0.17, 0.16	0.16		704	217		
	40 min. after degasing	3	0.18, 0.16	0.17		706	227		
	50 min. after degasing	3	0.15, 0.16	0.16		706	237	57	32
Launder	start of A drop	4	0.15, 0.18	0.16		687	285		
	10 min. into A drop	4	0.16, 0.16	0.16	0.22	692	297		
	end of A drop	4	0.15, 0.16	0.16	0.18	682	342		
	start of B drop	4	0.15, 0.14	0.14		685	382		
	10 min. into B drop	4	0.14, 0.16	0.15	0.18	684	395		
	end of B drop	4	0.14, 0.15	0.14	0.18	683	437	69	32

* Duplicate sample was damaged in preparation.

Table 8.3

Hydrogen content during the production of aluminium ingot alloy AA6063, cast 3.

Sampling location and sequence		Sampling point (Fig 7.1)	Hydrogen content (cm^3/100g)			Metal temperature (°C)	Time (minutes)	%Relative humidity	Ambient temperature (°C)
			Duplicate	Average	Telegas				
Crucible before charging into melter.		1	0.73, 0.71	0.72		820	0	73	23
Melting furnace befor transfer.		2	0.33, 0.34	0.34		754	50		
Casting furnace	after transfer.	3	0.33, 0.32	0.32		725	88		
	after stirring.	3	0.27, 0.25	0.26		719	108		
	after degasing	3	0.20, 0.21	0.20		710	163		
	10 min. after degasing	3	0.21, 0.20	0.20		703	173		
	20 min. after degasing	3	0.20, 0.20	0.20		702	183		
	30 min. after degasing	3	0.19, 0.19	0.19		701	193	68	27
	40 min. after degasing	3	0.17, 0.19	0.18		704	203		
	50 min. after degasing	3	0.19, 0.19	0.19		704	213		
Launder	start of A drop	4	0.18, 0.19	0.18		677	236		
	10 min. into A drop	4	0.19, 0.18	0.18	0.20	688	253		
	end of A drop	4	0.18, 0.17	0.18	0.18	688	287		
	start of B drop	4	0.18, 0.18	0.18		682	348		
	10 min. into B drop	4	0.18, 0.19	0.18	0.20	690	358		
	end of B drop	4	0.16, 0.15	0.16	0.18	684	391	74	27

Table 8.4

The chemical analysis*, wt%, throughout the melt preparation, Cast 1.

Sample		Si	Fe	Mg	Na	Other, each	Al
Crucible before charging into melter.		0.03	0.04	---	0.0050	< 0.05	Balance
Melting furnace before transferring.		0.09	0.10	0.08	0.0013	< 0.05	Balance
Casting furnace	after transfer	0.40	0.14	0.75	0.0011	< 0.05	Balance
	after alloying/stirring	0.43	0.15	0.51	0.0011	< 0.05	Balance
	after degassing	0.43	0.16	0.49	0.0004	< 0.05	Balance
Launder	start of A drop	0.41	0.15	0.47	0.0002	< 0.05	Balance
	end of A drop	0.43	0.16	0.48	0.0003	< 0.05	Balance
	start of B drop	0.41	0.15	0.46	0.0004	< 0.05	Balance
	end of B drop	0.43	0.17	0.49	0.0003	< 0.05	Balance

Table 8.5

The chemical analysis*, wt%, throughout the melt preparation, Cast 2.

Sample		Si	Fe	Mg	Na	Other, each	Al
Crucible before charging into melter.		0.03	0.10	---	0.0063	< 0.05	Balance
Melting furnace before transferring.		0.03	0.05	---	0.0016	< 0.05	Balance
Casting furnace	after transfer	0.43	0.17	0.64	0.0012	< 0.05	Balance
	after alloying/stirring	0.41	0.17	0.50	0.0012	< 0.05	Balance
	after degassing	0.41	0.17	0.52	0.0006	< 0.05	Balance
Launder	start of A drop	0.40	0.17	0.50	0.0005	< 0.05	Balance
	end of A drop	0.41	0.17	0.52	0.0006	< 0.05	Balance
	start of B drop	0.42	0.18	0.52	0.0005	< 0.05	Balance
	end of B drop	0.40	0.17	0.50	0.0004	< 0.05	Balance

Table 8.6

The chemical analysis*, wt%, throughout the melt preparation, Cast 3.

Sample		Si	Fe	Mg	Na	Other, each	Al
Crucible before charging into melter.		0.03	0.07	---	0.0027	< 0.05	Balance
Melting furnace before transferring.		0.07	0.10	0.06	0.0012	< 0.05	Balance
Casting furnace	after transfer	0.42	0.16	0.58	0.0012	< 0.05	Balance
	after alloying/stirring	0.37	0.15	0.50	0.0011	< 0.05	Balance
	after degassing	0.41	0.16	0.52	0.0005	< 0.05	Balance
Launder	start of A drop	0.41	0.16	0.53	0.0003	< 0.05	Balance
	end of A drop	0.40	0.16	0.51	0.0003	< 0.05	Balance
	start of B drop	0.40	0.16	0.51	0.0003	< 0.05	Balance
	end of B drop	0.42	0.18	0.51	0.0004	< 0.05	Balance

*Analysis by atomic emission spectroscopy, +/- 0.0001 wt%.

Table 8.7

Distribution of hydrogen content and metal temperature on casting table, drop A.
Sampling points as marked in Figure 7.2, page 122.

Time from start (min.)	Hydrogen content $cm^3/100g$ with temperature °C in parentheses					
	Point 1		Point 2	Point 3	Point 4	Point 5
15	0.22*	0.20 (688)	0.18 (685)	0.18 (668)	0.17 (667)	0.18 (676)
30	0.21*	0.17 (694)	0.17 (688)	0.18 (678)	0.18 (674)	0.18 (681)
45	0.21*	0.16 (689)	0.17 (684)	0.17 (671)	0.16 (669)	0.16 (677)
60	0.20*	0.16 (685)	0.17 (682)	0.17 (669)	0.16 (667)	0.17 (672)
* Corresponding telegas reading.						

Table 8.8

Distribution of hydrogen content and metal temperature on casting table, drop B.
Sampling points as marked in Figure 7.2, page 122.

Time from start (min.)	Hydrogen content $cm^3/100g$ with temperature °C in parentheses					
	Point 1		Point 2	Point 3	Point 4	Point 5
1	0.21*	0.17 (689)	0.17 (683)	0.16 (669)	0.17 (666)	0.17 (674)
2	0.20*	0.16 (681)	0.16 (677)	0.15 (666)	0.15 (664)	0.16 (669)
3	0.20*	0.16 (681)	0.15 (677)	0.16 (666)	0.16 (663)	0.15 (671)
4	0.19*	0.15 (683)	0.15 (679)	0.14 (667)	0.15 (663)	0.16 (672)
* Corresponding telegas reading.						

8.2 Hydrogen Content of the Billet

The results given in this section relate to section 7.3.

8.2.1 Structural characterisation

Figure 8.1 is a photograph of the macrostructure of a ingot cross-section

Figures 8.2 to 8.4 are macro-photographs of the edge, mid-radius and centre of the ingot.

Figures 8.5 to 8.7 are micro-photographs of the as cast ingot, etched.

Figures 8.8 to 8.10 are micro-photographs of the as cast ingot, un-etched.

Figures 8.11 to 8.13 are micro-photographs of the industrially homogenised ingot.

Figure 8.14 and 8.15 are photographs of the ingot surface.

Figure 8.16 gives a SIMS depth profile through the oxide on the as cast surface.

Figures 8.17 and 8.18 give SIMS depth profile through the oxide on the surface of the homogenised ingot.

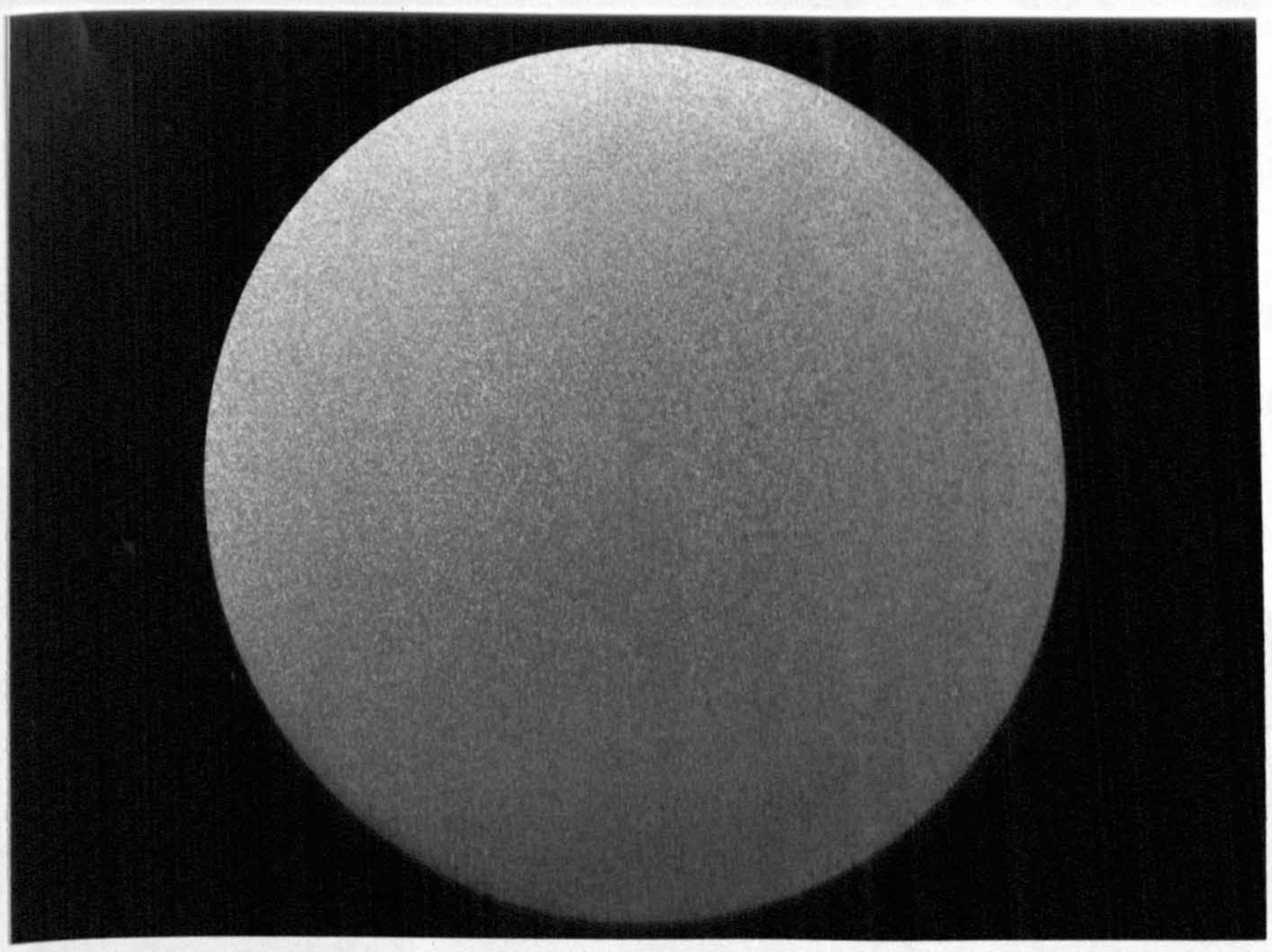

Figure 8.1 Cross section of AA 6063 alloy aluminium billet, 178 mm diameter. Etched in concentrated HNO_3 /HCl /HF mixture.

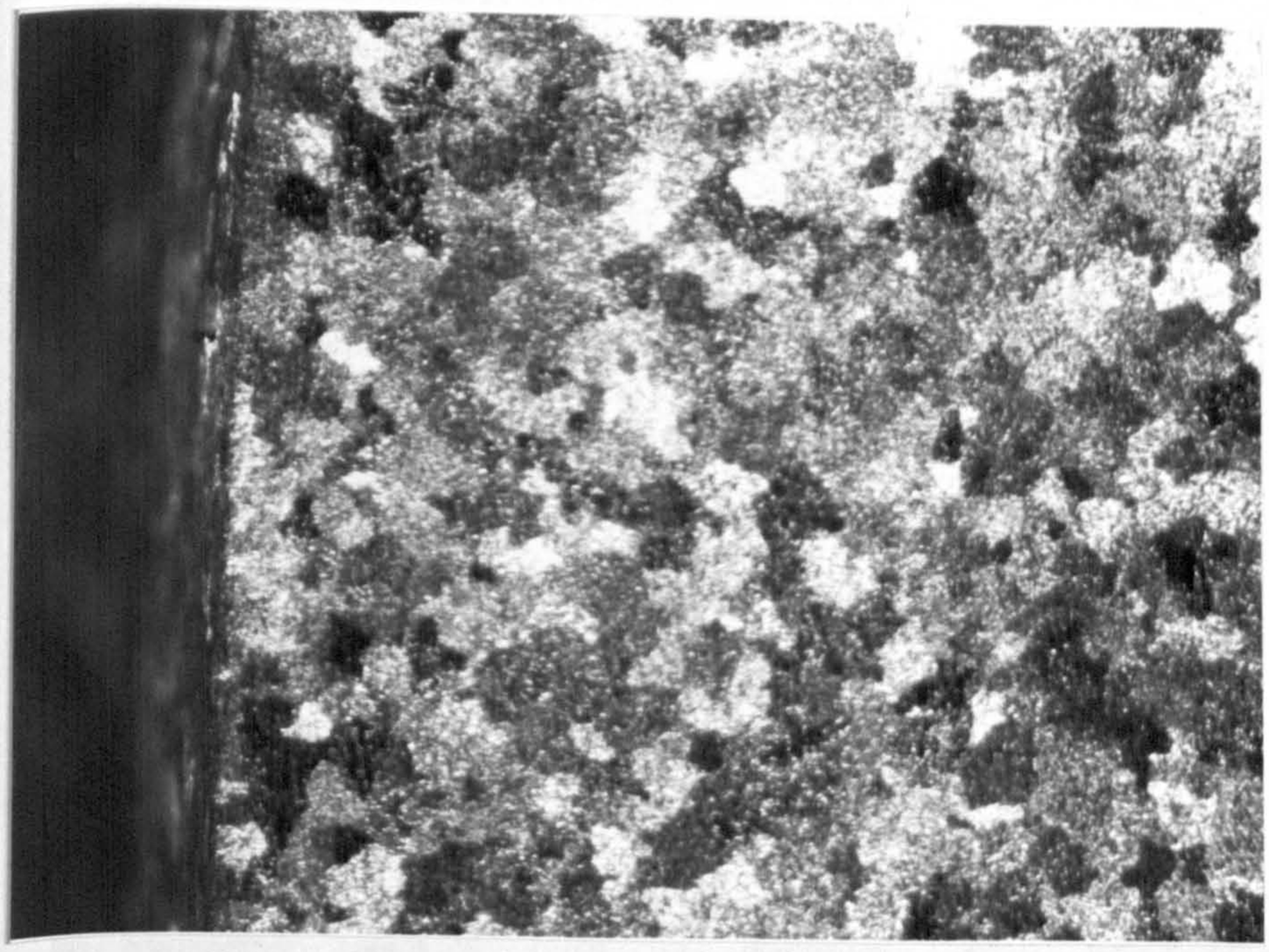

300 µm

Figure 8.2 Cross-section through cast edge of billet, shown in Figure 8.1, showing equi-axed grains nearly to the cast edge, characteristic of air-slip casting Etched in concentrated HNO_3 /HCl /HF mixture. x 20.

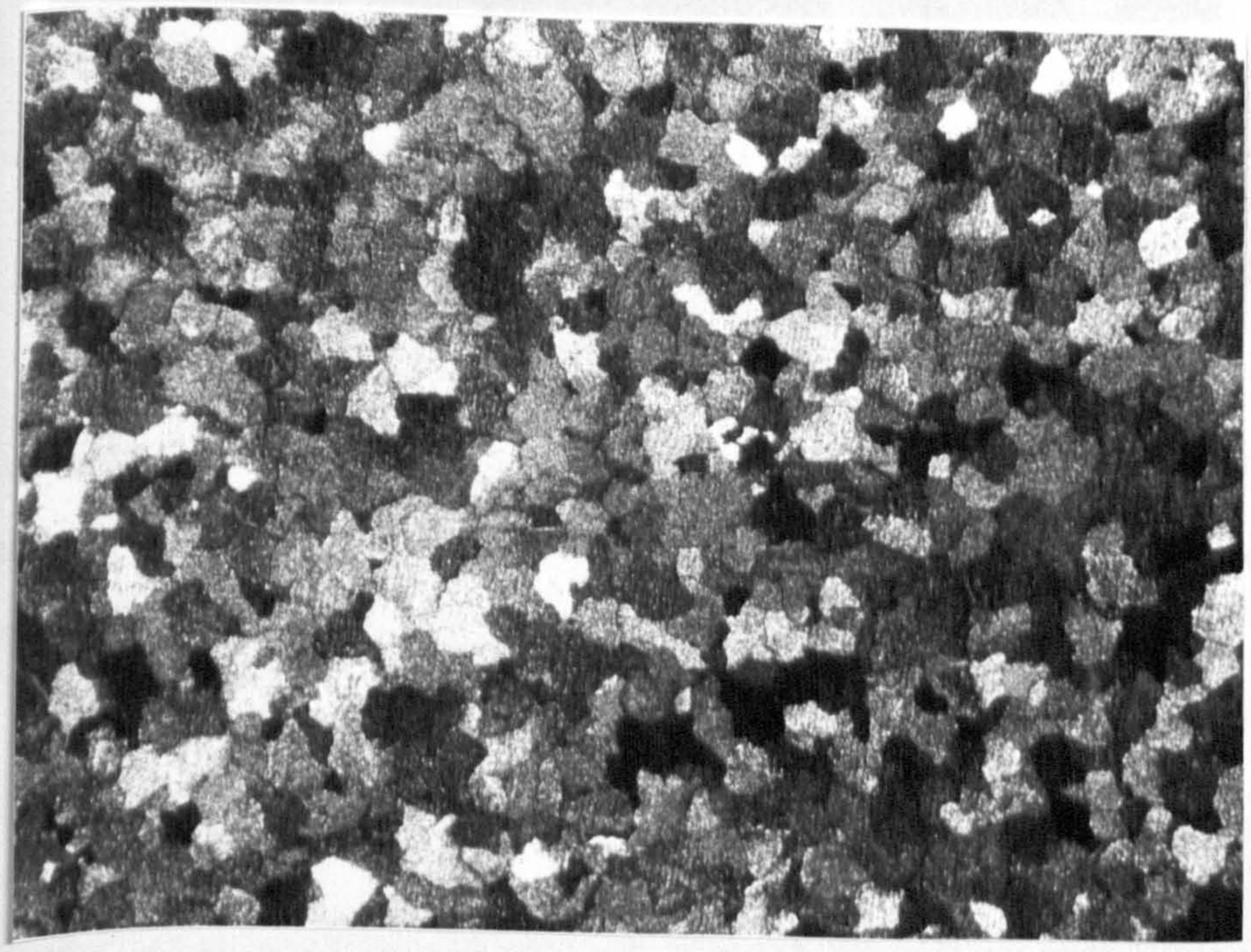

300 µm

Figure 8.3 Cross-section through mid-radius of billet, shown in Figure 8.1, showing equi-axed structure of similar size to that at the cast edge. Etched in concentrated HNO_3 /HCl /HF mixture. x 20.

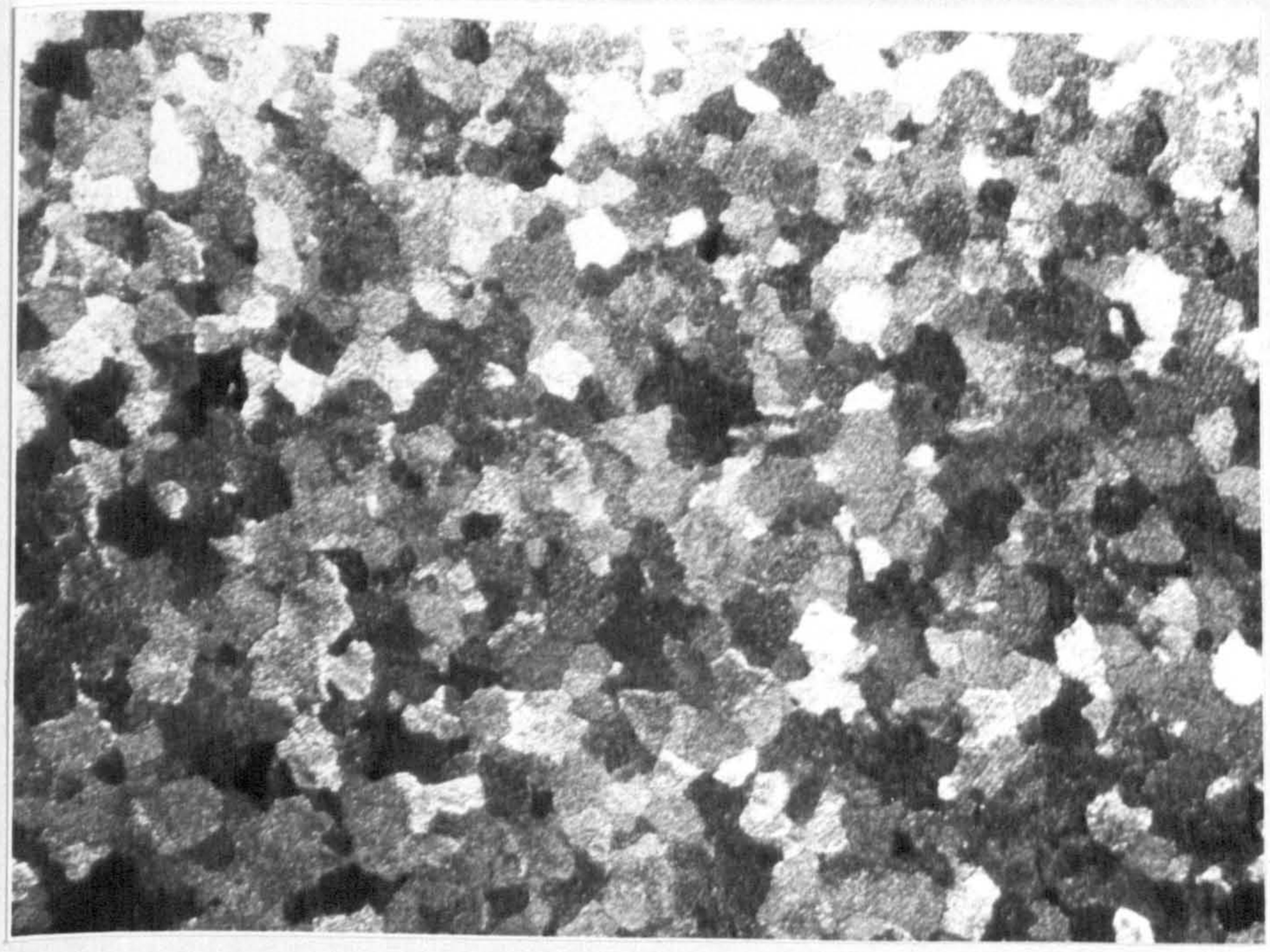

300 μm

Figure 8.4 Cross-section through centre of billet, shown in Figure 8.1, showing equi-axed structure of similar size to that at the cast edge. Etched in concentrated HNO_3 /HCl /HF mixture. x 20.

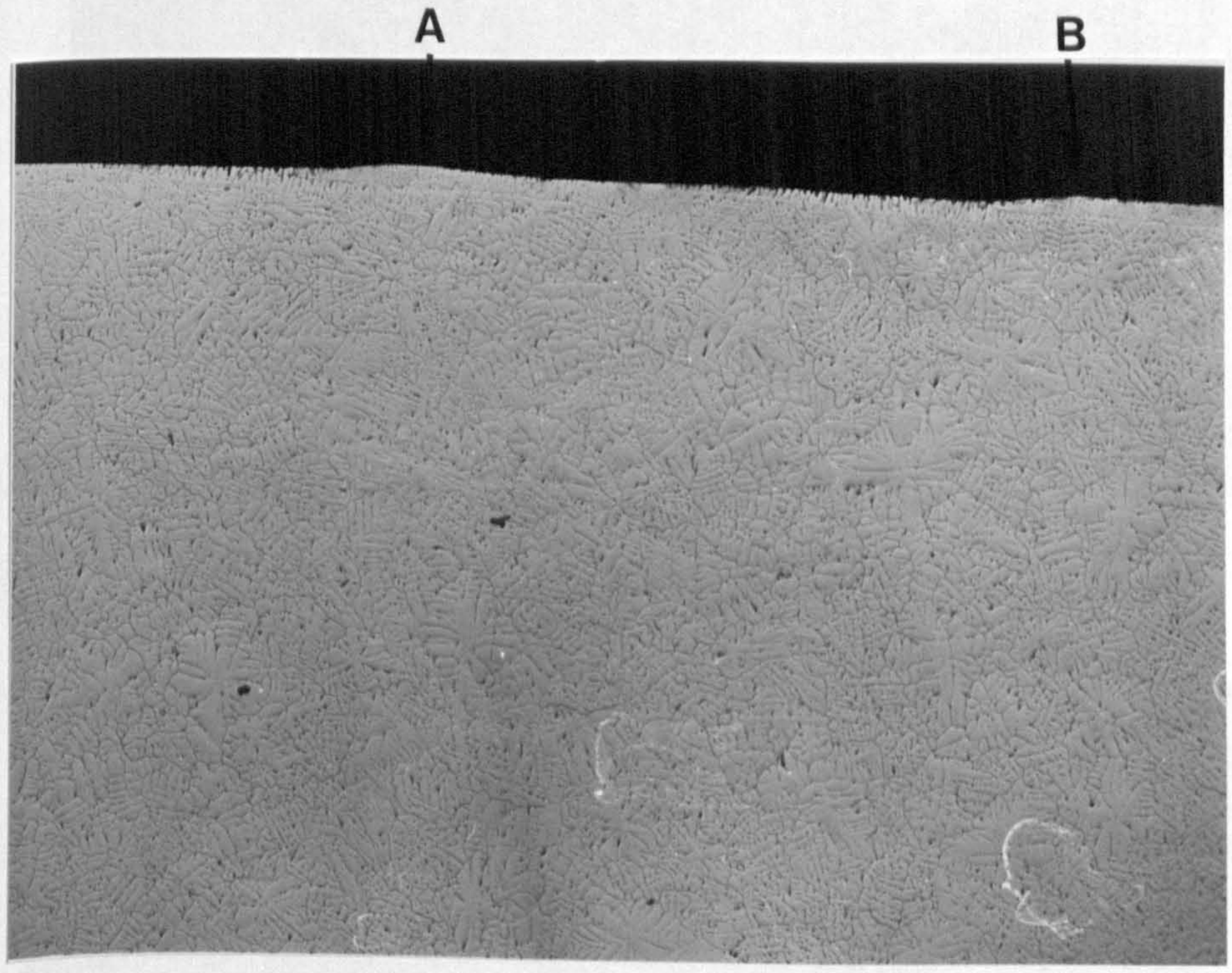

Figure 8.5 Longitudinal microstructure of near the cast edge of billet shown in Figure 8.1, showing typical dendritic structure. Typical "closed form folds", indicated arrows A and B are visible at the cast edge. Etched in Keller's reagent. x 50.

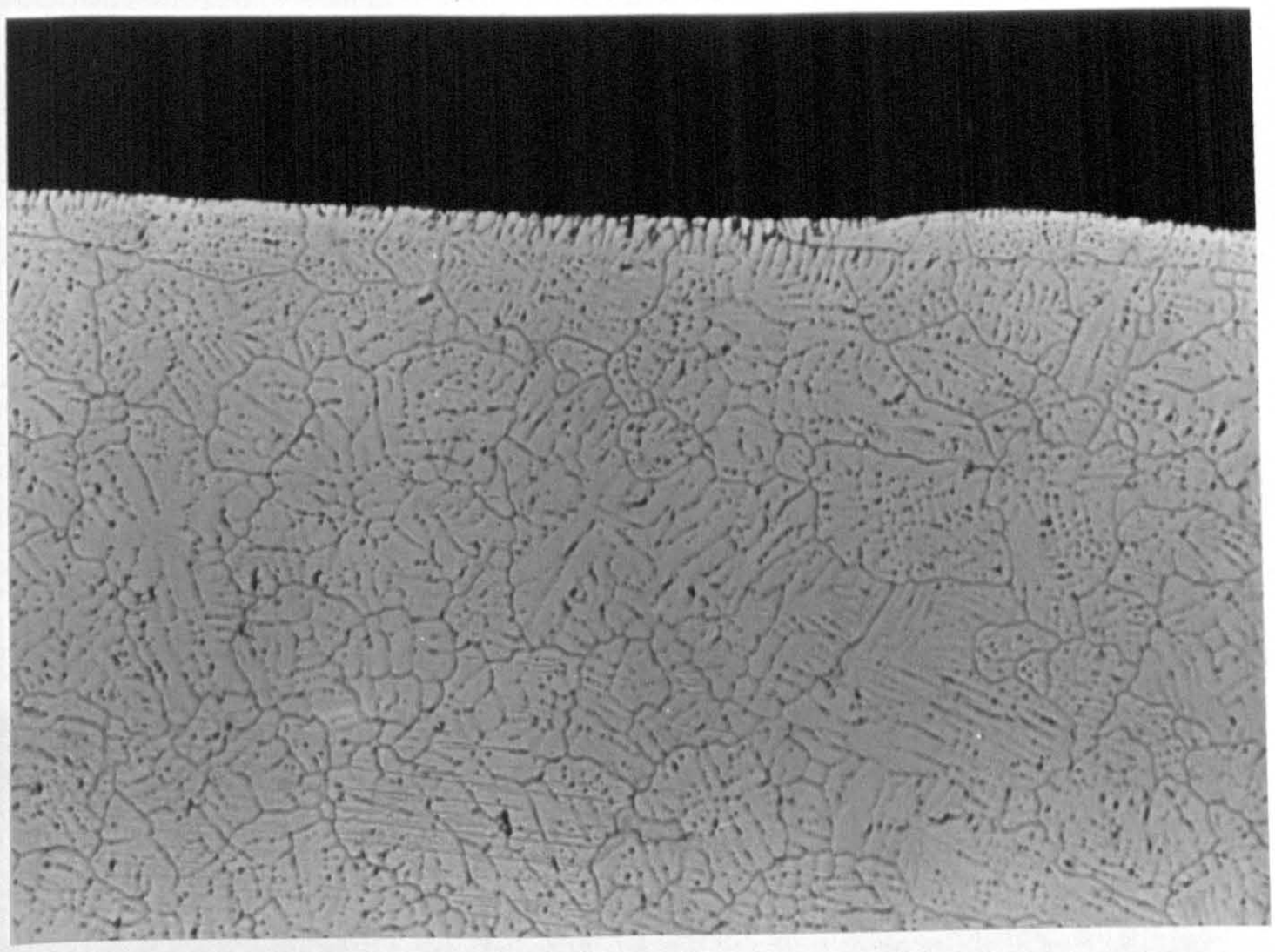

Figure 8.6(a) As Figure 8.5, at higher magnification, showing detail of close-form fold at B. x 100.

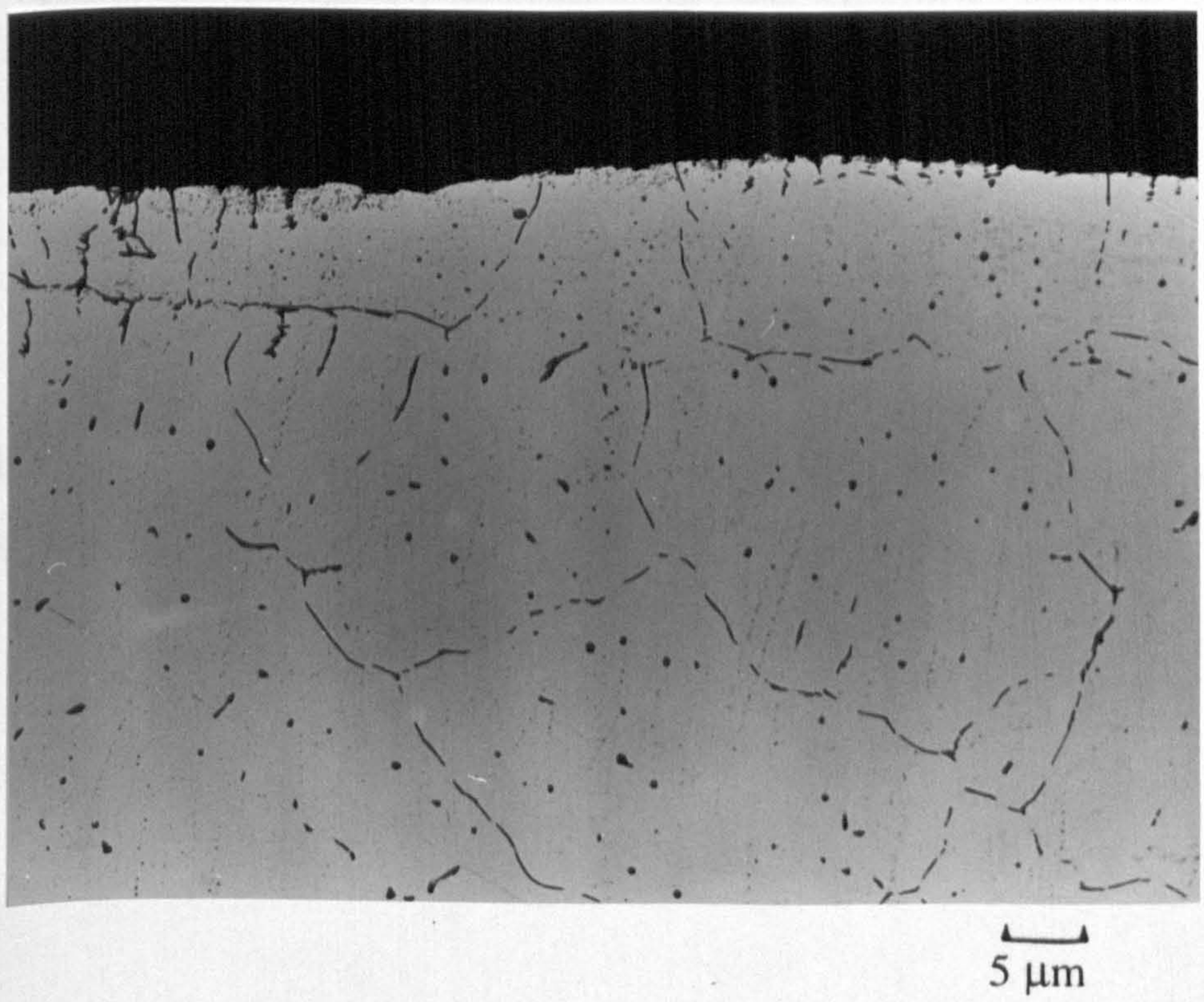

Figure 8.6(b) As Figure 8.5, at still higher magnification, showing relation betwwen close-form fold and a thin chill zone at the cast edge. x 400.

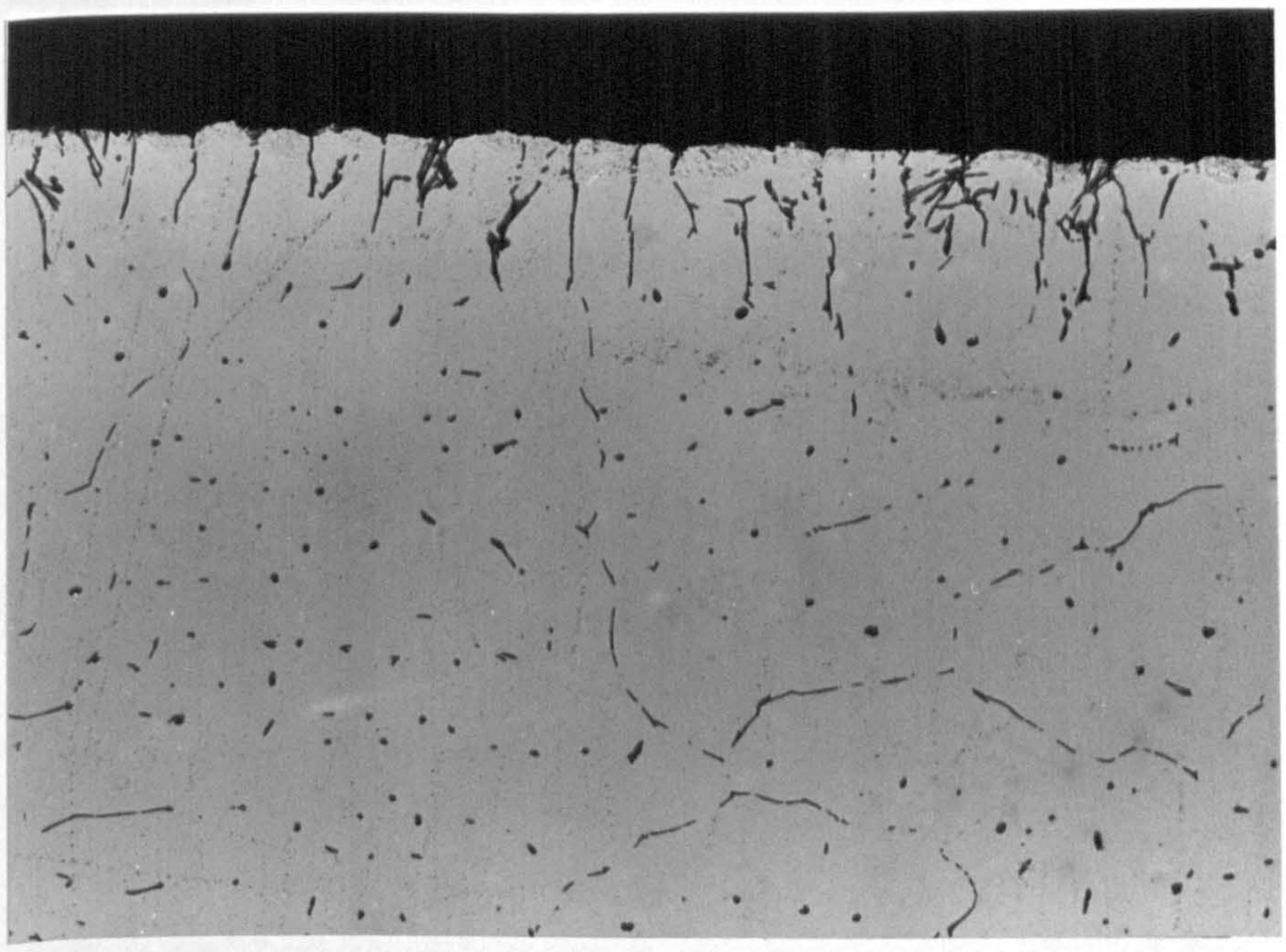

Figure 8.6(c) As Figure 8.6(b), showing typical inverse segregation in the chill zone at the cast edge. x 400.

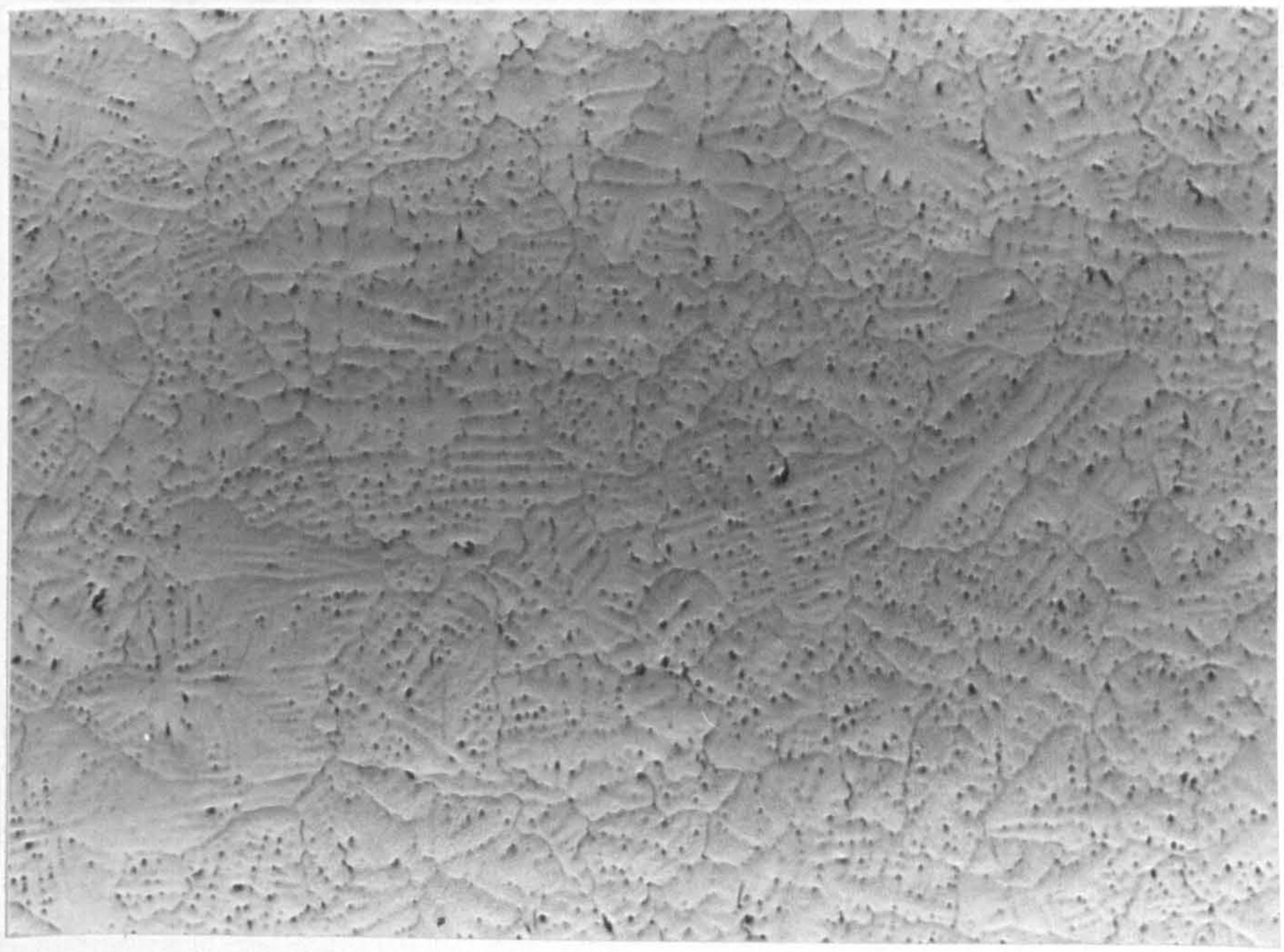

Figure 8.7(a) Longitudinal microstructure at the centre of billet shown in Figure 8.1, for comparison with Figure 8.6(a) showing dendritic structure Etched in Keller's reagent. x 100.

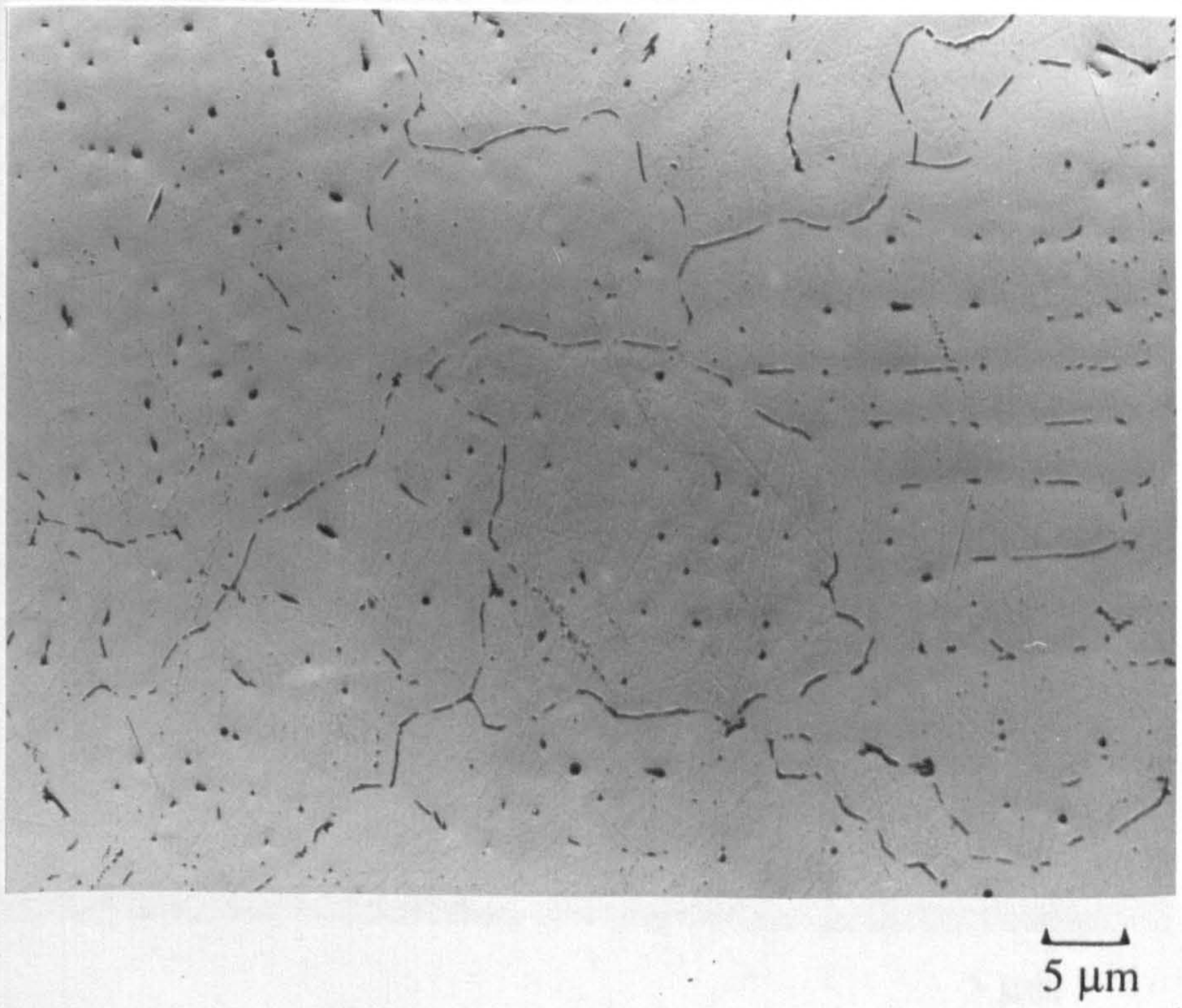

Figure 8.7(b) As Figure 8.7(a) at higher magnification for comparison with Figure 8.6(b). x 400.

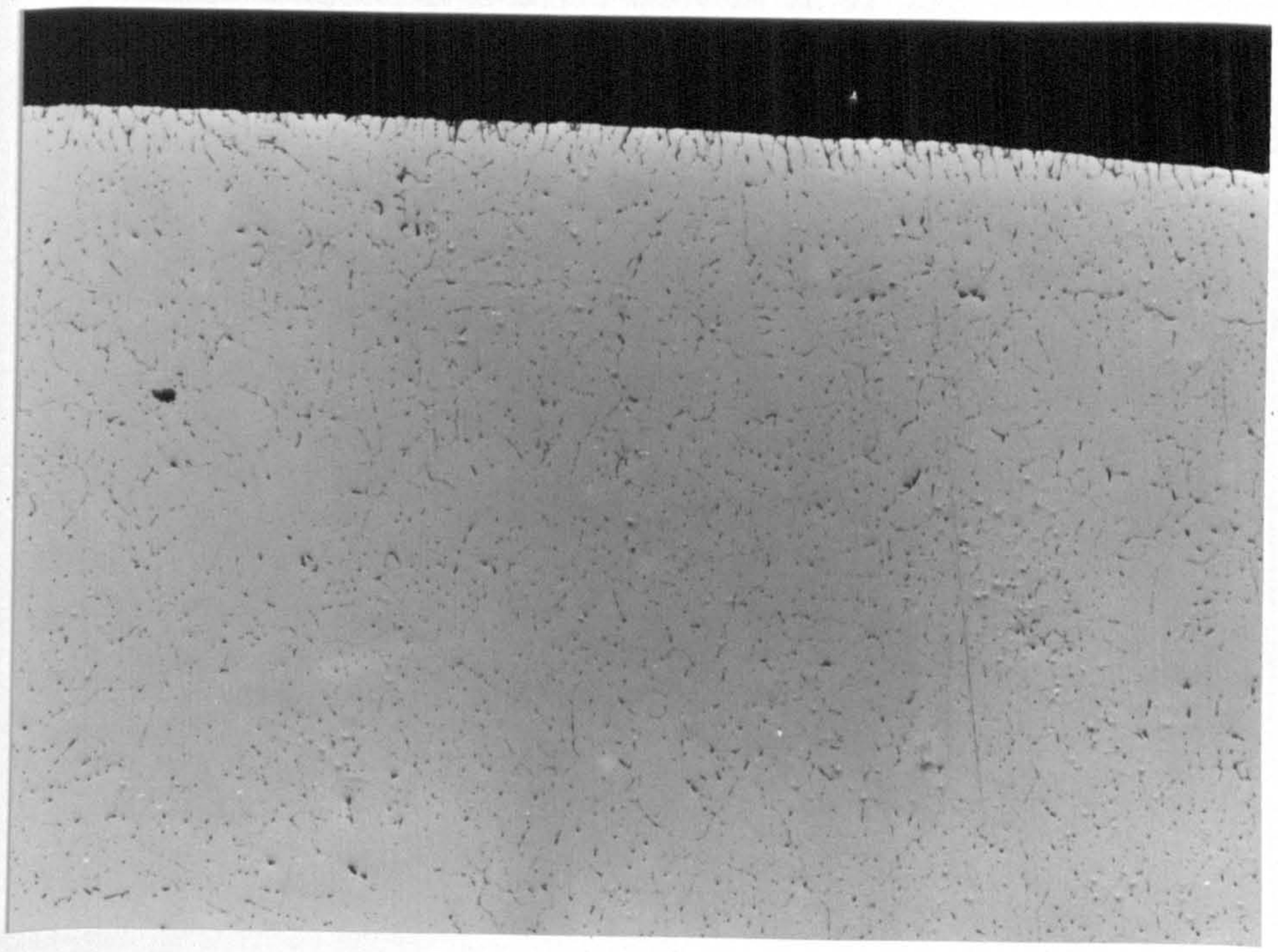

Figure 8.8(a) Porosity near the edge of the as-cast billet. It is difficult to differentiate between micropores of the order of 2 or 3 µm and constituents in the as-cast structure, although a few can be seen. Unetched. x 100.

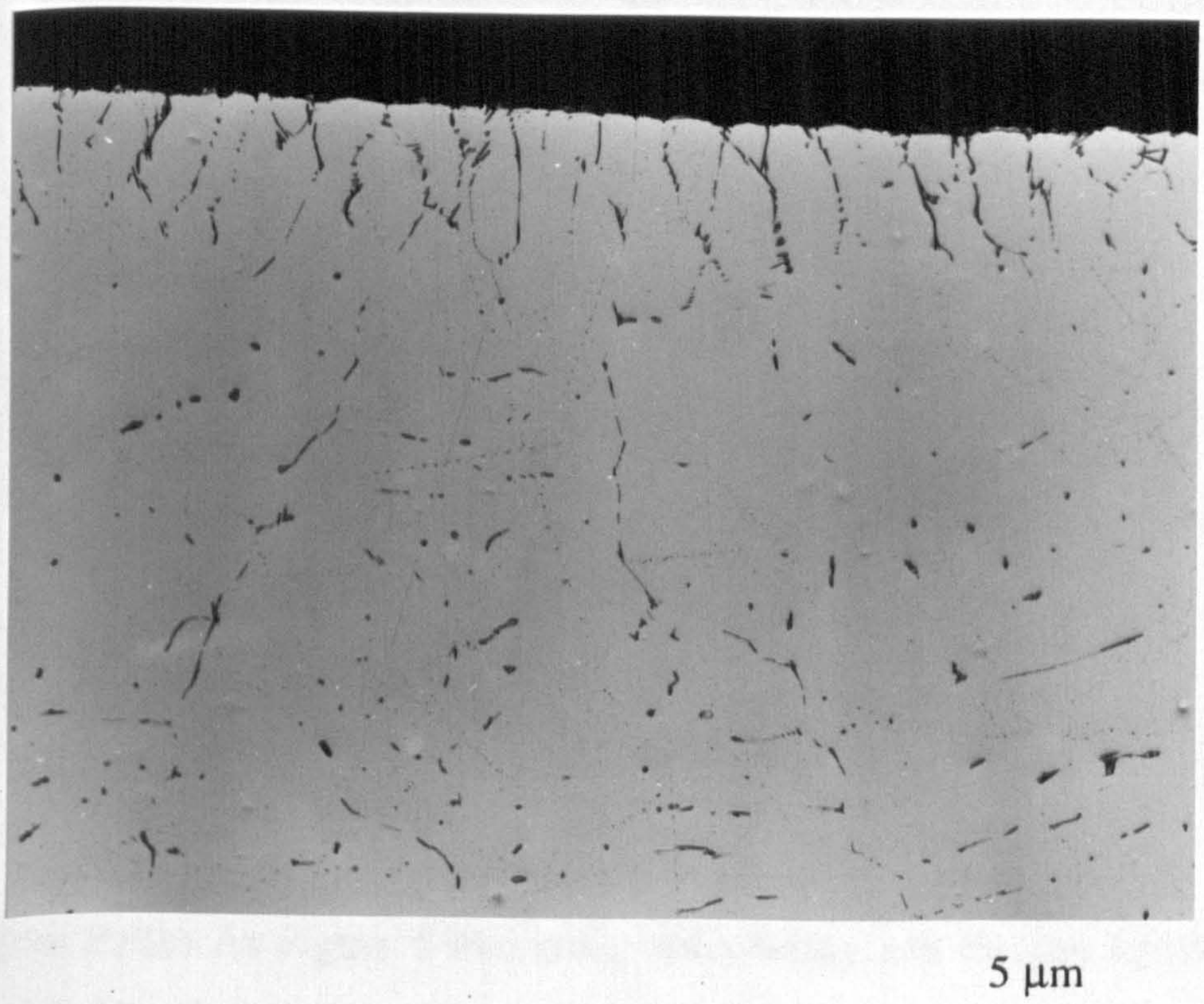

Figure 8.8(b) As Figure 8.8(a) at higher magnification, showing little advantage in resolving micropores due to shallower depth of field. Unetched. x 400.

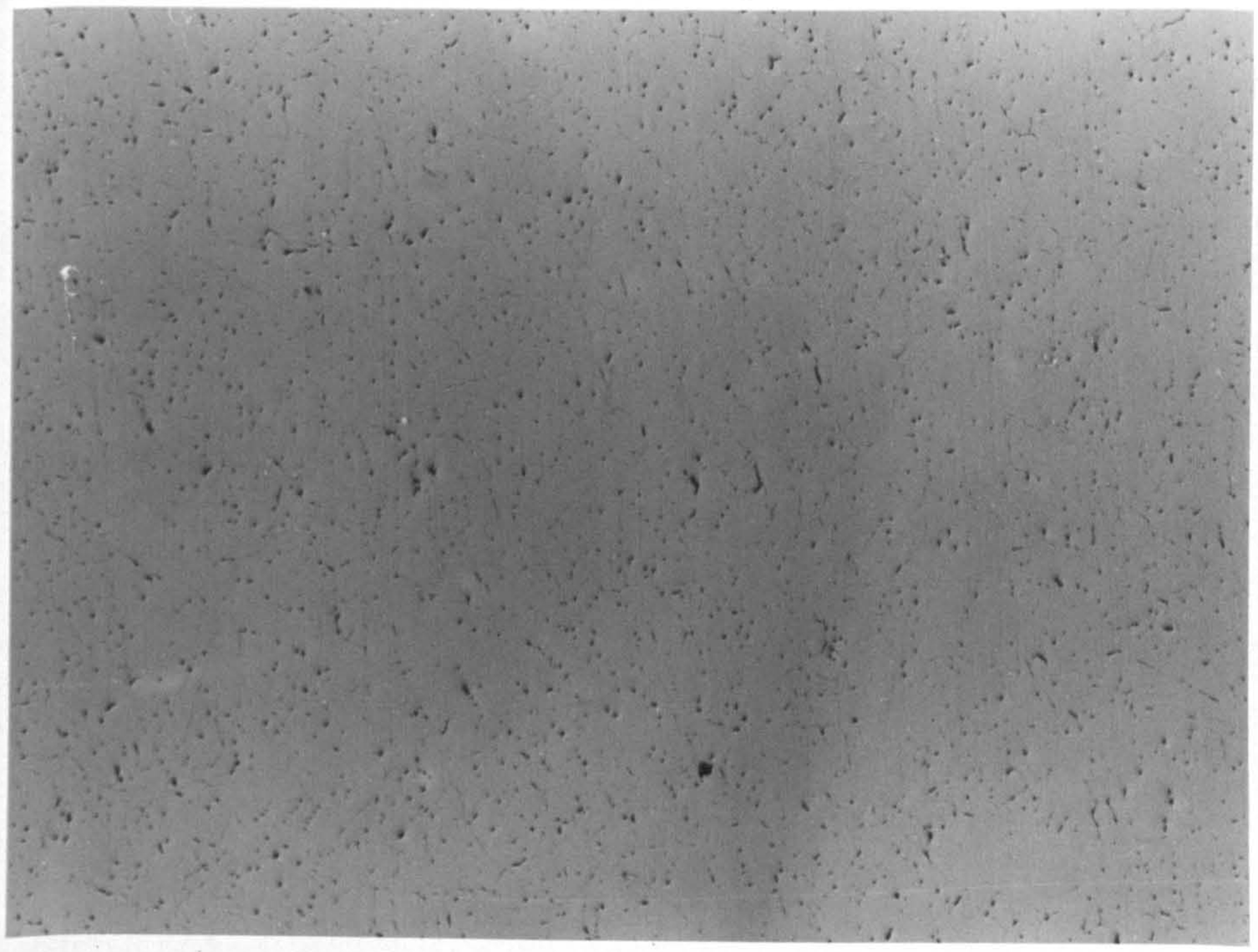

Figure 8.9(a) Porosity at mid-radius of as-cast billet. Unetched. x 100.

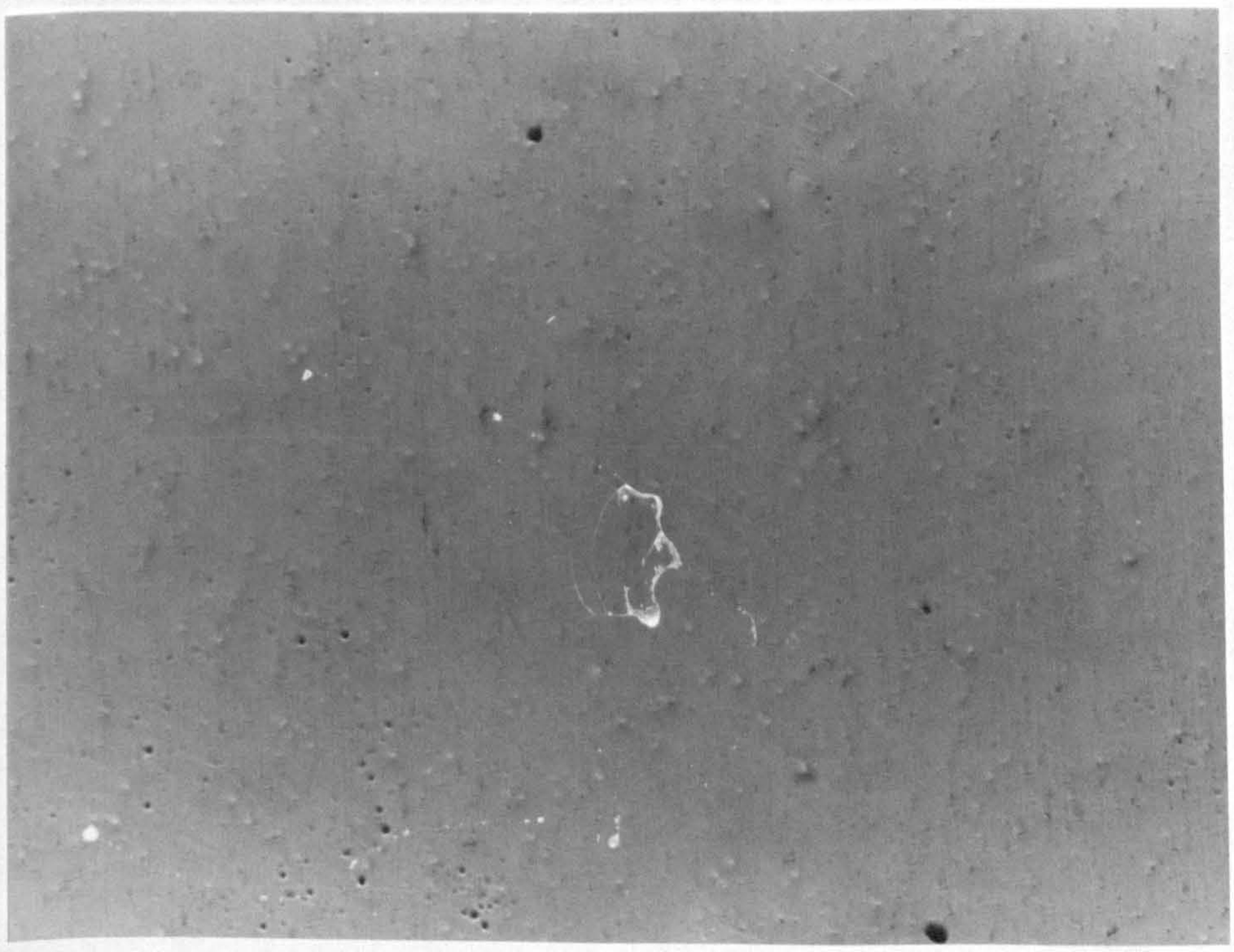

Figure 8.9(b) As Figure 8.9(a) using defocussing and oblique lighting to resolve micropores. Unetched. x 100

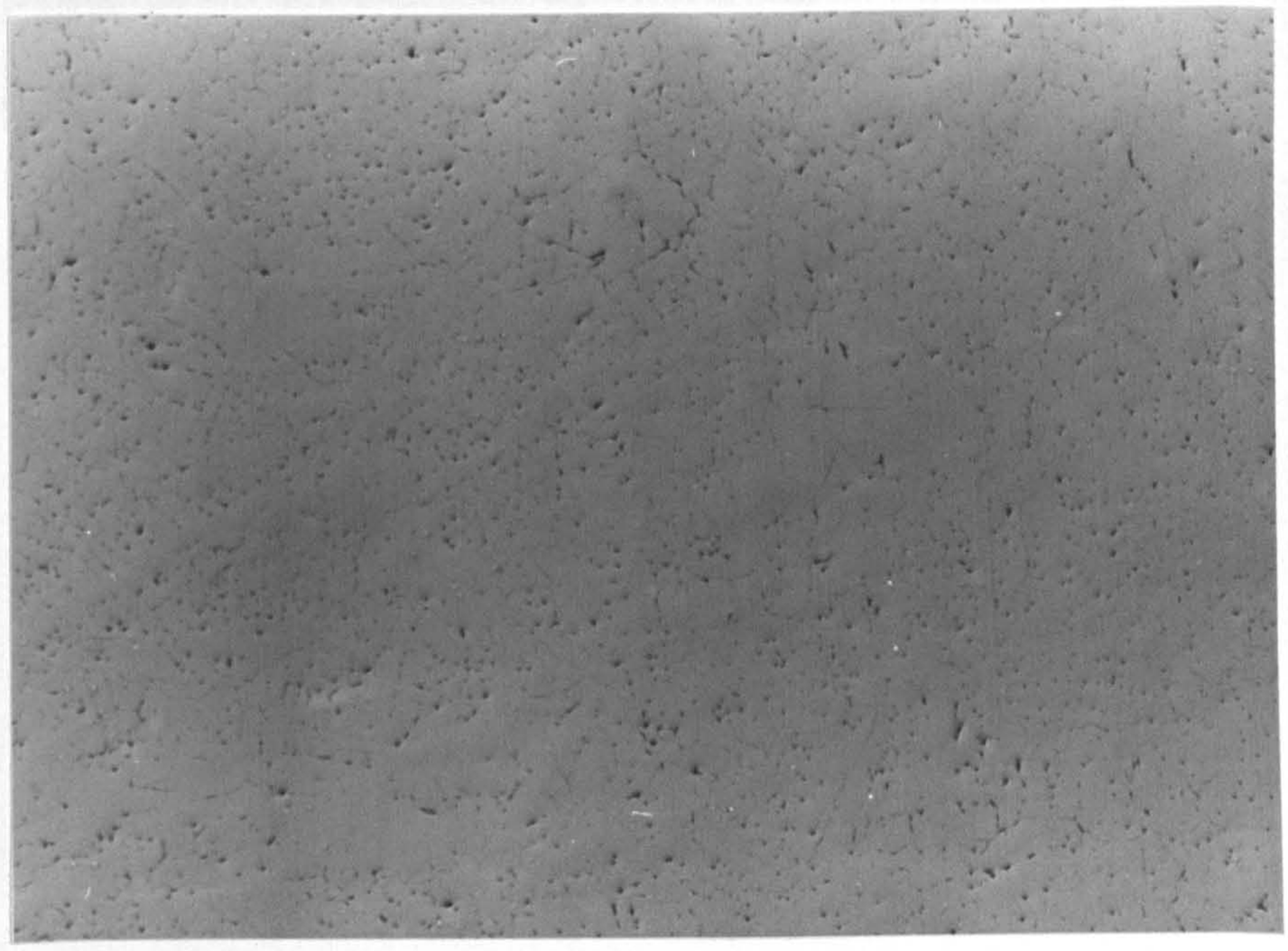

20 μm

Figure 8.10(a) Porosity at centre of as-cast billet. Unetched. x 100.

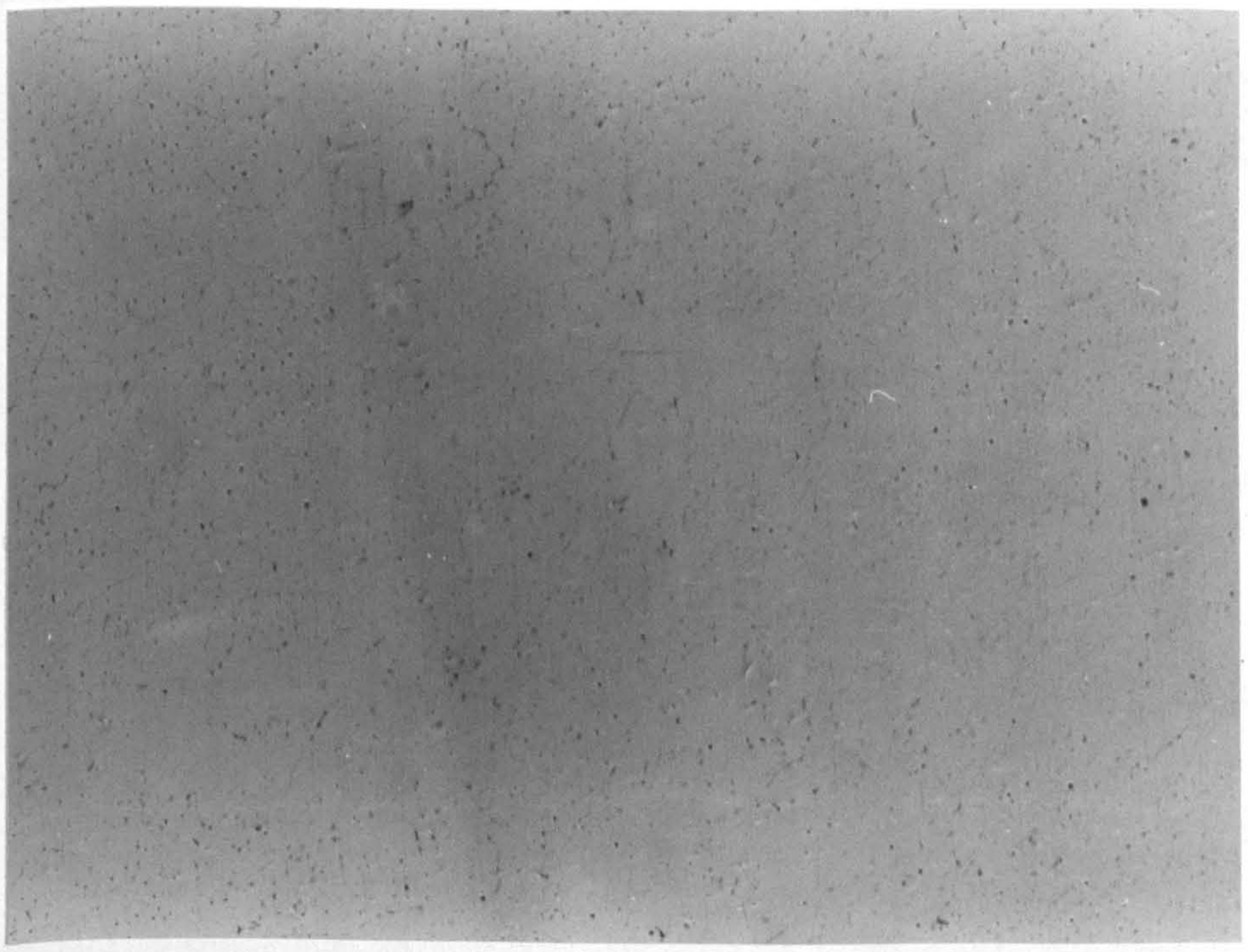

20 μm

Figure 8.10(b) As Figure 8.10(a) using defocussing and oblique lighting to resolve micropores. Unetched. x 100.

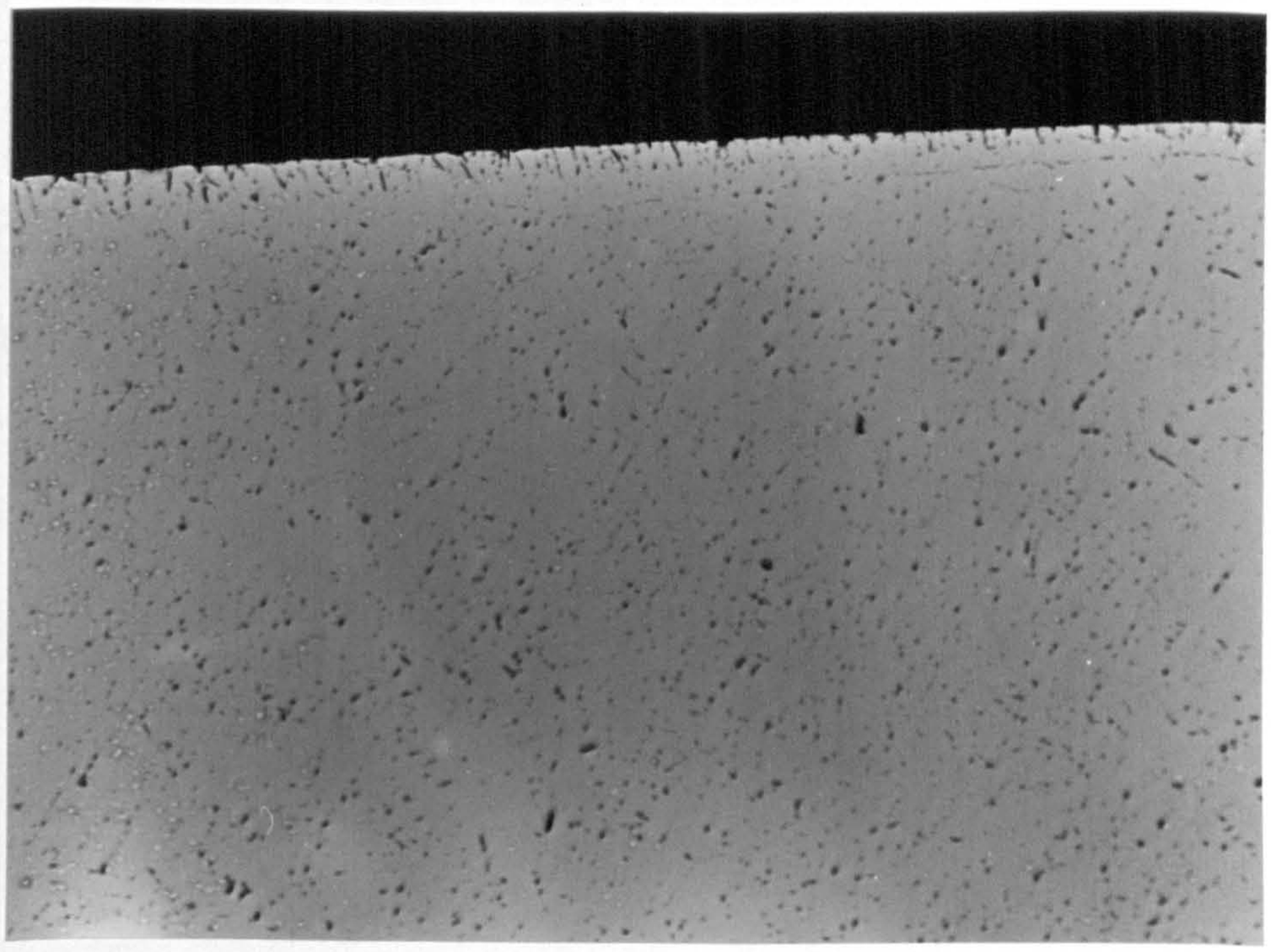

Figure 8.11(a) Porosity near cast edge of industrially homogenised billet. Unetched. x 100.

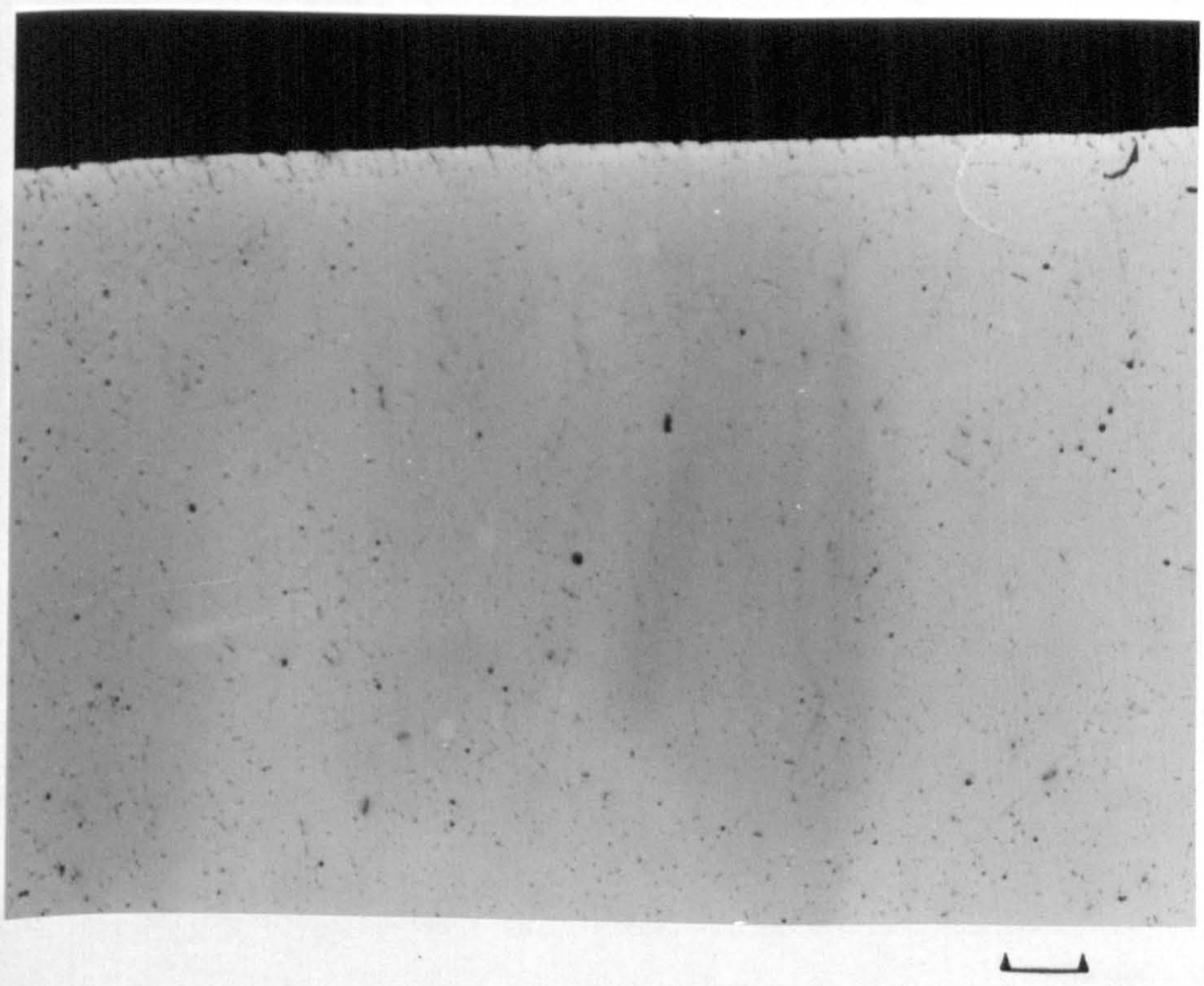

Figure 8.11(b) As Figure 8.11(a) with better resolution of the pores using defocussing and oblique lighting. The micropores are larger than those in the corresponding section through as-cast billet, shown in Figure 8.8(b).

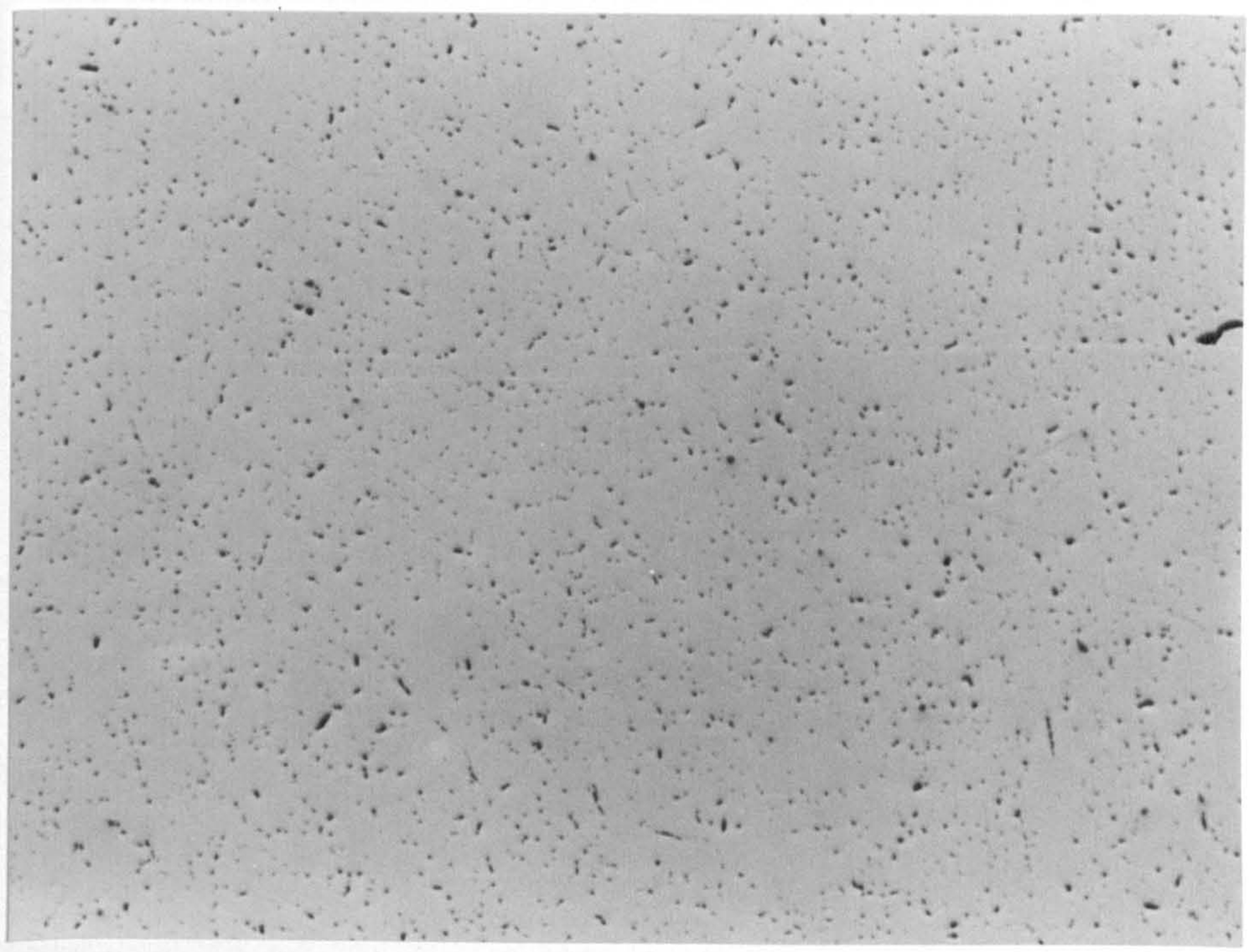

Figure 8.12(a) Porosity near mid-radius of industrially homogenised billet. Unetched. x 100.

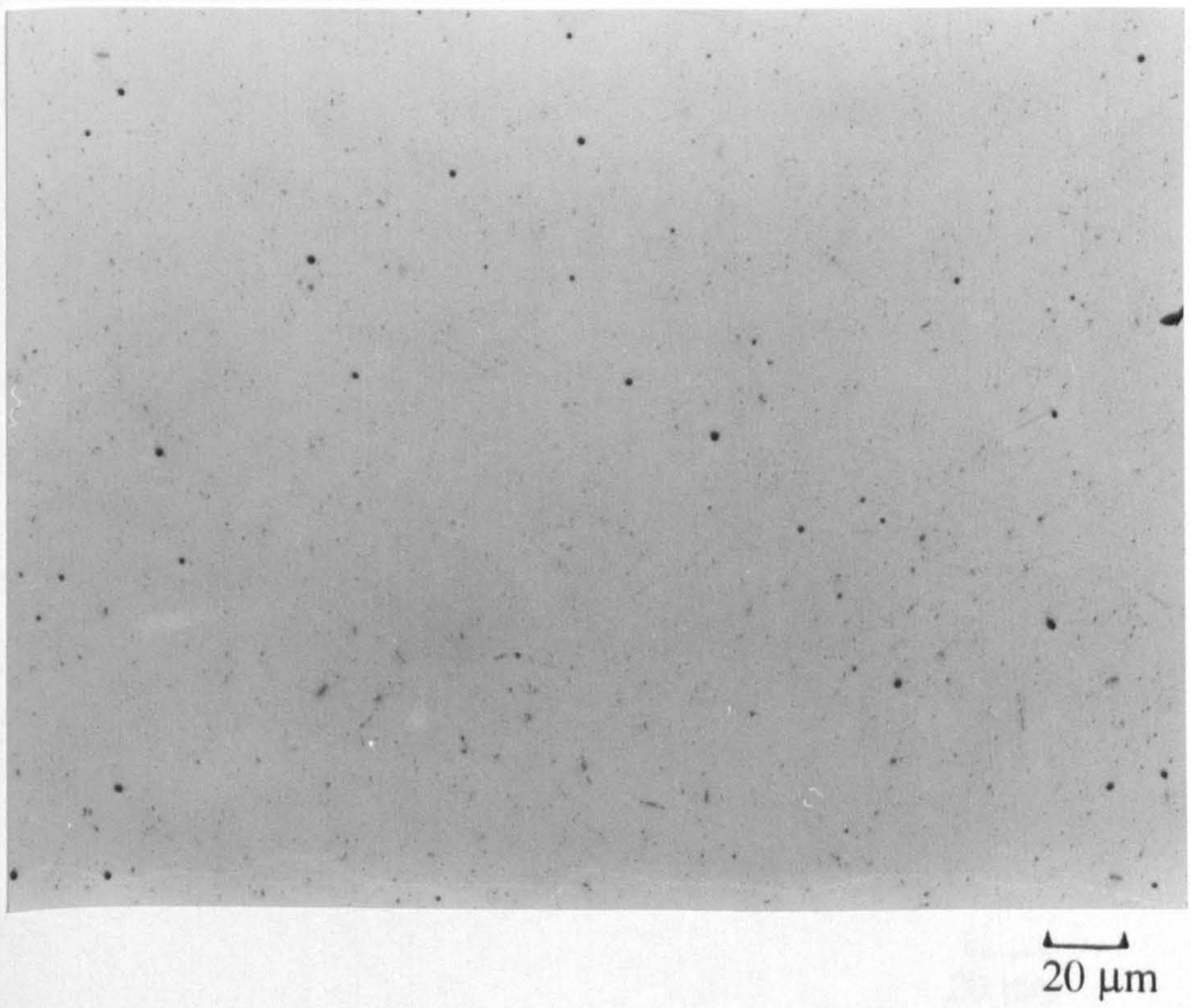

Figure 8.12(b) As Figure 8.12(a) with better resolution of the pores using defocussing and oblique lighting. The micropores are larger than those in the corresponding section through as-cast billet, shown in Figure 8.9(b).

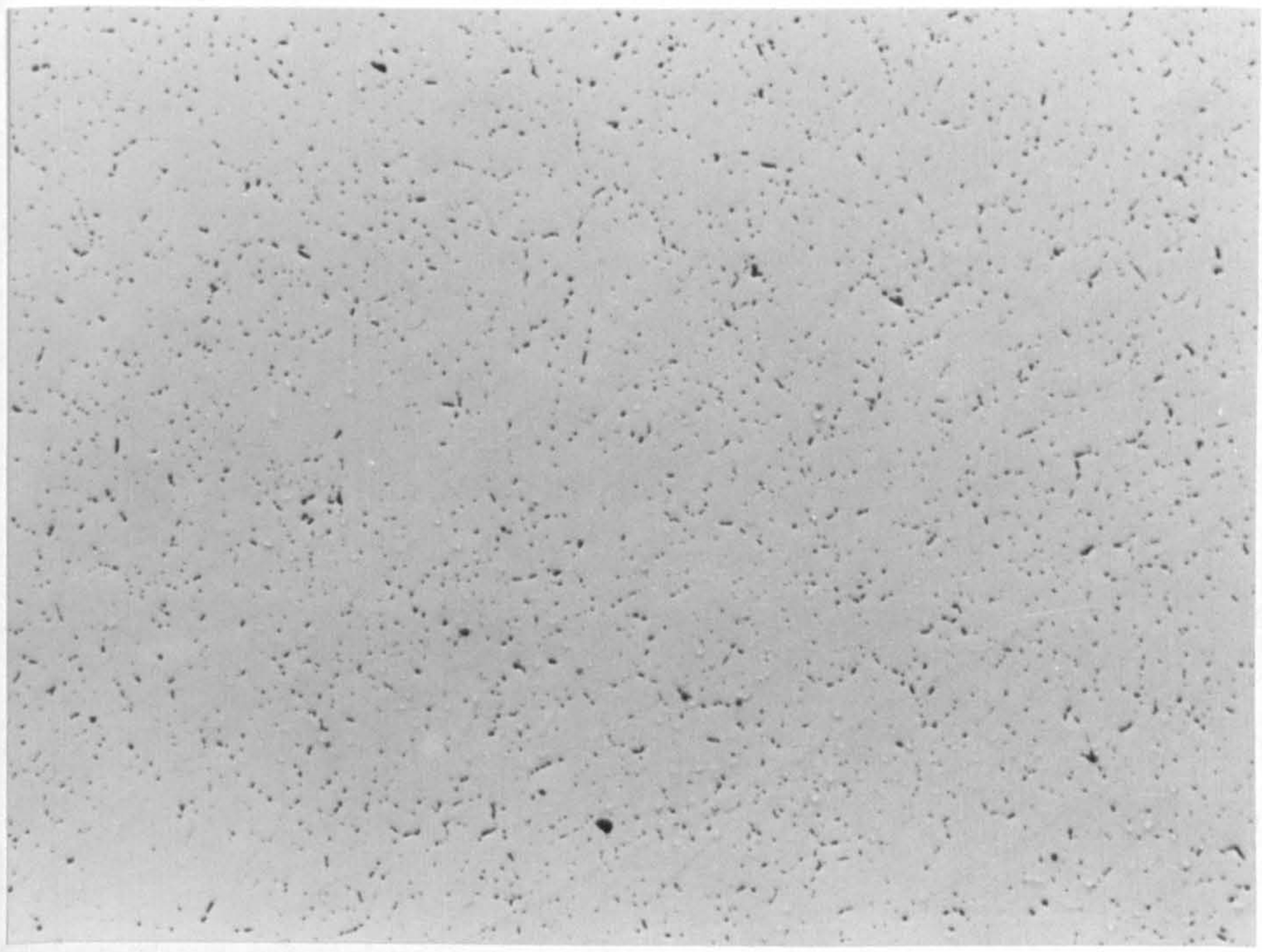

Figure 8.13(a) Porosity at the centre of industrially homogenised billet. Unetched. x 100.

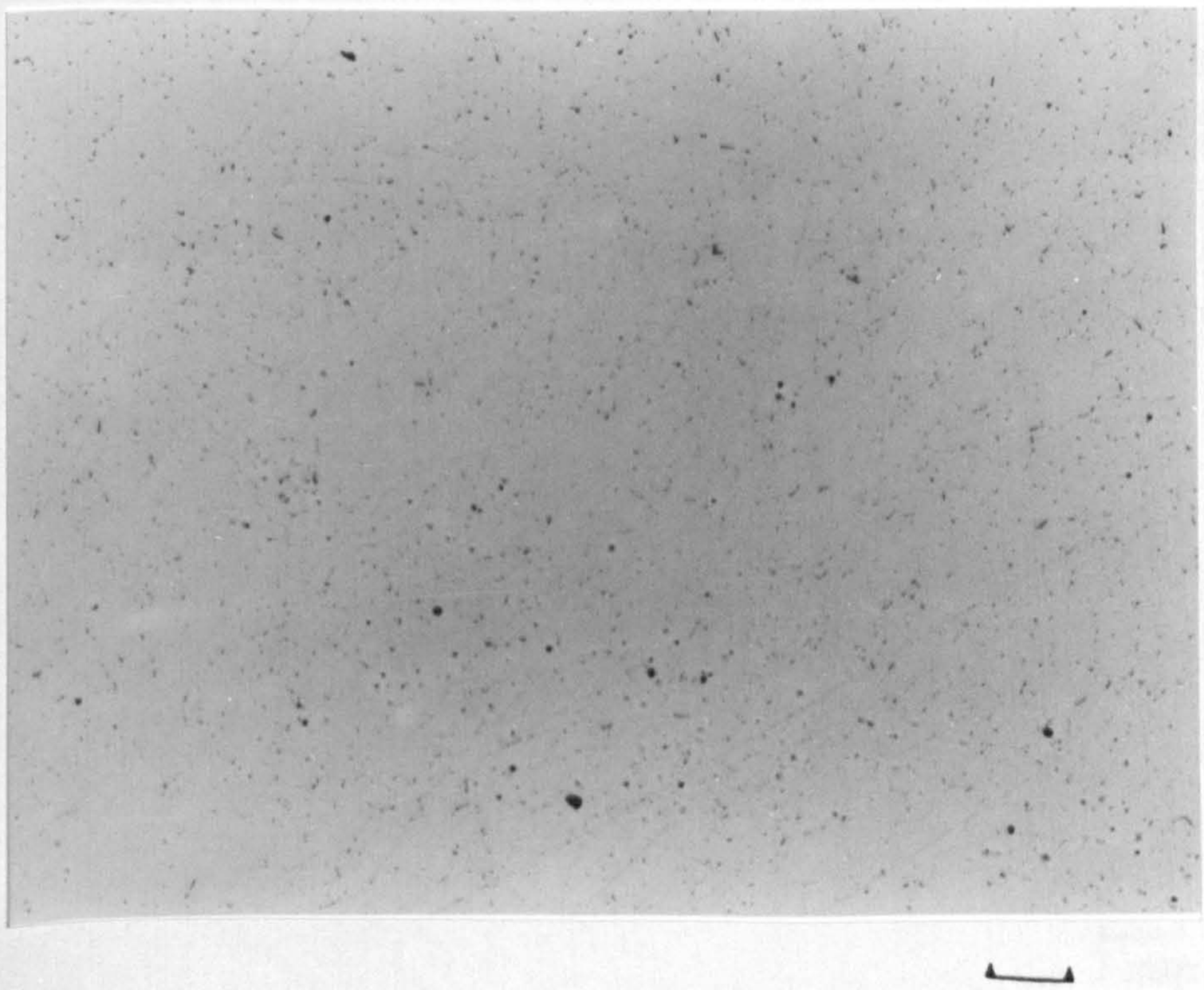

Figure 8.13(b) As Figure 8.13(a) with better resolution of the pores using defocussing and oblique lighting. The micropores are larger than those in the corresponding section through as-cast billet, shown in Figure 8.10(b).

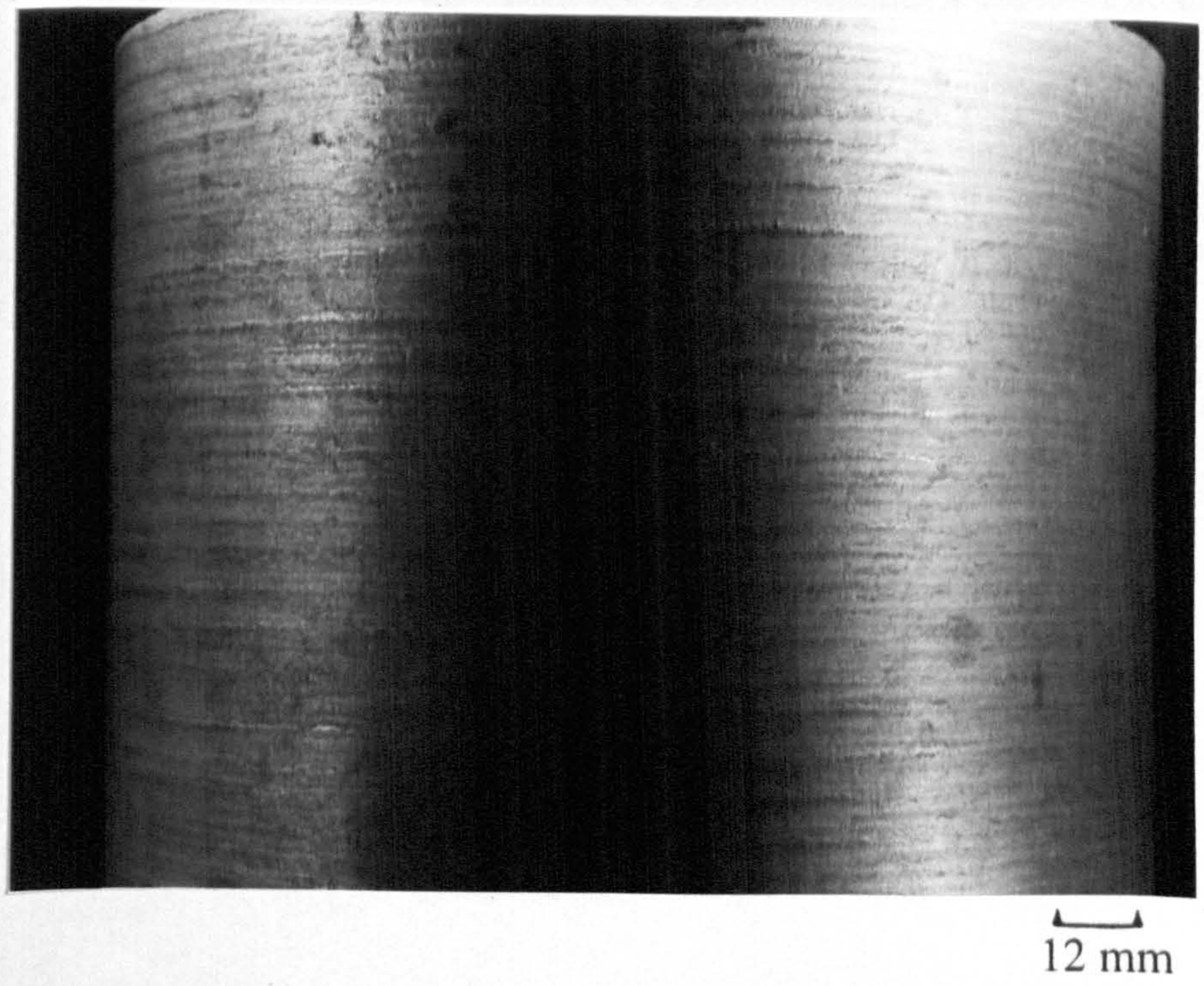

Figure 8.14 View of part of AA 6063 alloy air-slip cast billet, 7.5 m long x 178 mm diameter.

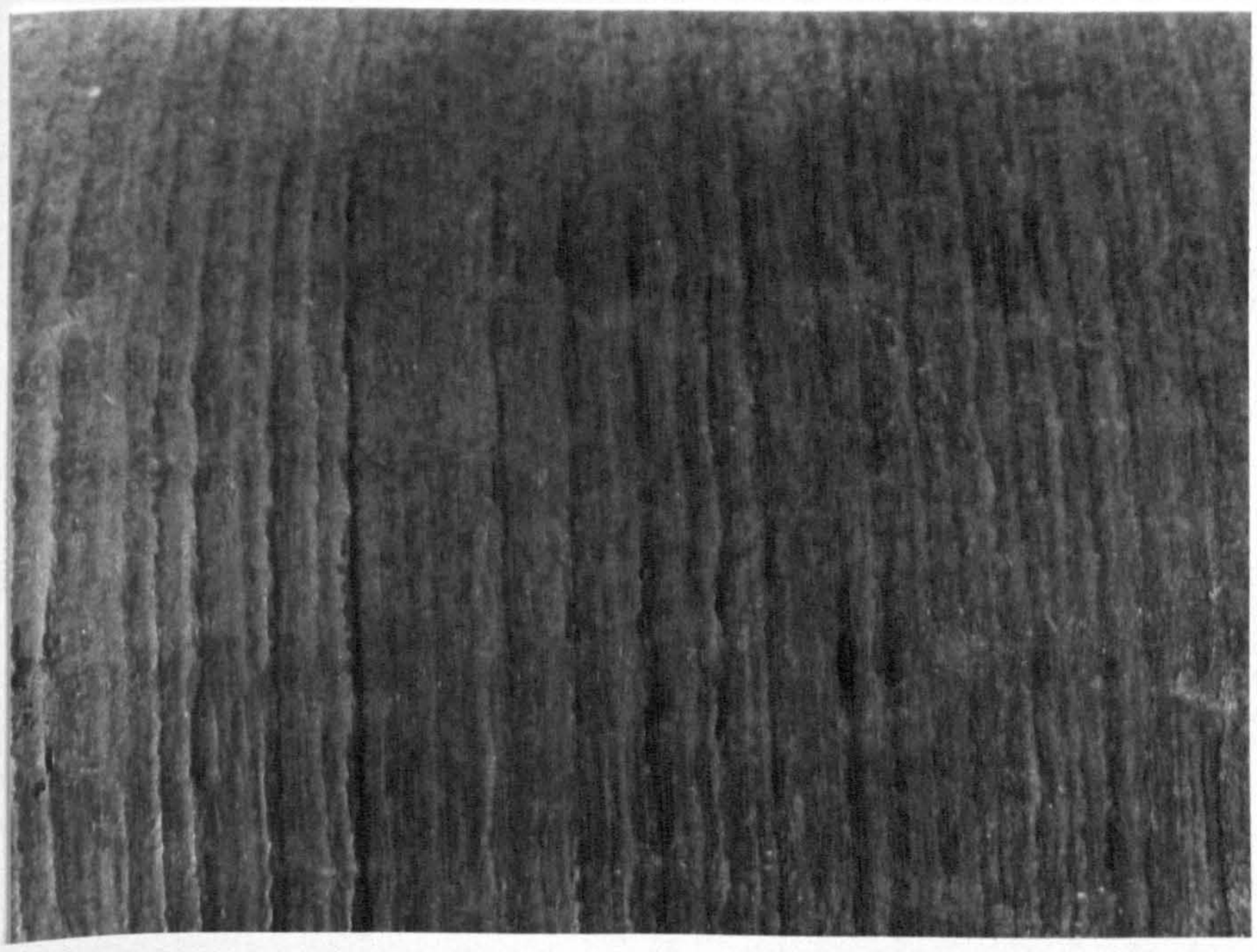

Figure 8.15 Close-up view of billet, showing close-form folds. The folds seem to be parallel in the photograph but they are in fact turns in a single spiral.

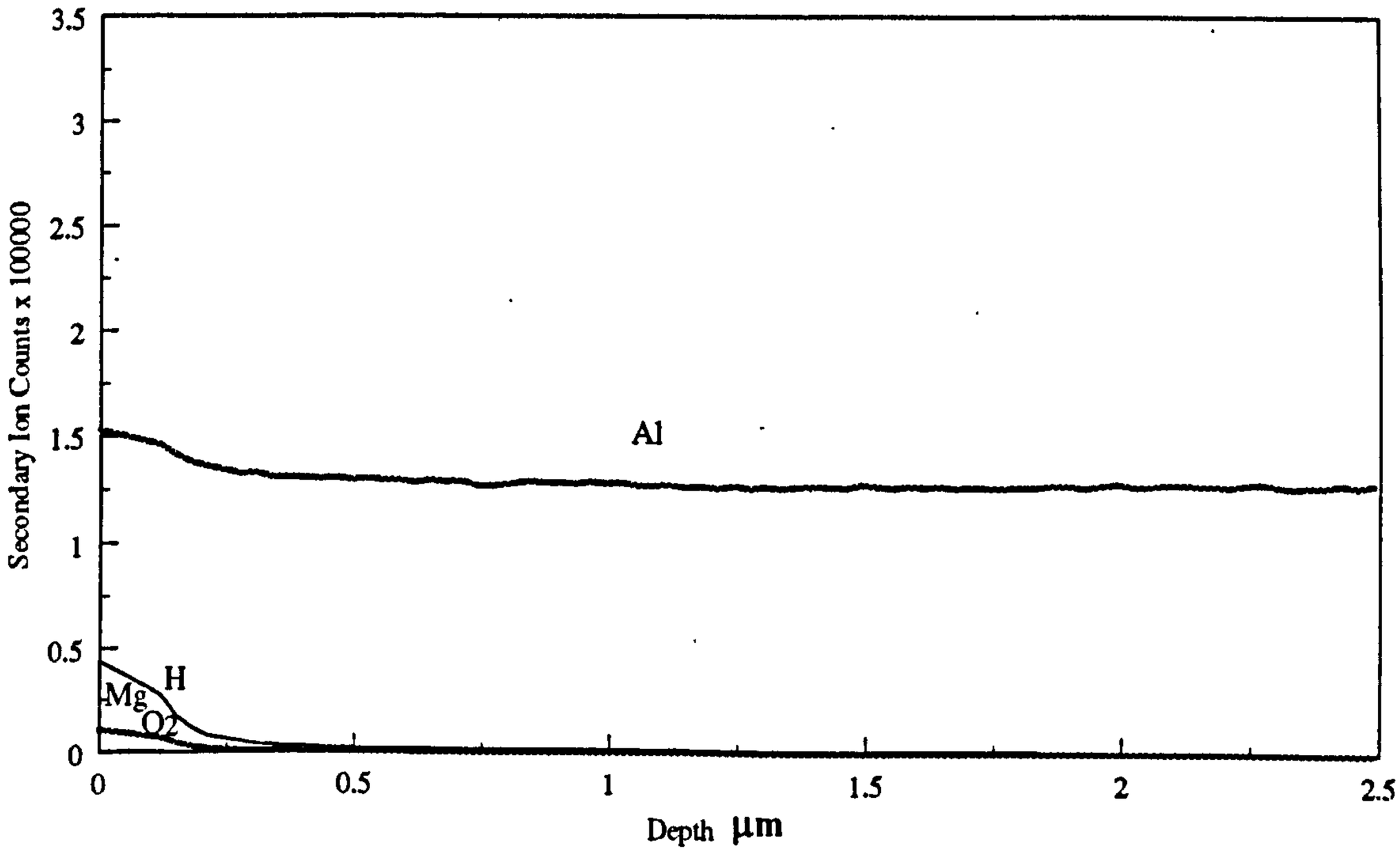

Figure 8.16 SIMS depth profile through the oxide on as-cast billet using a caesium (Cs^+) ion beam.

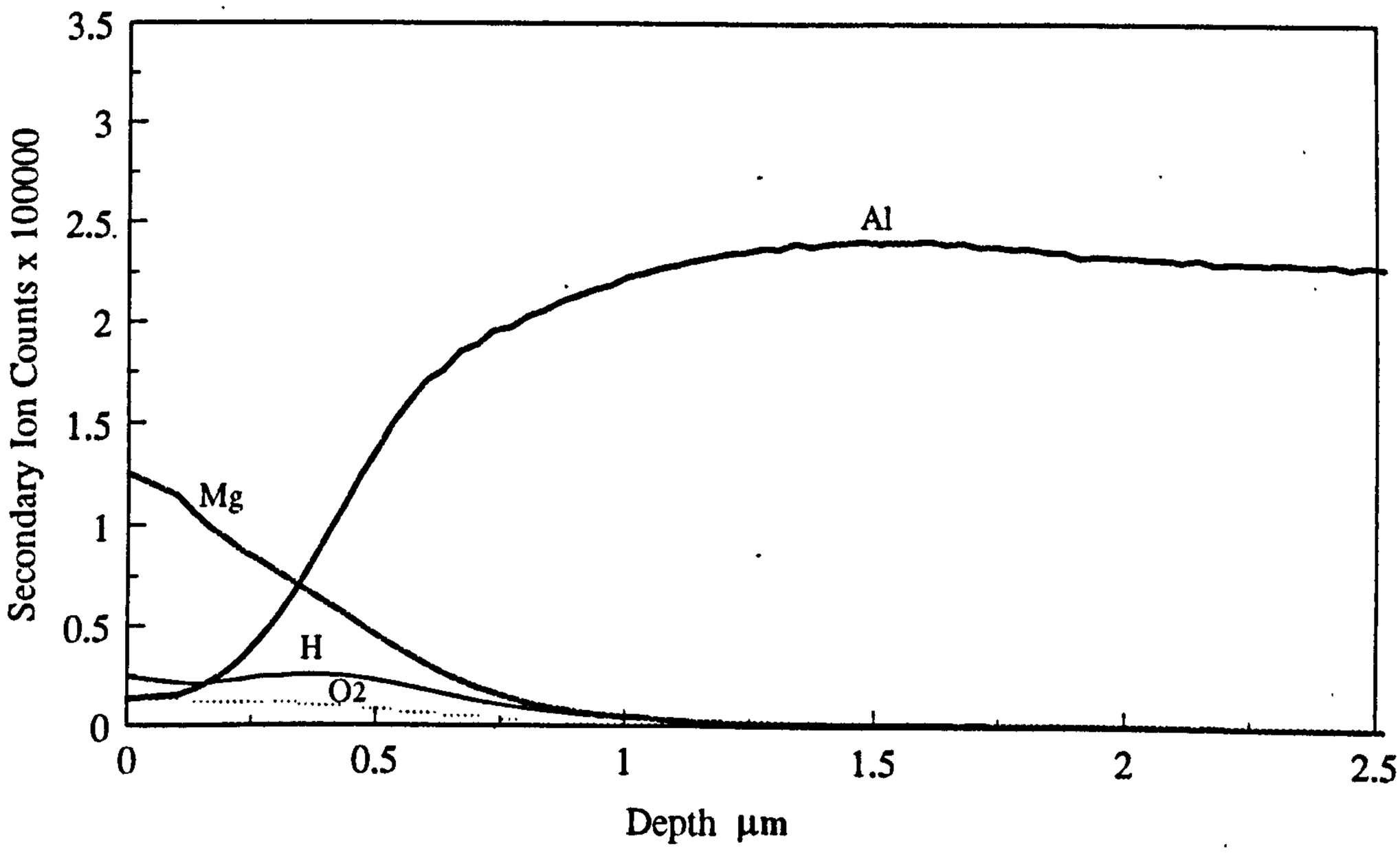

Figure 8.17 SIMS depth profile through the oxide on industrially homogenised billet, using a caesium (Cs^+) ion beam.

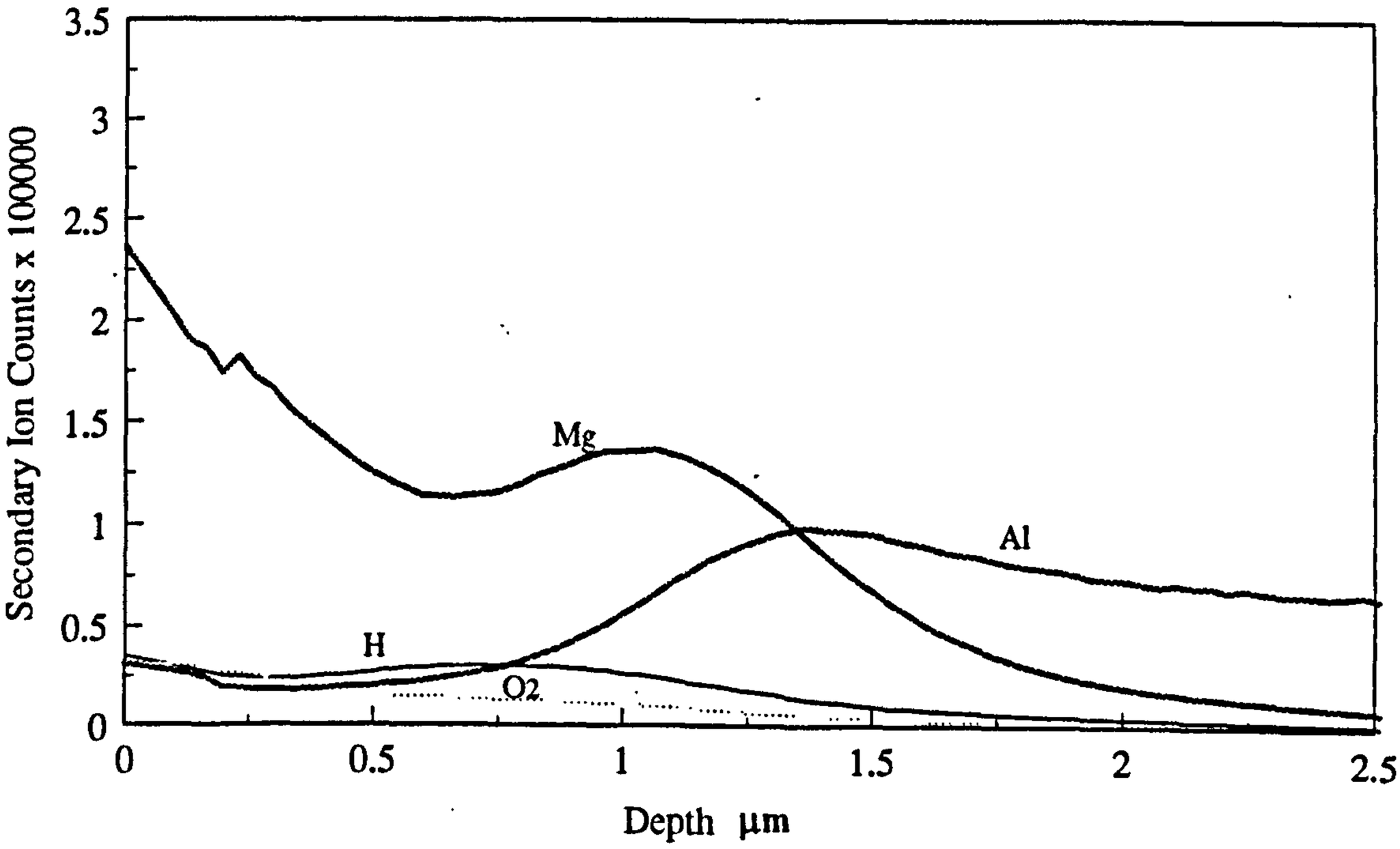

Figure 8.18 SIMS depth profile through the oxide on industrially homogenised billet, using a caesium (Cs^+) ion beam.

8.2.2 Distribution of hydrogen content in the billet

Tables 8.9 gives the results of hydrogen content determinations on the samples taken from the as cast billet.

Table 8.10 gives the results of hydrogen content determinations on the samples taken from the homogenised billet.

Table 8.9
Hydrogen content in aluminium billet, alloy AA6063,
along the cast length and across the diameter.

Cast length (mm)	Liquid metal temp. (°C) at casting	Hydrogen content in liquid metal (cm^3 / 100g)		Hydrogen content in the cast billet, (cm^3 / 100g) at:		
		Telegas	Hot Vac. Ext.	edge	mid. radius	centre
1200	676	0.20	0.18	0.17	0.18	0.17
2400	683	0.20	0.19	0.18	0.19	0.17
3600	680	0.19	0.17	0.16	0.17	0.18
4800	674	0.19	0.18	0.18	0.18	0.19
6000	677	0.18	0.17	0.17	0.17	0.16
7200	676	0.18	0.16	0.16	0.16	0.17

Table 8.10
Hydrogen content after homogenisation.

Sample	Hydrogen conten (cm^3 / 100g)					
	Edge of the billet		Mid-radius of the billet		Centre of the billet	
	sample 1	sample 2	sample 1	sample 2	sample 1	sample 2
as cast	0.17	0.18	0.18	0.19	0.18	0.17
homogenized in furnce 1	0.12	0.15	0.15	0.15	0.14	0.15
homogenized in furnce 2	0.11		0.15		0.15	
homogenized in furnce 3	0.11	0.14	0.16	0.16	0.15	0.14
Homogenization temperature set at 580 °C.						

8.3 Results of Heat Treatment in Simulated Environment

The results of hydrogen content determinations for heat-treatments in the experimental environments, described in Section 7.4 are given in sections 8.3.1 to 8.3.7.

SIMS depth profiles through the oxide films formed in various heat treatment environments are given in Section 8.3.8.

The results of XPS analysis of the oxide films are given in Section 8.3.9.

Micrographs showing the effect of the hydrogen absorbed in these treatments are given in section 8.3.10.

8.3.1 Hydrogen content after heat-treatment in dry air

8.3.1.1 Isothermal treatment

Table 8.11 - 590°C.

Heat treatment time (hrs)	1	2	4	6	8
Hydrogen content (cm^3 / 100g)	0.02	0.02	0.04	0.03	0.04

Table 8.12 - 500°C.

Heat treatment time (hrs)	1	2	4	6	8
Hydrogen content (cm^3 / 100g)	0.18	0.21	0.24	0.23	0.28

8.3.1.2 Isochronal treatment

Table 8.13 - 4 hours.

Heat treatment temperature (°C)	470	500	530	560	590
Hydrogen content (cm^3 / 100g)	0.22	0.24	0.32	0.27	0.04

8.3.2 Hydrogen content after heat-treatment in wet air

8.3.2.1 Isothermal treatment

Table 8.14 - 590°C.

Heat treatment time (hrs)	1	2	4	6	8
Hydrogen content (cm^3 / 100g)	0.19	0.20	0.26	0.03	0.07

Table 8.15 - 500°C

Heat treatment time (hrs)	1	2	4	6	8
Hydrogen content (cm^3 / 100g)	0.18	0.22	0.32	0.27	0.23

8.3.2.2 Isochronal treatment

Table 8.16 - 4 hours.

Heat treatment temperature (°C)	470	500	530	560	590
Hydrogen content (cm^3 / 100g)	0.21	0.32	0.25	0.21	0.26

8.3.3 Hydrogen content after heat-treatment in air containing HCl

8.3.3.1 Isothermal treatment

Table 8.17 - 590°C.

Heat treatment time (hrs)	1	2	4	6	8
Hydrogen content (cm^3 / 100g)	0.23	0.24	0.37	0.14	0.02

Table 8.18 - 500°C

Heat treatment time (hrs)	1	2	4	6	8
Hydrogen content (cm^3 / 100g)	0.28	0.33	0.37	0.55	0.36

8.3.3.2 Isochronal treatment

Table 8.19 - 4 hours.

Heat treatment temperature (°C)	470	500	530	560	590
Hydrogen content (cm^3 / 100g)	0.34	0.37	0.42	0.42	0.37

8.3.4 Hydrogen content after heat-treatment in air containing HCl and SO_2

8.3.4.1 Isothermal treatment

Table 8.20 - 590°C.

Heat treatment time (hrs)	1	2	4	6	8
Hydrogen content (cm^3 / 100g)	0.82	0.80	0.86	0.92	1.08

Table 8.21 - 500°C.

Heat treatment time (hrs)	1	2	4	6	8
Hydrogen content (cm^3 / 100g)	0.38	0.56	0.68	0.75	0.81

8.3.4.2 Isochronal treatment

Table 8.22 - 4 hours.

Heat treatment temperature (°C)	470	500	530	560	590
Hydrogen content (cm^3 / 100g)	0.59	0.68	0.82	0.84	0.86

8.3.5 Hydrogen content after heat-treatment in dry air and SO_2

8.3.5.1 Isothermal treatment

Table 8.23 - 590°C.

Heat treatment time (hrs)	1	2	4	6	8
Hydrogen content (cm^3 / 100g)	0.68	1.15	0.80	1.05	1.13

Table 8.24 - 500°C.

Heat treatment time (hrs)	1	2	4	6	8
Hydrogen content (cm^3 / 100g)	0.71	0.54	0.70	0.80	0.82

8.3.5.2 Isochronal treatment

Table 8.25 - 4 hours.

Heat treatment temperature (°C)	470	500	530	560	590
Hydrogen content (cm^3 / 100g)	0.76	0.70	1.00	1.41	0.80

8.3.6 Hydrogen content after heat-treatment in wet air and SO_2

8.3.6.1 Isothermal treatment

Table 8.26 - 590°C.

Heat treatment time (hrs)	1	2	4	6	8
Hydrogen content (cm^3 / 100g)	1.02	1.23	1.29	2.04	2.83

Table 8.27 - 500°C.

Heat treatment time (hrs)	1	2	4	6	8
Hydrogen content (cm^3 / 100g)	0.55	0.74	0.84	0.93	0.91

8.3.6.2 Isochronal treatment

Table 8.28 - 4 hours.

Heat treatment temperature (°C)	470	500	530	560	590
Hydrogen content (cm^3 / 100g)	0.84	0.84	0.98	1.18	1.29

8.3.7 Hydrogen content after heat-treatment in dry air and SO_2 contaminated furnace

Table 8.29 - 590°C

Heat treatment time (hrs)	2	6
Hydrogen content (cm^3 / 100g)	0.76	0.98

8.3.8 SIMS depth profiles

The profiles were obtained using a caesium ion (Cs^+) beam. The ions selected and recorded were $^{54}Al^{6+}$, $^{26}Mg^{2-}$, $^{16}O^{2-}$, $^{32}S^{2-}$ and $^{1}H^-$. $^{54}Al^{6+}$ and $^{26}Mg^{2+}$ were used because signals from the more abundant species, $^{27}Al^{3+}$ and $^{24}Mg^{2+}$, overwhelmed the signals from minority elements.

Figure 8.19 gives a SIMS depth profile through the air-formed oxide on the surface of a sample polished to 6 μm and not heated, to act a reference.

Figures 8.20 to 8.25 give the SIMS depth profiles through the oxides formed on the surface of samples from heat-treatments in various environments. Only a few selected samples could be submitted to SIMS analysis because use of the facility was on a very expensive commercial basis.

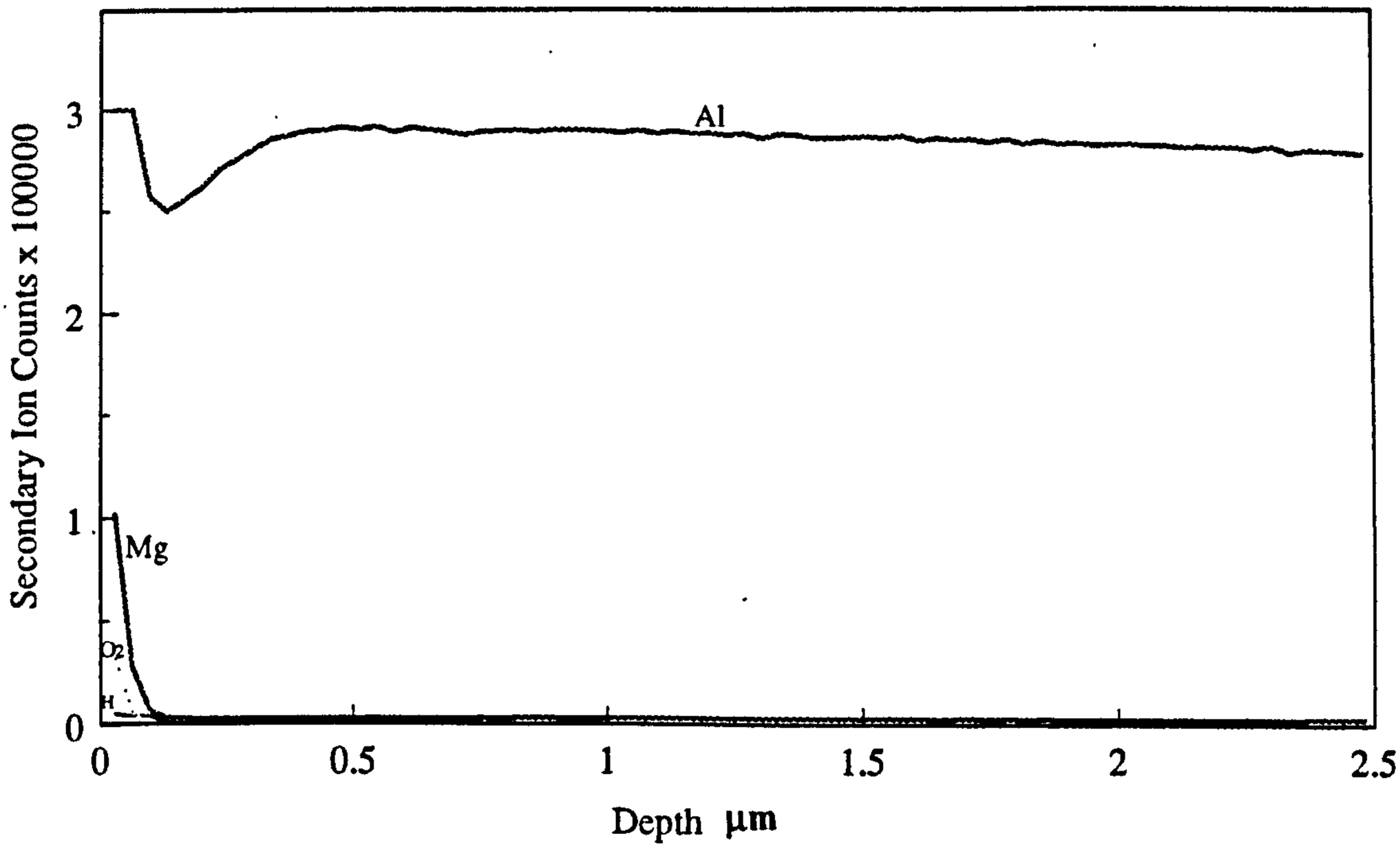

Figure 8.19. SIMS depth profile of clean reference sample - not heat-treated.

The $^{54}Al^{6+}$ signal is relatively constant and extends right to the surface.

The $^{26}Mg^{2+}$ signal is restricted to a narrow zone just below the surface.

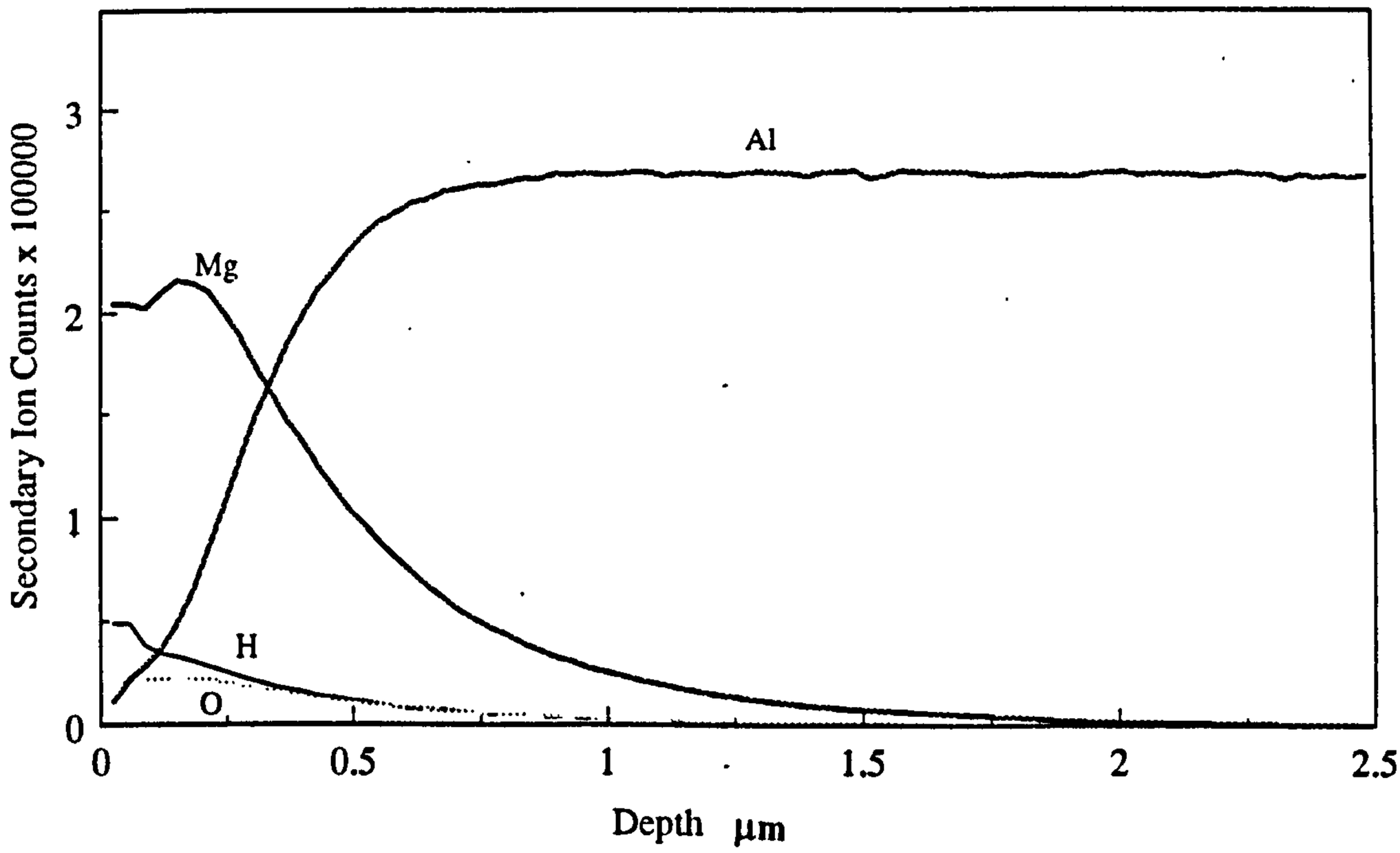

Figure 8.20. SIMS Depth profile through oxide film formed on sample heated 4 h at 500 °C in nominally dry air.

The $^{54}Al^{6+}$ signal rises from zero at the surface to a constant value at ~ 0.6 µm.

The $^{26}Mg^{2+}$ signal is high in the surface 0.3 µm and falls away at greater depths.

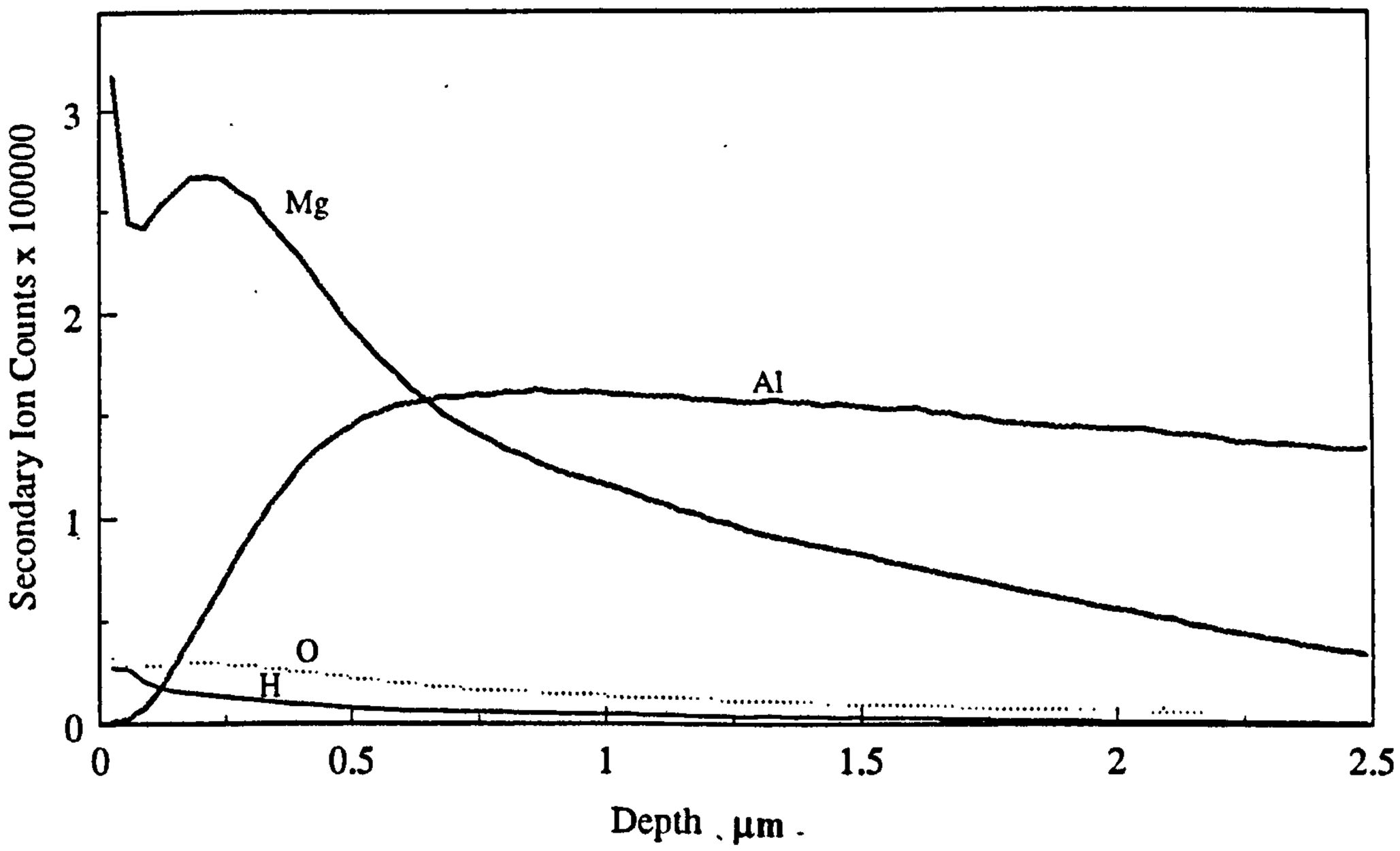

Figure 8.21. SIMS Depth profile through oxide film formed on sample heated 4 h at 590 °C in nominally dry air.

The $^{54}Al^{6+}$ signal rises from zero at the surface to a constant value at ~ 0.5 µm.

The $^{26}Mg^{2+}$ signal is high in the surface 0.4 µm and falls away at greater depths.

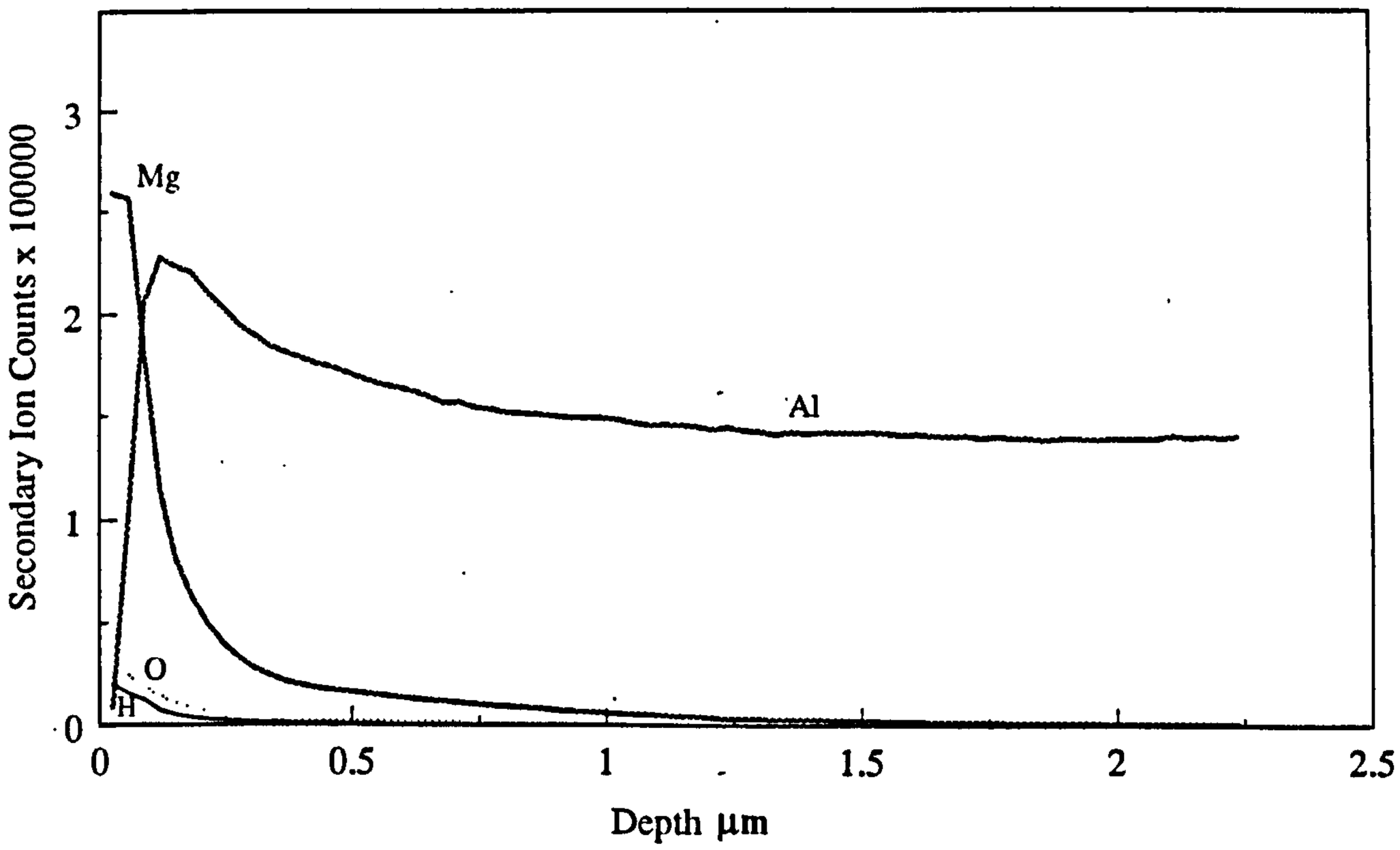

Figure 8.22. SIMS Depth profile through oxide film formed on sample heated 4 h at 500 °C in water-saturated air.

The $^{54}Al^{6+}$ signal rises from zero at the surface to a maximum value at ~0.1 µm.

The $^{26}Mg^{2+}$ signal is high in the surface 0.05 µm and falls away at greater depths.

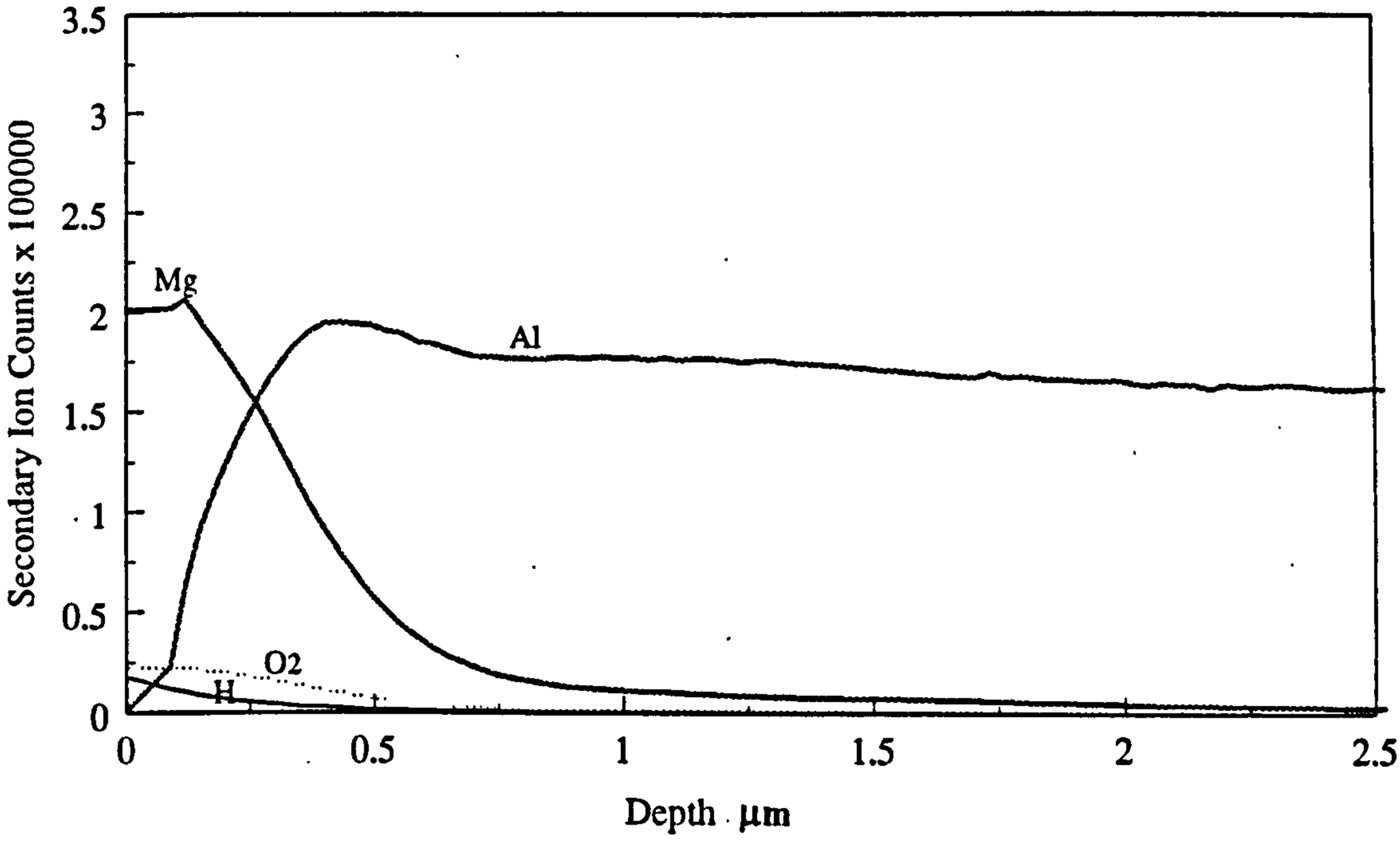

Figure 8.23. SIMS Depth profile through oxide film formed on sample heated 4 h at 590 °C in water-saturated air.

The $^{54}Al^{6+}$ signal rises from zero at the surface to a maximum value at ~0.4 µm.

The $^{26}Mg^{2+}$ signal is high in the surface 0.1 µm and falls away at greater depths.

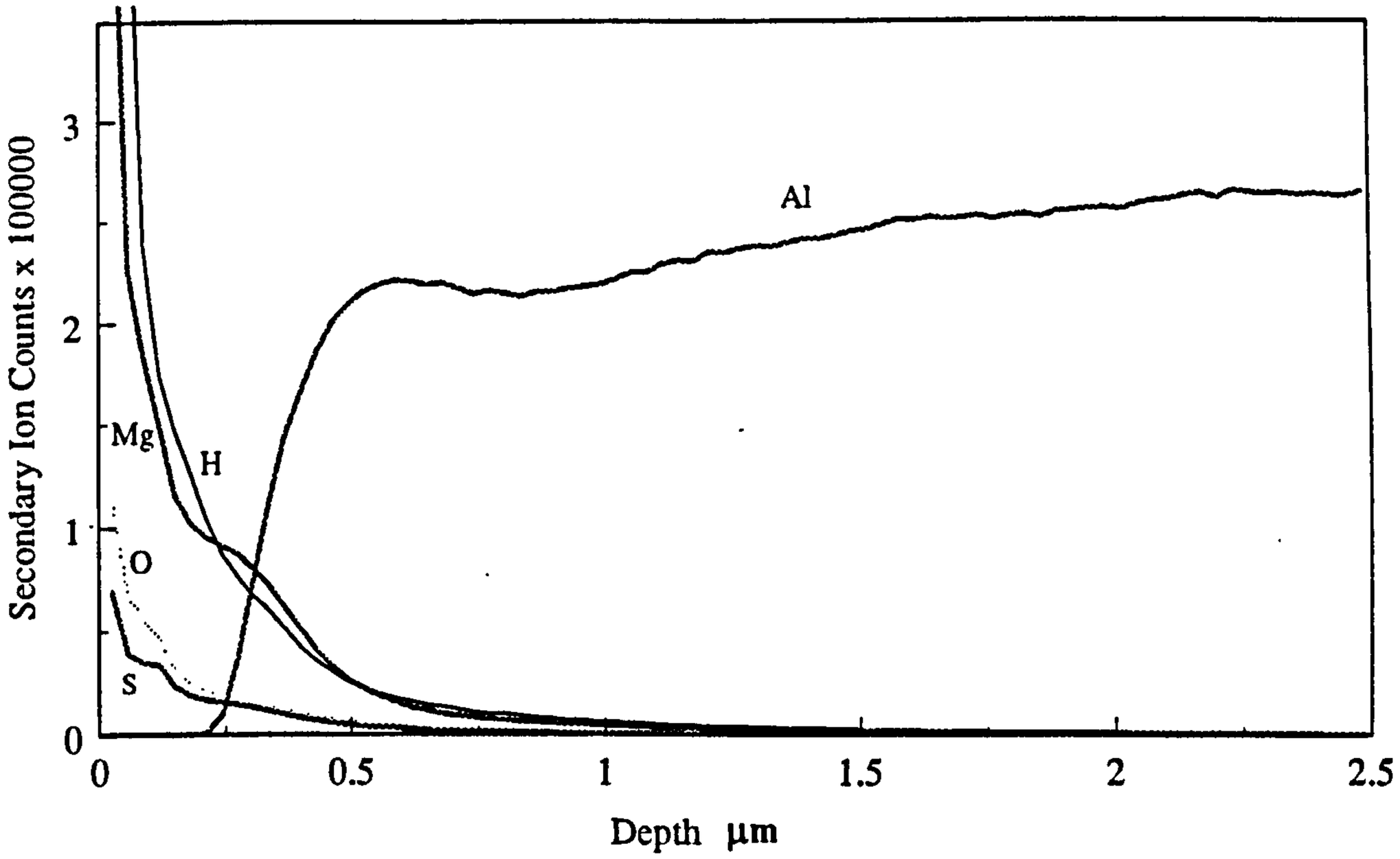

Figure 8.24. SIMS Depth profile through oxide film formed on sample heated 4 h at 500 °C in nominally dry air + 1% SO_2

The $^{54}Al^{6+}$ signal is not detected in a zone extending from the surface to a depth of 0.2 µm. Thereafter it rises to a maximum value at a depth of ~ 0.6 µm.

The $^{26}Mg^{2+}$ signal is high in the aluminium-free zone, falling at greater depths.

Significant $^{32}S^{2-}$, $^{16}O^{2-}$ and $^{1}H^{-}$ signals were detected in the aluminium-free zone.

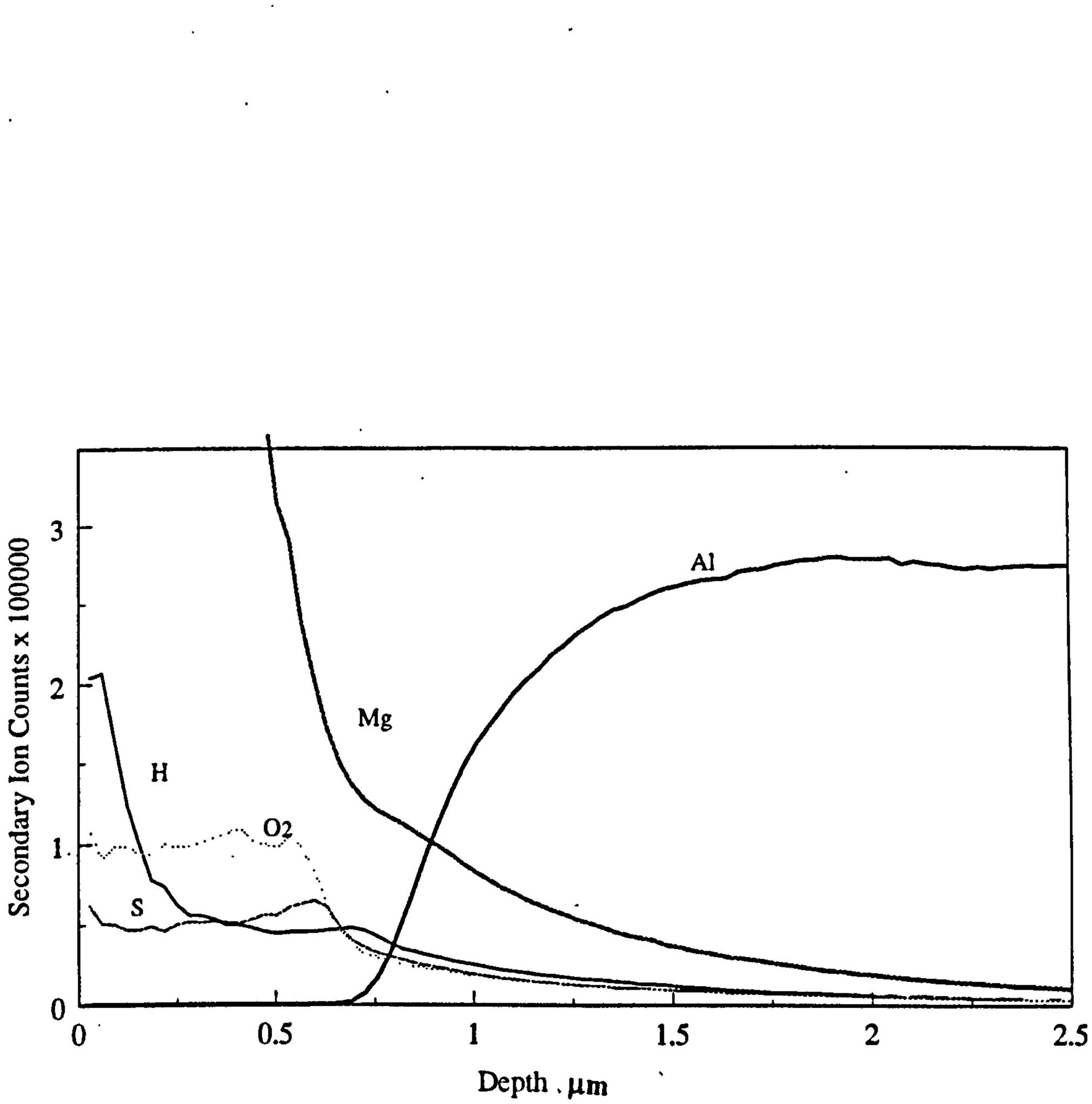

Figure 8.25. SIMS Depth profile through oxide film formed on sample heated 4 h at 590 °C in nominally dry air + 1% SO_2.

The $^{54}Al^{6+}$ signal is not detected in a zone extending from the surface to a depth of 0.7 µm. Thereafter it rises to a fairly constant value at a depth of ~1.5 µm.

The $^{26}Mg^{2+}$ signal is high in the aluminium-free zone, falling at greater depths.

$^{32}S^{2-}$, $^{16}O^{2-}$and $^{1}H^{-}$ signals were detected, lying on plateaus corresponding with the aluminium-free zone. The $^{1}H^{-}$ signal was enhanced towards the surface.

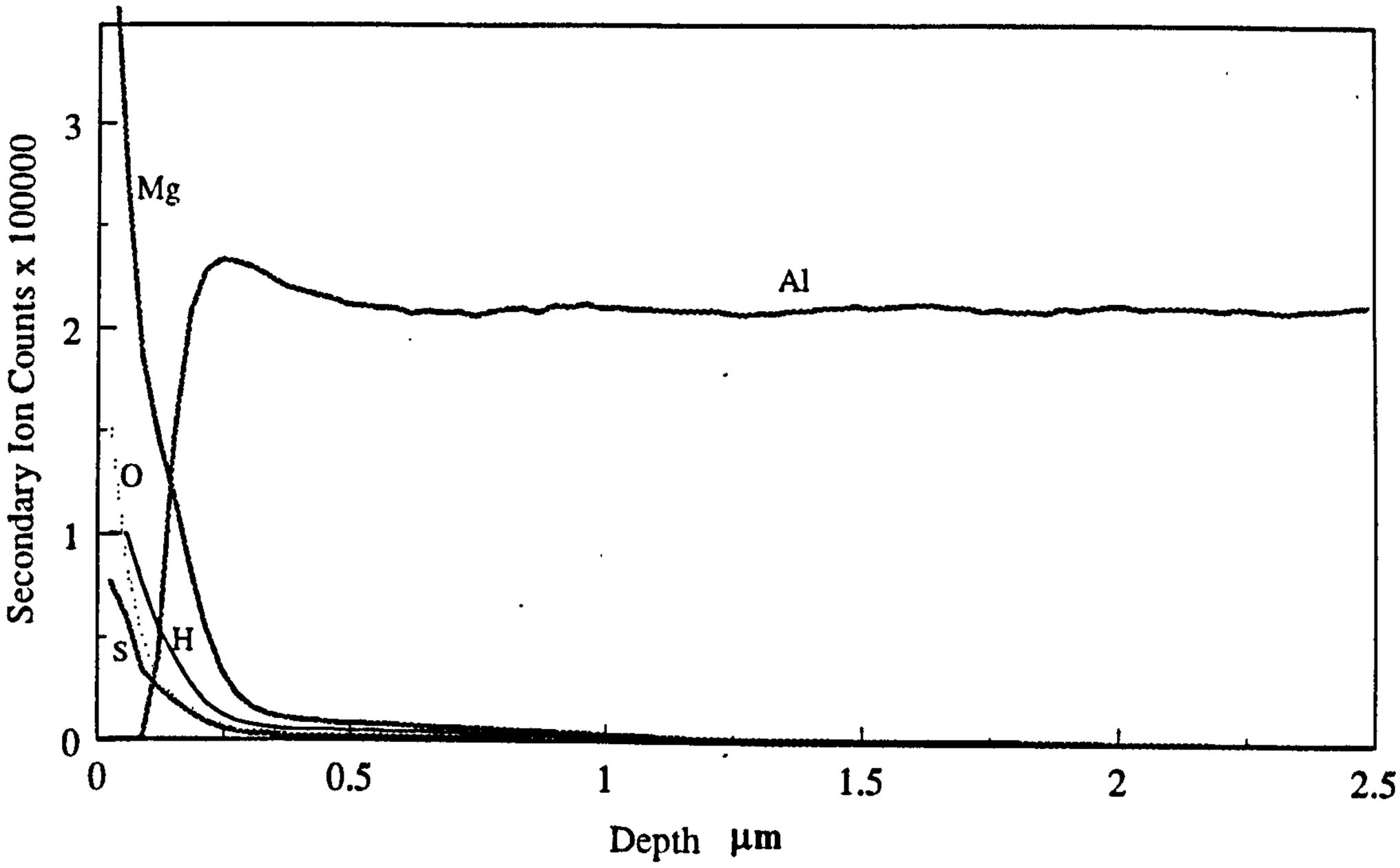

Figure 8.26. SIMS Depth profile through oxide film formed on sample heated 4 h at 500 °C in water-saturated air + 1% SO_2.

The $^{54}Al^{6+}$ signal is not detected in a zone extending from the surface to a depth of 0.1 µm. Thereafter it rises to a maximum value at a depth of ~ 0.25 µm.

The $^{26}Mg^{2+}$ signal is high in the aluminium-free zone, falling at greater depths.

Significant $^{32}S^{2-}$, $^{16}O^{2-}$ and $^{1}H^{-}$ signals were detected in the aluminium-free zone.

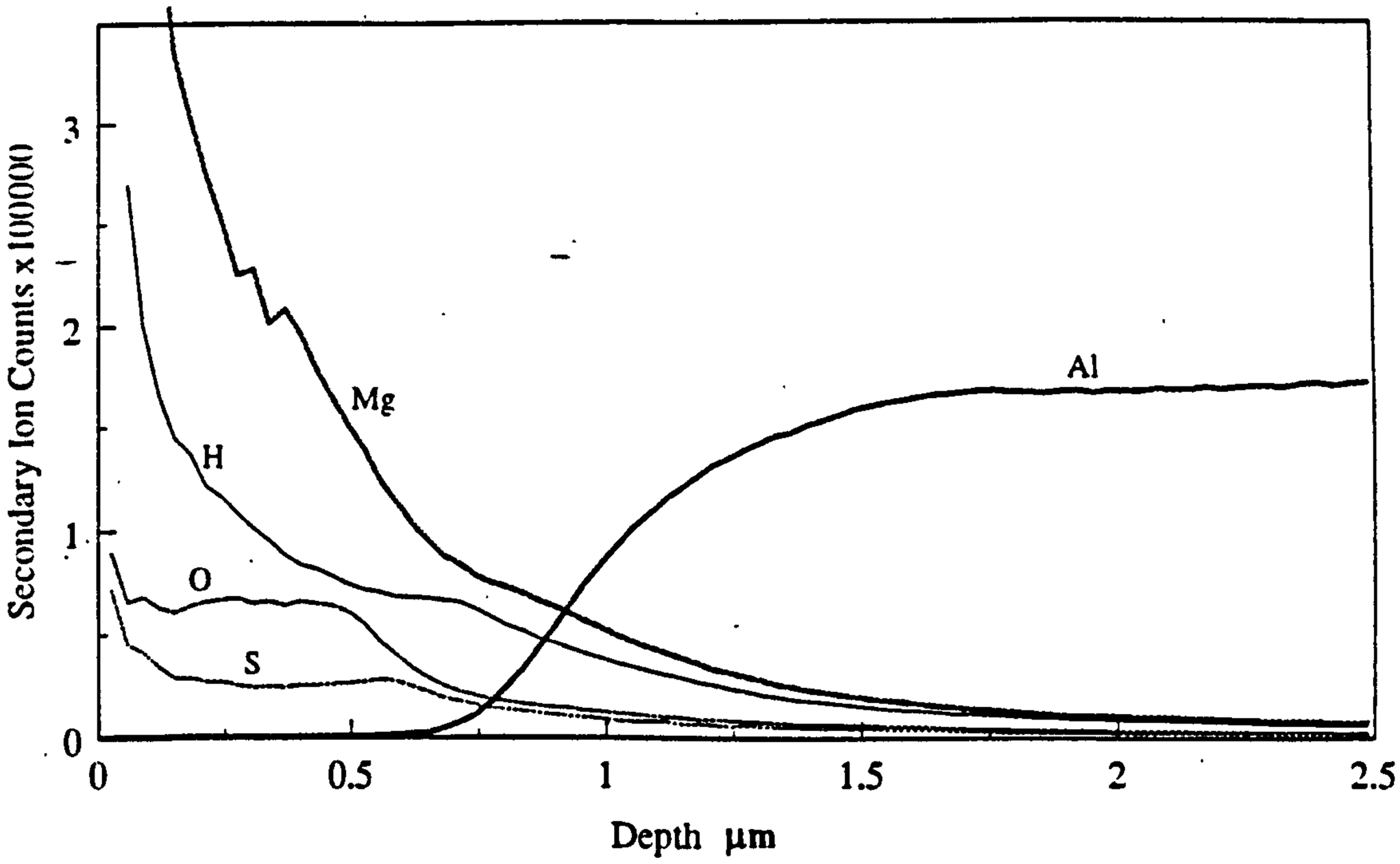

Figure 8.27. SIMS Depth profile through oxide film formed on sample heated 4 h at 590 °C in water-saturated air + 1% SO_2.

The $^{54}Al^{6+}$ signal is not detected in a zone extending from the surface to a depth of 0.6 µm. Thereafter it rises to a fairly constant value at a depth of ~1.5 µm. The $^{26}Mg^{2+}$ signal is high in the aluminium-free zone, falling at greater depths. $^{32}S^{2-}$, $^{16}O^{2-}$and $^{1}H^{-}$ signals were detected, lying on plateaus corresponding with the aluminium-free zone. The $^{1}H^{-}$ signal was enhanced towards the surface

8.3.9 XPS analysis

To interpret the XPS spectra as described later in Section 9.4 it was necessary to identify magnesium sulphate peaks. No suitable information was found in the literature, so a sample of magnesium sulphate heptahydrate was analysed as standard. The material was 99.5% pure BDH Anala R, $MgSO_4.7H_2O$. The results are given in Table 8.30 and in Figures 8.28 and 8.29.

Table 8.30 The binding energies for XPS analysis of 99.5% $MgSO_4.7H_2O$.

Peak	C_{1s}	Mg_{1s}	Mg_{2p}	Mg_{2s}	S_{2p}	O_{1s}
Binding energy (eV)	287.6	1307.6	54.0	92.8	172.5	535.3
Binding energy, charge corrected (eV)	284.6	1304.6	51.0	89.8	169.5	532.3

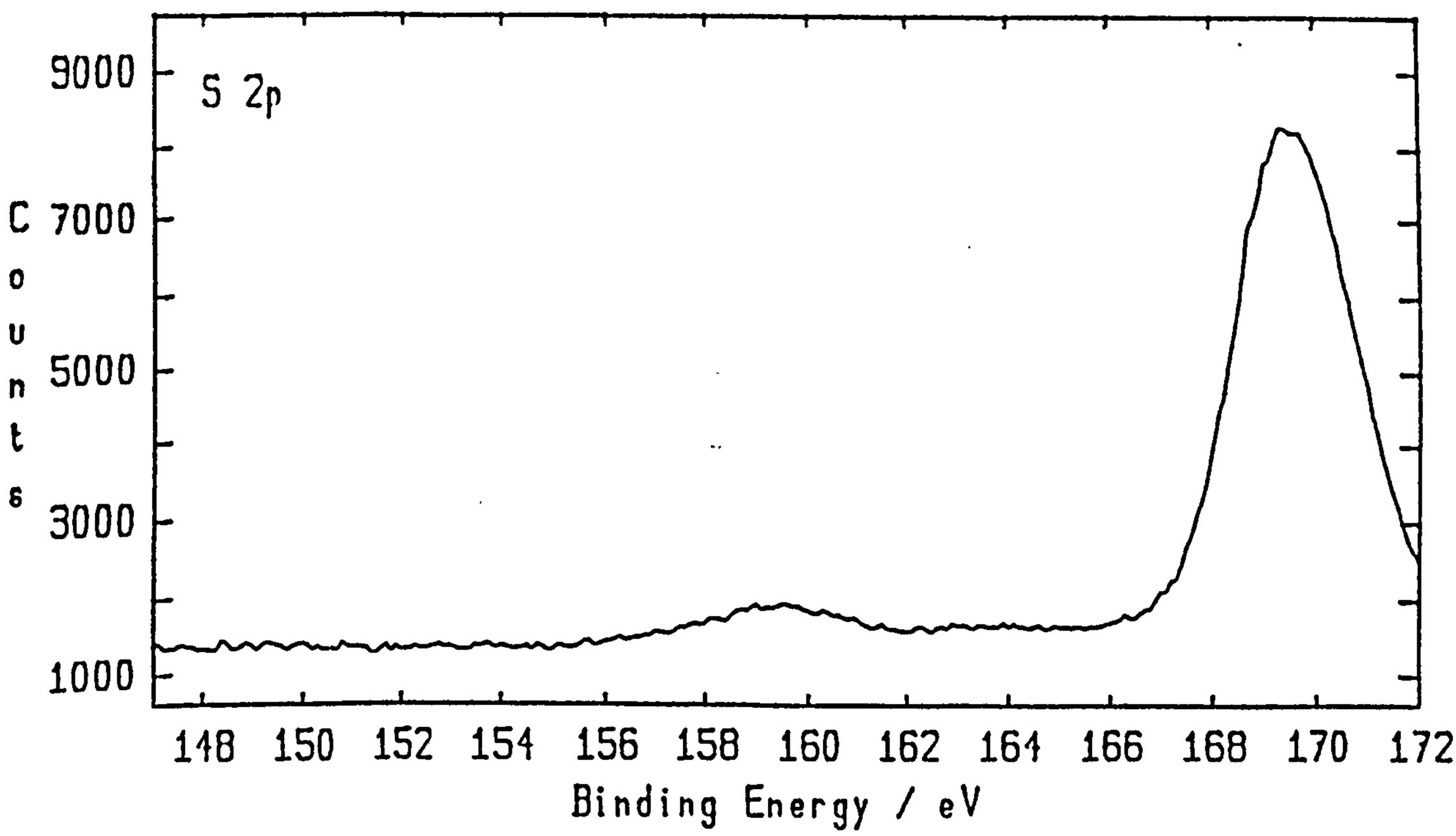

Figure 8.28. XPS spectrum of 99.5% pure $MgSO_4.7H_2O$, showing the S_{2s} peak.

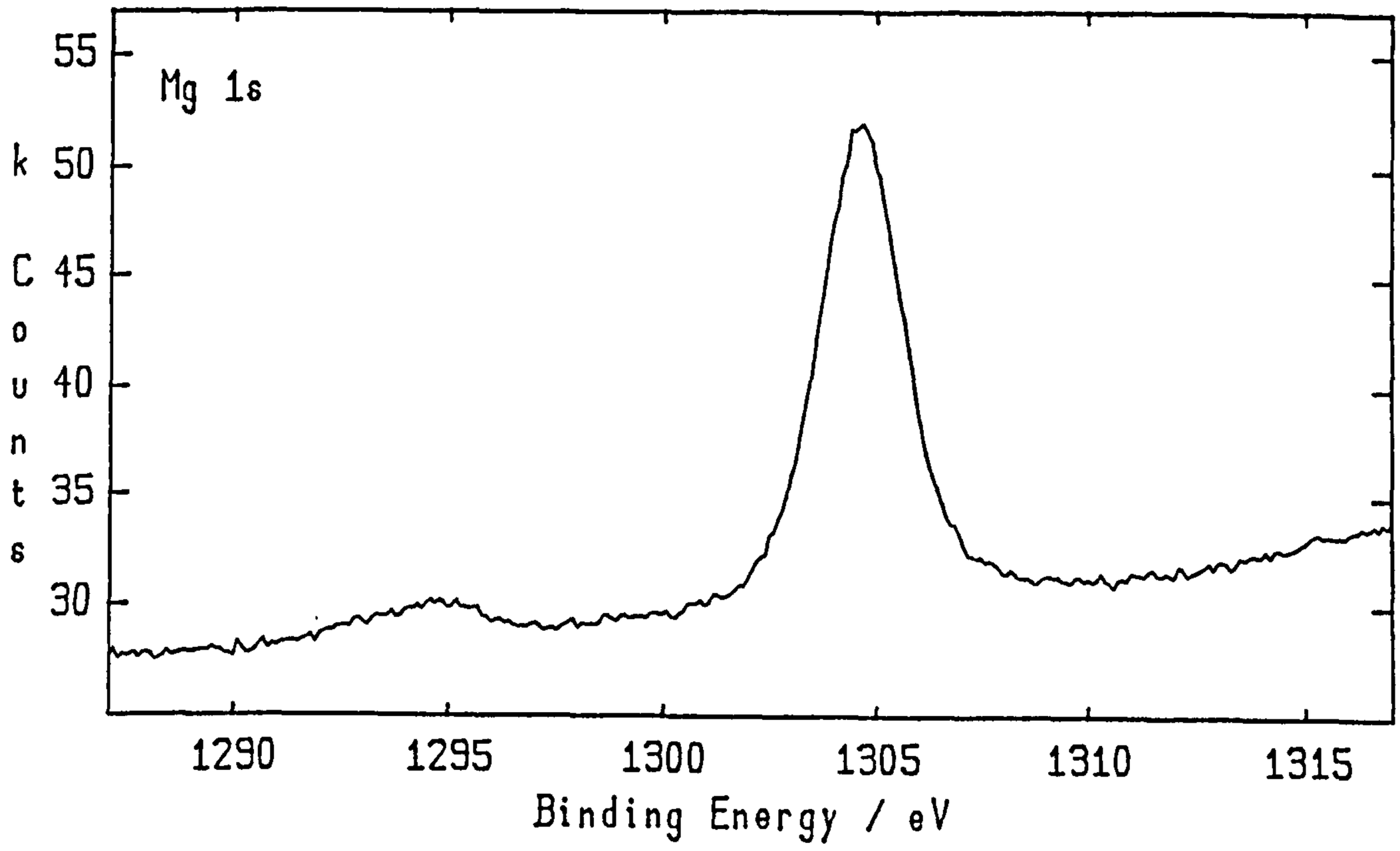

(a)

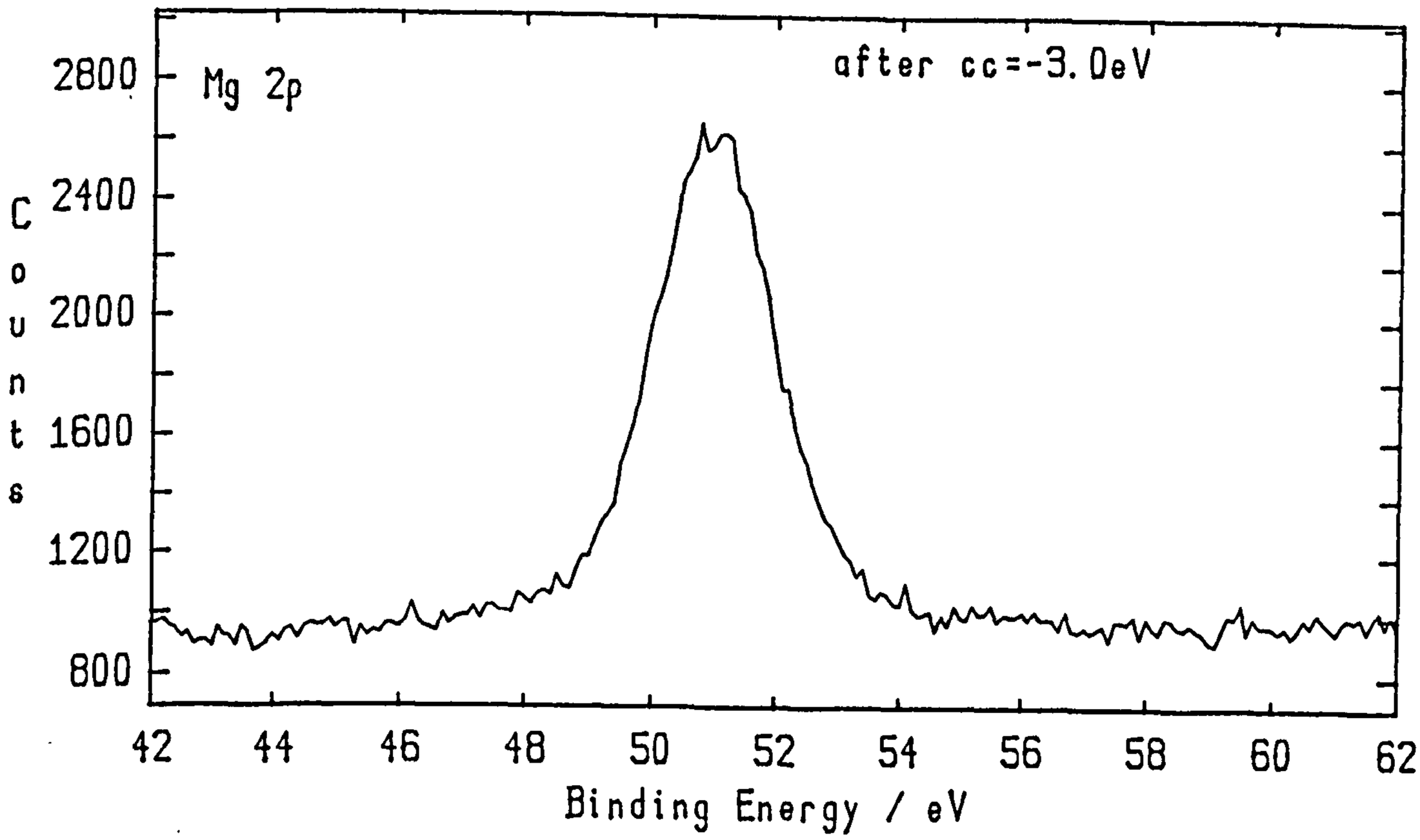

(b)

Figure 8.29 (a) and (b) XPS spectra of 99.5% pure $MgSO_4.7H_2O$.

(a) Mg_{1s} peak. (b) Mg_{2p} peak.

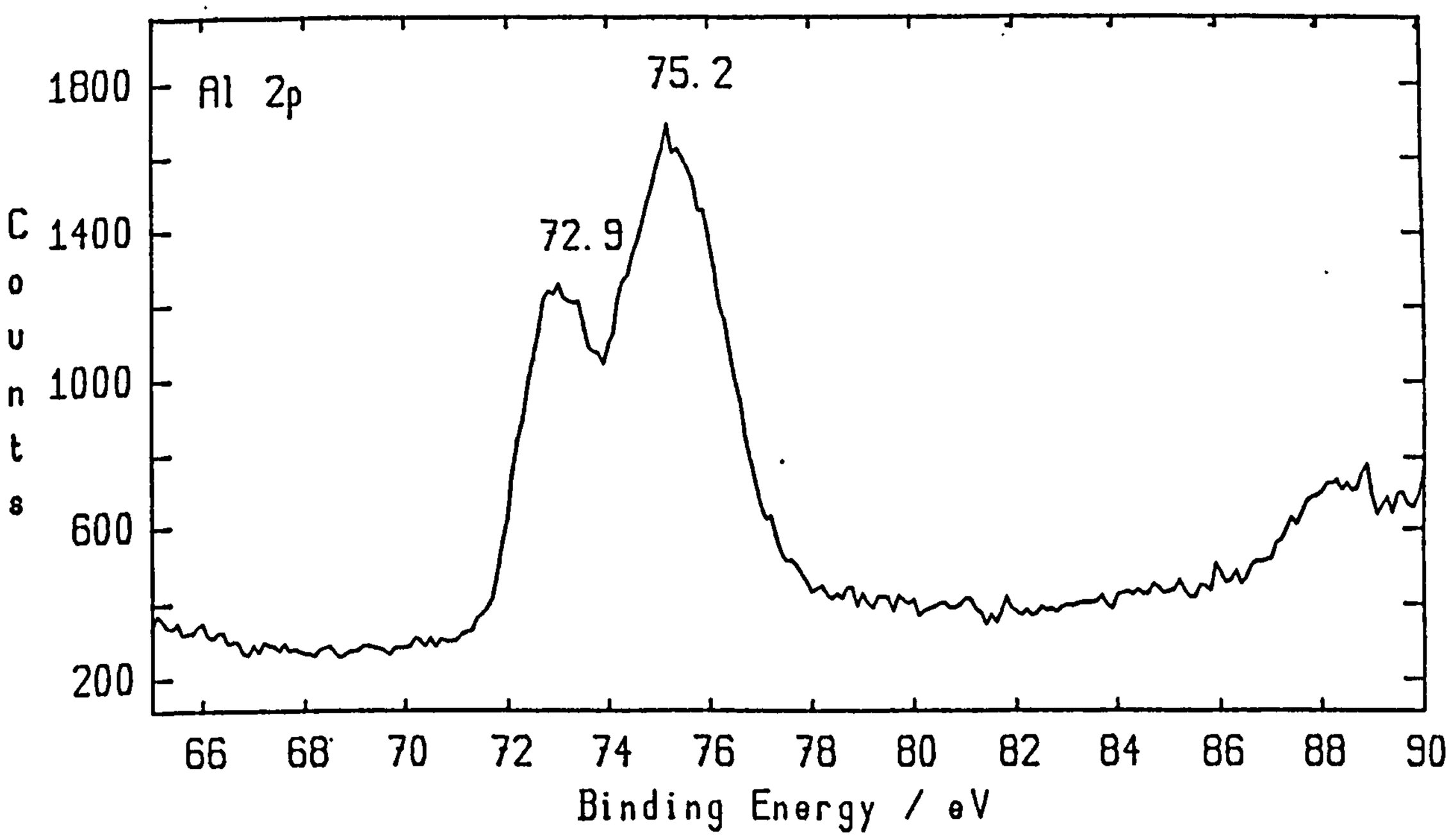

Figure 8.30 . XPS spectrum from surface of reference sample - not heat-treated. Al_{2p} peaks corresponding to metallic aluminium (72.9 eV) and Al_2O_3 (75.2).

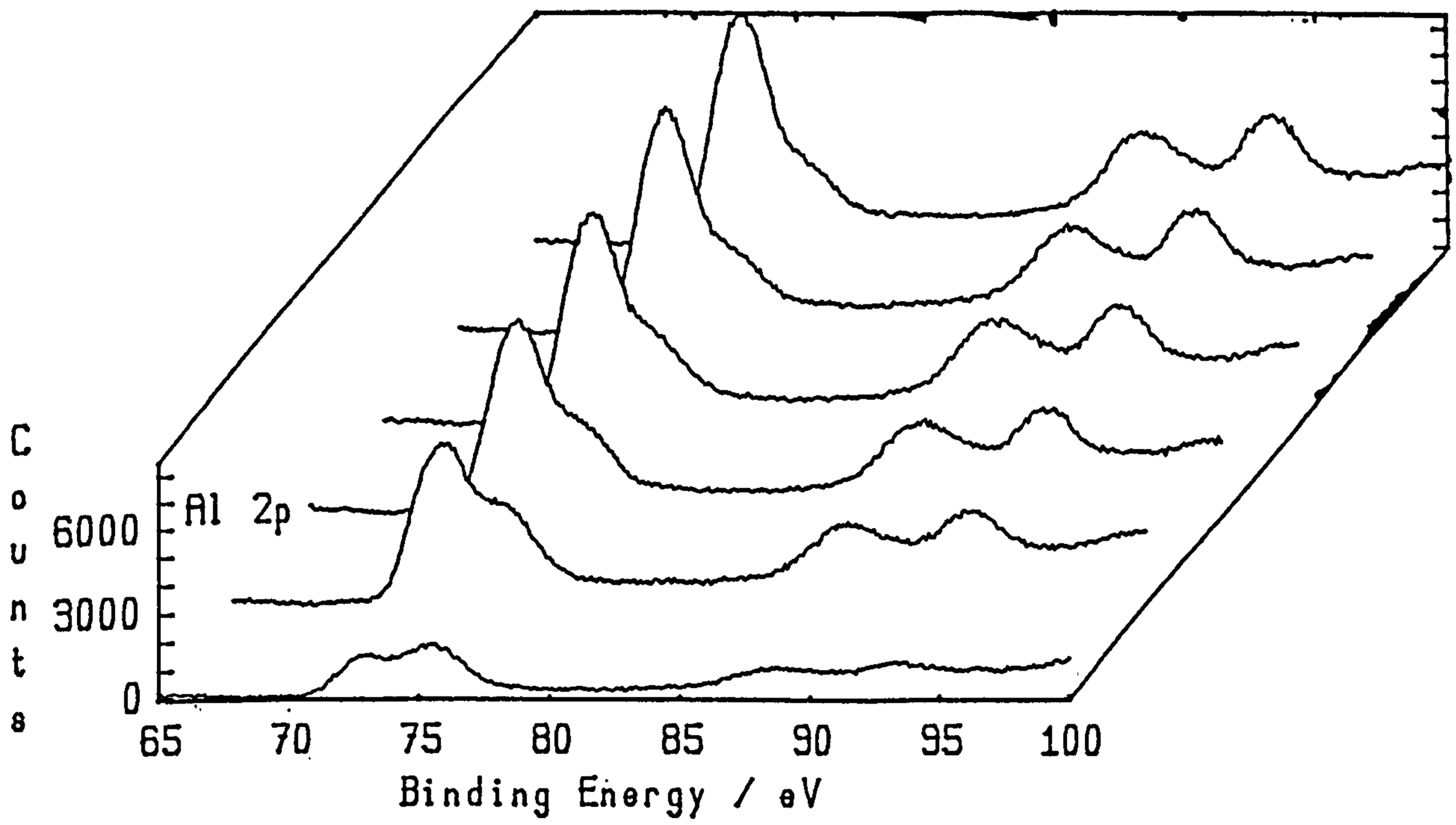

Figure 8.31 XPS depth profile montage from reference sample - not heat-treated.

Al_{2p} peaks corresponding to metallic Al (72.9 eV) and Al_2O_3 (75.2 eV). The two peaks at 88 and 93 eV are energy loss artefacts and have no significance. The metallic Al signal increases as material is removed by the ion beam etching .

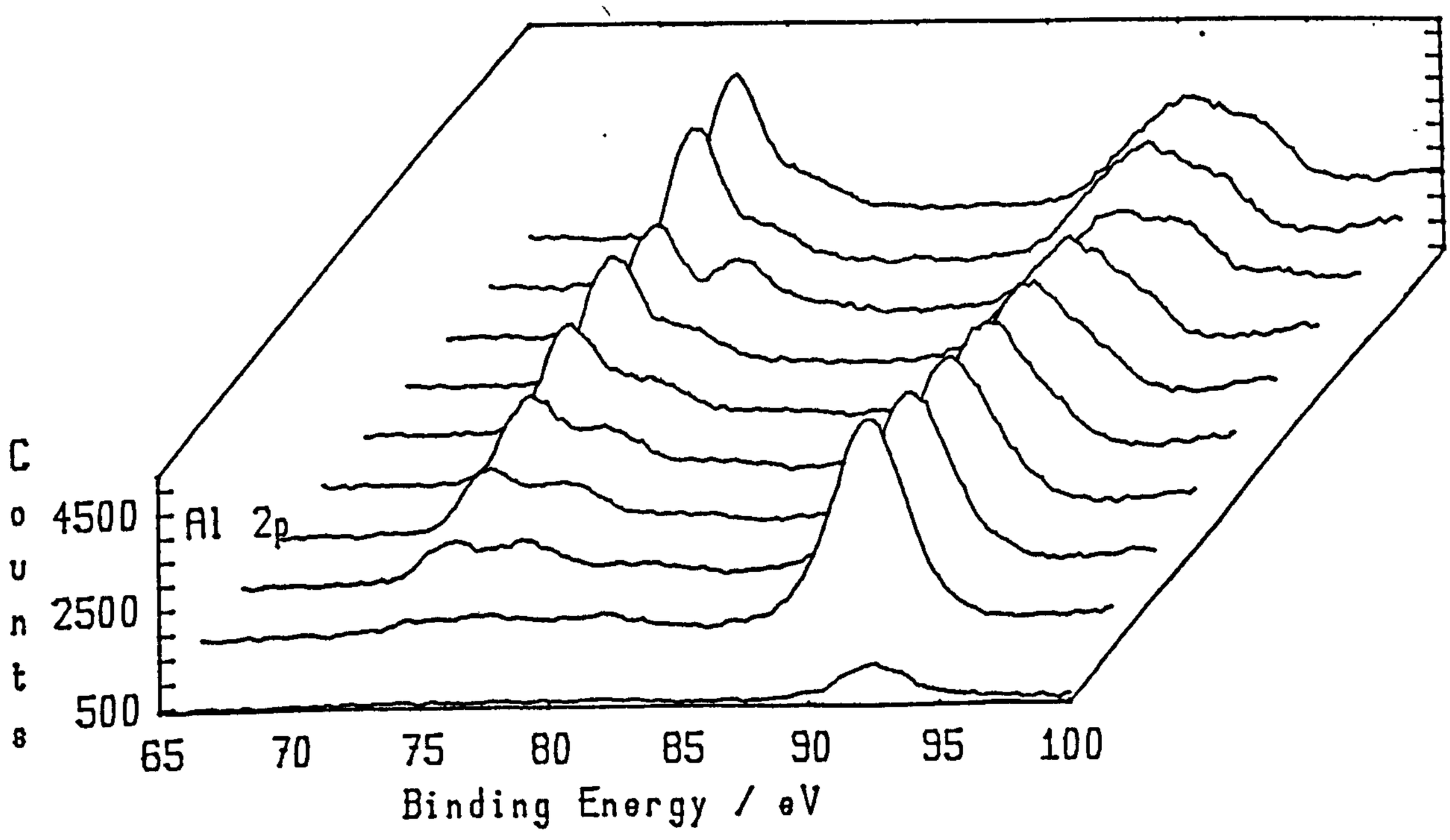

Figure 8.32. XPS depth profile montage of sample heated 4 h in dry air at 590 °C.

Al_{2p} peaks corresponding with metallic Al (72.9 eV) and Al_2O_3 (75.2 eV)

Mg_{2s} peak corresponding with MgO (90.3 eV).

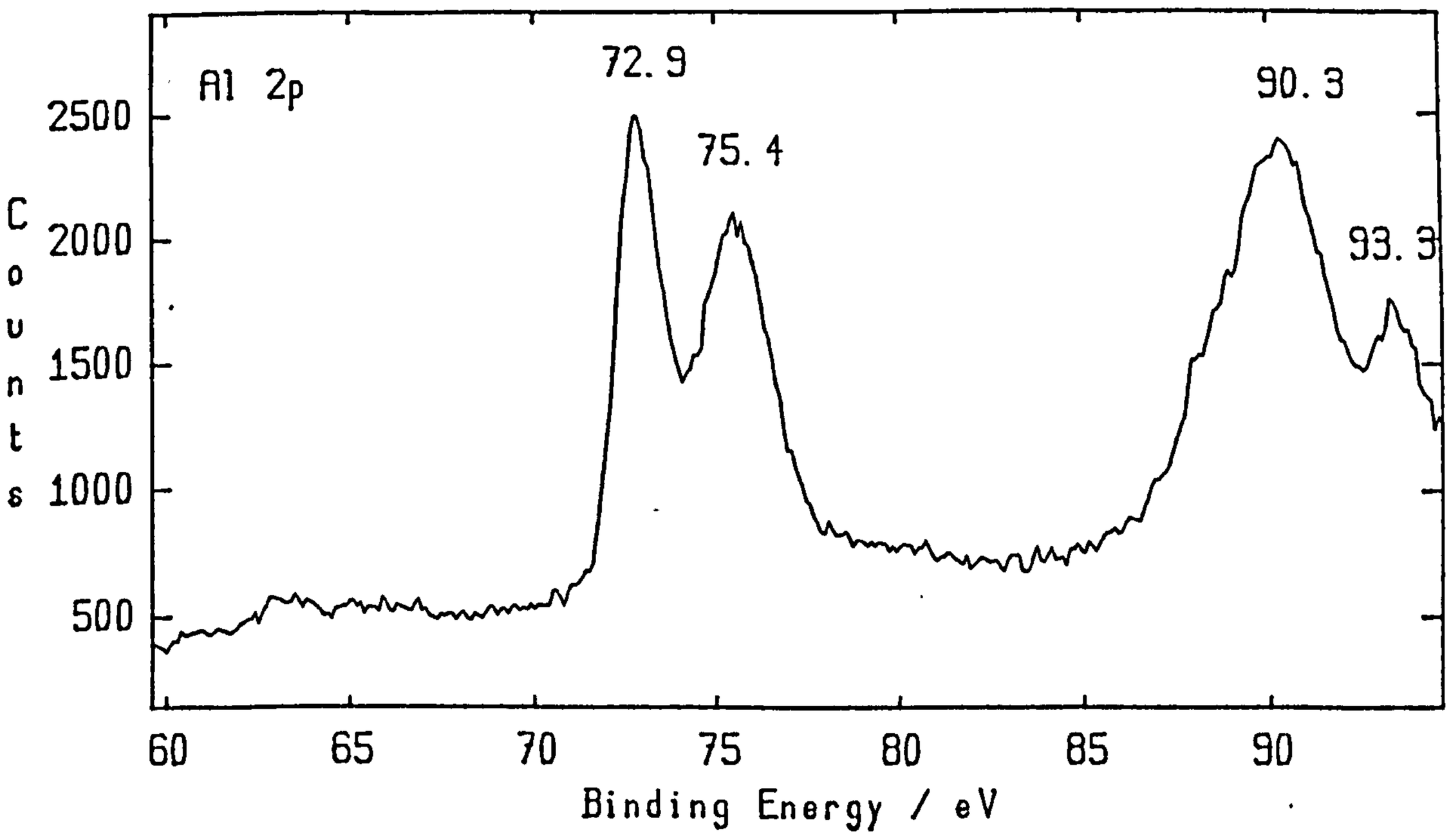

Figure 8.33. XPS spectrum corresponding to the 5th profile from the bottom of the depth profile montage in Figure 8.32.

Al_{2p} peaks corresponding with metallic Al (72.9 eV) and Al_2O_3 (75.4 eV).

Mg_{2s} peak corresponding with MgO (90.3 eV).

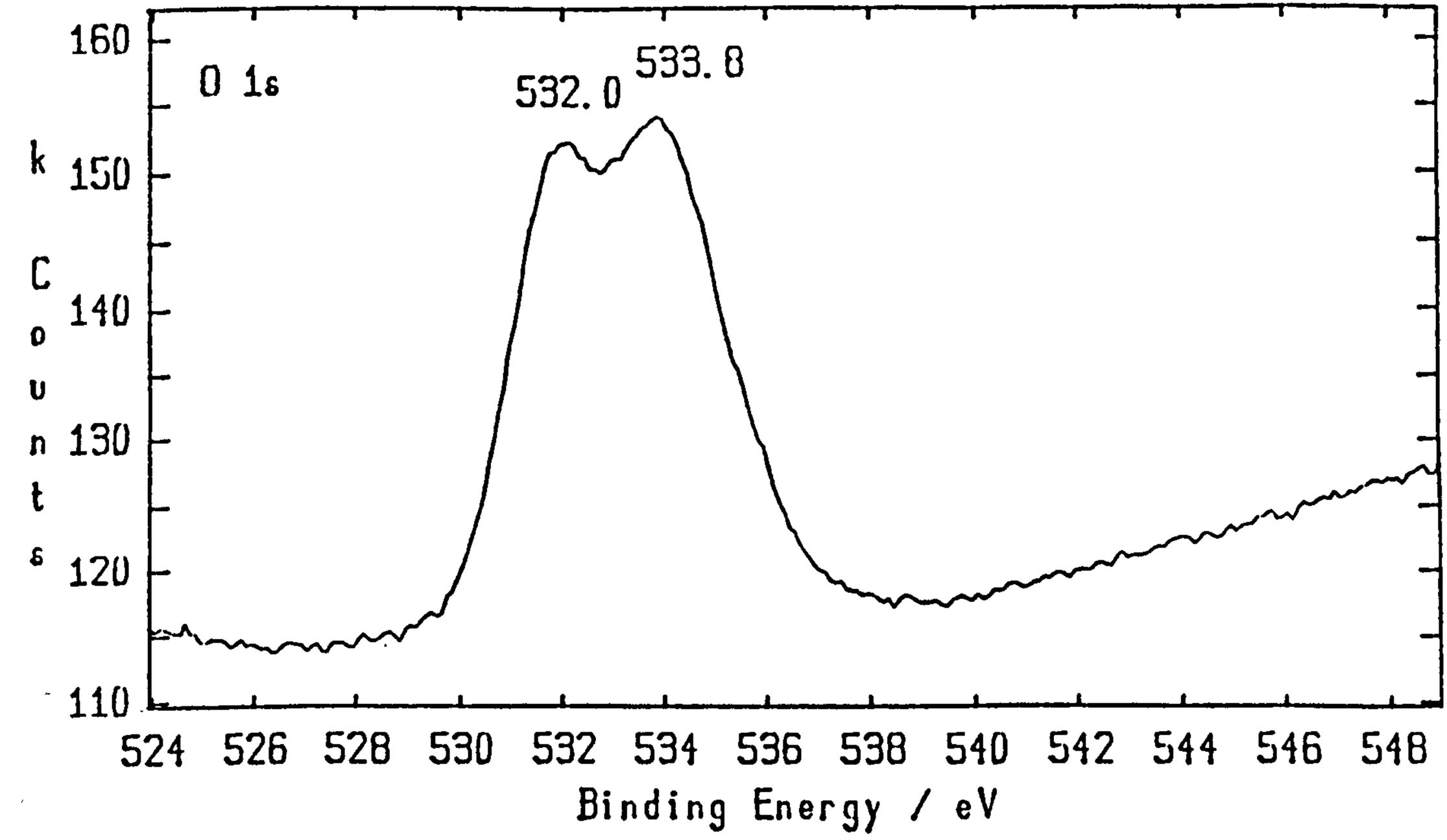

(a)

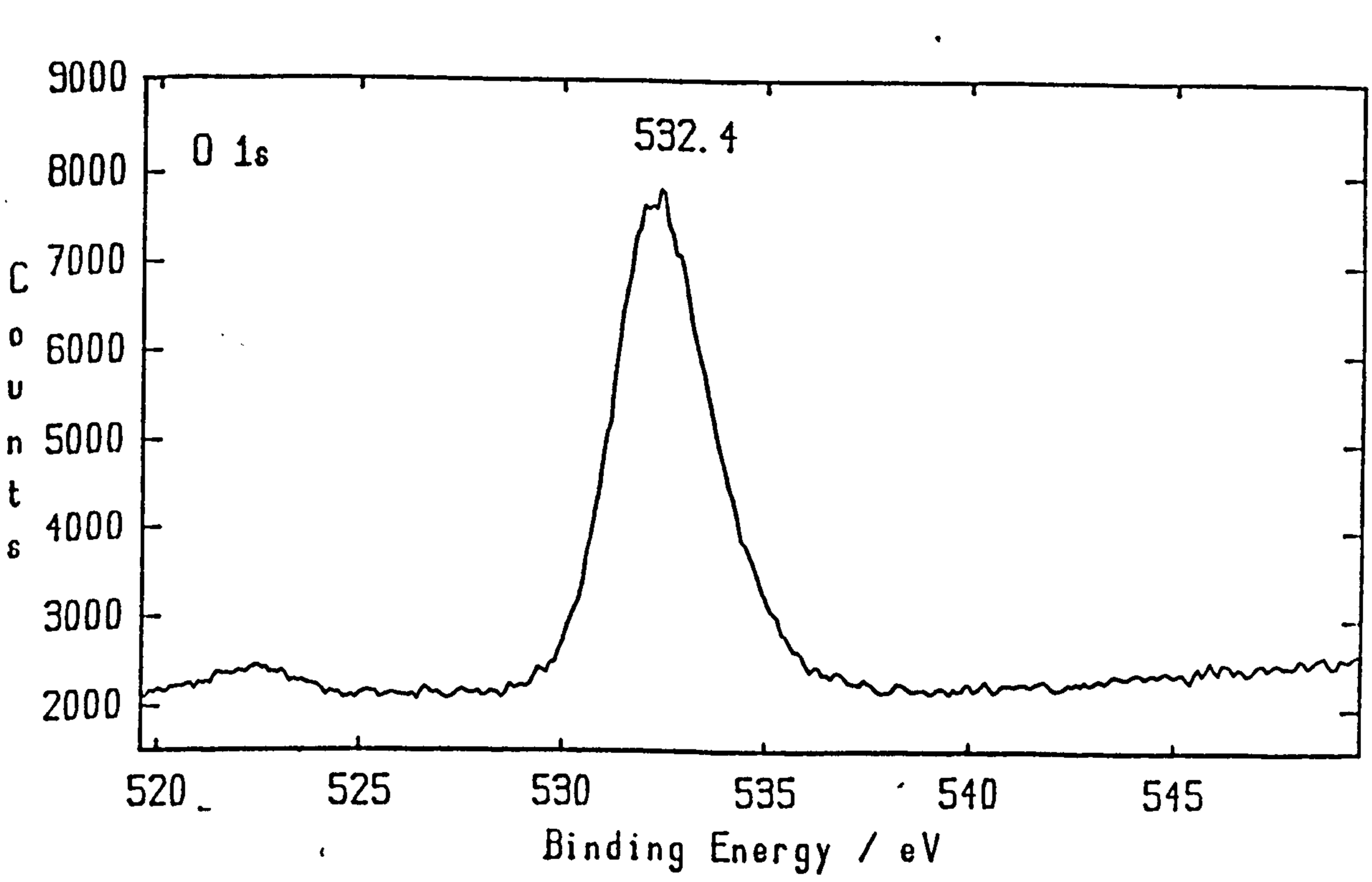

(b)

Figure 8.34 XPS spectra from sample heated 4 h in dry air at 590 °C.

(a) O_{1s} peak for MgO (532.0 eV) & OH (533.8 eV) at the oxide/air interface.

(b) O_{1s} peak for MgO (532.4 eV) inside the oxide film.

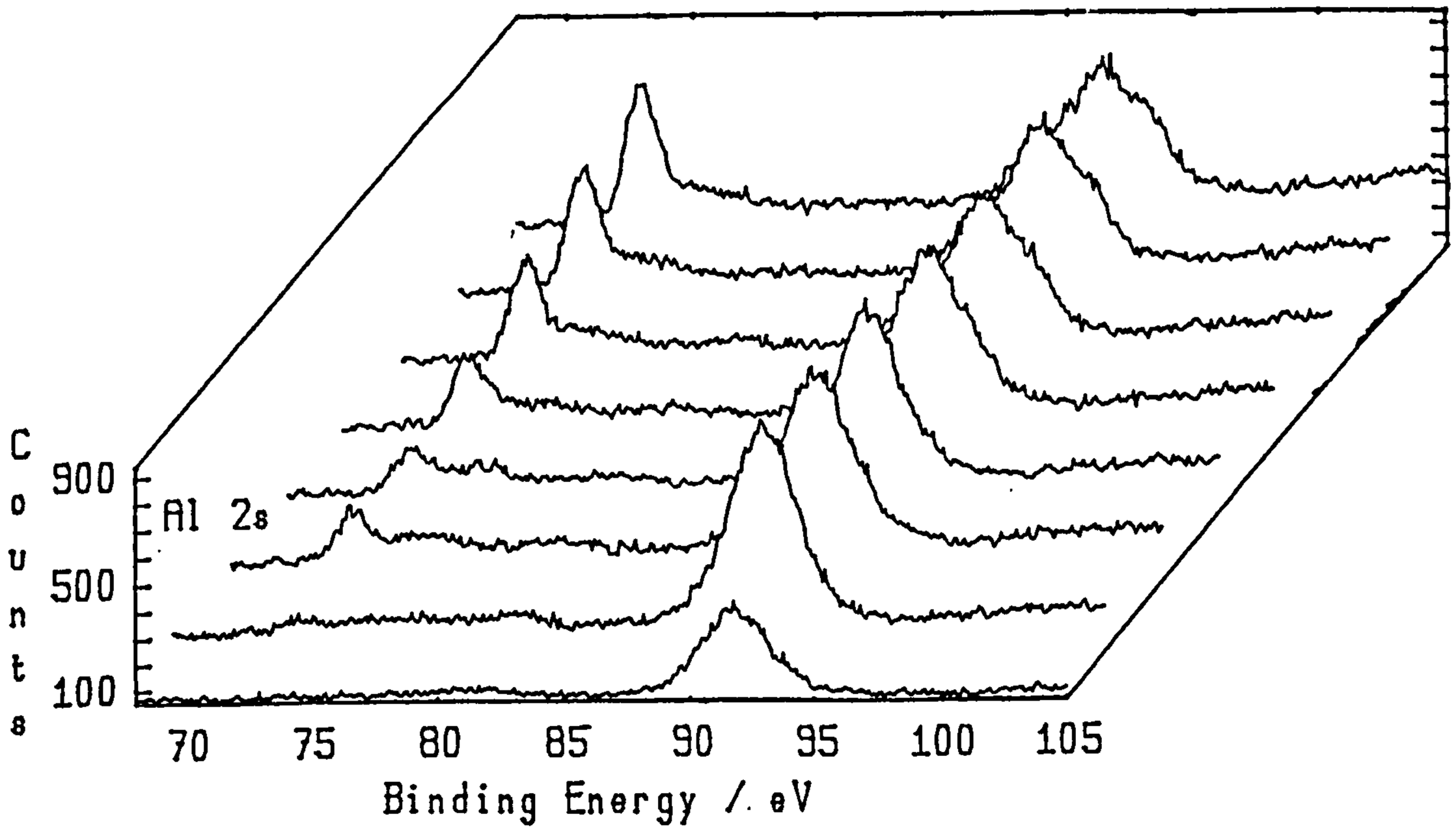

(a)

Figure 8.35 a, b & c. Extended XPS depth profile montage from sample heated 4 h in water-saturated air at 590 °C. (continued on next page).

Al_{2p} peaks, corresponding with metallic Al (72.9 eV) and Al_2O_3 (75.5 eV). No aluminium peaks are recorded at the air/oxide interface. At greater depths the peak for metallic Al becomes dominant.

Mg_{2s} peak, corresponding with MgO (90.2 eV).
The magnesium peak broadens at greater depths, suggesting a change in chemical state, e.g. transformation to $MgAl_2O_4$.

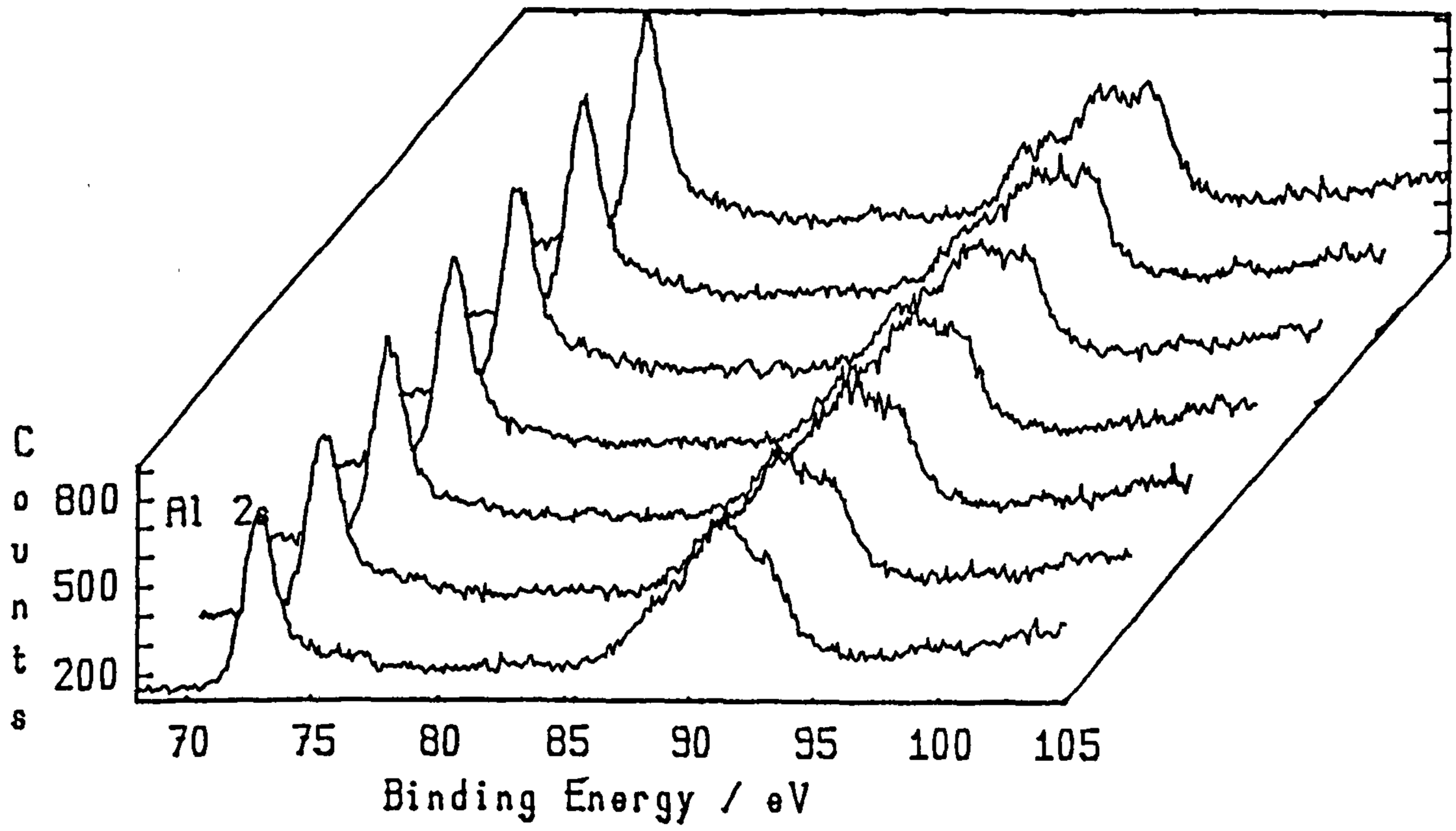

(b) *continued from* (a)

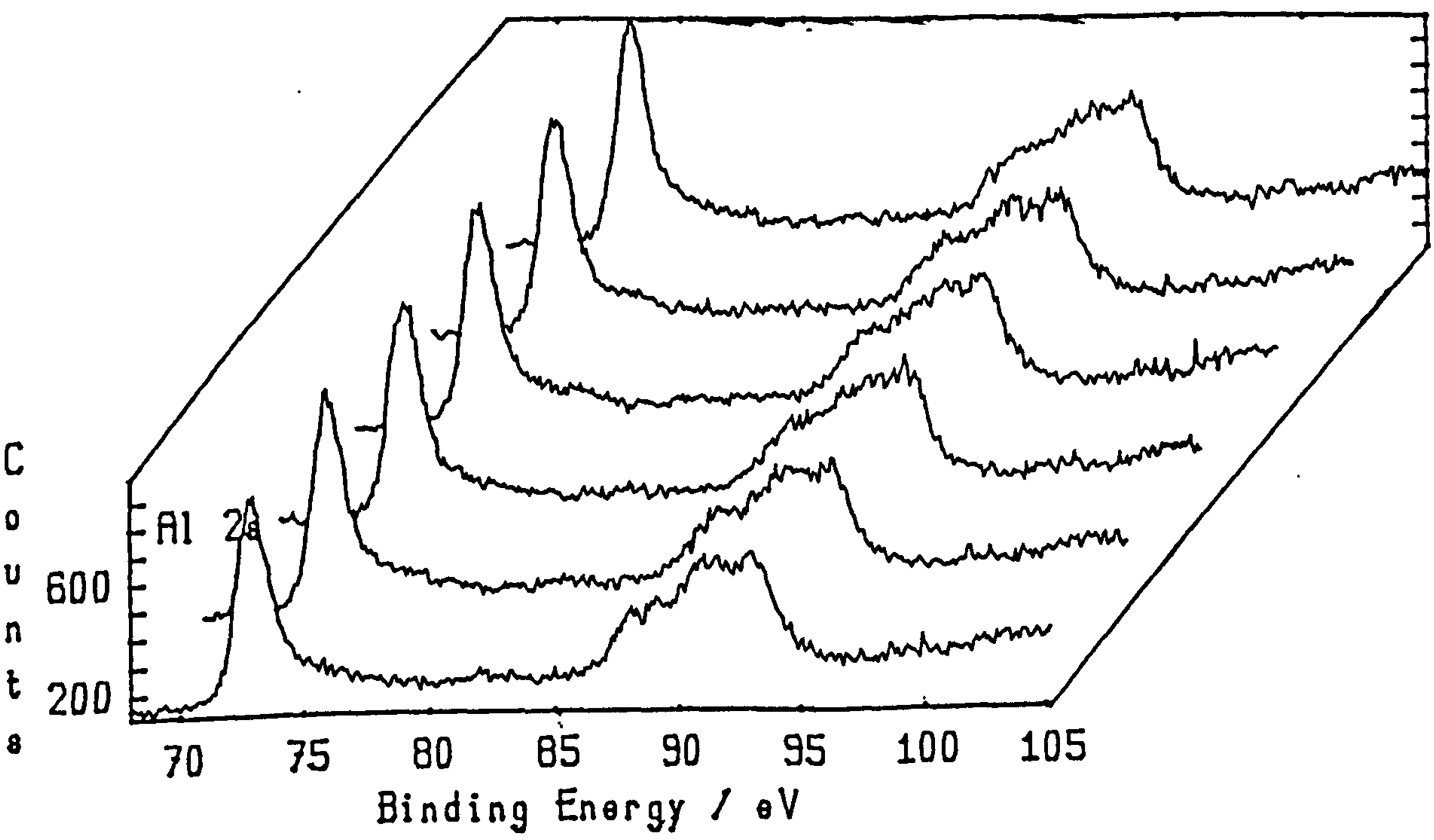

(c) *continued from* (b)

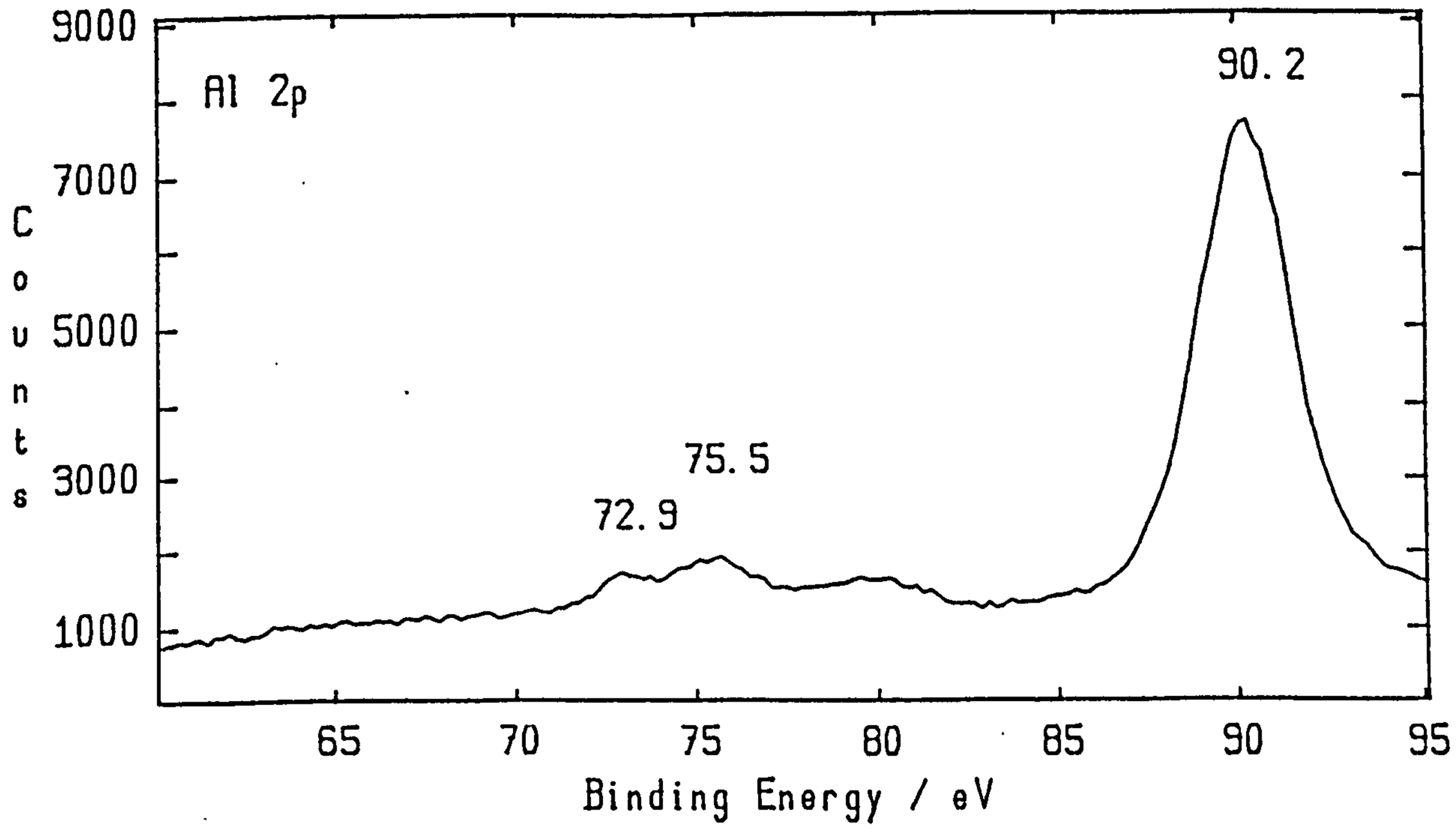

(a)

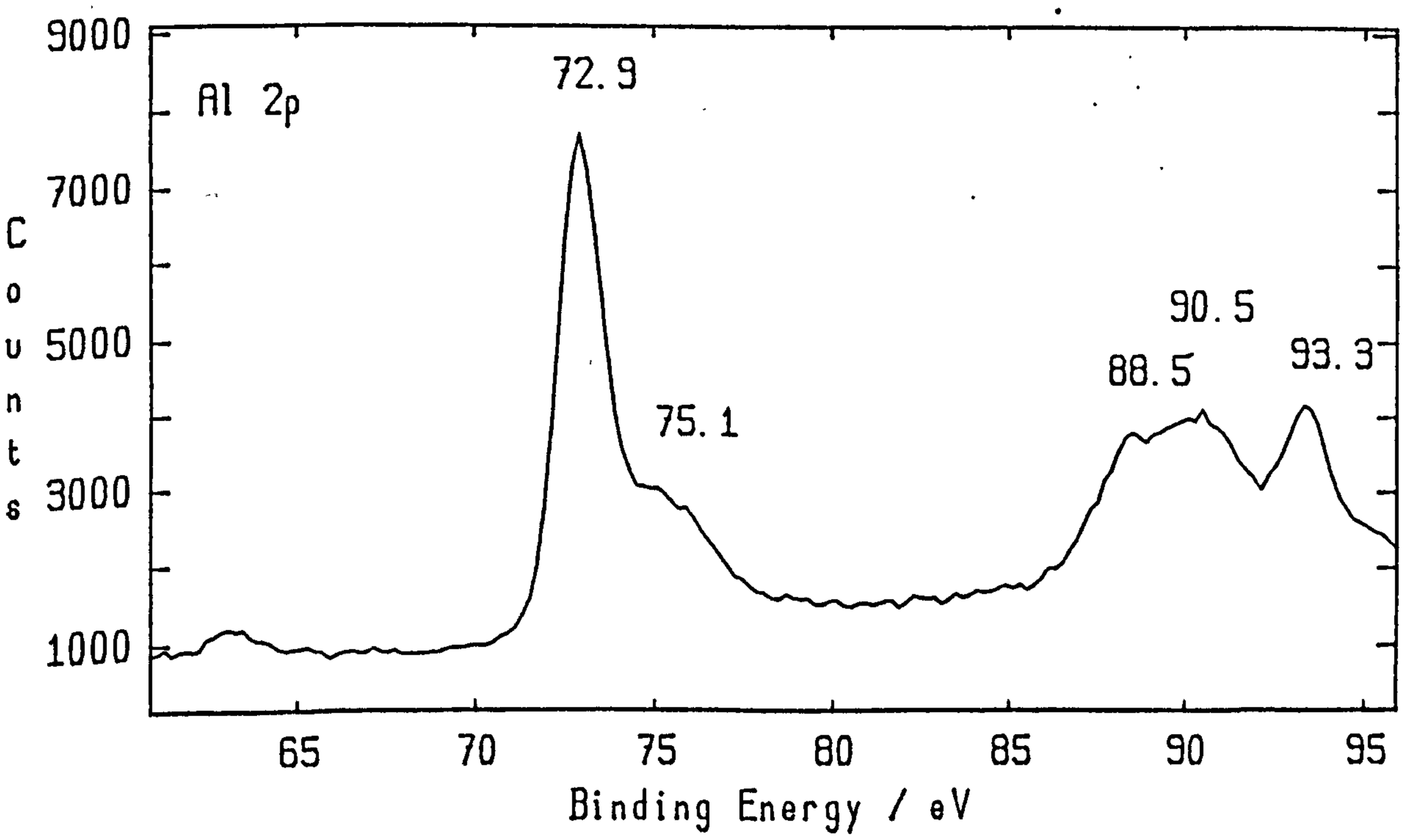

(b)

Figure 8.36. XPS spectra selected from the depth profile montage in Figure 8.35.

(a) Near surface - 4th profile from the bottom of the montage in Figure 8.35 (a).

(b) Inside the oxide - 5th profile from montage in Figure 8.35 (c).

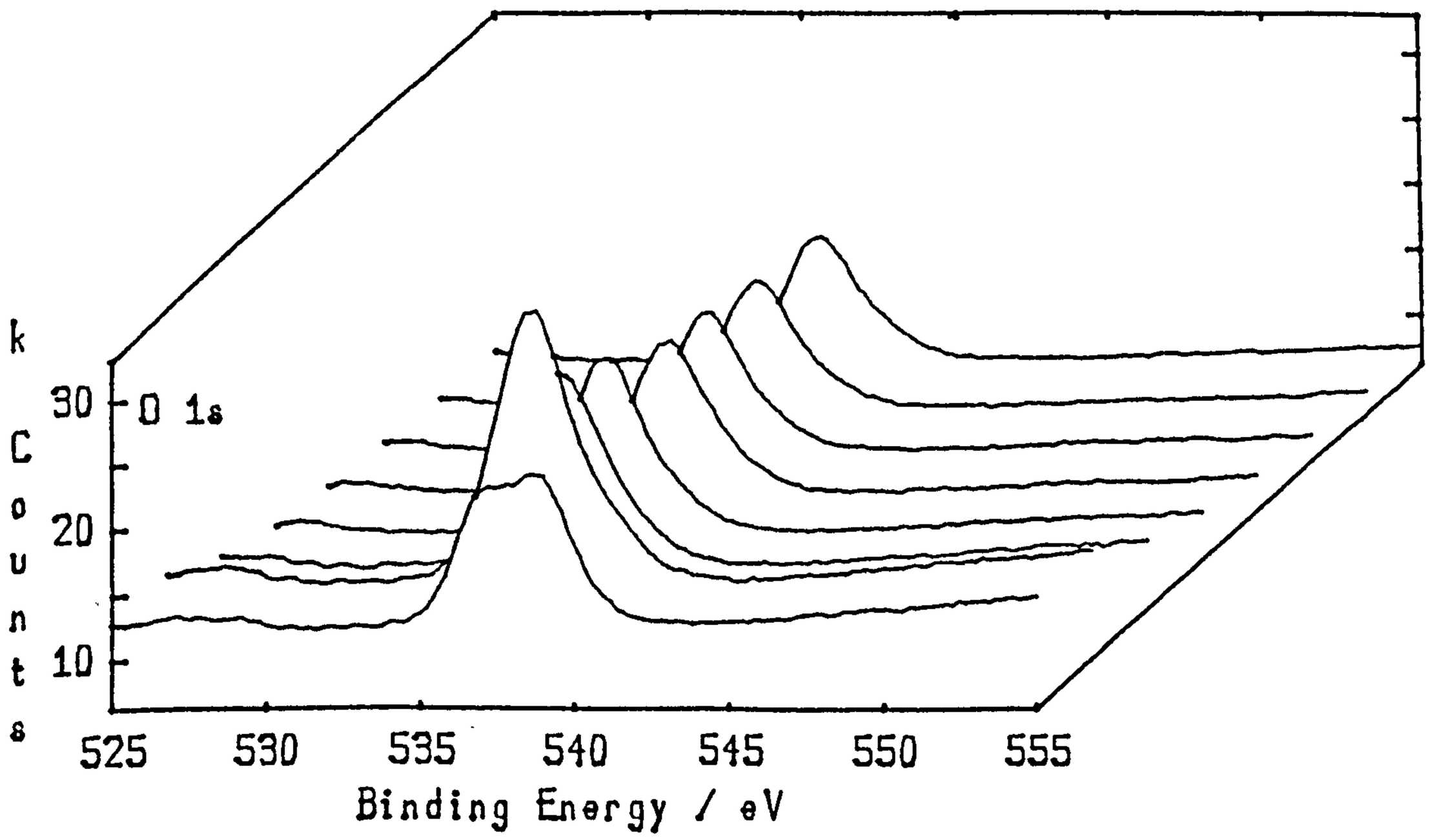

Figure 8.37. XPS depth profile montage from sample heated 4 h in water-saturated air at 590 °C.

O_{1s} peaks corresponding to MgO (532.5 eV) and OH (533.8 eV)

Note that the peak for OH is confined to the profile at the surface.

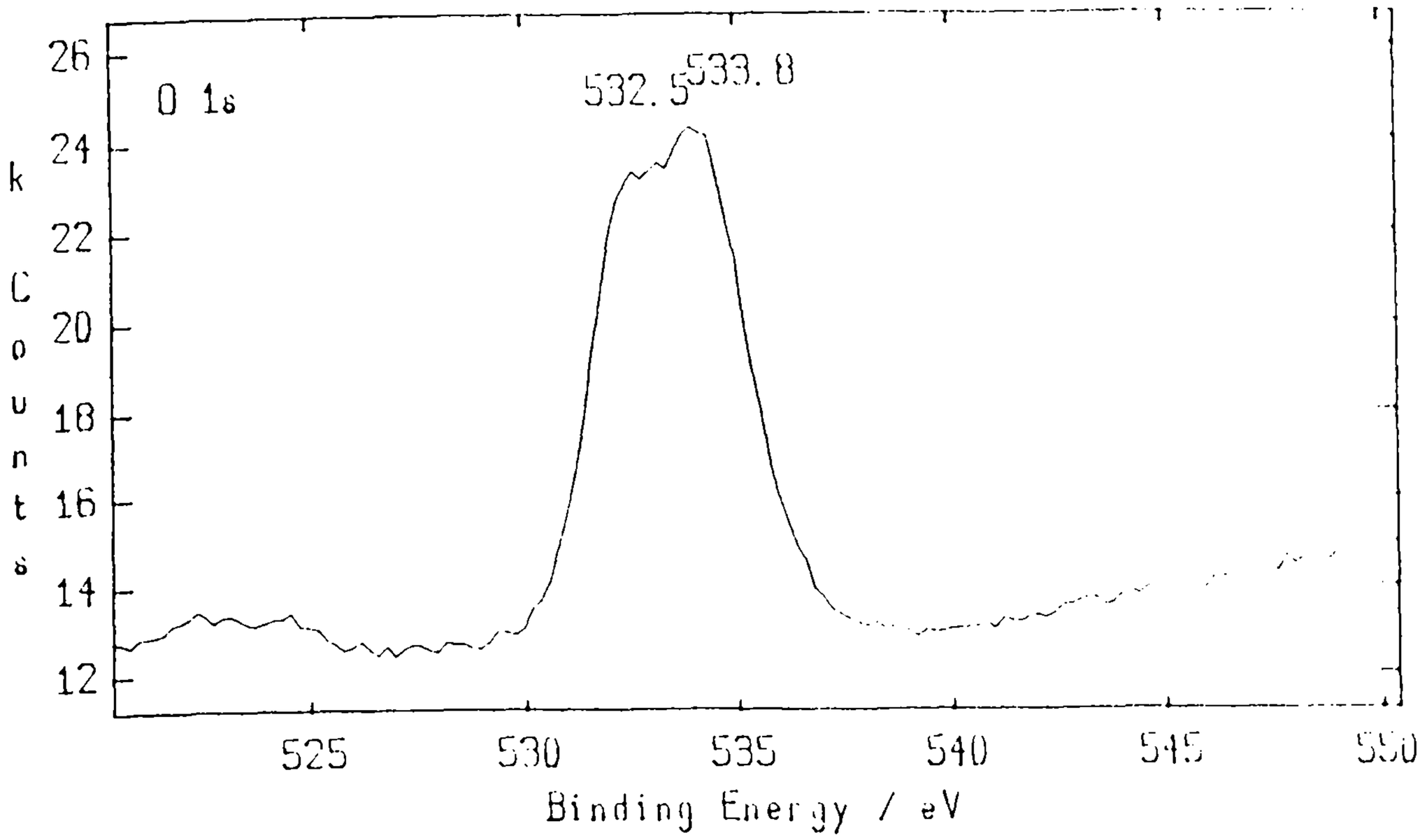

(a)

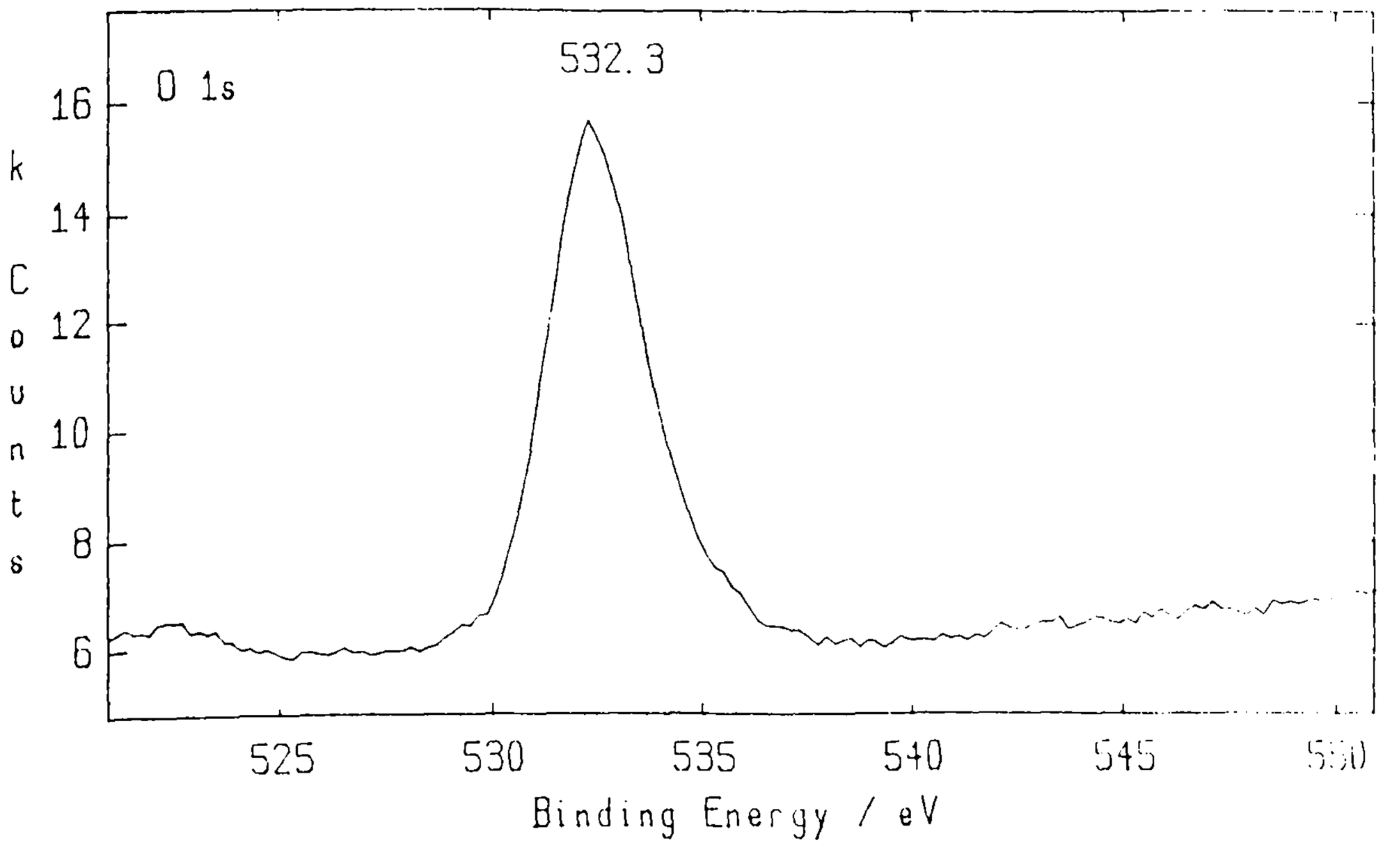

(b)

Figure 8.38. XPS spectra selected from the depth profile montage in Figure 8.37.

(a) O_{1s} peaks for MgO (532.5 eV) and hydroxyl (533.8) at the surface.

(b) O_{1s} peak for MgO (532.3 eV) inside the oxide film.

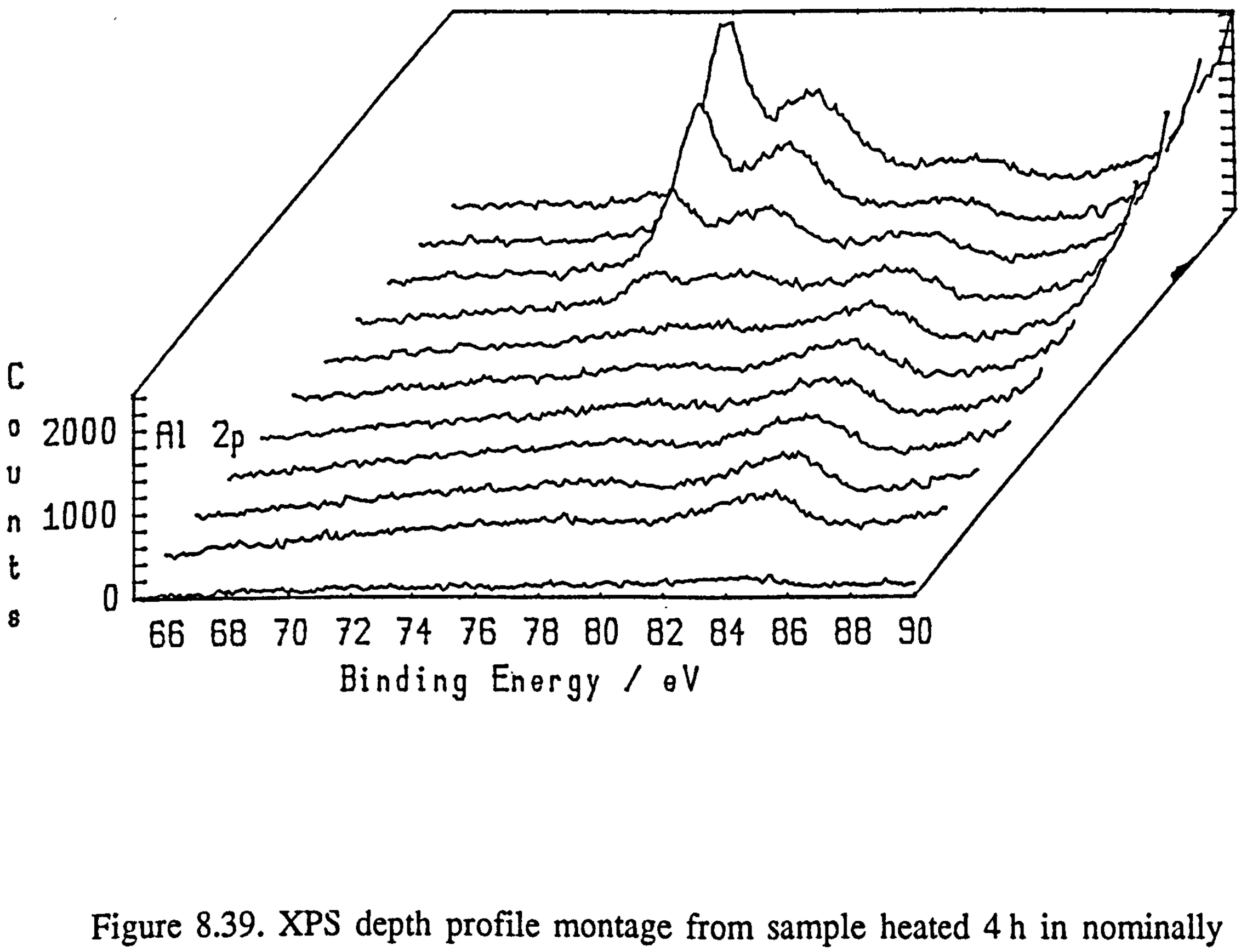

Figure 8.39. XPS depth profile montage from sample heated 4 h in nominally dry air + 1% SO_2 at 590 °C.

Al_{2p} peaks, corresponding to metallic Al (72.9 eV) and Al_2O_3 (75.7 eV). Note the complete absence of aluminium peaks in an extended surface zone.

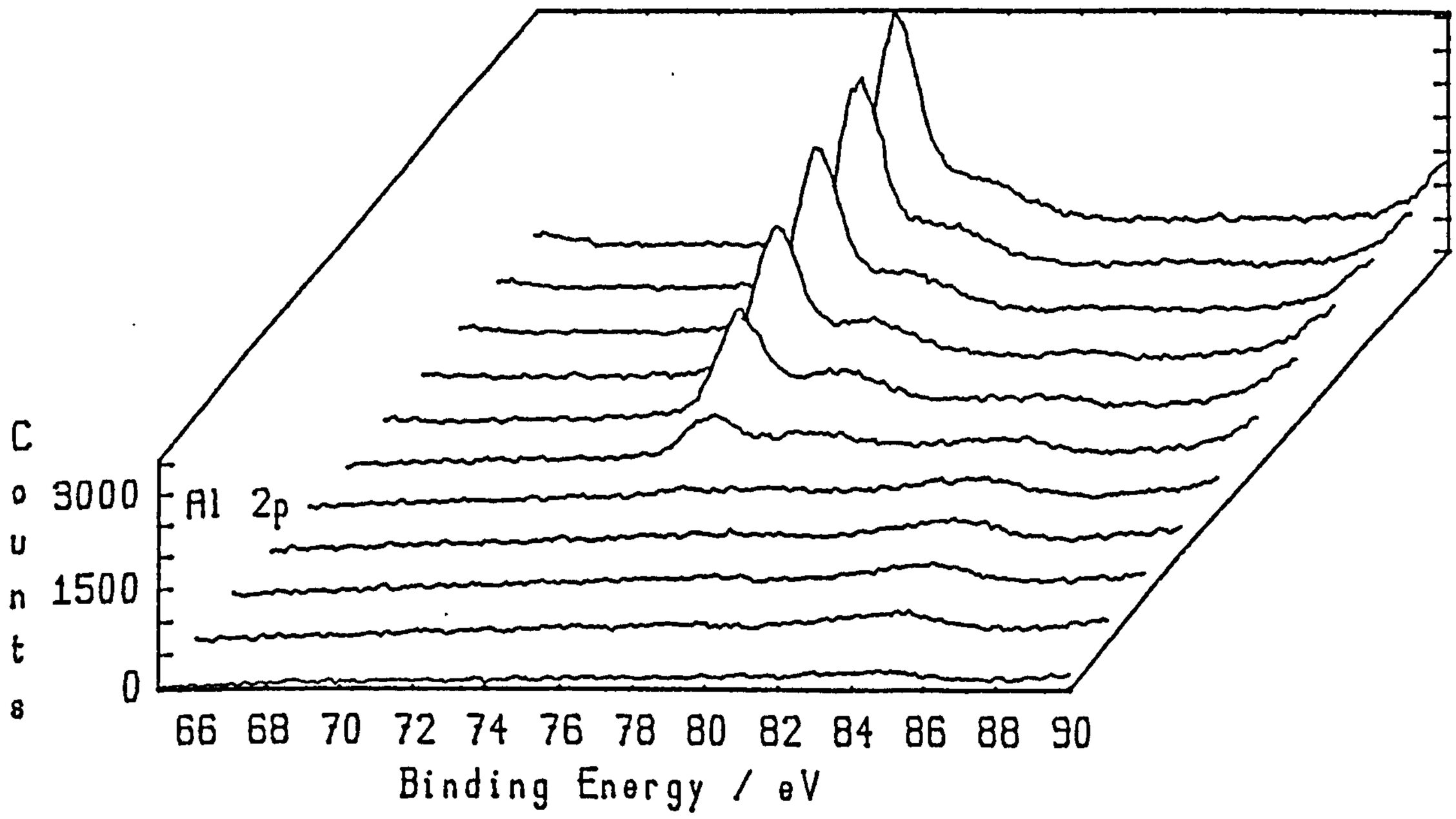

(a)

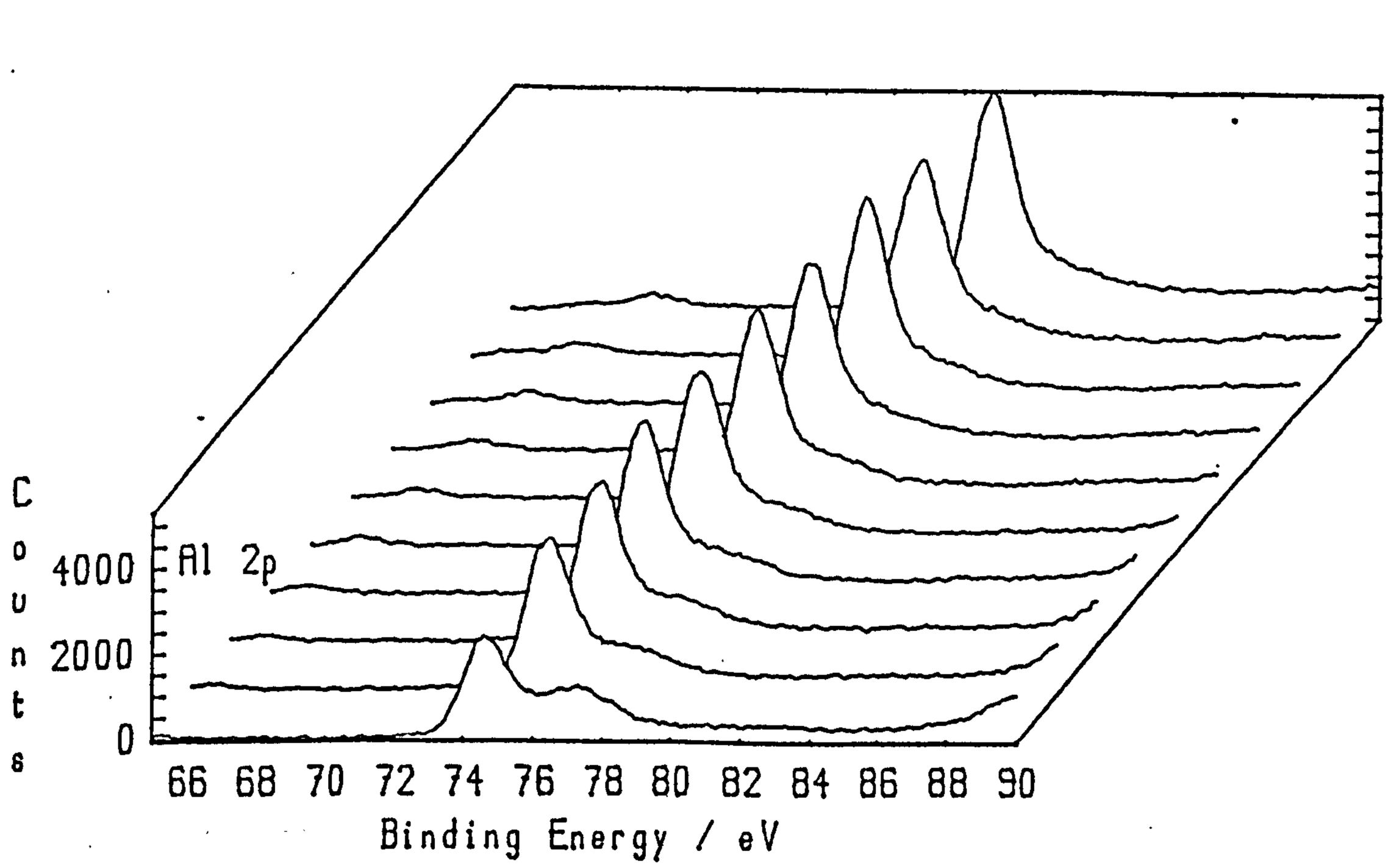

(b)

Figure 8.40. Extended XPS depth profile montage from sample heated 4 h in water-saturated air + 1% SO_2 at 590 °C.

Al_{2p} peaks, corresponding to metallic Al (72.9 eV) and Al_2O_3 (75.7 eV) Note the complete absence of aluminium peaks in an extended surface zone in (a).

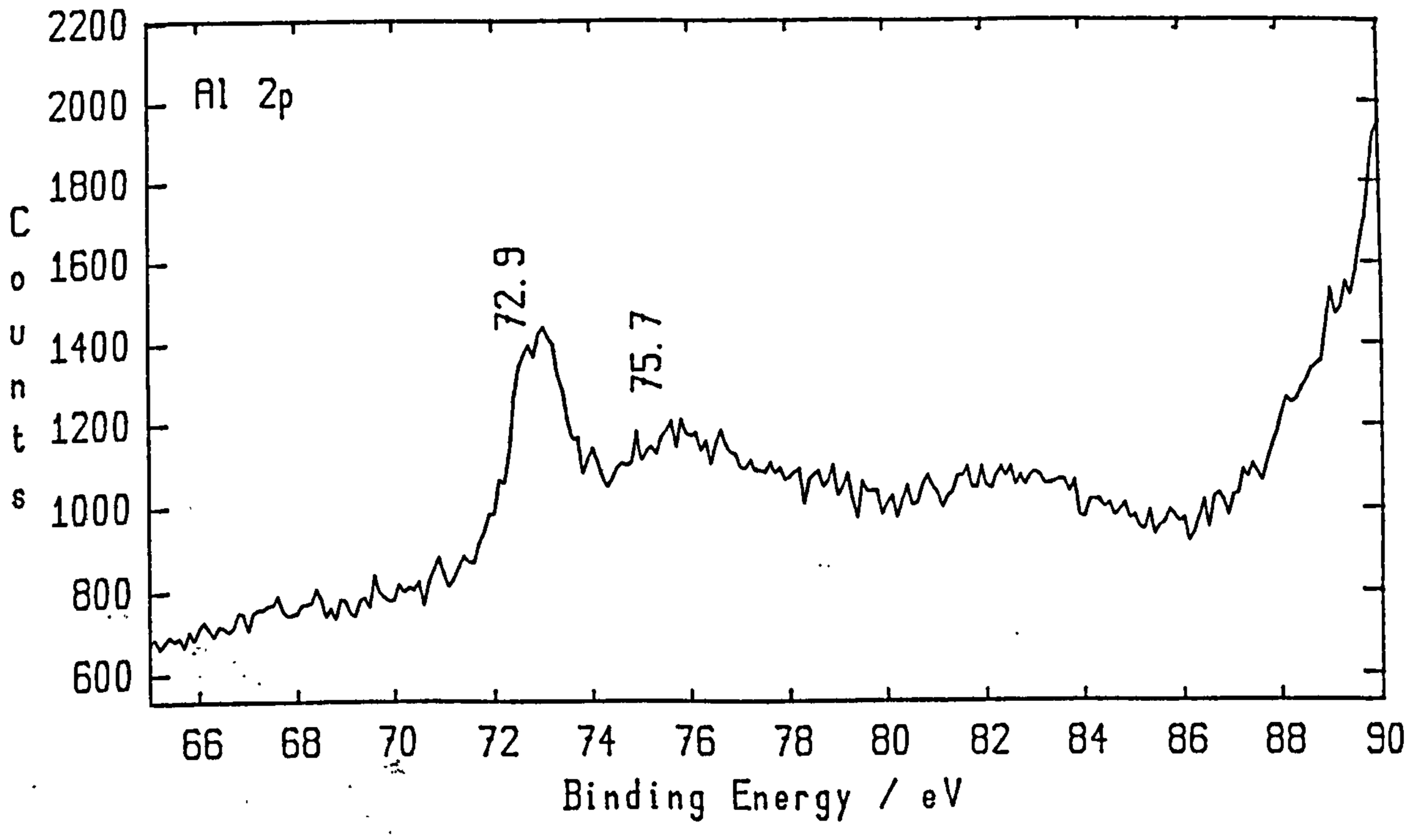

Figure 8.41. XPS spectra selected from the depth profile montage in Figure 8.40.

(a) Profile at the depth where the Al_{2p} peaks first appear - 6th profile from the bottom of the montage in Figure 8.40 (a).

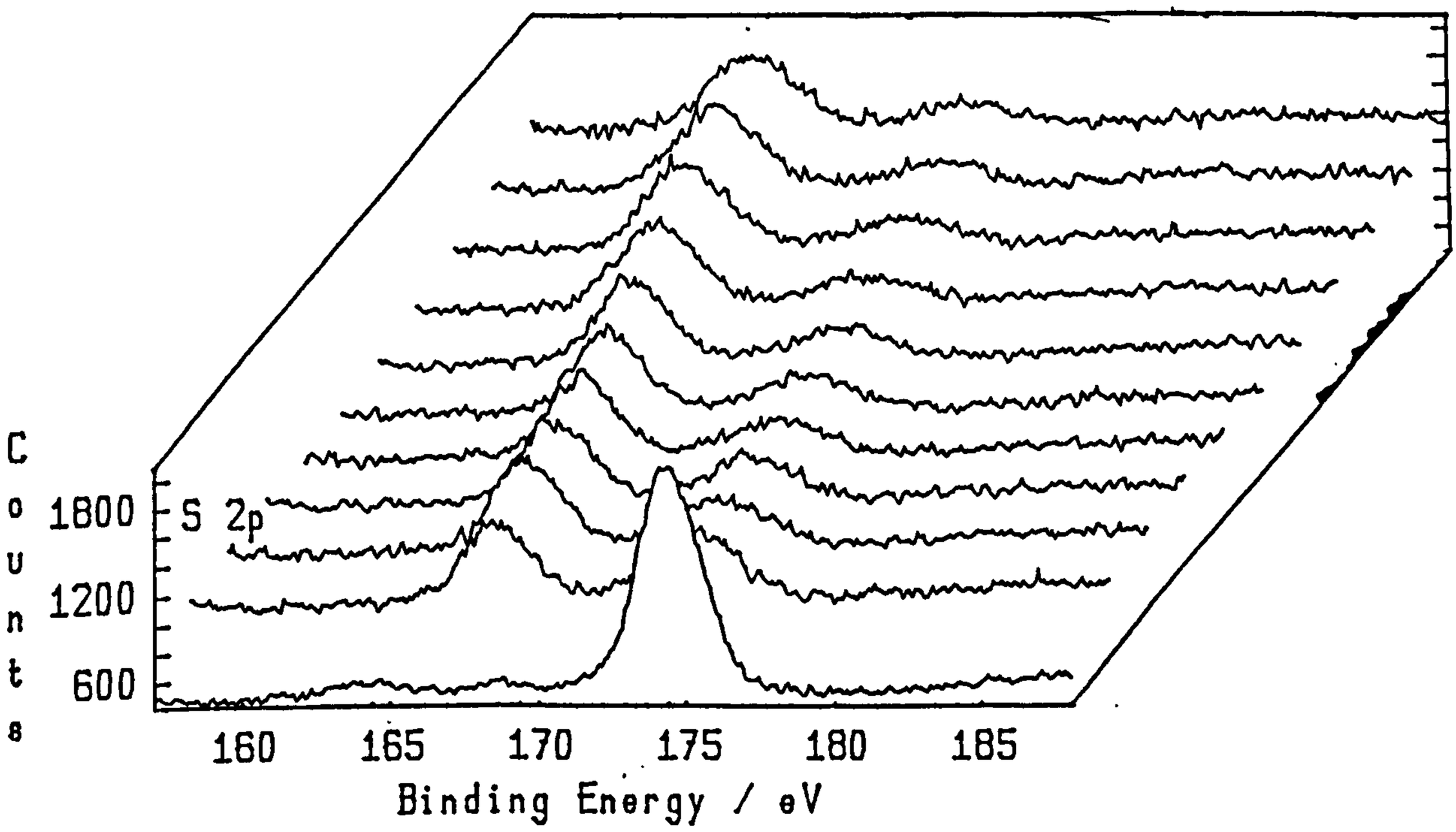

Figure 8.42. XPS depth profile montage from sample heated 4 h in nominally dry air + 1% SO_2 at 590 °C.

S_{2p} peaks for $MgSO_4$ (169.6 eV) and MgS (162.6 eV).

Note change in chemical state of sulphur immediately below the surface.

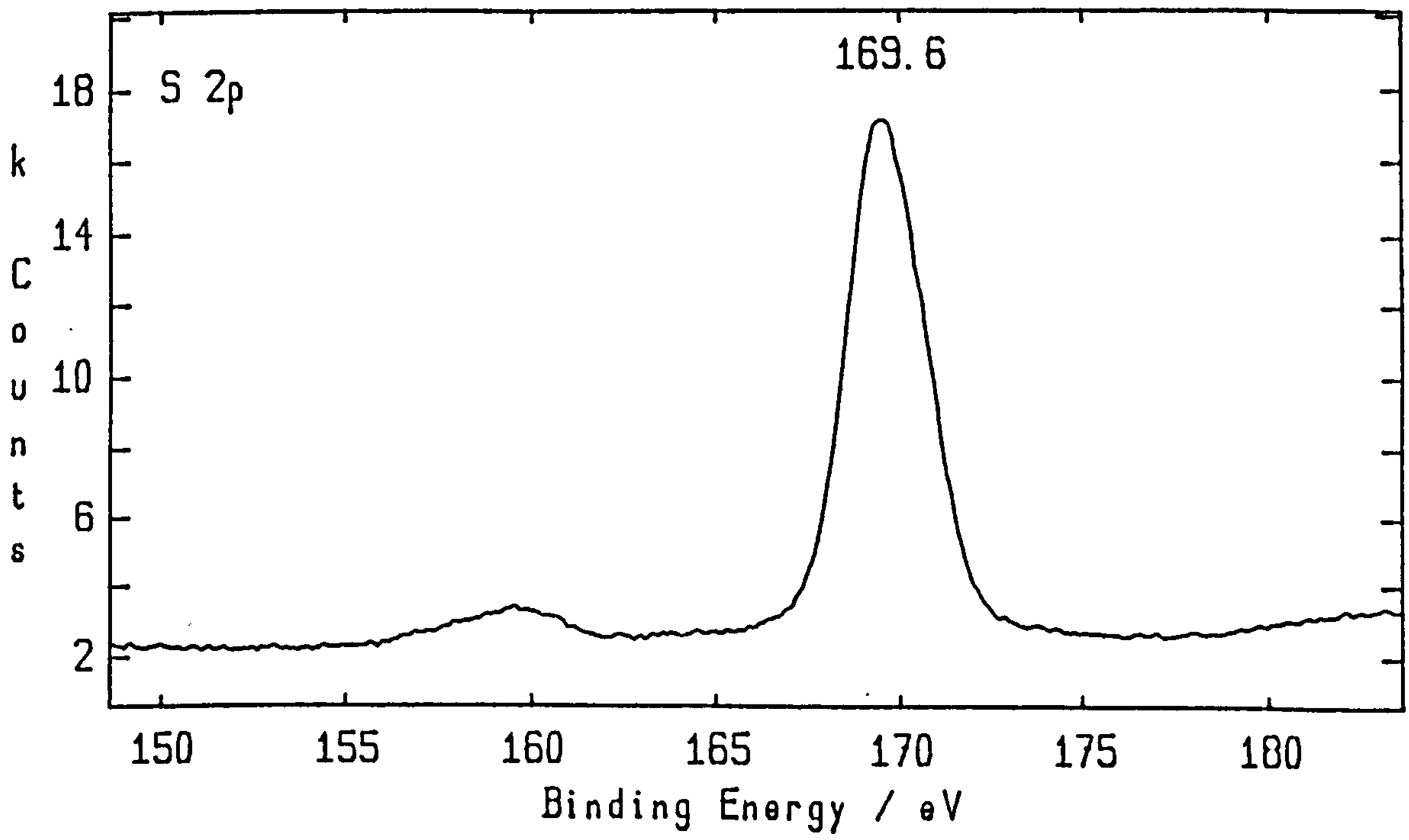

(a)

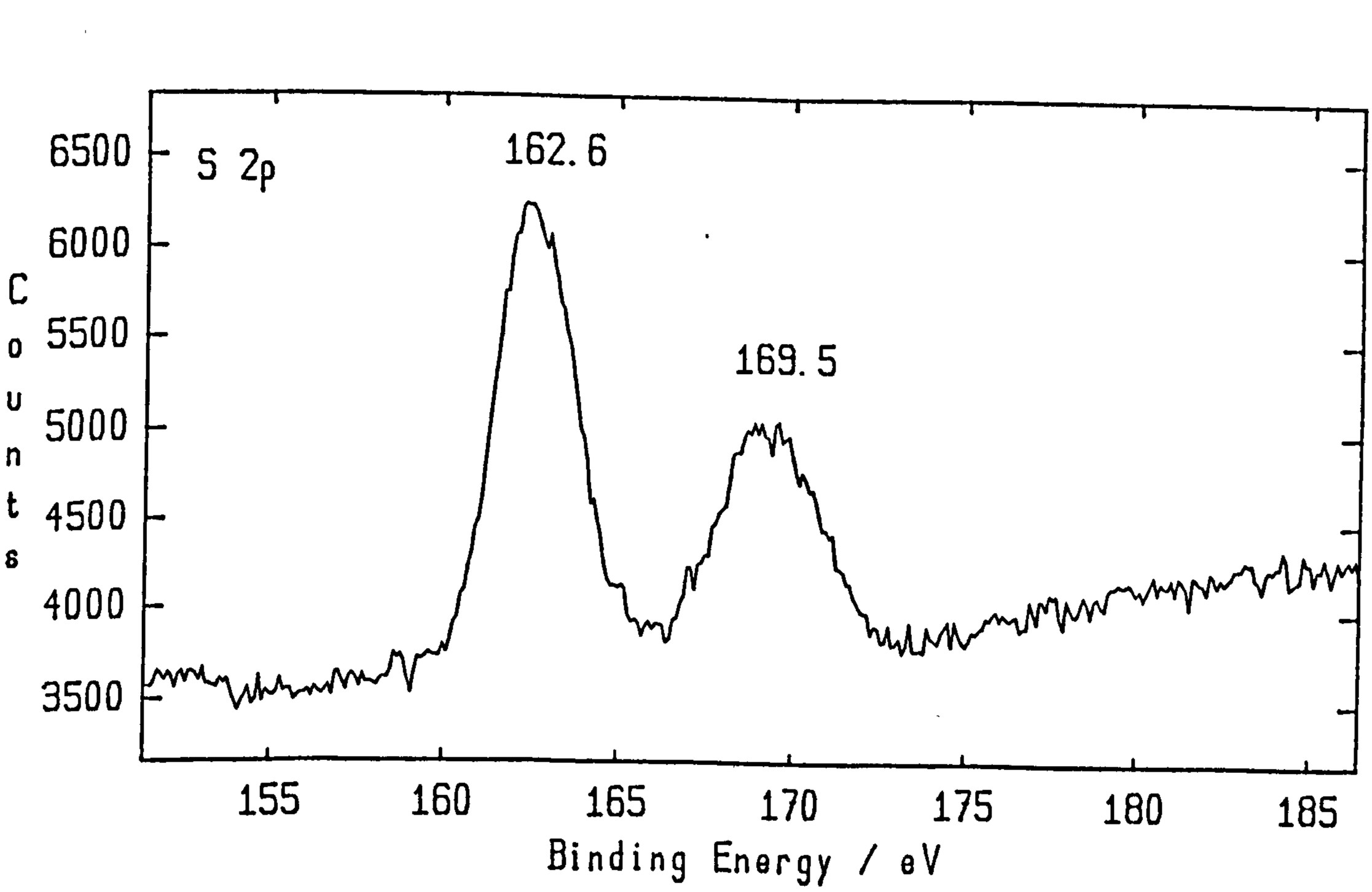

(b)

Figure 8.43. XPS spectra selected from the depth profile montage in Figure 8.42.

(a) S_{2p} peak for $MgSO_4$ (169.6 eV) at the surface - bottom profile .

(b) S_{2p} peaks for MgSO4 (169.5 eV) and MgS (162.6) - 6th profile.

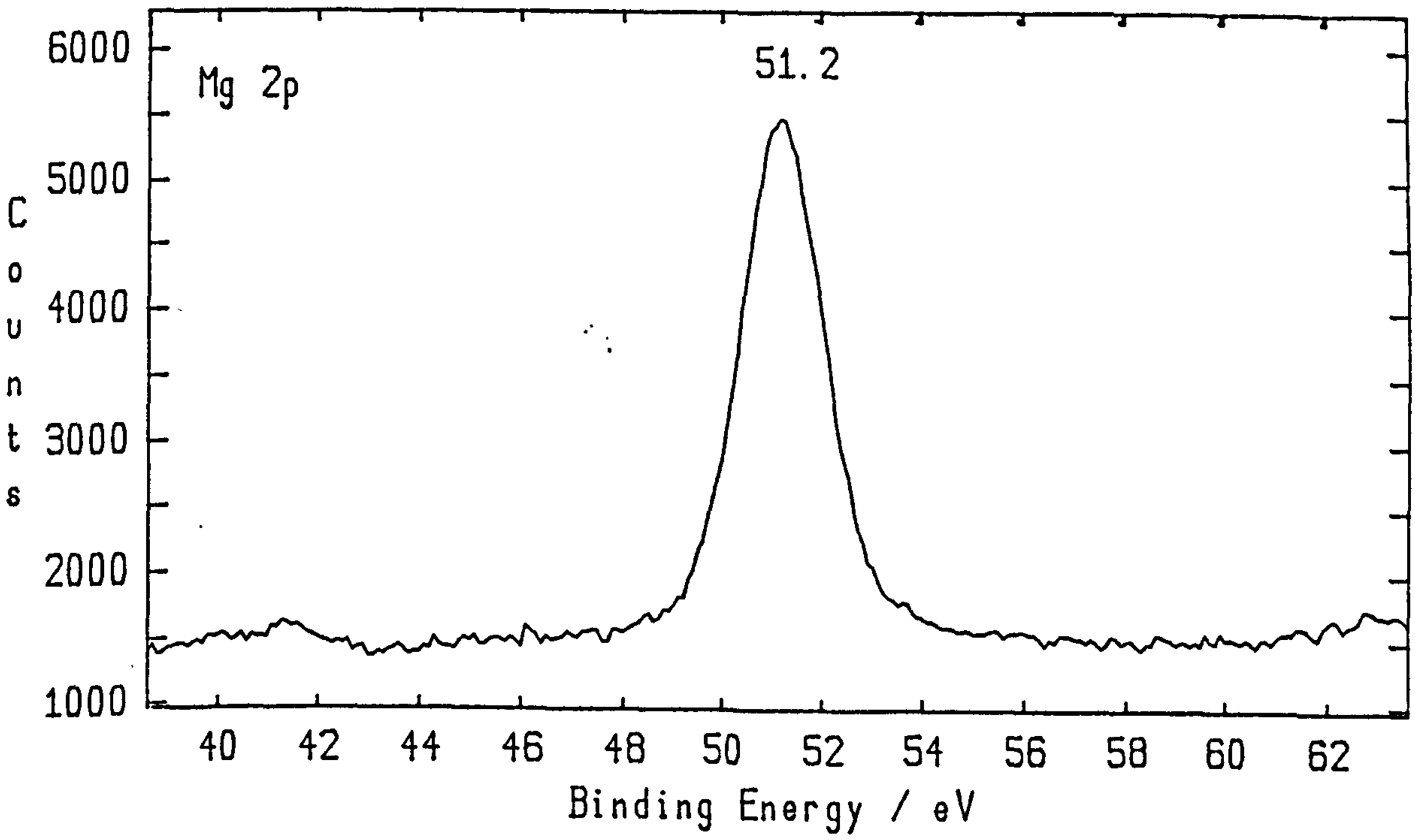

Figure 8.44. XPS spectrum from surface of sample heated 4 h at 590 °C in nominally dry air + 1% SO_2.

Mg_{2p} peak for $MgSO_4$ (51.2 eV)

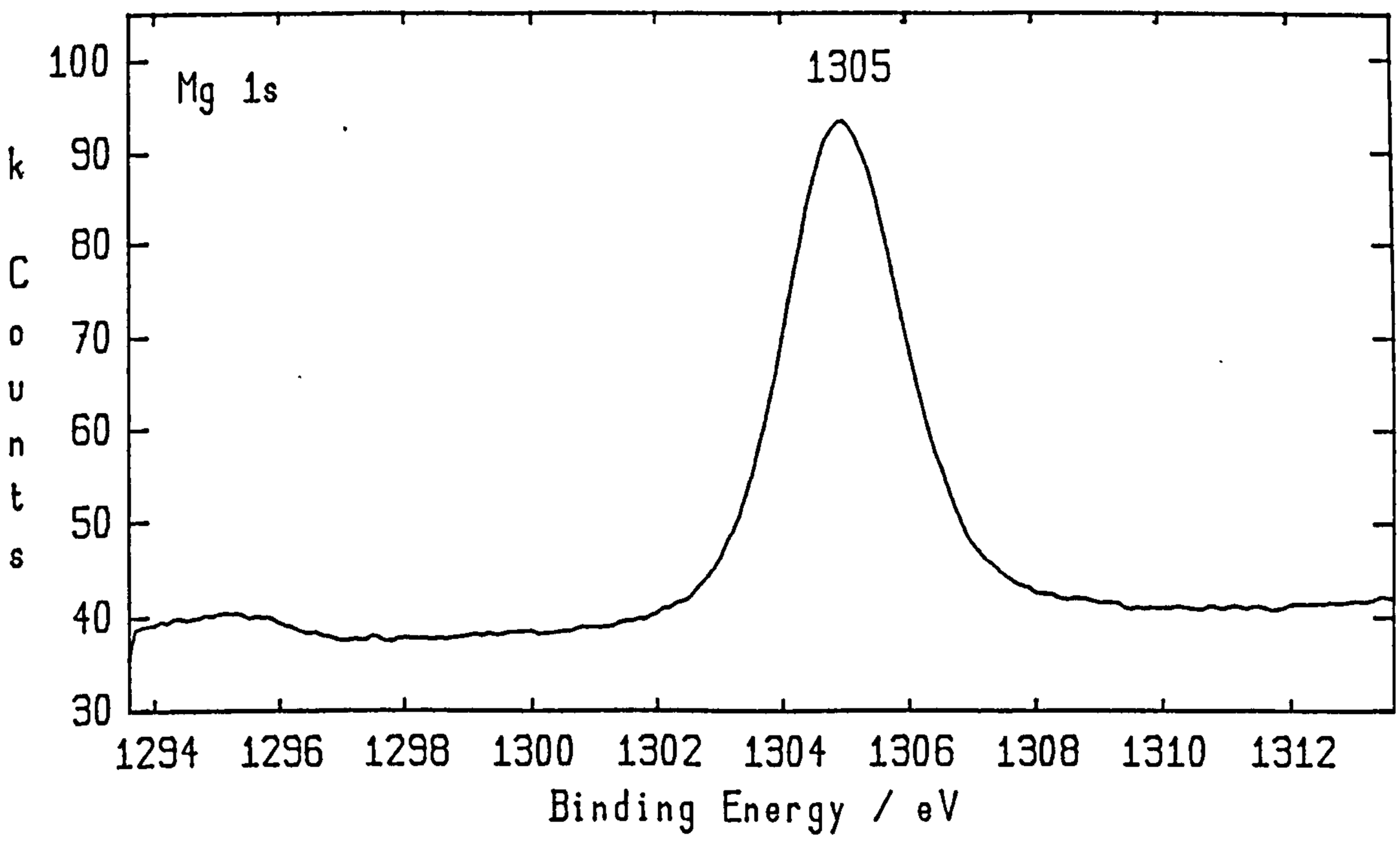

Figure 8.45. XPS spectrum from surface of sample heated 4 h at 590 °C in nominally dry air + 1% SO_2.

Mg_{1s} peak for $MgSO_4$ (1305 .0 eV)

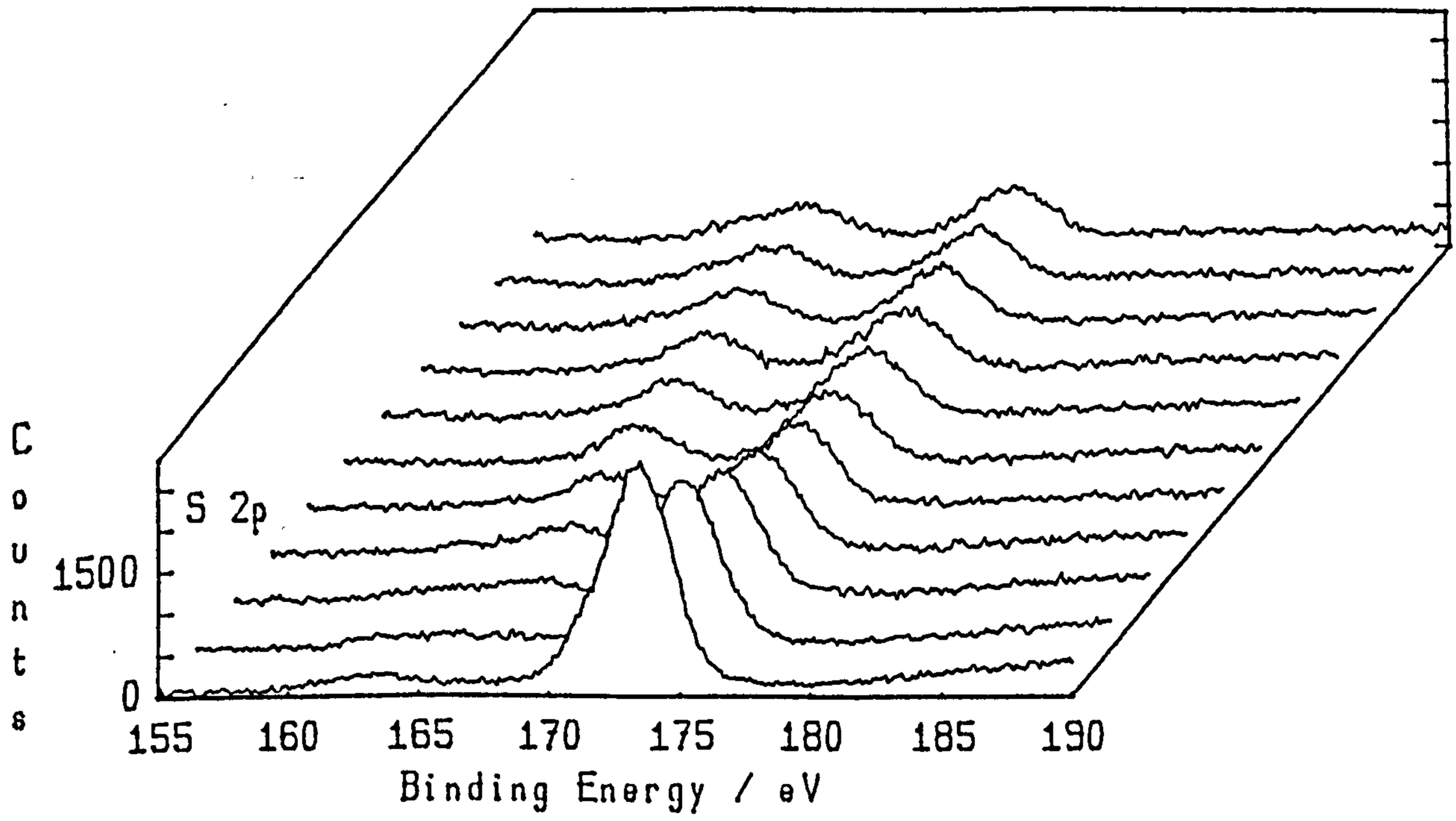

Figure 8.46. XPS depth profile montage from sample heated 4 h in water-saturated air + 1% SO_2 at 590 °C.

S_{2p} peaks for $MgSO_4$ (169.6 eV) and MgS (162.1 eV).

Note change in chemical state of sulphur immediately below the surface.

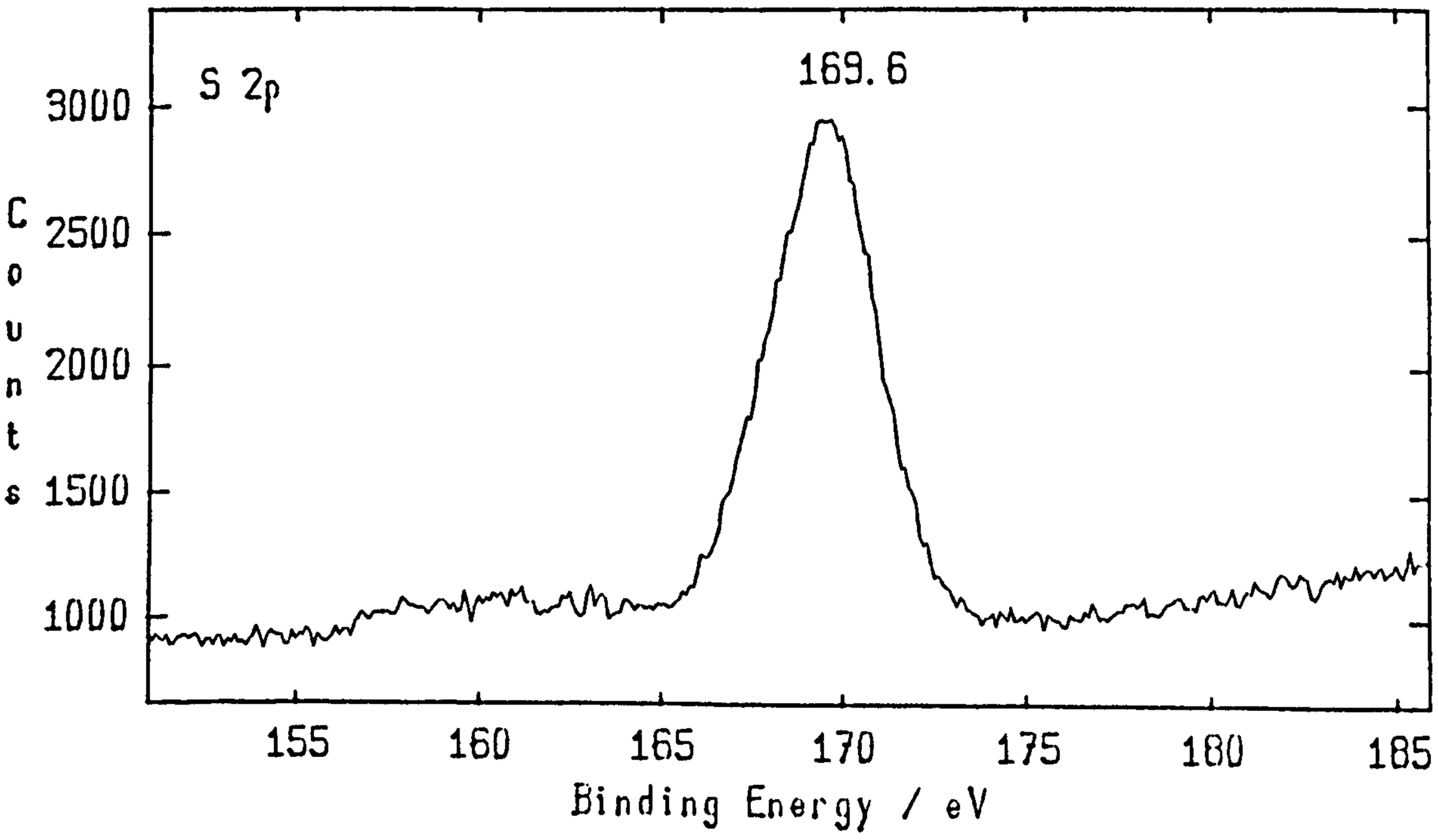

(a)

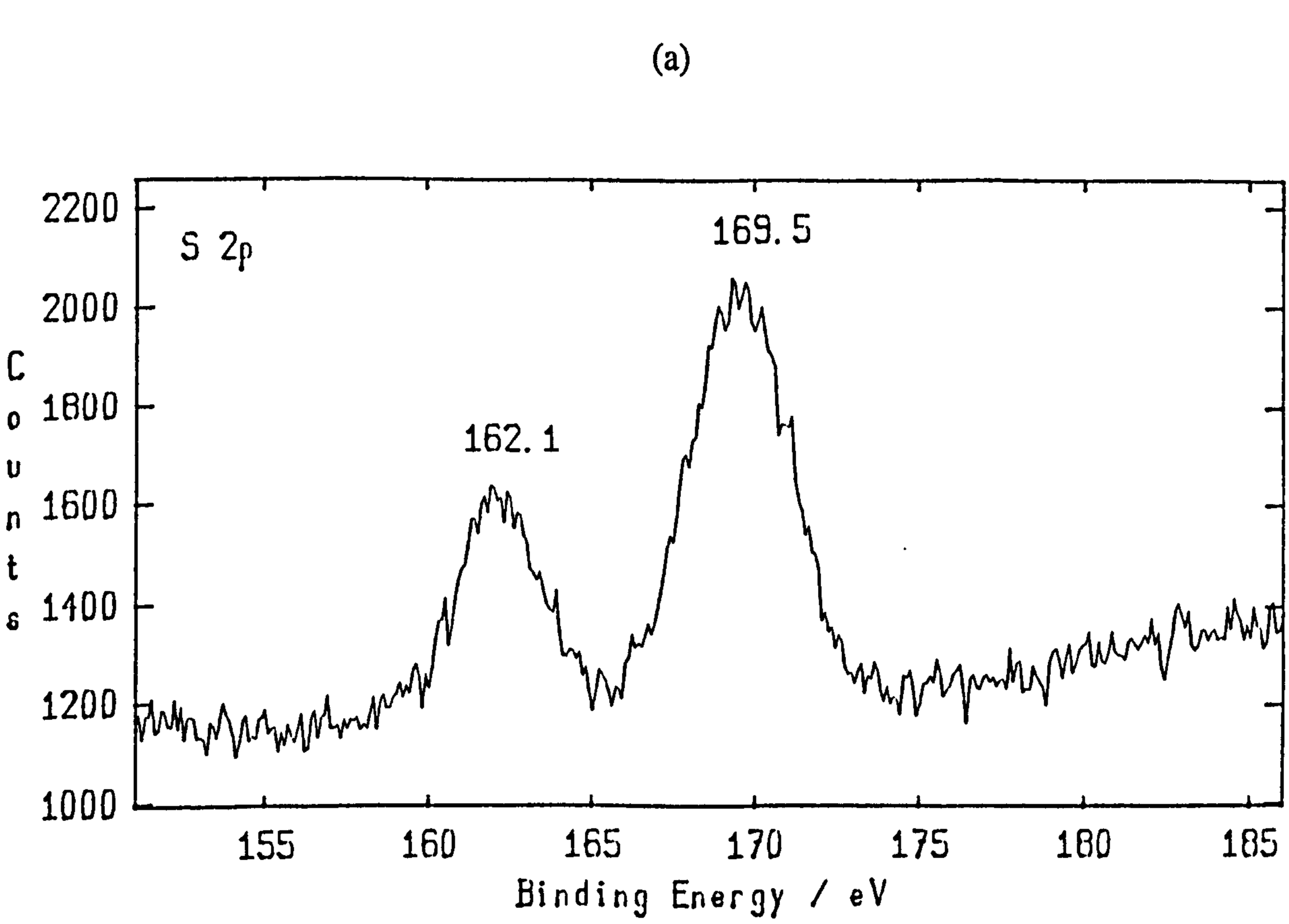

(b)

Figure 8.47 XPS spectra selected from the depth profile montage in Figure 8.46.

(a) S_{2p} peak for $MgSO_4$ (169.6 eV) at the surface - bottom profile.

(b) S_{2p} peaks for MgSO4 (169.5 eV) & MgS (162.1) - 6th profile.

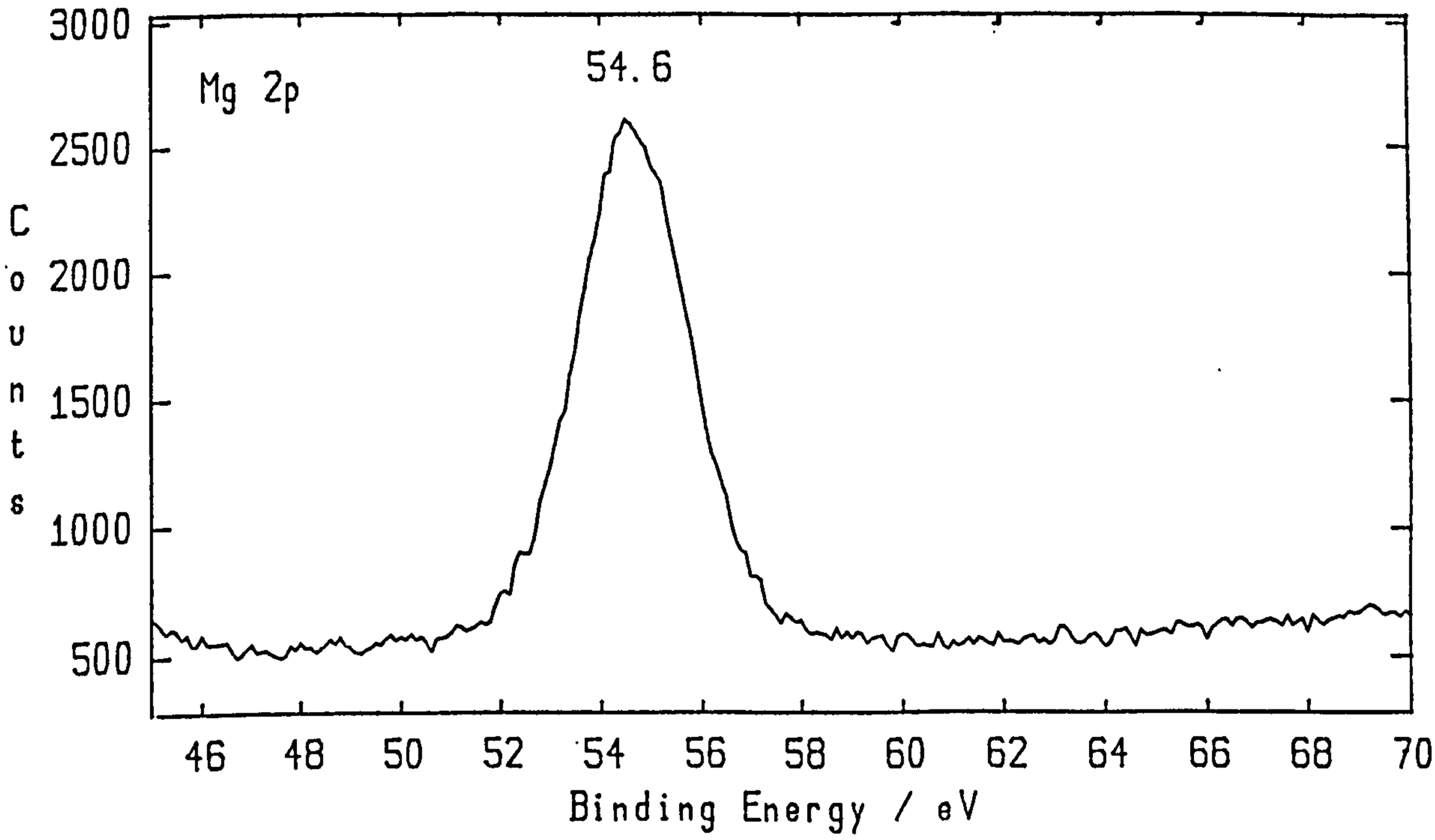

Figure 8.48. XPS spectrum (not charge corrected) from surface of sample heated 4 h at 590 °C in nominally dry air + 1% SO_2.

Mg_{2p} peak for $MgSO_4$ (51.0 eV after charge correction)

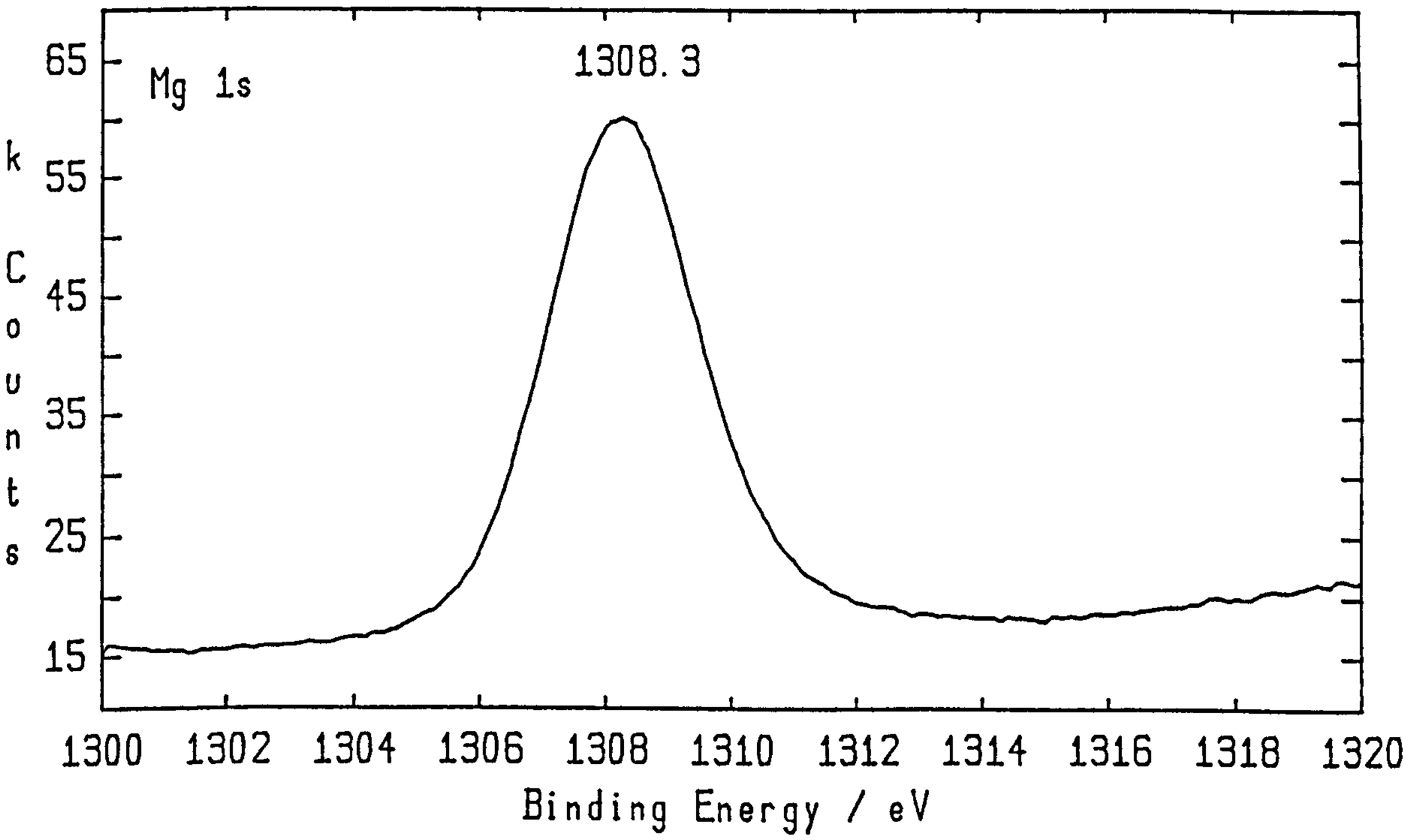

Figure 8.49. XPS spectrum (not charge corrected) from surface of sample heated 4 h at 590 °C in nominally dry air + 1% SO_2.

Mg_{1s} peak for $MgSO_4$ (1304.7 eV after charge correction).

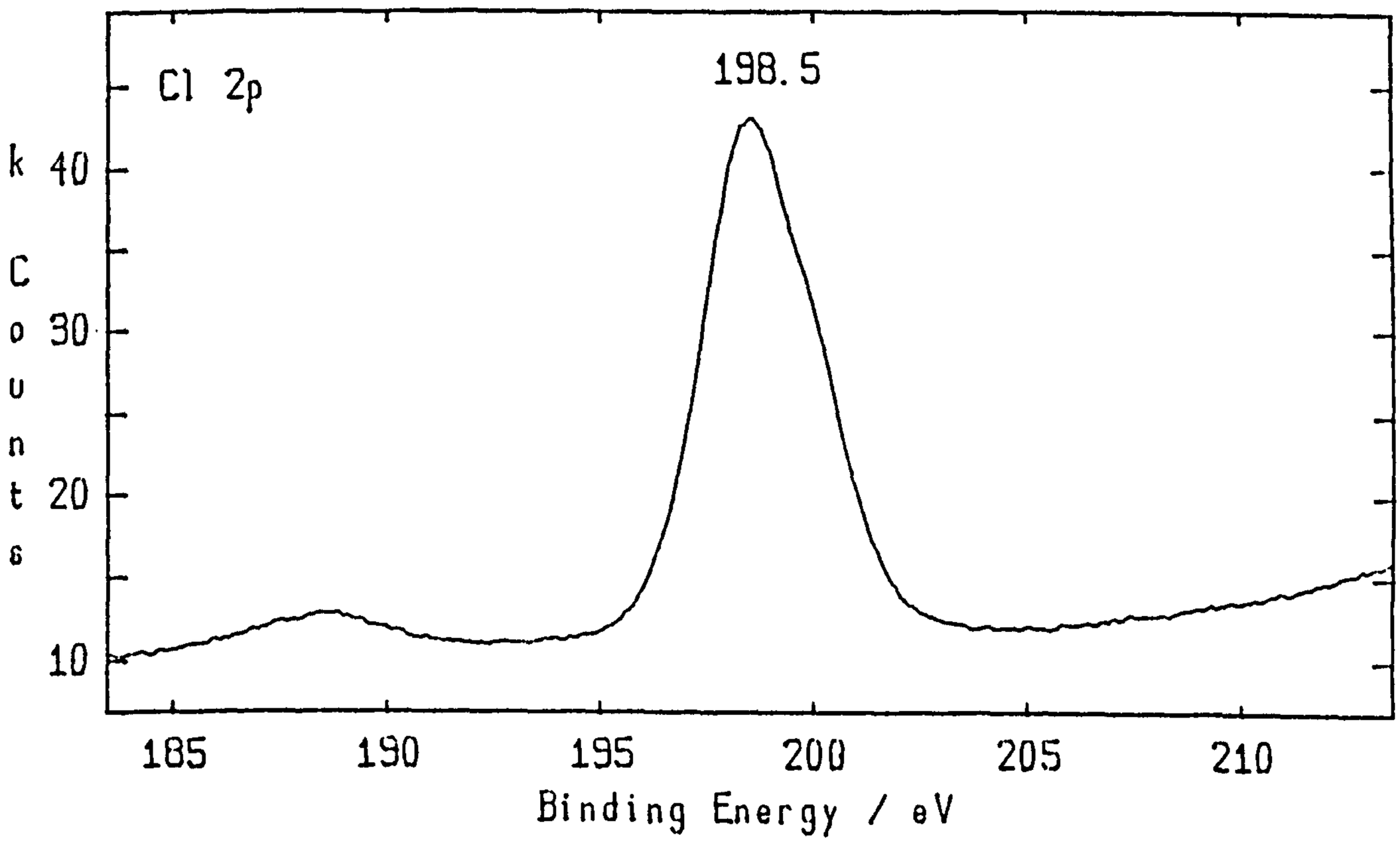

Figure 8.50. XPS spectrum from surface of sample heated 4 h at 500 °C in water saturated air + HCl.

Cl_{2p} peak for $MgCl_2$ (198.5 eV).

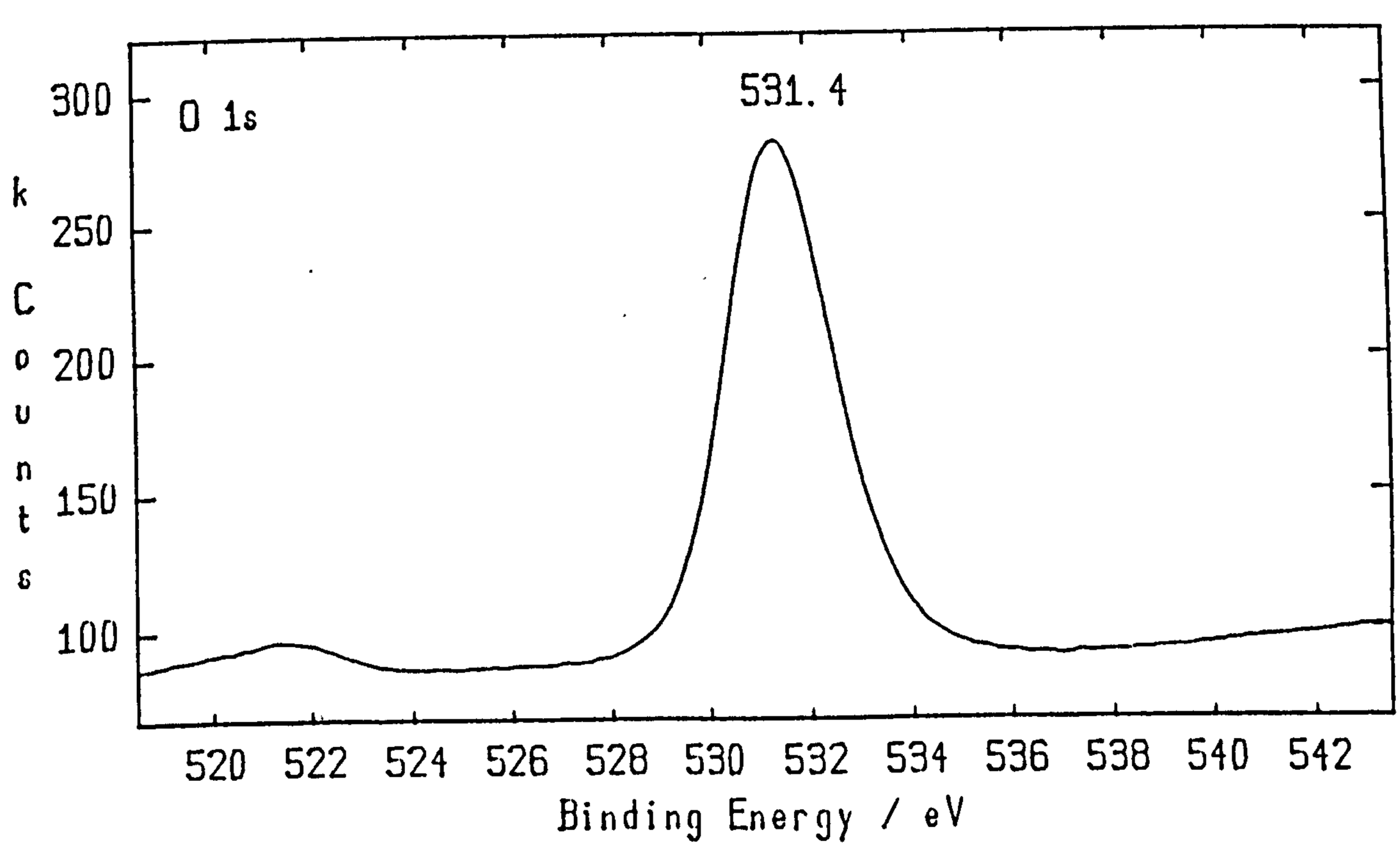

Figure 8.51. XPS spectrum from surface of sample heated 4 h at 500 °C in water saturated air + HCl.

O_{1s} peak for MgO (531.4 eV).

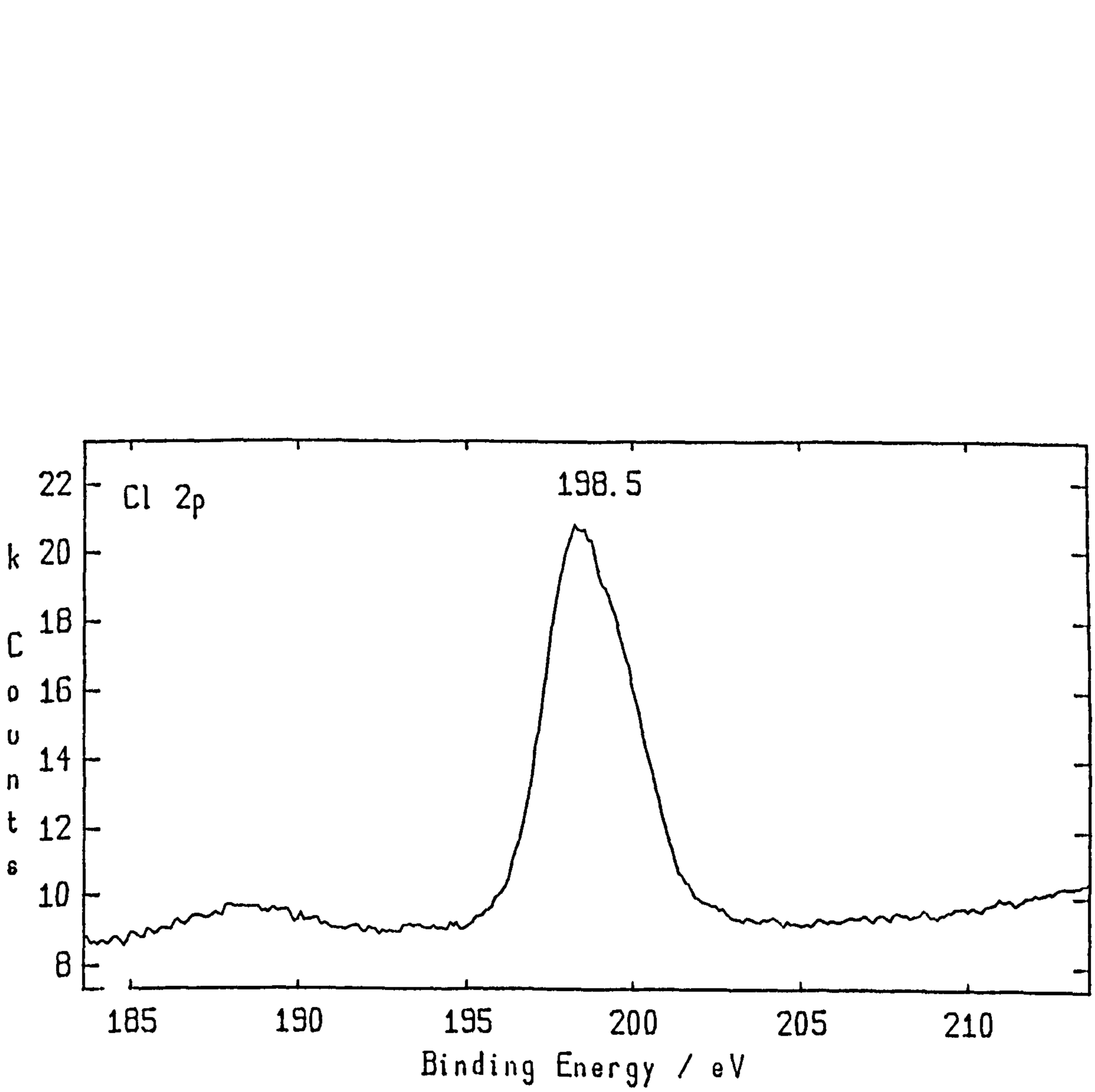

Figure 8.52. XPS spectrum from surface of sample heated 8 h at 590 °C in water saturated air + HCl.

Cl_{2p} peak for $MgCl_2$ (198.5 eV).

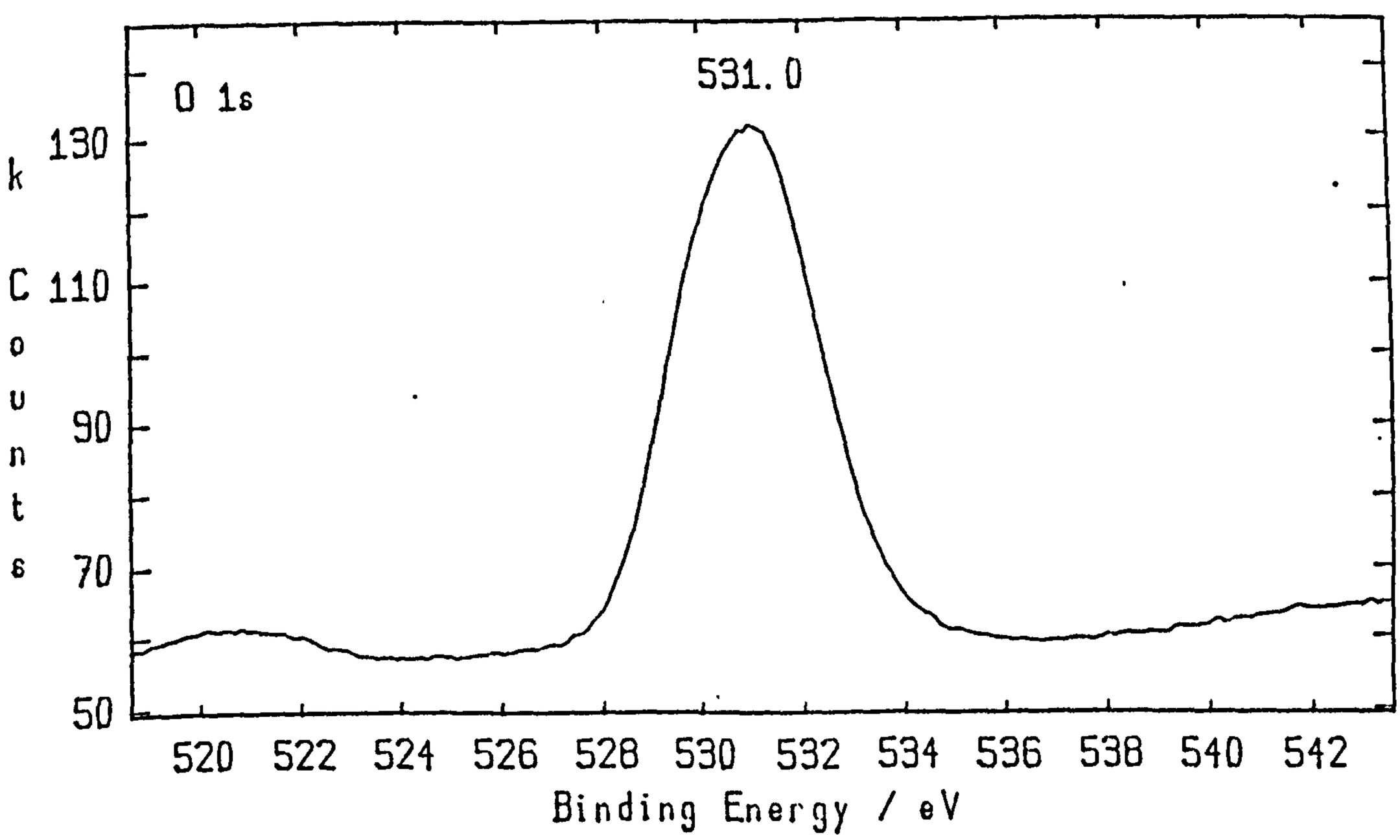

Figure 8.53. XPS spectrum from surface of sample heated 8 h at 590 °C in water saturated air + HCl.

O_{1s} peak for MgO (531.0 eV).

8.3.10 Micrographs of samples after heat-treatments are given in Figures 8.54 to 8.73 to show the effect of absorbed hydrogen on porosity.

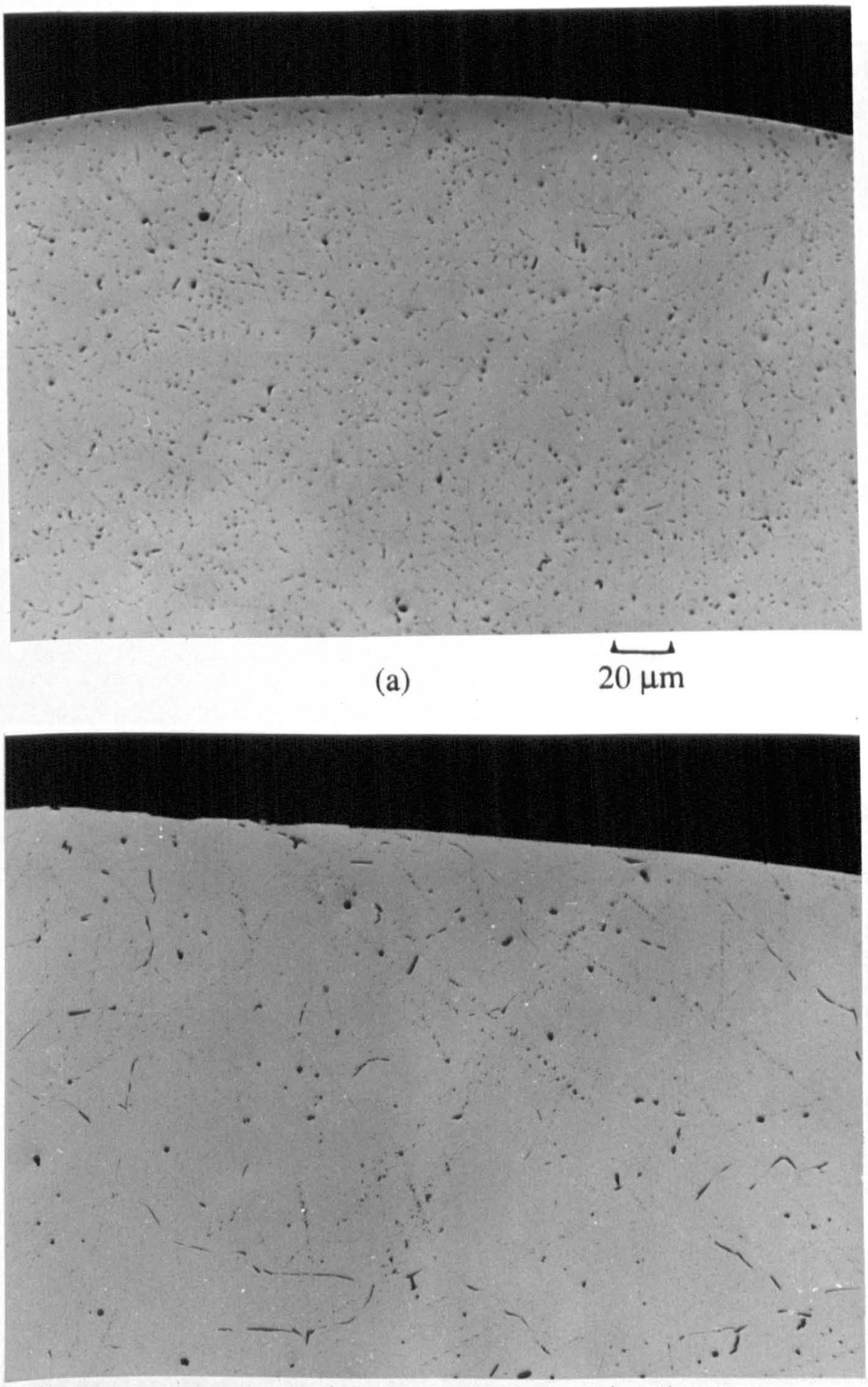

Figure 8.54. As cast sample of material used for experimental heat-treatments. Hydrogen content 0.18 cm^3/100g. Unetched. (a) x 100 and (b) x 400.

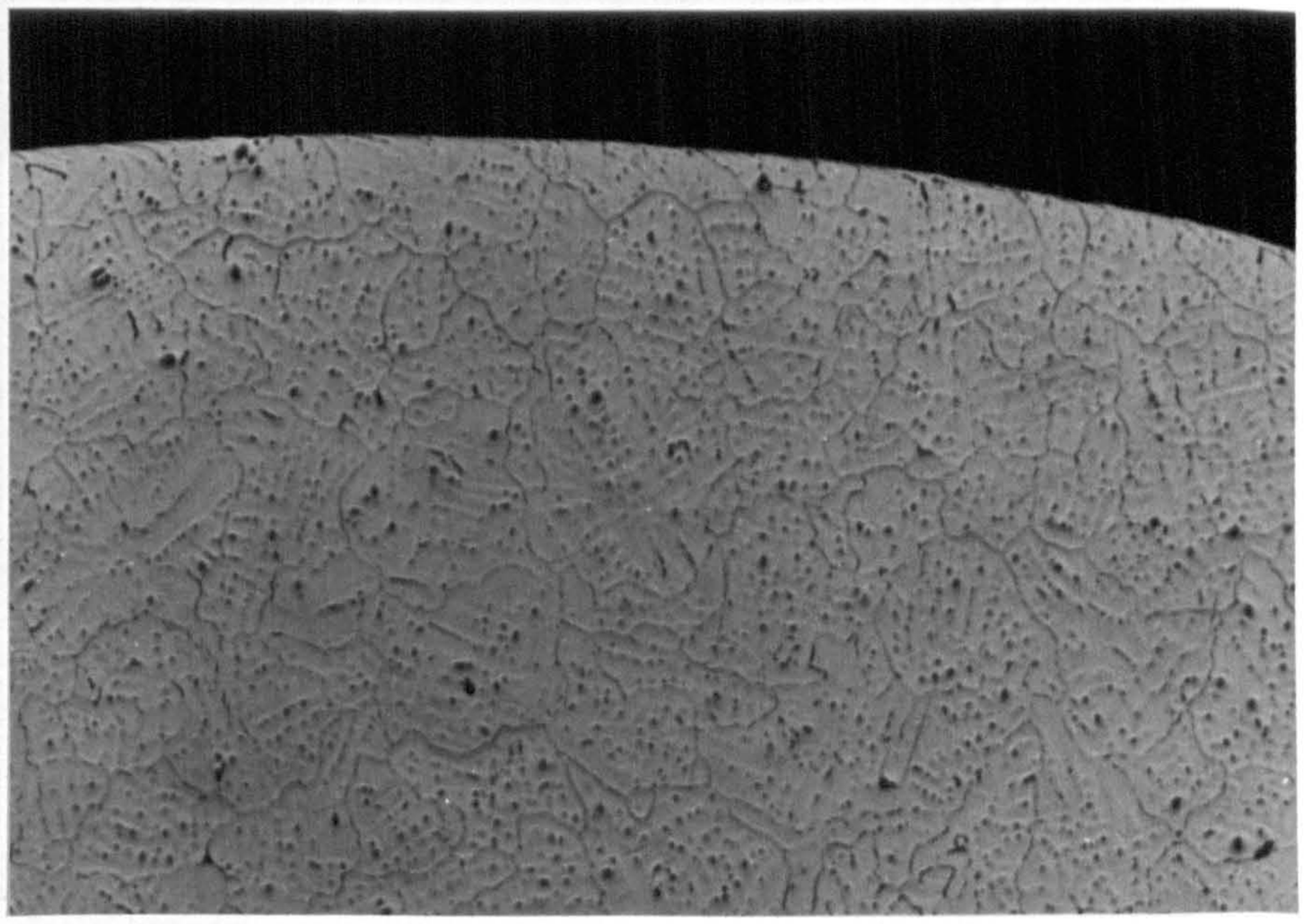

(a)

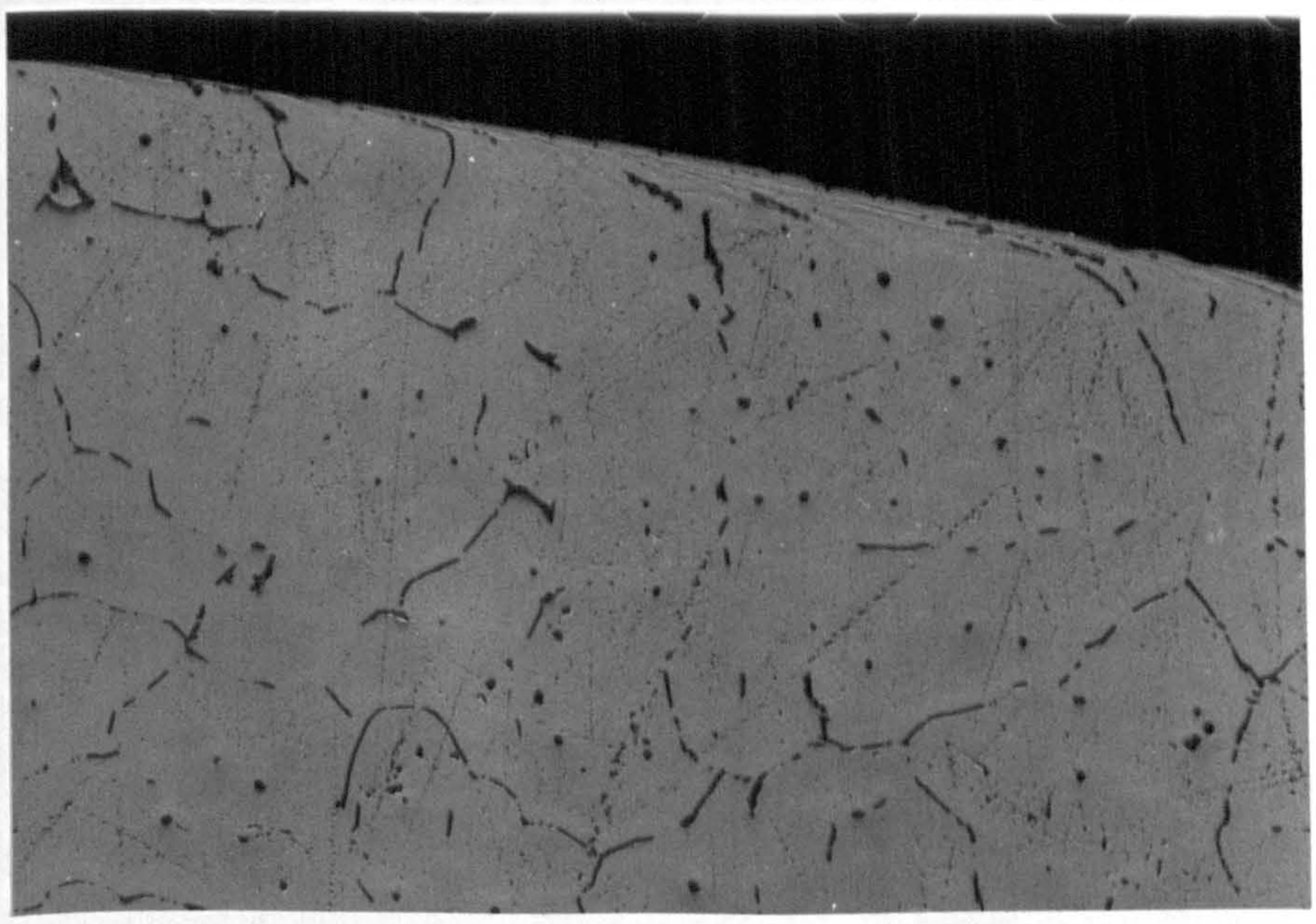

(b)

Figure 8.55. As cast sample of material used for experimental heat-treatments. Hydrogen content 0.18 $cm^3/100g$. Etched in Keller's reagent (a) x 100 and (b) x 400.

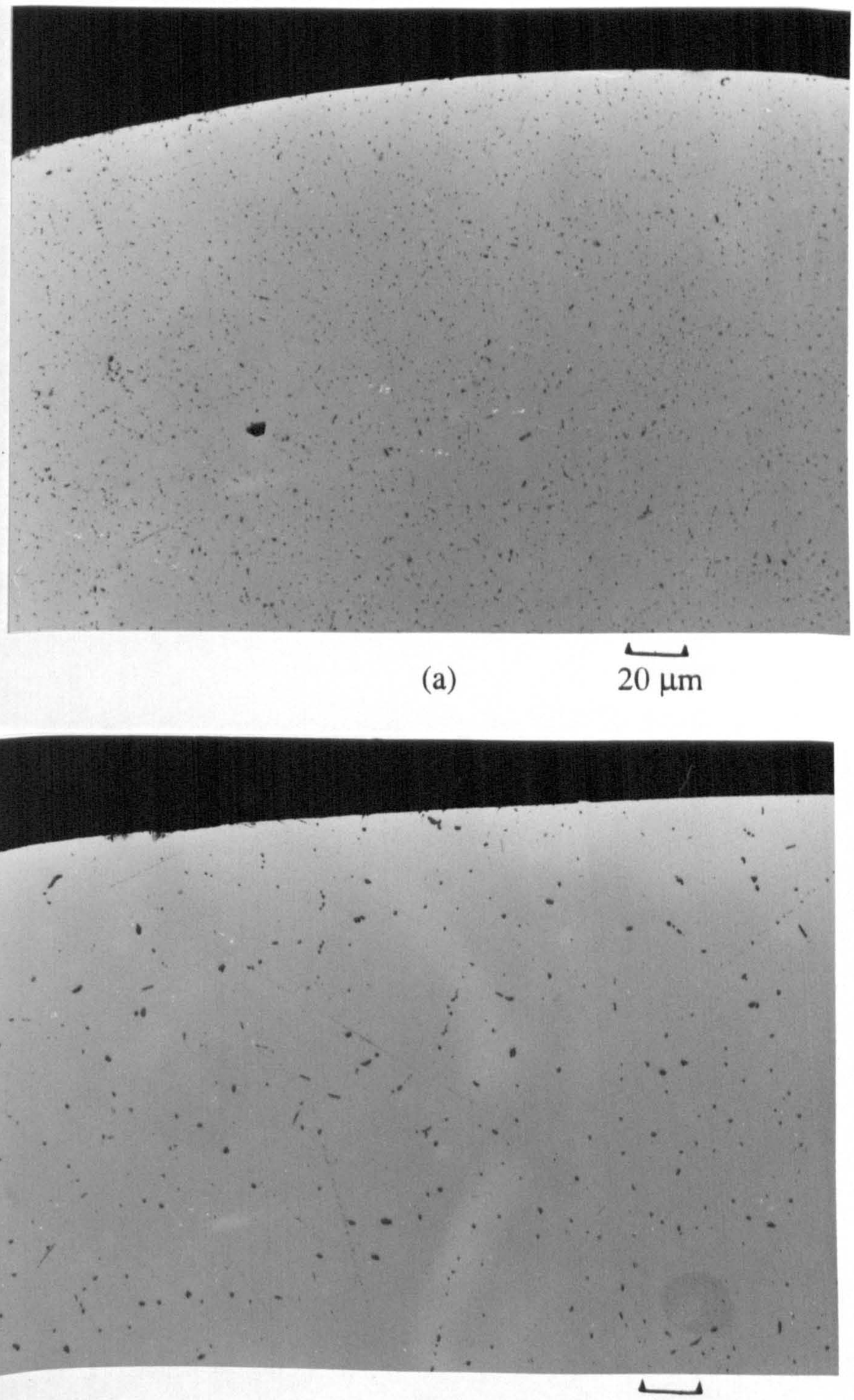

Figure 8.56.

Heat-treatment: nominally dry air for 4 h at 590°C.

Hydrogen content: 0.04 $cm^3/100g$.

Unetched. (a) x 100 (b) x 400.

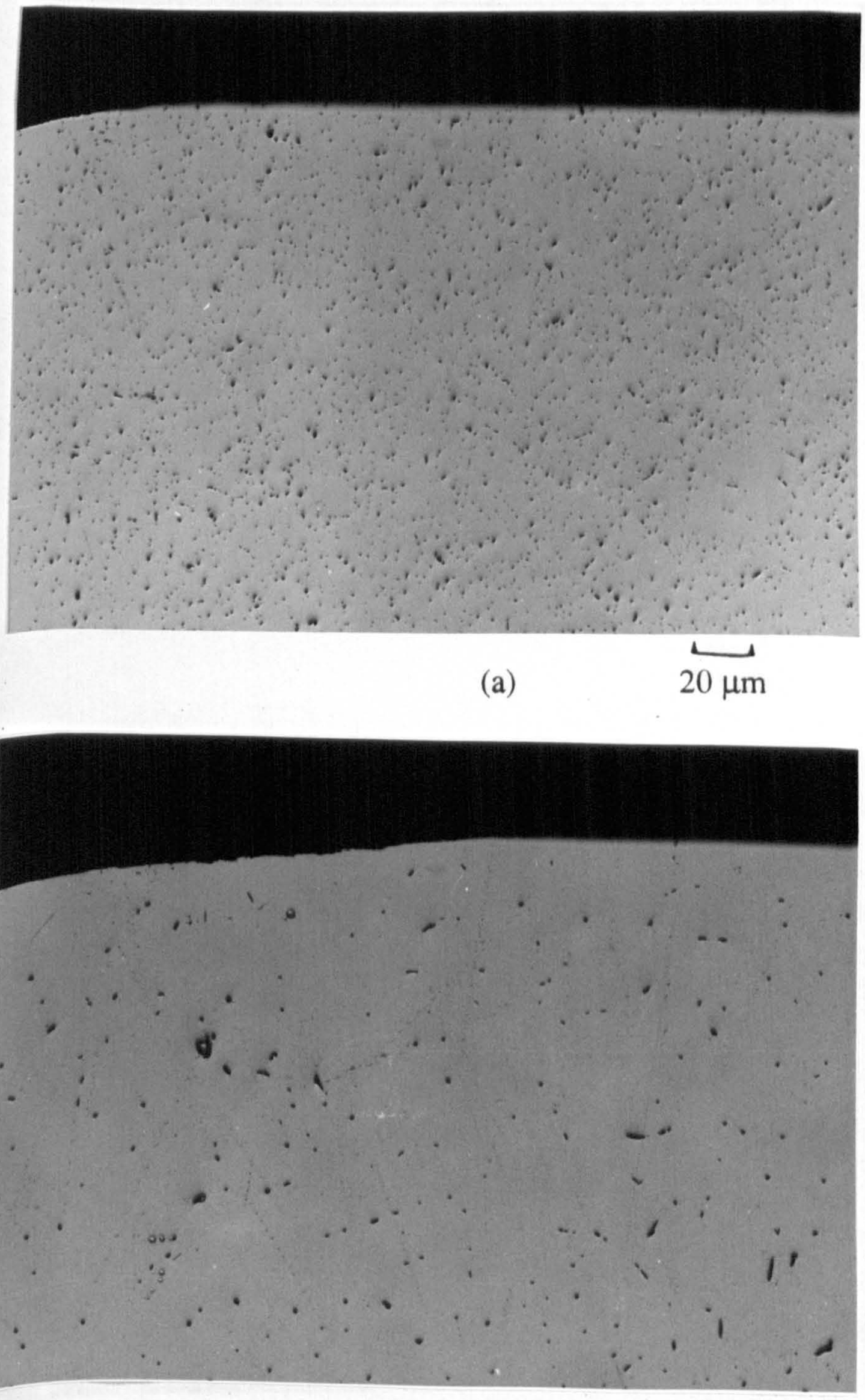

Figure 8.57.

Heat-treatment: water saturated air + HCl for 6 h at 590°C.

Hydrogen content: 0.14 cm^3/100g.

Unetched. (a) x 100 (b) x 400.

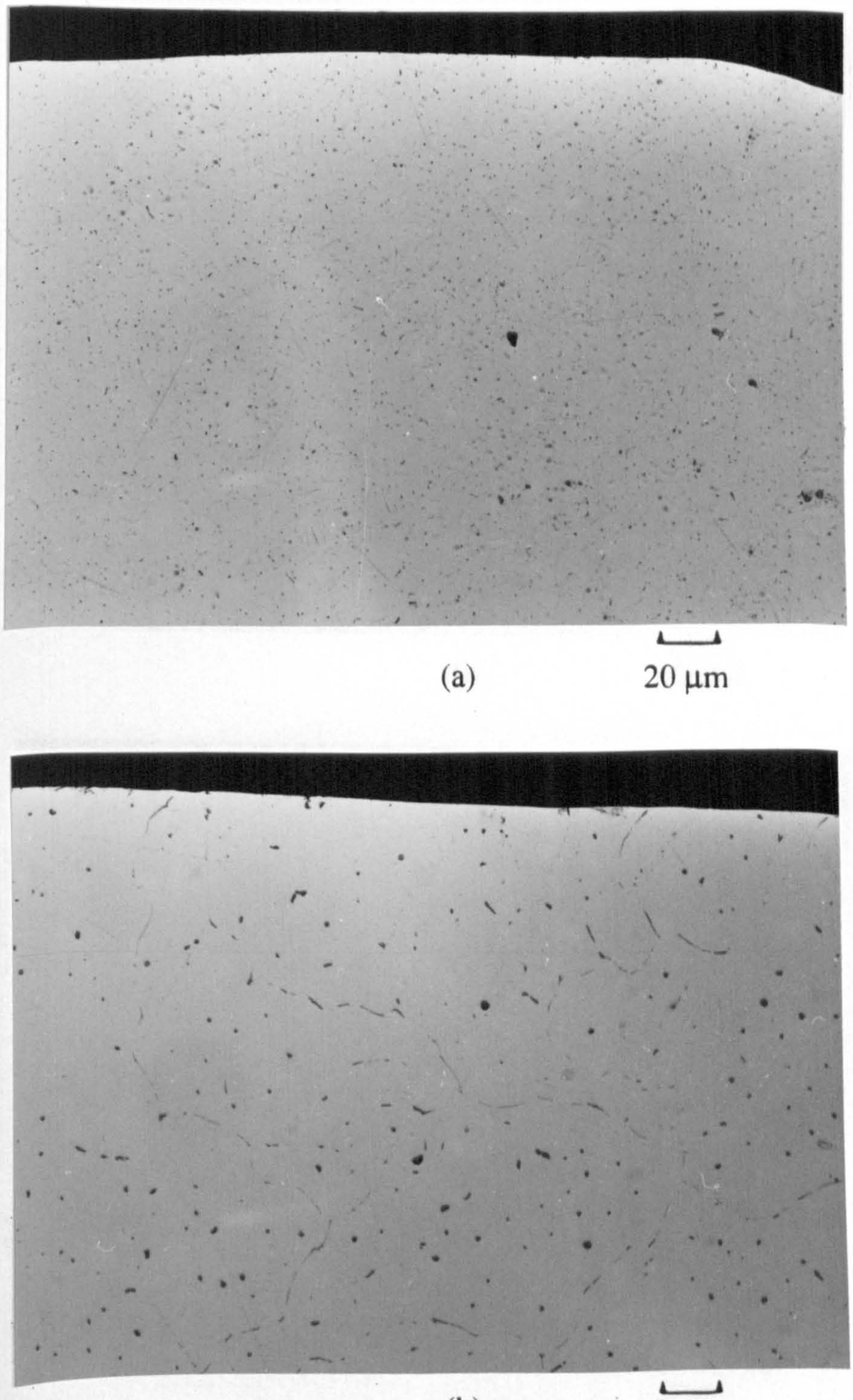

Figure 8.58.

Heat-treatment: nominally dry air for 4 h at 500°C.

Hydrogen content: 0.24 cm^3/100g.

Unetched. (a) x 100 (b) x 400.

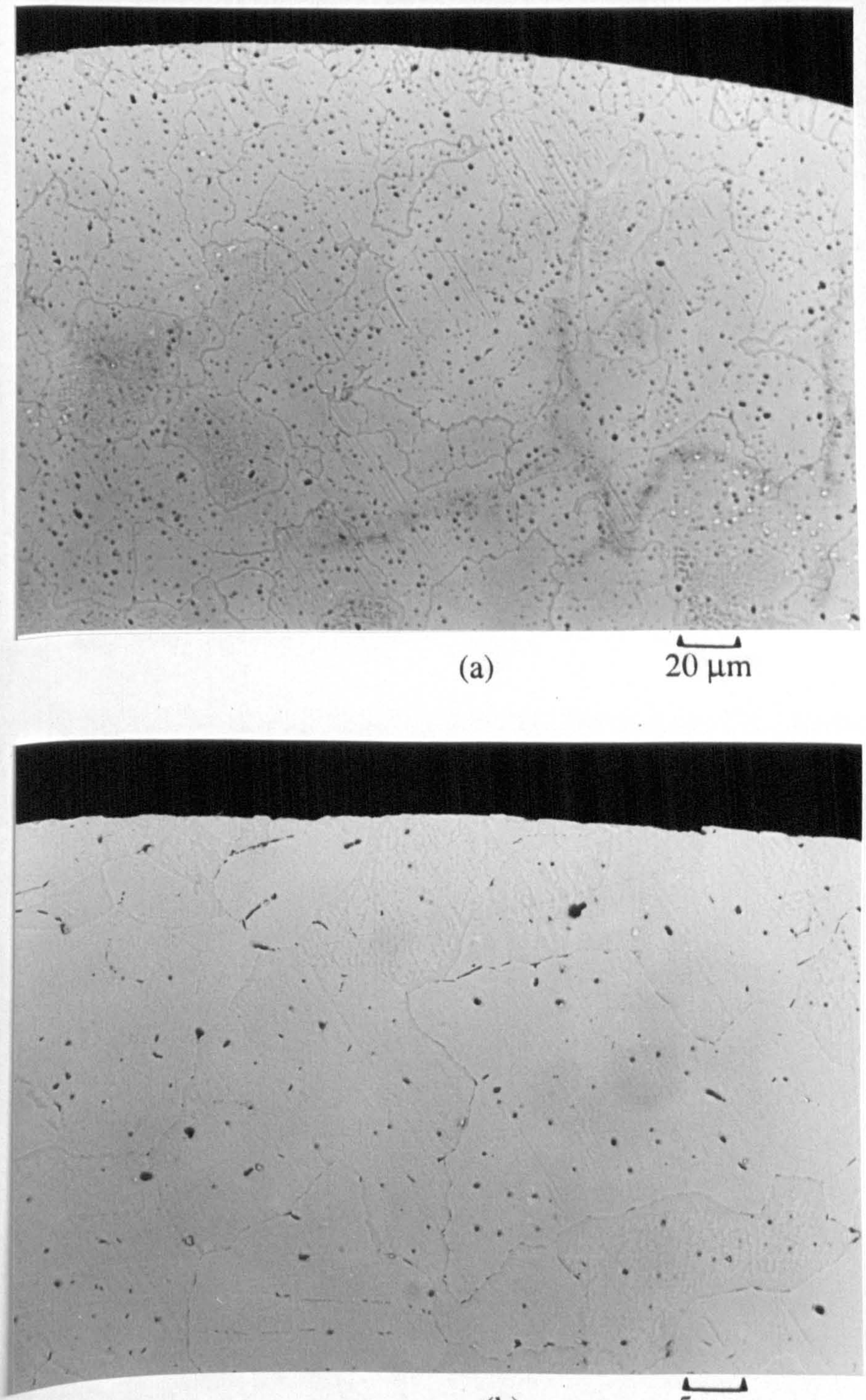

Figure 8.59.

Heat-treatment: in water saturated air + HCl for 4 h at 500°C.

Hydrogen content: 0.37 cm^3/100g.

Unetched. (a) x 100 (b) x 400.

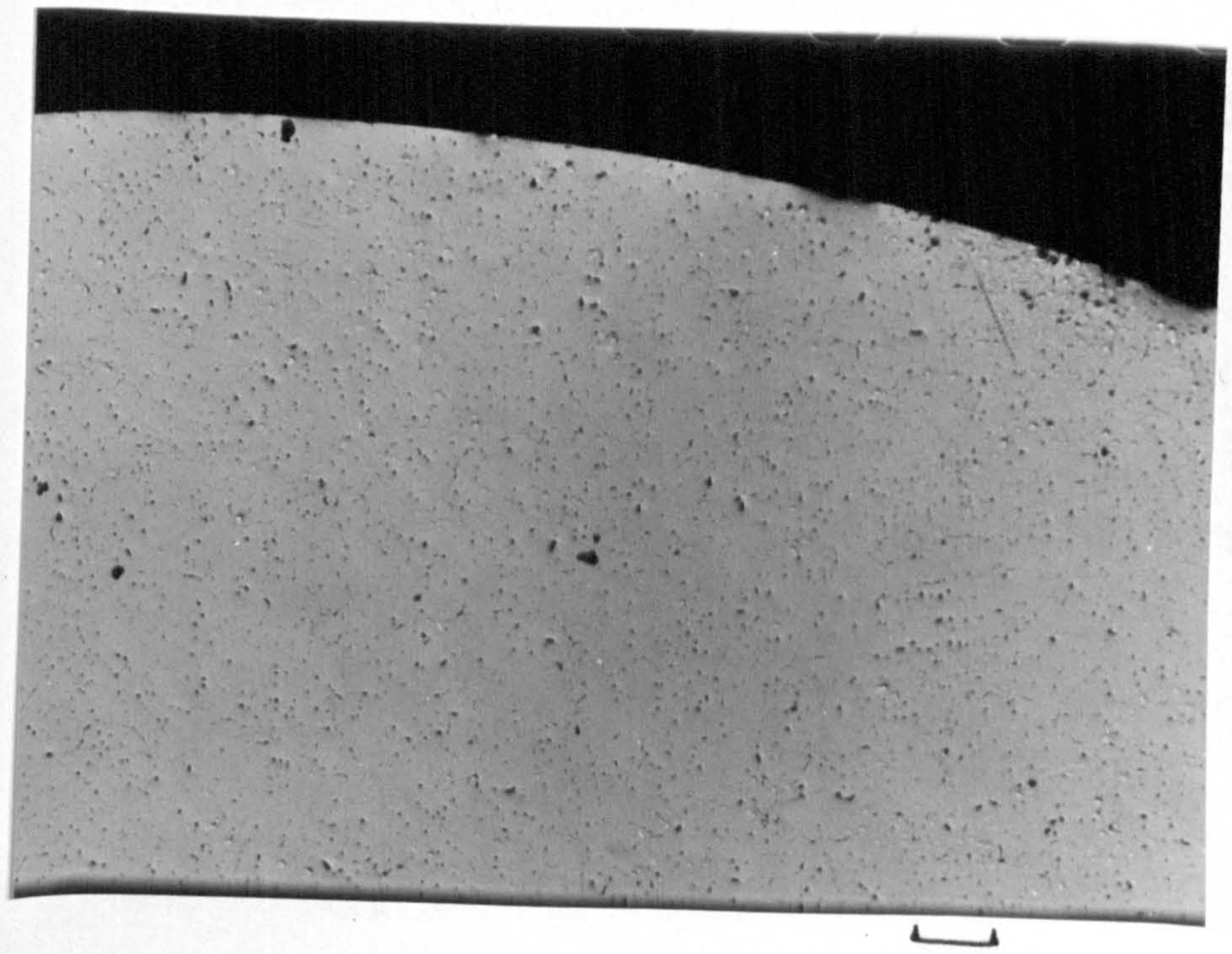

(a) 20 μm

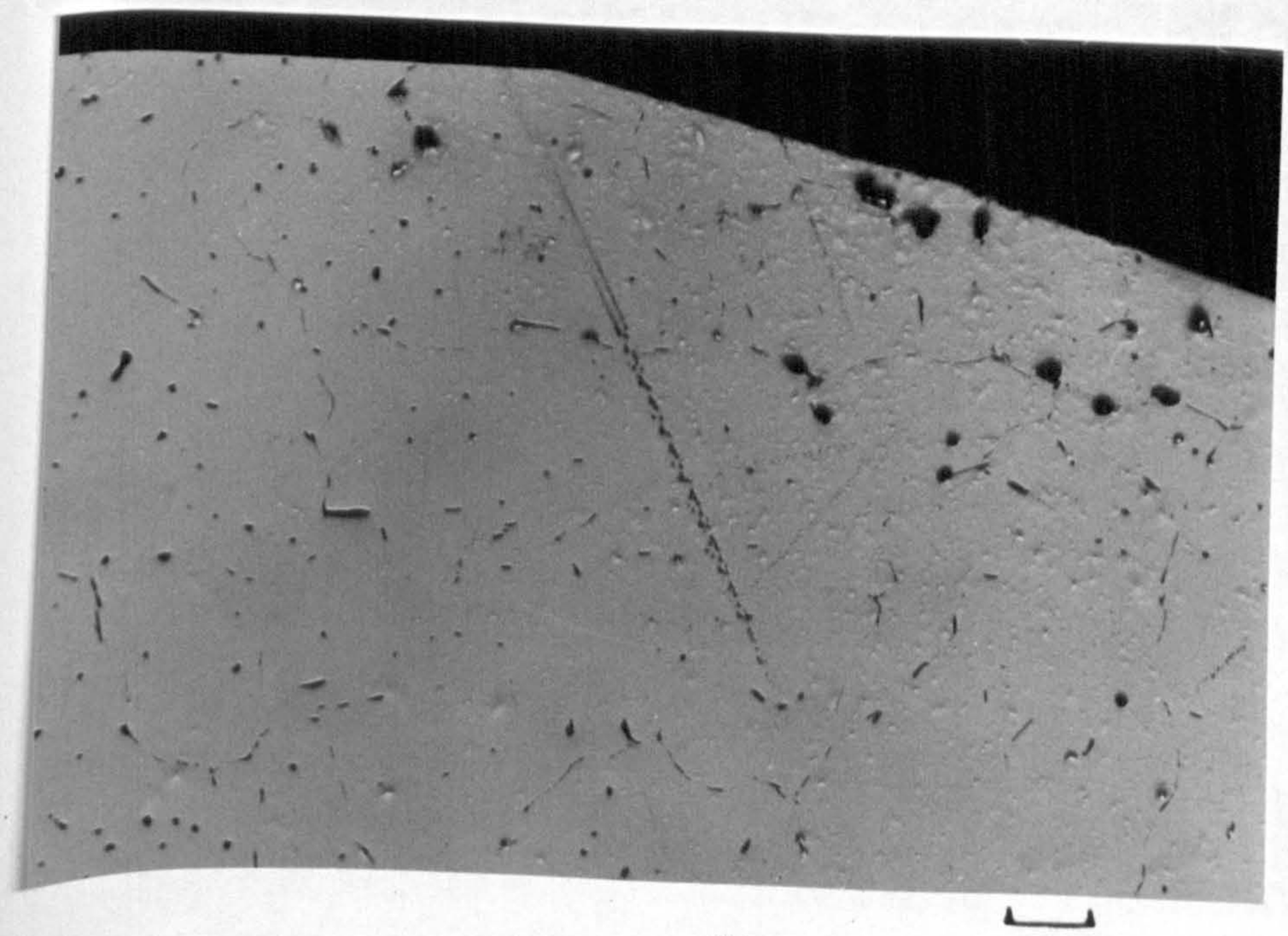

(b) 5 μm

Figure 8.60.

Heat-treatment: in nominally dry air + 1% SO_2 for 2 h at 500°C.

Hydrogen content: 0.54 cm^3/100g.

Unetched. (a) x 100 (b) x 400.

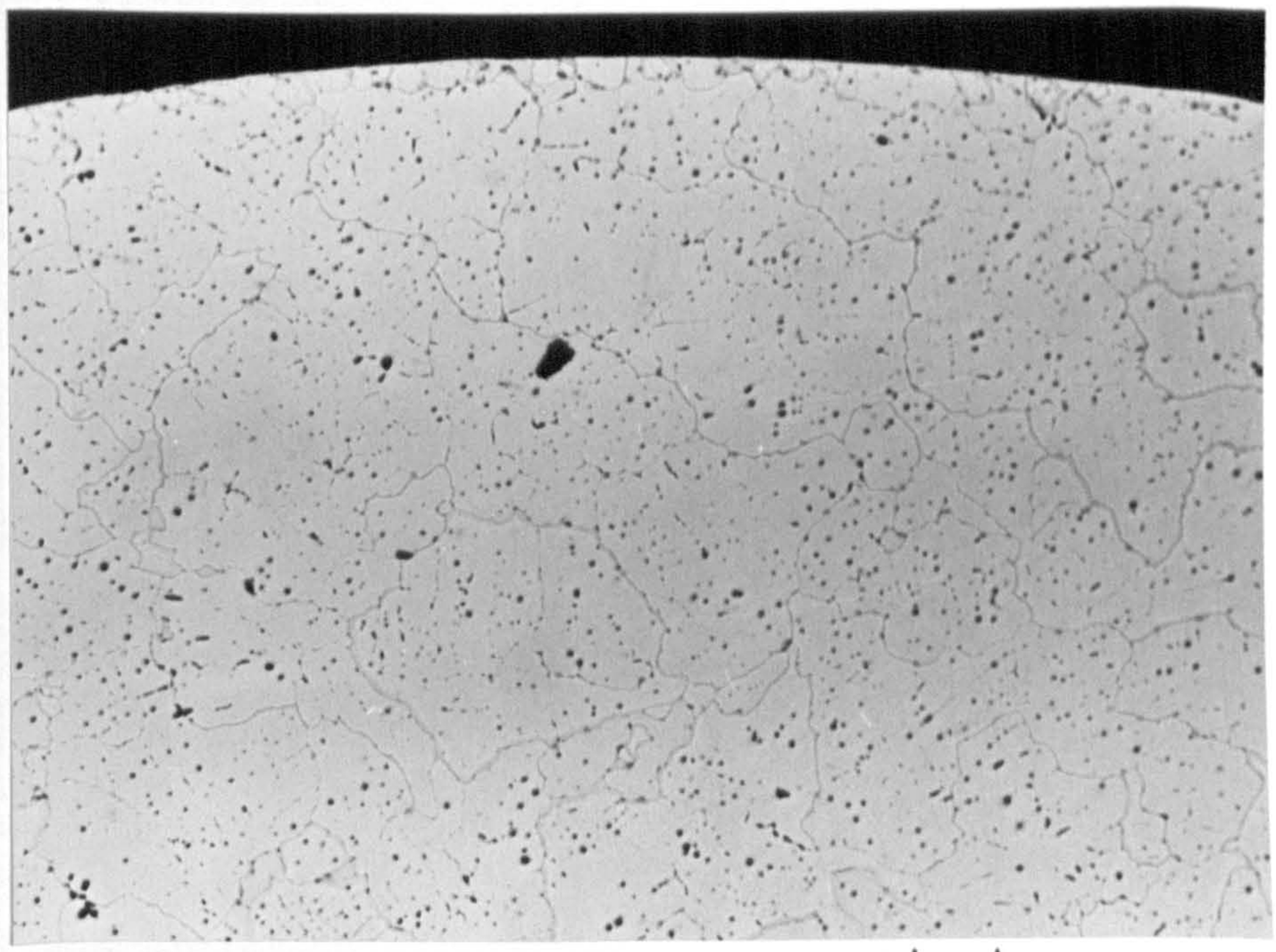

(a) 20 µm

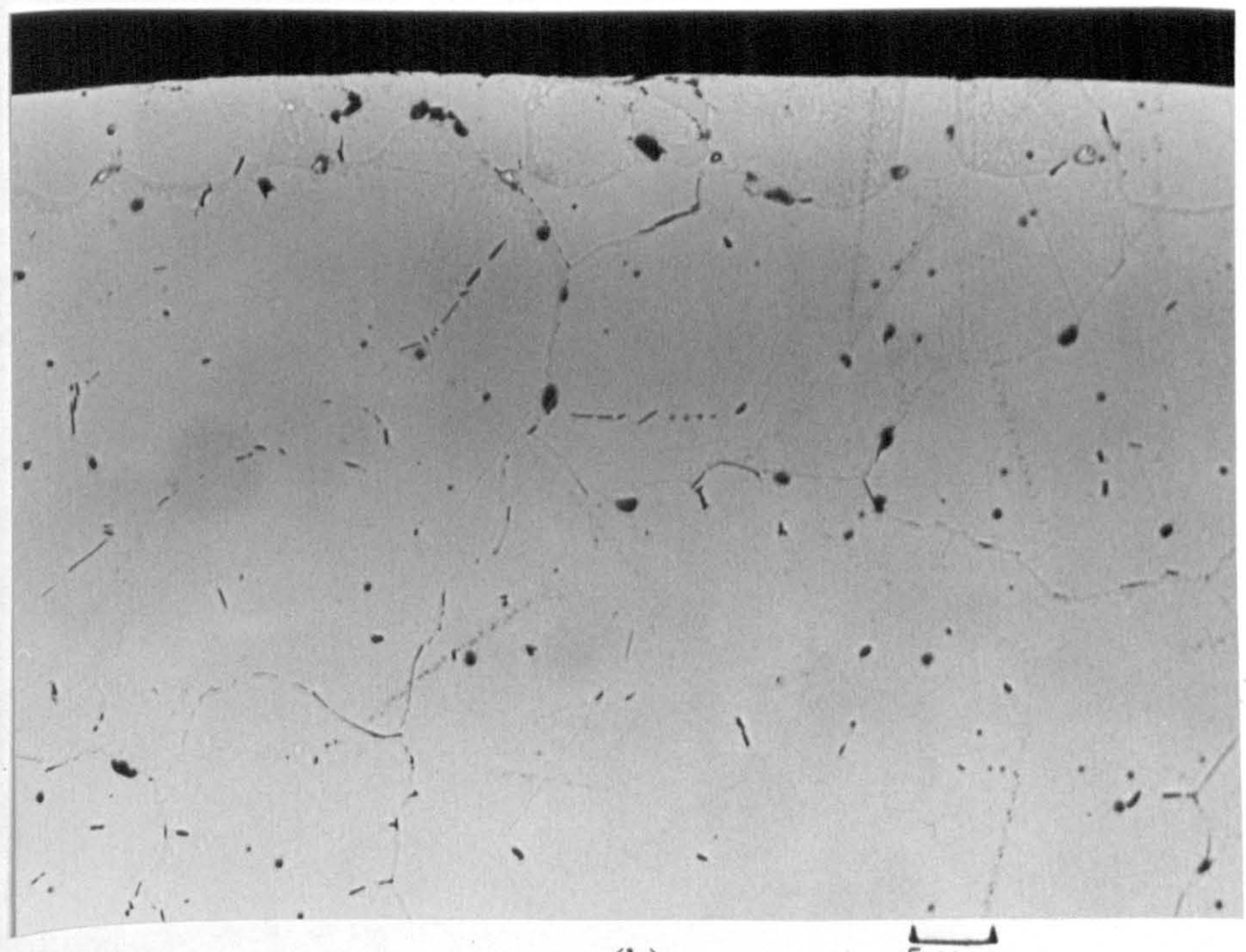

(b) 5 µm

Figure 8.61.

Heat-treatment: in water saturated air + 1% SO_2 + HCl for 4 h at 500°C.

Hydrogen content: 0.68 cm^3/100g.

Unetched. (a) x 100 (b) x 400.

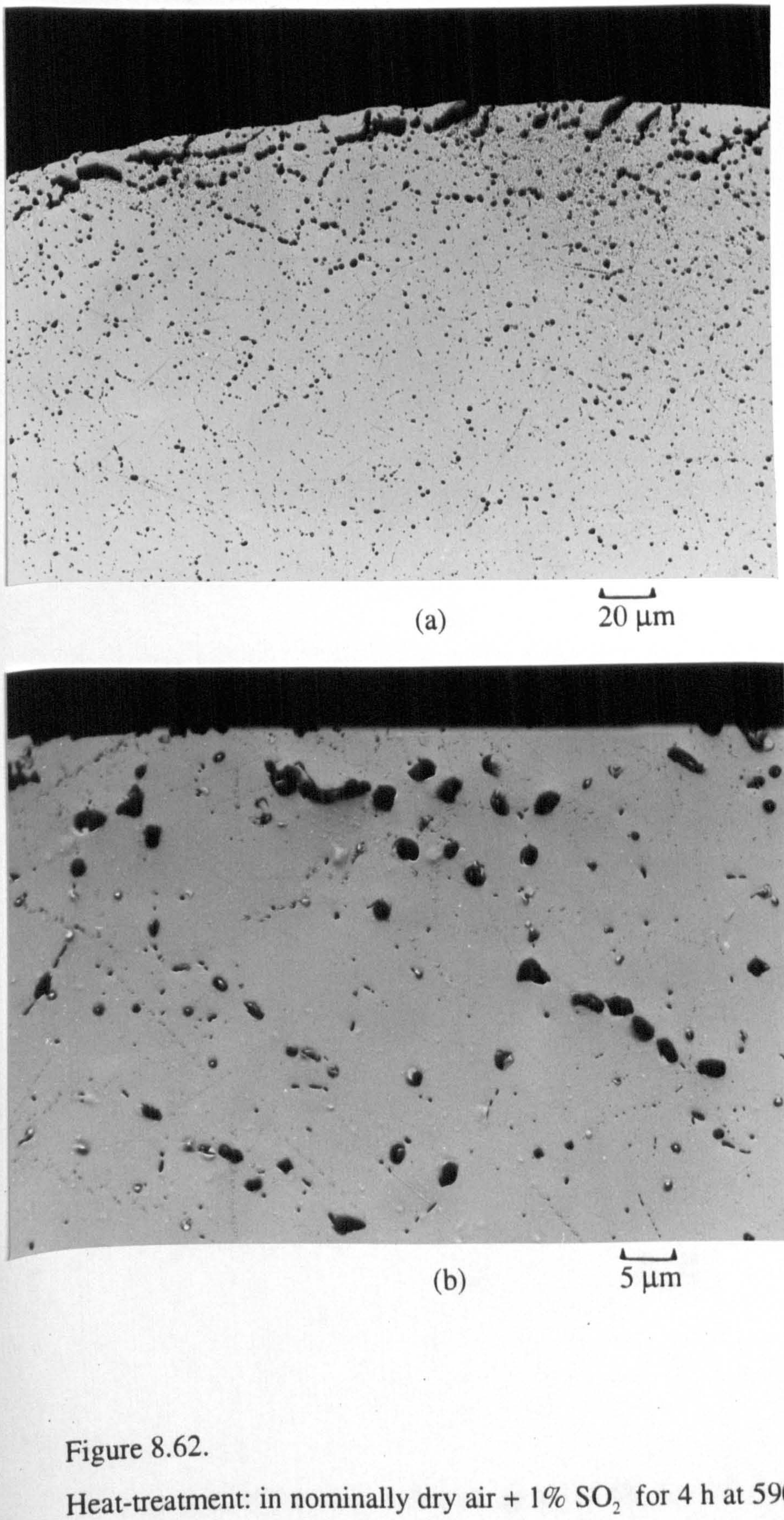

Figure 8.62.

Heat-treatment: in nominally dry air + 1% SO_2 for 4 h at 590°C.

Hydrogen content: 0.80 cm^3/100g.

Unetched. (a) x 100 (b) x 400.

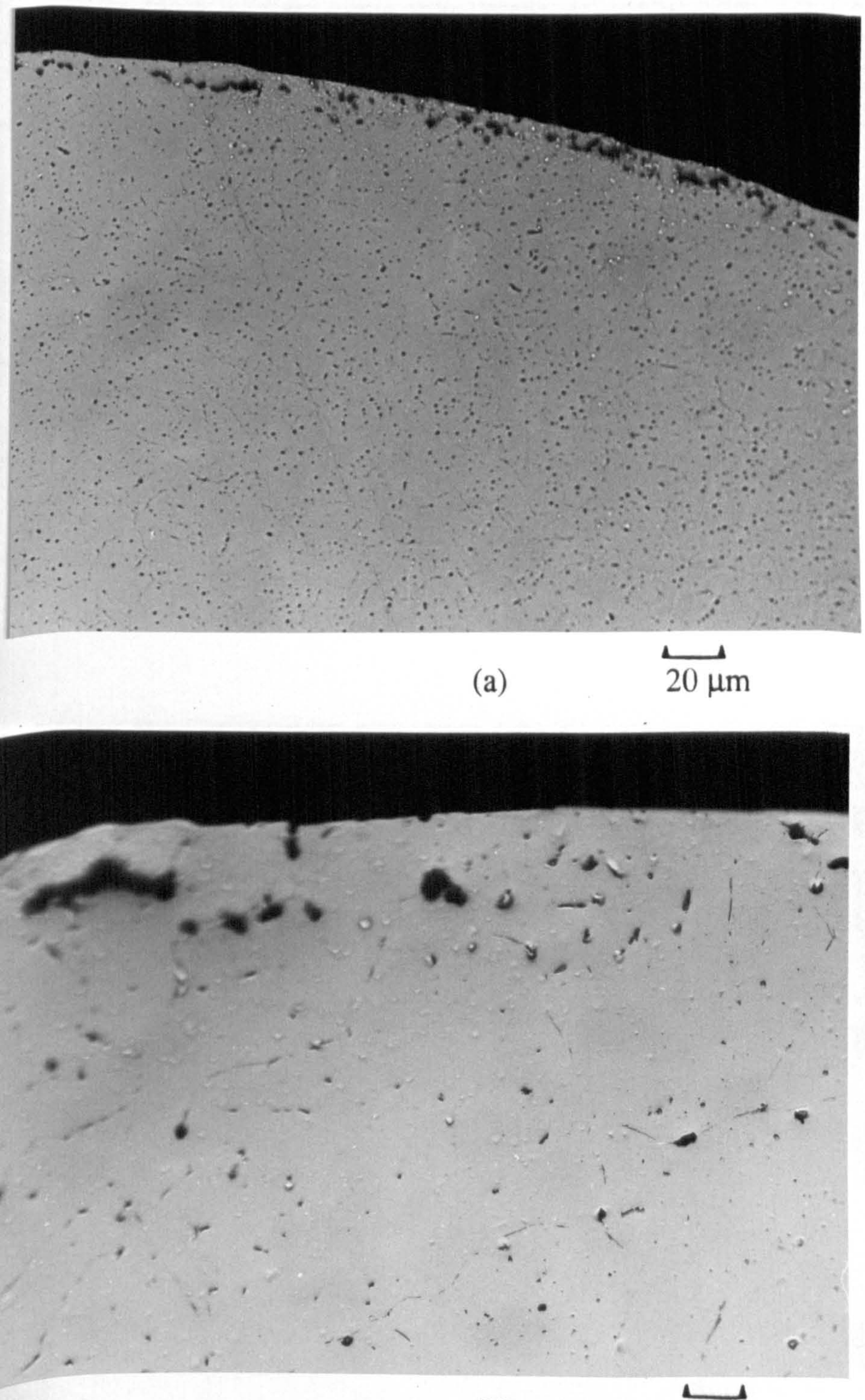

Figure 8.63.

Heat-treatment: in water saturated air + 1% SO_2 for 8 h at 500°C.

Hydrogen content: 0.91 cm^3/100g.

Unetched. (a) x 100 (b) x 400.

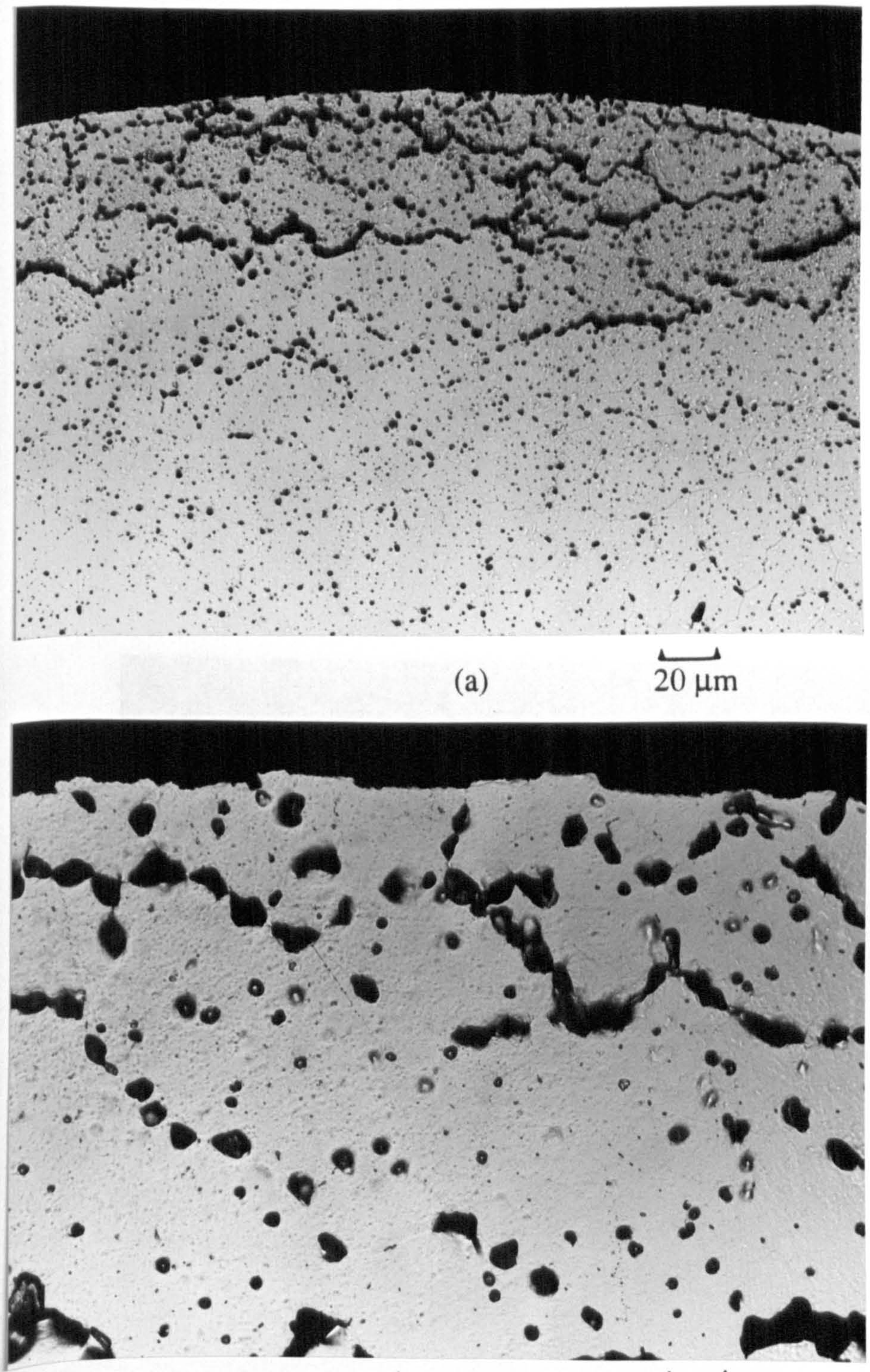

Figure 8.64.

Heat-treatment: in water saturated air + 1% SO_2 + HCl for 8 h at 590°C.

Hydrogen content: 1.08 $cm^3/100g$.

Unetched. (a) x 100 (b) x 400.

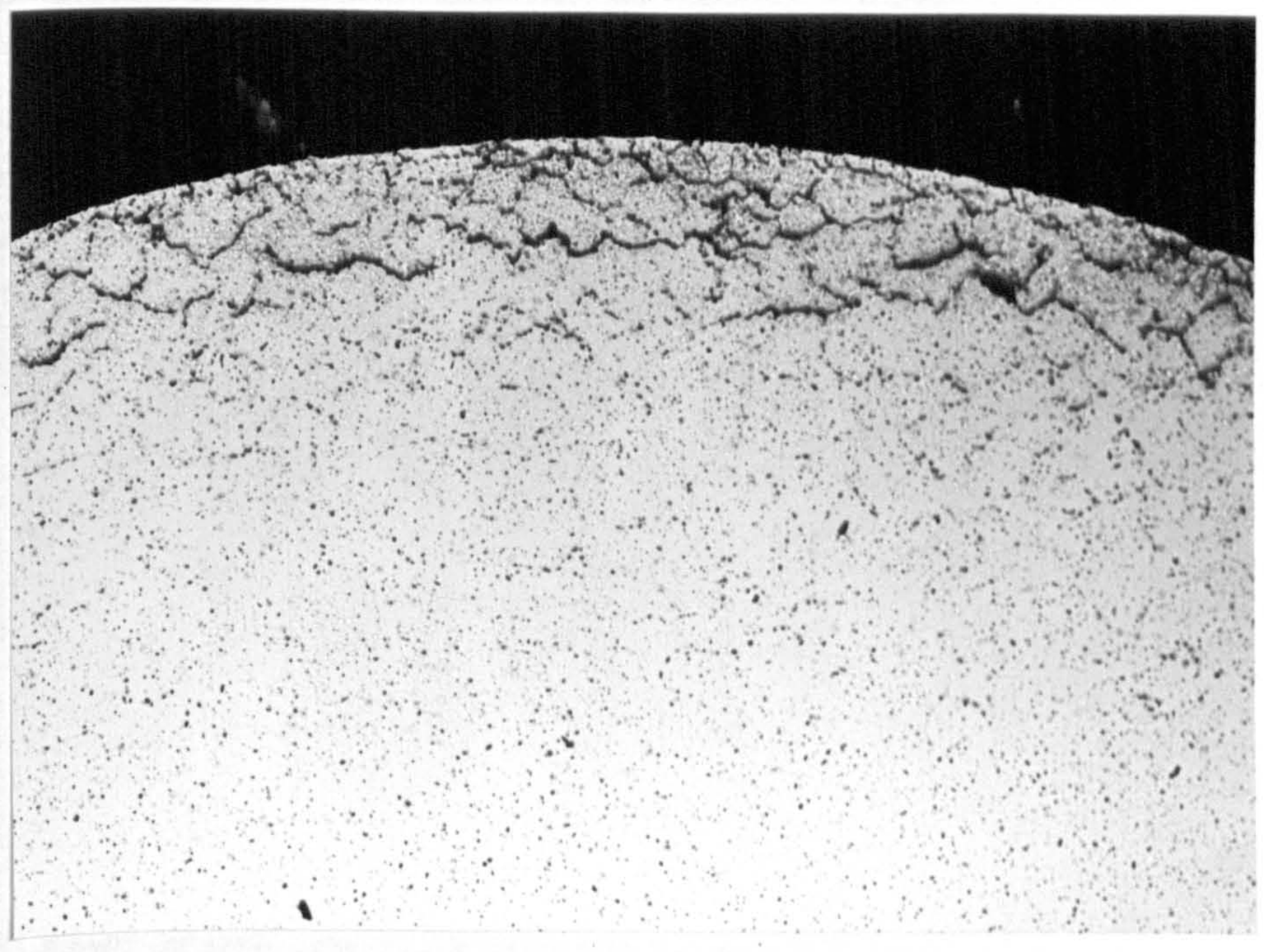

Figure 8.65.

Heat-treatment: in water saturated air + 1% SO_2 + HCl for 8 h at 590°C.

Hydrogen content: 1.08 $cm^3/100g$.

Unetched. x 50

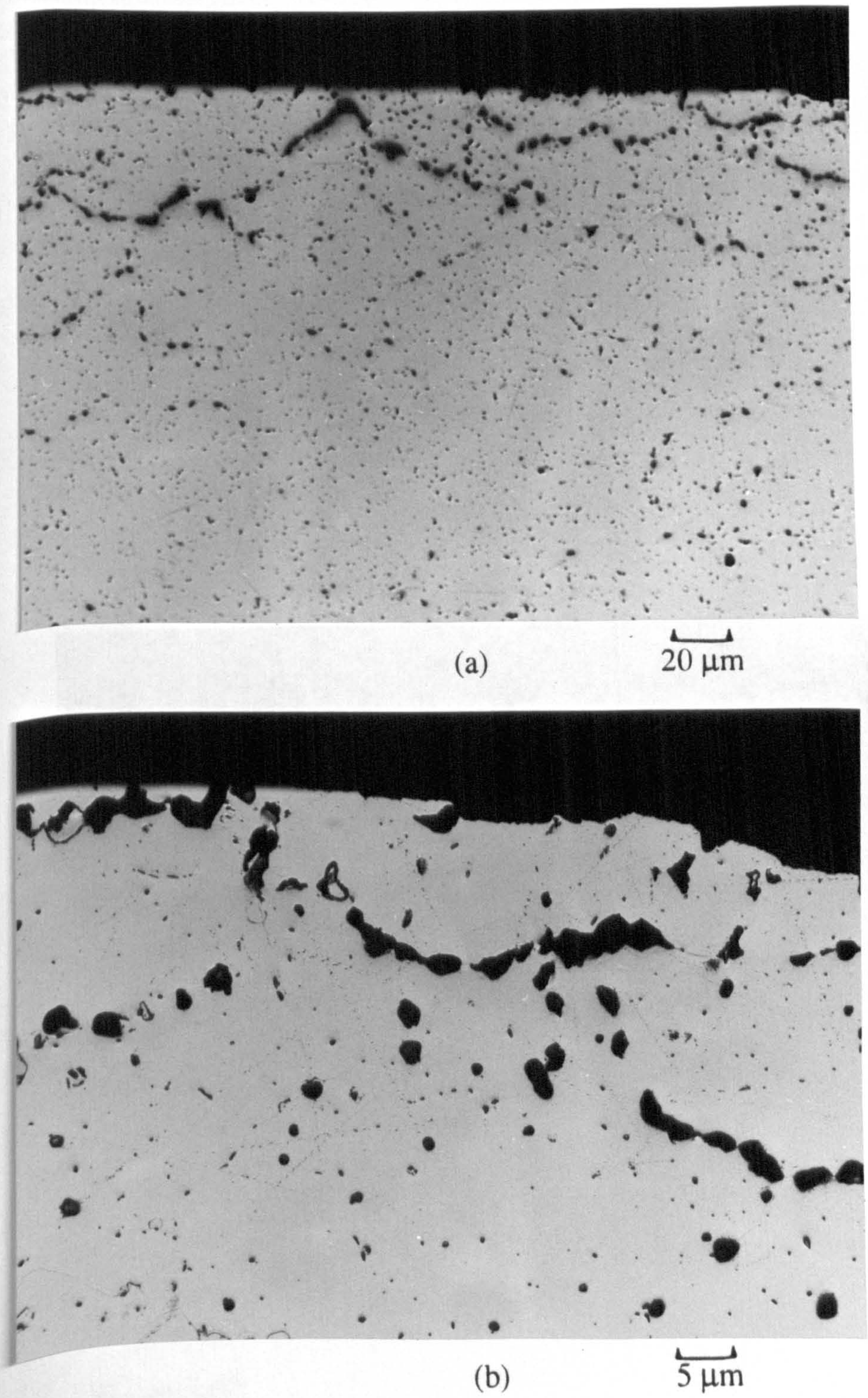

Figure 8.66.

Heat-treatment: in nominally dry air + 1% SO_2 for 8 h at 590°C.

Hydrogen content: 1.13 cm^3/100g.

Unetched. (a) x 100 (b) x 400.

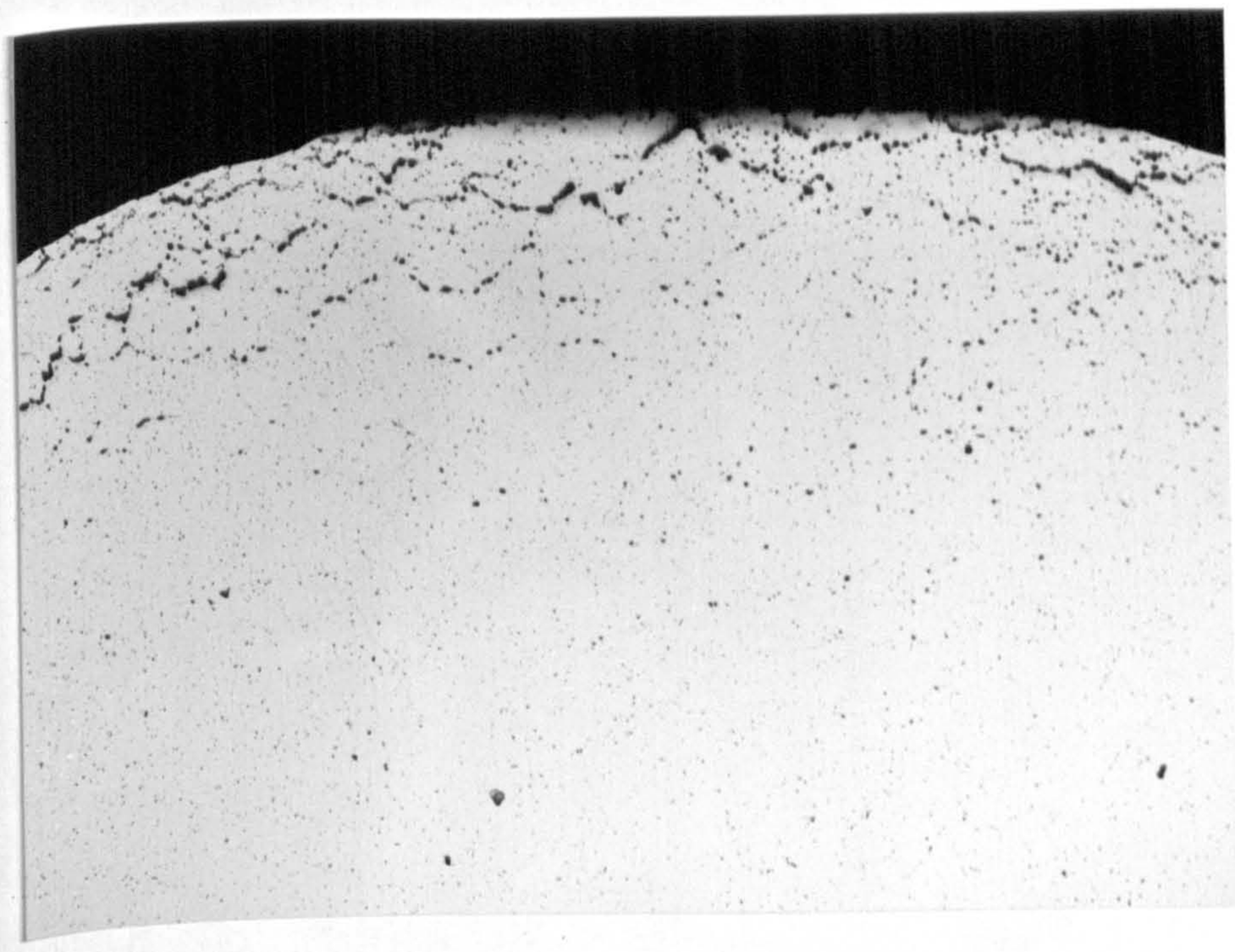

40 µm

Figure 8.67.

Heat-treatment: in nominally dry air + 1% SO_2 for 8 h at 590°C.

Hydrogen content: 1.13 cm^3/100g.

Unetched. x 50.

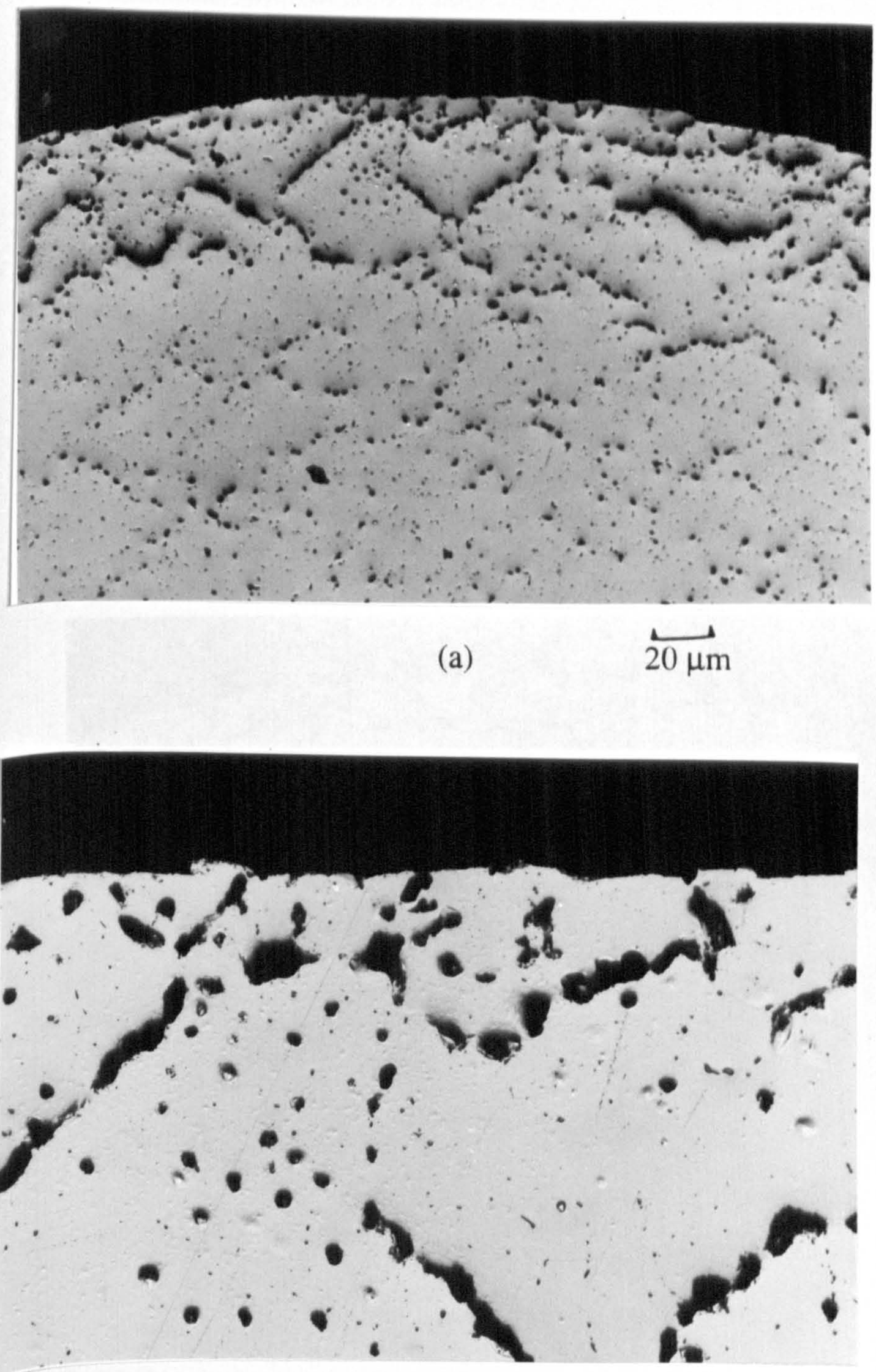

Figure 8.68.

Heat-treatment: in water saturated air + 1% SO_2 for 4 h at 590°C.

Hydrogen content: 1.29 $cm^3/100g$.

Unetched. (a) x 100 (b) x 400.

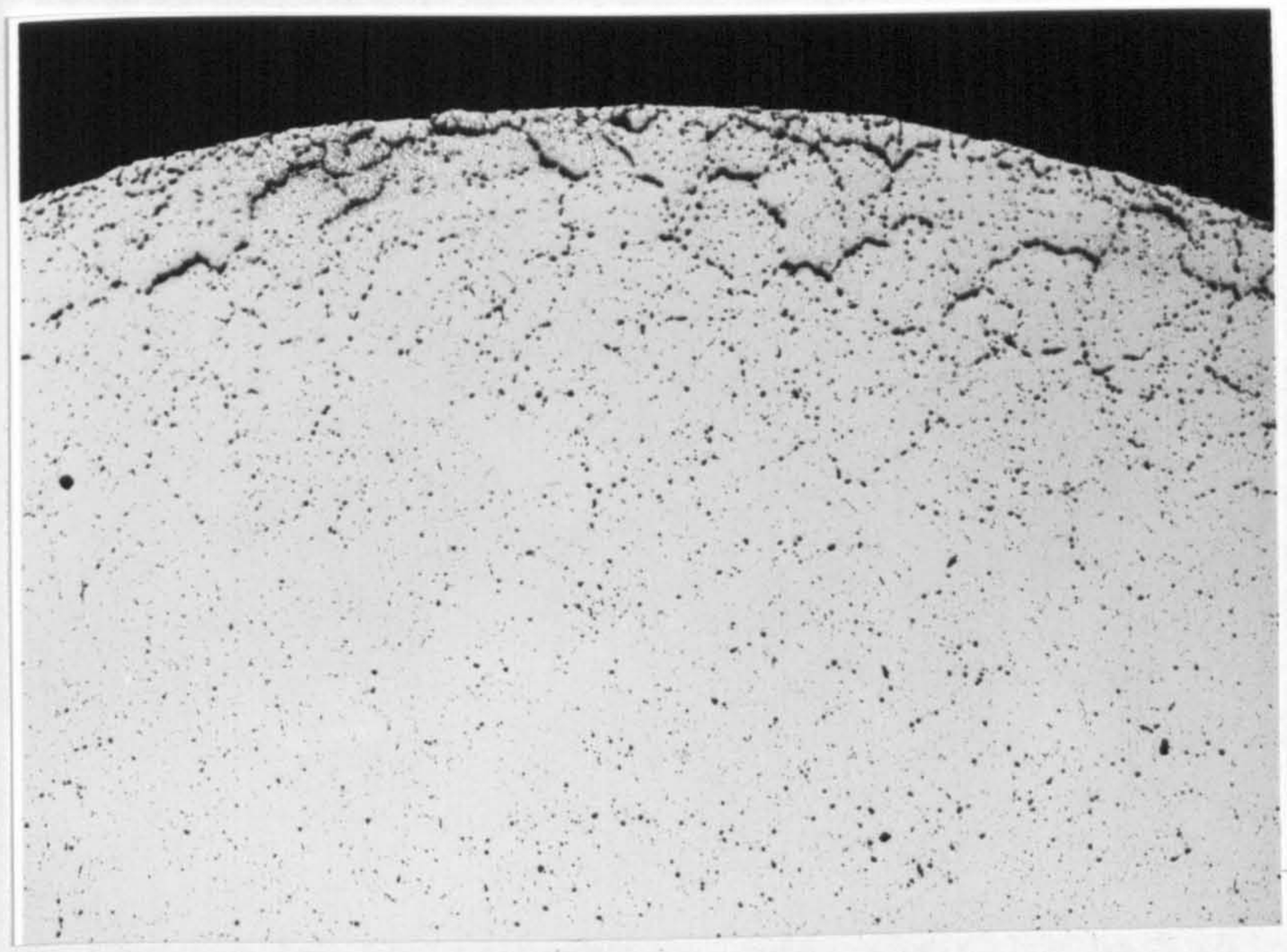

Figure 8.69.

Heat-treatment: in water saturated air + 1% SO_2 for 4 h at 590°C.

Hydrogen content: 1.29 $cm^3/100g$.

Unetched. x 50.

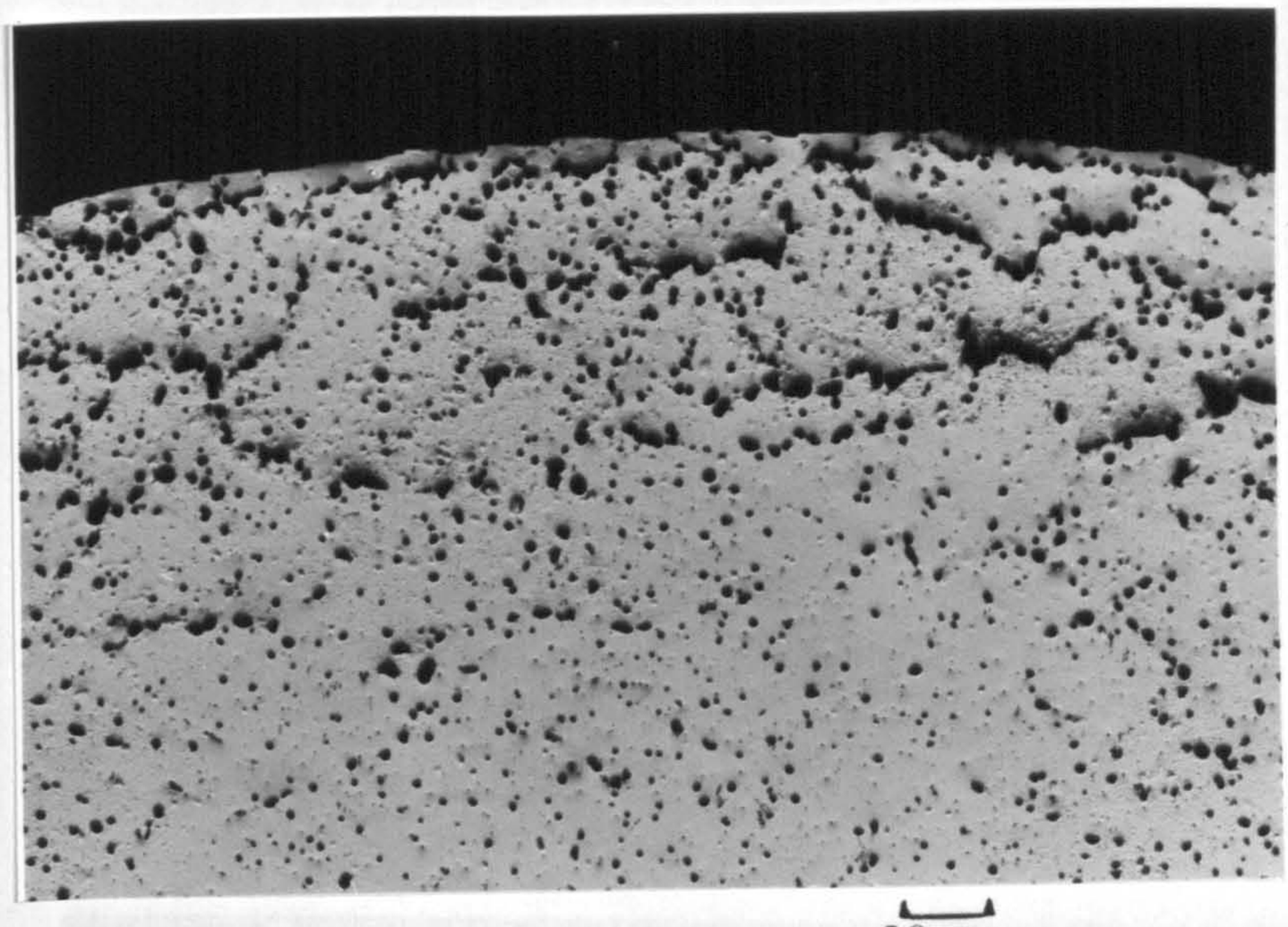

(a) 20 µm

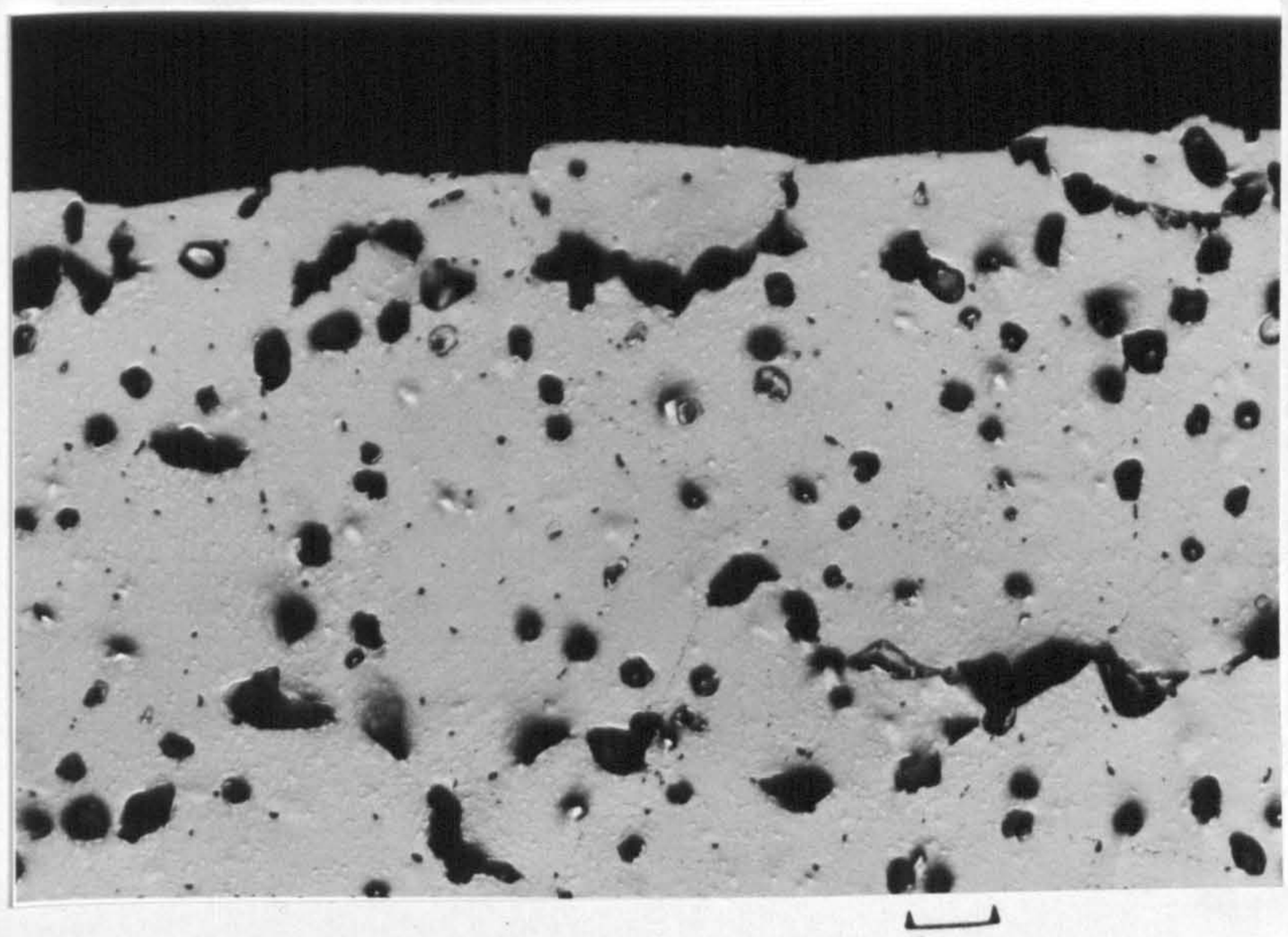

(b) 5 µm

Figure 8.70.

Heat-treatment: in water saturated air + 1% SO_2 for 6 h at 590°C.

Hydrogen content: 2.04 cm^3/100g.

Unetched. (a) x 100 (b) x 400.

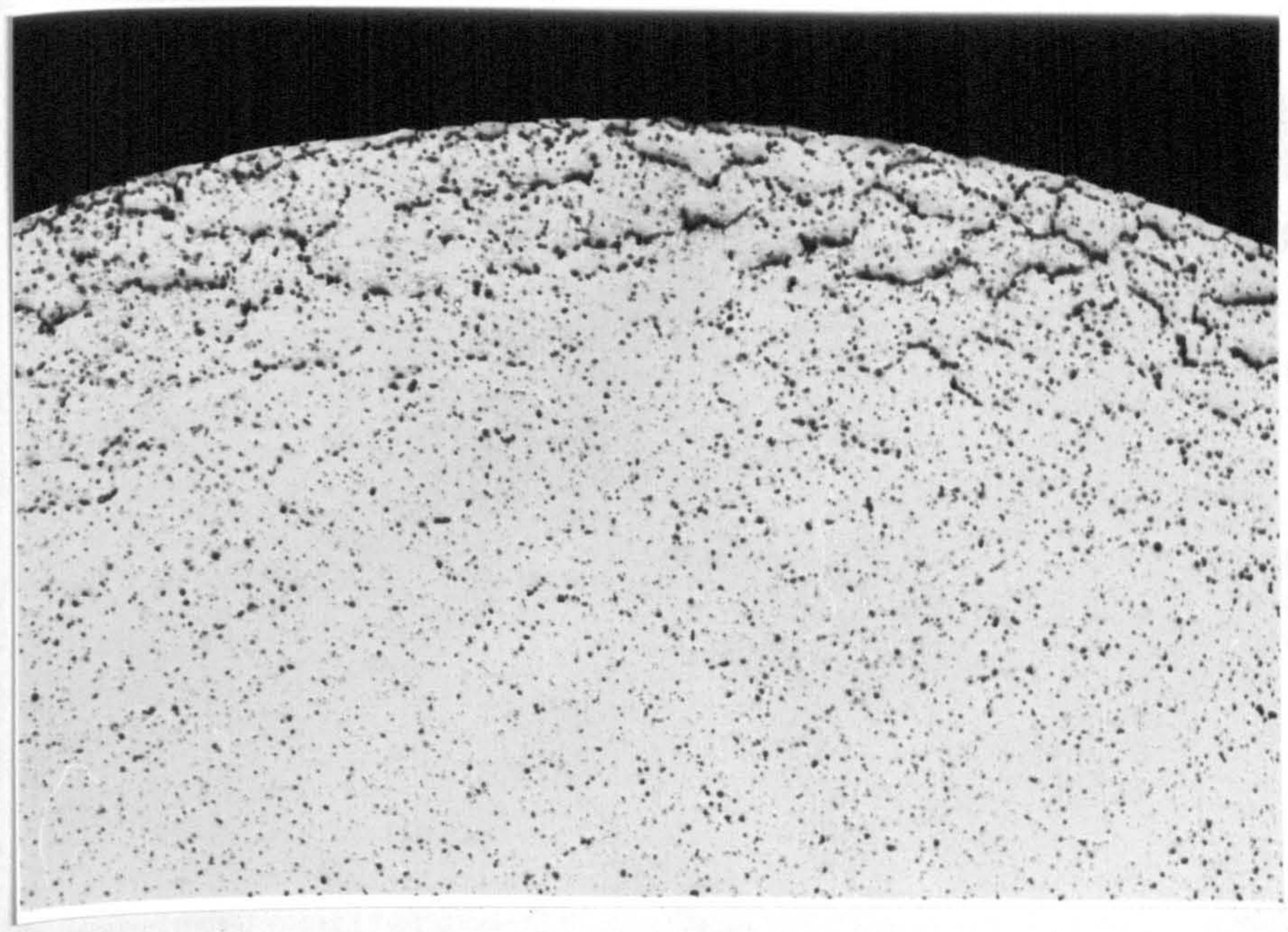

Figure 8.71.

Heat-treatment: in water saturated air + 1% SO_2 for 6 h at 590°C.

Hydrogen content: 2.04 cm^3/100g.

Unetched. x 50.

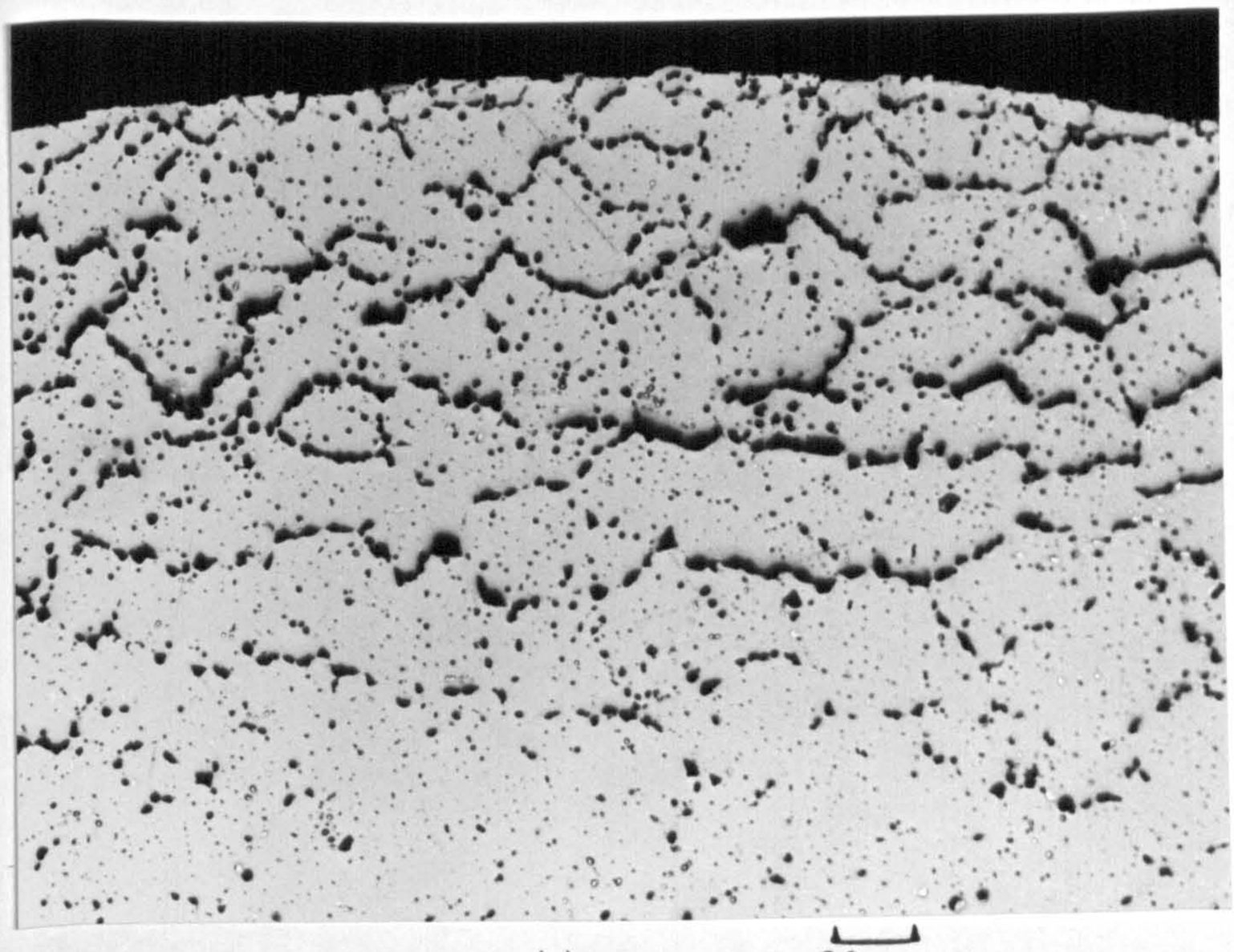

(a) 20 µm

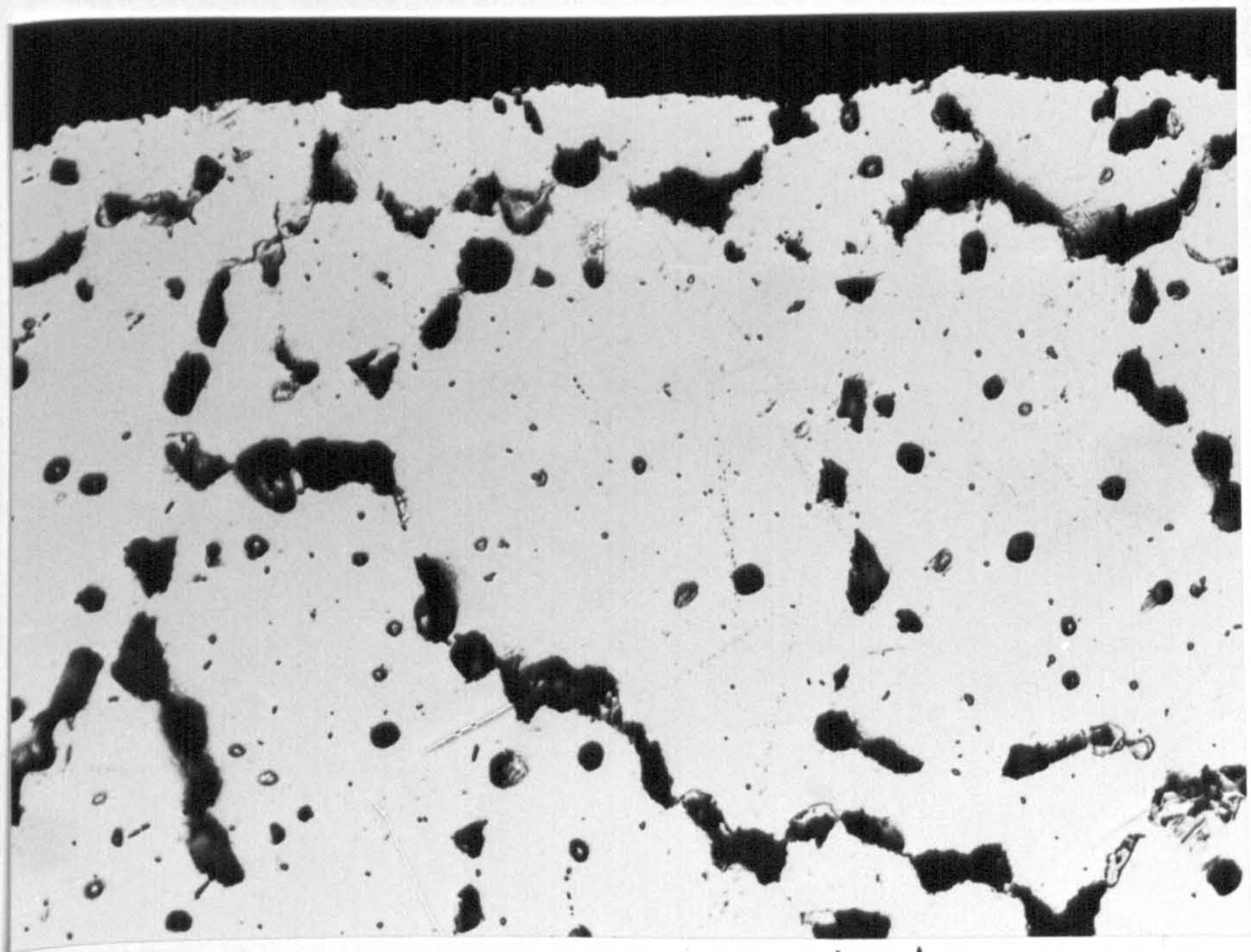

(b) 5 µm

Figure 8.72.

Heat-treatment: in water saturated air + 1% SO_2 for 8 h at 590°C.

Hydrogen content: 2.83 cm^3/100g.

Unetched. (a) x 100 (b) x 400.

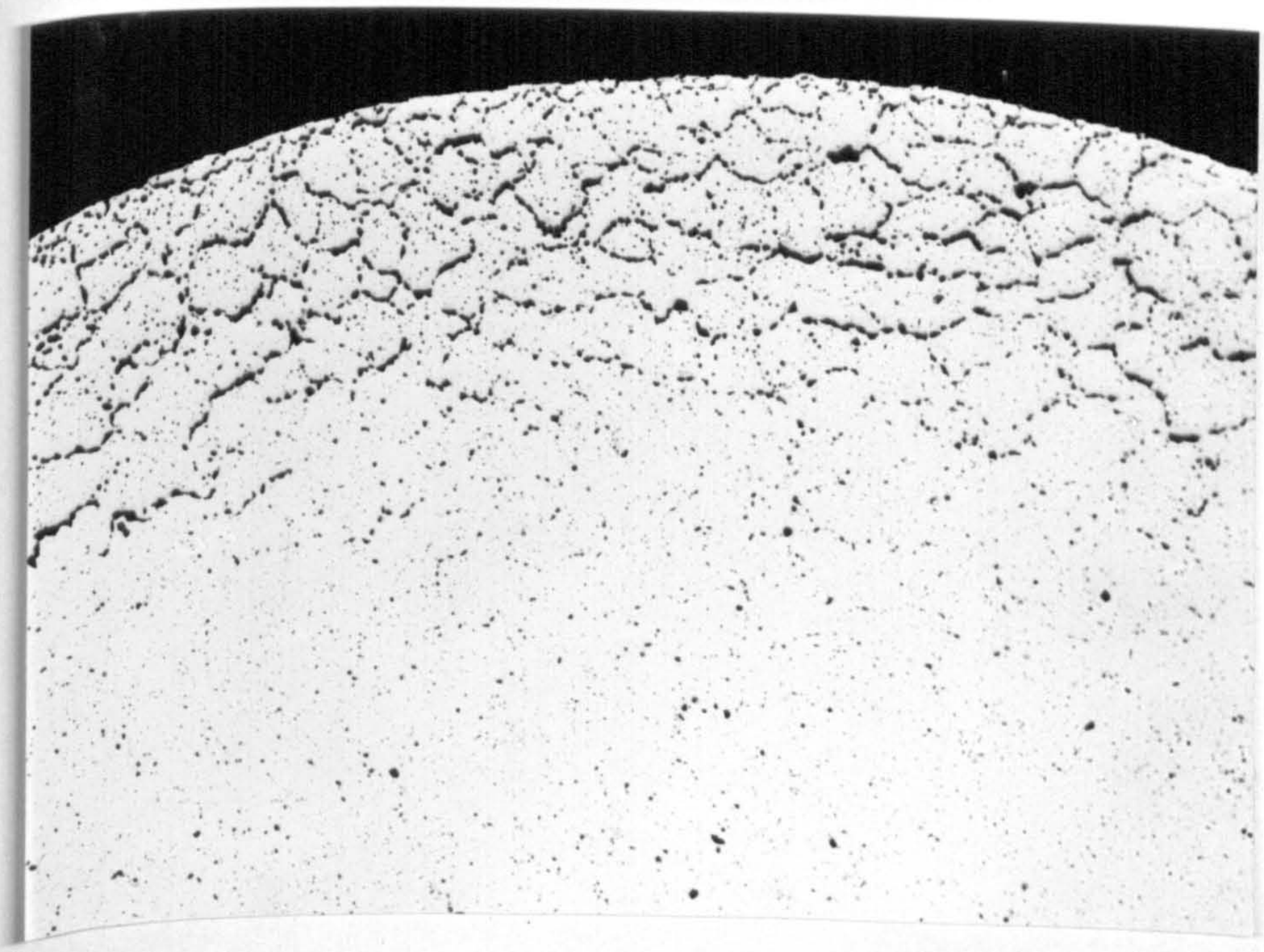

Figure 8.73.

Heat-treatment: in water saturated air + 1% SO_2 for 8 h at 590°C.

Hydrogen content: 2.83 cm^3/100g.

Unetched. x 50.

9. DISCUSSION

There are five aspects to the present work to be considered:

- The effects of industrial operations on the hydrogen content of liquid metal.
- The distribution of hydrogen in an industrial cast ingot and in the corresponding material after homogenisation in the prevailing industrial conditions.
- The influences of temperature and environment on the hydrogen content of the solid metal after laboratory heat-treatments simulating industrial homogenisation.
- Damage to the metal by hydrogen absorbed during the laboratory heat-treatments.
- The influence of the environment on the nature of the oxide formed on the metal surface and on the susceptibility of the metal to hydrogen absorption or loss.

9.1 Effects Of Industrial Operations On The Hydrogen Content Of Liquid Metal

The average results from Tables 8.1 to 8.3 are plotted in Figures 9.1 to 9.3 to show changes in hydrogen content of the metal throughout the process for Casts 1, 2 and 3.

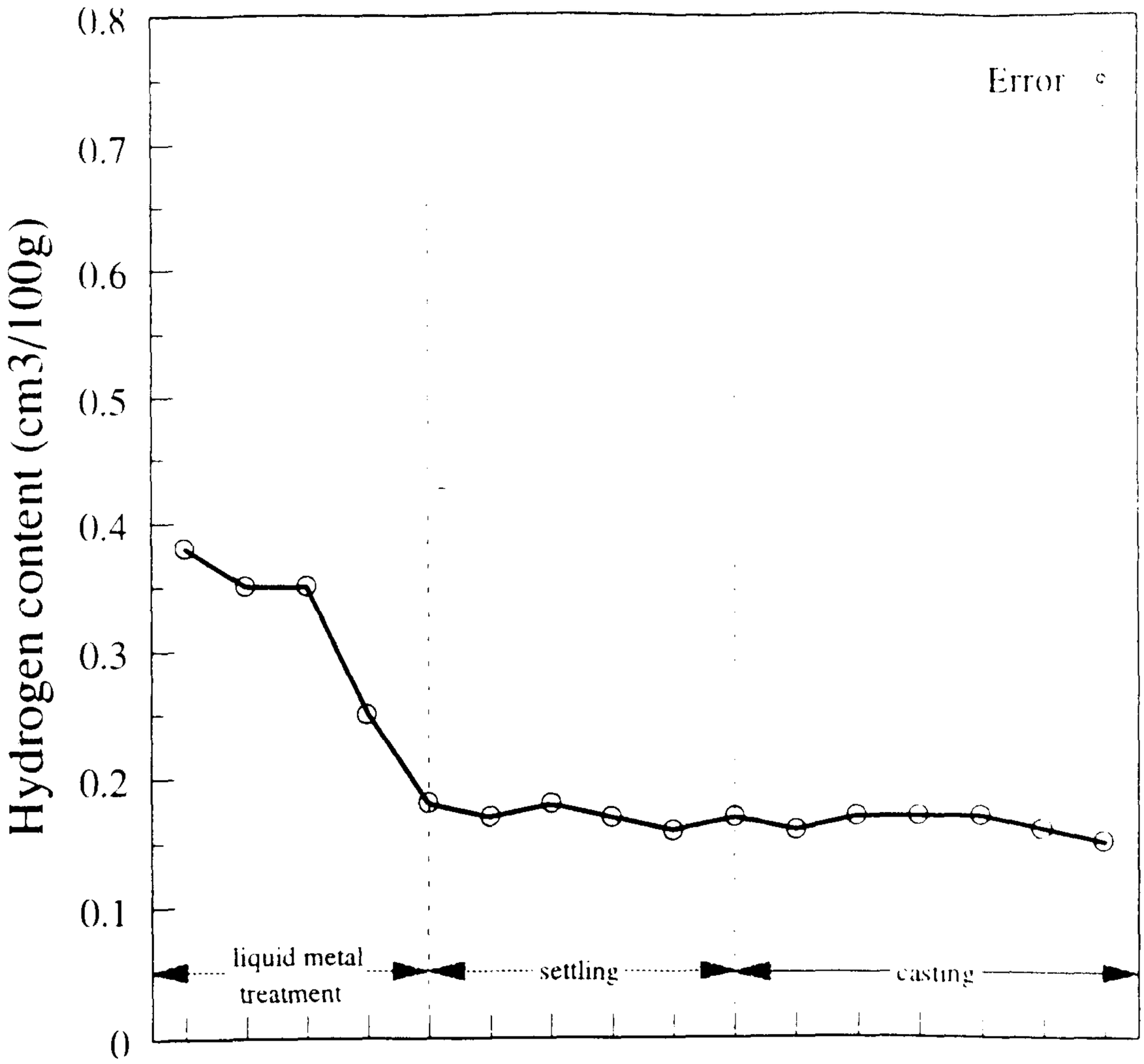

Figure 9.1 Hydrogen content of liquid metal throughout processing - Cast 1.

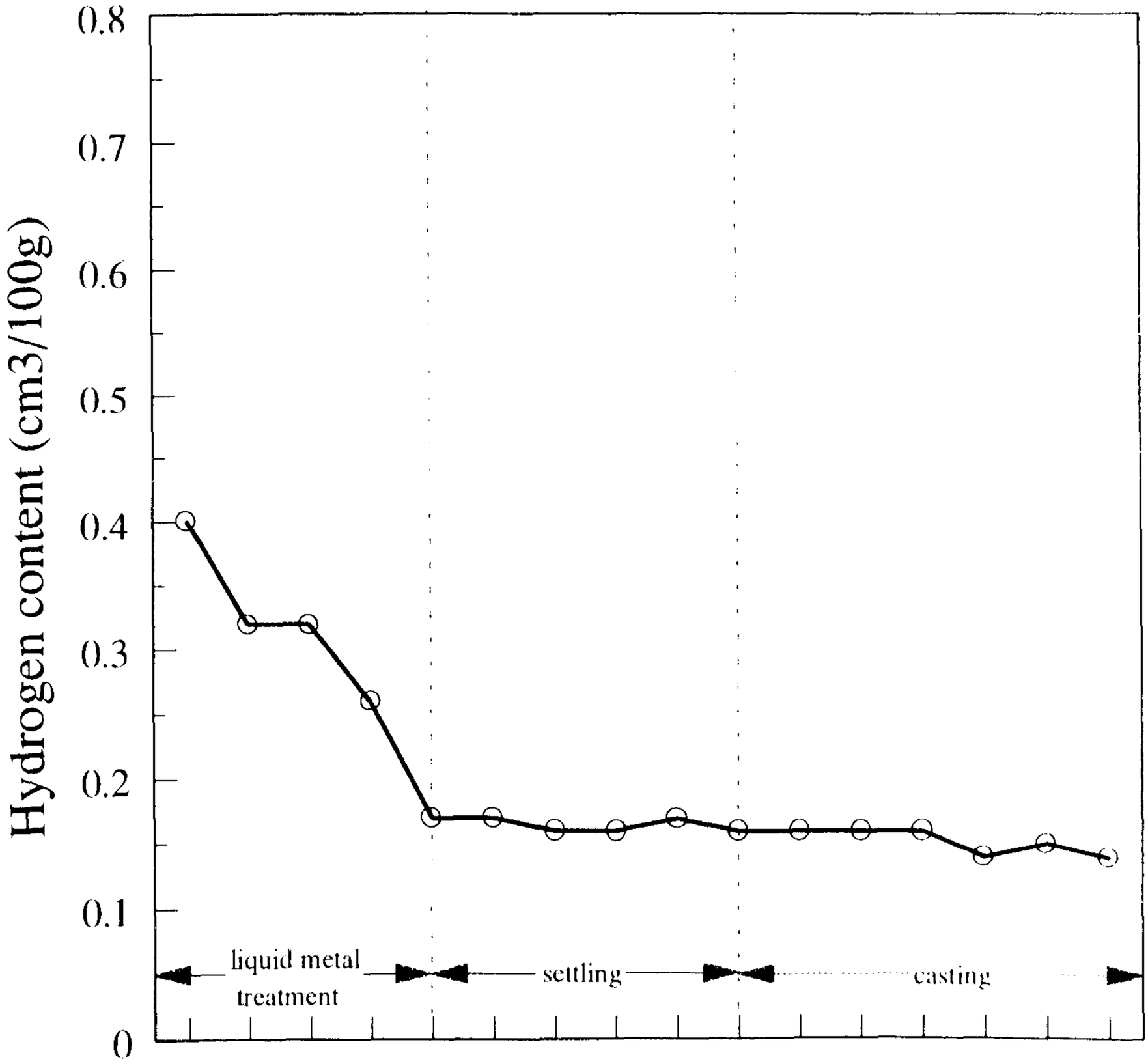

Figure 9.2 Hydrogen content of liquid metal throughout processing - Cast 2.

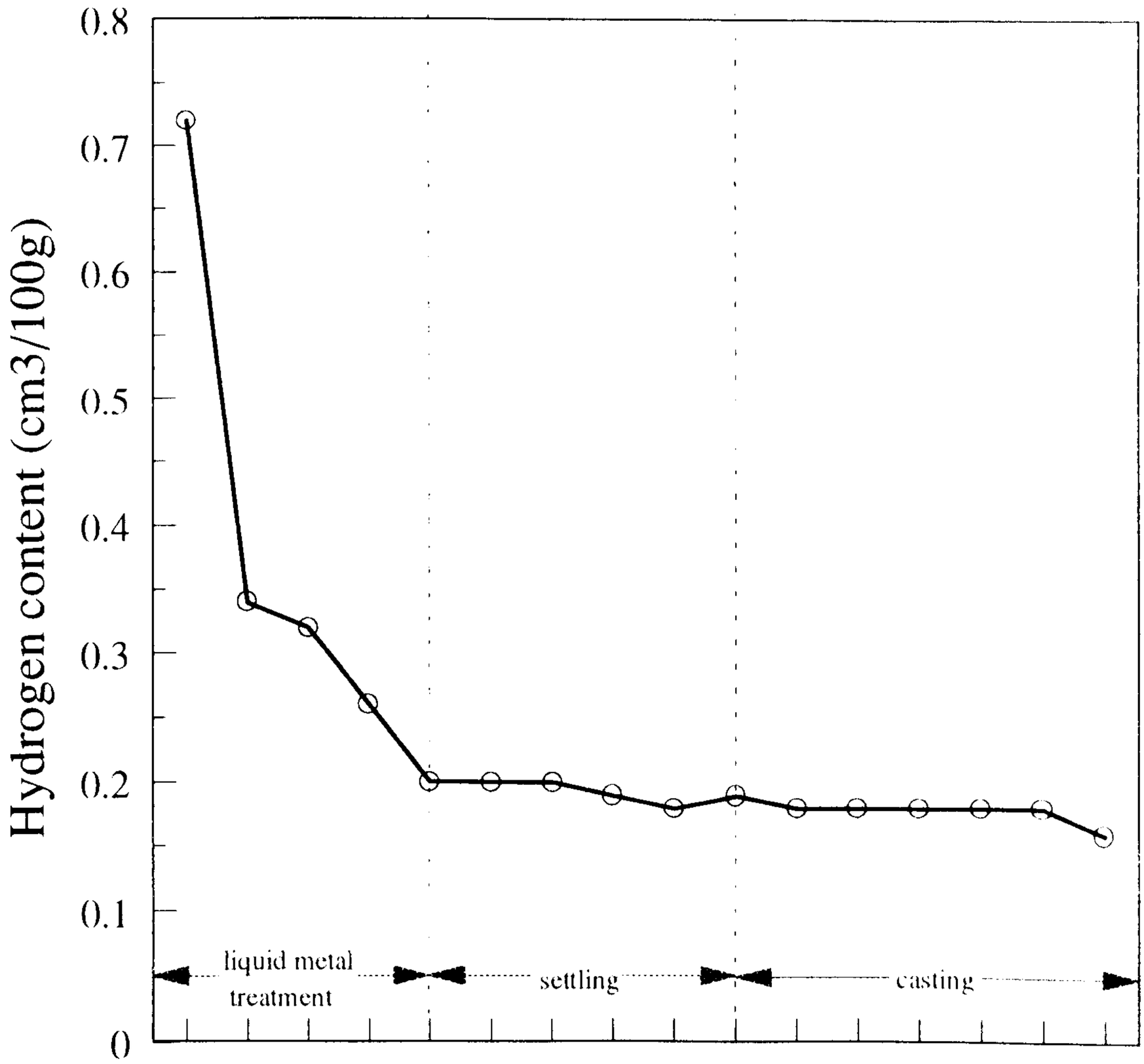

Figure 9.3 Hydrogen content of liquid metal throughout processing - Cast 3.

9.1.1 The basis of assessment

The hydrogen content of the metal must be considered in relation to the hydrogen content acceptable in the cast ingots. The essence of the discussion, given in Section 4.3.1 and illustrated in Figure 4.8, is that there exists threshold hydrogen contents below which ingots are free from interdendritic porosity and hence acceptable for fabricated products for less critical applications. The threshold values depend on alloy composition and ingot dimensions and are known for only a few standard alloys and ingot sizes[115, 135, 163,165] but industrial requirements can be assessed from the information given in Table 4.9 which shows that known threshold values are in the range 0.12 to 0.17 $cm^3/100$ g. Thus to ensure that ingots are free from interdendritic porosity, a reasonable criterion is to set a limit of 0.17 $cm^3/100$ g but to strive to reduce the hydrogen content to below 0.12 $cm^3/100$g.

The three stages in the process are:

i. Liquid metal treatment ii. Settling iii. Casting

These will now be considered in turn because different considerations apply.

9.1.2 Liquid Metal Treatment

The liquid metal is treated in the following sequences:

i. It is transferred in a crucible from the reduction pot-line to the melting furnace.
ii. Its approximate composition is established by stirring in alloying elements.
iii. It is transferred by launder from the melting furnace to the holding furnace.
iv. Its composition is adjusted by stirring in trimming alloy additions.
v. It is degassed by manually immersing tablets of hexachlorethane and skimmed.

Hydrogen contents, taken from Figures 9.1 to 9.3, are re-plotted in Figures 9.4 to 9.6 to show the detailed treatments and corresponding metal temperatures during this stage

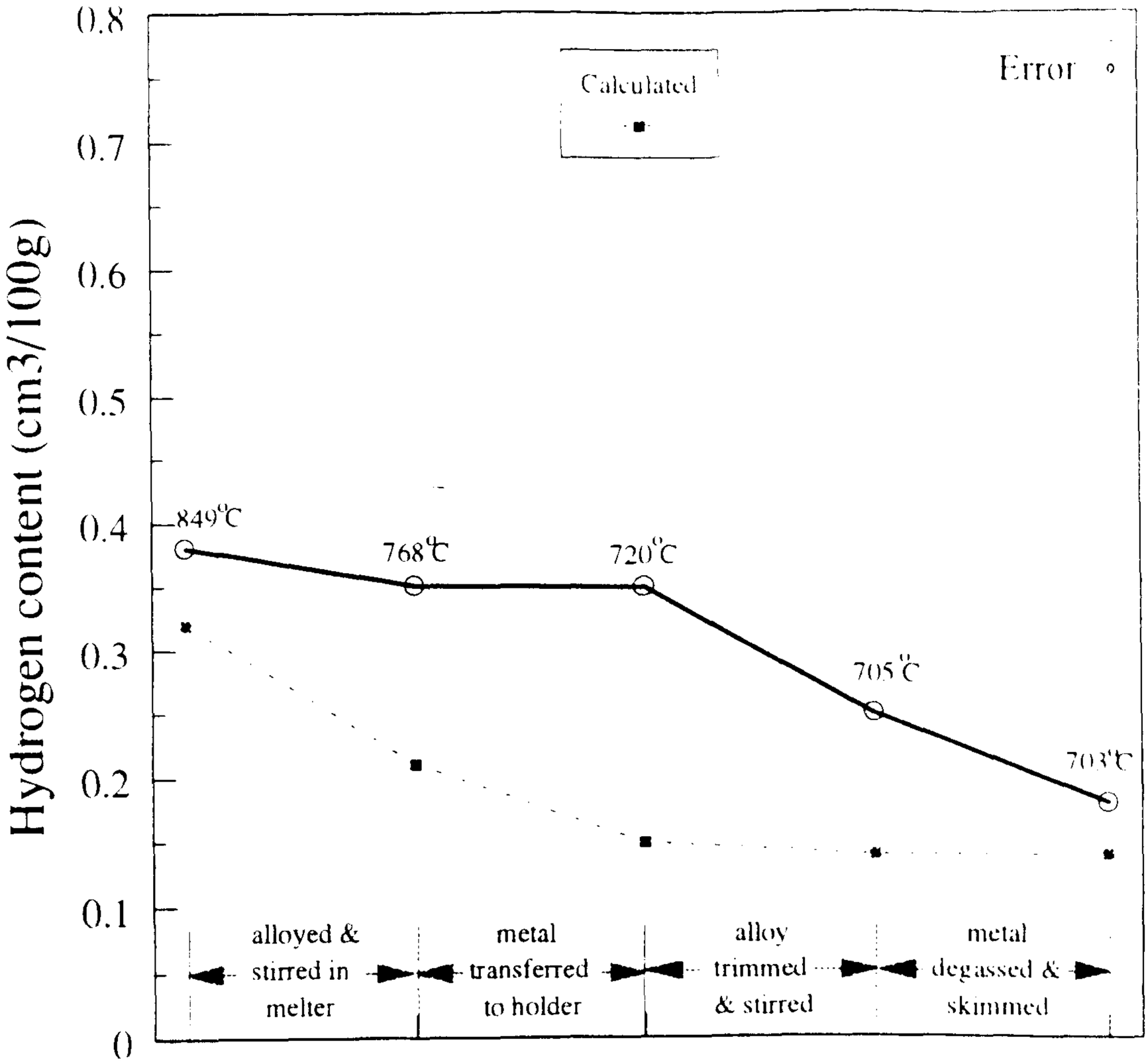

Figure 9.4 Hydrogen content of liquid metal during metal treatment - Cast 1.

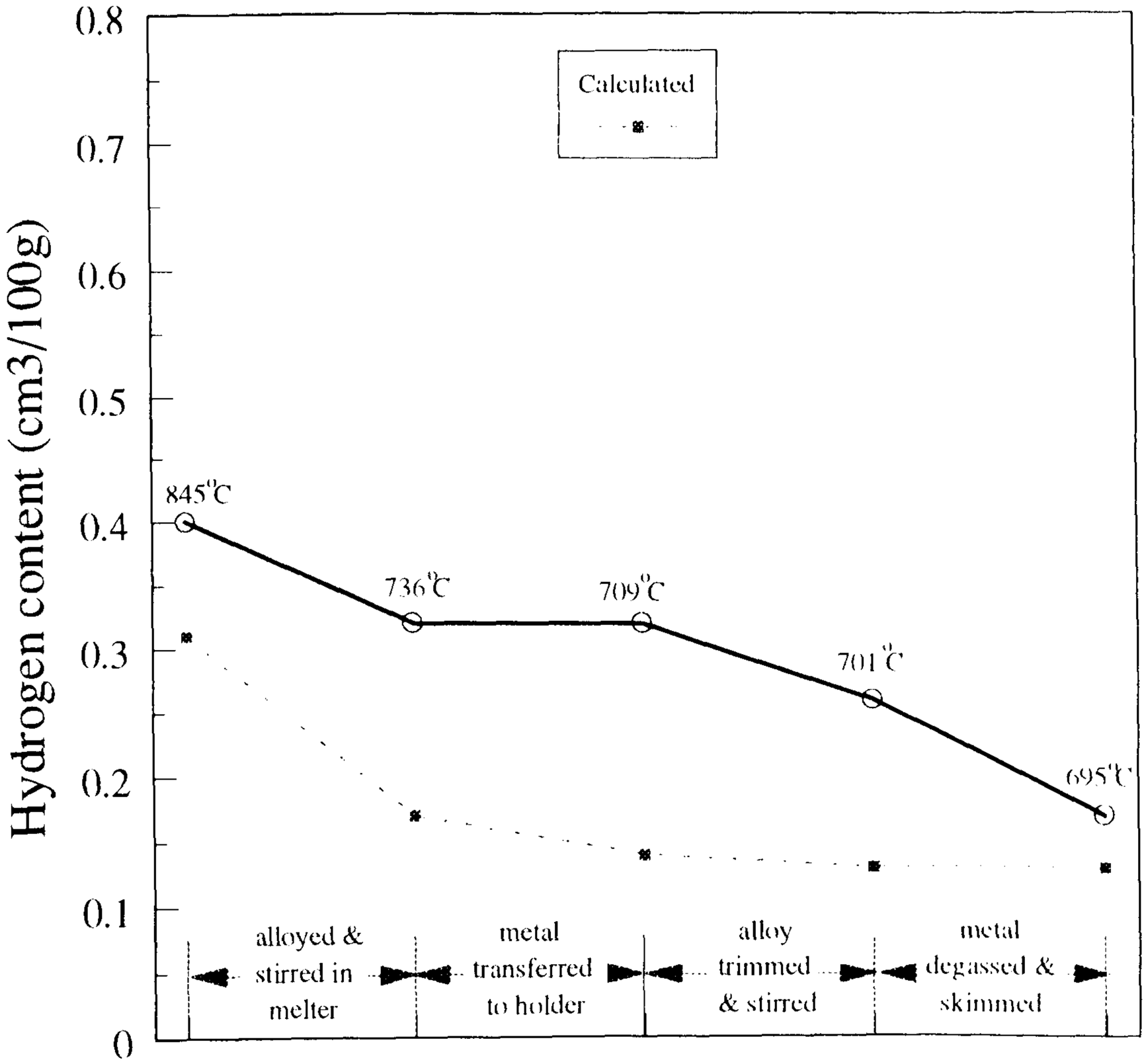

Figure 9.5 Hydrogen content of liquid metal during metal treatment - Cast 2.

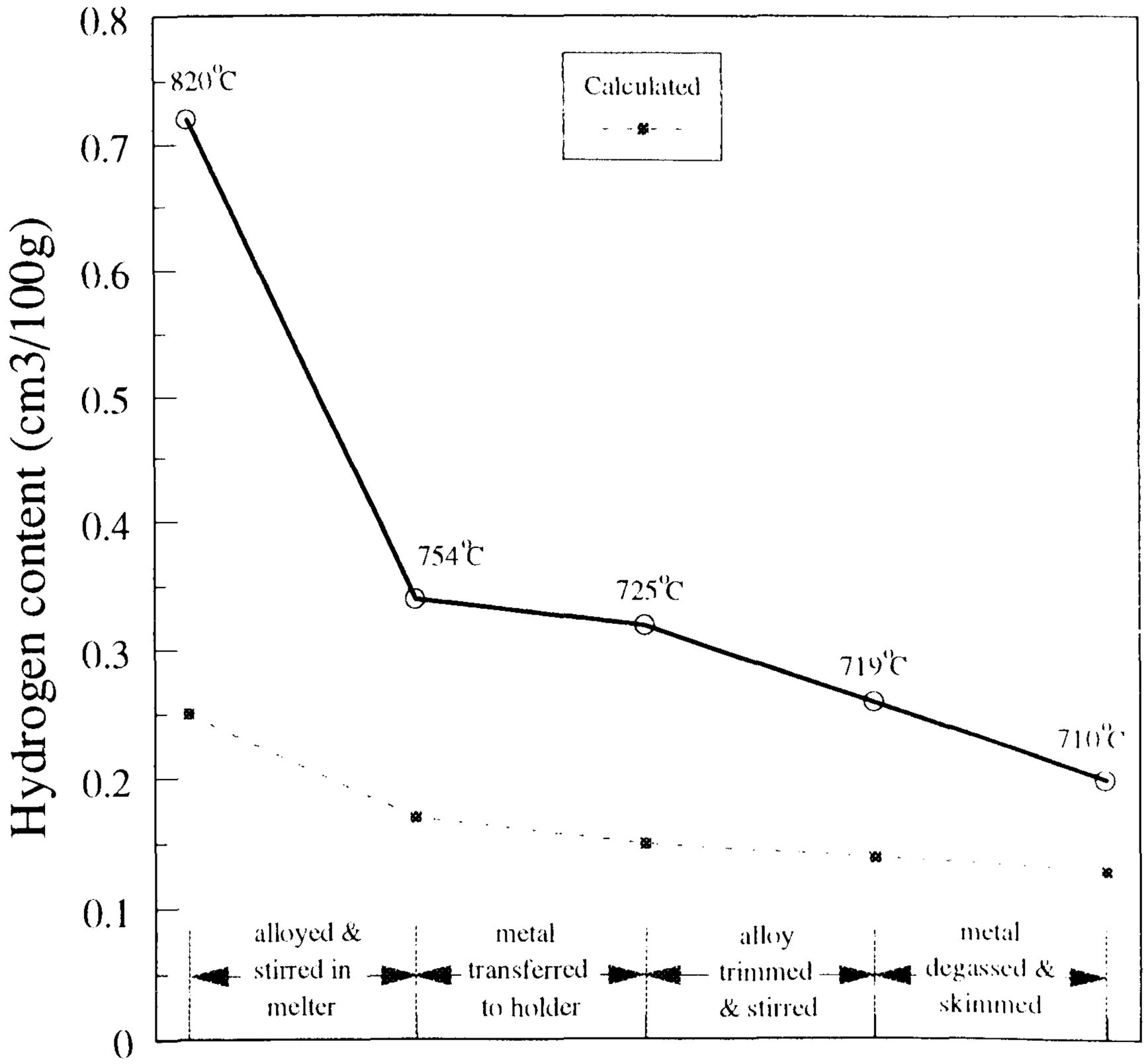

Figure 9.6 Hydrogen content of liquid metal during metal treatment - Cast 3.

Figures 9.4 to 9.6 all show that by the criteria presented in Section 9.1.1, the hydrogen contents of the metal as delivered from the pot line into the melting furnace is much too high. The hydrogen content falls progressively as the metal is alloyed and stirred, transferred to the holding furnace, trimmed to specification by further alloying and degassed. Two features of these result merit attention

i. The temperature of the metal falls progressively from its initial value of 830 +/- 10 °C to 700 +/- 10 °C at the end of the sequence of operations.

ii. All of the operations disturbed the metal to a greater or lesser degree. The metal was stirred after each of the two alloying sequences, it flowed along a launder during transfer from the melting furnace to the holding furnace and it experienced vigorous agitation during degassing.

9.1.2.1 Effect of temperature

An effect of temperature is expected, because the solubility of hydrogen is temperature-dependent. Ransley and Talbot[135] found that if a large mass, 15 tonnes, of pure aluminium was exposed to the atmosphere at a constant temperature for several hours, its hydrogen content approached a pseudo-equilibrium with the water vapour pressure of the atmosphere as if it were a hydrogen pressure, so that the hydrogen content could be predicted by modifying Sieverts' relation as below:

$$H = S\sqrt{p\left(H_2\right)} = S\sqrt{p\left(H_2O\right)} \tag{9.1}$$

If the solubility, S, of any particular alloy is known, Equation 9.1 yields values for "theoretical equilibrium hydrogen contents" by inserting the prevailing metal temperatures and water vapour pressures. This causes an apparent problem because as mentioned in Section 4.7.3, accurate values for solubility are available for only a few alloys, which do not include aluminium-magnesium alloys. This is because of experimental difficulties associated with the volatility of magnesium. Fortunately the solubility of hydrogen in a liquid aluminium-1%Mg alloy has been estimated[206] and found to be slightly higher than for pure aluminium, but by no more than 10%. For the AA6063 alloys used in the present work, which contain approximately 0.5%Mg, the solubility can be taken as equal to the solubility in pure aluminium, with the reservation that a calculation based on Equation 9.1 could be in error by up to - 10%.

Hydrogen contents calculated on this basis for Casts 1, 2 and 3 are given in the last column of Table 9.1 and plotted by the dashed line in Figures 9.4 to 9. 6.

Table 9.1 Hydrogen content calculated from prevailing metal temperatures and water vapour pressure.

	Sample	T/°C	T/K	S* $cm^3/100g$	p** (H_2O)	Calculated hydrogen $cm^3/100g$
CAST 1	Crucible, before charging into melter	849	1122	2.06	0.024	0.32
	Melter, after alloying & stirring	768	1041	1.34	0.024	0.21
	Holder, after transfer	720	993	1.00	0.024	0.15
	Holder, after alloy trimming & stirring	705	978	0.90	0.024	0.14
	Holder, after degassing	703	976	0.89	0.024	0.14
CAST 2	Crucible, before charging into melter	845	1118	2.02	0.023	0.31
	Melter, after alloying & stirring	736	1009	1.11	0.023	0.17
	Holder, after transfer	709	982	0.93	0.023	0.14
	Holder, after alloy trimming & stirring	701	974	0.89	0.023	0.13
	Holder, after degassing	695	968	0.85	0.023	0.13
CAST 3	Crucible, before charging into melter	820	1093	1.78	0.020	0.25
	Melter, after alloying & stirring	754	1027	1.23	0.020	0.17
	Holder, after transfer	725	998	1.03	0.020	0.15
	Holder, after alloy trimming & stirring	719	992	1.00	0.020	0.14
	Holder, after degassing	710	983	0.94	0.020	0.13

* Assumed equal to the solubility in pure aluminium[194].
** Calculated from relative humidities given in Tables 8.1 to 8.3.

Comparison of the actual values with the calculated values shows that the hydrogen content of the metal was always higher than the assumed equilibrium hydrogen content.

9.1.2.2 Effect of agitation

In all three casts the hydrogen content approached equilibrium most rapidly when the metal was vigorously agitated. The hydrogen content changed very little during the relatively quiescent operation of transferring the metal by launder from the holding furnace to the melting furnace, despite a considerable difference between the actual and calculated equilibrium values of hydrogen content and a significant fall in temperature, i.e. 48, 25 and 29°C in Casts 1, 2 and 3 respectively. In contrast, the alloying operation with stirring in the holding furnace was associated with a useful reduction in hydrogen although the temperatures fell by only 15, 8 and 6 °C respectively.

In all three casts, stirring in the holding furnace was as effective as degassing in reducing the hydrogen content.. This raises some doubt about the real mechanism of

furnace degassing. It is generally assumed, *without proof*, that it functions by a purging action in which hydrogen is removed by transfer of hydrogen from solution in the metal to the bubbles of purge gas as they ascend through the metal as explained e.g. by Geller[207]. The present results suggest that it is equally possible that the hydrogen is removed at the surface, as it is with stirring because of the vigorous agitation of the metal due to the injection of the purge gas. There is good reason to question the efficiency of furnace degassing because holding furnaces are of the reverberatory type, designed with a wide, shallow baths for good thermal transfer from the flame and ease of operation. They are geometrically incompatible with the requirements for purge gas degassing, which requires a deeper, more compact vessel. The capacity of the holding furnace used in the present investigation was 35 tonnes of metal distributed over a bath area of about 20 m^3 and a bath depth of 0.7 m. Application of the purge gas was by immersion of hexachlorethane tablets manually through the side doors. In such a situation, degassing is inevitably inefficient and erratic.

The poor efficiency can be quantified by comparing the actual quantity of degasser used with the theoretical minimum quantity required calculated using Gellers[207] equation:

$$V = Km\left[\left(S^{\theta}\right)^2\left(\frac{1}{C_F}-\frac{1}{C_I}\right)+\left(C_F-C_I\right)\right] \qquad (9.2)$$

where:

V is the volume of purge gas,

C_I and C_F are the initial and final hydrogen concentrations,

S^{θ} is the solubility of hydrogen at atmospheric pressure,

m is the mass of the liquid metal

K is 10^{-2} when m is in g and C_I, C_F are in $cm^3/100g$

Application of Equation 9.2 to Casts 1, 2 and 3 yields the degassing efficiencies, E., given in Table 9.2. E is the ratio of the theoretical volume of purge gas ,V, to the volume actually used, V_{actual}, expressed as a percentage. The mass of metal, m was 35×10^6 g and V_{actual} is calculated as follows. Hexachlorethane, yields the purge gas, aluminium trichloride by decomposition:

$$C_2Cl_6\,(s) + 2Al(l) = 2AlCl_3\,(g) + 2C(s) \qquad (9.3)$$

One mole of C_2Cl_6 (237 g) yields 2 moles of $AlCl_3$ (2 x 22400 cm^3 at 273 K), which is equivalent to 1.6×10^5 cm^3 at the degassing temperature., 720 °C (993 K).

V_{actual} is the volume of $AlCl_3$ produced from the 60 Kg addition

$$= [(60 \times 10^3)/237] \times 1.6 \times 10^5 = 4 \times 10^7$$

Table 9.2 Calculation of degassing efficiency

Cast	C_I $cm^3/100g$	C_F $cm^3/100g$	m/g	T/K	S^0	$V_{calculated}$	V_{actual}	E %
1	0.25	0.18	35×10^6	993	1.0	5.2×10^7	4.0×10^7	1.3
2	0.26	0.17	35×10^6	993	1.0	6.8×10^7	4.0×10^7	1.7
3	0.26	0.20	35×10^6	993	1.0	3.8×10^7	4.0×10^7	1.0

Another disadvantage with furnace degassing with hexachlorethane is the formation of highly undesirable carbides e.g. Al_4C_3 which provide nucleation sites for gas bubbles in the cast ingot. If inert gases such as nitrogen or argon are used, oxide is produced as the bubbles break the liquid metal surface.

Modern trends are away from furnace degassing and towards "in-line degassing" i.e. degassing and filtering the liquid metal during transfer from the furnace to the mould[208,209], by applying a purge gas countercurrent to the metal as it passes through a heated vessel containing a granular filter bed. This has the following advantages:

i. The purging gas is utilised effectively because it is dispersed as small bubbles, giving a large gas/metal interface and is conducted in a customised vessel designed to maximise the contact time. In these circumstances, the conventional model for the degassing mechanism probably applies[13, 14, 15, 207].
ii. The metal has little time to reabsorb hydrogen before casting.
iii. Fume emission can be eliminated
iv. The time spent on furnace degassing is saved.

9.1.3 Settling

Hydrogen contents, taken from Figures 9.1 to 9.3, are re-plotted in Figures 9.7 to 9.9 on a time scale. Equilibrium hydrogen contents, calculated as described in Section 9.1.2.1 are added to these figures.

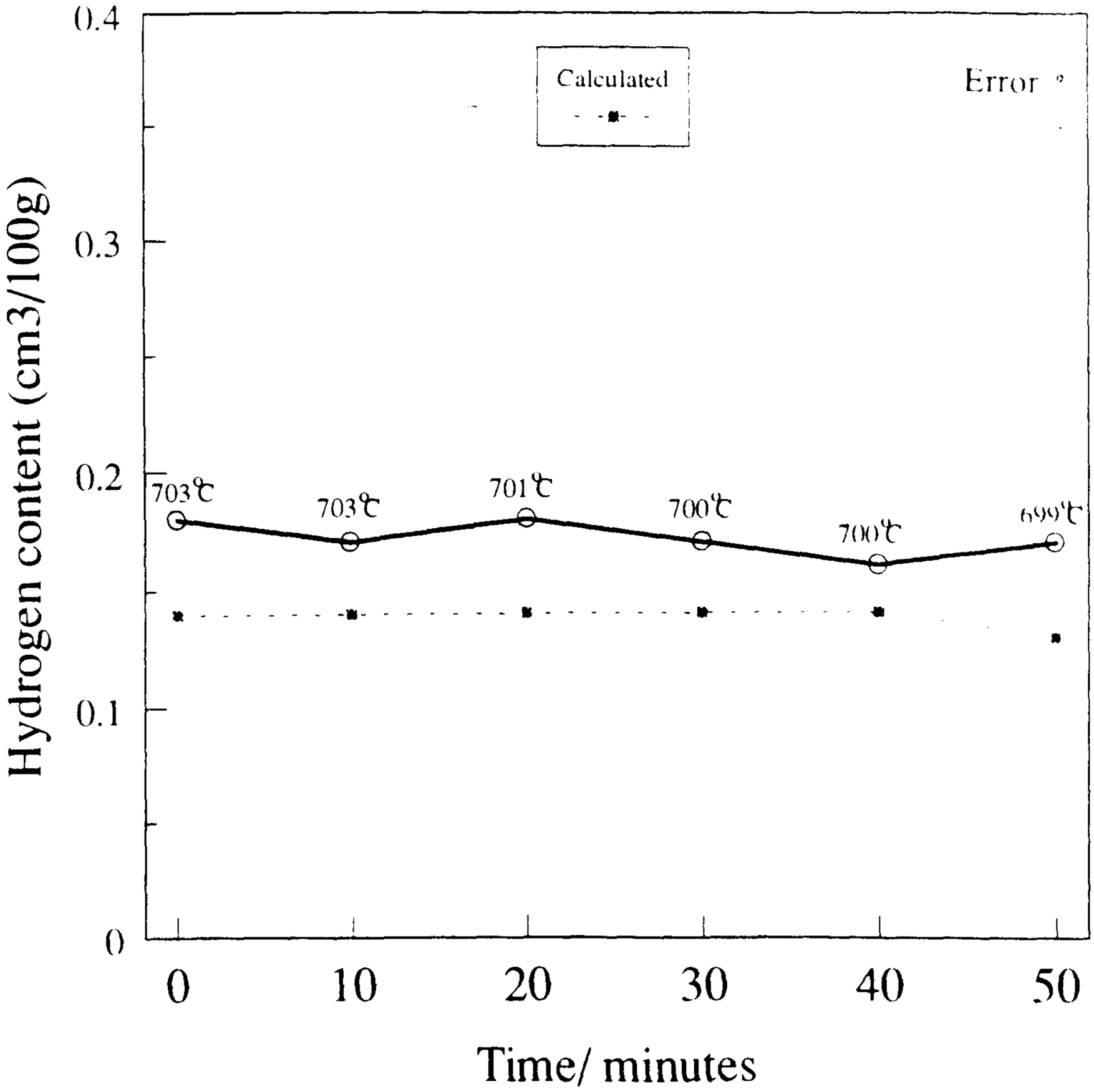

Figure 9.7 Hydrogen content of liquid metal during settling - Cast 1.

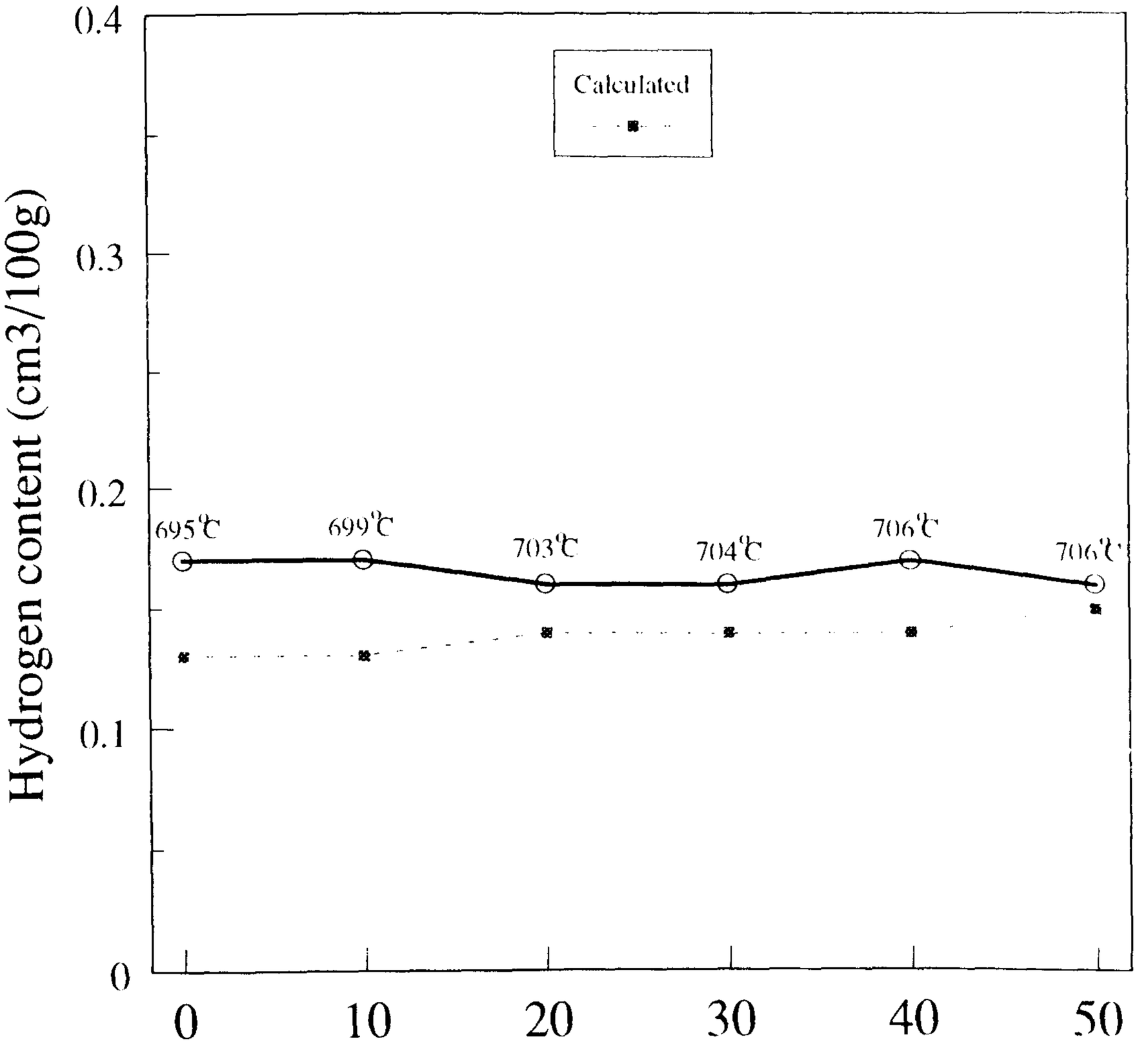

Figure 9.8 Hydrogen content of liquid metal during metal settling- Cast 2.

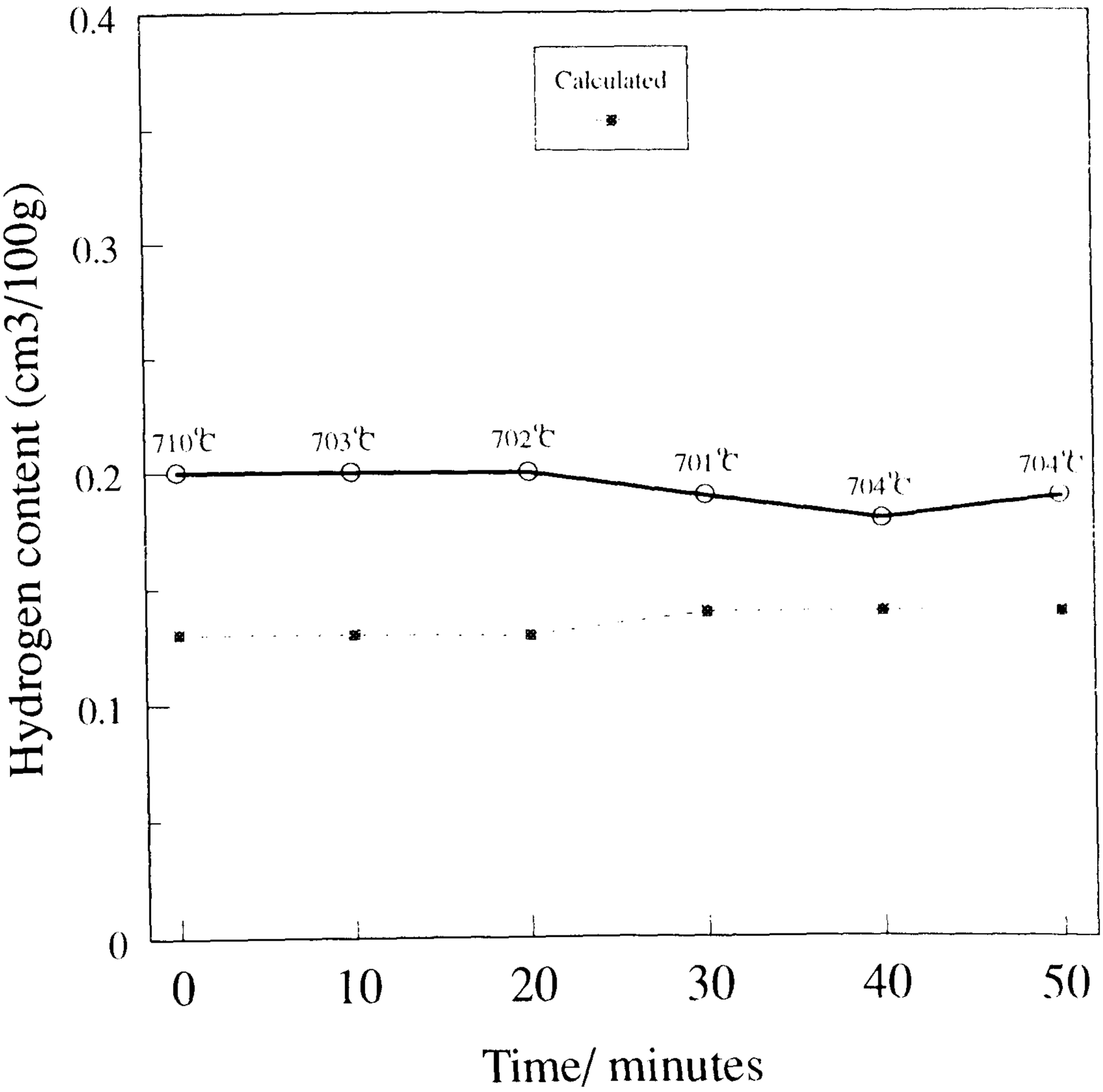

Figure 9.9 Hydrogen content of liquid metal during settling - Cast 3.

The information given in Figures 9.7 to 9.9 provides an opportunity to see what happens when a large bulk of quiescent metal with a low hydrogen content is held in a shallow bath at constant low temperature for a long time.

For all three casts, the metal was held undisturbed for 60 minutes at a constant temperature of 700 +/- 5 °C . During this period, the hydrogen content remained

virtually unchanged at 0.17, 0.16 and 0.19 $cm^3/100$ g for Casts 1, 2 and 3 respectively. At first, this appears unremarkable but there are two important conclusions to be drawn:

i. Comparison of the actual hydrogen contents with the calculated hydrogen contents shows that the hydrogen content is at most only slightly above that in equilibrium with the atmosphere. When allowance is made for the small uncertainty in solubility discussed in Section 9.1.2.1 , it may even be at equilibrium for Casts 1 and 2.

ii. This provides further evidence that the role of furnace degassing is to improve the kinetics of equilibration of the metal with the atmosphere rather than to remove hydrogen actively, as intended.

iii. It is a common belief that after degassing, the metal is susceptible to reabsorption of hydrogen from the atmosphere. It follows from point (i) above that this is an over simplistic view. Only if degassing has succeeded in reducing the hydrogen content *below* the equilibrium value is this possible. It does not seem to apply to furnace degassing but it must be borne in mind when metal is degassed by more efficient methods, such as in-line degassing, described in Section 2.1.2.2.

9.1.4 Casting

Hydrogen contents, taken from Figures 9.1 to 9.3, are re-plotted in Figures 9.10 to 9.12 on a time scale. Corresponding Telegas readings are also plotted.

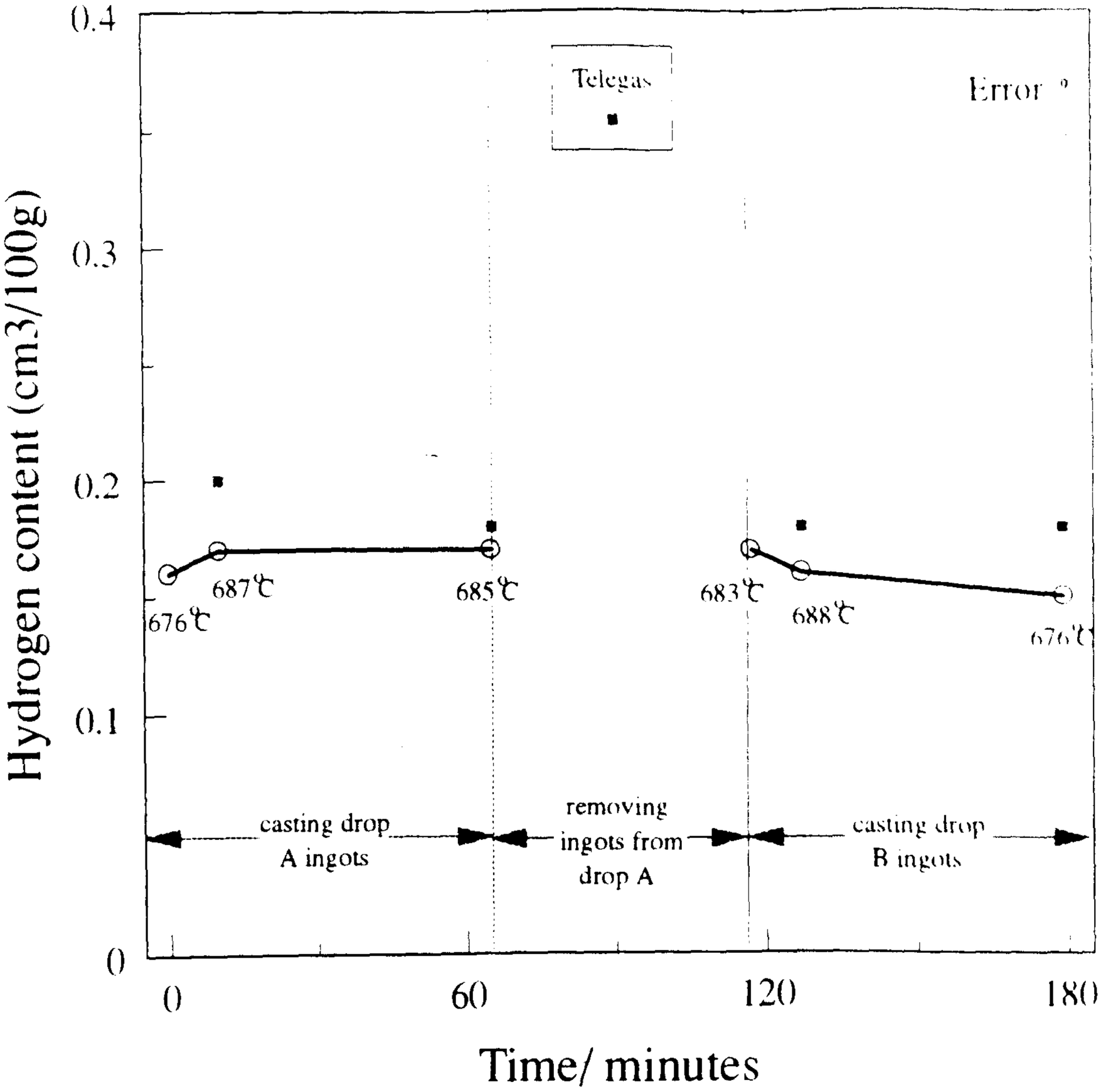

Figure 9.10 Hydrogen content of liquid metal during casting - Cast 1.

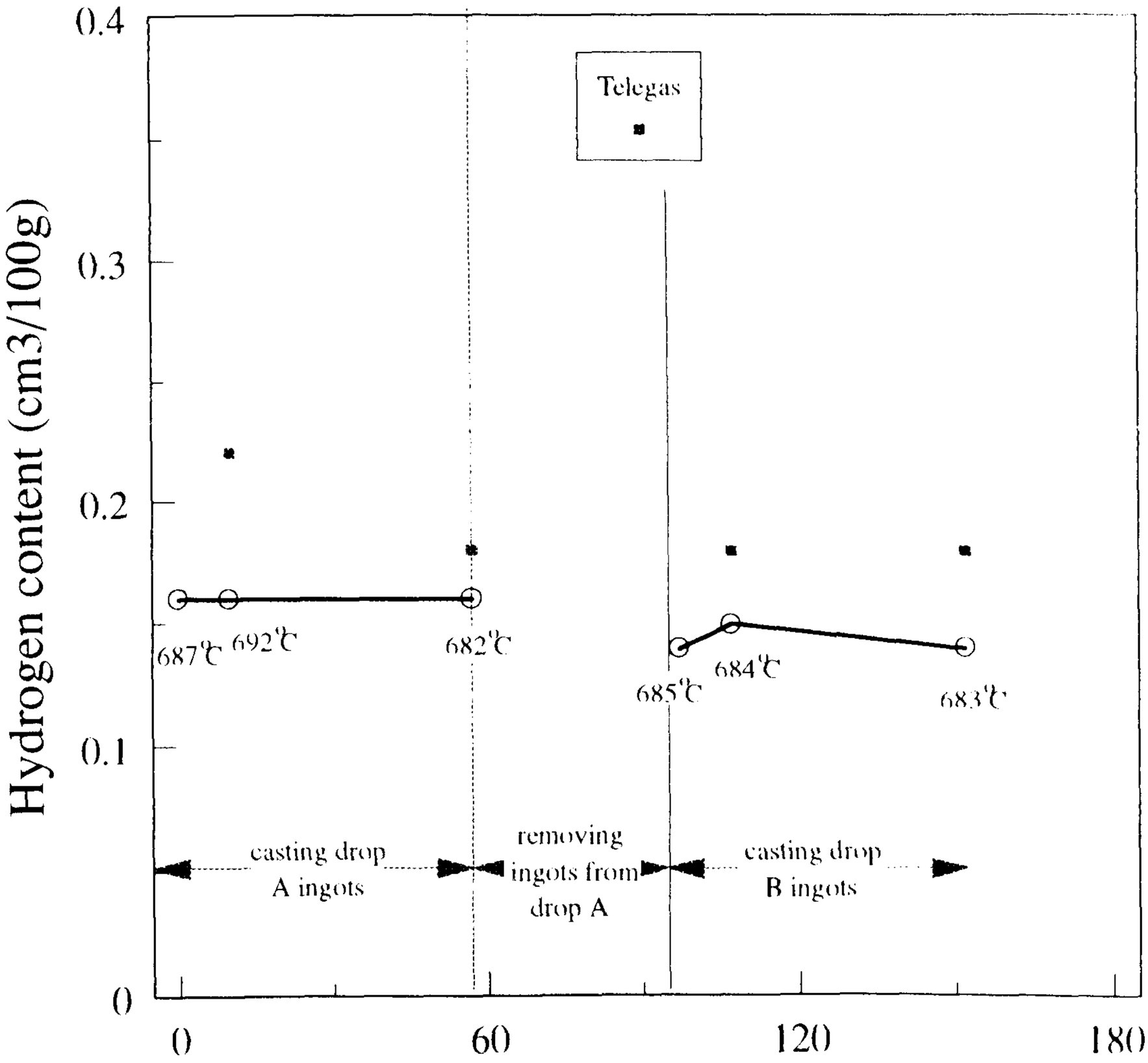

Figure 9.11 Hydrogen content of liquid metal during casting - Cast 2.

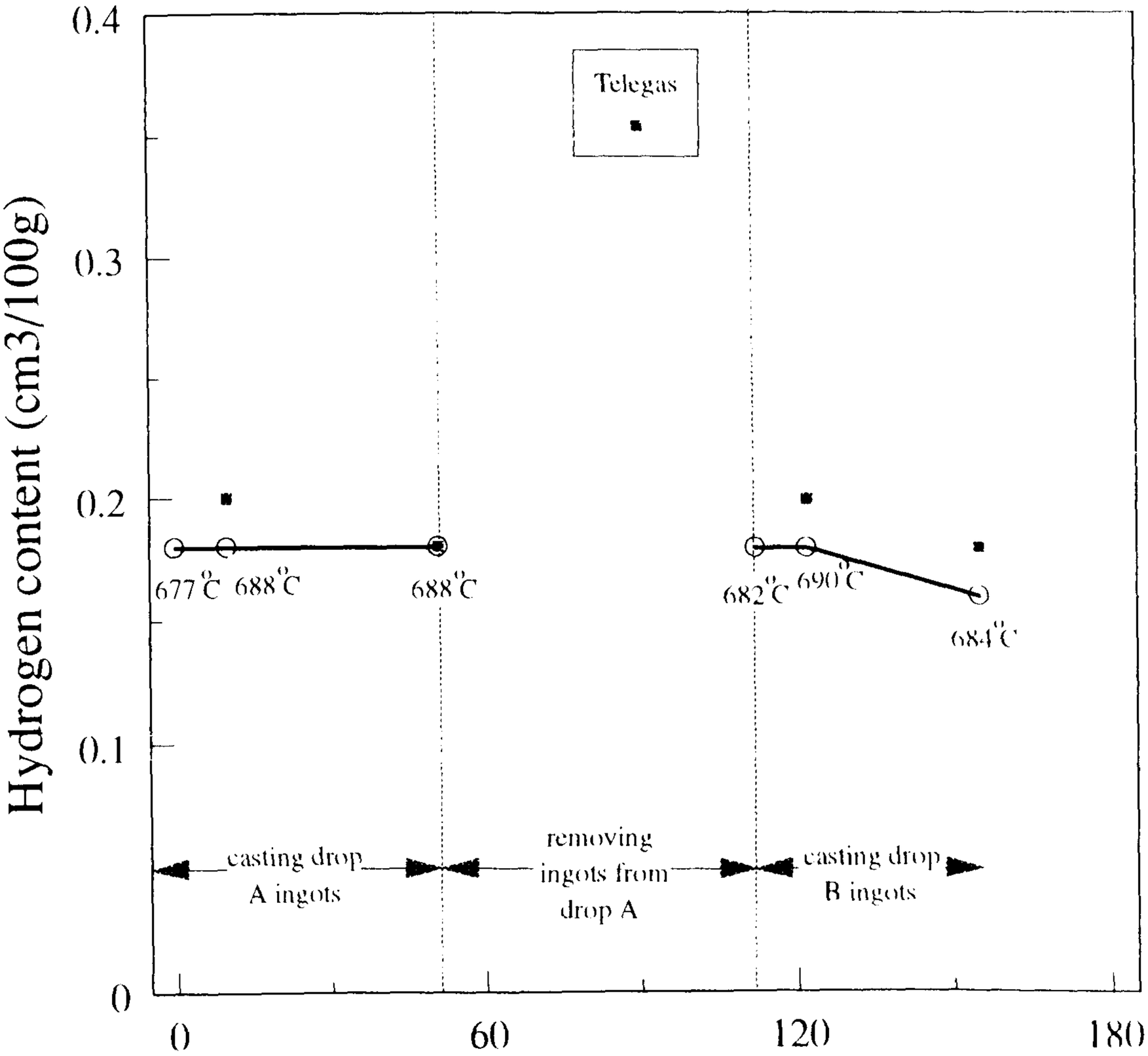

Figure 9.12 Hydrogen content of liquid metal during casting - Cast 3.

The results given in Figures 9.10 to 9.12 are also apparently unremarkable but they contain the following important information:

i. The results confirm the conclusions drawn so far because they are effectively a continuation of the results given in Section 9.1.2.3. The balance of the metal remained quiescent in the holding furnace throughout the whole period of casting and the last portion of the metal to be cast had been

in the furnace for a total of 220 to 240 minutes. There is a slight fall, i.e. of 0.01 to 0.02 cm^3 in hydrogen content towards the end of the second drop in all three casts, consistent with the reduction in equilibrium hydrogen content expected from the fall of 10 °C in temperature, calculated as in Section 9.1.2.1.

ii. The Telegas readings, plotted in Figures 9.10 to 9.12 are slightly higher than the corresponding results obtained by hot vacuum extraction. It is most probably due to drift in the calibration of the particular Telegas instrument used, a not uncommon effect. When such differences arise the hot vacuum extraction results are preferred, because the calibration of the equipment is absolute by the methods described in Section 6.1.3 and is not susceptible to drift, as is the Telegas. Nevertheless, the Telegas readings plotted in Figures 9.10 to 9.12 show the same trends in hydrogen content. The trends are confirmed by the author's previous industrial experience that the hydrogen content measured with the Telegas during a cast is always lower during the second drop than during the first

9.1.5 Distribution of hydrogen on the casting table

Tables 8.7 and 8.8 show that in all of the casts, the distribution of hydrogen across the extensive casting table, serving 36 moulds was perfectly uniform and virtually unchanged from its value on entry. This result dispels apprehension that conditions present on the table, e.g. moisture in the refractories, exposure to the atmosphere and process malfunction, such as the "bubbling mould" described in Section 7.2.1.2, might promote reabsorption of hydrogen . It must be borne in mind that these results apply to a *properly prepared* casting table, i.e. one which had been preconditioned by prolonged baking and well-maintained. In less meticulous practice, it would be quite possible for imperfectly dried refractory dressings or repairs to contribute water as a hydrogen source.

Incidentally, it is gratifying to note that as casting proceeded, there was a reduction in hydrogen content, especially towards the end, confirming the drift towards equilibrium noted in Section 9.1.4.

9.1.6 Implications for metal quality

Integrating results for all of the casts investigated, the final hydrogen contents of the liquid metal as it is delivered to the moulds, which determines the quality of the metal, is in the range 0.14 to 0.18. By the criteria of threshold values 0.12 to 0.17 cm^3/100 g, set out in Section 9.1.1, these hydrogen contents are approaching the upper limit for ingots to be free from interdendritic porosity.

The experiments were conducted in the Autumn in the Arabian Gulf region, when climatic conditions were not extreme but it is well-known that hydrogen-related defects are subject to a seasonal factor which has the effect of increasing their prevalence during long spells of hot and humid weather[115]. The theory of equilibration with atmospheric water vapour, developed in Section 9.1.2.1 gives an insight into the nature of the seasonal effect for the following reason. Throughout the liquid metal processing system under investigation, the hydrogen content approached but was never below the theoretical equilibrium hydrogen content calculated from the atmospheric water vapour pressure, which varies with climatic conditions. Accordingly, higher hydrogen contents are expected in the metal when the weather is hot and humid than when it is cool and dry. Figure 9.13 shows the range of equilibrium hydrogen contents as functions of metal temperature, expected from Winter to Summer in the Arabian Gulf region, calculated using Equation 9.1. The range of threshold values is added for comparison.

Figure 9.13 shows two important features:

i. Unless degassing can reduce the existing hydrogen content below the equilibrium value, it is probably difficult to produce metal with hydrogen contents low enough to yield ingots entirely free from interdendritic porosity in a humid season. This strengthens the argument for in-line degassing, which is both more efficient and minimises the risk that hydrogen can be reabsorbed to the equilibrium value.
ii. Irrespective of the climatic conditions, it is important to maintain the lowest possible metal temperatures.

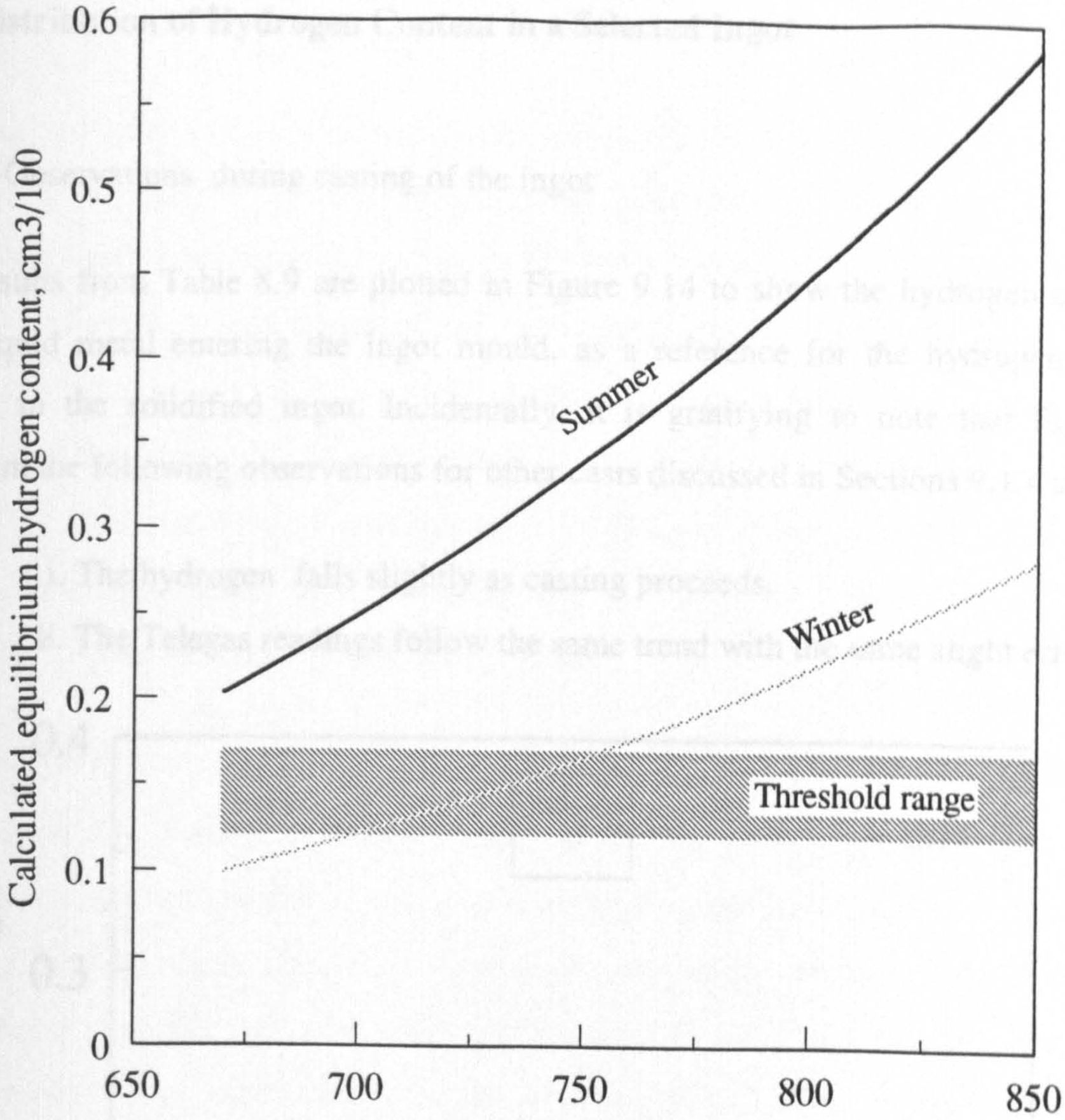

Range of Threshold values for D C ingots free from interdendritic porosity.

Typical ambient conditions:

Winter; Temperature- 25 °C, Relative humidity 60%.

Summer; Temperature- 45 °C, Relative humidity 85%.

Figure 9.13 Seasonal variation of calculated equilibrium hydrogen content of metal produced in the Arabian Gulf region.

9.2 Distribution of Hydrogen Content in a Selected Ingot

9.2.1 Observations during casting of the ingot

Results from Table 8.9 are plotted in Figure 9.14 to show the hydrogen content of the liquid metal entering the ingot mould, as a reference for the hydrogen contents found in the solidified ingot. Incidentally, it is gratifying to note that Figure 9.14 confirm the following observations for other casts discussed in Sections 9.1.4 and 9.1.5:

i. The hydrogen falls slightly as casting proceeds.

ii. The Telegas readings follow the same trend with the same slight error

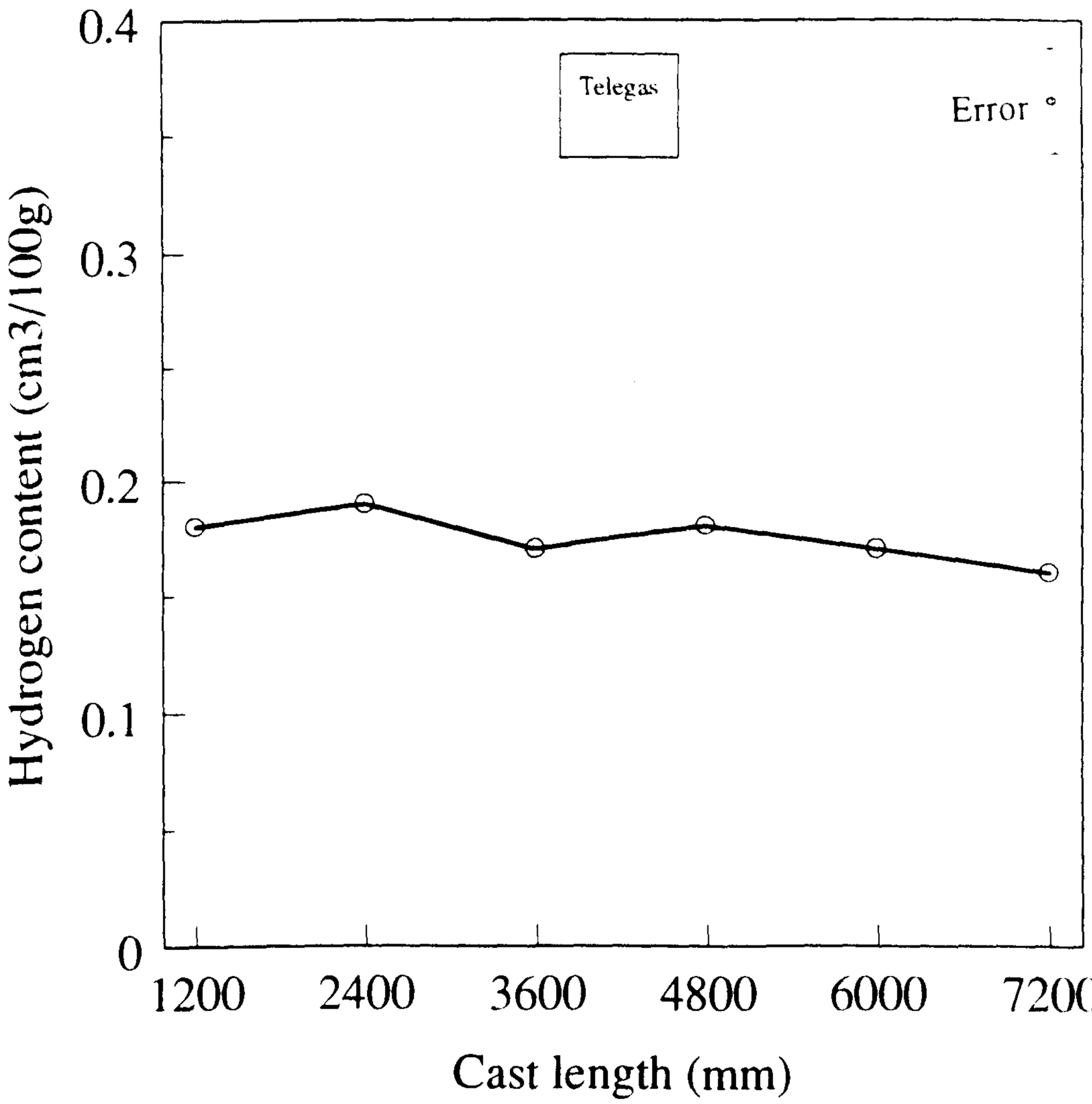

Figure 9.14 Hydrogen content of the liquid metal during casting.

9.2.2 Structural characterisation of the ingot

The photograph of the macroetched full cross-sectionof the ingot, given in Figure 8.1 reveals a completely equiaxed grain structure, difficult to resolve with unaided eye. Selected fields from the cross-section at the surface, mid-radius and centre of the ingot show a completely uniform grain size, 200 to 300 μm in diameter, with dendrite arm spacings of 21 to 29 μm, determined from corresponding micrographs at higher magnification, given later in Figures 8.7 (a) and (b). The dendrite arm spacing is consistent with the range of spacings given by Granger[73] for typical DC cast aluminium alloys and corresponds with a cooling rate of 1 to 10 Ks^{-1}, according to Spear and Gardner's criterion[74], reproduced in Figure 3.6.

The very narrow zone of inverse segregation, characteristic of hot-top mould castings is clearly visible in Figures 8.6 (a) to (c). The depth of the zone is 25 to 49 μm, which is of the same order of magnitude as the dendrite arm spacing. A characteristic feature of the inverse segregation is that on longitudinal microsections it appears as overlapping periodic segregate zones extending for 2 mm. Every zone is separated from the next by a fold, illustrated in Figure 8.5 and 8.6 (a) and (b) at successively greater magnifications. The apparently separate zones visible in microsection are, in reality, the result of sectioning through a continuous spiral of segregate on the ingot surface, evident in the photograph given in Figures 8.14 and 8.15.

In the rest of the ingot the microstructure was as expected in the non-equilibrium cast structure, exhibiting small quantities of intermetallic phases between the dendrite arms , principally Mg_2Si , and various Fe/Al/Si phases.

A feature of considerable importance discussed later in Section 9.2.4 is the incidence of secondary porosity, i. e. small spherical pores, ~ 2 μm in diameter, disseminated throughout the material. This porosity is very difficult to distinguish from small particles of intermetallic phases in micrographs without electropolishing to exaggerate the pores[121]. With careful scrutiny, it can be seen in the micrographs of the cast ingot, given in Figures 8.8 to 8.10, but the only certain way of identifying it is by de-focussing and manipulating the illumination in the microscope. This is difficult to record

record photographically. The most important observation is the enlargement of the porosity after homogenisation, evident in the micrographs given Figures 8.11 to 8.13. This effect corresponds to the same effect observed by Talbot and Granger[121] during the homogenisation of DC cast ingots of 99.2% aluminium.

9.2.3 Analysis of ingot surface

The surface profile of the as-cast ingot, produced by secondary ion mass spectrometry (SIMS), given in Figure 8.16 refers to metal covered by a very thin oxide film. The apparent rise in aluminium content in the surface 0.2 μm of the plot is an instrumental artefact due to initial stabilisation of the ion beam. In fact, the profile is consistent with uniform aluminium content right to the ingot surface. The profile for magnesium is more significant and identifies an enrichment in magnesium at the extreme surface, assumed to be due to selective oxidation, yielding a magnesium rich surface film. The trace for hydrogen suggest that the film is hydrated oxide.

The interpretation of the corresponding SIMS depth profiles for the ingot after homogenisation, given in Figures 8.17 and 8.18 is complicated by two effects:

i. Due to the roughness of the cast surface, the surface is not necessarily normal to the ion beam. For example, this creates difficulty in estimating the thickness of the oxide film formed.
ii. The inverse segregation pattern, noted in Section 9.2.2 means that the magnesium content at the ingot surface varies over distances of ~ 2 mm.

The best estimate for the oxide thickness is 0.5 to 1.0 μm. Figures 8.17 to 8.18 show that there is virtually no aluminium at the origin of the profile, corresponding to the air/oxide interface, implying that the outside of the film is either magnesium oxide or more likely a hydrated form of it in view of the significant signal for hydrogen. The gradual changes in the aluminium and magnesium signals could indicate an underlay of spinel between an outer oxide layer and the metal but they could equally well be due to surface roughness. The differences in the intensity of the aluminium signal between Figures 8.17 and 8.18 due to instrumental factors in the SIMS technique. When one component is dominant, the signal from the single ion - $^{27}Al^{3+}$ in the present case - is

overwhelming . The problem is solved by detecting less intense signal from the double ion $^{54}Al_2^{6+}$. Signals from double ions, e.g. $^{54}Al_2^{6+}$ are more sensitive than single ions, e.g. $^{24}Mg^{2+}$, to attenuation by sample charging due to variation in the non-conductive oxide thickness. This is why both the absolute intensity for the for the Al signal and its value relative to the Mg signals is less in Figure 8.18 than in Figure 8.17.

9.2.4 Distribution of hydrogen in the ingot as cast

The ingots studied in the present work were cast in the Airslip hot-top mould, designed to promote a shallow sump as described in Section 3.3.2, reducing the air gap. Also, the alloy, cast AA6063 has a relatively short freezing range. These two factors both conspire to reduce inverse segregation and the effect is very superficial as illustrated in Figure 8.6 (c) In these circumstances, lateral segregation of hydrogen, as has been observed in regular DC casting[135, 162] is not expected. This is confirmed by the results given in Table 9.3, extracted from Table 8.9.

Table 9.3 Lateral and longitudinal hydrogen content distribution in an as cast ingot.

Cast length, mm	Hydrogen content, $cm^3/100g$		
	Near the ingot edge	At the middle of ingot radius	At centre of the ingot
1200	0.17	0.18	0.17
2400	0.18	0.19	0.17
3600	0.16	0.17	0.18
4800	0.18	0.18	0.19
6000	0.17	0.17	0.16
7200	0.16	0.16	0.17

Although lateral segregation was not expected in an Airslip cast ingot vertical segregation of hydrogen was a possibility because the direction of solidification in the shallow mould is at a relatively small angle to the vertical, so that the cumulative effect of rejected hydrogen diffusing upwards, away from solidifying metal could introduce a vertical hydrogen content gradient. In the event, no such gradient was found, as shown in Figure 9.15, which is a plot of results given in Table 8.9.

The downward trend in hydrogen content during casting matched the downward drift in the metal entering the mould as casting proceeded, shown earlier in Figure 9.14.

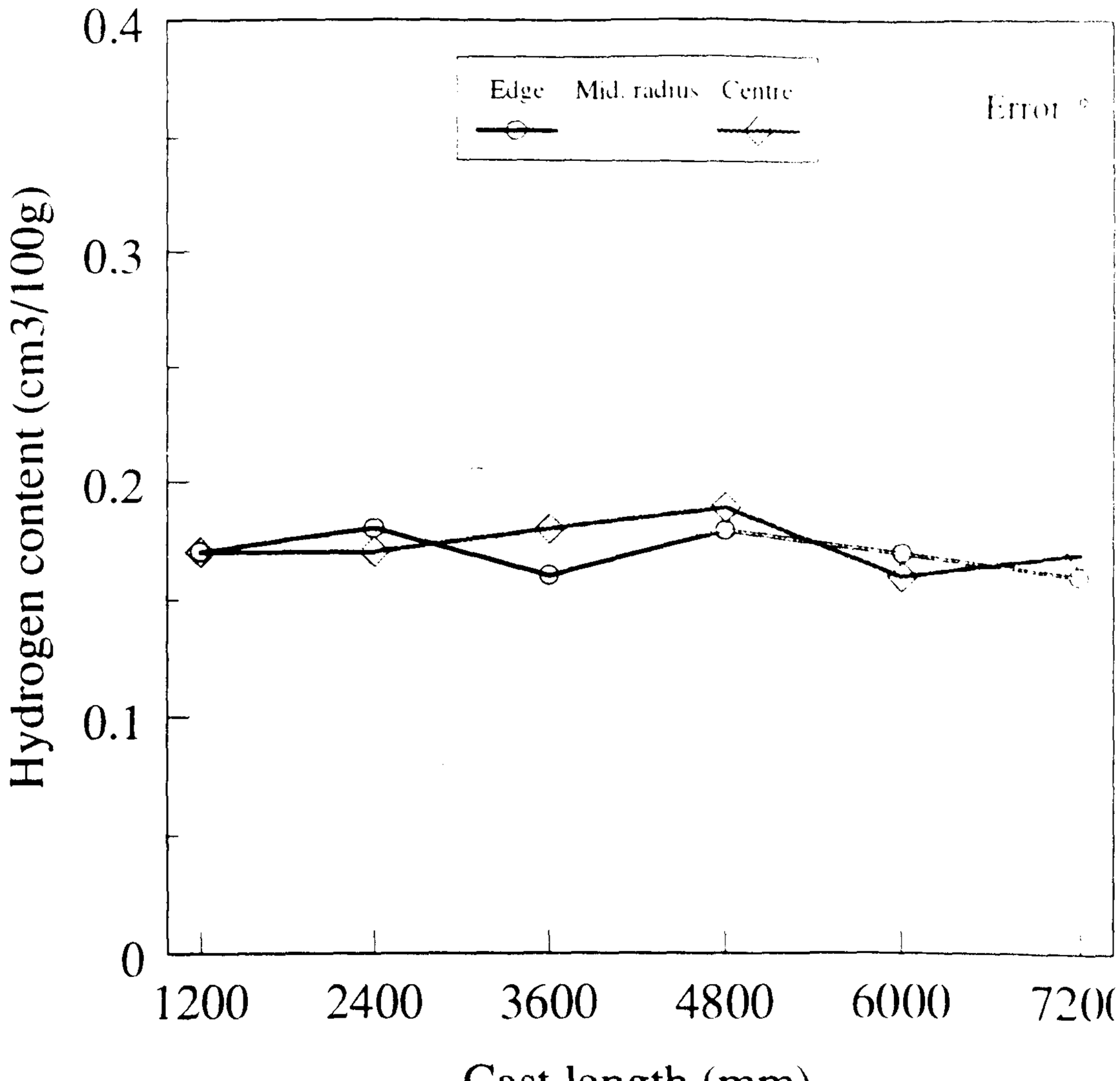

Figure 9.15 Distribution of hydrogen content along the length of the as-cast ingot.

9.2.5 Distribution of hydrogen in the same ingot after homogenisation

Talbot and Granger[121] showed that cast DC ingots of 99.2% pure aluminium lost hydrogen from the surface when heated for 12 hours at 580 °C in clean air, as illustrated by their results reproduced in Figure 9.16.

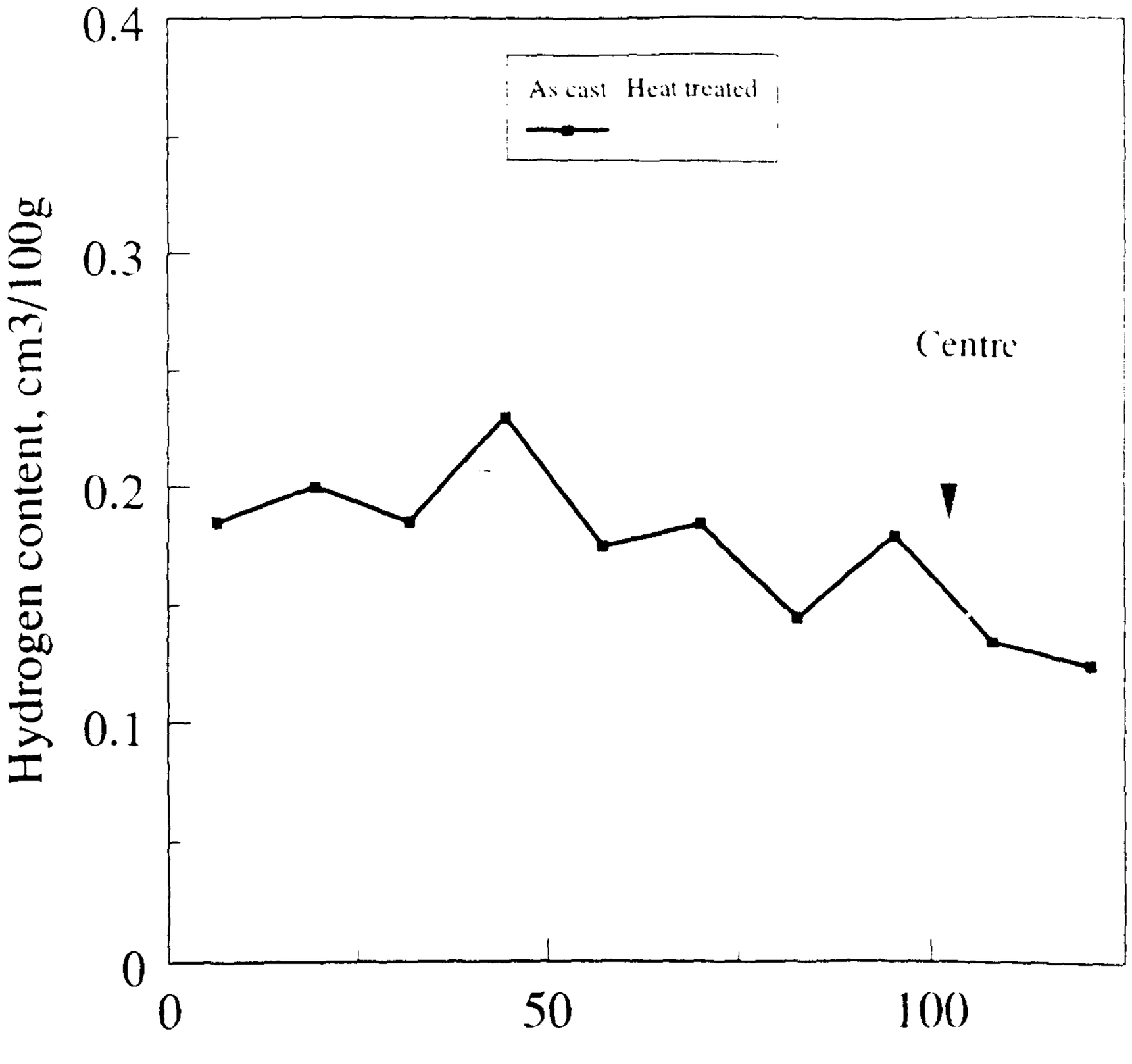

Figure 9.16 Distribution of hydrogen content across 200 mm thick rectangular DC cast ingot of 99.2% pure aluminium as cast and as heat-treated for 12 h at 580 °C, after Talbot and Granger [121].

In considering transfer of hydrogen at the metal surface, the nature of the oxide film, must be taken into account. The oxide film formed at elevated temperatures on pure aluminium is η– alumina[191]. No information on loss or absorption of hydrogen has been published for large industrial ingots of aluminium alloys where the oxide film on the cast surface is expected to be MgO or $MgAl_2O_4$[210]. The present results for AA6063, given in Table 8.10 and plotted in Figures 9.17 to 9.19 below therefore provide the only available information.

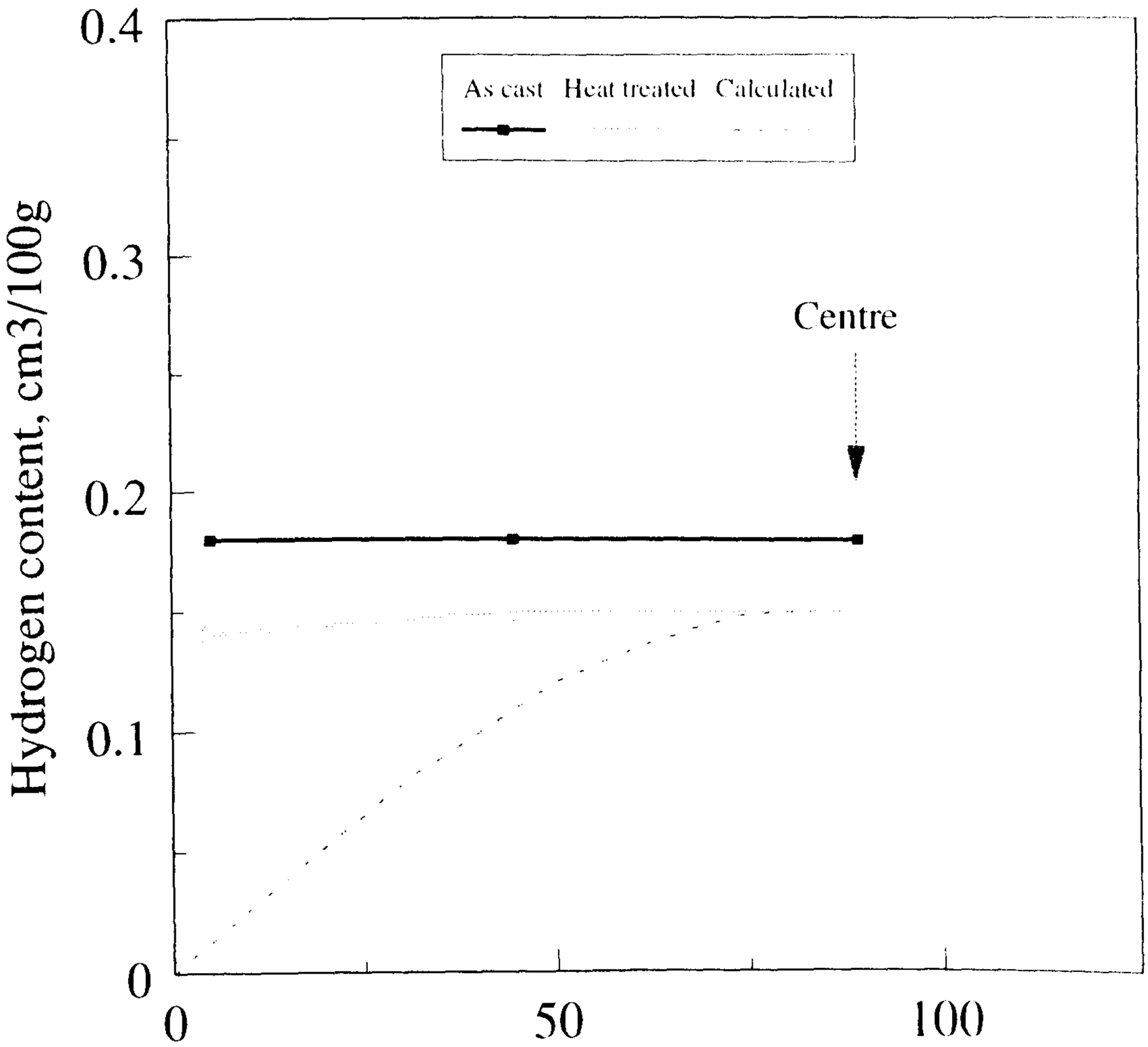

Figure 9.17 Lateral distribution of hydrogen content across ingot before and after industrial homogenisation in Furnace No. 1. Withdrawal temperature 590 °C. The calculated hydrogen profile after homogenisation is derived later in this Section.

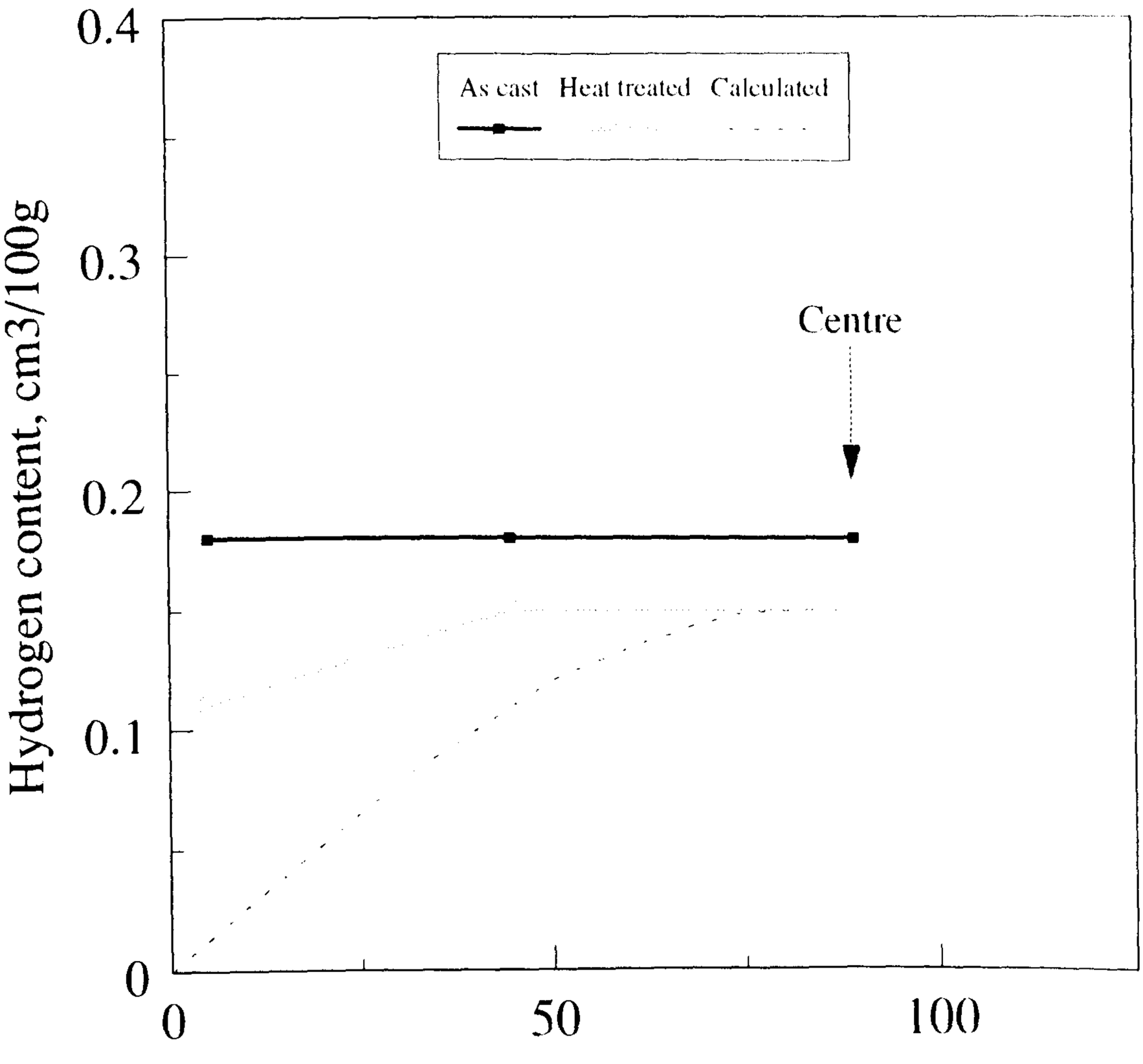

Figure 9.18 Lateral distribution of hydrogen content across ingot before and after industrial homogenisation in Furnace No. 2. Withdrawal temperature 590 °C. The calculated hydrogen profile after homogenisation is derived later in this Section.

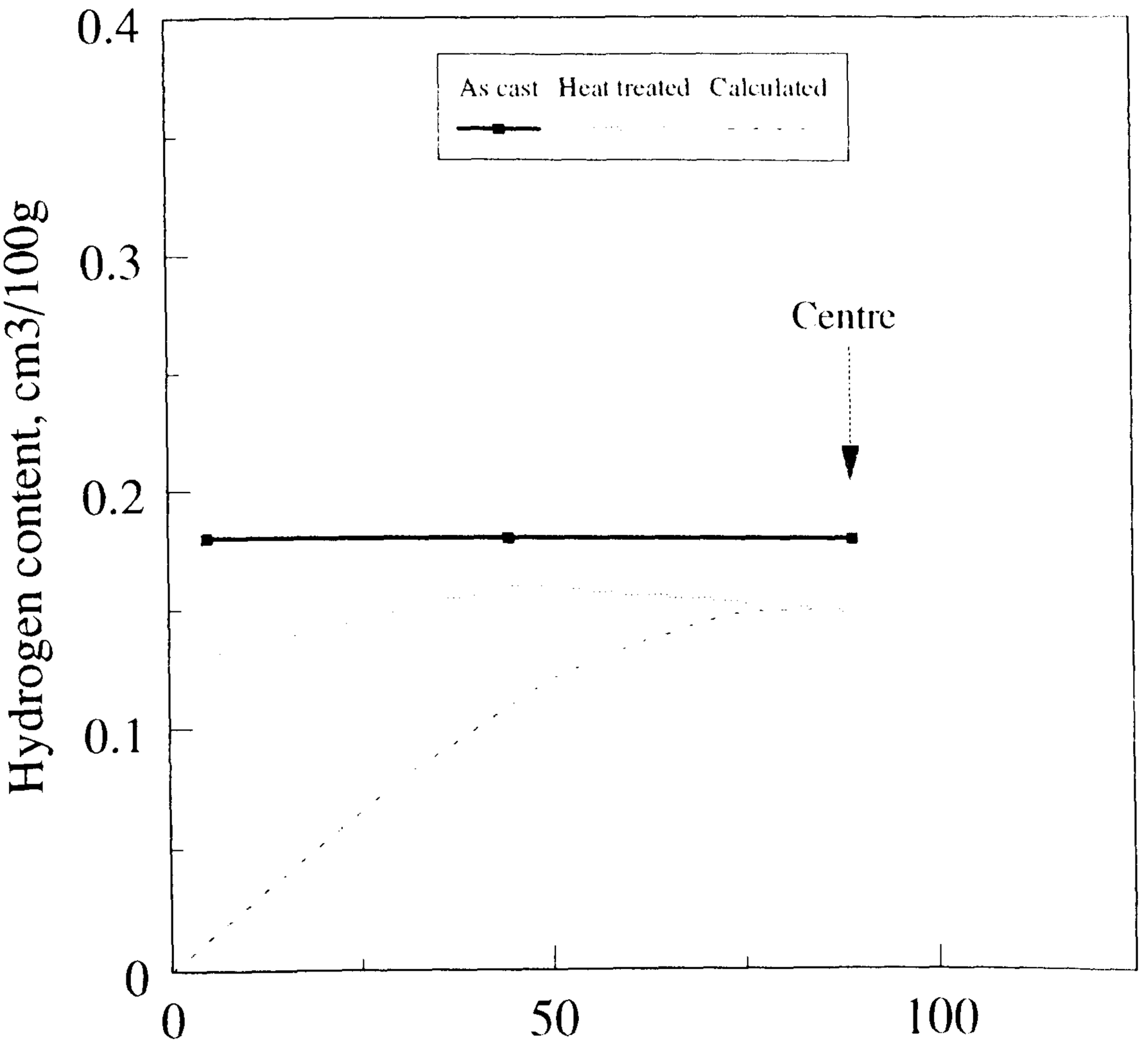

Figure 9.19 Lateral distribution of hydrogen content across ingot before and after industrial homogenisation in Furnace No. 3. Withdrawal temperature 590 °C. The calculated hydrogen profile after homogenisation is derived later in this Section.

The results of the present work for AA6063 plotted in Figures 9.17 to 9.19 are remarkably similar to those for pure aluminium plotted in Figure 9.16, suggesting that hydrogen is freely lost at the surface irrespective of the oxide film. Intuitively, it seems that there is no surface rate-control and the loss of hydrogen is controlled by the diffusion of hydrogen in the metal. To test this idea the hydrogen content profile after homogenisation can be estimated theoretically.

There are several problems to be solved in making the estimate:

i. True diffusion coefficients as given by Eichenauer and Pebler[127] do not describe transport of hydrogen in manufactured aluminium products[111] because it is subject to trapping, as described in Section 4.8.5 and must be replaced by mobility constants for the diffusion of hydrogen in a field of traps, i.e. by the apparent diffusion coefficients given by Eborall and Ransley[98] and Ransley and Talbot[161]
ii. The diffusion coefficient is variable because industrial heat-treatments are not isothermal, the high thermal capacity of the load and the metal temperature rises continuously throughout the process.

Provided that the variable diffusion coefficient is a function of time, t, only, a semi-empirical model can be devised to overcome the second problem, by Crank's approach, using the diffusion equations for constant D but replacing Dt by:

$$\int Dt\,dt = \int f(t)t\,dt \tag{9.4}$$

Using mobility constants for the manufactured metal, as explained in (i) above, Equation 9.4 becomes:

$$\int Mt\,dt = \int f(t)t\,dt \tag{9.5}$$

where the variable diffusion coefficient is given by: $D = f(t)$

To use this approach, the diffusion coefficient in the present problem must be expressed as a function of time. Since the temperature rise is linear during the effective heat treatment:

$$t = kT \tag{9.6}$$

the metal temperature rises linearly from 560 to 590 °C in 3.5 hours (12600 s):

$$k = 2.4 \times 10^{-3}\ Ks^{-1} \tag{9.7}$$

The mobility coefficient is given by the equation, introduced in Section 4.8.5:

$$M = 12 \exp -(16900/T) \tag{9.8}$$

Using Equation 9.6, substituting for f(t), k and M from Equations 9.6, 9.7 and 9.8 and inserting $a = 0.089$ for the ingot radius expressed in m:

$$\frac{Mt}{a^2} = \frac{\int 12 \exp[-16900\ (T_0 + 2.4\times10^{-3}t)]}{(0.089)^2} \tag{9.9}$$

Integrating this function between the limits $t = 0$ and $t = t_f$, yields:

$$\frac{Mt}{a^2} = \frac{12\times16900}{2.4\times10^{-3}(0.089)^2}\left[\frac{e^{-y}}{y^2}\left(1 - \frac{2!}{y} + \frac{3!}{y^2} - \cdots\right) - \frac{e^{-x}}{x^2}\left(1 - \frac{2!}{x} + \frac{3!}{x^2} - \cdots\right)\right] \tag{9.10}$$

where $x = 16900/T_0$ and $y = 16900/T_F$ and T_0 and T_F are the initial and final temperatures.

Inserting T_0 =560 °C and T_F =590 °C into Equation 9.10, for the effective range of the heat treatments:

$$\frac{Mt}{a^2} = 0.087 \tag{9.11}$$

Carslaw and Jaeger[211] give the concentration profiles in cylinders for selected values of Mt/a^2 in terms of the dimensionless parameters $(C - C_1)/(C_0 - C_1)$ and r/a reproduced in Figure 9.20.

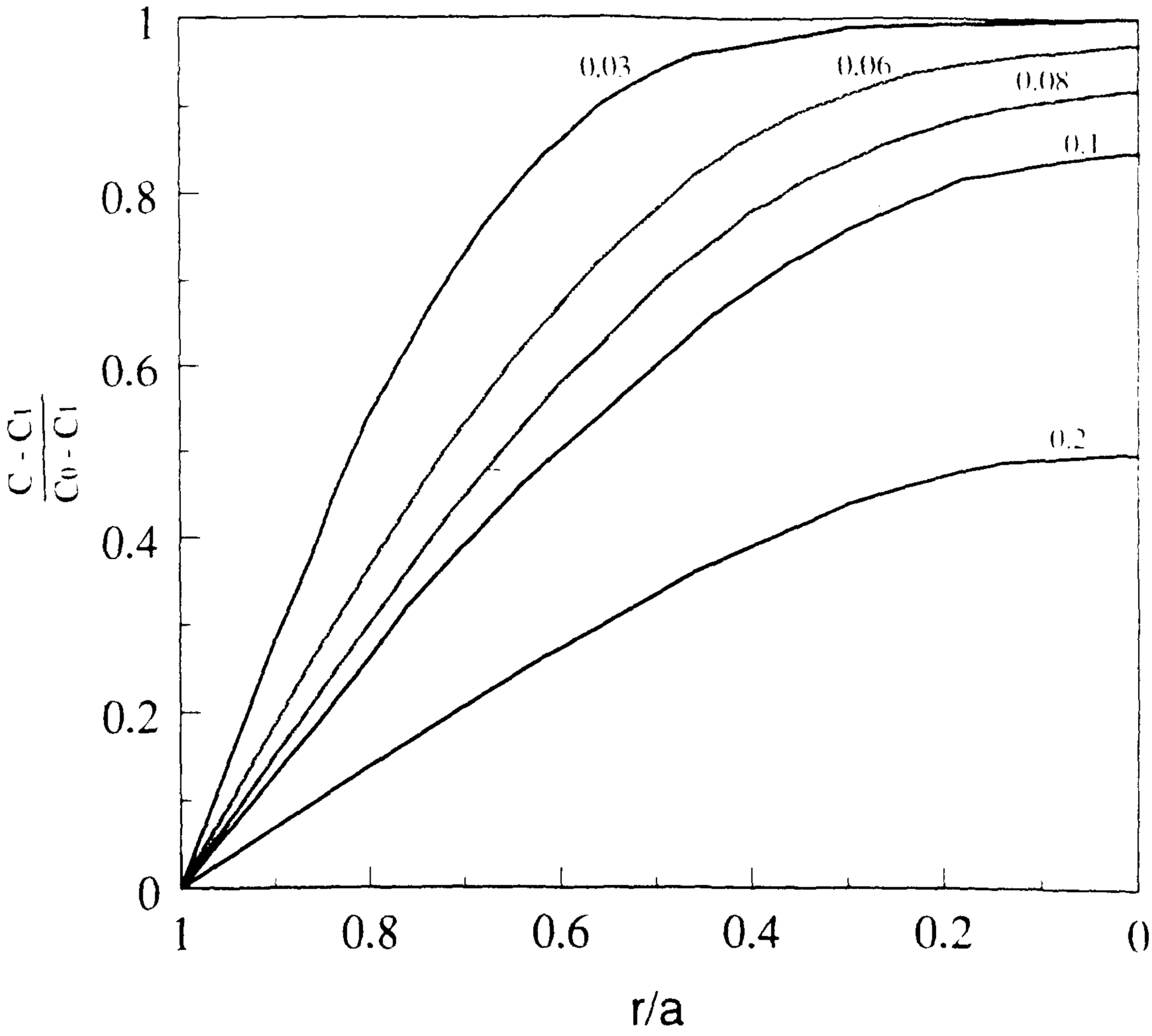

Figure 9.20 Concentration distribution at various times with initial concentration C_1 and surface concentration C_0. Numbers on curves are values of Dt/a^2. Reproduced from Carslaw and Jaeger[211].

Selecting the profile for $Dt/a^2 = 0.087$ by interpolating between the profiles for $Dt/a^2 = 0.08$ and $Dt/a^2 = 0.10$ and converting the dimensionless parameters into dimensioned values yields the theoretical profile of hydrogen content against ingot radius. This profile is superimposed on Figures 9.17 to 9.19.

Comparison of the actual and theoretical hydrogen profiles shows that the theoretical model correctly predicts the actual loss of hydrogen from the centre of the ingot but overestimates the loss from the surface. Reference to Figure 9.20 shows that the actual

hydrogen profiles in Figures 9.17 to 9.19 are untypical of ordinary diffusion control, showing the intervention of some other factor. Comparison of the micrographs of as cast ingot structures in Figures 8.8 to 8.10 with corresponding micrographs of the structures after homogenisation in Figures 8.11 to 8.13 reveals significant increases in the number and size of spherical pores, especially in the mid-radius and surface zones of the ingot. This implies that an increasing fraction of hydrogen is trapped in the metal as the gas phase as diffusion proceeds, depleting the diffusible solute concentration. This can explain the discrepancy between the predicted and actual profiles.

9.3 Heat Treatments In Clean Air

Results for the isothermal heat-treatments in clean dry air and water-saturated air, given in Tables 8.11, 8.12, 8.14 and 8.15, are plotted in Figures 9.21 to 9.24.

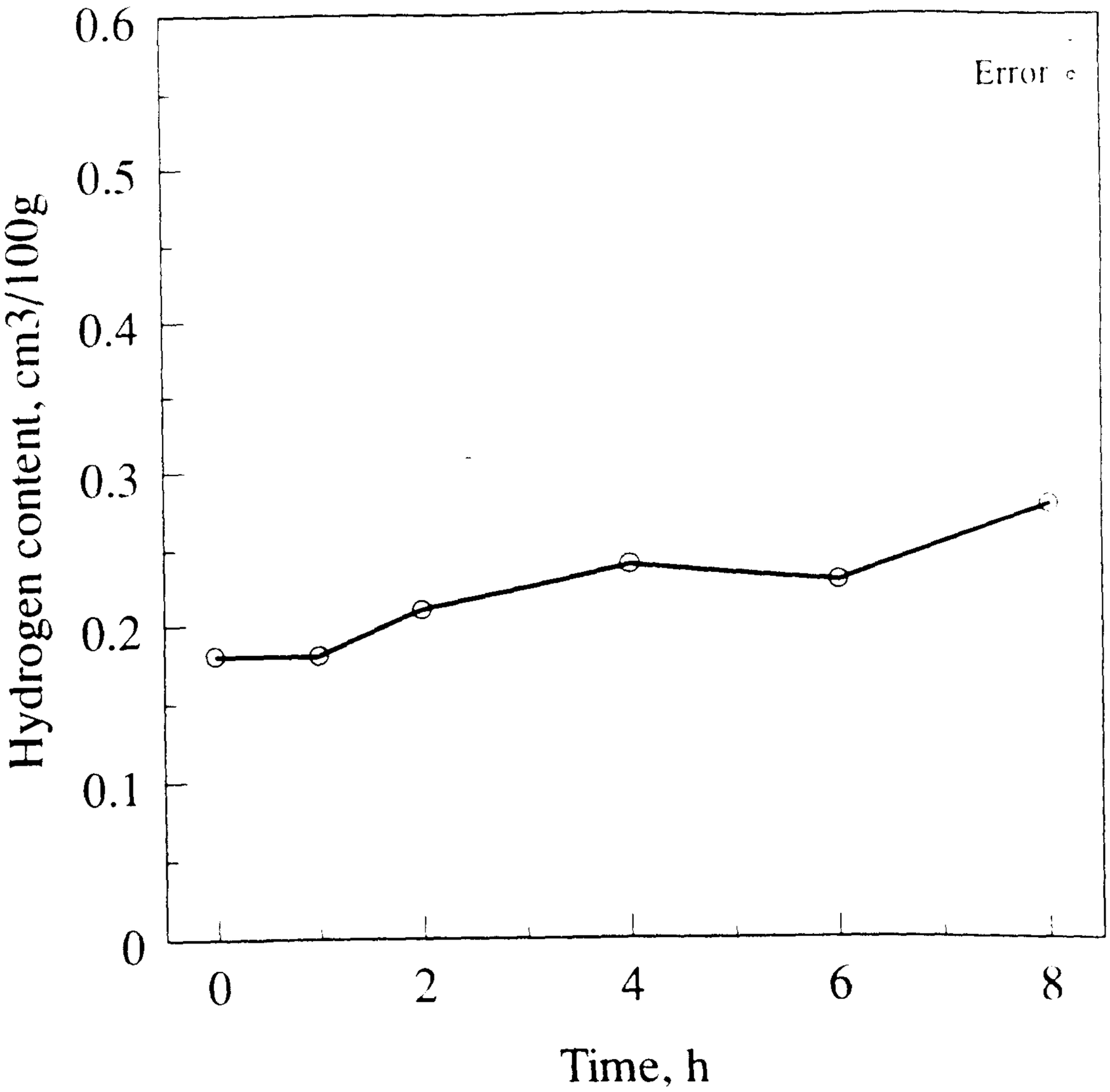

Figure 9.21. Hydrogen content of 10 mm diameter samples machined from the interior of a DC cast Al-0.5%Mg-0.4%Si alloy ingot. Response to isothermal heat-treatment at 500 °C in nominally dry air.

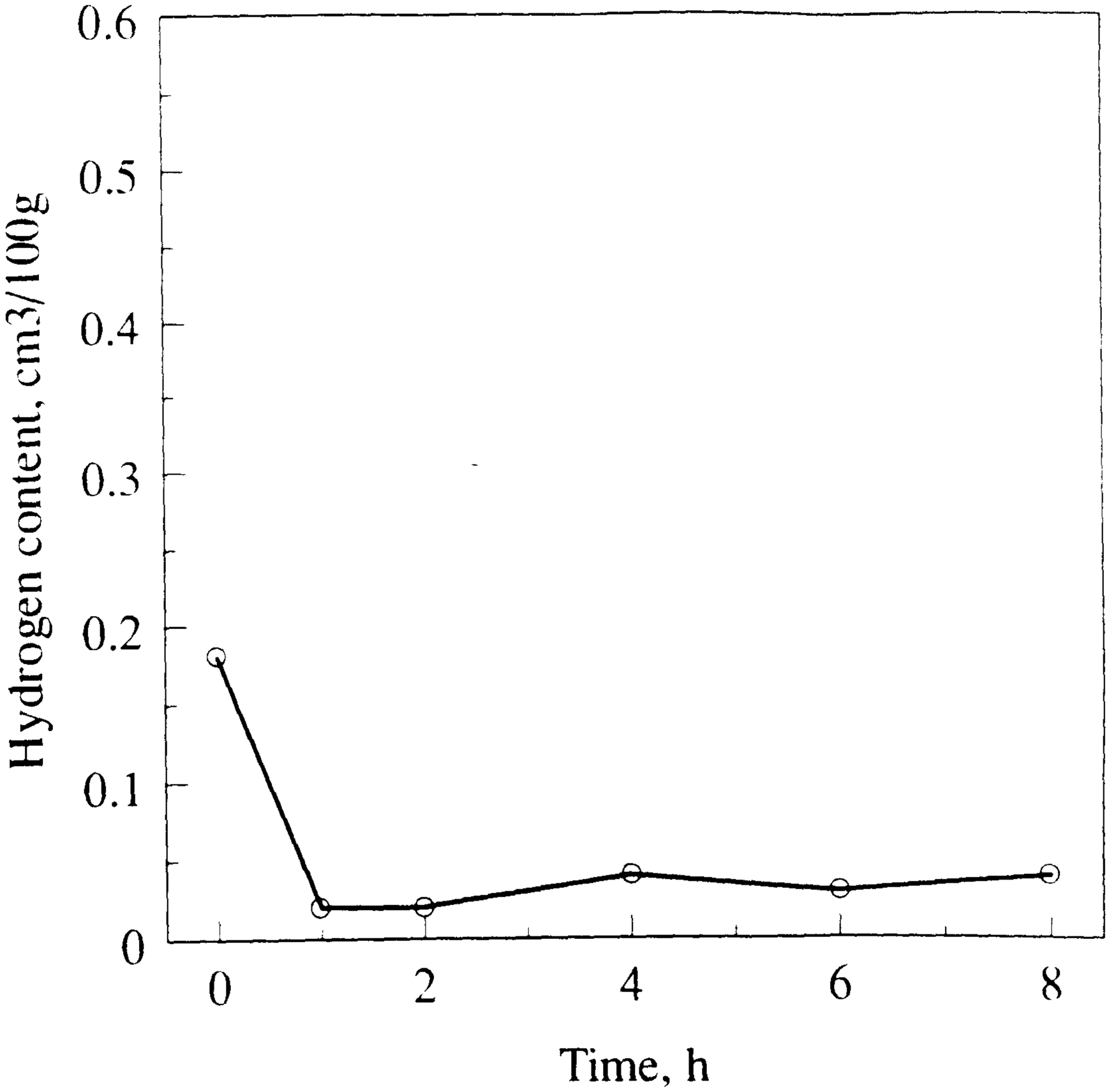

Figure 9.22 Hydrogen content of 10 mm diameter samples machined from the interior of a DC cast Al-0.5%Mg-0.4%Si alloy ingot. Response to isothermal heat-treatment at 590 °C in nominally dry air.

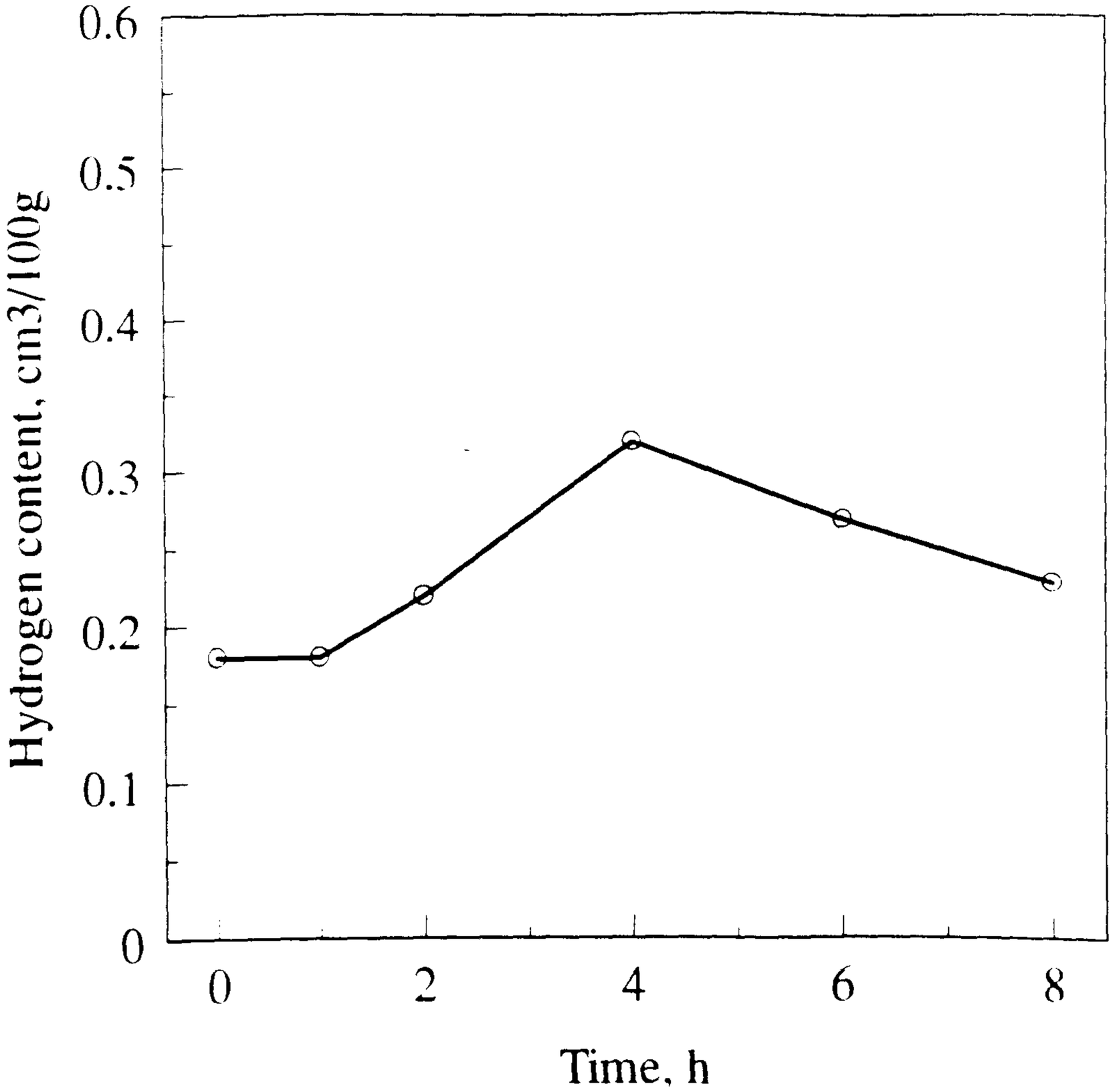

Figure 9.23. Hydrogen content of 10 mm diameter samples machined from the interior of a DC cast Al-0.5%Mg-0.4%Si alloy ingot. Response to isothermal heat-treatment at 500 °C in water-saturated air (p_{H_2O} = 0.03 atm).

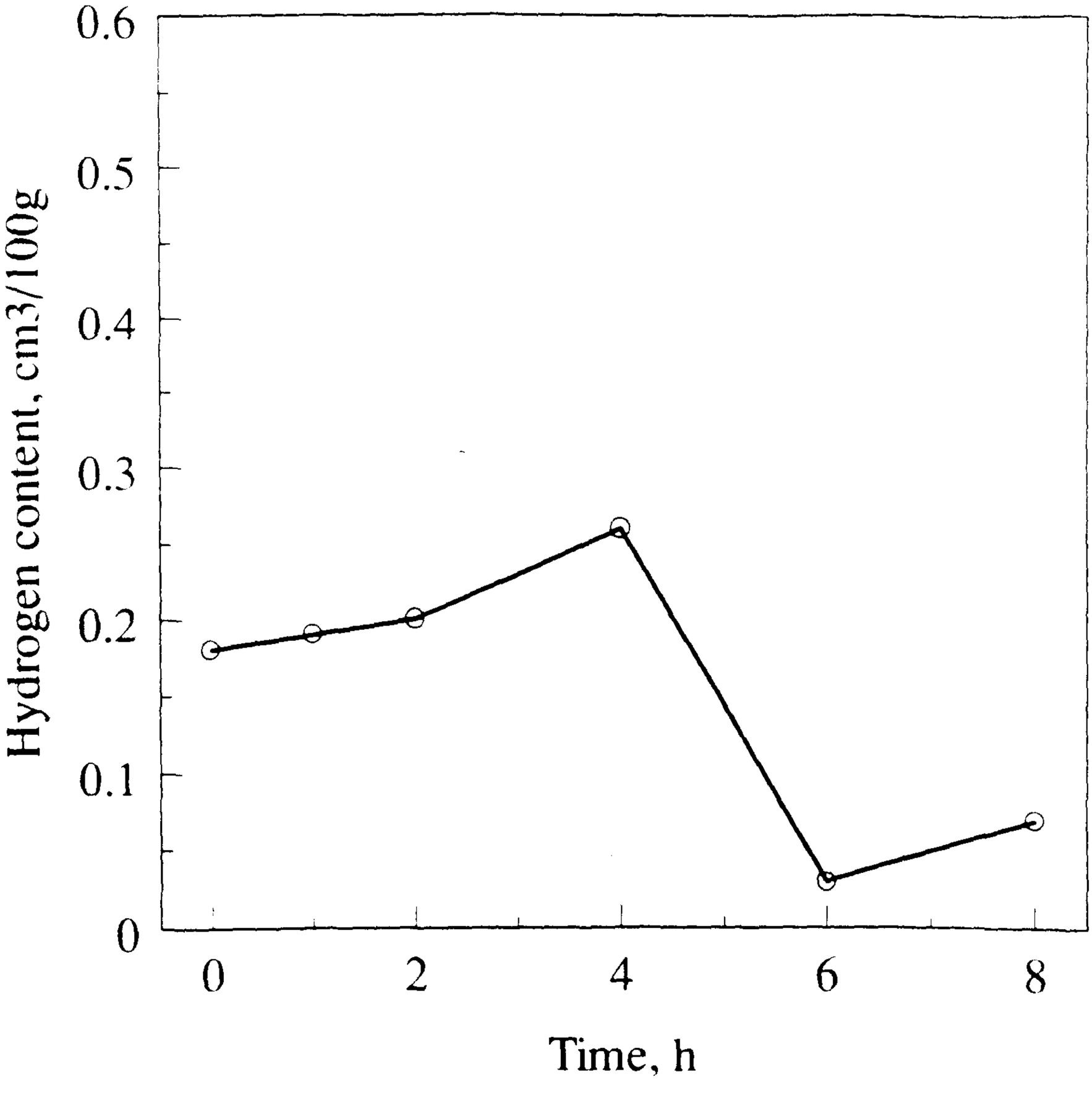

Figure 9.24. Hydrogen content of 10 mm diameter samples machined from the interior of a DC cast Al-0.5%Mg-0.4%Si alloy ingot. Response to isothermal heat-treatment at 590 °C in water-saturated air (p_{H2O} = 0.03 atm).

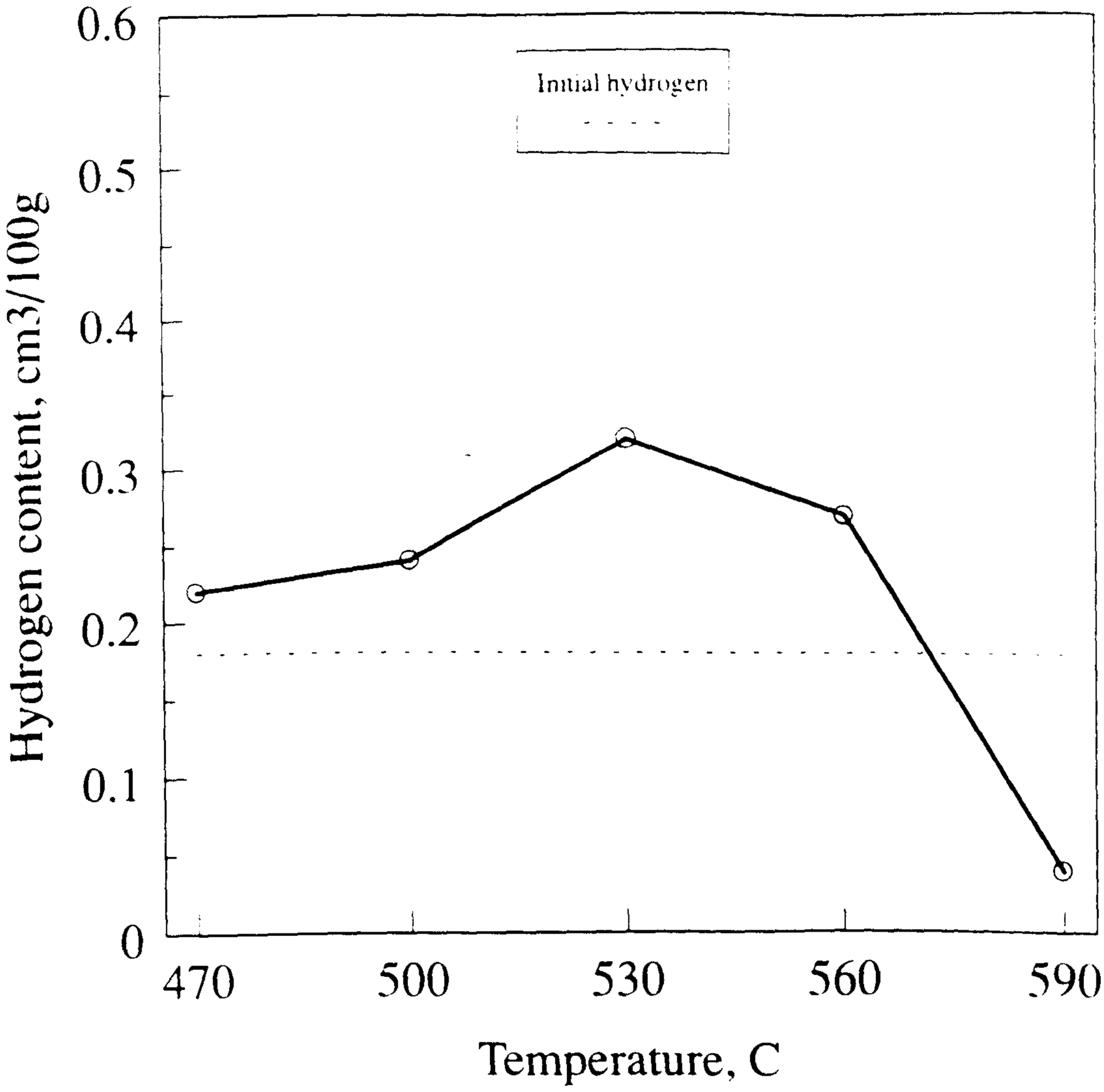

Figure 9.25. Hydrogen content of 10 mm diameter samples machined from the interior of a DC cast Al-0.5%Mg-0.4%Si alloy ingot. Response to isochronal heat-treatment for 4 h in nominally dry air.

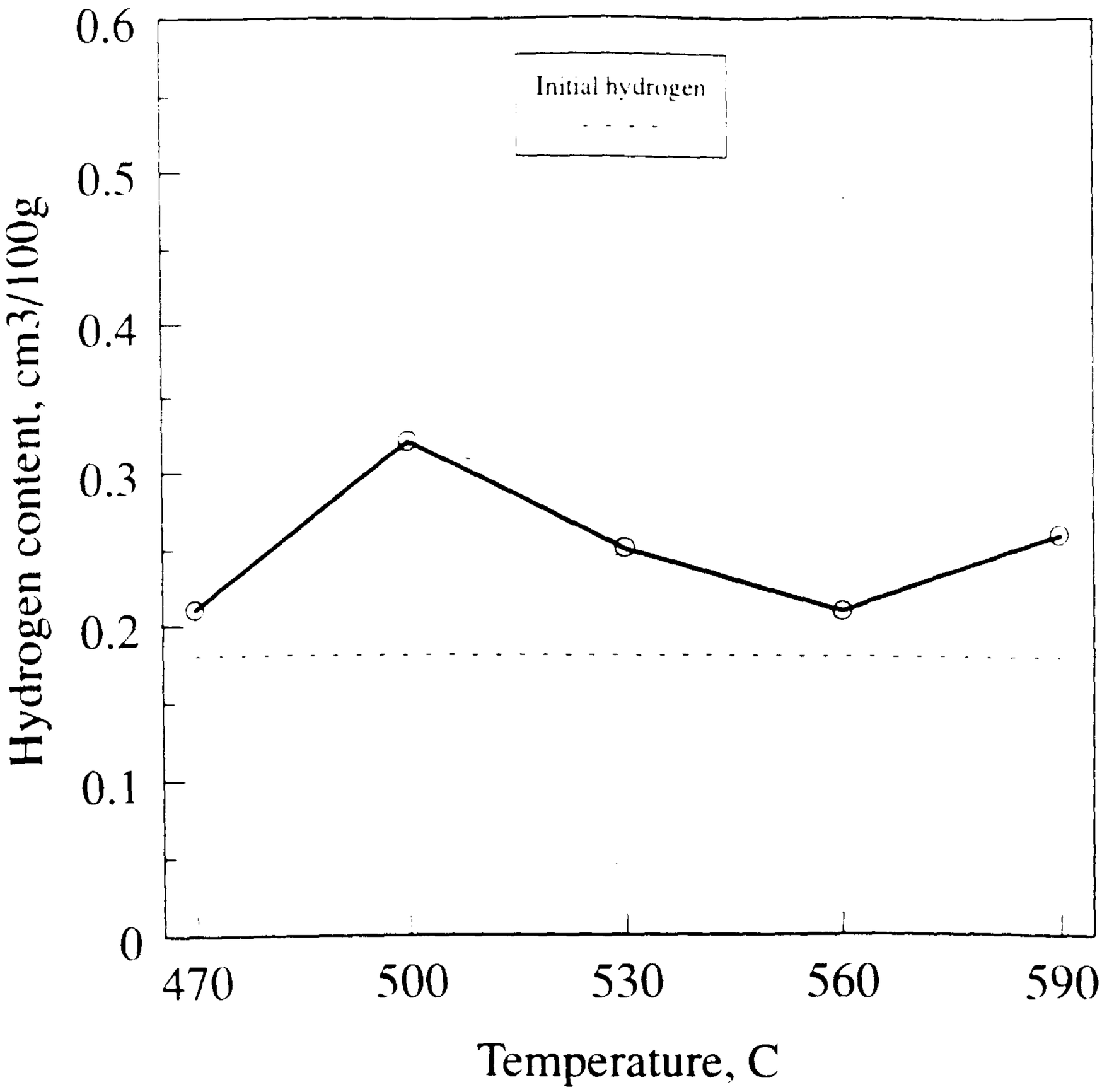

Figure 9.26. Hydrogen content of 10 mm diameter samples machined from the interior of a DC cast Al-0.5%Mg-0.4%Si alloy ingot. Response to isochronal heat-treatment for 4 h in water-saturated air (p_{H2O} = 0.03 atm).

Purely thermodynamic considerations suggest that hydrogen would always be absorbed by the metal by the overall reactions:

$$2Al(s) + 3H_2O(g) = Al_2O_3(s) + 3H_2(g) \qquad (9.12)$$
$$\Delta G^{\theta} = -937675 - 16.7T\log T - 202.1T \quad J$$

$$Mg(s) + H_2O(g) = MgO(s) + H_2(g) \qquad (9.13)$$
$$\Delta G^{\theta} = -357522 - 12.3T\log T + 87.2T \quad J$$

Inserting the Gibbs free energy changes[213] into the Van't Hoff isotherm for T = 773 K and $p(H_2O)$ = 0.03 atm, a typical water vapour pressure in a humid atmosphere:

$$\Delta G^{\theta} = -RT\ln K = -RT\ln [p(H_2)/p(H_2O)] \qquad (9.14)$$

yields hydrogen pressures of 3 x 10^{53} atm, and 9 x 10^{19} atm for reactions 9.12 and 9.13 respectively.

The results given in Figures 9.21 to 9.24 show that, contrary to thermodynamic considerations, hydrogen is not always absorbed but is sometimes even lost from the metal in the presence of water vapour. Similar variable results were obtained by Tahbaz[114] on the same alloy. The determining factors must therefore be kinetic, rather than thermodynamic.

Stephenson[137] encountered an analogous problem with liquid pure aluminium in which the hydrogen content first rose and then fell when it was exposed to a humid atmosphere. He explained these effects by a shift in the dynamic balance between competing absorption and a desorption processes due to structural changes which he identified in the oxide film separating the metal from the atmosphere. This concept offers a reasonable prospect for finding an explanation for the present results. The first step is to characterise the surface oxides formed on the metal samples by the heat-treatments in clean dry and water-saturated atmospheres.

9.3.1 Characterisation of the oxide films

The SIMS depth profiles given in Figures 8.19 to 8.23 and XPS spectra given in Figures 8.30 to 8.38 yield information on the oxide films formed in the heat-treatments.

9.3.1.1 Constitution

Reference sample - natural air-formed oxide film

The surface analyses on the reference sample characterise the surface condition of all samples before heat-treatment.

The SIMS depth profile, given in Figure 8.19, shows an $^{54}Al^{6+}$ signal extending right to the surface of the sample with surface signals for oxygen and magnesium.

The XPS spectrum, given in Figure 8.30 exhibits peaks at 72 .9 and 75.2 eV, corresponding to aluminium 2p electrons for metallic Al and Al_2O_3 respectively[213,214,215]. No magnesium peaks were detected. In the XPS depth profile montage, given in Figure 8.31, the spectrum with two distinct aluminium 2p peaks is confined to the extreme surface. Spectra from deeper levels exhibit one major aluminium 2p peak corresponding to the metallic state, with a only a small shoulder peak corresponding to Al_2O_3. Metallic aluminium was detected because the electron beam penetrated into the metal substrate and since the depth resolution of the XPS instrument was 10 nm, the natural air-formed film was a layer of alumina or alumina + $MgAl_2O_4$, < 10 nm thick.

Film formed on sample heated 4h at 500°C and at 590 °C in nominally dry air.

The SIMS depth profiles, given in Figures 8.20 and 8.21, exhibit the following features:

i. The $^{54}Al^{6+}$ signals are zero at the surfaces and rise to maxima at distances of ~ 0.5 and ~ 0.6 μm below the surface for 500 and 590 °C respectively. These values are taken to indicate the position of the oxide/metal interfaces.

ii. The $^{26}Mg^{2+}$ signals are inverse to the aluminium signals. They are high close to the surfaces and diminish to relatively constant low values at the assumed oxide/metal interfaces.

The corresponding XPS montage for the sample heat-treated at 590 °C, given in Figure 8.32, exhibits peaks with the following characteristics:

i. Aluminium 2p peaks first appear not at the air/oxide interface but at a finite distance below it confirming the SIMS profile for $^{54}Al^{6+}$.

ii. Two aluminium 2p peaks were identified, one at 72.9 and the other at 75.4 eV, corresponding respectively to metallic Al and Al_2O_3. The peak for metallic Al grows and the peak for Al_2O_3 attenuates progressively in spectra from successive depths. The layer of material removed by ion beam etching to produce the XPS profile was much thinner than the oxide layer, estimated as 0.6 μm thick from the SIMS depth profile. Hence the metallic aluminium detected was within the oxide film, since the depth resolution of the XPS instrument was 10 nm.

iii. There is a magnesium 2s peak at 90.3 eV corresponding to MgO[216] at the oxide/air interface. The peak attenuates but broadens progressively in spectra from successive depths. This correlates well with the SIMS profile for $^{26}Mg^{2+}$.

Figure 8.33, extracted from the montage in Figure 8.32, is an example of a spectrum used to identify the aluminium 2p and magnesium 2s peaks from their energies.

Film formed on sample heated 4h at 500 °C and at 590 °C in water-saturated air.

The SIMS depth profiles, given in Figures 8.22 and 8.23, exhibit features which are very similar to those described for the films formed in nominally dry air, with the proviso that for both temperatures the films are somewhat thinner. These features are:

i. The $^{54}Al^{6+}$ signals are zero at the surfaces and rise to maxima at distances of 0.1 and 0.4 μm below the surface for 500 and 590 °C respectively. As before, these values are taken to indicate the oxide thickness.

ii. The $^{2+}Mg^{2+}$ signal is inverse to the aluminium signal as described before.

The extended montage of XPS spectra, given in Figures 8.35 (a) to (c) exhibits the same features as the corresponding montage for the sample heated in nominally dry air, i.e. a peak for MgO in the surface spectrum and peaks for MgO, metallic Al and Al_2O_3 in subsurface spectra. The peak for MgO diminished and the aluminium peaks increased in intensity as successive spectra approached the oxide/metal interface. Figure 8.36 (a) was taken at the air/oxide interface and exhibited only the MgO peak . Figure 8.36 (b) was taken from deep inside the oxide and exhibited a peak for MgO and a peak for metallic aluminium with a shoulder peak for Al_2O_3.

9.3.1.2 Surface hydroxylation

Figures 8.34(a) & (b) and 8.38 (a) & (b) are pairs of XPS spectra for the films formed in nominally dry and water-saturated atmospheres respectively. Figures 8.34 (a) & 8.38 (a) were taken at the air/oxide interfaces and Figures 8.34 (b) & 8.38 (b) were taken immediately below. The two films exhibit the same characteristics, as follows:

Figures 8.34 (a) and 8.38 (a) exhibit two oxygen 1s peaks, one at 532 eV, corresponding to MgO[217,218] and the other at 533 eV, equal to the OH bond in water[213], showing the presence of hydroxyl groups at the air/oxide interface.

Figures 8.34(b) and 8.38 (b) exhibit only the 532 eV oxygen 1s peak for MgO, showing that there are no hydroxyl groups below the surface.

The implication is that hydroxyl groups are confined to an adsorbed layer at the extreme surface of the oxide. This is best illustrated in the montage of XPS spectra for the film formed in water-saturated air, given in Figure 8.37.

It may seem surprising to find hydroxyl groups adsorbed on an oxide film formed in nominally dry air but dew-point hygrometer measurements[111]show that it is virtually impossible to reduce water vapour pressure to $<5 \times 10^{-7}$ atm in laboratory glassware.

9.3.1.3 Interpretation of oxide structure

The following concept of the oxide structure emerges from the surface analyses:

The oxide is not of uniform composition through its thickness. There is an underlay of Al_2O_3 or $MgAl_2O_4$ adjacent to the metal surface, containing a dispersion of metallic aluminium, overlaid by an outer layer of MgO. Whether formed in water-saturated or nominally dry air, the MgO bears an adsorbed layer of hydroxyl groups on its surface.

The generation of this complex structure is explained as follows:

It is well known that Al-Mg alloys bear an air-formed alumina film of a few nm thick, which thickens as the temperature rises up to 350 °C [219,220,221,222,223]. The alumina layer is thermodynamically unfavourable but its formation at temperatures <350 °C is explained by slow diffusion of magnesium to the oxide/alloy interface.. For higher temperatures, selective oxidation of magnesium has often been reported[224,220,221], as would be expected. Subsequently as the temperature exceeds 350 °C, and magnesium becomes accessible through increased diffusivity[225], an approach toward thermodynamic equilibrium becomes theoretically possible. It is established that the reaction:

$$MgO + Al_2O_3 = MgAl_2O_4 \qquad (9.15)$$

can occur at the MgO/Al_2O_3 interface[226]

It has been suggested in the literature that the process goes further producing metallic aluminium by the reaction:

$$3Mg(s) + Al_2O_3 = 3MgO(s) + 2Al(s) \qquad (9.16)$$

but both of the oxides Al_2O_3 and MgO are very stable and a reduction to metal is unlikely in the prevailing high oxygen potential.

The observation of metallic aluminium is most probably an artefact of the XPS technique due to either (i) surface roughness of the samples combined with low lateral resolution of the x-ray, or (ii) decomposition of Al_2O_3 by the highly energetic ion beam.

9.3.2 Competing absorption and desorption processes

9.3.2.1 Absorption

For the reaction to proceed, the primary reactants or species derived from them must meet in an environment where the oxygen potential is low enough for the production of hydrogen. Such a low oxygen potential occurs only at the metal/oxide interface, so some species carrying the hydrogen from its ultimate source in atmospheric water vapour must be able to migrate through the oxide. The molecules of water itself are too large to diffuse through the interstices in the oxide to the metal/oxide interface so that an alternative scheme must be considered.

It is known from the information given in Section 9.3.1.2 that the air/oxide interface bears an adsorbed layer of hydroxyl ions. These must have been produced from atmospheric water vapour by protonation of the surface oxygen ions on the MgO lattice:

$$H_2O\ (\text{atmosphere}) + O^{2-}\ (\text{MgO lattice surface}) = 2OH^-\ (\text{MgO lattice surface}) \quad (9.17)$$

illustrated schematically in Figure 9.27.

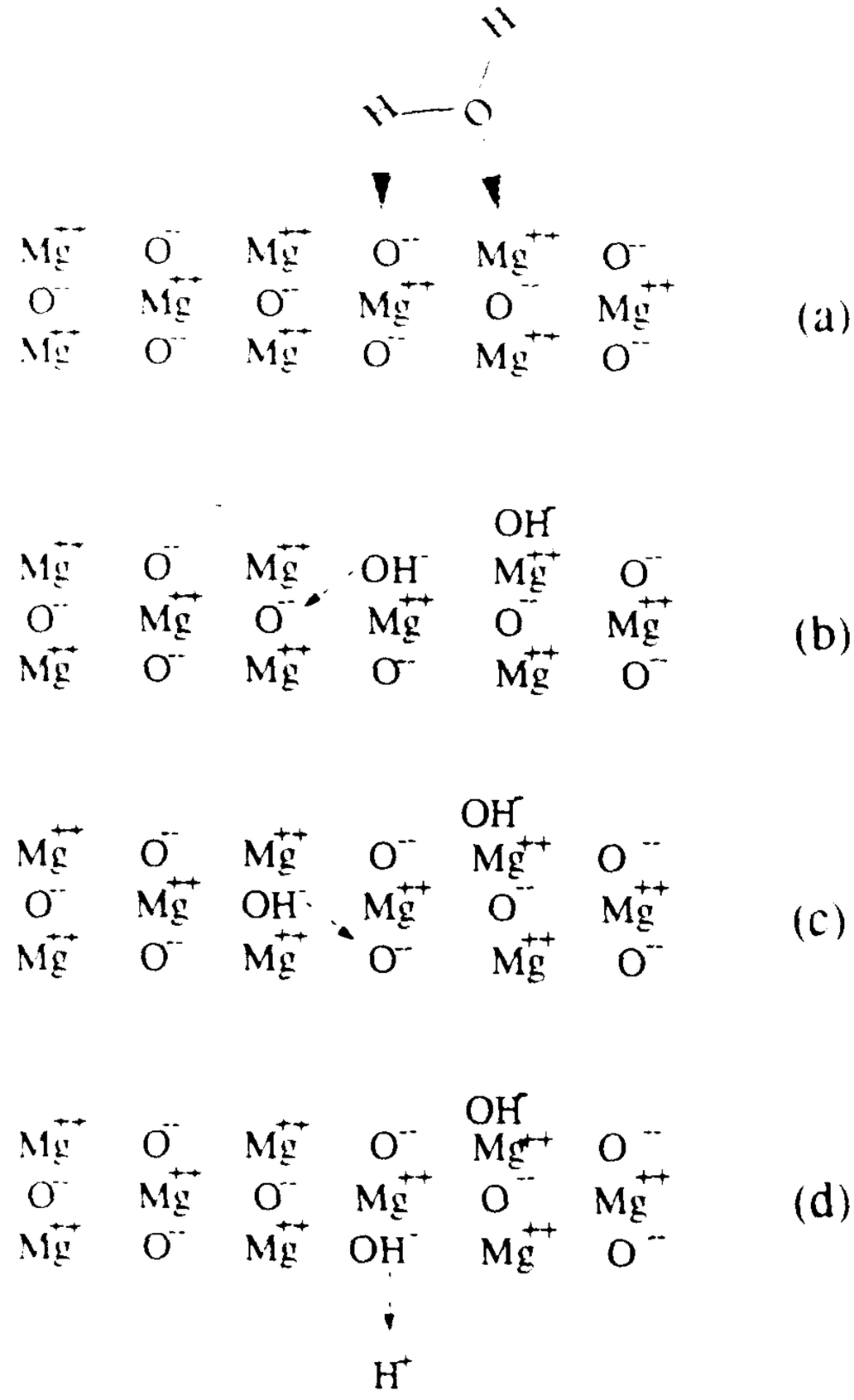

Figure 9.27. Schematic diagram representing protonation of MgO surface and subsequent proton migration by a Grotthus-type chain.

If protons can be conveyed to the oxide/ metal interface by a Grotthus-type chain, as indicated, in Figure 9.27, hydrogen can be produced by the reaction:

$$Mg\ (metal) + 2H^{+} = Mg^{2+}\ (oxide) + 2H \qquad (9.18)$$

The driving force for the process is the high negative Gibbs free energy change of the overall reaction which is the sum of reactions 9.17 to 9.19:

$$Mg + H_2O = MgO + 2H \qquad (9.19)$$

The problem is that the MgO matrix is a poor conductor of protons. It is almost completely ionic with a large electron energy band gap so it is intolerant to the replacement of an intrinsic ion by an ion of different valency, i.e. the replacement of the divalent O^{2-} ion by the monovalent OH^- ion which results from protonation of the O^{2-} ion. The low population of Shottky defects in MgO also precludes significant alternative pathways for protons.

The situation is therefore as follows. There is a supply of hydroxyl ions at the air/oxide interface and a driving force for Reaction 9.19 but the MgO matrix blocks the transport of protons ions needed for the reaction to proceed. Since hydrogen was absorbed during some of the heat-treatments, there must be some conditions in which an alternative proton path is activated. A potential path is offered by grain boundaries, where the regularity of the structure and charge balance in the MgO lattice is locally disturbed. A grain boundary path for protons is worthy of consideration, because Silva[226] has shown that the growth of MgO on aluminium-magnesium alloys is due almost entirely to magnesium diffusion through the grain boundaries and that the rate of oxide growth became slower as the grain boundary area diminished due to grain growth. Therefore a reasonable proposition is that the transport of protons through the oxide and consequently absorption of hydrogen by the metal also depends on the grain size of the oxide and, of course also on length of the path, i.e. on the film thickness.

9.3.2.2 Desorption

In the desorption process, the hydrogen moves through the oxide in the opposite direction, i.e. from the oxide/metal interface to the air/oxide interface. This cannot be in the form of *protons*, as in the absorption process, because the proton concentration gradient is adverse. The interstices of the oxide are large enough to accommodate *neutral hydrogen atoms* and since there is no gaseous hydrogen at the air/oxide interface, the concentration gradient is favourable for outward diffusion.

9.3.2.3 Dynamic balance between absorption and desorption

From the arguments given in Sections 9.3.2.1 and 9.3.2.2, hydrogen absorption and desorption are to be regarded as independent competing processes, whose relative rates

depend on different parameters. It is clear from the discussion in Section 9.3.1 that these opposing processes operate within a very complex structure and the dynamic balance between them, which determines whether the metal absorbs or loses hydrogen, must be very sensitive to prevailing conditions.

If protons are unable to migrate through the oxide, only physical desorption prevails and the metal loses hydrogen continuously, as in the heat-treatment recorded in Figure 9.22. Conversely, if protons migrate easily through the oxide, hydrogen absorption can overwhelm the loss by physical desorption and the metal absorbs hydrogen continuously as apparently happened in the heat-treatment recorded in Figure 9.21.

The merit of the concept of a dynamic balance is that it can provide an explanation for a change from hydrogen absorption to loss during the same heat-treatment as recorded in Figures 9.23 and 9.24. The explanation lies in a shift in the dynamic balance from net hydrogen absorption to net hydrogen loss due to structural change in the oxide. The diffusion of hydrogen atoms through the oxide matrix is less structure-sensitive than the diffusion of protons through selective grain boundary paths for the reasons given in Section 9.3.2.1. As a heat-treatment continues, grain boundary paths for protons become longer and fewer because the oxide thickens and the grain size increases. Silva[226] provided evidence for grain growth in MgO films formed on aluminium-3% magnesium alloys. He found that films formed at 525 °C had grain diameters of ~ 2 nm after 30 minutes and ~ 10 nm after 2 h, as illustrated in the TEM micrographs and electron diffraction patterns reproduced in Figure 9.28. Silva's temperature and time-span are relevant to the present results.

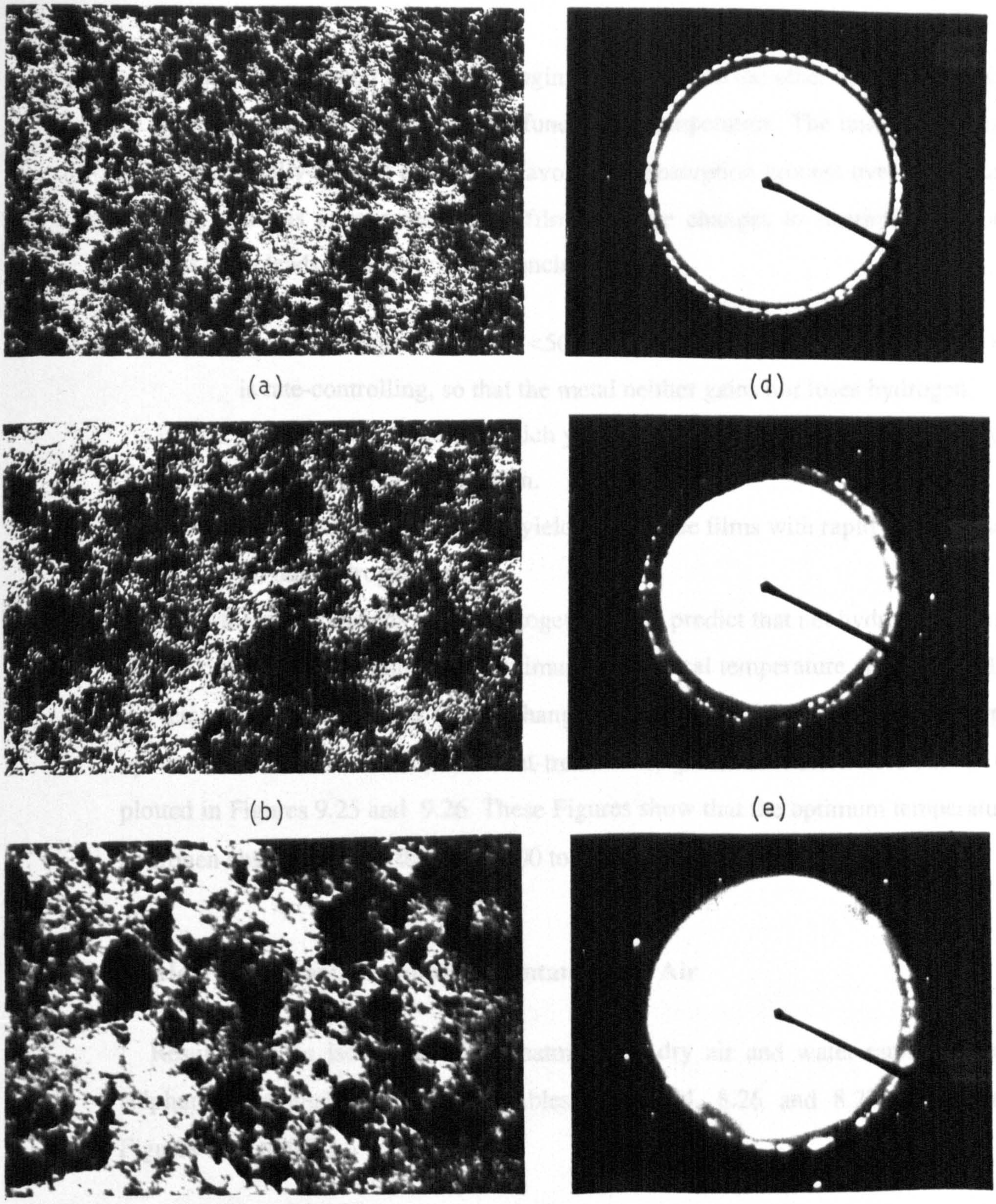

Figure 9.28. TEM micrographs and related electron diffraction patterns from fragments of oxide films formed on solid Al-3.1% Mg alloy after varous exposures in the moist atmosphere at 525 °C, showing grain growth of MgO film[226].

(a), (d) : after 30 min (x 120,000)
(b), (e) : after 1h (x 120,000)
(c), (f) : after 2h (x 120,000)

The above discussion assists in bringing some logic to the otherwise arbitrary pattern of hydrogen absorption and loss as a function of temperature. The underlying principle is that the intially-formed oxide film favours the absorption process over the desorption process, and this is reversed as the film structure changes to restrict the absorption process. This leads to the following conclusions:

i. At low temperatures, i.e. <500 °C, slow diffusion of hydrogen in the metal is rate-controlling, so that the metal neither gains nor loses hydrogen.
ii. Moderate temperatures which yield thin oxide films with slow grain growth favour hydrogen absorption.
iii. High temperatures, which yield thick oxide films with rapid grain growth, favour hydrogen loss.

When these conclusions are taken together, they predict that net hydrogen absorption should rise with temperature to a maximum at a critical temperature and then decline as the temperature rises further finally changing to hydrogen loss. This idea is supported by the results for 4h isochronal heat-treatments, given in Tables 8.13 and 8.16 and plotted in Figures 9.25 and 9.26. These Figures show that the optimum temperature for hydrogen absorption is in the range 500 to 530 ^{0}C.

9.4 Heat Treatments In Sulphur-Contaminated Air

Results for the isothermal heat-treatments in dry air and water-saturated air with sulphur contamination, given in Tables 8.23, 824, 8.26 and 8.27, are plotted in Figures 9.29 to 9.32.

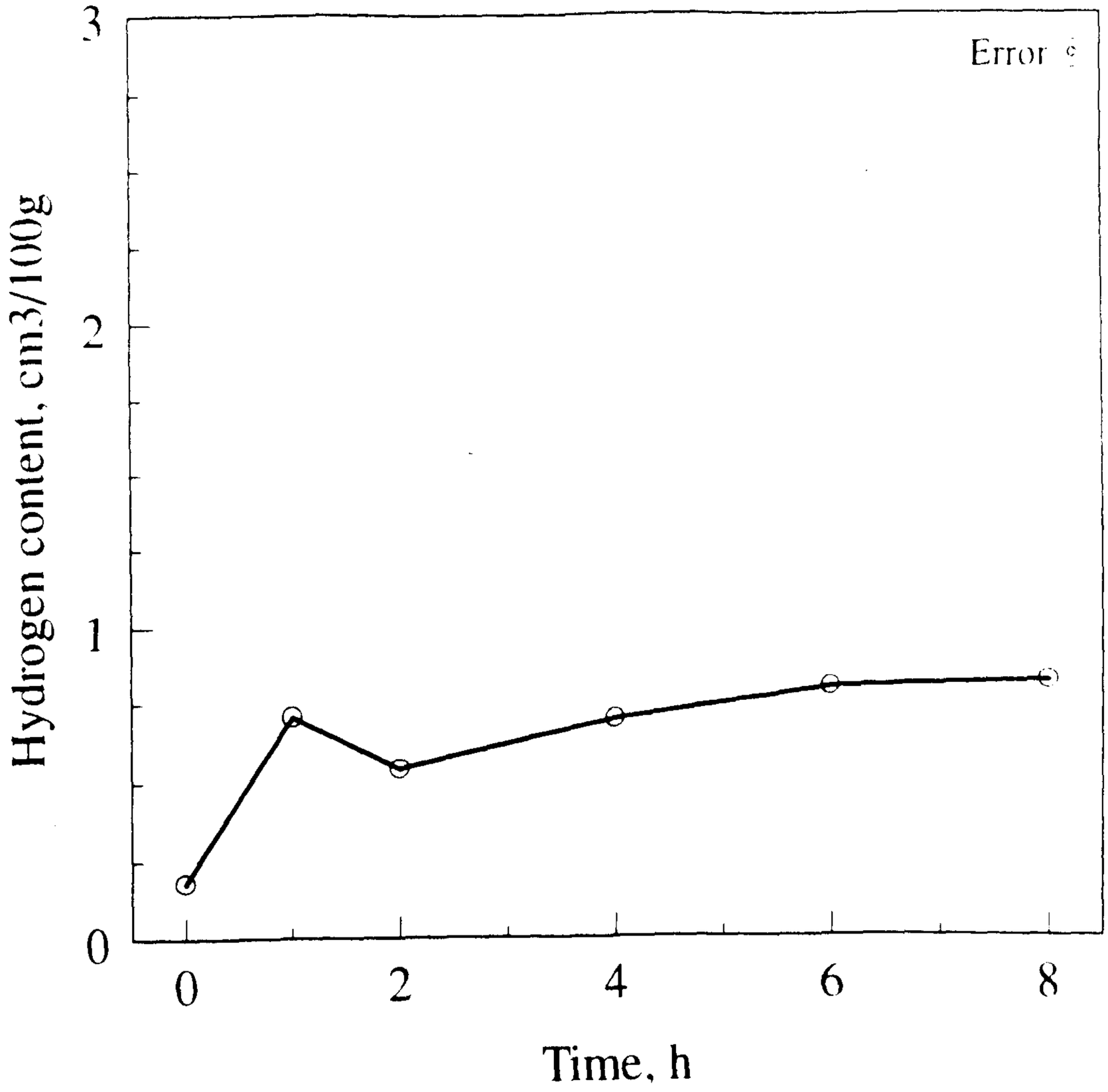

Figure 9.29. Hydrogen content of 10 mm diameter samples machined from the interior of a DC cast Al-0.5%Mg-0.4%Si alloy ingot. Response to isothermal heat-treatment at 500 °C in nominally dry air + 1% SO_2.

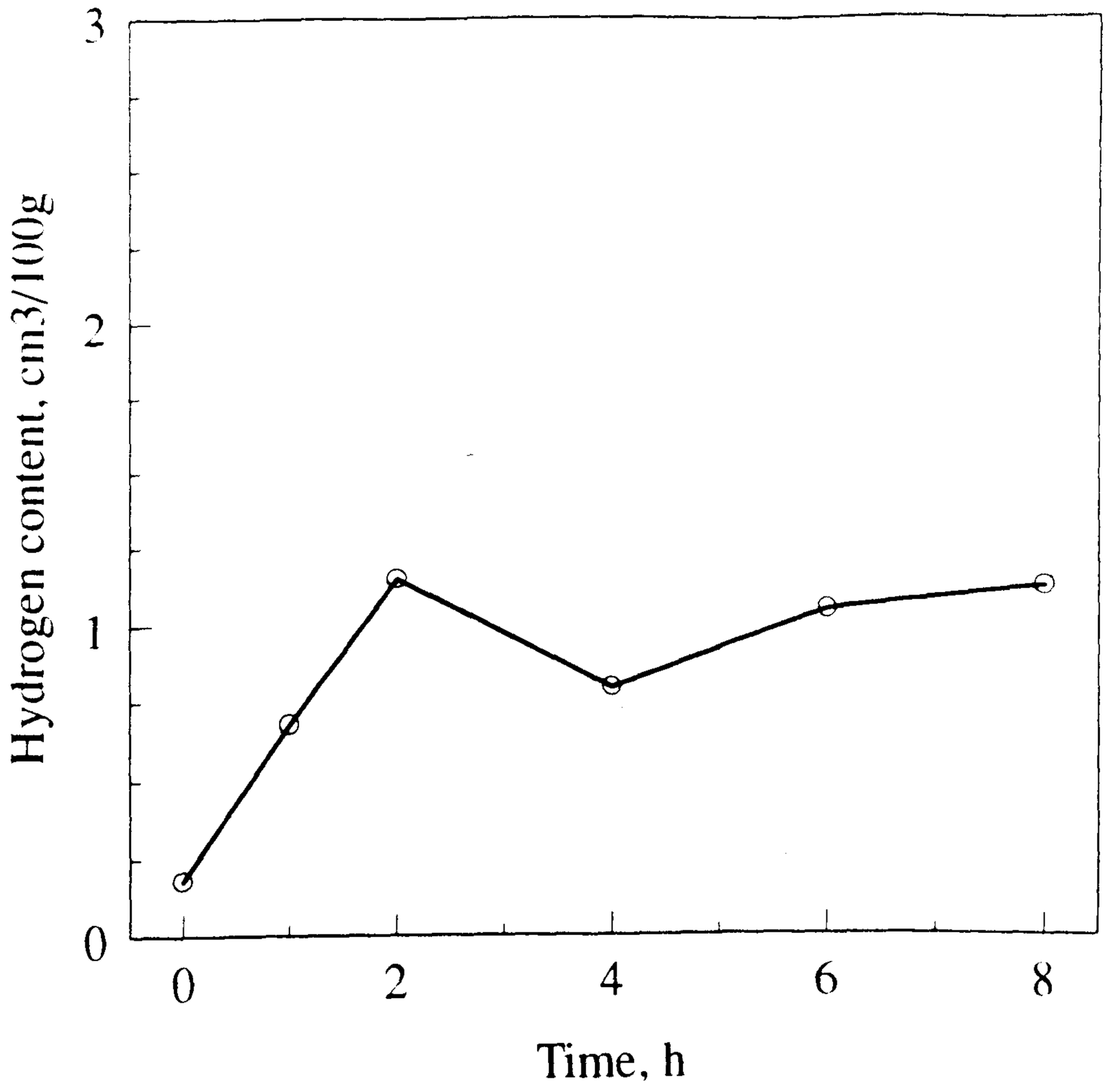

Figure 9.30. Hydrogen content of 10 mm diameter samples machined from the interior of a DC cast Al-0.5%Mg-0.4%Si alloy ingot. Response to isothermal heat-treatment at 590 °C in nominally dry air + 1% SO_2.

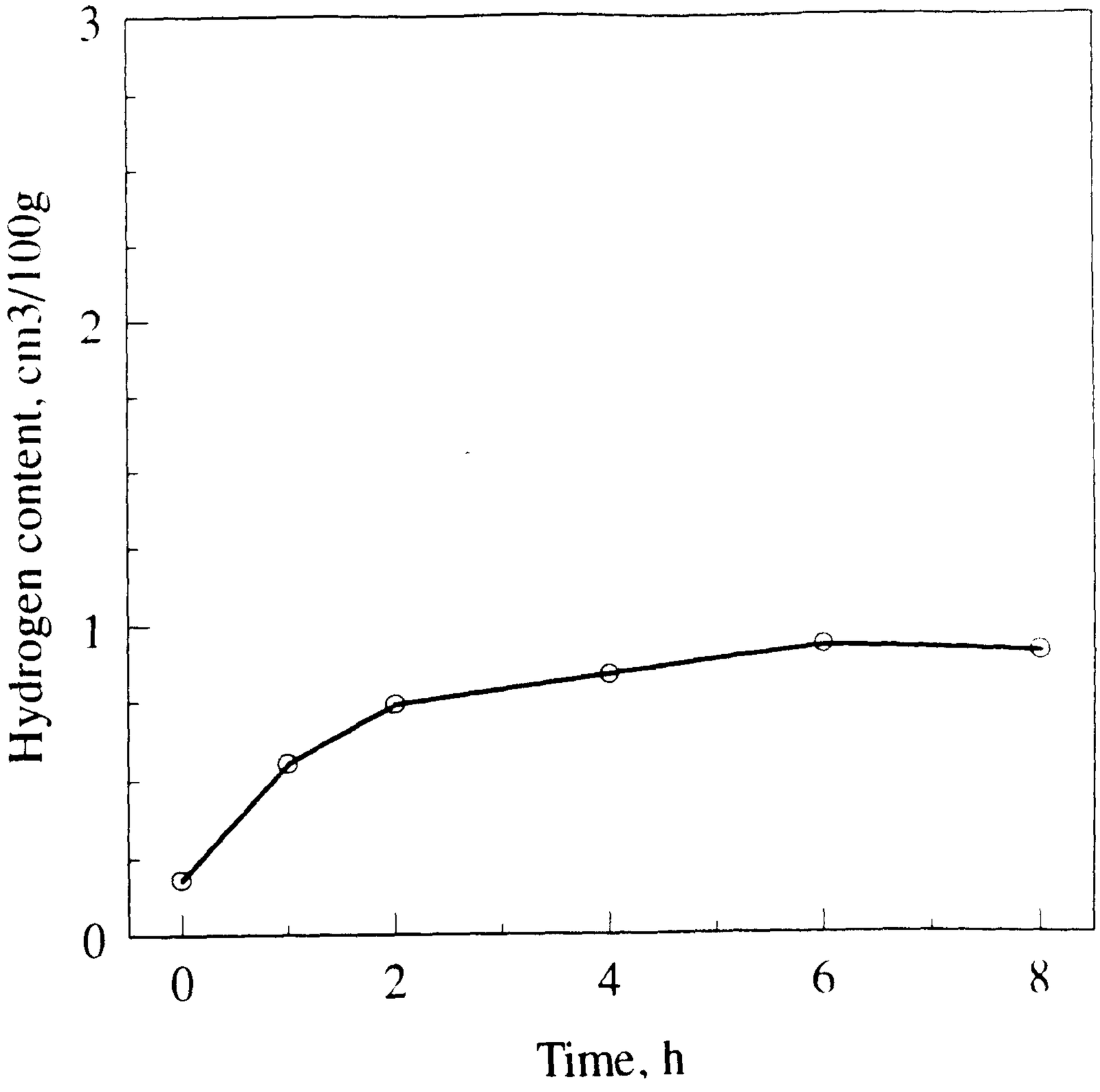

Figure 9.31. Hydrogen content of 10 mm diameter samples machined from the interior of a DC cast Al-0.5%Mg-0.4%Si alloy ingot. Response to isothermal heat-treatment at 500 °C in water-saturated air + 1% SO_2 (p_{H2O} = 0.03 atm).

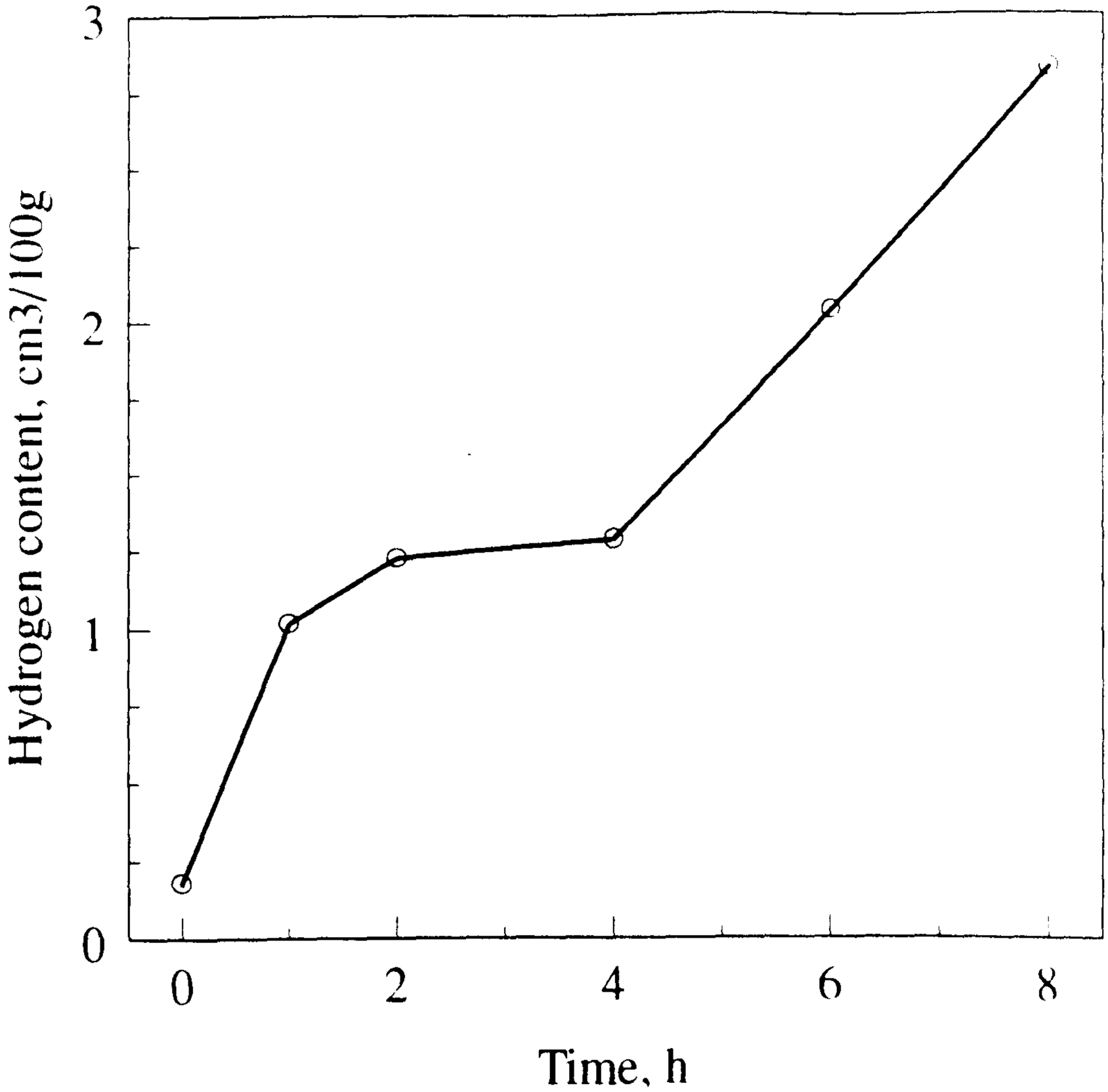

Figure 9.32. Hydrogen content of 10 mm diameter samples machined from the interior of a DC cast Al-0.5%Mg-0.4%Si alloy ingot. Response to isothermal heat-treatment at 590 °C in water-saturated air + 1% SO_2 (p_{H2O} = 0.03 atm).

The results given in Figures 9.29 to 9.32 show that hydrogen was always absorbed from sulphur-contaminated air and that the quantity absorbed was an order of magnitude greater than the maximum quantity absorbed from clean air. (Note that the hydrogen content scale is extended by a factor of five compared with corresponding results for clean air). Again it is apparent that even the nominally dry atmosphere contributed a sufficient source of water vapour to supply the absorbed hydrogen.

Results for the isochronal heat-treatments, given in Table 8.25 and 8.28 are plotted in Figures 9.33 and 9.34. They show the same tendency to optimise hydrogen absorbtion as discussed in Section 9.3.2.3 but at a somewhat higher temperature, as expected from the enhanced absorption process when sulphur is present.

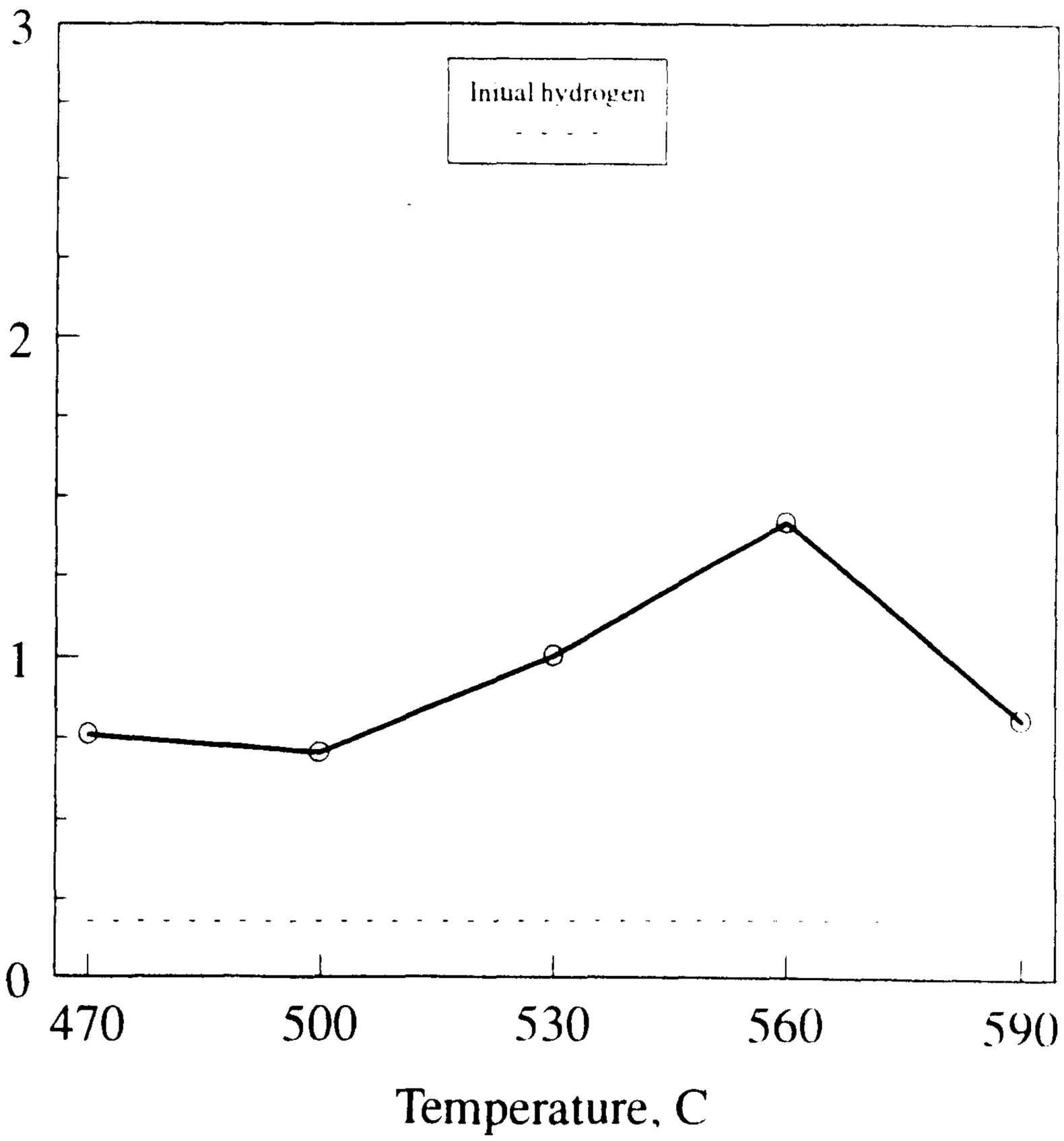

Figure 9.33. Hydrogen content of 10 mm diameter samples machined from the interior of a DC cast Al-0.5%Mg-0.4%Si alloy ingot. Response to isochronal heat-treatment for 4 h in nominally dry air + 1% SO_2.

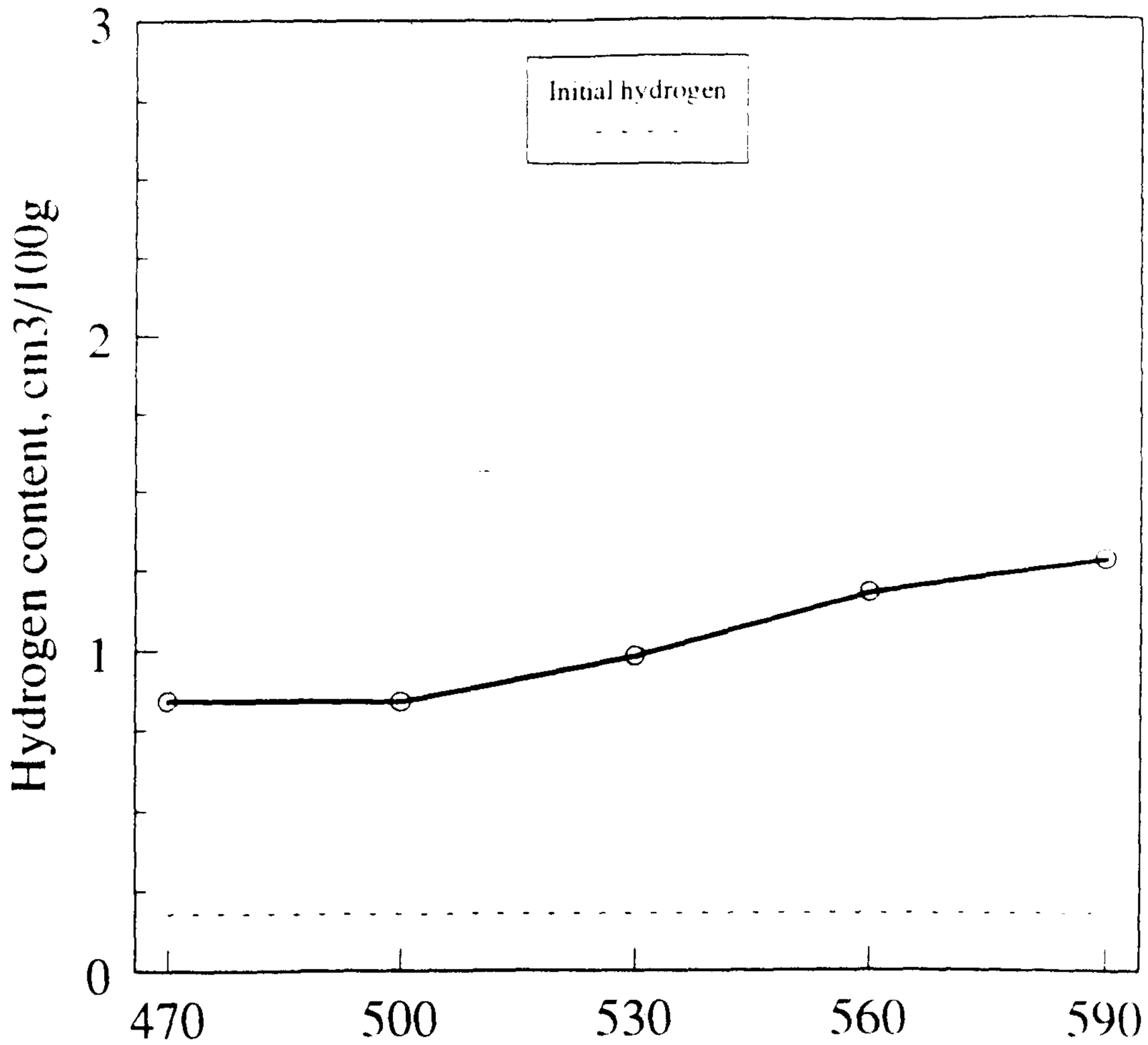

Figure 9.34. Hydrogen content of 10 mm diameter samples machined from the interior of a DC cast Al-0.5%Mg-0.4%Si alloy ingot. Response to isochronal heat-treatment for 4 h in water-saturated air + 1% SO_2 (p_{H2O} = 0.03 atm).

Table 8.29 gives an interesting insight into the sensitivity of the metal to sulphur contamination. The results given in the table were obtained during preliminary experiments when a thermocouple used with a sample heated in air with 1% SO_2 was subsequently used with a sample heated in an air-flow free from SO_2 . There was enough transfer of sulphur on the thermocouple to cause the two samples affected to absorb 0.76 and 0.98 cm^3/100 g of hydrogen.

Following the line of reasoning developed in Section 9.3 the marked increase in the quantity of hydrogen absorbed must have been due to a change in the character of the oxide film, which promoted reaction between atmospheric water vapour and the metal. This directs attention to the results of surface analysis, described in Section 9.4.1 next.

9.4.1 Characterisation of the sulphur-bearing oxide films

Figures 8.24 to 8.27 give the SIMS depth profiles for the samples heated at 500 °C and at 590 °C for 4h in dry and in water-saturated air, both contaminated with sulphur dioxide. Figures 8. 39 to 8.49 give the related XPS spectra.

9.4.1.1 Constitution.

In the SIMS profiles given in Figures 8.24 to 8.27 differ from the corresponding profiles for clean air, given in Figures 8.20 to 8.23, as follows:

i. The $^{54}Al^{6+}$ signal was first detected at a greater depth below the air/oxide interface, i.e. 0.1 to 0.25 μm and 0.6 μm for heat-treatments at 500 °C and 590 °C respectively.
ii. Strong $^{16}O^{2-}$, $^{32}S^{2-}$ and $^{1}H^{-}$ signals as well as $^{26}Mg^{2+}$ signals were recorded in the zone between the air/oxide interface and the plane at which the Al signal was detected . A significant feature of the profiles is that the $^{16}O^{2-}$, $^{32}S^{2-}$ and $^{1}H^{-}$ signals fall from the air/oxide interface to plateaus terminating at the plane where the $^{54}Al^{6+}$ signal is first detected.

Figures 8.39 and 8.40 a & b are montages of XPS depth profiles showing the development of aluminium 2p peaks as a function of the depth below the air/oxide interface. These montages exhibit two significant features:

i. the peaks first appear at a greater depth below the air/oxide interface than in the corresponding montages for clean air, given in Figures 8.32 and 8.35 a-c, confirming the information derived from the SIMS profile.
ii. As for the corresponding information for clean air, twin peaks are identified, one at 72.9 and the other at 75.7 eV, corresponding respectively

to metallic Al and Al_2O_3. Figure 8.41 gives one of the spectra selected from the montage to show how the peaks were identified by their energies.

Figures 8.42 and 8.46 are montages of XPS spectra showing the development of 2p electron peaks for sulphur as a function of the depth below the air/oxide interface. These are of great significance in assessing the character of the film. The spectrum taken at the air/oxide interface exhibits only peak, at 169.6 eV, corresponding to $MgSO_4$. Immediately below the interface, a second peak was detected at 162.6 eV, corresponding to MgS. The sulphate peak diminishes and the sulphide peak increases in amplitude in successive spectra at greater depths below the air/oxide interface.

The identification of surface sulphate and deeper sulphide is crucial in assessing the character of the oxide film. Table 9.4 confirms the presence of sulphate by comparing the energies attributed to the sulphur and magnesium peaks in the film with the energies of the known corresponding peaks from the standard sample of $MgSO_4$. $7H_2O$. The sulphide peak was then confirmed by comparing the difference in energies between the two peaks, i.e. 7 eV, with the known difference between sulphate and sulphide peaks for other metallic elements[227].

Table 9.4. Comparison of S_{2p}, Mg_{2p} and Mg_{1s} peaks with $MgSO_4.7H_2O$ standard

Source	Figures	Peak (eV)			
		S_{2p}		Mg_{2p}	Mg_{1s}
$MgSO_4.7H_2O$ (standard)	8.28 & 8.29	169.5	-	51.0	1304.6
Heated in nominally dry air + SO_2	8.43, 8.44 & 8.45	169.6	162.6*	51.2	1305.0
Heated in water-saturated air + SO_2	8.47, 8.47 & 8.49	169.6	162.1*	51.0	1304.7
* Peak corresponding to MgS					

9.4.1.2 Structure of the surface film

Comparison of the SIMS profiles for sulphur-contaminated air, given in Figures 8.24 to 8.27 with the corresponding profiles for clean air, given in Figures 8.20 to 8.23 shows that the effect of the SO_2 contamination was to stimulate the growth of a thick overlay containing magnesium, oxygen, sulphur and hydrogen.

Combining this information with the information from the XPS spectra yields a concept of the oxide constitution as follows:

i. There is an underlay of Al_2O_3 or $MgAl_2O_4$ adjacent to the metal surface, containing dispersed metallic aluminium. This is similar to the underlay in films formed in clean air, described in Section 9.3.

ii. There is an overlay of a phase or phases containing magnesium ,sulphur, oxygen and hydrogen.

iii. Sulphur at the air/oxide interface, is entirely in the form of SO_4^{2-}

iv. Sulphur in the overlay below the air/oxide interface is in the form of S^{2-}.

Figure 9.35 gives a schematic section through the oxide/sulphide system, illustrating these features.

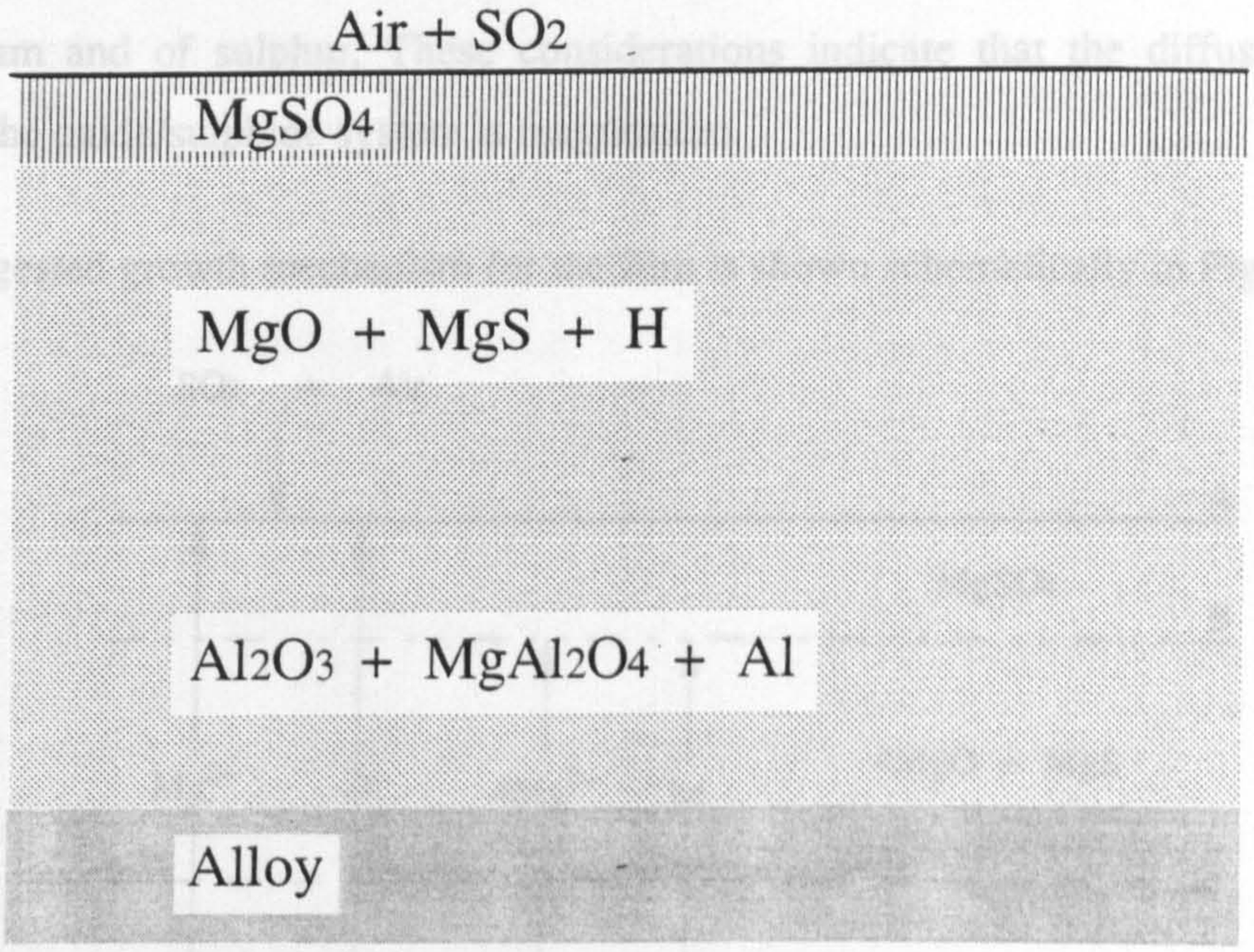

Figure 9.35. Schematic section through oxide/sulphide film system

9.4.1.3 Oxide growth mechanism

Diffusion coefficients for magnesium and oxygen in MgO are known only at very high temperatures:

Magnesium[228]: $D = 0.25 \exp(79/RT)\ cm^2s^{-1}$ for1400 - 1600 °C (9.20)

Oxygen[229]: $D = 2.5 \times 10^{-6}\exp(62.4/RT)\ cm^2s^{-1}$ for 1300 - 1750 °C (9.21)

At the lower temperatures relevant to the present work, the diffusivity of magnesium must still be orders of magnitude greater than the diffusivity of oxygen. No information is available for the diffusion of magnesium or sulphur in MgS but since it has the same simple cubic structure as MgO and the S^{2-} ion (0.184 nm radius[230]) is larger than the O^{2-} ion (0.140) nm radius[230], the same disparity must apply between the diffusivity of magnesium and of sulphur. These considerations indicate that the diffusing species through the oxide/sulphide system is magnesium.

A suggested growth mechanism for the film is shown schematically in Figure 9.36.

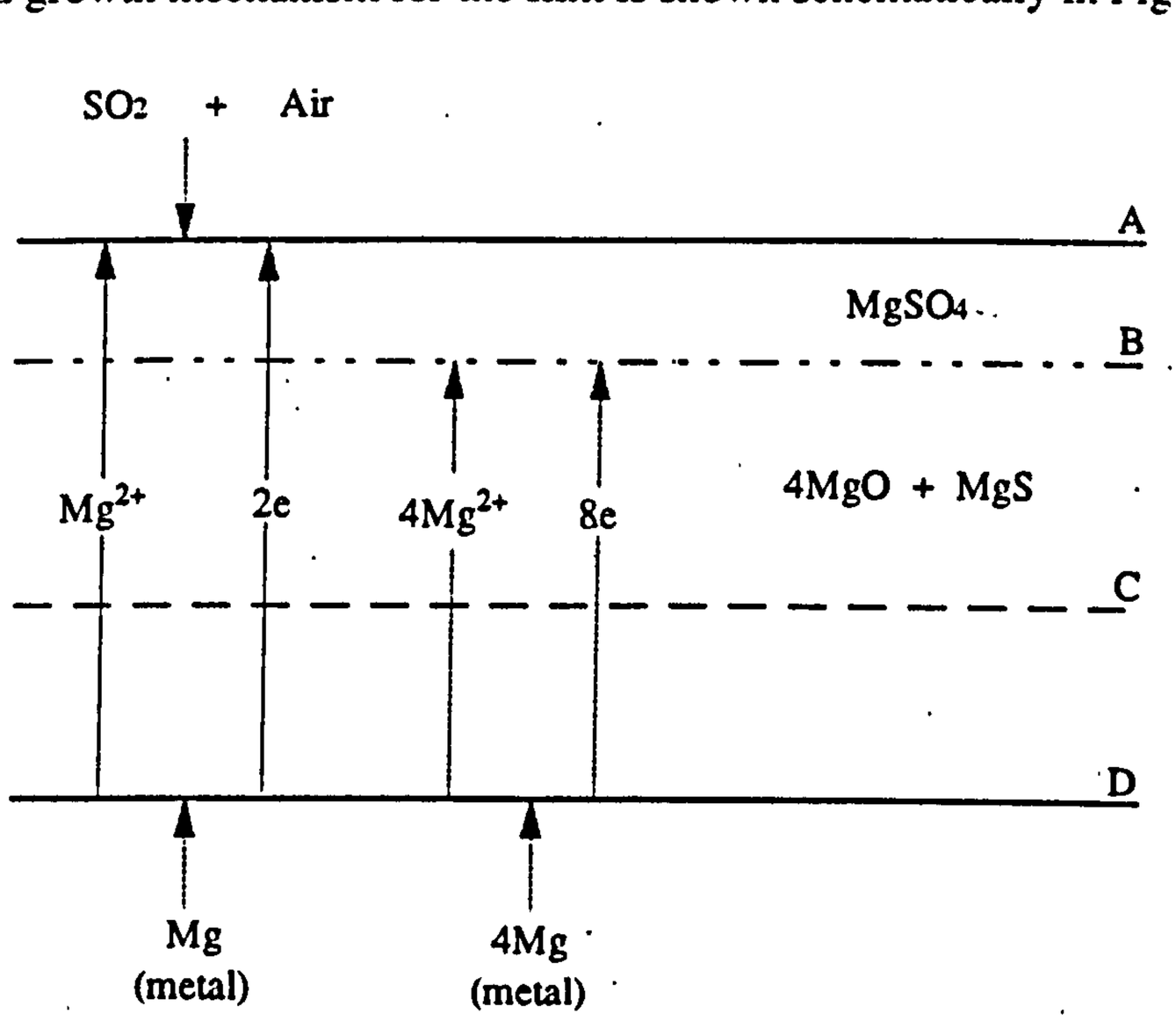

Figure 9.36. Schematic growth mechanism for oxide.

Expressed in ionic terms, the following overall reactions at the interfaces in Figure 9.36 are suggested:

i. Air/oxide interface, A

$$2e + SO_2 + O_2 = SO_4^{2-}$$

ii. Sulphate/sulphide interface, B

$$8e + SO_4^{2-} = S^{2-} + 4O^{2-}$$

iii. Oxide/metal interface, D

$$(4 + 1)Mg = (4 + 1)\,Mg^{2+} + (2 + 8)e$$

Of the ten electrons produced at the air/oxide interface A, two are transmitted to the air/oxide interface, where they sustain oxide growth and eight are consumed at the sulphate/sulphide interface in reducing SO_4^{2-} to S^{2-}, as shown in Figure 9.36. Four of the Mg^{2+} ions are retained as counter ions to maintain charge balance at the sulphate/sulphide interface, B and the other is transmitted to the air/oxide interface, A, where it fulfils the same function.

The overall oxidation process is slow because rate-control is exercised by magnesium diffusion through the film[226]. At this stage, it is uncertain whether the proposed sulphating scheme occurs simultaneously with normal oxidation or replaces it.

9.4.2 Absorption of Hydrogen

Figures 9.29 to 9.34 show that the hydrogen absorption process completely overwhelmed the loss by desorption. It is clear that the theory of a limited absorption process considered in Section 9.3.2.1 is inadequate to explain the acquisition of the very high hydrogen contents absorbed.

The high $^1H^-$ signals in the magnesium/oxygen sulphur overlay identified in the SIMS profiles given in Figures 8.24 to 8.27 suggest an explanation. The kinetic problem for hydrogen absorption from clean air was identified as the poor proton conduction of the highly ionic oxide MgO. Replacement of some of the MgO by $MgSO_4$ and/or MgS is expected to provide much better conducting paths for protons for the following reasons:

i. MgS has less ionic character than MgO. The ionic character of a compound is determined by the difference in electronegativity between the constituent elements. The electronegativities of magnesium, sulphur and oxygen are 1.2, 2.5 and 3.5 respectively on Pauling's scale[230]. This gives electronegativity differences of 2.3 for MgO and 1.3 for MgS. From Pauling's chart[230], reproduced in Figure 9.37, the ionic characters expected are 75% for MgO and 35% for MgS. This means that the electron energy band gap in MgS is smaller than in MgO and it is hence more amenable to accepting ions with mismatching valencies, if size factors permit. The smaller band gap improves electronic conductivity, facilitating electron flow to maintain charge balance.

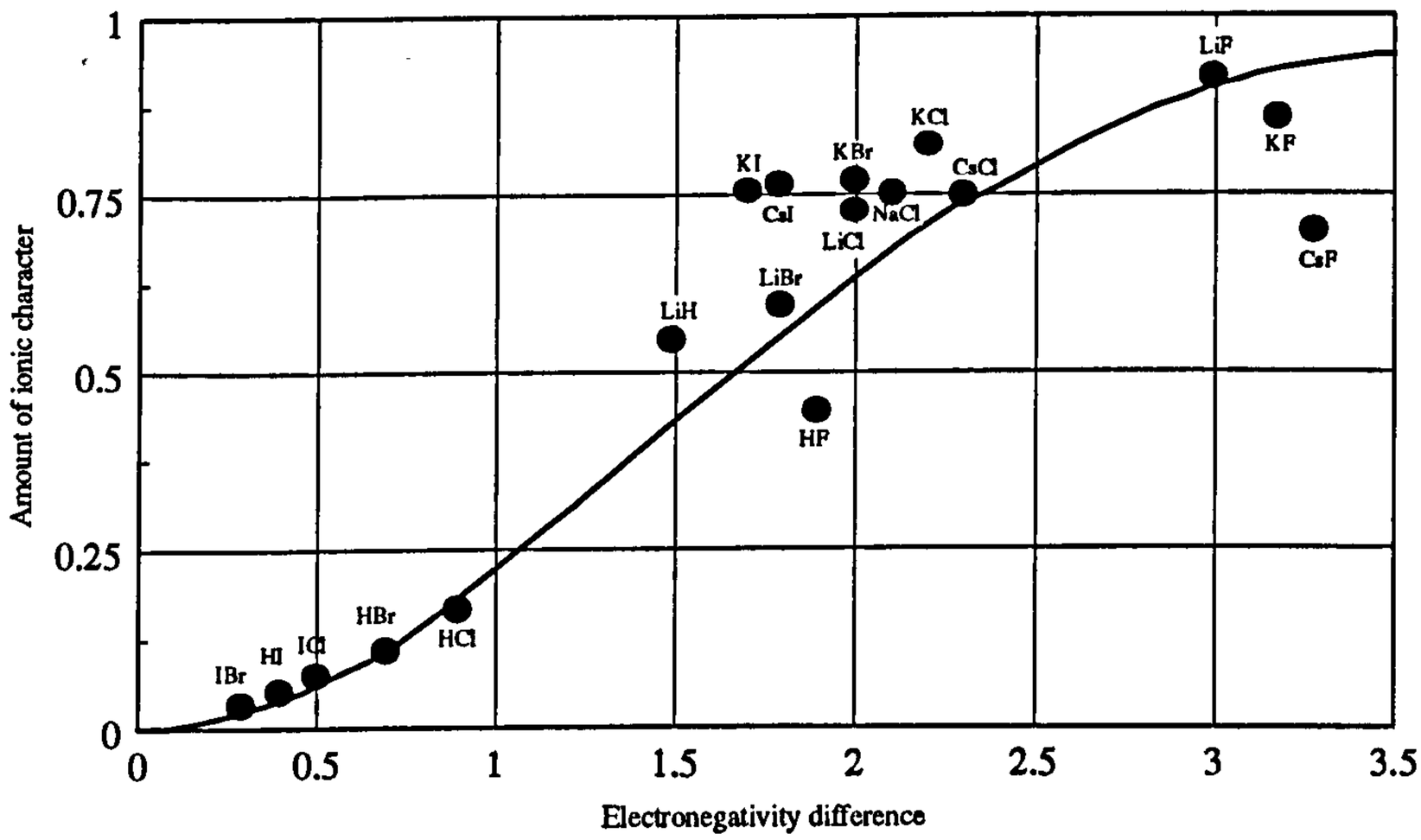

Figure 9.37. Ionic character of bonds as a function of electronegativity difference[230].

ii. protons can diffuse along a path provided by the anions of a dibasic acid. This amounts to a linear exchange between the primary and secondary ions. The activation energies for diffusion along such a path depends on the strength of the bond between the protons and the host ions, which is indicated by the values of the second dissociation constants of their parent acids. The parent acids of the ions of interest in the present discussion, i.e. O^{2-}, S^{2-} and SO_4^{2-} are H_2O, H_2S and H_2SO_4. The second dissociation

constants at 25 °C are[231.205]:

$$H_2O : \quad OH^- = H^+ + O^{2-} \quad K = 10^{-36} \tag{9.22}$$

$$H_2S : \quad HS^- = H^+ + S^{2-} \quad K = 10^{-12} \tag{9.23}$$

$$H_2SO_4 : \quad HSO_4^- = SO4^{2-} \quad K = 10^{-2} \tag{9.24}$$

Equations 9.22 to 9.24 indicate that the activation energies for diffusion along S^{2-} or SO_4^{2-} paths are much less than along O^{2-} paths. Hence protons should be much more mobile in MgS and $MgSO_4$ media than in MgO.

This provides a convincing explanation for the vulnerability of the alloy to absorb hydrogen in atmospheres contaminated with sulphur. The considerations apply irrespective of whether proton diffusion is through the matrix or selectively along disturbed lattice order at grain boundaries.

9.5 Heat Treatments In Chloride -Contaminated Air

Results for isothermal heat-treatments in water-saturated air with chloride contamination, from Tables 8.17 and 8.18, are plotted in Figures 9.38 and 9.39. Corresponding results for 4 h isochronal heat-treatments from Table 8.19 are plotted in Figure 9.40.

Results for isothermal heat-treatments in water-saturated air + 1% SO_2 with chloride contamination, from Tables 8.20 and 8.21 are plotted in Figures 9.41 and 9.42. Corresponding results for 4 h isochronal heat-treatments from Table 8.22 are plotted in Figure 9.43.

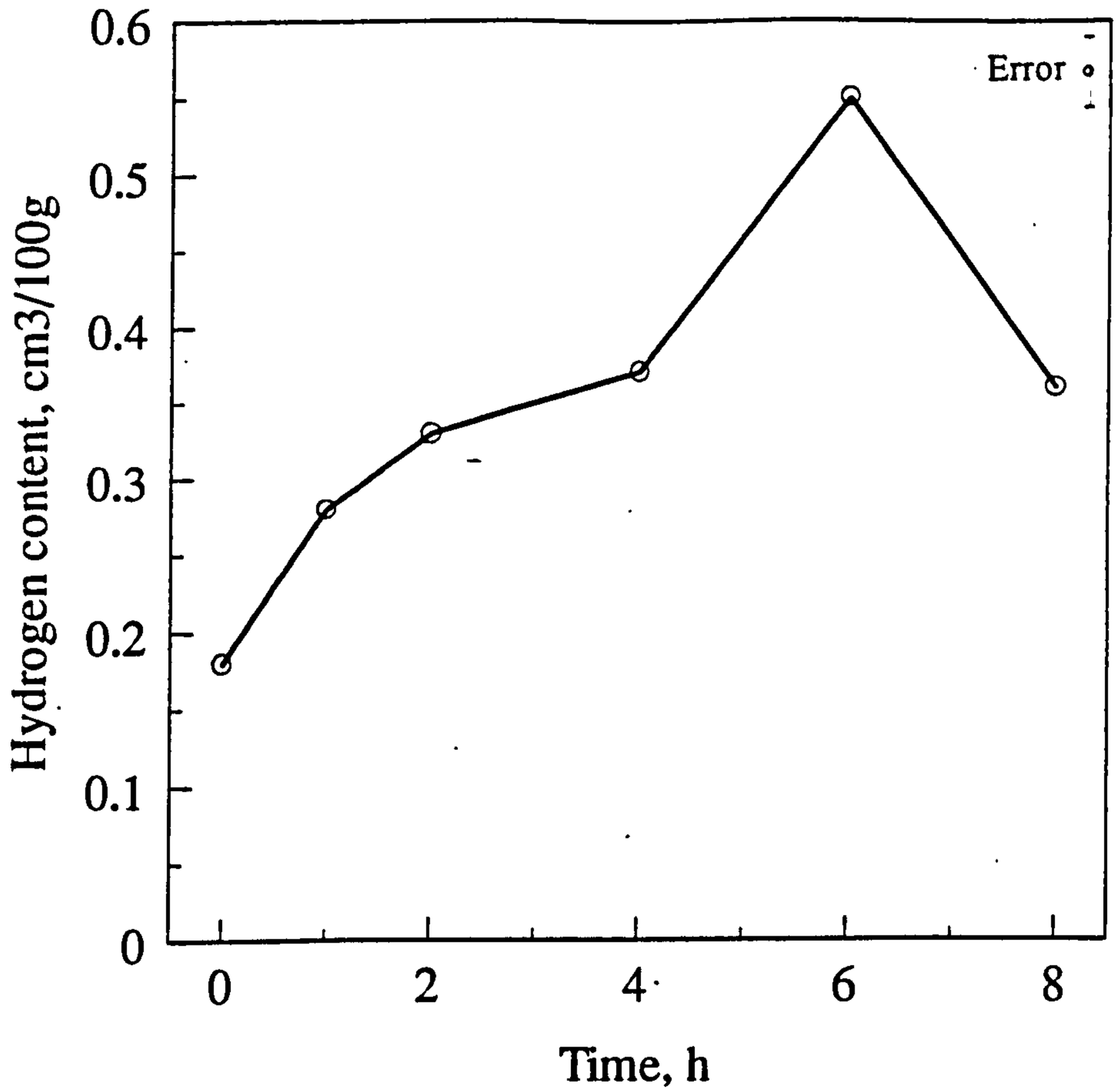

Figure 9.38. Hydrogen content of 10 mm diameter samples machined from the interior of a DC cast Al-0.5%Mg-0.4%Si alloy ingot. Response to isothermal heat-treatment at 500 °C in water-saturated air + HCl (p_{H_2O} = 0.03 atm).

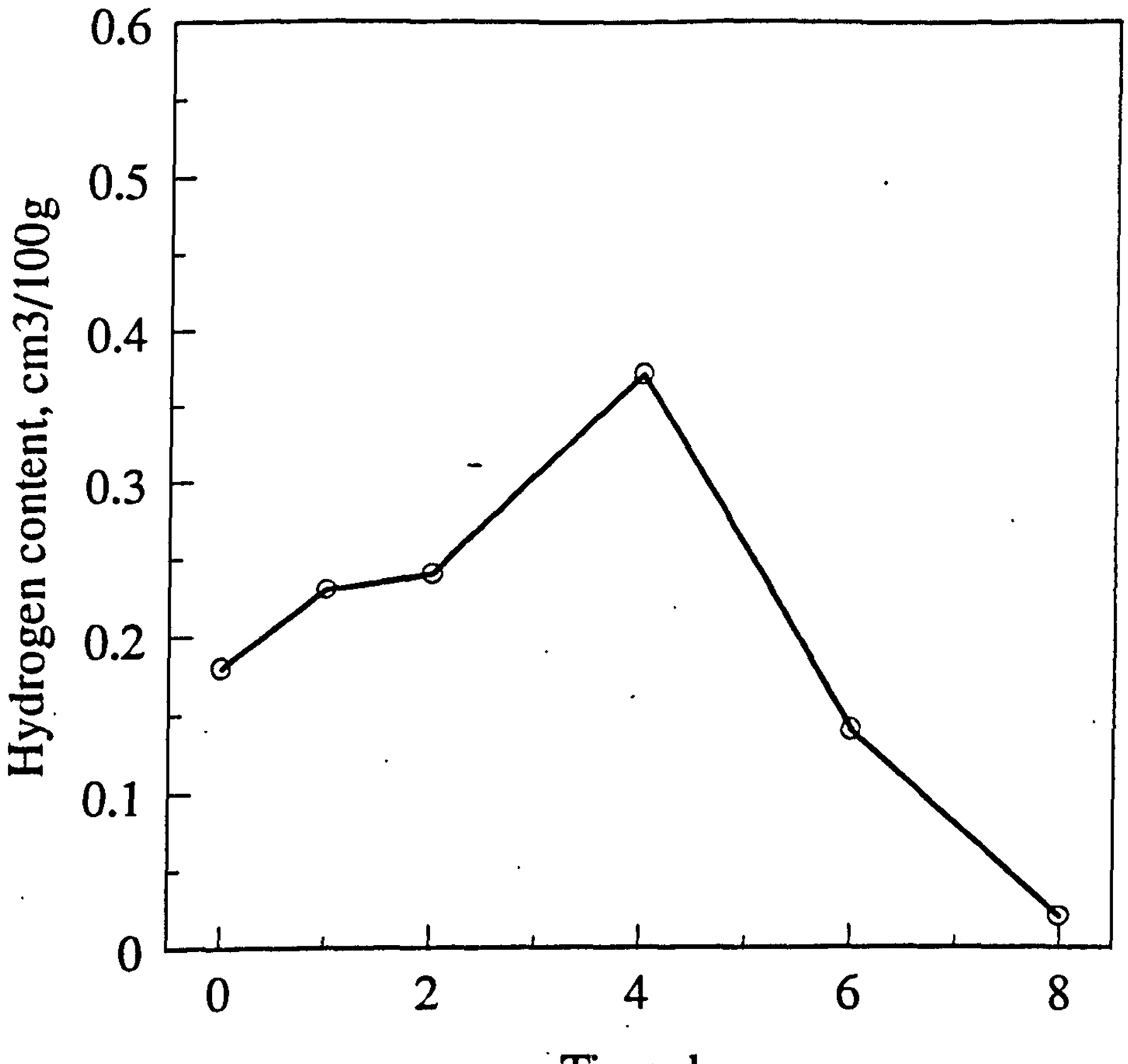

Figure 9.39. Hydrogen content of 10 mm diameter samples machined from the interior of a DC cast Al-0.5%Mg-0.4%Si alloy ingot. Response to isothermal heat-treatment at 590 °C in water-saturated air + HCl (p_{H2O} = 0.03 atm).

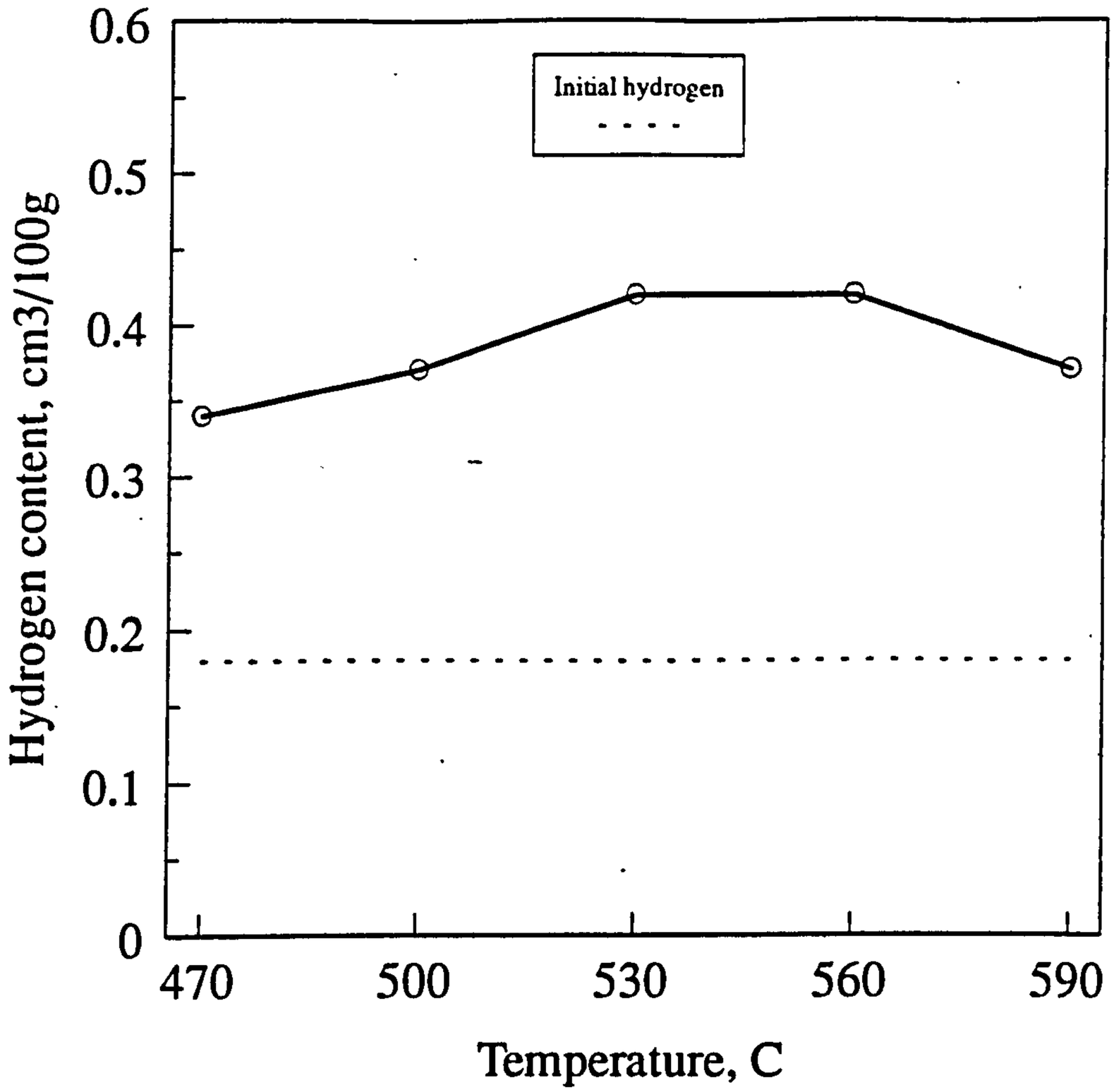

Figure 9.40. Hydrogen content of 10 mm diameter samples machined from the interior of a DC cast Al-0.5%Mg-0.4%Si alloy ingot. Response to isochronal heat-treatment for 4 h in water-saturated air + HCl (p_{H2O} = 0.03 atm).

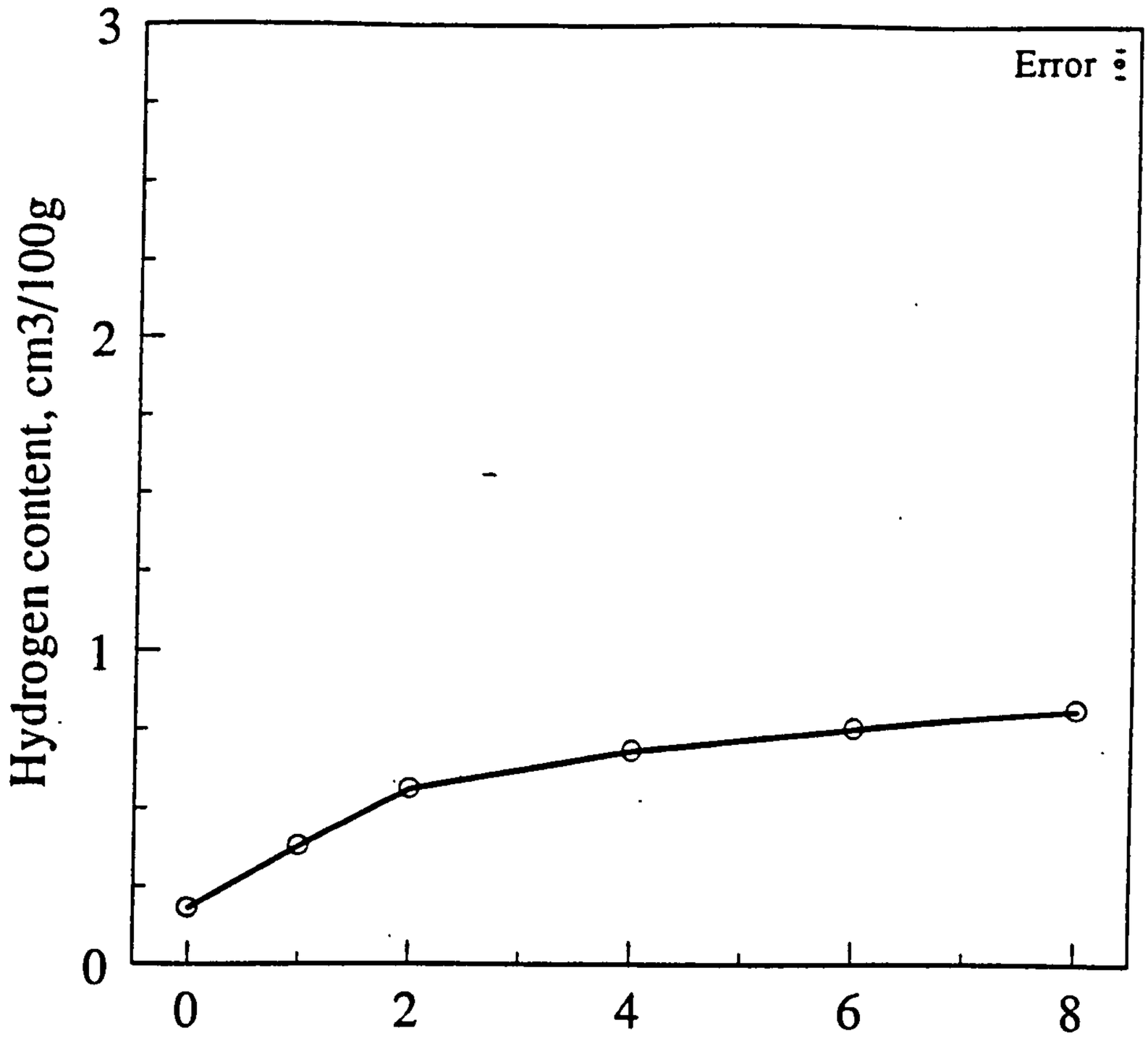

Figure 9.41. Hydrogen content of 10 mm diameter samples machined from the interior of a DC cast Al-0.5%Mg-0.4%Si alloy ingot. Response to isothermal heat-treatment at 500 °C in water-saturated air + 1% SO_2 + HCl. (p_{H2O} = 0.03 atm).

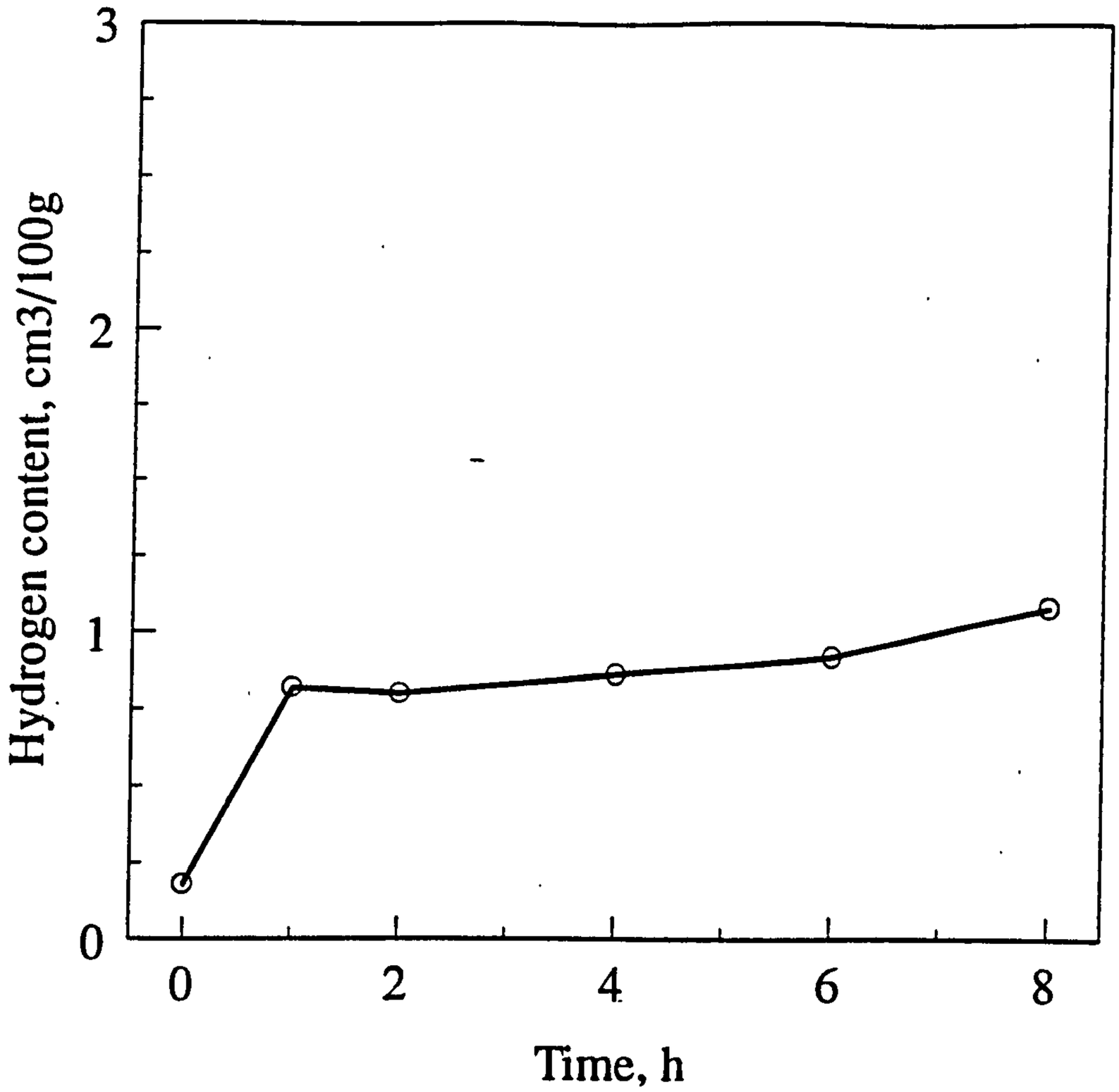

Figure 9.42. Hydrogen content of 10 mm diameter samples machined from the interior of a DC cast Al-0.5%Mg-0.4%Si alloy ingot. Response to isothermal heat-treatment at 590 °C in water-saturated air + 1% SO_2 + HCl (p_{H2O} = 0.03 atm).

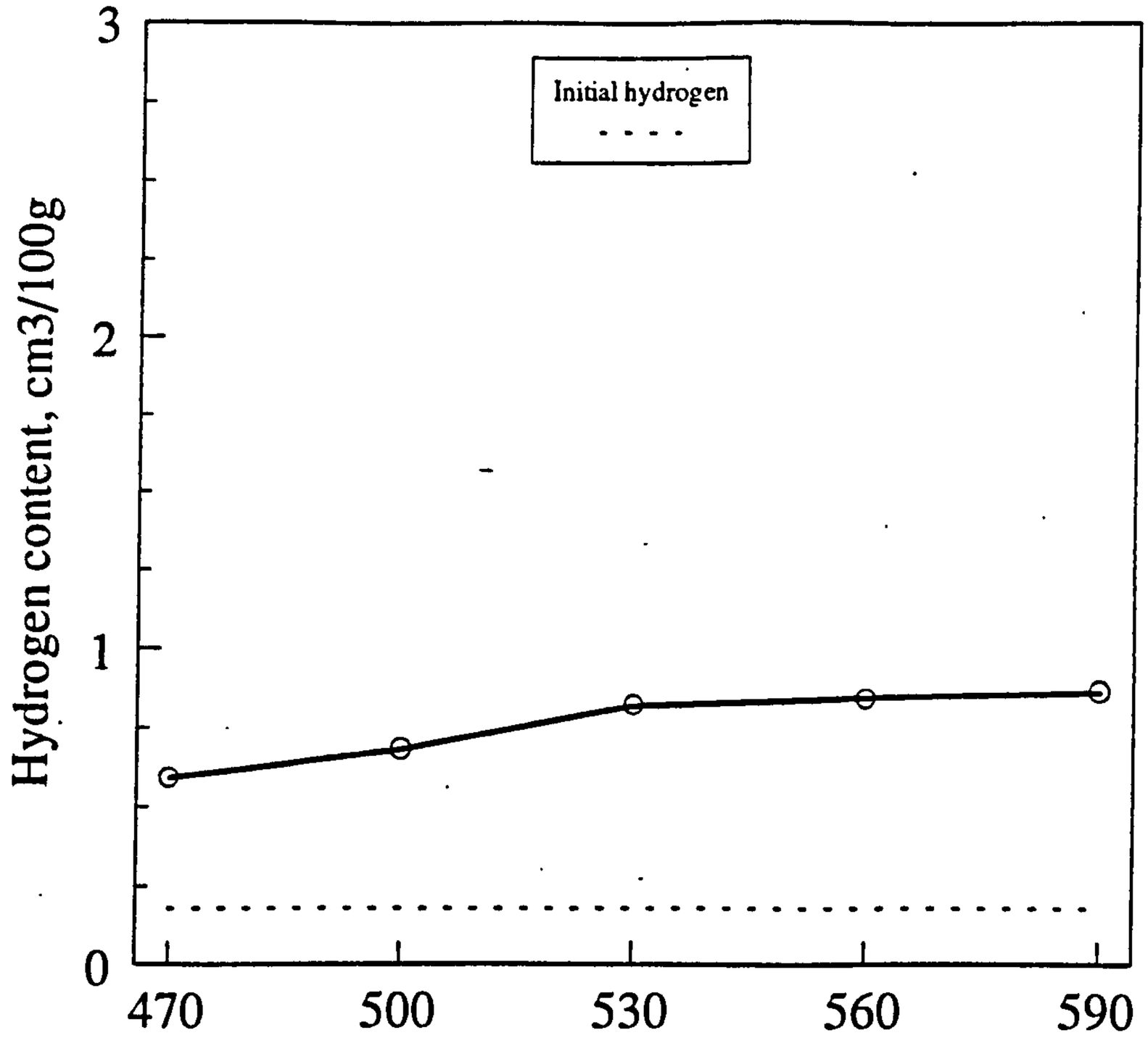

Figure 9.43. Hydrogen content of 10 mm diameter samples machined from the interior of a DC cast Al-0.5%Mg-0.4%Si alloy ingot. Response to isochronal heat-treatment for 4 h in water-saturated air + 1% SO_2 + HCl (p_{H2O} = 0.03 atm).

The results given in Figures 9.38 to 9.43 show different effects of chloride contamination, depending on whether or not the atmosphere contained SO_2 .

9.5.1 Heat-treatments in clean water-saturated air contaminated by chloride

The results given in Figures 9.38 to 9.40 show that when chloride was present in the atmosphere, the samples experienced a cycle of net gain of hydrogen followed by net loss similar to that described in Section 9.3.2.3 for air free from chloride, but the peak hydrogen contents, 0.55 and 0.37 $cm^3/100$ g at 500 and 590 °C respectively were much higher. The implication is that chloride stimulates the absorption process.

9.5.2 Heat-treatments in water-saturated air + 1% SO_2 contaminated by chloride

In view of the stimulated absorption described in Section 9.5.1, the effect of chloride contamination in air containing SO_2 were unexpected. Comparison of Figures 9.41 to 9.43 with Figures 9.31 to 9.33 (Section 9. 4, pages 273-275) shows that the effect of chloride is not to *stimulate* but to *attenuate* the absorption.

9.5.3 Characterisation of oxide

Limited time and funding available permitted only the cursory surface analysis represented by the XPS spectra from the surfaces of two samples heated in clean air, given in Figures 8. However, in Figures 8.50 and 8.52 the spectra from both samples exhibit strong peaks with an energy of 198.5 eV. The energy for the Cl_{2p} peak for $MgCl_2$ is unknown but the value obtained is very close to the values for Cl_{2p} peaks for both KCl and NaCl. and is therefore taken as evidence for incorporation of Cl in the oxide film. It was surprising to find, in Figures 8.51 and 8.53, that only single O_{1s} peaks (531 eV) were obtained with no indication of second peaks corresponding to OH.

With such slender evidence, it is impossible to advance an explanation for the effect of chloride in stimulating hydrogen absorption but one or two general points are

relevant. The strongly electronegative Cl^- ion is expected to interact with the surface ions of an ionic substance such as MgO. Thus, HCl may, perhaps compete with H_2O for adsorption, i.e. by replacing the surface reaction:

$$O^{2-} + H_2O = 2OH^- \quad (9.25)$$

with :

$$O^{2-} + HCl = OH^- + Cl^- \quad (9.26)$$

Cl^- is a larger ion (0.18 nm radius[230.]) than O^{2-} (0.14 nm radius[230.]) and is thus expected to be selectively absorbed at defect sites, where it could stabilise lattice steps or grain boundaries, inhibiting oxide development.

In a metal-rich environment, the most stable form of chlorine is as chloride. The XPS measurements show that the most abundant metal in the film is magnesium and thus it is reasonable to assume that chloride is present as $MgCl_2$. Thermodynamically, $MgCl_2$ formation is strongly favoured from HCl gas and magnesium

$$Mg(s) + 2HCl(g) = MgCl_2 + H_2(g) \quad (9.27)$$

and so it is not unexpected that $MgCl_2$ is present as well as phases normally formed in atmospheres free from HCl gas, i.e. MgO etc.

$MgCl_2$ and MgO are structurally incompatible because their structures are hexagonal and simple cubic respectively. Therefore $MgCl_2$ areas on the oxide constitute defects in the MgO film.

It must be emphasised that to elucidate the true role of chloride in the film structure would be a major undertaking in its own right, outside of the scope of the present investigation.

9.6 Porosity Development During Heat-Treatments

The brief of the present investigation did not include a study of factors governing the growth of porosity in the metal as a result of hydrogen absorption during heat-treaments, because this has already been studied both theoretically and experimentally by Morton.[232.] Nevertheless it was naturally of considerable interest to

observe the effects in the samples from the current heat-treatments. The microgaphs, given in Figures 8.54 to 8.73 were selected from the examination of 100 samples from the heat treatments. The overriding factor determining the porosity development was the final hydrogen content of the samples. The micrographs are given in order of hydrogen content to illustrate the progressive damage done to the metal.

The industrial lesson from this series of micrographs is the great importance of avoiding hydrogen absorption in the solid metal, irrespective of its form and of the atmosphere from which the hydrogen is absorbed. The sequence of events as more and more hydrogen is absorbed is:

i. Expansion of pre-existing microporosity (secondary porosity) at the surface of the metal as in Figure 8.60 for a hydrogen content of 0.54 cm^3/100 g. It is easy to see how this surface porosity can coalesce to give surface blistering.
ii. Extension of the porous zone deeper into the metal as illustrated by the sequence of micrographs in Figures 8.61 to 8.63 for hydrogen contents in the range 0.68 to 0.91 cm^3/100 g.
iii. Finally, deeper penetration and relocation of pores along grain boundaries, completely destroying the metal, illustrated in Figures 8.64 to 8.73 for hydrogen contents over 1cm^3/100 g..

The experiments are comparable because they were all conducted on samples from the same ingot. The damage to the metal arises because the absorbed gas is able to exploit the pre-existing secondary porosity. It would be interesting to explore the effect of gas absorption in metal *completely free from secondary porosity* but this is not presently a feasible industrial objective, because it implies consistently reducing the hydrogen content to below the solid solubility[121], which is of the order of 0.04 cm^3/100 g[127]. Presumably, such metal would be much less vulnerable to damage by hydrogen absorption.

10. IMPLICATIONS AND SUGGESTIONS

10.1 Conclusions

i. The hydrogen contents of large industrial melts of AA 6063 alloy (Al - 0.5%Mg - 0.4%Si) alloy are determined primarily by the prevailing humidity and metal temperature. The actual hydrogen content follows the theoretical hydrogen content with marked hysteresis. Reduction in hydrogen content by degassing in a reverberatory furnace is due more to the effect of turbulence in assisting the approach to equilibrium than to positive removal of hydrogen in the standard physical model of gas purging.

ii. Hydrogen in the liquid metal is retained in and uniformly distributed throughout the length and breadth of 178 mm diameter x 7m long ingots produced by airslip hot-top DC casting.

iii. Hydrogen is lost from the as-cast surface of the ingots when heated to 590 °C in gas-fired industrial furnaces with apparently clean air atmospheres. The hydrogen loss is under diffusion control but is hindered by the growth of microporosity, which traps some of the hydrogen.

iv. In small-scale experimental heat-treatments in clean air, the metal is exposed to competing processes of hydrogen absorption and loss . These processes are controlled respectively by the migration of protons and neutral hydrogen atoms through the oxide film. Whether the net result is to increase or decrease the hydrogen content of the metal is governed by the growth of the oxide film , which depends on the time and temperature of treatment.

v. Sulphur dioxide in the heat-treatment atmosphere massively stimulates the absorption process, seriously damaging the metal by promoting the expansion of microporosity. Surface analysis shows that the effect is due to partial replacement of MgO by $MgSO_4$ and MgS in the surface film on the metal, which facilitates the inward migration of protons.

vi. Chloride ions in the heat-treatment atmosphere stimulates both the hydrogen absorption and the hydrogen loss processes. Time and funds did not permit detailed analysis of these effects.

10.2 Industrial Recommendations

i. To minimise the hydrogen content of cast ingots, keep liquid metal temperatures to the minima consistent with viable operation, throughout liquid metal processing.

ii. Replace all furnace degassing with in-line degassing systems.

iii. In homogenisation heat-treatments, raise the temperature of ingots or other metal products to the final temperature as quickly as possible to minimise the time spent at in the temperature range 500 to 550 °C, where the metal is most vulnerable to hydrogen absorption.

iv. Use gas or oil with low sulphur content for firing heat-treatment furnaces and remove all traces of sulphonated lubricants and coolants from the metal charge before loading it. Monitor heat-treatment furnace atmospheres for traces of sulphur and eliminate if present .

v. Consider whether chloride in marine atmospheres is damaging in practice.

10.3 Suggestions For Further Work

1. An extended programme of hydrogen content measurements throughout liquid metal processing in different seasons to assess the influence of ambient temperatures and humidities.

2. Surveys of hydrogen content across the sections of ingots (i) withdrawn from an industrial furnace at various temperatures in the range 550 to 590 °C (ii) heated to the same withdrawal temperature but at different rates. This information will allow the thermal cycles to be optimised, to benefit from surface loss of hydrogen.

3. Small-scale experimental heat-treatments to investigate the following:

i. The effect of trace quantities of sulphur on hydrogen absorption.

ii. The effect of magnesium content on sulphur-induced hydrogen absorption.

iii. The detailed effects of chloride in the atmosphere on hydrogen absorption.

iv. Greater exploitation of modern surface analysis techniques, e.g. SIMS and XPS surface analysis to characterise surface films on aluminium alloys.

REFERENCES

1. John E. Hatch; Aluminium: Properties and Physical Metallurgy, American Society for Metals, 1984.

2. C. J. Simensen, Sources of Impurities in Aluminium Melts and Their Control, [Conf. Proc.] Aluminium *Melt Refining* and Alloying, July 10-12, 1989 University of Melbourne, Australia

3. J. F. Grandfield, Sources of Inclusions and The Defects They Generate, [Conf. Proc.] Aluminium Melt Refining and Alloying, July 10-12, 1989 University of Melbourne, Australia

4. C. J. Simensen, Inclusion Removal by Floatation, [Conf. Proc.] Aluminium Melt Refining and Alloying, July 10-12, 1989 University of Melbourne, Australia

5. C. E. Eckert, R. E. Miller, D. Apelian, and R. Mutharasan, Light Metals , 1984, TMS- AIME

6. J. F. Grandfield, Inclusion Removal Techniques, [Conf. Proc.] Aluminium Melt Refining and Alloying, July 10-12, 1989 University of Melbourne, Australia

7. R. Guthrie, General Principles of Melt Treatment, [Conf. Proc.] Aluminium Melt Refining and Alloying, July 10-12, 1989 University of Melbourne, Australia

8. J. P. Martin, G. Dube, D. Frayce, and R. Guthrie, Light Metals 1988, TMS-AIME. p. 445.

9. M. Nilmani, P. K. Thay, C. J. Simensen, and D. W. Irwin, Gas Fluxing operation in Aluminium Melt Refining Laboratory and Plant Investigations, Light Metals 1990, pp. 747-754, TMS-AIME.

10. C. Celik and D. Doutre, Light Metals 1989, TMS-AIME, pp. 793-799.

11. Materials Engineering Institute, course 26, Aluminum and its Alloys. Lesson 5: Aluminum Casting Principles, ASM International.

12. A. Szekely, Met. Trans., B, 1976, **7B**, 259

[13.] T. A. Engh and G. K. Sigworth, Light Metals 1982, pp 983-1001, TMS-AIME.

[14.] T. A. Engh, Removal of Impurity Element, Sodium in Aluminium, [Conf. Proc.] Aluminium Melt Refining and Alloying, July 10-12, 1989 University of Melbourne, Australia

[15.] T. A. Engh and T. Pedersen, Light Metals 1984, pp 1329-1344, TMS-AIME.

[16.] J. F. Grandfield, D. W. Irwin, S. Brumale and C. J. Simensen, Light Metals 1990, pp. 737-746, TMS-AIME

[17.] Judith G. Stevens and Ho Yu, Mechanisms of Sodium, Calcium and Hydrogen Removal from an Aluminium Melt in Stirred Tank Reactor-The Alcoa 622 Process, [Conf. Proc.] Aluminium Melt Refining and Alloying, July 10-12, 1989 University of Melbourne, Australia

[18.] J. P. Desmoulins, Light Metals 1989, pp. 757-767, TMS-AIME

[19.] J. P. Desmoulins, H. d'Hondt, J. M. Hicter, and P. Netter, Efficiency and Reliability in Aluminium Filtering, [Conf. Proc.] Aluminium Melt Refining and Alloying, July 10-12, 1989 University of Melbourne, Australia

[20.] P. Netter and C. Conti, Light Metals 1986, pp. 847-860, TMS-AIME.

[21.] J. A. Ford and J.E. Dore, Fine pore Ceramic Foam Filtration, Selee Corporation.

[22.] D. V. Neff, Improving Extrusion Billet Quality Through Molten Metal Degassing and Filtration, [Conf. Proc] Aluminum Extrusion Technology Seminar 1988, pp. 55-60, Aluminum Association.

[23.] R. M. Mutharasan, D. Apelian and C. R. Romanowski, J. Metals, 1981, Dec.

[24.] T. A. Engh, B. Rasch, and E. Bathen, Light Metals 1986, pp. 829-836, TMS-AIME

[25.] Seymour G. Epstein: Aluminium and its Alloys, Technical report C-6, The Aluminium Association, 818 Connecticut Ave., N.W., Washington, D.C. 20006, U.S.A., 1984.

[26.] J. T. Staley; in "Treatise on Materials Science and Technology", Vol. 31, 1989, Academic Press, Inc., p. 6.

[27.] Metals Handbook® , Desk Edition, Edited by H. E. Boyer & T.L.Gall , American Society for Metals, 1986.

[28.] Edgar A. Starke, Jr; in "Treatise on Materials Science and Technology", Vol. 31, 1989, Academic Press, Inc., p. 54.

[29.] Lucio F. Mondolfo, Metallography of Aluminum Alloys, J. Wiley & sons inc., New York , 1943

[30.] N. Raghunathan, T. Sheppard, and Xianhua Yin, Mat. Sci. Tech., 1991, 7, 341.

[31.] A. Annenkoff, in 4th International Aluminium Extrusion Technology Ceminar, 1988, p. 97.

[32.] D. Turnbull and J. C. Fisher, J. Chem. Phys., 1949, **17**, 71.

[33.] J. H. Holloman, and D. Turnbull, Progress Met. Physics, 1953, **4**, 333.

[34.] G. J. Davies, "Solidification and Casting", Applied Science Publishers Ltd., London, 1973, p. 12.

[35.] W. Kurz and D. J. Fisher, "Fundamentals of Solidification", Trans Tech Publications Ltd., Switzerland, 1986.

[36.] D. Turnbull, J. Chem. Phys., 1950, **18**, 198.

[37.] R. Becker, Ann. Phys., 1938, **32**, 128.

[38.] D. Turnbull and R. E. Cech, J. Appl. Phys., 1950, **21**, 804.

[39] D. A. Porter and K. E. Easterling, "Phase Transformtions in Metals and Alloys", 2nd edition, Chapman & Hall, London, 1992.

[40] K. A. Jackson, "Liquid Metals and Solidification", ASM, Cleveland, 1958.

[41] M. C. Flemings, "Solidification Processing", McGraw-Hill Inc., 1974.

[42] K. A. Jackson and B. Chalmers, Can. J. Phys., 1956, **34**, 473.

[43] H. A. Wilson, Phil. Mag., 1900, **50**, 238.

[44] J. Frenkel, Physik. Z. Sowjet Union, 1932, **1**, 498.

[45] M. Volmer and M. Mander, Z. Physik. Chem., 1931, **A154**, 97.

[46] F. C. Frank, Disc. Faraday Soc., 1949, **5**, 48.

[47] W. B. Hillig and D. Turnbull, J. Chem. Phys., 1956, **24**, 219.

[48] R. W. Ruddle, J. Inst. Metals, 1950, **77**, 1.

[49] R. W. Ruddle, A. L. Mincher, J. Inst. Metals, 1950-51, **78**, 229.

[50] H. F. Bishop and W. S. Pellini, Foundry, 1952, **80**, (2), 86.

[51] F. A. Brandt, H. F. Bishop, and W. S. Pellini, Amer. Found. Soc., 1954, **62**, 646.

[52] R. W. Ruddle, "The Solidification of Castings, The Institute of Metals, London, 1957.

[53] F. Weinberg and B. Chalmers, Can. J. Phys., 1951, **29**, 382.

[54] J. W. Rutter and B. Chalmers, Can. J. Phys., 1953, **31**, 15.

[55] W. A. Tiller, J. W. Rutter, K. A. Jackson and B. Chalmers, Acta Met., 1953, **1**, 428.

[56] B. Chalmers, Trans. A.I.M.E., 1954, **200**, 519.

[57] K. Somboonsuk and R. Trivedi, Acta Metal., 1985, **33**, 1051.

[58] R. Trivedi, J. A. Sekhar and V. Seetharaman, Met. Trans., 1989, **20A**, 769.

[59] R. Trivedi and W. Kurz, Acta Metall. Mater., 1994, **42**, 15.

[60] R. Trivedi and W. Kurz, Int. Mat. Rev., 1994, **39**, (2), 49.

[61] G. H. Gulliver, "Metallic Alloys" (Appendix), Charles Griffin & Co. Ltd., London, 1922.

[62] E. Scheil, Z. Metallk., 1942, **34**, 70.

[63] B. Chalmers, "Principles of Solidification", John Wiley & Sons, Inc. 1967.

[64] M. C. Boichenko, "Continuous Casting of Steel", Butterworth's, London, 1961.

[65] T. P. Battle, Int. Mat. Rev., 1992, **37**, (6), 249.

[66] D. Altenpohl, "Aluminium Viewed from Within", Aluminium-Verlag, Dusseldorf, 1982.

[67] W. C. Winegard and B. Chalmers, Trans. A.S.M., 1954, **46**, 1214.

[68] K. A. Jackson and J. D. Hunt, Trans. Met. Soc. A.I.M.E., 1966, **236**, 1129.

[69] A. Papapetrou, Z. Kristallogr., 1935, **A92**, 89.

[70] M. O. Klia, Kristallografiia, 1956, **1**. 577.

[71] D. R. Ullmann, T. P. Seward III, and B. Chalmers, Trans. Met. Soc. A.I.M.E., 1966, **236**, 527.

[72] M. C. Flemings, in "Solidification of Metals", ISI Publication, London, 1967, 277.

[73] D. A. Granger, in "Aluminum Alloys Contemporary Research and Applications", Edited by: A. K. Vasudevan and R. D. Doherty, Academic Press Inc., 1989, 109.

74. R. E. Spear and G. R. Gardner, Trans. Amer. Foundrymen's Soc., 1963, **71**, 209.

75. J. E. Hatch (Ed), "Aluminum, Properties and Physical Metallurgy", Amer. Soc. Met., 1984, 25.

76. M. C. Flemings, in "Solidification Technology in the Foundry and Cast House", The Metals Society, 1983

77. T. F. Bower, H. D. Brody, and M. C. Flemings, Trans. Met. Soc. A.I.M.E., 1966, **236**, 624.

78. L. Aitchison and V. Kondic, "The Casting of Non-Ferrous Ingots", Macdonald & Evans Ltd., London, 1953.

79. M. C. Flemings and R. Mehrabian, in "Solidification", Amer. Soc. Met., 1971, 311.

80. J. W. Martin and R. D. Doherty, "Stability of Microstructure in Metalic Systems", Cambridge University Press, 1976.

81. J. S. Kirkaldy and W. V. Youdelis, Trans. Met. Soc. A.I.M.E., 1958, **212**, 833.

82. N. B. Vaughan, J. Inst. Metals, 1937, **61**, 35.

83. D. E. Adams, J. Inst. Metals, 1948-1949, **75**, 805.

84. W. C. Winegard, Trans. Amer. Foundrymen's Soc., 1953, **61**, 352.

85. W. V. Youdelis and D. R. Colton, Trans. Met. Soc. A.I.M.E., 1960, **218**, 628.

86. H. Yu and D. A. Granger, in "Fundamentals of Alloy Solidification Applied to Industrial Processes", [Proc. Conf.], NASA Conference Publication 2337, 1984, 157.

87. A. Kroupa and J. S. Kirkaldy, in "Modeling of Casting, Welding and Advanced Solidification Processes", TMS, 1993, 269.

[88] W. V. Youdlis, in "The Solidification of Metals", The Iron and Steel Institute, London, 1967, 112.

[89] E. Scheil, Metallforschung, 1947, **2**, 69.

[90] E. F. Emley, Int. Met. Rev., 1976, **21**, 75.

[91] H. D. Merchant, T. Z. Kattamis and G. Scharf, in "Homogenization and Annealing of Aluminum and Copper Alloys", Edited by: H. D. Merchant, J. Crane and E. H. Chia, The Metallurgical Society, Inc., 1988, p.1.

[92] T. S. Sheppard and N. Raghunathan, Mat. Sci. and Tech., 1989, **5**, 268.

[93] F. King, "Aluminium and Its Alloys", John Wiley, 1987, p.188.

[94] Y. G. Grishkovets, L. V. Budanova and D. A. Morgacheva, Met. Sci. Heat Tr., 1983, **25**, (7/8), 604.

[95] R. A. Hine and R. D. Gruminsky, J. Inst. Met., 1960/61, **89**, 417.

[96] K. J. Holub and L. J. Matienzo, Appl. Surf. Sci., 1981, **9**, 22.

[97] L. J. Matienzo, Aluminium, 1983, **59**, (11), E453.

[98] R. Eborall and C. E. Ransley, J. Inst. Metals, 1945, **71**, 525.

[99] A. J. Swain, J. Inst. Metals, 1951-52, **80**, 125.

[100] C. E. Ransley, J. Inst. Metals, 1953-54, **82**, 588(discussion).

[101] J. D. Fast, "Interaction of Metals and Gases", Vol. 2, Kinetics and Mechanism, Philip Technical Library, Eindhoven (1971), chap. 1.

[102] W. Shockley, J. Appl. Phys., 1939, **10**, 543.

[103] J. K. Norskov, Phys. Rev. B, 1982, **26**, 2875.

[104] M. S. Daw and M. I. Baskes, Phys. Rev. B, 1984, **29**, 6443.

[105] M. J. Stott and E. Zaremba, Phys. Rev. B, 1980, **22**, 1564.

[106] J. K. Norskov, Phys. Rev. Lett., 1982, **48**, 1620.

[107] M. J. Puska, R. M. Nieminen and M. Manninen, Phys. Rev. B, 1981, **24**, 3037.

[108] F. C. Tompkins, "Chemisorption of Gases on Metals", Academic Press, Inc., London (1978).

[109] J. J. Moore, "Chemical Metallurgy", Butterworth & Co. Ltd., 1981, p. 79.

[110] C. J. Smithells, "The Metals Reference Book", 7th Edition, E. A. Brandes and G. B. Brook (Ed.), Butterworth-Heinemann Ltd., Oxford, 1992.

[111] D. E. J. Talbot, "Hydrogen in Aluminium and Its Alloys", PhD. Thesis, Department of Materials Technology, Brunel, The University of West London, 1989.

[112] "Manual of Symbols and Terminology for Physicochemical Quantities and Units", Pure Appl. Chem., 1970, **21**, 1.

[113] M. L. McGlashan, "Physicochemical Quantities and Units", Royal Institute of Chemistry Monographs for Teachers No. 15, London: 1971.

[114] M. R. Tahbaz, "Absorption of Hydrogen by a Solid Aluminium-Magnesium Alloy From Humid Atmospheres", M. Phil. Thesis, Brunel University, London, 1977.

[115] D. E. J. Talbot, Int. Met. Rev., 1975, **20**, 166.

[116] R. A. Swalin, "Thermodynamics of Solids", John Wiley & Sons, Inc., New York, 1962.

[117] L. M. Foster, A. S. Gillespie, T. H. Jack, and W. W. Hill, Nucleonics, 1963, **21**, 53.

[118] H. A. Wriedt and L. S. Darken, Trans. Met. Soc. A.I.M.E., 1965, **233**, 111 and 121.

[119] M. Mokaram, "The Solution and Diffusion of Hydrogen in Solid Copper and Copper Alloys", Ph. D. Thesis, Brunel University, London, 1974.

[120] J. Langerweger, in "Light Metals 1981", The Metallurgical Society A.I.M.E, 1981, 685.

[121] D. E. J. Talbot and D. A. Granger, J. Inst. Metals, 1963-64, **92**, 290.

[122] J. E. Harris and P. G. Partridge, J. Inst. Metals, 1964-65, **93**, 15.

[123] A. Sieverts, Z. Physical Chem., 1911, **77**, 591.

[124] C. E. Ransley and H. Neufeld, J. Inst. Metals, 1948, **74**, 599.

[125] W. R. Opie and N. J. Grant, Trans. A.I.M.E., 1950, **188**, 1237.

[126] W. Eichenauer, W. Loser and H. Witte, Z. Mettalk., 1965, **56**, 287.

[127] W. Eichenauer and A. Pebler, Z. Metallk., 1957, **48**, 373.

[128] F. G. Jones and R. D. Pehlke, Met. Tran., 1971, **2**, 2655.

[129] C. L. Thomas, Trans. Met. Soc. A.I.M.E., 1967, **239**, 485.

[130] P. N. Anyalebechi, "The Solubility of Hydrogen in Pure Aluminium and Binary Aluminium-Lithium Alloys", Ph. D. Thesis, Brunel University, London, 1985.

[131] P. Rotgen and H. Braun, Metall., 1932, **11**, 459 and 471.

[132] L. Bircumshaw, Trans. Faraday Soc., 1935, **31**, 1439.

[133] W. Baukloh and F. Oesterlen, Z. Metallk., 1938, **11**, 386.

[134] W. Baukloh and M. Redjali, Metall., 1942, **21**, 683.

[135] C. E. Ransley and D. E. J. Talbot, Z. Metallk., 1955, **46**, 328.

[136] W. Eichenauer, K. Hattenbach and A. Pebler, Z. Metallk., 1961, **52**, (10), 682.

[137] D. J. Stephenson, "The Absorption of Hydrogen From Humid Atmosphere by Molten Aluminium and Aluminium-Magnesium Alloy", Ph. D. Thesis, Brunel University, London, 1978.

[138] M. A. Sargent, "The Solubility of Hydrogen in Some Commercial Aluminium -Lithium Alloys", Ph. D. Thesis, Brunel, The University of West London, 1989.

[139] C. G. McCracken, "The Intrinsic and Extrinsic Solubility of Hydrogen in Aluminium -Lithium Based Alloys", Ph. D. Thesis, Brunel, The University of West London, 1994.

[140] A. Fick, Progg. Ann., 1855, **94**, 59.

[141] J. B. Fourier, "Theorie analytique de la chaeur", Paris, 1822.

[142] L. S. Darken, R. W. Gurry and M. B. Bever, "Physical Chemistry of Metals", McGraw-Hill Book Co, Inc., (1953).

[143] J. Crank, "The Mathematics of Diffusion", Oxford Science Publication, 1992, p. 47.

[144] K. Papp and E. Kovacs-Csetenyi, Scripta Met., 1981, **15**, 161.

[145] S. Matsuo and T. Hirata, Nippon Kinzoku Gakkaishi, 1967, **31**, 590.

[146] E. Hashimoto and T. Kino, J. Phys. F: Met. Phys., 1983, **13**, 1157.

[147] L. A. Andreew et al., Izv. Vuz. Cvetn. Met., 1975, **5**, 123.

[148] K. Papp and E. Kovacs-Csetenyi, Scripta Met., 1977, **11**, 921.

[149] P. N. Anyalebechi, in "Light Metals 1991", E. L. Rooy (Ed.), The Mineral, Metals & Materials Society A.I.M.E., 1990, 1025.

[150] Y. Dardel, Metals Technology, 1948, **15** TP No. 2484.

[151] Y. Dardel, Metal Industry, 1950, **76**, 203.

[152] P. D. Hess, J. Metals, 1973, **10**, 46.

[153] P. D. Hess, in "Light Metas 1972", The Metallurgical Society, A.I.M.E., 367.

[154] C. E. Ransley, D. E. J. Talbot and H. C. Barlow, J. Inst. Metals, 1957-58, **86**, 212.

[155] British Patent No. 684865.

[156] F. Degreve, J. Metals, 1975, March, 21.

[157] F. Degreve and C. Jardin, Met Trans. B, 1975, **6B**, 545.

[158] U. Manweiler, Aluminium, 1978, **54**, (12), 765.

[159] Chr. J. Simensen and J. L. Lauritzen, Aluminium, 1980, **56**, (2), 156.

[160] P. N. Anyalebechi, M. Phil. Thesis, Brunel University, London, 1982.

[161] C. E. Ransley and D. E. J. Talbot, J. Inst. Metals, 1955-56, **84**, 445.

[162] M. F. Jordan, G. Denyer, and A Turner, J. Inst. Metals, 1962-63, **91**, 48.

[163] B. R. Deoras and V. Kondic, Foundry Trade J. 1956, **100**, 361.

[164] G. J. Metcalfe, J. Inst. Metals., 1945, **71**, 618 (discussion).

[165] P. M. Thomas and J. E. Gruzleski, Met. Trans. B, 1978, **9B**, 139.

[166] Q. T. Fang, P. N. Anyalebechi, R. J. O'Malley and D. A. Granger, in Conference Proceeding 1987, Institute of Metals, 33.

[167] R. W. Ruddle and A. Cibula, J. Inst. Metals, 1956-57, **85**, 265.

[168] K. J. Brondyke and P. D. Hess, Trans. A.I.M.E., 1964, **230**, 1542.

[166] M. C. Celik and G. H. Bennet, Met. Tech., 1977, **4**, 138.

[167] F. Seitz, Acta Met., 1953, **1**, 355.

[168] R. S. Barnes and D. J. Mazey, Acta Met., 1958, **6**, 1.

[172] P.E. Doherty and B. Chalmers, Trans. Met. Soc. A.I.M.E., 1962, **224**, 1124.

[173] P. D. Hess and G. K. Turnbull, in "Hydrogen in Metals", I. M. Bernstein and A. W. Thompson (Ed.), American Society for Metals, 1974, p.277.

[174] K. B. Das, E. C. Roberts and R. G. Bassett, in "Hydrogen in Metals", I. M. Bernstein and A. W. Thompson (Ed.), American Society for Metals, 1974, p. 289.

[175] H. Chadwick, J. Inst. Metals, 1954-55, **83**, 513 (discussion).

[176] H. Kostron, Z. Metllk., 1952, **43**, 269 & 373.

[177] I. Weisshaus and A. Kaufman, in "Effect of Hydrogen on Behavior of Materials", A. W. Thompson and I. M. Bernstein (Ed.), TMS-AIME, 1976, p. 623.

[178] L. J. Barker, Iron Age, 1946, **157**, (No. 19), 60.

[179] E. H. Dix Jr., "Physical Metallurgy of Aluminium Alloys", American Society for Metals, 1949, p. 200.

[180] I. J. Polmear, J. Australian Inst. Metals, 1956, **1**, (2), 169.

[181] I. J. Polmear, J. Australian Inst. Metals, 1957, **2**, (2), 71.

[182] I. J. Polmear, J. Australian Inst. Metals, 1958, **3**, (1), 267.

[183] T. Mills, J. Australian Inst. Metals, 1957, **2**, (2), 72.

[184] A. E. Jenkins, J. Australian Inst. Metals, 1957, **2**, (1), 79.

[185] O. Kubaschewski, A. Cibula and D. C. Moore, "Gases and metals", 1970, London. Iliffe.

[186] J. H. O'Dette, Trans. AIME, 1957, **208**, 924.

[187] A. N. Turner and A. J. Bryant, J. Inst. Metals, 1967, **95**, 353.

[188] G. M. Scamans, R. Alani and P. R. Swann, Corros. Sci., 1976, **16**, 443.

[189] G. M. Scamans, J. Mat. Sci., 1978, **13**, 27.

[190] G. M. Scamans, Aluminium, 1982, **59**, 332.

[191] M. S. Hunter and P. Fowle, J. Electrochem. Soc., 1956, **103**, 482.

[192] J. M. Walls, in "Methods of Surface Analysis", J. M. Walls (Ed.), Cambridge University Press 1989,.

[193] J. M. Walls and A. B. Christie, in "Surface Analysis and Pretreatment of Plastics and Metals", D. M. Brewis (Ed.), Applied Science Publishers, London and New Jersy. 1982, p. 13.

[194] D. E. J. Talbot and P. N. Anyalebechi, Mat. Sci. Tech., 1987, **4**, 1.

[195] D. A. Granger, Light Metal Age, 1984, Dec., 17.

[196] D. A. Anderson,D. A. Granger and J. G. Stevens, Light Metal Age, 1989, Dec., 5.

[197] P. D. Hess, J. Met., October 1973.

[198] D. E. J. Talbot, Private communication.

[199] H. H. Willard, L. L. Merritt, Jr., J. A. Dean, and F. A. Settle, Jr., "Instrumental Methods of Analysis", Wadsworth Pub. Co., 1988, p. 340.

[200] D. R. Penn, Phys. Rev. B., 1976, **13**, 5248.

[203] M. P. Seah and W. A. Dench, Surf. Interface Anal., 1979, **1**, 2.

[204] D. E. Sykes, in "Methods of Surface Analysis", J. M. Walls (Ed.), Cambridge University Press 1989, p. 216.

[205] J. A. McHugh, in "Methods of Surface Analysis", A. W. Czanderna (Ed.), Elsevier Scientific Publishing Co. 1975, p. 223.

[206] P. T. Stroup, US Patent Nos 2092033 and 2092034.

[205] R. C. Weast (ed.), "CRC Handbook of Chemistry and Physics", Boca Raton, FL, USA: 1982 (CRC Press).

[206] D. E. J. Talbot, Unpublished work, private communication.

[207] W. Geller, Z. Metallkunde, 1950, **41**, 124.

[208] L. C. Blayden and K. J. Brondyke, J. Met., Feb. 1974, p. 25. See also Light Metals, 2, 1973, AIME, and US Patent Nos 3737303-3737305

[209] M. V. Brant, D. C. Bone and E. F. Emley, J. Met., 1971, p. 48.

[210] M. P. Silva and D. E. J. Talbot, Light Metals, 1989, p. 1035

[211] H. S. Carslaw and J. C. Jaeger, "Conduction of Heat in Solids, Oxford: 1948.

[212] O. Kubaschewski and C. B. Alcock, "Metallurgical Thermochemistry", 5th Ed. London: 1979 (Pergamon Press)

[213] D. Briggs and M. P. Seah (Ed.), "Practical Surface Analysis", New York: 1990 (John Wiley)

[214] C. D. Wagner, W. M. Riggs, L. E. Davis, J. F. Moulder and G. E. Muilenberg, "Handbook of X-Ray Photoelectron Spectroscopy", Minnesota: 1978 (Perkin-Elmer)

[215] R. L Tapping, I. Aitcheson and D. G. W. Goad, Can. J. Spectroscopy, 1983, **28**, 87.

[216] A. I. Lenov, Yu P. Kostikov, E. M. Trusova, I. K. Ivanov and N. S. Andreeva, Izv. Akad. Nauk USSR, Neorganisheskie Materialy, 1978, **14**, 498.

[217] J. C. Fuggle, L. M. Watson, D.J. Fabian and S. Affrossmann, J. Phys. F: Metal Phys. 1975, **5**, 375.

[218] S. Hagstrom and S. E. Karlsson, Arkiv. Fys., 1964, **26**, 451.

[219] L. DeBrouckiere, J. Inst. Metals, 1945, **71**, 131.

[220] D. J. Field, G. M. Scamens and E. P. Butler, Proc. 2nd Int. Conf. on Al Li Alloys, California, 1983, page 393.

[221] K. Wefers, Aluminium, 1981, **57**, 722.

[222] I. M. Ritchie, J. V. Sanders and P.L. Weiekhard, Oxid. Metals, 1971, **3**, 91.

[223] A. J. Brock and M. A. Hine, J. Electrochem. Soc., 1972, **119**, 1123.

[224] W. W. Smeltzer, J. Electrochem. Soc., 1958, **105**, 67.

[225] C. Lea and C. Molinari, J. Mat. Sci., 1984, **19**, 2336.

[226] M. P. Silva, "Oxidation of Aluminium-Magnesium Alloys in the Solid, Semi Liquid and Liquid States", Ph. D. Thesis, Brunel University, 1987.

[227] G. E. Muilenberg, Ed. "Handbook of X-Ray Photoelectron Spectroscopy" Eden Prairie, Minnesota:1978 (Perkin -Elmer)

[228] Y. Oishi and W. D. Kingery, J. Chem. Phys., 1960, **33**, 480 & 905.

[229] R. Lindner and G. D. Parfitt, J. Chem. Phys., 1957, **26**, 182

[230] L. Pauling, "The Nature of the Chemical Bond" , London:1960 (Oxford University Press).

[231] F. A. Cotton and G. Wilkinson, "Advanced Inorganic Chemistry", 4th edition, New York, 1980 (John Wiley)

[232] J. M. Morton, " Hydrogen Absorption and Loss During Heat-treatment of Aluminium Alloys containing Magnesium and Lithium" Ph. D. Thesis, Brunel University, 1990